



The University of
Nottingham

**SCHOOL OF ELECTRICAL AND
ELECTRONIC ENGINEERING**

**USE OF 3D ULTRASOUND DATA SETS TO
MAP THE LOCALISED PROPERTIES OF
FIBRE-REINFORCED COMPOSITES**

ROBERT A SMITH, MA MSc

**Thesis submitted to the University of Nottingham
for the degree of Doctor of Philosophy.**

JULY 2010

This thesis contains information protected by United Kingdom Patent Application No. 0818383.2 and No. 0818088.7 and, until July 2012, is restricted in circulation to employees of the Faculty of Engineering, University of Nottingham and any external examiners of this PhD. Applications for further dissemination should be made in the first instance to the author at QinetiQ Ltd.

ABSTRACT

This thesis documents a programme of work undertaken from mid-2005 to mid-2009 as a part-time PhD, investigating the application of signal-processing methods to ultrasonic non-destructive evaluation (NDE) data from fibre-reinforced composite materials. The aims of the project were:

- to push the boundaries of defect detectability by applying knowledge-based filtering methods to remove the response of the structure;
- to produce 3D profile maps of various measured parameters to assist in differentiating between defects and structural effects;
- to present the NDE information in terms of actual material properties that can be easily interpreted.

These aims are linked to specific NDE problems in inhomogeneous materials:

- 3D characterisation of the material properties and defects in composite materials such as carbon-fibre reinforced plastic (CFRP);
- 3D mapping of ply wrinkling and fibre orientation in CFRP and glass-fibre reinforced plastic (GFRP).

By developing and using a model, it was possible to understand the ultrasonic response of multi-layered structures when the layers themselves comprise both fibres and matrix. Various defects were inserted into the model to determine which parameters from the ultrasonic response would provide good distinction between defect types and enable quantitative 3D profiling of the required material properties.

A toolset of signal-processing and image-processing algorithms was used to apply the methods to both simulated and real ultrasonic data from the above NDE problems in order to demonstrate the benefits of the new methods. At various stages through the project a validation process was undertaken to evaluate the methods for use on real composite aerostructures.

This thesis contains information protected by United Kingdom Patent Application No. 0818383.2 and No. 0818088.7.

ACKNOWLEDGEMENTS

Firstly, I would like to acknowledge the excellent guidance and encouragement of my supervisor: Professor Richard Challis, throughout the period of this part-time PhD. Secondly, I am very grateful to the other members of the Applied Ultrasonics Laboratory at the University of Nottingham, including Dr Valerie Pinfield and Mr Martin Mienczakowski for their collaboration and numerous useful and interesting discussions, and to my examiners: Dr Marion Unwin from the University of Nottingham and Prof Peter Cawley FRS from Imperial College.

I acknowledge the support of my employer: QinetiQ Ltd, and of my colleagues at QinetiQ, in particular: Dr Luke Nelson, Dr Albert Phang, Mr Lyn Jones, Mr Jamie Bending and Mr Rob Pitts. And I am grateful to Mr Andrew Bond-Thorley of Airbus, who has provided specimens and a considerable amount of support for much of the work on inspection of carbon-fibre composites.

Finally I am totally indebted to my dear wife Anne, who has encouraged and supported me throughout this project, and to my children Mark and Katie, now adults, for their forbearance and understanding.

TABLE OF CONTENTS

Abstract	i
Acknowledgements	ii
Table of contents	iii
Nomenclature	vi
Glossary of terms	viii
1. Introduction	1
1.1. Background	1
1.2. Objectives	4
1.3. Overview of the project	7
1.4. Structure of the thesis	9
2. Review of NDE Methods and Current Position	10
2.1. Early NDE methods for composite materials	10
2.2. A review of composite inspection from the 1990s	16
2.3. Porosity characterisation in composite materials	27
2.4. Fibre volume fraction	42
2.5. Ply stacking sequence	46
2.6. In-plane fibre waviness	48
2.7. Out-of-plane ply wrinkling	50
2.8. Discussion	55
3. Review of Modelling of Ultrasound Propagation	56
3.1. Motivation	56
3.2. Particulate structures	57
3.3. Layered structures	62
3.4. Equivalent media	65
3.5. Discussion	76
4. Modelling of Ultrasound Propagation In Layered Structures	78
4.1. Introduction	78
4.2. Frequency-dependence of ultrasonic interactions	81
4.3. Analytical layer modelling	88

4.4. Multi-layer analytical modelling	93
4.5. Convolution with realistic pulses	105
4.6. Modelling a porous layer	113
4.7. Modelling a thick resin layer	133
4.8. Distinguishing between porosity and a thick resin layer	137
4.9. Benefits of the model	138
5. Isolation of localised properties in layered structures	139
5.1. Motivation	139
5.2. Presentation of 3D localised properties	141
5.3. Fibre-resin effects	146
5.4. Porosity – Amplitude method	165
5.5. Porosity – Model-based decomposition method	173
5.6. Summary of property isolation in layered structures	200
6. Fibre Orientation Measurement and Mapping	201
6.1. Introduction	201
6.2. 2D FFT method	206
6.3. Angular power distribution	210
6.4. 2D map of orientation	225
6.5. 1D profile of stacking sequence	229
6.6. Spatial-frequency energy distribution and spatial filtering	236
6.7. Discussion	241
7. Validation and Application	243
7.1. Ply spacing and fibre volume fraction mapping	243
7.2. Porosity and thick resin layer mapping – The Porosity Meter	250
7.3. Fibre orientation mapping	258
7.4. Ply stacking sequence	259
7.5. In-plane wrinkling	266
7.6. Out-of-plane wrinkling	270
7.7. Applications summary	278
8. Discussion and Conclusions	279
8.1. Initial position and motivation	279
8.2. Approach	280
8.3. The wave propagation model	281
8.4. 3D characterisation of composites	283

8.5. 3D fibre orientation in composites	286
8.6. Benefits	288
8.7. Recommendations for future work	289
8.8. Final conclusions	290
References	291
Appendices	
A. Ultrasonic interaction with thin layers	327
B. Reflection and transmission at a rough surface	332
C. Use of the analytical model for FVF measurement	334
D. Bezier curves and Hilbert Transforms	345
E. Focused ultrasonic fields	348
F. Equivalent media modelling	353
G. Simulating fibre orientation images	384
H. Accuracy of fibre orientation measurements	390

NOMENCLATURE

Symbols for complex variables and matrices are in bold face type. Vector quantities are denoted by an over-bar. Descriptions of symbols which have more than one meaning are separated by a semi-colon.

Roman Symbols:

a	Radius of pores
A	Pressure amplitude at $x = 0$
c	Sound velocity
C_{ij}	Stiffness matrix
D	Element diameter of a circular transducer
E	Young's modulus
G	Shear modulus
I	Intensity
k	Wavenumber: $2\pi/\lambda$
K	Bulk modulus
K_f	Focal gain: z_f/N
M	Compression modulus
N	Near-field distance (distance to last axial maximum): $D^2/4\lambda$
p	Acoustic pressure
r	Complex pressure reflection coefficient
R	Intensity reflection coefficient
t	Complex pressure transmission coefficient
T	Intensity transmission coefficient
u	Particle velocity
w_f	Focal beamwidth
w_t	Fibre-tow width
z_f	Focal distance
z_{ps}	Ply spacing
Z	Acoustic impedance

Greek symbols:

α	Attenuation coefficient. Also used as a local coefficient, usually together with β
α_n	The reciprocal of the product of the n th resonant frequency and the ply spacing
β	Scattering function which governs the long-wavelength behaviour of the reduced scattering cross-section. Also used as a local coefficient, usually together with α
η	Ratio of shear-wave to compression-wave velocities
θ	Usually an angle
λ	Wavelength of ultrasound
ν	Poisson's ratio
ρ	Density of a material
ϕ	Volume fraction: proportion of one material in the whole, by volume
ψ	Value of ka below which the long-wavelength limit applies
Γ	Reduced scattering cross-section

GLOSSARY OF TERMS

CFRP	Carbon-Fibre Reinforced Epoxy
CNR	Contrast-to-noise ratio. The ratio of a) the difference between a signal and the background, and b) the surrounding noise level.
FMC	Full Matrix Capture
FVF	Fibre volume fraction. The proportion of a composite that is fibres, by volume.
GFRP	Glass-Fibre Reinforced Epoxy
GLARE	GLass-fibre Aluminium hybrid Reinforced Epoxy laminate
NDE	Non-destructive evaluation.
NDT	Non-destructive testing.
POD	Probability of detection of a defect.
RIFT	Resin infusion through flexible tooling.
RFI	Resin film infusion.
RTM	Resin transfer moulding.
SNR	Signal-to-noise ratio
TFM	Total Focusing Method

CHAPTER 1 INTRODUCTION

1.1 Background

1.1.1 *Non-destructive Evaluation (NDE) in aerospace*

Non-destructive evaluation (NDE) methods are in widespread use for both detection and characterisation of defects in metals and composites in most fields of engineering and manufacturing, both in production and in service. In the vast majority of cases the application of conventional NDE methods is straightforward, well qualified and adequate for the task. But it is the few cases where conventional methods are less effective that consume the majority of the resources spent on NDE and become a source of constant frustration for the end-users. This is the same across the user spectrum from car manufacturers to military fighter squadrons, and applies to both detection and characterisation of defects.

The civil aerospace industry is currently undergoing a massive culture change as it scales up the proportion of composite structural components on new aircraft almost ten-fold within just a few years. Manufacturers now need to inspect the actual material they are using to construct the aircraft, whereas the older metallic raw materials did not require inspection. The first substantially-composite airliners will each contain at least 1800 m² of structural composite, much of it including complex structures such as co-cured stiffeners.

Military aircraft operators are facing a different challenge – their largely metallic fleets are being required to fly beyond their original design lives, requiring life-extension programmes and a reliance on NDE to assure damage tolerance is maintained. In complex structures that were built before the days of CAD packages and CNC machines, and which have often been repaired in a way that changes the structure significantly, NDE is becoming a significant financial and resource burden.

Thus virtually the entire aerospace industry is moving towards an NDE reliance that is unprecedented and requires solutions that will dramatically raise the effectiveness of NDE methods on complex structures, both metallic and composite.

The effectiveness of NDE methods is determined statistically through probability-of-detection (POD) trials (Berens, 2001; Spencer, 2001) if the objective is defect detection, or through calibration if the objective is characterisation of either the material or a defect. Ultimately the governing factor for image-based defect detection is the contrast-to-noise ratio (CNR) when the structure is simple (Smith and Hugo, 2001). This is the difference between the responses from the defect and from the surrounding structure, relative to the 'noise' fluctuations in the same area. For simple materials and structures the contrast achievable will change with location and material properties according to well-known physical effects such as diffraction, diffusion, dispersion etc. The point at which the CNR falls below 2.5 is often regarded as the limit of defect detectability (Smith and Hugo, 2001). But, when the materials or structures are inhomogeneous, the causes of the 'noise' become location-dependent and much more complex, often swamping the contrast from the defect. It is then much more difficult to predict the effectiveness of the technique from simple POD trials.

1.1.2 *Inspection of inhomogeneous materials and structures*

Many of the most difficult unresolved problems in the field of NDE involve the detection and characterisation of defects in inhomogeneous materials and structures, where the basic response of the structure can overshadow the response of the defect. In the author's experience, this is especially true when defects are just a particular variation of the basic inhomogeneity of the structure, such as fibre-volume fraction changes in carbon-fibre reinforced plastic (CFRP) composites (Smith et al, 1999a). This is less of a signal-to-noise (SNR) problem than a defect-to-structural-response problem - the structural response cannot be classified as 'noise' as it is rarely random. In each case, the optimum solution to extract the defect response depends on whether the structural response is predictable or random, or a combination of the two.

NDE techniques that are highly successful on simple structures can rapidly become unusable as the structure becomes more inhomogeneous, either by the inclusion of extra layers, fasteners or edges, or because the materials themselves are inhomogeneous, as in composite materials.

1.1.3 *Ultrasonic response of inhomogeneous materials*

The ultrasonic NDE method generally uses acoustic frequencies above 0.5 MHz in either a through-transmission (two transducers, one either side of the specimen) or pulse-echo mode (one transducer), requiring a liquid couplant such as water to transfer the energy into the component under test. The full-waveform ultrasonic response is analysed at each location on the surface of the structure and either the results of this analysis, or the full-waveform data, are stored for further post-processing and analysis (Smith, 2004).

Ultrasound is an extremely useful NDE method for inspecting inhomogeneous materials for several reasons:

- the wavelengths can be of the order of the size of any particles or layers, allowing the use of resonance and/or scattering methods
- the beamwidth can be big enough to average over a distribution of inhomogeneities, or small enough to map them individually
- energy is reflected or scattered at boundaries of acoustic impedance - local changes in density or stiffness – allowing both inhomogeneities and defects to be characterised.
- by storing the full-waveform response at each location on the structure, a 3D dataset has effectively been captured representing the 3D structure itself (Smith, 2004).

The challenge when interpreting ultrasonic signals from inhomogeneous materials is that simple amplitude variations within the ultrasonic waveform, or even more complex spectral variations, are often insufficient to identify their cause. Often it is necessary to compare the 3D location of the source of the amplitude variation with the 3D locations of structural components such as

fasteners and edges, or with the expected resonance response from multiple layers or plies in a composite.

1.1.4 *Ultrasonic 3D characterisation*

As mentioned above, 3D characterisation is often essential for defect detection and identification in inhomogeneous materials due to the complexity of the ultrasonic response. Essentially the response of each volume element needs to be extracted from the overall response of the structure. This may be achieved in several ways, but the one covered in this project is beam focusing, for in-plane zone definition and time-delay gating for out-of-plane zone depth.

1.1.5 *Ultrasonic mapping of material properties*

Ever since the first ultrasonic signals were obtained from static objects, over 60 years ago, the interpretation of those signals has remained a specialist skill. Even modern computer-based mapping methods generally map ultrasonic parameters that are meaningful only to trained NDE personnel. However, it should be possible to combine the ultrasonic ability to map structures with a knowledge of how ultrasound interacts with materials in order to reprocess the data and produce maps of actual material properties such as: density, modulus, ply spacings in monolithic composites, porosity levels, degree of bonding at an adhesive/adherend interface, consolidation and uniformity of fibre spacing in a metal matrix composite, etc.

1.2 Objectives

1.2.1 *Aims*

The primary aim of this project is to produce 3D profile maps of various measured parameters for inhomogeneous materials and structures to assist in differentiating between defects and structural effects, and to provide a higher degree of material characterisation for subsequent use by materials engineers.

A second aim for the project is to present quantitative NDE information in terms of actual material properties that can be easily interpreted, rather than ultrasonic

response parameters that require considerable understanding and expertise to interpret in terms of material properties.

A third and final aim of the project is to develop visualisation methods for each of the parameters to help NDT engineers to present convincing information to structures and design engineers, who then need to make decisions on allowing defects (concession or disposition) or repair strategies.

1.2.2 Specific requirements

With the rapidly escalating usage of composite materials, not only in military aircraft but in civil airliners as well, production NDT throughput is already stretched to its limit internationally. NDT data analysis is set to become the bottleneck preventing the required rise in production rates of composite civil aircraft in the next few years. Thus there is an urgent requirement for rapid, automated analysis of up to a Terabyte of data per airliner, escalating to over 200 Terabytes per year - worldwide. The primary aim of automated analysis is to release operators from the time-consuming analysis of all scans and focus operator attention on non-compliant structures. A secondary aim is to provide three-dimensional quantitative information that lightens the operator's decision-making burden. The latter aim is one of the requirements for the current project.

Through advanced characterisation methods, NDT also has the potential to provide crucial feedback to control the composite production process, increase production yield and decrease costs. Current analysis methods for ultrasonic scans produce through-thickness average parameters, which provide little useful information to assist the stress analysis for defects, or the production process. Three-dimensional characterisation of defects can increase yield by informing the concession/disposition process for defects. For future process control, information is required about the 3D distribution of material properties in the structures on the production line, providing comprehensive long-term trend analysis.

After consulting composites design engineers and materials scientists, the following list of composite material properties was generated, where accurate 3D measurements would be advantageous:

- distributed porosity
- layer porosity
- ply spacing
- fibre volume fraction (thick resin layers etc)
- ply stacking sequence
- in-plane fibre waviness
- out-of-plane fibre wrinkling

All of these material properties are important for both CFRP and glass-fibre reinforced polymer (GFRP).

Most of the critical material properties for CFRP and GFRP, such as void volume fraction and fibre volume fraction (FVF), are currently measured indirectly using ultrasonic parameters related to bulk properties. Direct measurements of material properties would be of more use to structural designers, especially if they could be mapped as a function of 3D location in the structure. This would allow structural designers to vary the acceptance criteria on these parameters depending on the predicted stress at each location, resulting ultimately in a lighter design.

Full-waveform acquisition and storage is now becoming commonplace for both production and in-service ultrasonic inspection, so there is potential for the direct measurement of various important material properties through signal processing and spectral analysis of the full-waveform data. Ultimately it should be possible to generate 3D profiles of these material properties by analyzing separately each 3D volume element in the structure. A short time gate placed on a particular ultrasonic waveform effectively isolates the ultrasound reflected or scattered from a specific 3D volume element. The extent to which the time-gate response is actually isolated from the effects of material in advance or in the rear of this volume element depends on the technique used to analyze the response and on the structure itself, and is an important consideration in any validation exercise.

In this work, the author has investigated new ways of decomposing the ultrasonic volume-element response into contributions from fibre-resin effects

(fibre volume fraction, ply spacing and thick resin layers), porosity and fibre orientation.

1.2.3 Scope and originality

The scope of the project in terms of inhomogeneous materials is confined to just CFRP and GFRP composite laminates. Only ultrasonic inspection of these composite laminates is included, although the first review chapter (Chapter 2) has a wider scope in order to justify the use of ultrasound.

The project is broad in terms of the range of material properties that are characterised and mapped and, for this reason, not all of the 3D characterisation toolset has been fully validated by the end of the project.

The originality in this project is in the application of signal- and image-processing methods to the isolation and characterisation of various material properties of composite laminates and then refining the methods of application, all in ways that have not been done before.

1.3 Overview of the project

1.3.1 Modelling of ultrasonic propagation in layered composites

A multi-layer ultrasonic bulk wave propagation model, MLM-Propmat, has been developed at the University of Nottingham to simulate the reflection and transmission responses of composite materials. Each layer is modelled as an effective medium using conventional mixture rules for the physical properties (Greszczuk, 1971). During the period of this project this model has been augmented by other workers to include the frequency dependence of ultrasonic attenuation due to porosity in the resin, based on the scattering theories of Epstein and Carhart (1953) and Allegra and Hawley (1972).

The effects of porosity and other panel defects were investigated by using a flexible simulation of ultrasonic wave propagation through multi-layered structures. For the purposes of simulation it was assumed that a monolithic composite could be considered to contain multiple layers which could consist of resin alone, resin with fibres, or either of these with the inclusion of porosity.

The model was essentially a transfer matrix formulation, and followed the earlier work of Freemantle (1995). The model simulates acoustic wave propagations in multi-layered media on the basis of a well-established transfer matrix model which originated from the works of Thompson (1950), Haskell (1955), Knopoff (1964) and Pialucha (1992). A description of the model was presented recently by Mienczakowski et al (2008).

For benchmarking purposes, a different and completely separate model was developed in parallel by the author, using similar mixture rules but a different software architecture. Also, the ultrasonic attenuation due to porosity was calculated using a different method – that described by Adler et al (1986) because it has an analytical formulation that does not require access to scattering-model software. This model is based on analytical expressions for the complex reflection coefficients at groups of interfaces, which can then be built into larger structures of interfaces. It was built by the author into QinetiQ's ANDSCAN[®] Waveform Analysis software for easy comparison with experimental data. The ability to compare the two models proved invaluable during this project and the models have been used to develop techniques to detect, localize and characterize flaws in composite materials.

1.3.2 Development of an ultrasonic signal processing toolset

The author had already developed substantial waveform-processing, image-processing, and spectral analysis toolsets in QinetiQ's ANDSCAN[®] application (Smith 1995a; Smith 1995b; Smith 2004). As the aims of this project included making the methods developed here available in the industry, it was appropriate to develop the new capabilities within this framework and it was obviously familiar to the author.

In many cases the pre-existing toolset just needed to be applied to the problems of inhomogeneous material inspection and then refined based on the knowledge gained from modelling and experiment. However, in certain cases new tools had to be added to the toolset.

As in most applications of signal processing and image processing, it is not the process itself that is new, but the specific optimisation of parameters for its

application to a particular problem. Hence most of the techniques used in this project already existed and were freely available as code fragments or algorithms in books or on the internet. This thesis focuses on their application to the above requirements and the originality in the optimisation of the solutions.

1.3.3 *Mapping of Inhomogeneous Material Properties*

Having extended the new toolset of image- and signal-processing tools, they were applied to each of the above requirements for inhomogeneous materials mapping. This process involved understanding the problem through modelling and experiment, followed by several stages, each including: application of the tools, optimisation of the parameters, and assessment of the outcome. Finally, in cases where a particularly successful process was defined, a validation stage followed where the accuracy and precision of the method was assessed.

1.4 Structure of the thesis

This thesis is divided into eight chapters and eight appendices. It was decided to put most of the scientific detail into the appendices in the interests of clarity and to maintain the flow of the main chapters.

Two literature review chapters are provided – Chapter 2 covers NDE methods for composite materials and the current position whilst Chapter 3 reviews modelling methods relevant to ultrasound propagation in composites. Chapter 4 describes the development of a model for normal-incidence ultrasonic propagation in a multi-ply composite. Then Chapter 5 covers the original use of this model for model-based decomposition in order to isolate the contributions in the response from different material properties. Moving away from the use of the model, Chapter 6 describes the development of novel methods for mapping fibre orientation and ply inclination. Chapter 7 is a discussion of applications of these new methods to various types of composite materials whilst Chapter 8 gives the conclusions.

This thesis contains information protected by United Kingdom Patent Application No. 0818383.2 and No. 0818088.7 dated October 2008.

CHAPTER 2 REVIEW OF NDE METHODS AND CURRENT POSITION

This chapter reviews the development of NDT methods targeted at composite materials but focuses on innovations of the last ten years. The chapter begins with two historical review sections: the first covering the early developments from the 1960s to the early 1990s and the second covering the 1990s to the start of the project in 2005. The subsequent sections then focus on individual material properties or defect types, namely: porosity, fibre volume fraction, ply stacking sequence, in-plane fibre waviness and out-of-plane ply wrinkling. Finally a discussion section summarises this review chapter.

2.1 Early NDE Methods for composite materials

This section reviews the development of non-destructive testing (NDT) methods for composite materials since the 1960s, as well as summarising relevant technical achievements and current work in academia, industry, and research organizations.

2.1.1 *Scope and availability of literature*

Much of the very early research was conducted in the defence establishment where composite materials were being developed – the Royal Aircraft Establishment (RAE) – and reports of this work, although often restricted in circulation, were made available to the author for this review. Some defence-based work in the USA is still restricted and not accessible. More recently the use of composite materials has become more widespread and filtered into the civil arena, resulting in a broader research base and more accessible literature.

A range of defect types is covered in this chapter, and materials include monolithic carbon fibre reinforced plastic (CFRP), glass fibre reinforced plastic (GFRP), sandwich structures such as honeycomb or foam between CFRP skins.

2.1.2 Historical NDT of Composites – 1960s and 1970s

Early in the development of CFRP (initially at the RAE in Farnborough, UK) it was realised that non-destructive testing would be essential in order to detect internal defects that were not visible on the surface. A small Non-destructive Evaluation (NDE) Group was established at RAE in the late 1960s to support the development of CFRP, drawing on expertise in image processing and coherent optical methods, such as holography. Reports in 1972/3 included work on holography (Sanders, 1973; Chubb and Abbiss, 1973; Wright, 1973), Moiré imaging (Wadsworth et al., 1972) and stress-wave sensing, later called acoustic emission (Dingwall, 1973). Work also commenced around this time on the ultrasonic NDT of composites. This was linked with work by the Materials and Structures groups at the RAE on, for example, compressive failure in CFRP (Ewins and Ham, 1973), buckling performance (Snell, 1979), and fracture mechanisms (Bishop and McLaughlin, 1979).

In parallel, an NDT Group within the Admiralty Materials Laboratory at Holton Heath in Dorset had started looking at acoustic emission for metallics and pressure vessels. This work was recognized as potentially useful for CFRP (Green, 1974; Green and Lane, 1978; Green et al., 1979). By 1974, holographic interferometry had been demonstrated at the RAE on honeycomb sandwich panels (Marchant, 1974) and acoustic emission on CFRP missile fins (Dingwall and Mead, 1974). In 1978 holography was applied to CFRP wing tips (Marchant, 1978) at the RAE and then used to determine the flexural stiffness of thin plates (Marchant and Snell, 1981). Laser holography was then used in industry by Westland Helicopters (Worsdell, 1982) for composite components.

In the USA, NDT of composites seemed to precede a thorough understanding of failure mechanisms and defect types, leading to some conclusions that now seem surprising, with hindsight. For example, Hagemaiier et al (1970) performed an early review of NDT techniques for carbon, glass and boron fibre epoxy composites but ultrasound was only noted as being useful for disbonded areas. X-radiography was found to be suitable for most sub-surface defects that were tested for, including fibre patterns, fibre gaps, broken fibres and resin-rich areas. Maigret and Jube (1971) also drew a strange conclusion from their

survey of NDT methods for composites – that the defect detection problem had largely been solved using X-radiography!

At the US Air Force Materials Lab, Anderson and deLacy (1972) found radiographic and ultrasonic tests to be the most effective for detecting open bonds and laminar defects. By 1982 deLacy (deLacy 1982) was using passive acoustic emission for GFRP structures on telecommunications satellites. Rose et al (1973) were some of the first researchers to realise the potential for using the ultrasonic spectroscopic signature of a composite to characterise its properties. At Sikorsky, Nevadunsky et al (1975) looked for early fatigue damage in composites using a range of NDT methods but found ultrasonic and holography to be the most effective. Sheldon (1978) systematically evaluated NDE techniques for in-service inspection of composites using an acoustic positioning system to allow the building up of 2D images from ultrasonic or optical methods. Knollman et al (1978) also evaluated a similar positioning system.

Double through-transmission ultrasonic systems for detecting voids in composites were developed by Markham (1969) and Compton (1971) as well as at the RAE. From Harwell, Reynolds (1974) reported on ultrasonic and vibration methods and the importance of porosity measurement. Stone (1974) highlighted the need for alignment between NDT developments and mechanical testing programmes to determine the importance of defect types, based on his work at RAE. A breakthrough in ultrasonic NDT of composites was reported by Stone and Clarke (1974) - the ultrasonic measurement of porosity. They demonstrated that ultrasonic attenuation increases due to the scattering of ultrasound by voids, that this is a frequency-dependent effect, and that it could be used to measure volume void content provided a calibration curve for the particular fibre-resin system had already been established. This was groundbreaking work and was published in the public domain (Stone and Clarke, 1975). Work at the RAE to check whether calibration data could be read across to other fibre-resin systems was published by Jones and Stone (1976) and showed approximately a 1 dB difference between two fibre-resin systems of the same fibre-volume fraction. Their data were re-analyzed and described in a

review by Birt and Smith (2004), showing that the agreement between the two systems was within the accepted $\pm 0.5\%$ error in the acid-digestion method used by Jones and Stone to determine volume void content. Sturgeon (1978) confirmed the important role that NDT was playing at the time in the development of composite materials. For the next thirty years this ultrasonic method of assessing porosity levels has prevailed in the production NDT of aerospace composites. It is only now, because civil airliners will soon contain a much higher proportion of composite structure, that improved methods are being sought to reduce production costs, weight, and hence operating costs.

Burchett (1972) successfully used holographic interferometry to inspect composite laminates. Meanwhile, under UK defence funding, electronic speckle-pattern interferometry (ESPI) was developed at the University of Loughborough (Bergquist, 1978) and this went on to form the backbone of the laser shearography method that is now being used in many composite applications, particularly for disbonding of sandwich components.

2.1.3 Historical NDT of Composites – 1980s and early 1990s

A group in British Aerospace was working on developing B-scan capability with Diagnostic Sonar Ltd (Figure 2-1) and carried out feasibility studies on an array-based 'System 185', with 394 elements at 5 MHz, in the early 1980s (Gassert, 1983).



Figure 2-1 - Diagnostic Sonar's 'System 185' for array-based B-scanning of CFRP was developed following interest from British Aerospace for military composite aircraft inspection, and was on sale in 1978 (Gassert, 1983).

They also reported on NDT of defects in CFRP (Thacker, 1984), on attenuation and velocity of acoustic emissions in composites (Hall, 1985) and, of particular interest, on ultrasonic spectroscopy for characterization of the composite itself (Brant, 1984). At this time there was also acoustic pulsing (later known as acousto-ultrasonics) work on GFRP at the Welding Institute (Bartle, 1983), and work at the Atomic Energy Authority's Harwell Laboratory on measurement of moisture content in CRFP from positron annihilation lifetime measurements (Allen et al, 1986). Also, at Harwell, Reynolds was investigating porosity using ultrasonic velocity measurements in CFRP (Reynolds and Wilkinson, 1978). He went on to use thermography for composite inspection in the early 1980s (Reynolds, 1985). With Milne he developed pulsed video thermography (UKAEA, 1983), later known as transient thermography (Milne and Reynolds, 1985). Hobbs continued evaluating transient thermography for use on composites in the 1990s at Harwell (Hobbs et al, 1991; Hobbs and Temple, 1993; Hobbs et al, 1994).

Other research was being carried out in the UK on the use of electromagnetic acoustic transducers (EMATs) by Tube Investments (Connor, 1988), and on computed tomography for helicopter rotor blades by Westland Helicopters Ltd (Powell, 1988).

Apart from some work on high-frequency eddy-currents for CFRP, by the end of the 1980s research at RAE on the NDT of CFRP was focused on ultrasonics and penetrant-enhanced X-radiography. Early ultrasonic immersion tanks from Meccasonics Ltd and C-scanning using electrostatic paper to produce six quantized gray levels were state-of-the-art (Lloyd and Wright, 1986). Computers were becoming useful for processing data from digitizers and the first pseudo-3D ultrasonic images of impact damage in CFRP were produced by Lloyd (1989) from one of the first full-waveform capture systems (see Figure 2-2). The author recalls that each 3D representation required at least ten minutes to calculate and display on a PDP-11 computer.

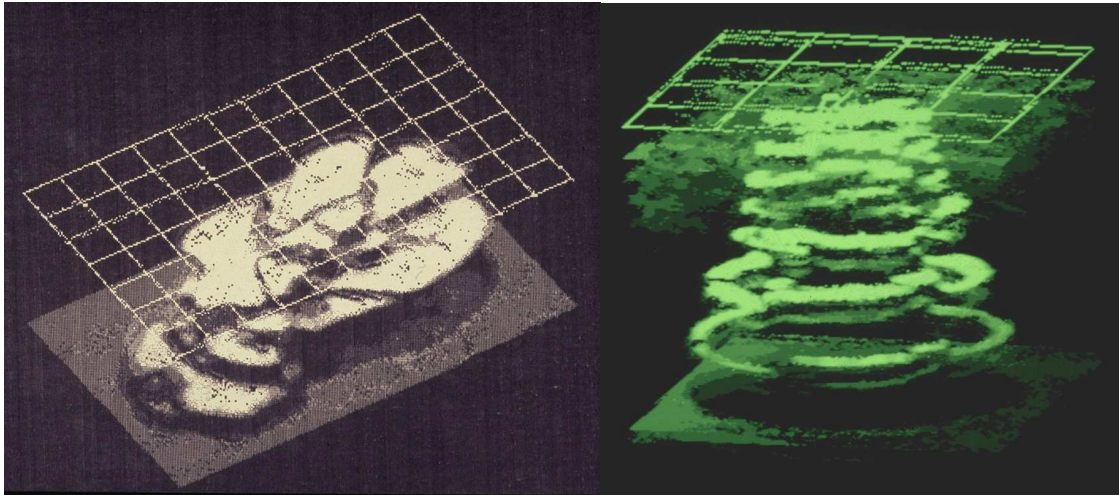


Figure 2-2 - Pseudo-3D images of impact damage in CFRP (Lloyd, 1989) generated from a Krautkramer KB6000 linked to a PDP-11 computer.

At this time in the Admiralty Research Establishment (ARE, formerly AML), the NDE Group was using acoustic emission (Jemison et al, 1989), eddy-currents (Lane, 1988), ultrasound, and X-ray (Jemison and Culpan, 1989) methods for some of the first aluminium metal-matrix composites (MMC) (Jemison et al, 1993). Meanwhile, at the Harwell Laboratory, acoustic methods were being tested for these MMC materials (Buttle and Scruby, 1988), and acoustic emission source location was being studied in CFRP (Buttle and Scruby, 1989). Acoustic microscopy was investigated for a range of composite materials, including MMCs, by Briggs, Lawrence and Scruby (Briggs et al, 1993; Lawrence et al, 1993a; Lawrence et al, 1993b; Lawrence et al, 1993c), and acoustic emission was investigated for MMCs (Mummery et al, 1991; Mummery et al, 1993).

In the late 1980s at Imperial College, London, Cawley and Adams were developing an understanding of the low-frequency vibrational response of composite structures and how to harness this for inspection purposes (Cawley, 1985; Cawley et al, 1985; Cawley, 1987; Adams and Cawley, 1988; Cawley and Adams, 1988; Cawley, 1989; Cawley and Adams, 1989; Cawley, 1990). Then Cawley turned his attention to the potential for using ultrasonic guided-wave modes to inspect large areas of composite structures using sparsely distributed sensors (Guo and Cawley, 1993; Cawley, 1994; Guo and Cawley, 1994a), with some work on normal-incidence pulse-echo ultrasound for porosity

measurement in composite repairs (Guo and Cawley, 1994b). Also, at Imperial at this time, an acousto-ultrasonic method was being investigated for composite inspection by Rawlings (Thompson and Rawlings, 1991; Aduda and Rawlings, 1990).

2.2 A review of composite inspection from the 1990s

2.2.1 *Ultrasonic Composite Inspection*

The availability of personal computers led to the transfer of C-scanning to computer operation at RAE Farnborough from 1989. Immersion-tank scanning was transferred first, and then a portable in-service inspection system, soon to be known as ANDSCAN[®], was developed (Smith and Jones, 1992; Smith, 1995a; Smith, 1995b). These systems allowed the gathering of ultrasonic data from a flaw detector followed by storage and imaging as coloured maps of the ultrasonic response of the structure. In addition, the pseudo-3D imaging capability developed by Lloyd (1989) was reproduced within the ANDSCAN imaging system. The increase in computer speed in just three years allowed the 3D images to be calculated and displayed in just a few seconds and soon it was possible to manipulate them on the screen, at a viewing angle controlled by the computer mouse.

By this time the RAE had been merged with the ARE and two other non-nuclear defence research establishments (RSRE and RARDE) to form the Defence Research Agency (DRA). A few years later this became the Defence Evaluation and Research Agency (DERA) when some other establishments were amalgamated.

Having started capturing full waveforms from every point in the scan in the 1980s, the benefits were well understood at RAE Farnborough and the new computerized systems were designed to continue with this method (Smith, 1996). An early benefit was the ability to determine ply stacking sequence by imaging sequential C-scans generated by moving a narrow time gate down through the 3D ultrasonic data set that represented the structure (Smith and Clarke, 1994). Examples of these early scans are shown in Figure 2-3. The

stacking sequence was determined by noting the two dominant fibre-tow directions by eye from each scan and tracking them down through the structure. An automated system to measure fibre orientation was developed later and is described below.

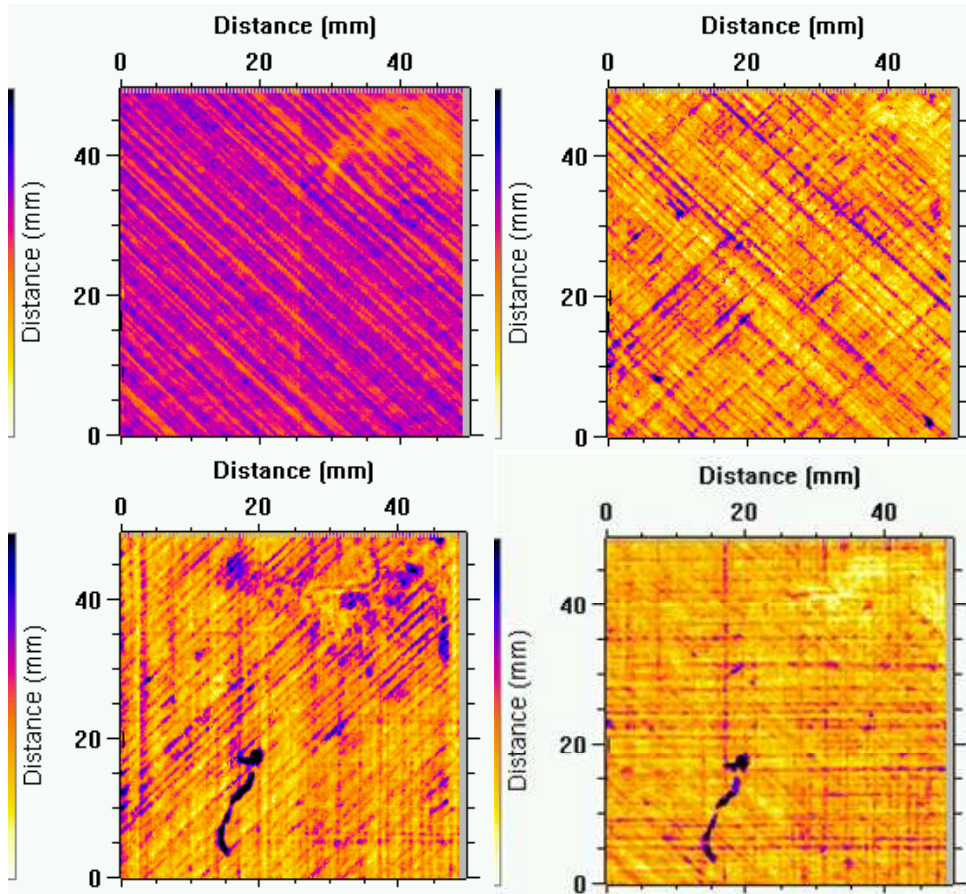


Figure 2-3 - Examples of amplitude C-scans obtained from half-ply wide time gates at different depths in a 6-ply skin, from near-surface (top left) descending (top right, bottom left, etc). The imprint of fibre tows from plies both above and below the reflecting interfaces is clearly evident. A significant void defect is also detected in a deeper ply.

Defect sizing for accurate measurement of defect growth became an issue, resulting in several papers that assessed the errors in the -6 dB and amplitude sizing methods, and recommended procedures to minimize these errors (Smith, 1994; Smith et al, 1997; Smith et al., 1998). In collaboration with the Ultrasonics Section of the National Physical Laboratory (NPL), the NDT Group at Farnborough investigated the effect on immersion NDT measurements of nonlinear propagation in water – a phenomenon that had been overlooked, and

still is, due to the relatively narrowband sensors used for NDT, but which can cause significant errors in attenuation and spectroscopic measurements (Smith et al, 1998b; Smith, 1999; Smith et al, 1999b). One of the effects of nonlinear propagation in water is that energy is transferred into higher harmonics, often creating a saw-tooth waveform with positive pressure peaks being sharper and exceeding the negative pressure peaks. Figure 2-4 shows the high-frequency harmonics that are evident when a broadband sensor is used to measure the acoustic pressure waveform from a conventional commercially available transducer and flaw detector.

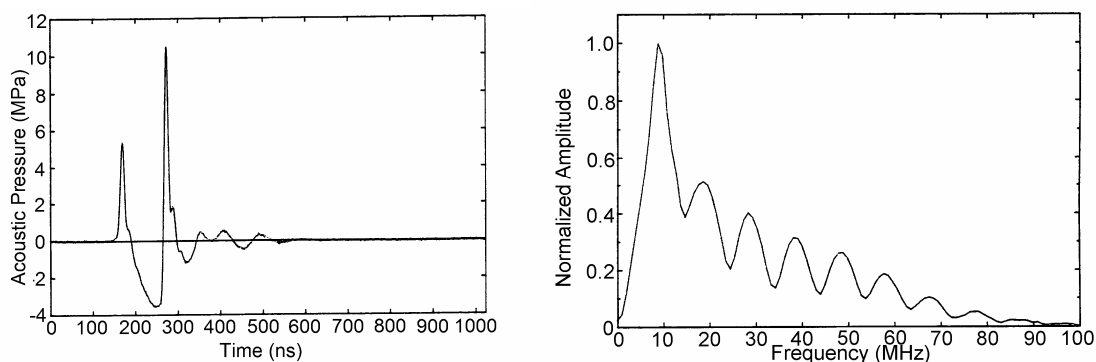


Figure 2-4 - Acoustic waveform (left) and its spectrum (right) from a conventional commercially available 10 MHz focused NDT transducer measured at the focus, 34 mm, using a broad-band PVDF membrane hydrophone (Bacon, 1982). Measurements made at the National Physical Laboratory.

It was becoming clear in the early 1990s that large-area in-service inspection of composites would prove necessary. Two strands of work were undertaken at DERA Farnborough: Lamb wave inspection of large composite panels, and multi-element ultrasonic arrays. The Lamb wave method was investigated in terms of the potential for different modes of propagation in CFRP and to detect delaminations at different depths in the material (Percival and Birt, 1997; Birt, 1998). As ultrasonic-array technology had been successfully used in the medical field for years, it seemed obvious that this was the way forward for rapid NDT of composites. The author's history in medical ultrasound at the National Physical Laboratory (NPL) prior to joining RAE in 1989 led to a strong collaboration with Diagnostic Sonar Ltd, a company that had been producing

modified medical array systems for B-scan inspection of composites since 1978 – see Figure 2-1 (Gassert, 1983; Lines, 1998; Lines et al, 1999). By linking this array technology to accurate positional scanning systems such as ANDSCAN[®], it became possible to produce C-scan images and capture full waveforms over large areas (Figure 2-5) (Willsher and Smith, 1998a; Willsher and Smith, 1998b; Smith et al, 1999a; Lines et al, 2003).

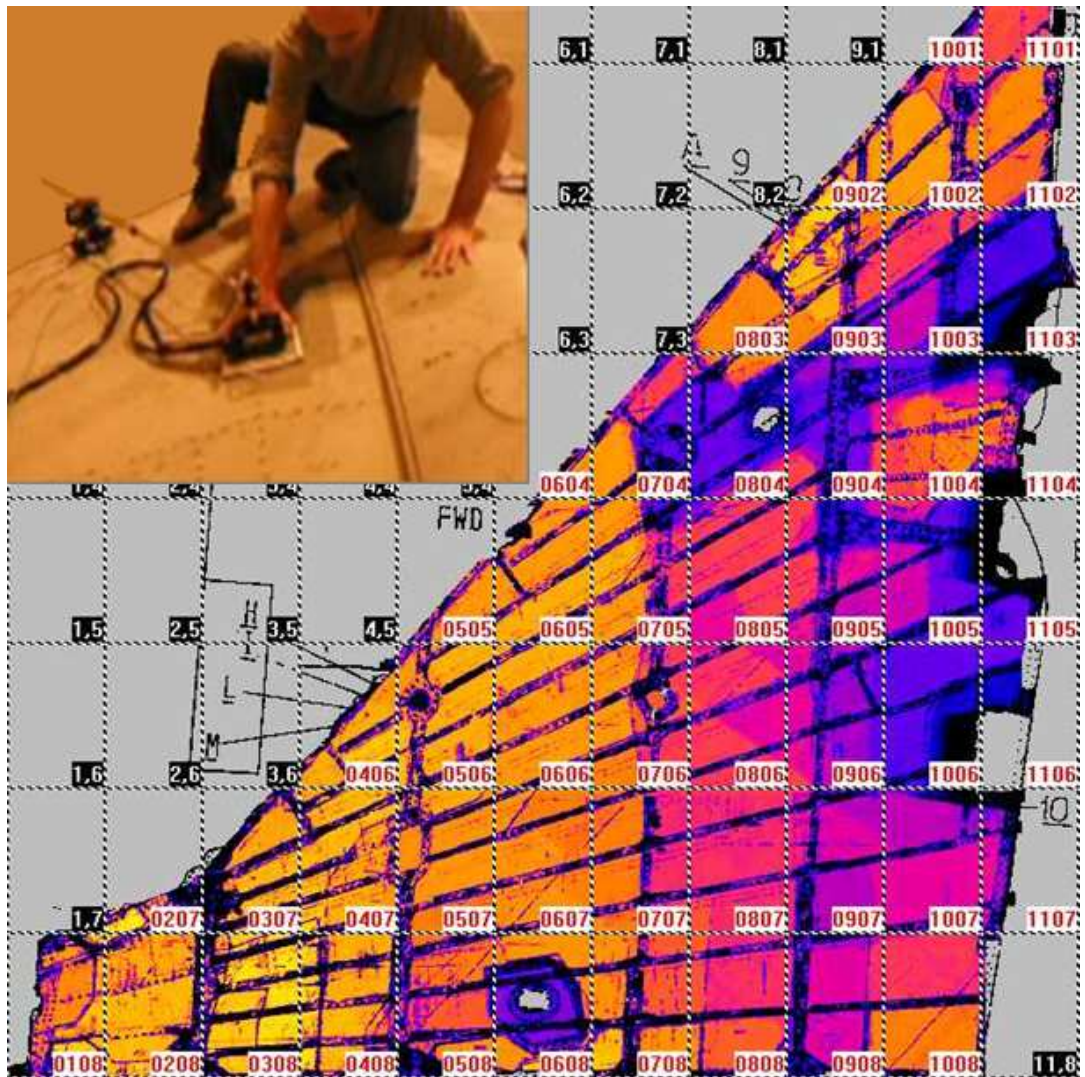


Figure 2-5 - Large-area thickness scan produced from a full-waveform ultrasonic-array scan of an 8.5 m² (91.5 ft²) wing structure. A manual scanning method was used with Diagnostic Sonar's FlawInspecta[®] array attached to an R-theta scanning arm (inset) and DERA's ANDSCAN[®] software. Each individual 'slave' scan is scanned and stored at high resolution and automatically stitched into the large 'master' scan shown. The 'large-area grid' shown is used to select and open a specific high-resolution 'slave' scan for detailed analysis.

The NDE Group at DERA Farnborough was involved early in the development of new low-cost manufacturing methods for CFRP, such as resin transfer moulding (RTM), resin film infusion (RFI) and resin infusion with flexible tooling (RIFT). Projects funded by the Department of Trade and Industry in the UK included: ultrasonic methods for detecting and characterizing any new types of defect (Jones et al, 1998), a study of porosity, fibre volume fraction, and fibre waviness measurement, as well as the effects of rough surfaces on measurements. Another project investigated the ultrasonic inspection of thick-section monolithic CFRP and foam-sandwich structures produced using RTM. The difficulties of mapping changes in fibre volume fraction and fibre orientation were first encountered during these projects and are only now being solved by the author in collaboration with the University of Nottingham under this PhD project.

2.2.2 *Development of Standards for Ultrasonic C-scan Production Inspection of CFRP*

Following a study by the NPL, funded by the Department of Trade and Industry (Broughton and Sims, 1996a; Broughton and Sims, 1996b), a program commenced to respond to a need for improved standardization of ultrasonic C-scan inspection. This collaborative program involved NPL, DERA and a large number of industrial advisers. A considerable amount of research was carried out to underpin the standards and most of this was documented in a special issue of *INSIGHT – the Journal of the British Institute of NDT* (Broughton et, 1998; Smith et al, 1998a; Smith et al, 1998b; Smith et al, 1998c; Zeqiri et al, 1998;) and in other papers (Smith et al, 1998d; Broughton et al, 1999, Smith et al, 1999b).

Three draft standards were produced covering: a) operational procedures, b) transducer calibration, and c) preparation of reference defects and reference panels (BSI, 1999a; BSI, 1999b; BSI 1999c). Two round-robin comparisons were then carried out – one in the UK and the other in the USA and Europe. The standards are still at the draft stage.

2.2.3 Automated Analysis and Sentencing

As the use of composites in military and civil aircraft became more widespread, it became clear that large-area automated analysis and sentencing capabilities would be required for both production and in-service inspection. QinetiQ's NDE Group embarked on a project for the Ministry of Defence to develop automated analysis and sentencing software, specifically targeted at analyzing large full-waveform capture scans at high resolution (Connor, 2005). A reference scan is used for comparison. This can be either an earlier scan of the same component or a scan of a 'reference' component. Two images from the data, such as C-scans, are automatically aligned in both translation and rotation. Then the two data sets are subtracted (see Figure 2-6) and the resulting differences are classified in terms of the cause of the difference (structural misalignment, noise, or a defect), and various measurements are performed. This information is then used to form a priority list for an operator to investigate. It is expected that this process could reduce the amount of data that needs to be analyzed by an operator to less than 10%.

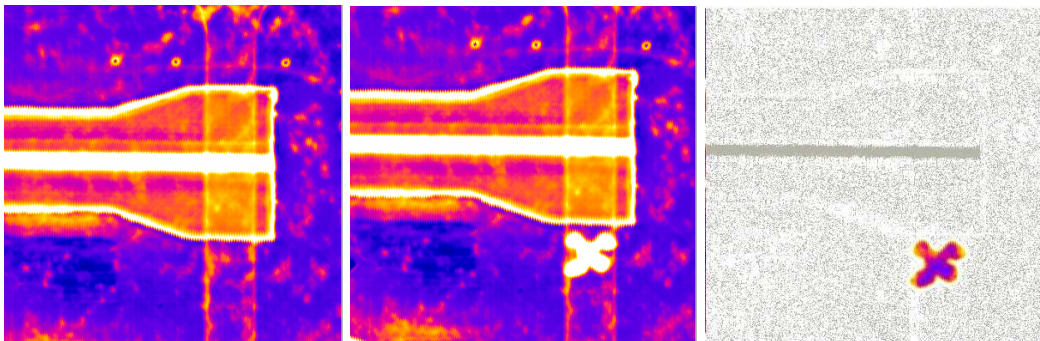


Figure 2-6 - Demonstration of automated registration (translation and rotation) in QinetiQ's PinPoint[®] software, followed by image subtraction to highlight the defect. The back-wall amplitude C-scan on the left is prior to impacting, the middle C-scan is after impacting, and the right-hand image is after automated registration and image subtraction.

In recent years the NDE Group in BAE Systems at Warton in Lancashire has collaborated with the University of Central Lancashire to develop software for image registration of NDT images with CAD wire-frame models, and hence with other NDT images for data fusion purposes (Matuszewski, 2000; Matuszewski,

2001; Shark et al, 2001; Bach et al, 2002; Deng et al, 2002; Matuszewski, 2002).

2.2.4 Advanced Low-frequency Vibration Methods

To improve the defect detection and characterization capabilities of the low-frequency vibration method for honeycomb sandwich structures, Nelson et al (2006) at QinetiQ Ltd have been modelling the low-frequency response of honeycomb structures. From this work a new model-assisted inspection mode has been developed that is single-sided whilst being equally sensitive to front and rear skin-to-core disbonds, as well as to core crushing from impact damage. Some commercially available low-frequency vibration instruments have the ability to make use of the parameters recommended by the structural model. However, the optimum implementation of this method requires more advanced instrumentation and signal processing, and is currently being evaluated by QinetiQ using various existing modules within the ANDSCAN[®] software application. This includes the use of a multi-element linear-array version of the traditional pitch-catch arrangement, with ANDSCAN[®] storing the response from each element at its correct location on the scan, thus providing large-area scanning coverage of honeycomb structures.

2.2.5 Microwaves

Under a Ministry of Defence program, microwave imaging methods have been applied by QinetiQ Ltd (in collaboration with the University of Missouri at Rolla) to various applications, including the inspection of thick-section GFRP and various sandwich-construction composite maritime structures for disbonds, delaminations and core crushing. The microwave response of a composite structure is governed by the locations and thicknesses of dielectric materials. An assessment of the potential for using this method on maritime structures has been presented by Green (2004) and an example is given in Figure 2-7 of the type of image possible from a 150 mm (6 inches) wide region of impact damage in the PVC foam core of a sandwich structure with 3.5 mm thick GFRP skins. A relatively low frequency of 15 GHz was used to penetrate into the core of the structure. Skin and core material dielectric properties, as well as their thicknesses, govern the optimum operating frequency and the ultimate defect

detection capability. At present, minimum detectable defect sizes have not been formally established because critical defect sizes in this form of construction are generally large for maritime structures.

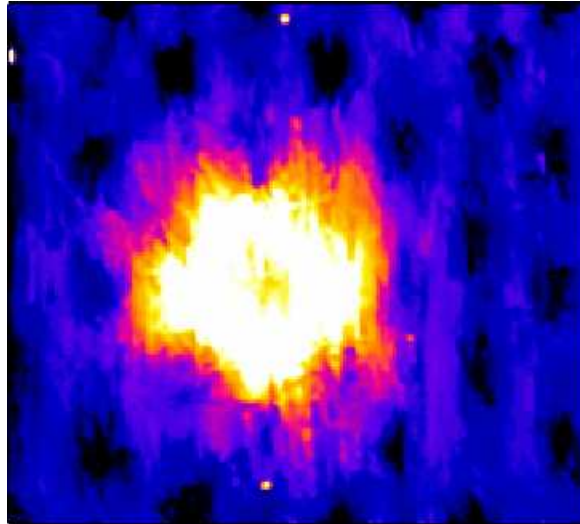


Figure 2-7 – 15 GHz microwave-NDT image of impact-damage core crushing in a 3.5 mm thick e-glass GFRP-skinned, PVC foam-cored specimen. The image covers an area 300 mm (12 inches) wide.

2.2.6 Laser Shearography

Over the past 30 years the University of Loughborough has been developing electronic speckle pattern interferometry (ESPI) for NDT applications. In more recent years, under the direction of Dr John Tyrer, the group has evaluated laser speckle shearing interferometry for use on composites (Zhang et al, 1997a; Zhang et al, 1997b; Zhang et al, 1997c; Richardson et al, 2000; Nurse et al, 2000; Petzing et al, 2002). These techniques have become known collectively as Laser Shearography and some are commercially exploited world-wide for particular NDT applications where a surface displacement can be produced above a defect such as a delamination or disbond using a vacuum or the application of heat.

2.2.7 Thermal methods

For some years a group at the University of Bath headed by Prof Darryl Almond has been researching thermal NDT methods and transient thermography in particular. In a transient thermographic inspection powerful flash lamps are

used to flash heat the surface of a test piece and its subsequent cooling transient is monitored by an infrared camera. Delaminations in composites block the conduction of heat from the surface into the composite. Consequently, the surface above a delamination defect cools relatively slowly and an image of the defect appears brighter in infrared camera frames collected during the cooling transient (Figure 2-8). This technique has the advantages of providing a large area inspection of a composite structure that is non-contacting and rapidly produces defect images that are simple to interpret. The technique is well suited to composite inspection because composites have low thermal conductivities, making thermal transients long (several seconds) and surface temperature rises adequate (a few degrees Celsius) for modest flash powers. In addition, composites are often black and/or non-reflective, ensuring good absorption of optical flash energy and good emission of infrared. The technique is, however, limited to the detection of defects within a few millimetres of the surface (Quek and Almond, 2005). It is now used commercially to inspect thin section composite structures and their bonding to, for example, honeycomb cores.

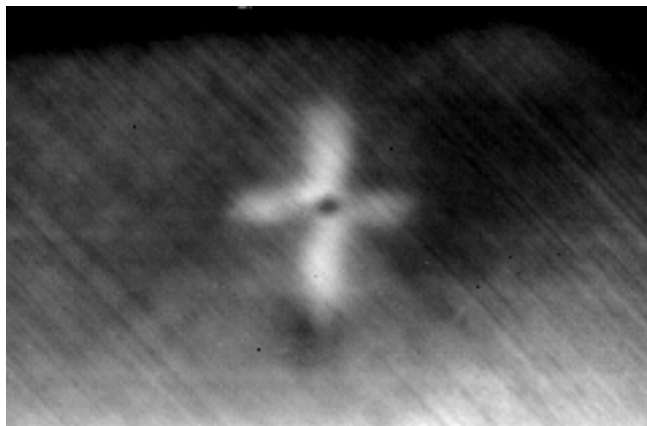


Figure 2-8. Transient thermographic image showing near-surface damage caused by a 51 J impact on an 8 mm thick CFRP composite sample. (Image courtesy of S. Pickering, University of Bath)

2.2.8 Acoustography

At the University of Bath, acoustography has been investigated in terms of its suitability for composite NDT. Acoustography is a medium-area ultrasonic imaging system that provides an alternative to ultrasonic C-scanning. A broad

beam of ultrasonic waves is passed, water coupled, through a test piece to an acousto-optic imager formed by a layer of ultrasound-sensitive liquid crystal. On exposure to ultrasound the layer becomes birefringent, showing a brightness change that increases with ultrasonic intensity. Consequently, a shadow image of defects that block ultrasound is formed on the imager that can be captured by a standard visible light CCD camera. The acoustographic system used by the University of Bath produces full-field images in a few seconds of inspection areas up to 150 mm x 150 mm using 3.3 MHz ultrasound. It has been shown that acoustographic images can potentially reveal more detail than conventional C-scans (Bond-Thorley et al, 2000) because the image is not broken up into scan-step sized elements. Acoustography applications include large-area ultrasonic inspection of composite sheets and the inspection of tight radii in parts that can be manipulated in the broad ultrasonic beam. The technique has been used by Chen et al (2001) at the University of Bath to study, in real time, the growth of impact damage in composite test pieces during fatigue loading in a mechanical testing machine – see Figure 2-9. This was groundbreaking work because it was possible to image the specimen with an in-plane compressive load applied, thus opening the delaminations and showing that, when loaded, delaminations appear larger to ultrasound than when unloaded. The reason for this effect is thought to be that the edges of delaminations are effectively tightly-closed cracks in intimate contact and are transparent to ultrasound. An in-plane compressive load tends to open the delaminations, resulting in an ultrasonically reflecting gap (Figure 2-9 and Figure 2-10).

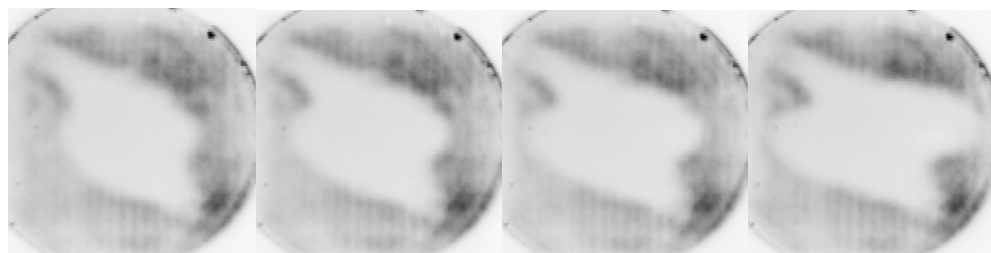


Figure 2-9. Acoustography images of impact damage growth in aerospace composite subjected to compressive fatigue, peak stress 170 MPa. Number of fatigue cycles (from left to right): 0, 2880, 5760, 8640 cycles. Images courtesy of Professor D Almond of the University of Bath.

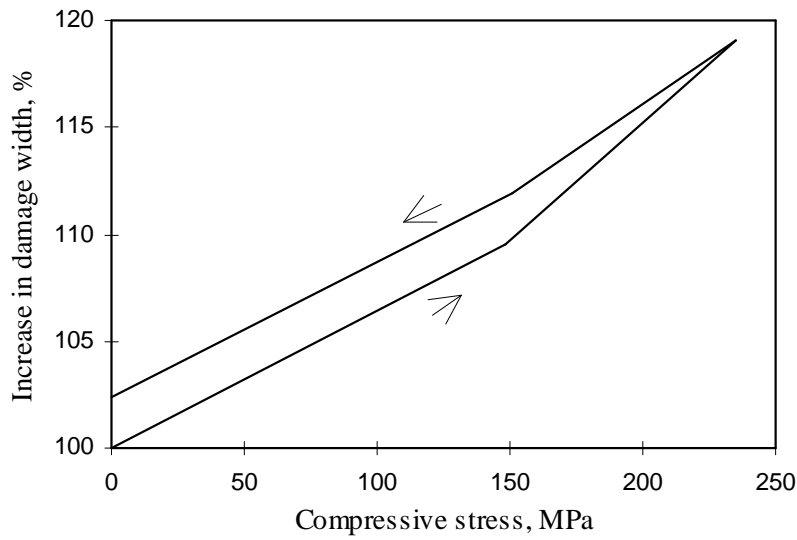


Figure 2-10. Damage width change during load/unload test, measured from acoustographic images. Image courtesy of Professor D Almond of the University of Bath.

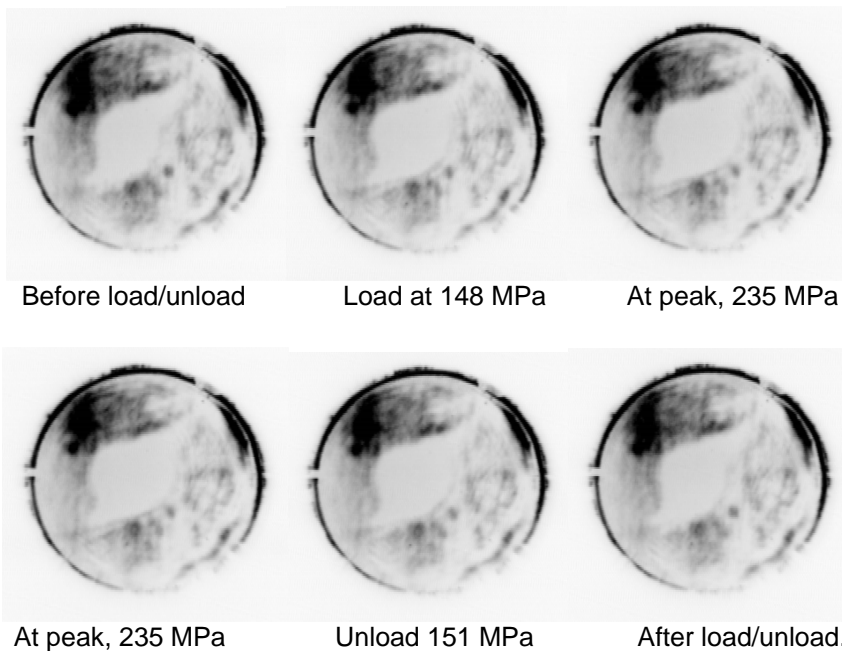


Figure 2-11. Image of damage area changes under static loading (top row) and unloading (bottom row). Images courtesy of Professor D Almond of the University of Bath.

2.3 Porosity Characterisation in Composite Materials

2.3.1 *Introduction to porosity defects in composites*

There are several types of defect that can occur during the manufacture of carbon fibre-reinforced composites. One of the most serious is voids in the matrix, which can be further classified as:

- **Delaminations:-** these are large planar voids occurring at the interfaces between the plies and can also be described as layer porosity. They are easily detected by ultrasonic methods as they act as almost perfect reflectors of the ultrasonic beam.
- **Discrete voids:-** these are large enough to be of structural significance and can also be individually detected and measured by ultrasound.
- **Porosity:-** this can be described as a large number of micro-voids, each of which is too small to be of structural significance or to be detected individually by a realistic inspection technique, but which collectively may reduce the mechanical properties of the components to an unacceptable degree. It is usually produced during the curing cycle from entrapped air, moisture or volatile products.

The distinction between discrete voids and porosity is a matter of convenience but, for practical purposes, porosity may be thought of as sub-millimetre voids whereas voids of several millimetres dimension would be considered as discrete defects.

The occurrence of high levels of porosity has been recognised as a serious problem for composite materials for many years. As the compressive and interlaminar shear strength of carbon fibre-reinforced composites depend primarily on the matrix properties, these are reduced by the presence of porosity. In contrast, tensile properties, which are determined almost exclusively by the fibre properties, are relatively unaffected by the presence of porosity (Garrett 1983). An extensive review of the effects of porosity on the mechanical properties of composites was undertaken by Judd and Wright (1978) and

subsequent work has been reported by Uhl et al (1988). These studies have concluded that the interlaminar shear strength is more seriously affected by the presence of porosity than the compression strength. It has generally been found that the interlaminar shear strength decreases by about 7% per 1% of voids, up to a total void content of about 4%. Other mechanical properties are also affected, although not to the same degree.

A figure of 2% porosity has commonly become the nominal acceptance threshold for many composite components. As an example, Hagemmaier and Fassbender (1979) state that for secondary aircraft structure, composite with void contents in excess of 2% are unacceptable. Research programmes in NDE have therefore concentrated on providing techniques that could detect and measure porosity in the range of 1 to 5% by volume. Ideally an NDE technique is required that could determine the level of porosity in a composite laminate independent of other variables such as pore morphology and the fibre and matrix materials. However, to date, no single NDE method has been able to provide this universal 'porosity meter'. The majority of the work on porosity measurement has concentrated on ultrasonic techniques. This sub-section reviews these in some detail but also describes some other methods that have been proposed for porosity measurement.

2.3.2 *Review of porosity measurement in composites*

Ultrasonic velocity and attenuation can both be used to estimate the porosity level in composite material. The velocity and attenuation of an ultrasonic pulse travelling in a fibre-reinforced composite will be dependent on both the porosity (void fraction) and the fibre volume fraction of the composite. Measurements of attenuation have been used in many studies as it is simpler to measure and less affected by variation in the volume fraction of fibres in the reinforcement.

Both velocity and attenuation measurements depend on the frequency of the ultrasound used for the inspection. Williams et al (1980) studied the variation of attenuation and velocity with frequency in carbon composite. Longitudinal velocity was found to be only very weakly frequency dependent while the attenuation increased significantly with increasing frequency. In principle, the

visco-elastic attenuation in matrix resin should increase linearly with frequency for low frequencies. This should be true for composite material at practical inspection frequencies (0.5 to 10 MHz), where the ultrasonic wavelength (6 to 0.3 mm) is much greater than the diameter of the reinforcing fibres.

Stone and Clarke (1975) carried out one of the earliest investigations into ultrasonic methods for porosity measurement at the Royal Aircraft Establishment (RAE), Farnborough. They performed an extensive series of experiments on a set of panels made from pre-preg material with HTS carbon fibre and ERLA 4617/DDM resin matrix, giving nominally 60% fibre volume fraction. The panels were manufactured in an autoclave to a nominal thickness of 2 mm using a unidirectional lay-up. An attempt was made to vary the porosity in the panels by altering the pressures used during the cure cycle. Porosity values were obtained by destructive examination using acid digestion. The panels were found to have porosity in the range of approximately 0.4% to 4.0%, with an estimated measurement error of $\pm 0.5\%$. Both surfaces of the panels were ground flat so that all the panels were of constant thickness and surface finish. All the ultrasonic measurements were taken with the ultrasound propagating perpendicular to the carbon fibres.

Stone and Clarke investigated the use of ultrasonic velocity measurements for determining void content. The velocity in 2 mm thick CFRP with no porosity was measured to be 2980 ms^{-1} . Experimentally, they found that a void content of 5% reduced the velocity by about 6%. Assuming this to be a linear dependence of velocity on porosity, a specimen with 1% voids would have a velocity of about 2944 ms^{-1} - a change in transit time of just 17 ns for 2 mm thickness. Although precision ultrasonic test equipment could measure this small difference, most commercial test sets are not capable of the required accuracy. Moreover, the temperature of the water bath is very important for accurate velocity measurements. They therefore concluded that, for general inspection purposes, the use of attenuation measurements was preferable to velocity measurements.

The ultrasonic attenuation was measured for the panels using three different pairs of transducers with measured centre frequencies of 2.5, 5 and 7 MHz in through-transmission geometry. The results were used to define a calibration

curve for the initial resin system; see Figure 2-12. The measured attenuation of the signal was corrected for surface insertion losses before being converted to a value of the attenuation coefficient, α , in dB/mm. In the absence of a theoretical treatment two ways of fitting the data empirically were explored.

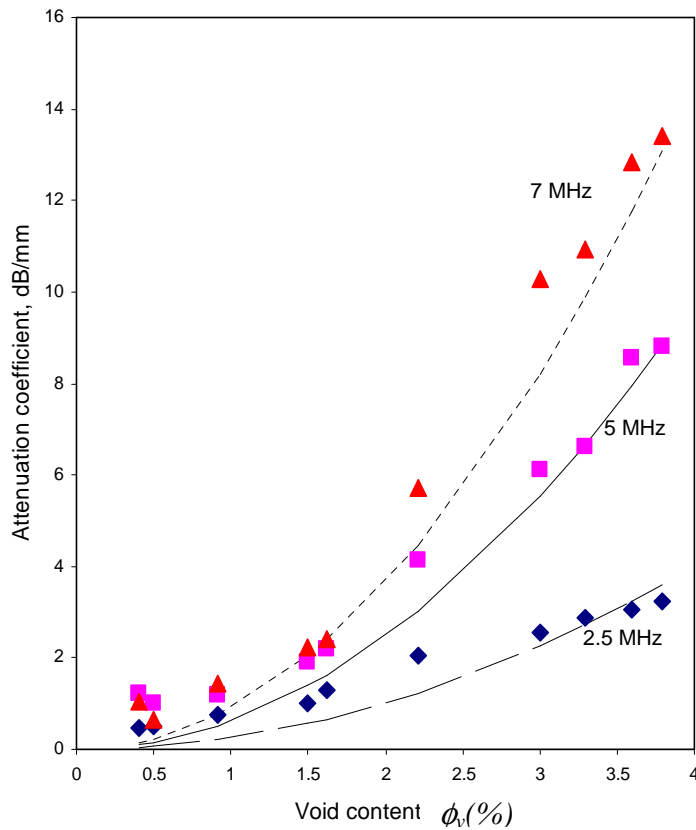


Figure 2-12. Variation of attenuation coefficient with void content (Stone & Clarke 1975). The curves show the best fit to the data using Equation 2-1.

Initially a parabolic fit to the data was attempted using the form:-

$$\alpha = n(f)\phi_v^2 \quad (2-1)$$

where n is a constant for a given frequency, f , and ϕ_v is the void volume fraction. The constant n was found to be 0.251 for the 2.5 MHz data, 0.616 for the 5 MHz data and 0.912 for the 7 MHz data. The fitted curves using these three constants are reproduced by the author and shown in Figure 2-12.

The dependence of n on frequency can be approximated from the above three values and the three theoretical curves may be expressed as:-

$$\alpha = 0.0794 f^{1.27} \phi_v^2 \quad (2-2)$$

Figure 2-13 shows these curves reproduced by the author using Equation 2-2, compared to the experimental data.

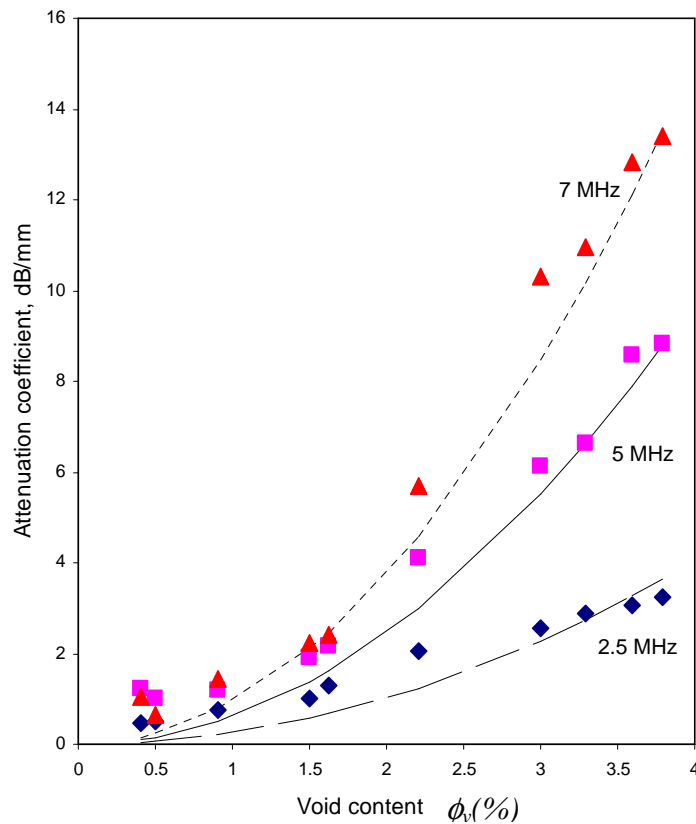


Figure 2-13. Variation of attenuation coefficient with void content (Stone & Clarke 1975). The curves show the best fit to the data using Equation 2-2.

A second fitting method took a bilinear form:-

$$\alpha = a_1(f)\phi_v + b_1(f) \quad \phi_v < 1.5 \% \text{ porosity} \quad (2-3)$$

$$\alpha = a_2(f)\phi_v + b_2(f) \quad \phi_v > 1.5 \% \text{ porosity} \quad (2-4)$$

where a_1 , b_1 , a_2 , and b_2 are constants for a given frequency. This bilinear form (see Figure 2-14) was motivated by the observation, during destructive examination of the specimens, that there was a qualitative change in the character of the voids at about 1.5% porosity. Up to 1.5% porosity, the voids tended to be spherical, with the void diameter ranging from 5 to 20 μm . These voids were thought to be due to the various volatile elements present and there is some evidence that the size of the individual voids increases with ϕ_v .

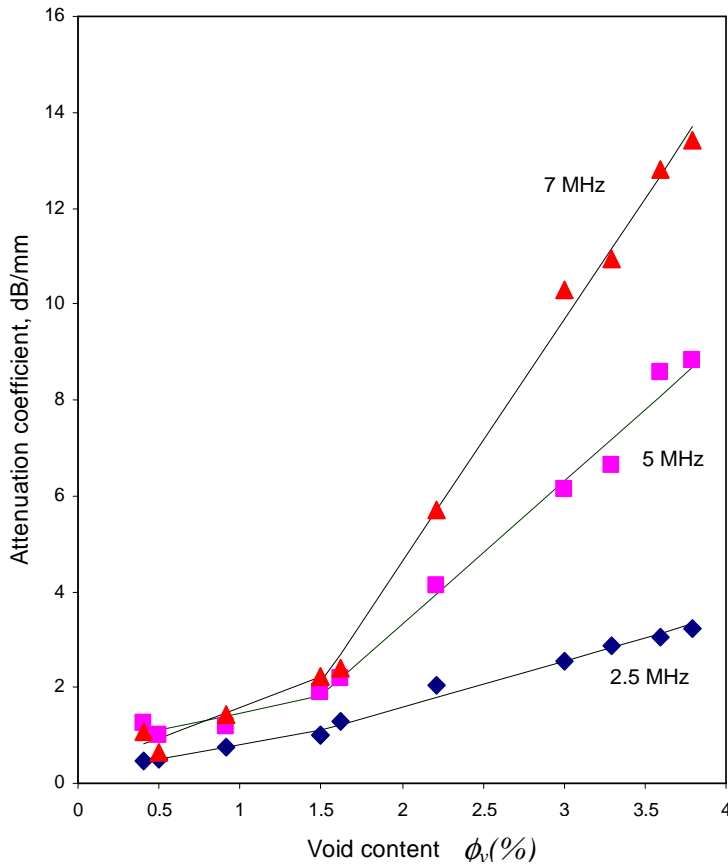


Figure 2-14. Variation of attenuation coefficient with void content (Stone & Clarke 1975). The curves show the fit to a bilinear form.

Beyond a ϕ_v of about 1.5%, interlaminar voids caused by air entrapped between the laminates start to predominate. These were flattened and elongated and tended to be significantly larger than the volatile-induced voids; see Figure 2-15.

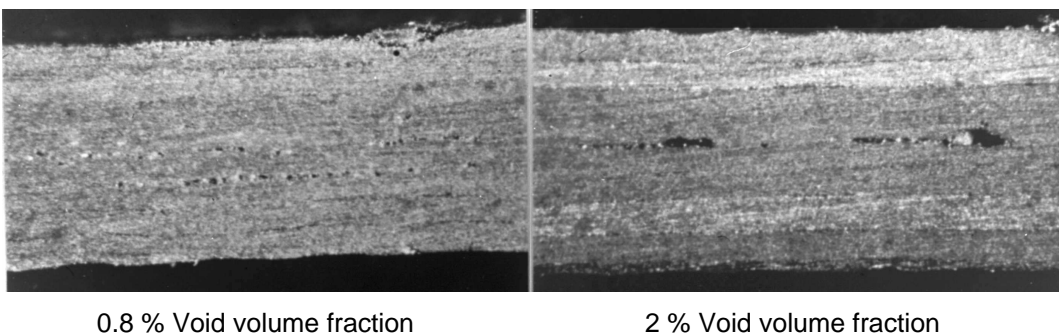


Figure 2-15. Typical void structure in carbon-fibre composite below 1.5% ϕ_v (mostly spherical voids) and above 1.5% ϕ_v (mostly flattened and elongated voids) as found by Stone and Clarke (1975).

Stone and Clarke concluded that the bilinear form appeared to provide a better fit to the experimental data. Hale & Ashton (1988) developed a combined sphere / disc model capable of predicting this bilinear form, although the fit is not as good as the one in Figure 2-14. It is discussed further in Chapter 3.

Finally, Stone and Clarke (1975) correlated ultrasonic attenuation measurements at 7 MHz with the interlaminar shear strength (Figure 2-16).

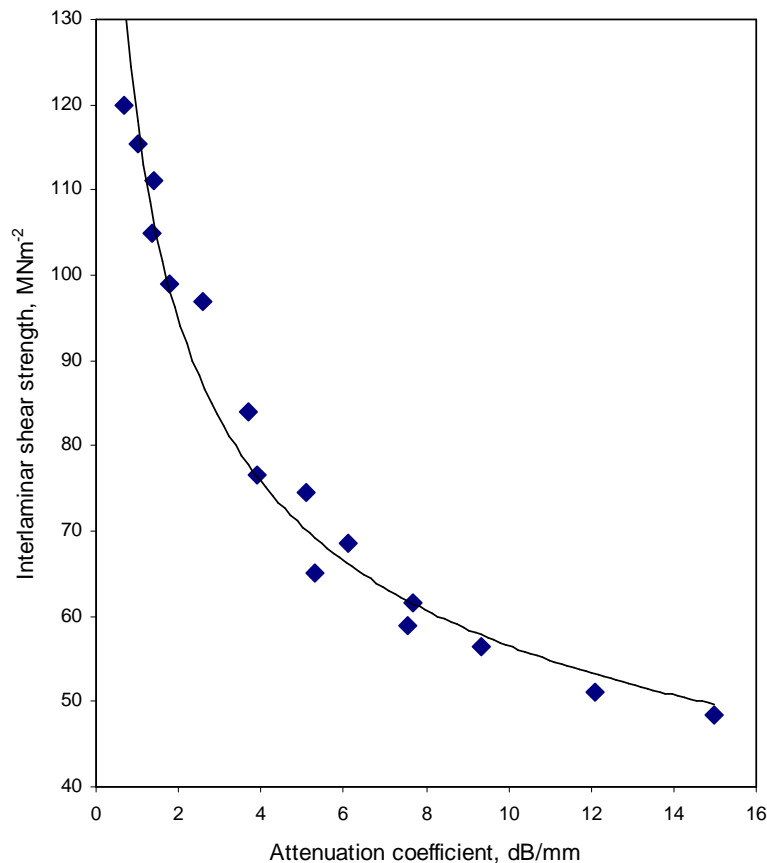


Figure 2-16. Relationship of interlaminar shear strength to the 7 MHz attenuation coefficient for HTS fibres in ERLA 4617/DDM matrix (Stone & Clarke 1975).

Other studies (Judd & Wright 1978; Uhl et al 1988) showed that the interlaminar shear strength was most seriously affected by the presence of porosity. The ultrasonic attenuation measurements were used instead of the porosity measurements as it was considered that the ultrasonic attenuation measurements were more reproducible than the porosity figures from the acid digestion method. For the fibre-resin system considered in this work, it can be seen that there was a good correlation between the ultrasonic attenuation and the interlaminar shear strength.

Attenuation due to porosity arises from elastic scattering of the ultrasound due to the acoustic mismatch at the voids. As the mismatch in acoustic impedance between the matrix material and void is several orders of magnitude, it is reasonable to assume that the scattering will be dominated by the geometrical considerations alone and not by the material properties of the resin. In this approximation the increase in attenuation due to porosity would be similar for all resins, providing the morphology of the porosity does not change. It was therefore assumed that the data for the ERLA 4617 system could be read across to other resin systems.

A further programme of work was undertaken at RAE to check the validity of this assumption (Jones & Stone 1976). The resin used for the follow-up study was DX 210 with the same volume fraction as the original study. The attenuation measured at 7 MHz centre frequency for the two resin systems is shown in Figure 2-17.

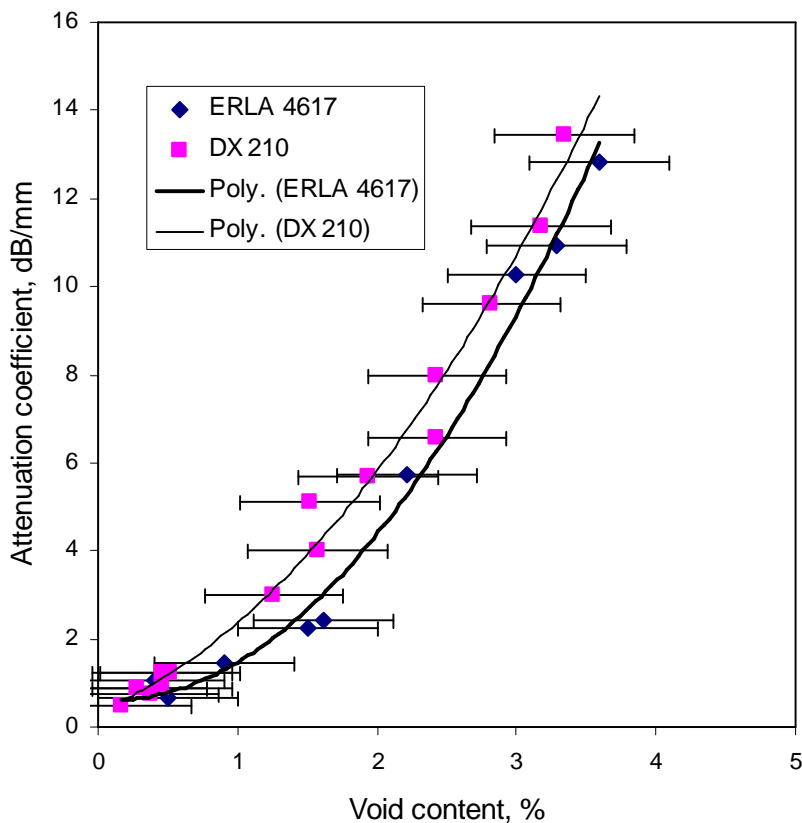


Figure 2-17. Variation in attenuation for two resin systems at 7 MHz centre frequency (Jones & Stone 1976).

It can be seen that the results are similar, although the attenuation for the DX 210 system appears to be up to 1dB higher for intermediate void contents. The ± 0.5 % error bars for the acid digestion measurements have been added to the original Jones and Stone results and are based on accepted overall uncertainties in this method.

Martin (1976) presented a theoretical treatment of the relationship of the ultrasonic attenuation to the void diameter. In this analysis all the voids were assumed to be spherical. He compared his results to the experimental work by Stone and Clarke (1975). Martin derived an expression for the ultrasonic attenuation making it inversely proportional to the cube of the void radius and proportional to the void content, but this is only valid when the ultrasonic wavelength was much larger than the diameter of the void. So, if the void radius changed by a factor of two, the attenuation changed by a factor of eight. It was also shown that for measuring void content ultrasonically it was best to use the highest frequency possible that will not be totally attenuated for void contents in the range ≤ 4 % by volume. However, this is likely to move out of the regime where the ultrasonic wavelength is much larger than the diameter of the void.

Hsu and Nair (1987) related the slope of an attenuation verses frequency measurement to the void content. The work was based on a model of the voids, which assumed long cylindrical voids with an elliptical cross-section. This shape of void was chosen as it had been observed that in composite the voids tend to occur at the interface between the plies and are generally flattened and elongated along the axial direction of the adjacent fibres. For a set of seven unidirectional and quasi-isotropic laminates, reasonably good agreement was observed between the porosity measured ultrasonically from the attenuation slope and acid digestion measurements; see Table 2-1 and Figure 2-18.

It was also noted by Hsu and Nair that porosity affects the spectral content of a broadband pulse. The shift in the centroid frequency, when normalised by dividing by the centroid frequency of the void-free specimen, showed a linear correlation with void content; see Figure 2-19.

Sample	Porosity by attenuation slope, %	Porosity by acid digestion, %
1	0.5	0.2
2	0.2	0.32
3	0.8	1.14
4	1.1	1.25
5	1.8	2.04
6	2.5	2.82
7	3.4	4.05

Table 2-1. Porosity measured by attenuation slope and acid digestion (Hsu and Nair 1987).

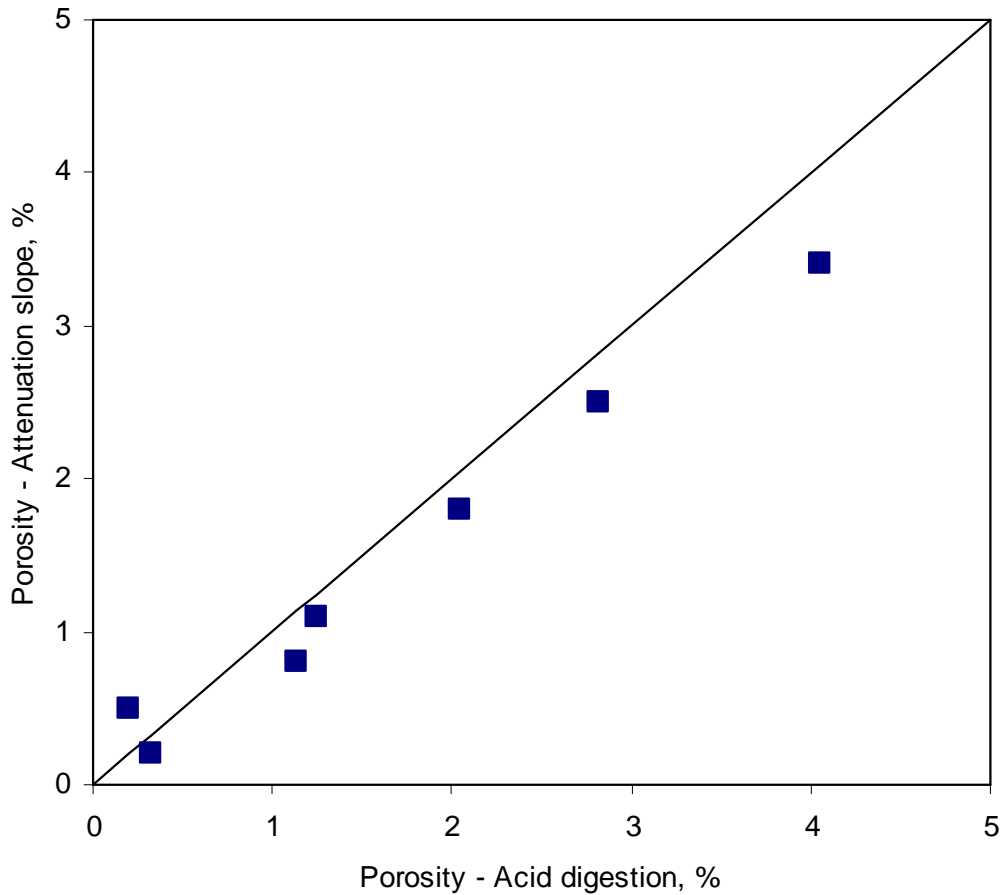


Figure 2-18. Comparison of porosity measured by attenuation slope and acid digestion (Hsu and Nair 1987). The line represents exact agreement and is for comparison with the experimental data.

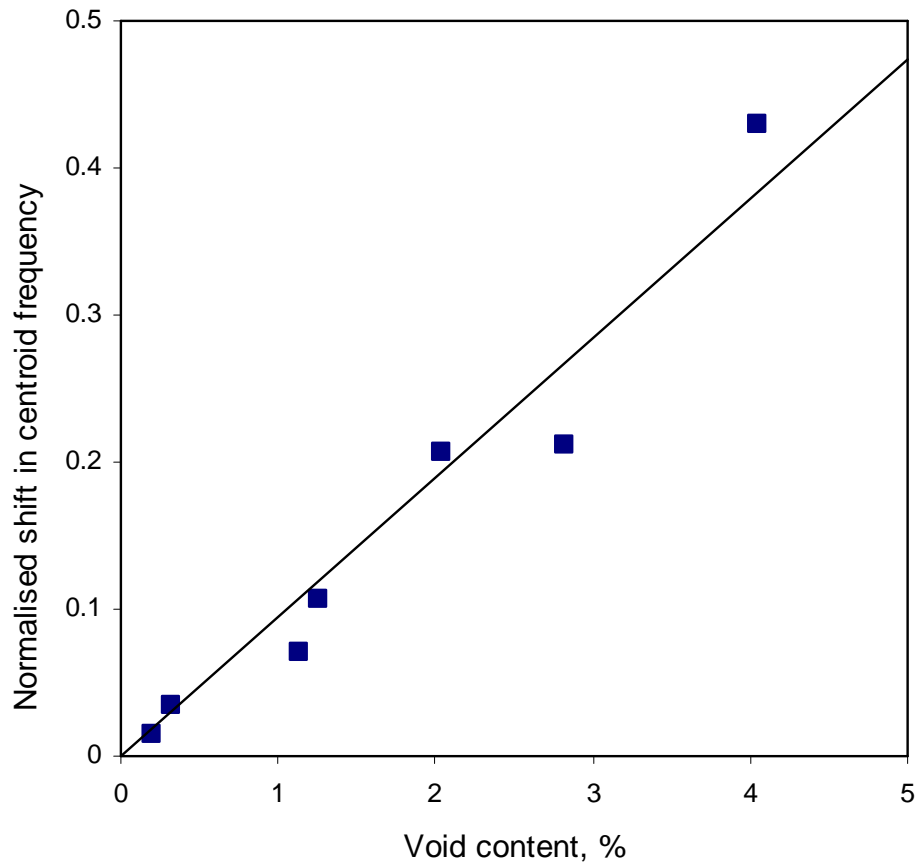


Figure 2-19. Correlation between void content and normalised centroid frequency shift for a 10 MHz transducer (Hsu and Nair 1987). The line is a linear best fit to the experimental data and has a slope of 0.095 %-1.

The use of ultrasonic velocity measurements to determine both porosity and fibre volume fraction has been considered by other investigators. Reynolds and Wilkinson (1978) described a method to calculate the elastic constants of unidirectional fibre-reinforced materials containing matrix voids. This permitted the construction of calibration curves for given materials by means of which the measurement of two or more ultrasonic wave velocities may be converted to estimates of fibre volume fraction and porosity. Martin (1977) also developed a model relating ultrasonic velocities to both fibre volume fraction and porosity.

More recent work by Jeong and Hsu (1995) investigated the frequency dependence of the phase velocity (dispersion), which was ignored by both Reynolds and Wilkinson (1978) and Martin (1977). When the wavelength of the ultrasound is of the same order of magnitude as the characteristic dimension of the voids it would be expected that over this frequency range the medium should show velocity dispersion. Dispersion effects are detected as frequency-

dependent ultrasonic velocities. A pulse, being a superposition of many frequencies, will change its shape as it propagates through a dispersive medium. Jeong and Hsu undertook a theoretical analysis followed by an experimental study. The ultrasonic attenuation and dispersion due to scattering are not independent according to Kramers-Kronig relations (O'Donnell et al 1978). Jeong and Hsu tested the relationship between the attenuation and dispersion using the theoretical local form of the Kramers-Kronig relation, which was found to hold experimentally for porous composite materials over the frequency range 2 to 10 MHz. The attenuation was found to be linearly dependent on frequency, with the attenuation slope ($d\alpha/df$) higher for laminates with higher void contents. The shape of the voids was found to have a great effect on the constant that relates void content to $d\alpha/df$ and this could explain almost a factor of two difference in attenuation compared with the Stone and Clarke (1975) experimental data. It was therefore considered important to use prior knowledge about the laminate structure and pore morphology in order to estimate the void content from the attenuation slope measurements.

The ultrasonic velocity decreased with increasing void content and the velocity dispersion increased as the frequency decreased. The velocity decrease was highest in unidirectional and quasi-isotropic samples, lower in the woven carbon/epoxy samples and lowest in the woven carbon/polyimide samples.

B T Smith 1990 proposed a method for fitting the back-surface reflection to that generated by a scattering model convolved with the front-surface echo (giving the system response). The fitting parameters would be sound velocity, reflection coefficient and porosity level. A nonlinear least-squares fitting routine was used and results looked promising for artificial porosity of a known pore size distribution. It is thought by the author that this method would be unreliable in real situations where the pore size is unknown.

Methods based on the Bar-Cohen & Crane (1982) observation of polar backscattering from composites have been developed by Yuhas et al (1986) and Blodgett et al (1986). They measured the azimuthal-angular dependence of the oblique-incidence backscattered amplitude. Backscatter from porosity should be independent of azimuthal angle, whereas backscattering from the

anisotropic composite is highly directional. Experimental results confirmed that this is potentially a highly sensitive method, but it requires numerous measurements for each location in the structure. It is too onerous a method for a single-element transducer, but with the advent of phased arrays and full-matrix capture, this method could be revisited in the future. Grolemond & Tsai (1998) used a statistical approach to understand the polar backscattering. Their results confirmed that the statistical behaviour of the echo amplitudes from porous laminates followed predictions based on circular Gaussian statistics for void contents in the range 2 to 5%.

Daniel et al (1992) proposed a method that combined pulse-echo and through-transmission measurements to measure attenuation accurately. Whilst this method may prove more accurate for attenuation measurement, the measurement of attenuation is not the biggest source of error – it is the relationship between attenuation and porosity level that is the biggest unknown.

2.3.3 Summary of ultrasonic porosity measurement

Measurement of the ultrasonic attenuation of composite laminates was found in the review by Birt & Smith (2004) to be the most frequently used method to try to measure porosity. From the literature it is clear that several factors affect the relationship between the measured ultrasonic attenuation and the void content. It can be assumed that there is a general equation relating the measured ultrasonic attenuation, α , in dB/mm to the volume void content, ϕ_v of the form:-

$$\alpha = K(f, d, s)C(\phi_v) \quad (2-5)$$

where K is dependent on the ultrasonic frequency, f , and the void shape, s and size, d . $C(\phi_v)$ is the function relating attenuation to void volume fraction, ϕ_v .

Stone and Clarke (1975) initially assumed:-

$$C(\phi_v) = \phi_v^2 \quad (2-6)$$

and that K was a function of the ultrasonic frequency only, i.e.

$$K = 0.0794 f^{1.27} \quad (2-7)$$

However Stone and Clarke (1975) concluded that a better fit was obtained using a bi-linear relationship of the form:-

$$C(\phi_v) = a_1(f)\phi_v + b_1(f) \quad \text{for } \phi_v < 1.5\% \quad (2-8)$$

$$C(\phi_v) = a_2(f)\phi_v + b_2(f) \quad \text{for } \phi_v > 1.5\% \quad (2-9)$$

Jeong and Hsu (1995) found a linear relationship between the void content and the attenuation slope, $d\alpha/df$:-

$$\frac{d\alpha}{df} = K(s)\phi_v \quad (2-10)$$

The parameter K was found to be dependent only on the void shape, s . This study was based on composite laminates manufactured from unidirectional, quasi-isotropic and woven laminates. The different material types produced different void shapes. The unidirectional and quasi-isotropic materials tended to have voids, which were flatter and longer. However, the voids in the woven laminates were more spherical in shape.

2.3.4 Ultrasonic 3D characterisation of porosity

An early method for 3D porosity mapping was proposed by B T Smith et al (1986). This converts the waveform response from the structure into a magnitude-versus-time profile, which can then be plotted in 3D. The conversion method starts with a deconvolution of the waveform with the system response, obtained by reflecting off a planar metallic reflector. The next stage is to apply a digital band-pass filter that approximately matches the system response, presumably to remove the noise that would have resulted from the deconvolution. The resulting waveform has its 'analytic magnitude' calculated – rather like an instantaneous reflection coefficient – and this forms the magnitude-versus-time profile. The method is mentioned again by B T Smith (1990) and a comparison is made with the porosity levels in an induced-porosity specimen. The porosity had been created by introducing hollow carbon micro-

spheres with a known size distribution in each layer. The 3D profiles were displayed as a movie and porosity could clearly be seen at the correct depths.

2.3.5 Other NDE methods for porosity measurement

Other methods for measuring porosity have also been reported in the literature. Connolly (1992) reported the use of a thermographic method to measure the porosity of six carbon composite samples. The technique consisted of heating one face of the sample with a laser and observing the temperature rise on the other face as the heat diffused through the sample. A good correlation was obtained between the diffusivity and porosity for all six samples.

Gray et al (1995) investigated the use of microwaves for the estimation of porosity in polymer composites. This work is currently at an early stage and the reported results apply to air-filled microballoon inclusions in epoxy resin samples. They estimate that porosity changes of about 2% should be detectable using the method. The technique reported should be applicable to glass fibre composite but is not a method easily adaptable for in-service use.

Kite et al (2008) investigated destructive methods of measuring porosity for comparison with NDT methods for calibration purposes and to make reference standards. An image processing method for micrographic sections is compared with the acid digestion method. Neither method is new although they do explain what image processing was used within a free open-source software package. Agreement between the two methods was good ($\pm 1\%$ porosity) for specimens with evenly distributed spherical pores, but non-spherical pores and uneven distribution both resulted in significantly poorer agreement ($\pm 4\%$ porosity) between the methods. These comparisons are useful to show the state-of-the-art for destructive methods looking at through-thickness average void content.

2.3.6 Porosity standards

Kollgaard et al (2008) reported work aimed at producing reproducible standards for porosity and providing an improved relationship between NDT measurements and void content. The paper reviews effects of porosity on mechanical strength and methods of porosity determination and then highlights

the problem that the relationship between ultrasonic attenuation and void content is dependent on void size and morphology. Thus a given volume fraction of small voids would produce a smaller attenuation than the same volume fraction of large (flatter) voids. The historical result was that standards were produced that used clouds of fine pores, which resulted in over-sensitivity to larger pores. The next part of the paper focuses on how to produce artificial standards that replicate the response to porosity, although the potential is addressed for using a parameter other than attenuation that is better related to actual void content. Kollgaard then presents a study of commercial ultrasonic instrument responses to porosity, showing that frequency content of the signal is the most important factor to control in order to obtain consistent results. Velocity measurements, on the other hand, showed remarkable immunity to the spectral variations across instruments; but velocity measurements require a knowledge of the component thickness at every location. They felt that this would be possible for relatively uniform shapes such as I-stiffeners, blade stiffeners and hat stiffeners.

2.4 Fibre Volume Fraction

2.4.1 *Introduction to fibre volume fraction measurement*

Changes in fibre volume fraction (FVF) in carbon-fibre composites affect both ultrasonic attenuation and surface losses – reflection and transmission coefficients change due to changes in the acoustic impedance (the product of density and ultrasonic velocity). It is possible for these two effects to cancel out for through-transmission measurements. Hence simple through-transmission attenuation is an unsatisfactory method for detection of fibre volume fraction. An ideal solution would be to use the combined ultrasonic information to generate a ‘volume-fraction’ meter. This may be possible by collecting full waveforms and analysing the frequency-dependence of the transmitted ultrasound.

Resin Transfer Moulding (RTM) processes use rigid matched metallic moulds, which control the finished size of the component. It is therefore possible to produce, from this tooling, panels with significantly different fibre volume

fractions, in a way that cannot be determined with a simple mechanical thickness measurement.

The following sub-sections summarise the work that had been done by the author and colleagues at the start of the current project, as well as reviewing work by other workers.

2.4.2 Ultrasonic attenuation

As the fibre volume fraction increases there should be a reduction in the bulk ultrasonic attenuation of the material (due to reduced resin content – the resin causes a higher ultrasonic attenuation than the fibre). But, due to the increase in density and velocity and, therefore, the acoustic impedance, there can be a complementary increase in the surface transmission losses. This is seen clearly in the 10 MHz double through-transmission scan in *Figure 2-20*.

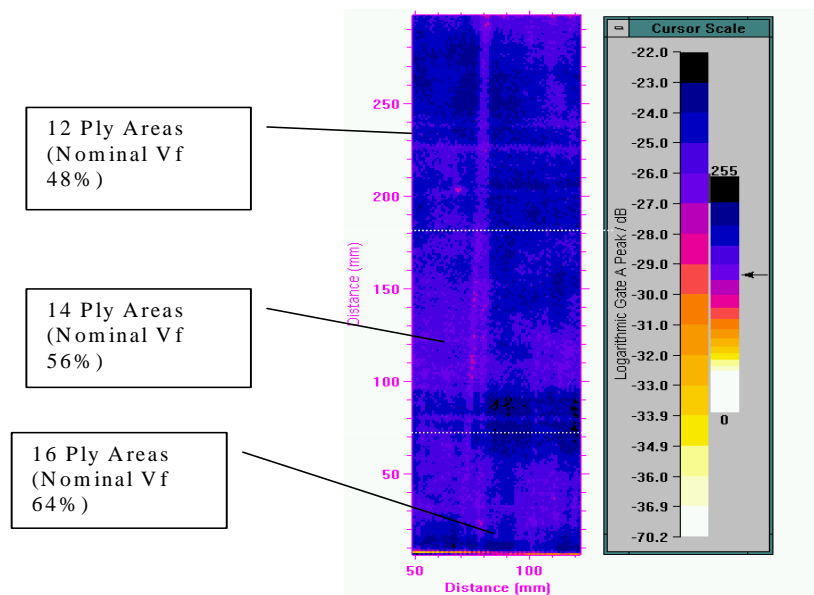


Figure 2-20. 10 MHz attenuation C-scan of a panel with variable fibre volume fraction which has 12 plies in the top section, 14 in the middle, and 16 in the bottom section. Note that there is very little variation in measured attenuation despite considerable variations in volume fraction. This is attributed to the cancelling effects of the attenuation and the surface losses.

This suggests that, at 10 MHz, the expected reduction in attenuation within the material at higher volume fractions was directly offset by the increased surface transmission losses due to the higher density and velocity. This self-cancelling

effect will be dependent on the thickness of the material as well as the changes in volume fraction but, most significantly, it will depend on the inspection frequency because the bulk attenuation is frequency-dependent whilst the surface losses are not, for normal incidence on a smooth surface (neglecting beam profile effects).

2.4.3 Acoustic Impedance Method

Although through-transmission ultrasonic measurements are affected by both bulk attenuation and surface-loss changes, it is possible to isolate the acoustic impedance effect by plotting the reflection amplitude from the surface of the specimen. An example of this type of scan is shown in Figure 2-21.

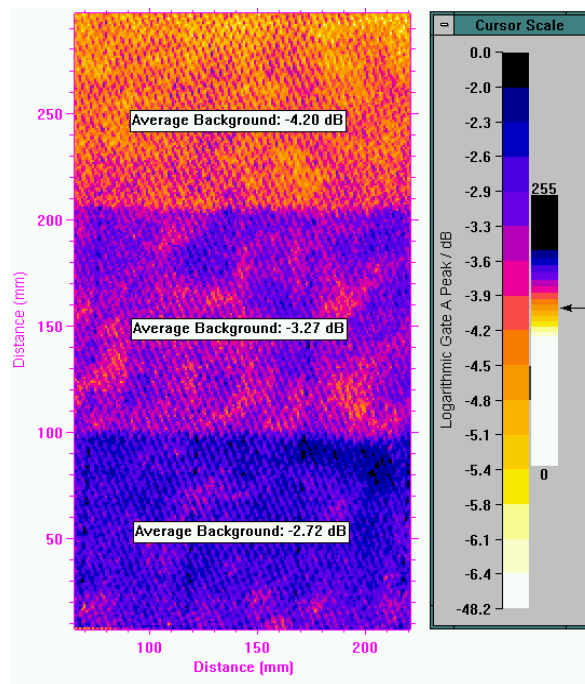


Figure 2-21. Front-surface reflection amplitude plotted for the variable volume-fraction specimen with 12 plies (top), 14 plies (middle), and 16 plies (bottom).

The effective impedance at the surface is a combination of the impedances of the fibres and resin matrix and is therefore sensitive to the fibre volume fraction according to a mixture rule. Mixture rules will be investigated in Chapter 3.

2.4.4 Ultrasonic Velocity Method

Another alternative to through-transmission attenuation measurement is to measure ultrasonic velocity. This is appropriate for RTM materials where rigid

moulds maintain accurate thicknesses and changes in velocity can be observed by plotting the time-of-flight to traverse the specimen. An example of this type of scan is shown in Figure 2-22 where the same variable volume-fraction panel has been scanned. The ultrasonic velocity through the material is frequency independent and can be measured to a high degree of accuracy. Although velocity would appear to be the most satisfactory measure of volume fraction it should be noted that the velocity can also be influenced by other factors such as porosity and foreign bodies.

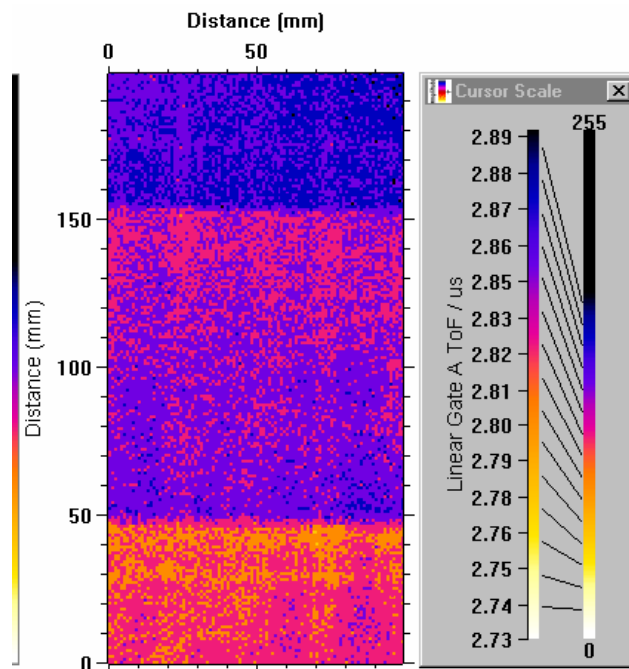


Figure 2-22. Time-of-flight (corresponding to $1/\text{velocity}$) through a variable volume fraction panel

2.4.5 B-scan Method

The third method investigated for determination of fibre volume-fraction (FVF) changes involves the use of high-frequency B-scan cross-sectional slices through the specimen (see Figure 2-23). The number of plies can be counted to determine the volume fraction. In addition, the velocity changes can be seen as changes in the apparent depth of the back surface.

In summary, isolation of surface loss can give an indication of volume fraction, but only near the surface, and may be influenced by the local resin thickness

before the first ply, depending on frequency. Bulk attenuation can be affected by porosity levels and small variations in fibre volume fraction can be masked by changes in surface losses and/or porosity. Velocity measurements may be affected by porosity levels, whereas B-scan ply-counting is satisfactory assuming plies can be imaged throughout the thickness.

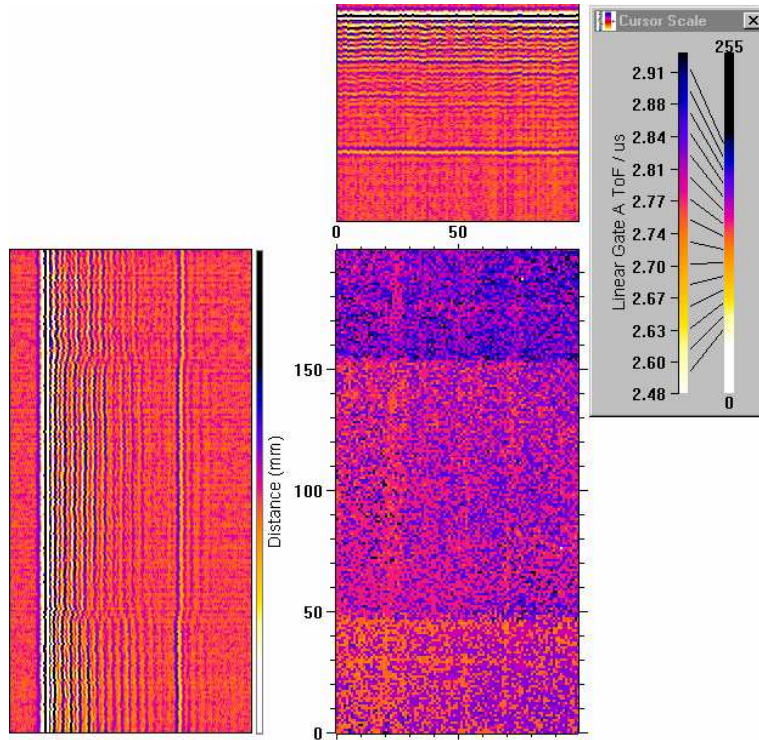


Figure 2-23. Image shows B-scan slices (left and top) and time-of-flight (bottom-right) through variable volume fraction panel. Change in number of plies and distortion at ply drop-offs can be clearly seen. Ply reflections nearer the back surface are less easily distinguished.

2.5 Ply stacking sequence

2.5.1 Introduction to ply stacking sequence methods

Non-destructive inspections for many types of defect are performed routinely at manufacture and during the service life of carbon-fibre composite structures. However, checking of the ply stacking sequence present in a component is rarely performed non-destructively due to tight quality controls during manufacture. These usually require the destructive inspection of an offcut of the

same lay-up as the component itself. In some instances it is necessary for the stacking sequence to be checked independently.

Standard fractographic techniques, involving polishing and examination using a conventional optical microscope, can be performed at the edges of components. However, many components have complex ply reductions in the central area, away from any edges, and these components may need to be checked in the centre to verify which ply orientations extend across the whole component.

2.5.2 *Review of earlier work*

Previous techniques have involved the use of eddy currents (Prakash & Owston 1976, Owston 1976 and Summerscales 1990b) and ultrasonics (Prakash & Owston 1977; Dreumel & Speijer 1983) but both methods produced a polar diagram which required comparison with specimens of identical stacking sequence. Thus it would be possible to deduce that a deviation from the expected sequence existed but difficult to determine the exact sequence that was present. Theoretical models were developed for both the eddy-current and ultrasonic techniques but no further work to develop the stacking sequence capabilities was felt necessary at the time by any of the authors.

In 1993 a technique was developed by the author at QinetiQ (Smith & Clarke 1994) to ultrasonically inspect each ply of unidirectional pre-preg CFC and determine the ply stacking sequence. This proved useful for determining that the incorrect plies had been terminated in the middle of the skin of a honeycomb structure.

In a unidirectional pre-preg CFC material the inter-ply interfaces are generally flat and the ply thickness constant. By using a gate width equivalent to half the ply thickness it is possible to image the dominant fibre directions at this depth – see Figure 2-3. In general two ply directions can be seen on the resultant C-scan, corresponding to the plies above and below the inter-ply reflecting layer. By repeating this for all depths the stacking sequence can be obtained. This is done using a high frequency pulse-echo technique and capturing the entire ultrasonic waveform representing the thickness of the panel.

The reason for two ply directions being visible was thought to be due to the fact that the main reflection at the ply interface is from the inter-ply resin layer, where the thickness of the layer is approximately proportional to its reflection coefficient. It therefore seems natural that the thickness of the inter-ply resin layer should be influenced by the fibre tows both above and below it.

2.5.3 More recent work

Subsequent work by Hsu et al (2002), reproduced the author's original work and then went on to use 2D Fourier Transforms to accurately determine ply orientation for carbon-fibre composites (CFCs). They introduced the idea of producing a greyscale map of angular distribution against depth, which has been further developed and refined in this PhD project.

2.6 In-plane Fibre waviness

The above technique was also successfully applied by the author and colleagues for the detection of in-plane fibre waviness in RTM panels manufactured in non-crimp fabric (NCF) for a previous project (Figure 2-24).

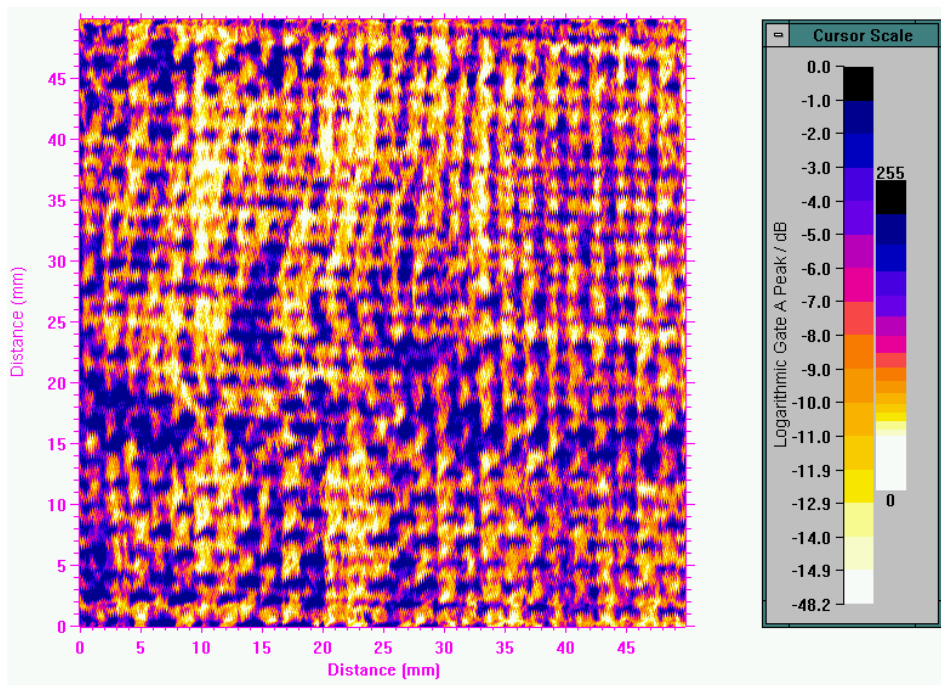


Figure 2-24. Fibre distortions in a non-crimp fabric RTM specimen caused by deliberately teasing the fibres in one ply after cutting the stitching. The scan was produced by gating over one inter-ply reflection.

The significant differences when applied to RTM materials are the use of thicker plies and variable ply thickness depending on fibre volume fraction. Non-crimped fabric laminates emulate normal unidirectional pre-preg in that each ply contains fibres in one direction and the inter-ply interfaces are nominally flat. However, woven materials have two orthogonal fibre directions (warp and weft) within each ply and the inter-ply interface has a more variable thickness.

Several panels were manufactured from five-harness satin-weave material to test the suitability of the ultrasonic de-plying technique for the detection of in-plane wavy fibres. The central region of these 6-ply panels contained deliberate fibre distortions in the middle one or two plies. Attempts to ultrasonically de-ply these panels revealed a strong interference effect caused by the interaction of adjacent plies that does not appear on scans of plies above that with the in-plane waviness (see Figure 2-25).

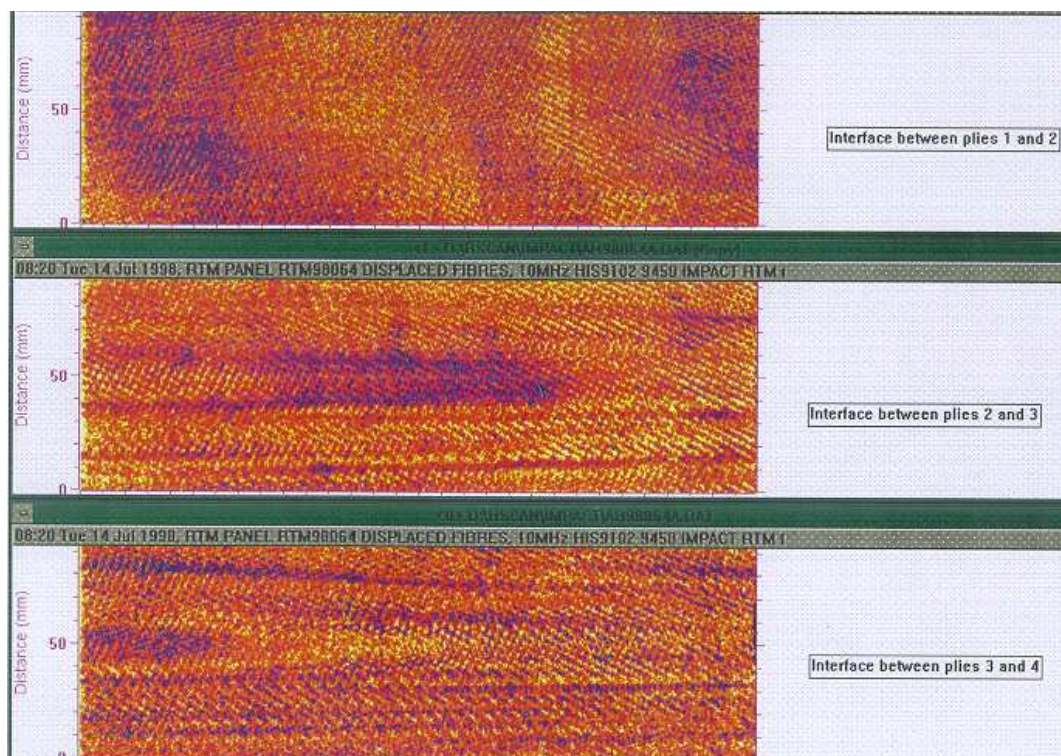


Figure 2-25. C-scans gated on ply boundary reflections in an in-plane waviness panel. The waviness was in the 3rd ply with a periodicity of around 100 mm and an amplitude of 15 mm in the centre of the panel, decreasing to the top and bottom of the scans. Note the interference effects (horizontal lines in the lower images) caused by the interaction of adjacent plies. In the middle and lower scans, which both include ply 3, but not in the top scan, which does not.

As the number of plies that the ultrasound has to pass through increases, so the interference effects increase. It is however possible to extract the information with the use of image processing techniques although the image is not as clear as those obtained from the NCF materials. Another effect noticed when stepping through the inter-ply reflection is that the interference effects can be either constructive or destructive. It is possible that this information could be used to infer the presence of fibre distortions.

In order to reduce the high level of noise on the C-scans a bandwidth limit was applied to the ultrasonic waveforms that were gated to generate the C-scan. Unfortunately this failed to have any positive effect on the detection of in-plane fibre waviness.

There is a possibility of using image processing and pattern recognition techniques (such as a Hough transform for detecting lines in an image) to highlight the inter-ply signals and enhance the imaging of waviness.

Another method that worked well when attempted during the author's earlier project was the use of kevlar tracer fibres which were then imaged using X-radiography. This method worked well for thin panels but is non-preferred on grounds of the effect on the structural properties.

2.7 Out-of-plane ply wrinkling

2.7.1 *Volume fraction as an indicator of out-of-plane ply wrinkling*

In thin RTM panels, out-of-plane ply wrinkling will usually take the form of fibre crimping, where fibres are folded back upon themselves. This can lead to a local increase in volume fraction associated with the crimping, but with relatively thin panels this crimping represents a large increase in volume fraction, often leading to poor fibre wet-out and porosity. It is therefore possible to image this severe out-of-plane wrinkling as changes in attenuation due to local volume-fraction changes caused by the crimping method, but there would be no ability to characterise the cause of the attenuation change. In addition, there are the same problems of potential complementary surface loss changes, requiring the isolation of surface loss from bulk attenuation.

Ultrasonic velocity changes are also indicators of local fibre volume fraction changes and may be imaged in order to identify locations of out-of-plane fibre waviness.

2.7.2 *B-scan imaging for out-of-plane ply wrinkling*

In a large stack, a single wavy ply is insignificant in terms of volume fraction change, but it could be seen by B-scan imaging of the plies. A B-scan system such as the author's ANDSCAN software allows a slice through the thickness to be displayed in both x and y orientations showing all the inter-ply reflections in a stack, enabling out-of-plane fibre waviness to be imaged. This system is now flexible enough to rapidly process the large full waveform data files and display a real time B-scan image for any point on the C-scan. Other features incorporated include 256 level colour or monochrome resolution, RF or rectified display, an adjustable bandwidth limit, and distance amplitude correction (DAC) facilities to compensate for the effects of attenuation.

2.7.3 *Experimental results for out-of-plane fibre wrinkling*

Out-of-plane fibre wrinkling was created in a series of carbon fibre RTM6 panels by distorting the dry fibre pre-form prior to moulding. The panels were manufactured with two different fibre volume fractions, both 2 mm thick but with either 6 or 7 plies. Control panels with the same number of plies were manufactured with no distorted plies. Initially the panels were C-scanned using a standard through-transmission technique to check for variability or any evidence of the distorted fibres. Both control panels appeared acceptable from the attenuation scans although both 7 ply panels had a small area of gross porosity. The attenuation scan of the 7 ply fibre waviness panel showed no obvious evidence that distorted fibres were present but had a similar area of gross porosity as the control panel. The 6 ply fibre waviness panel had a distorted line running across its entire width which showed a significant increase in attenuation.

The full waveform ultrasonic data was initially collected at a modest frequency of 10 MHz using a weakly-focused transducer. B-scan slices through both control panels showed no significant fibre distortions. Those small distortions

imaged were consistent with the use of a woven fabric, although it should be noted that as the volume fraction increases it becomes more difficult to extract the B-scan information as the inter-ply reflections appear to become weaker. The B-scan images of the 6 ply panel with deliberately introduced fibre waviness (see Figure 2-26) show significant distortions in the central plies over the area identified in the attenuation C-scan, and in areas extending into the plies above and below. The distortion introduced in the pre-form will have caused the fabric to buckle in these areas and may have cause either a variation in volume fraction or some porosity which is imaged in the amplitude C-scan.

The 7-ply panel (see Figure 2-27) showed significant distortion distributed through the mid plies in the central region. In some areas the distortion was so severe that the interface reflection was lost totally, again suggesting fibre buckling but to a lesser extent than seen in the lower volume-fraction panel. The panels were subsequently re-scanned at both 15 and 22 MHz to see if the quality of the B-scan image could be further improved, but the increased attenuation at these higher frequencies offset the potential increase in axial resolution.

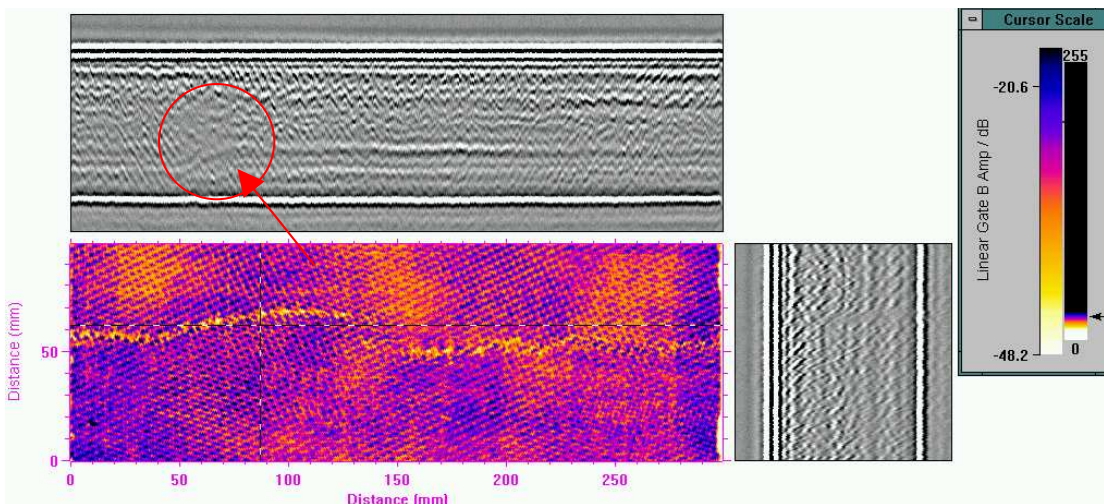


Figure 2-26. B-scan image of through thickness waviness in 6-ply specimen. A large angular displacement of fibres makes it difficult to get a reflection back from ply interfaces and porosity around fibre waviness also reduces reflected amplitude. Hence the indicated region shows distorted fibres.

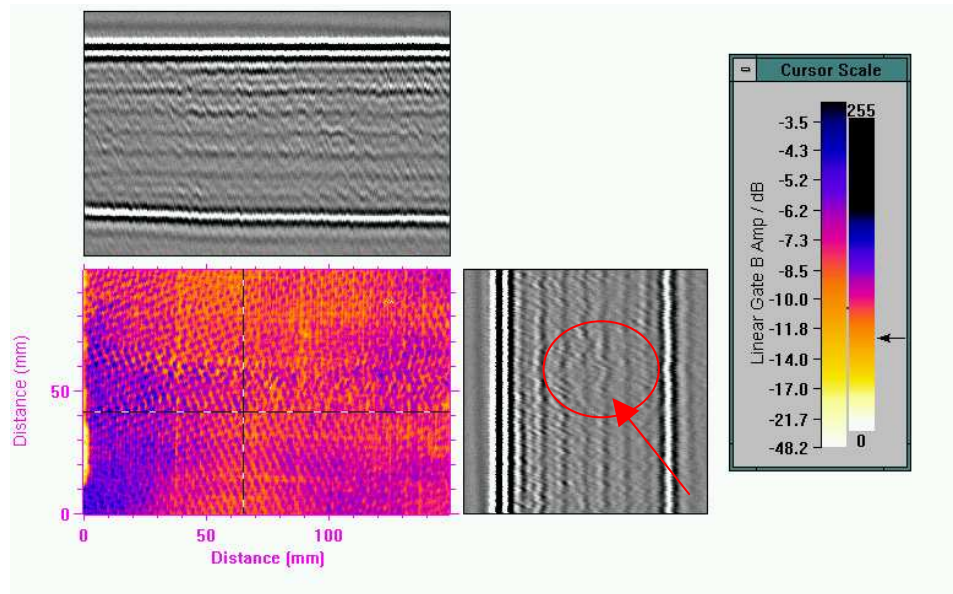


Figure 2-27. B-scan image of through thickness waviness in 7 ply specimen. A large angular displacement of fibres makes it difficult to get a reflection back from ply interfaces and porosity around fibre waviness also reduces reflected amplitude. Hence the indicated region shows distorted fibres.

A 4 mm RTM6 woven carbon panel produced with 12, 14 and 16 ply areas was scanned at 10 MHz. This panel had the extra plies added at its mid plane, therefore the plies either side of here would become distorted through the thickness at the step volume fraction changes. B-scan images across the volume fraction changes proved excellent at imaging the distortions in these areas (see Figure 2-28).

There are several methods for enhancing the inter-ply reflections, including use of the DAC, by bandwidth limiting and by performing a deconvolution with the front-surface signal as the reference.

Figure 2-28 and Figure 2-29 show the effects of introducing a DAC and a bandwidth limit – the deep inter-ply reflections are much clearer than in the raw images in Figure 2-23 and Figure 2-26 respectively and the actual two plies that stop at two locations can be seen in the left-hand B-scan.

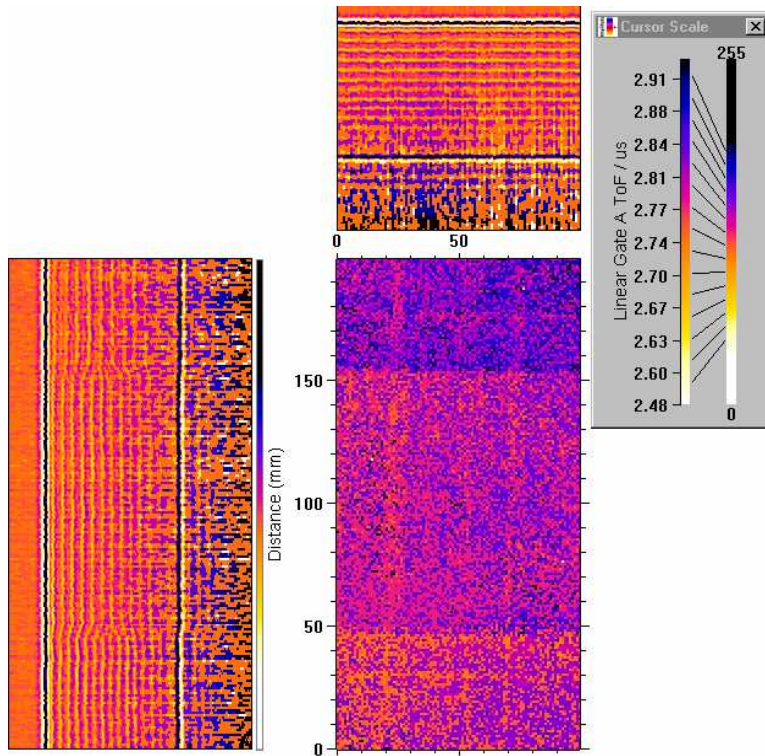


Figure 2-28. This image should be compared with the raw, unprocessed image in Figure 2-23. In the above image a distance-amplitude correction (DAC) has been applied plus an 8 MHz bandwidth limit. The bandwidth limit helps to reduce noise levels and cleans up inter-ply reflections, whereas the DAC allows imaging of plies nearer to the back surface.

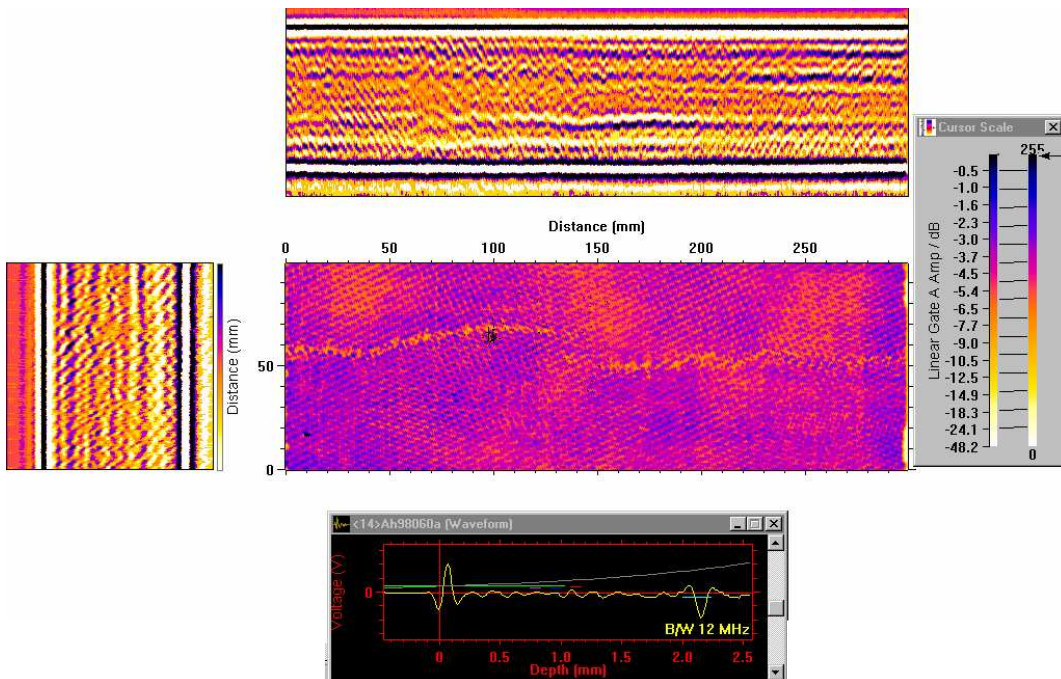


Figure 2-29. A 12 MHz upper frequency limit and DAC applied to the waveform data shown in Figure 2-26.

2.8 Discussion

This chapter has reviewed the development of various NDT methodologies for the inspection of composites over the past 40 years. It is clear that ultrasonic methods were recognised as offering great potential right from the early development of composite materials. However, despite considerable research effort since then, the real benefits of ultrasound inspection had still not been fully exploited for composites by 2005 when this project began. For example, most inspection was performed using analysis of either A-scan waveforms, or two-dimensional in-plane C-scan maps. These C-scans generally provided a through-thickness average parameter representing the attenuation (or insertion loss) for the whole specimen. A variant of the C-scan, the Depth-scan (or D-scan) did plot the depth of a signal, and Pseudo-3D images of the same data were developed in the 1990s, but depth-dependent information was uncommon and full B-scan cross-sections were rarely used.

The main reason for this predominance of through-thickness average information was the complexity of the pulse-echo response of the laminated structure to ultrasound compared with the apparent simplicity of a through-transmission or back-wall echo signal. Attempts to understand the full pulse-echo response and generate parameters that accurately reflected structural variations in the laminate had merely shown how difficult the problem was.

Another impasse in the development of composite inspection methods was the inability to provide measurements of actual material properties and thereby remove the need for expert NDT interpretation of results. This has been a constant source of frustration for manufacturers of composite materials who have repeatedly requested advanced automated analysis methods, which can output quantitative plots of real material properties, requiring no interpretation.

The current project aims to extend the inspection of composites to include 3D quantitative characterisation of the laminate itself and any deviations from the designed structure in terms of porosity, ply spacing, fibre-volume fraction, ply stacking sequence, in-plane fibre waviness or out-of-plane ply wrinkling. The project is necessarily broad in terms of the range of material properties so much of the validation of new methods will be covered in future work.

CHAPTER 3 REVIEW OF MODELLING OF ULTRASOUND PROPAGATION IN INHOMOGENEOUS MATERIALS

3.1 Motivation

In order to develop and evaluate new ultrasonic methods for three-dimensional characterisation of composite materials, it is necessary to use ultrasonic propagation modelling to gain a deep understanding of the interaction of ultrasound with these composites. The use of a model can make evaluation and refinement of new methods both possible and rapid when it is impractical to use experimental data due to the sheer number of possible scenarios and the difficulty of destructive characterisation – often the only other way to determine the exact properties of the materials and to map them in three dimensions.

The composite materials under consideration include multi-ply layered materials such as carbon-fibre or glass-fibre in a polymer-resin matrix, GLARE – a layered hybrid material comprising thin aluminium layers alternating with glass-fibre composite layers, and metal-matrix composites such as Titanium with Silicon-Carbide fibres in a periodic lattice – usually hexagonal. The types of defects to be modelled include porosity, which can be thought of as particulate scatterers, thick resin inter-ply layers, and changes in ply spacing. Hence this review of modelling methods includes particulate, periodic and layered structures.

As the objective of this work is to develop 3D characterisation methods from normal-incidence ultrasonic inspection, it is appropriate to restrict this review of modelling methods, and the development of the model itself, to normal-incidence compression-wave insonification of composite materials with in-plane layers. This constraint reduces the modelling problem to a much simpler one, where anisotropy can be largely neglected and the normal-incidence ‘effective medium’ properties can be determined for each composite layer using appropriate mixture rules.

An important part of modelling inhomogeneous composite layers is this mixture-rule method used for combining the properties of two or more different materials to obtain 'effective medium' properties that realistically represent the combined material. These mixture rule methods are reviewed and compared in Chapter 4, which describes the model developed in this project.

3.2 Particulate structures

The main reason to include modelling of ultrasonic interaction with particulate structures is to allow for the presence of porosity in composite materials. However, it should be noted that the modelling of ultrasonic scattering is a huge subject in its own right and is not part of the project work reported here. It was always intended to include the effects of scattering from porosity by collaboration with other members of the Applied Ultrasonics group at the University of Nottingham specialising in this area, and this collaborative work is covered in Chapter 4 as part of the mixture-rule development. However, the following review of modelling methods for particulate structures is included for completeness and for reference in the rest of this thesis.

3.2.1 *Ultrasonic scattering theory*

The first mathematical investigation of the scattering of sound was by Lord Rayleigh (1896) but he only considered the long-wavelength (small scatterers) limit. Morse (1948) considered larger scatterers and eventually extended his work to include the propagation of sound inside the scatterer. Faran (1951) extended this further to include shear waves, which can exist inside scatterers.

Then followed the three classical formulations of the diffraction problem for a compression wave incident on a single particle: the first by Epstein and Carhart (1953) for liquid particles in a liquid medium, the second by Ying and Truell (1956) for solid particles in a solid medium, and the third by Allegra and Hawley (1972) for solid or liquid particles in liquid. The equivalence of these three formulations has more recently been demonstrated by Challis et al (1998a) who have shown the Allegra-Hawley formulation to be adaptable to provide a basis for calculation in all three scenarios. It is this formulation that underpins the

model used at the University of Nottingham (Challis et al 1998b) to calculate the ultrasonic attenuation and velocity in scattering fields.

Habeger (1982) described the Allegra-Hawley formulation as an exact solution to the basic governing equations, which reduces to the less-complete models, such as those of Sewell (1910), Epstein (1941), Lamb (1945) and Urick (1953), as limiting cases. It should be noted that Davis (1979) has more recently corrected a sign error in the Allegra-Hawley boundary conditions and discussed its extension to more dense suspensions. Attenborough & Walker (1972) performed calculations with cylindrical inclusions for the long-wavelength case, whereas Habeger (1982) was concerned about shorter wavelengths – of the order of a radius of the cylinders they were considering.

A completely different theory, originating from the classical resonance theory of nuclear reactions, has been applied by Flax & Dragonette (1978) to acoustic scattering from elastic cylinders and spheres in a liquid. The resonance effects are in the particles themselves and these are superimposed on the rigid-body scattering. The study reveals that the elastic particles are relatively impenetrable to the incident wave except at the resonant frequencies, which occur at the eigenfrequencies of the elastic vibrations of the body.

3.2.2 Scattering from particulate fibres

The Gaunard and Uberall (1983) paper is of interest because it determines an effective medium via a scattering approach, and also investigates what concentration of scatterers is the limit before multiple scattering needs to be taken into account – yielding a limit of approximately 25% concentration. Otherwise, this paper is of little interest because it deals with particulate solid composites modelled as an aggregate with a random 3D distribution of solid elastic spheres in an elastic matrix. This situation is substantially different to long-fibre composites with porosity.

A more complex approach for random fibrous composites is given in a letter by Beltzer and Brauner (1984). This uses a theoretical determination of attenuation based on the microstructure and then the Kramers-Kronig relations to determine the wave speed in composite where fibres are aligned parallel to

an axis. Only the fibre volume fraction ϕ_f is required to determine the attenuation as a function of the frequency and fibre-radius product. However, the method applied appears to use an axially polarized shear wave and it is not clear to what extent this has influenced the outcome, or whether it is also applicable to the normal-incidence compression-wave case required for the current project.

3.2.3 Scattering from porosity in solids.

The review in Chapter 2 of experimental measurements of porosity in composites mentions models generated by Martin (1976, 1977), Reynolds and Wilkinson (1978), Hsu and Nair (1987), as well as Jeong and Hsu (1995), by way of comparison with experimental data. These are revisited briefly here after discussing the model of Adler (1986) used in this project.

Adler et al (1986) developed a theory for determining ultrasonic attenuation from porosity in solids based on the frequency dependence of scattering as a function of the size and volume fraction of the pores. This theory was based on the formally exact expressions developed by Gubernatis and Domany (1984) and used, for the scattering cross-section, numerical evaluations of the series expansion of Ying and Truell (1956). The useful aspect of this work is that they generate analytical expressions for the frequency-dependent attenuation as a function of pore size and volume fraction in both the short-wavelength and long-wavelength limits. For this reason, this method was chosen to calculate analytically the attenuation due to porosity in the model developed for this project – see Chapter 4.

The equation for the scattering attenuation coefficient $\alpha(k)$ derived from Adler

$$\text{is:} \quad \alpha(k) = \frac{3\phi_v}{4a} \Gamma(ka) \quad (3-1)$$

where ϕ_v is the void volume fraction, k is the wavenumber, a is the radius of the pores, and Γ is the reduced scattering cross-section. A scattering cross-section describes the area of a single scatterer that acts as an effective ‘source’ of ultrasound at a particular angle relative to the incident ultrasound – in this case

0° because it is forward scattering being considered here. The *reduced* scattering cross-section is a dimensionless function defined as the proportion of the actual cross-sectional area of the scatterer (perpendicular to the incident angle) that acts as an effective source of ultrasound propagating in a particular direction. This actual cross-sectional area is effectively the geometrical limit of the scattering cross-section for high ka values (ie the short-wavelength limit). Adler explains that the reduced scattering cross-section depends on the host medium's Poisson ratio only, which is also manifested in the ratio of shear to longitudinal velocities, η and is plotted in the graph reproduced from Adler et al (1986) in Figure 3-1.

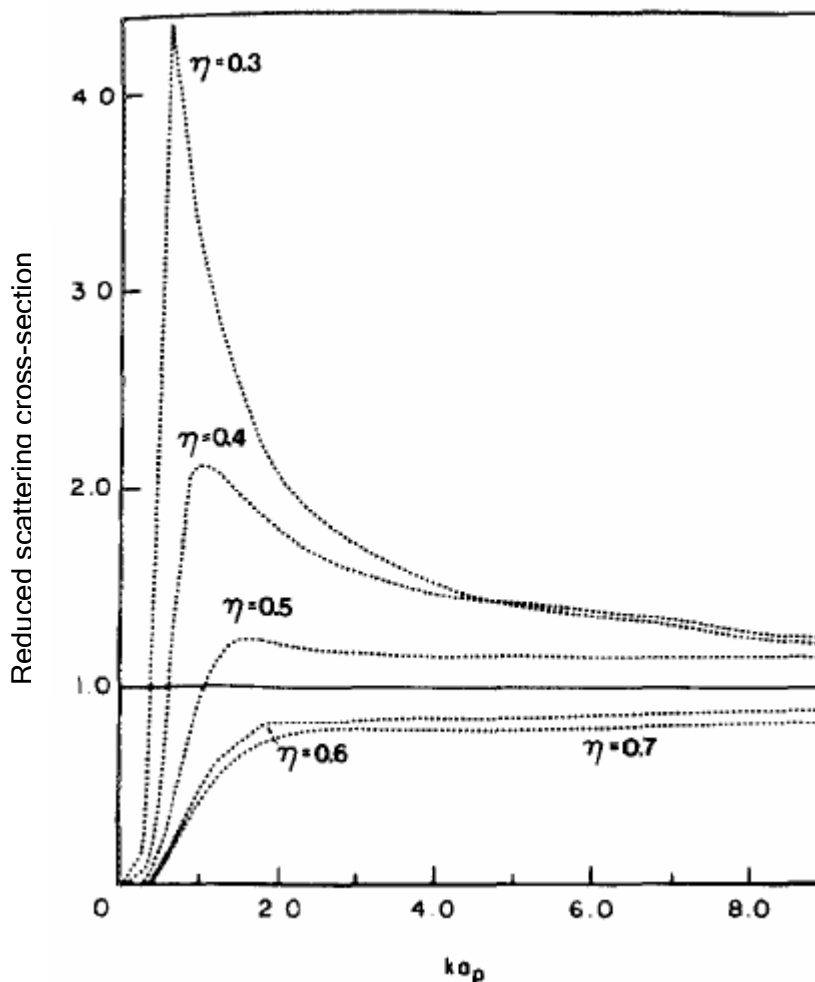


Figure 3-1. The reduced scattering cross-section determined by Adler et al (1986), based on a series expansion of Ying and Truell (1956) and reproduced here from the Adler et al (1986) paper.

The long-wavelength (low ka) equation given by Adler et al (1986) for the reduced scattering cross-section is:

$$\Gamma(ka) = \beta(\eta)k^4 a^4 \quad (3-2)$$

where β is a function of η plotted graphically by Adler et al (1986) from the series expansion of Ying and Truell (1956), and reproduced in Figure 3-2.

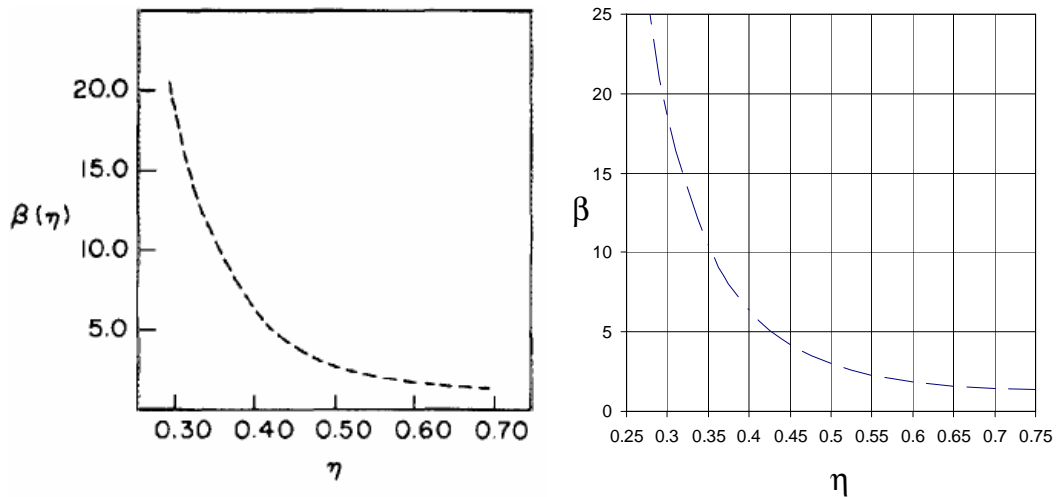


Figure 3-2. Graphical representation of $\beta(\eta)$ derived by Adler et al (left) and by the author (right) from the series expansion of Ying and Truell (1956) given in Equation 3-3.

Ying and Truell (1956) use a definition of η that is the reciprocal of the one used by Adler et al (1986) so their expansion has been modified to be consistent with Adler et al (1986) and is given in Equation 3-3:

$$\beta(\eta) = \frac{2}{9} \left(\frac{4}{3} + 40 \frac{2 + 3\eta^{-5}}{(4 - 9\eta^{-2})^2} - \frac{3}{2}\eta^{-2} + \frac{2}{3}\eta^{-3} + \frac{9}{16}\eta^{-4} \right) \quad (3-3)$$

The short-wavelength limit scattering attenuation coefficient $\alpha(k)$ derived from Adler, where $\Gamma(ka) \rightarrow \Gamma(\infty)$ as $ka \rightarrow \infty$ is given in Equation 3-4:

$$\alpha(k) = \frac{3\phi_v}{4a} \Gamma(\infty) \quad (3-4)$$

Martin (1976) uses the same expressions as Adler et al (1986) derived from Ying and Truell (1956) considering scattering from a single spherical void. However, Martin proposed that, for high concentrations of multiple voids, the ultrasonic velocities of the surrounding medium should be modified to allow for the void content. The author feels that this is debatable, and Martin's results, by comparison with the experimental measurements of Stone and Clarke (1975) are far from convincing.

Hale and Ashton (1988) have proposed a refinement of the model of Martin (1976) in order to fit the data of Stone and Clarke (1975). The refinement is that they assume small spherical voids at low concentrations (<1.5%), but flattened discs at higher concentrations, as observed experimentally by Stone and Clarke (1975). Attenuation due to disc voids was calculated by Hale and Ashton and takes the functional form:

$$\alpha(k) = \frac{\phi_v}{t} \Gamma(ka) \quad (3-5)$$

where t and a are the thickness and radius of the disc respectively, and the reduced scattering cross-section in the long-wavelength limit is given by the spherical version in Equation 3-2. Distributions of void sizes were incorporated prior to the comparison of this model with the Stone and Clarke (1975) data, which is reasonable at 7 MHz, but poor at the two lower frequencies: 5 MHz and 2.5 MHz.

3.3 Layered structures

Having reviewed particulate structures, this section now considers modelling of the layered composite structures that are the main focus of this project. Limiting the ultrasonic propagation to normal-incidence and compression waves does simplify the modelling, and therefore the literature review, because the majority of models consider oblique incidence propagation through anisotropic media, often including guided waves as well. For normal incidence plane waves, each composite layer can be considered to be transversely isotropic.

3.3.1 Previous reviews

An excellent review of the layer models developed in the last 60 years was published by Lowe (1995), clearly distinguishing between response models, which calculate reflection and transmission response of a multilayered system to an incident plane wave, and modal models, which address plate-wave propagation properties of the system.

The current project is only considering response models, and only for normal-incidence plane waves, where the layers can be considered to be isotropic effective media. Thus most of the formalisms reviewed by Lowe are far more complex than necessary for this project, although they do provide more general models against which the model for this project can be benchmarked.

Transfer-matrix response models are applicable to this project, where the displacements and stresses at the bottom of a given layer can be expressed in terms of those at the top of the layer, and a matrix can be used to express them at the bottom of a multilayered stack in terms of the top of the stack. Thomson (1950) and Haskell (1953) pioneered this method, often referred to as a 'propagator matrix' approach according to Lowe. A problem with the Thomson-Haskell propagator matrix was discovered by Dunkin (1965) and concerns the ill-conditioning of the matrix for large thicknesses and high frequencies, known as the 'large fd problem' (where f is the frequency and d is the thickness of a layer). Although several attempts have been made to resolve this limitation (Castaings and Hosten; 1993, 1994), it is unlikely to be of concern in the current project where layer thicknesses are of the order of a wavelength due to the need to exploit the low-order ply resonances in all the methods implemented here.

Many developments of the early work since 1980 have been inspired by the need to model propagation in composites, introducing viscoelastic and anisotropic media. In particular, the work by Hosten and Castaings (1993), and by Nayfeh and Chimenti (1991) contain general solutions for arbitrary angles of incidence on composite materials, but are far more complex than necessary for the normal-incidence, transversely isotropic case considered here.

Pialucha (1992) also generated a transfer-matrix model based on the Thomson-Haskell method but in order to solve the ‘large $f d$ problem’ resorted to using a global matrix approach, effectively a stiffness-matrix method similar to the one subsequently used by Wang and Rokhlin (2001).

3.3.2 More recent work, or from other fields

3.3.2.1 Skelton-James model

Interestingly, a completely separate line of work on acoustic propagation through anisotropic solids had been developed for underwater acoustics (sonar) applications by the UK’s Admiralty Research Establishment, culminating in the publication of a propagation-matrix model by Skelton and James (1992), which also uses a stiffness (or compliance) matrix as part of the formulation. This line of work converged with the above work reviewed by Lowe when Skelton moved to Imperial College and the work began to focus on the use of composites in maritime applications. More recently the model, which is now owned by QinetiQ, has been used to benchmark the model in the current project.

The Skelton-James model also deals with arbitrary angles of incidence through multi-layered anisotropic media and can determine plane-wave reflection and transmission coefficients. Each layer can be characterised by a complex infinite-plate compliance matrix. This matrix can be found analytically using a mixture rule of Wilczynski and Klasztorny (2000). Using the Skelton-James model, the behaviour of the individual layers in a sandwich composite may be combined and the overall acoustic behaviour of the infinite plate determined.

3.3.2.2 Stiffness matrix method

Wang and Rokhlin (2001) overcame the instabilities in the transfer matrix approach of Thomson-Haskell by using a layer stiffness (compliance) matrix to replace the layer transfer matrix. This method is shown to be ‘unconditionally stable’ and more computationally efficient than the transfer-matrix method. A recursive method is used to calculate the stiffness matrix in Rokhlin and Wang (2002a) and the method is used to determine the effective elastic properties of layers in composites in Rokhlin and Wang (2002b). The

final paper by Wang and Rokhlin (2003) describes the use of this recursive stiffness matrix method to generate time and frequency domain responses of multi-layered laminates and compares these with experiment. A normal-incidence transversely-isotropic version of this Wang and Rokhlin (2003) model was chosen as the most suitable for the current project in terms of the computation speed required for model-based decomposition – the ultimate objective for 3D characterisation of porosity in composites.

3.3.2.3 *MLM-Propmat*

A multi-layer model, *MLM-Propmat*, has been developed by Mienczakowski et al (2008) at the University of Nottingham, based on earlier work by Freemantle (1995). It is essentially a transfer matrix model using mixture rules to calculate the properties of each layer as effective media and is similar to the work of Pialucha (1992). This model assumes isotropic layer properties but can calculate propagation at an arbitrary angle. It was used for benchmarking the transversely-isotropic model developed in this project.

3.4 Equivalent media

A detailed critique and comparison of the various models proposed in the literature for equivalent media calculations is given in Appendix F with just a summary here for taking forward into the model used in this project

3.4.1 *Basic physics of mixtures*

It is assumed that composite materials can be described adequately by an elastic, homogeneous, isotropic matrix in which inclusions of another elastic, homogeneous, isotropic material exist, and that the density and moduli of both materials are known. Furthermore, it is assumed that the volume concentration is known and is uniform throughout the region considered, and that the material may be regarded as a quasi-homogenous and quasi-isotropic equivalent medium and described by effective elastic moduli and an effective density.

Until 1960, the determination of elastic moduli for solid mixtures of elastic media had only been studied for small concentrations (Eshelby, 1957; Hashin, 1958). Early attempts to extend these treatments to finite concentrations resulted in

numerous different formulae which were often contradictory. A review of these latter studies is beyond the scope of this thesis but summaries can be found in Frisch and Simha (1956) and Reiner (1958).

The models that were subsequently developed were based either on 1) a 'self-consistent approach' where stress or strain fields are analysed as a result of applying an external load, or 2) a 'variational method' considering the change in strain energy stored in a loaded homogeneous body as a result of inserting inhomogeneities (inclusions). For the variational method it was assumed that Hooke's law could be applied to relate stresses and strains in each direction, resulting in a stiffness matrix relating the multi-dimensional strain and stress tensors. This analysis was initially applied to spherical inclusions assuming that stress and strain are continuous across the boundary of each inclusion. Then, for fibres in a matrix, infinite elements of either circular or hexagonal cross-section were used, each containing a single fibre surrounded by a matrix, with similar boundary conditions and assumptions.

3.4.2 Spherical or cylindrical inclusions in an elastic matrix

A breakthrough occurred when Hashin (1962) abandoned the search for exact formulae for the moduli of equivalent media and proceeded by considering the generation of expressions for the upper and lower bounds of the effective elastic moduli. These expressions were found to coincide for the bulk modulus and to be very close for the shear modulus, allowing an expression to be derived that always lay between the upper and lower bounds. Two basic assumptions were made: firstly that the particles are spherical and secondly that the action of the bulk material on any one inclusion is transmitted through a 'virtual' spherical shell which lies wholly in the matrix. Long-fibre composites do not comply with the spherical-inclusion assumption but in fact the biggest deviation from a simple volumetric mixture rule is for dissimilar materials such as air and resin for porosity, rather than for carbon fibre and composite. However, glass fibre has about eight times the cross-axis compression modulus of carbon, and also violates this spherical requirement, so glass-fibre composites may need a different treatment.

Hashin derived expressions for the moduli (shear and bulk) for both very large and very small concentrations and showed that when the difference between the moduli of matrix and inclusions is small, then the equations reduce to a simple volumetric-ratio mixture rule.

Martin (1977) used the Hashin (1962) model for porosity in composite materials but realised the need for a different model for fibres in a matrix, before considering the porosity.

In a completely different approach, Pinfield et al (2010) has presented a treatment of a layer of porosity where the backscattered signals from the pores can be integrated over a random distribution of pores in a layer to determine the frequency-dependent backscattering cross-section. The layer can then be represented as an equivalent medium with a complex impedance, the imaginary part of which accounts for the frequency-dependent backscattering process. Spherical and cylindrical pores are dealt with and the backscattering amplitude includes consideration of the morphology type of the pores.

3.4.3 *Isotropic fibre reinforcement of an elastic matrix*

A useful review of models for predicting elastic constants in composite materials has been produced by Halpin (1992) in Section 6.3 of his book, a second edition of the earlier Ashton et al (1969).

Specific extensions of the Hashin (1962) 'variational method' to the case of long-fibre reinforced composites have been undertaken by Hashin and Rosen (1964), Hill (1964a) and Greszczuk (1966), whilst Hill (1965a) and Whitney and Riley (1966) pursued a 'self-consistent model' approach.

3.4.3.1 *Variational models*

Hashin and Rosen (1964) developed the composite cylinder assemblage (CCA) model, which looks specifically at the case where each fibre can be considered as a cylinder of fibre material surrounded by a matrix material, extending from one end of the specimen to the other, so end effects can be neglected. Two cases were considered – the first with fibres of equal circular cross-sections arranged in a hexagonal array, the second being a randomised arrangement of

fibres of different circular cross-sections whose diameters range from finite to infinitesimal. As with the spherical inclusions of Hashin (1962), upper and lower bounds were generated for the bulk and shear moduli. In the normal fibre-composite case, the lower and upper bounds coincide for the bulk modulus but not the shear modulus.

Tsai (1962a; 1962b) and Azzi and Tsai (1965a; 1965b) developed a model that is similar to Hashin and Rosen (1964) and uses a variational principle based on theorems of minimum potential energy to generate upper and lower bounds of the elastic constants.

Hill (1964a) produced analogous equations for the bounds to those of Hashin and Rosen (1964), considering a mathematical model of a large number of filaments so that local irregularities have negligible effect.

Hashin (1965) generalised the geometrical cases considered by Hashin and Rosen (1964) - the CCA model - to include a range of fibre sizes surrounded by larger cylinders of matrix material where the only restriction is that of transverse isotropy in the statistical sense.

Behrens (1967a; 1967b; 1969a; 1969b) developed an independent model using rectangular symmetry which produces an identical equation to Hashin (1965) for the bulk modulus, but a single equation for the shear modulus. This shear modulus must be for shear modulus parallel to the fibres because it matches Whitney and Riley (1966) and is equivalent to the lower bound of Hashin (1965), once it is corrected to the version that R E Smith (1972) quotes (equation 8b of his paper) - see Appendix F.

3.4.3.2 *Self-consistent models*

Hill (1965a) used the 'self-consistent' method to model the composite as a single fibre embedded in an unbounded homogeneous medium, indistinguishable from the composite. Whitney and Riley (1966) modelled, using the 'self-consistent method', a hexagonal array of repeating cylindrical elements, each containing a fibre surrounded by resin matrix. Although their method is claimed to be "written to appeal to the engineer rather than the

mathematician”, it appears to be considerably more complex than Hashin’s and contains several errors which are revealed in Appendix F.

Greszczuk (1966), with little reference to any previous work, modelled a rectangular array of circular filaments embedded in a continuous elastic matrix, rather than using repeating composite elements. He generated separate expressions for longitudinal (in fibre direction) and transverse Young’s modulus and compared his equations with “a more rigorous method” apparently using numerical methods and claimed agreement within 10% in the range 50% to 73% fibre volume fraction. However, above 90% fibre volume fraction the Geszczuk equations become unstable (see Appendix F for a full discussion). This method also ignores any interaction between fibres and matrix.

Martin (1977) took the equations of Greszczuk (1966) and Whitney and Riley (1966) and combined them into an isotropic-fibre model yielding equations for all the relevant elastic (stiffness) constants. He then went on to extend this to anisotropic fibres (eg. Carbon and Graphite) – dealt with in the following section.

3.4.3.3 *Comparison of models*

A comparison of the various methods discussed above is given in Figure 3-3 for the compression modulus, M , calculated from the bulk and shear moduli using Equation F-8, and in Figure 3-4 for compression velocity, $c = \sqrt{M/\rho}$. For Hashin (1965), Equations F-32 (transverse bulk), F-33 (transverse shear) and F-35 (longitudinal shear) are used. For Whitney and Riley (1966) Equation F-38 is used for bulk modulus but they use the Hashin (1965) lower-bound longitudinal shear modulus equation so this (Equation F-35) is used for the graph. For Behrens (1969a), the Equations F-56 and F-57 quoted by R E Smith (1972) are used. It can be seen that, apart from the Greszczuk method (Equation F-51), there is reasonable agreement. Possible reasons for the discrepancies shown by the Greszczuk method are discussed in Appendix F.

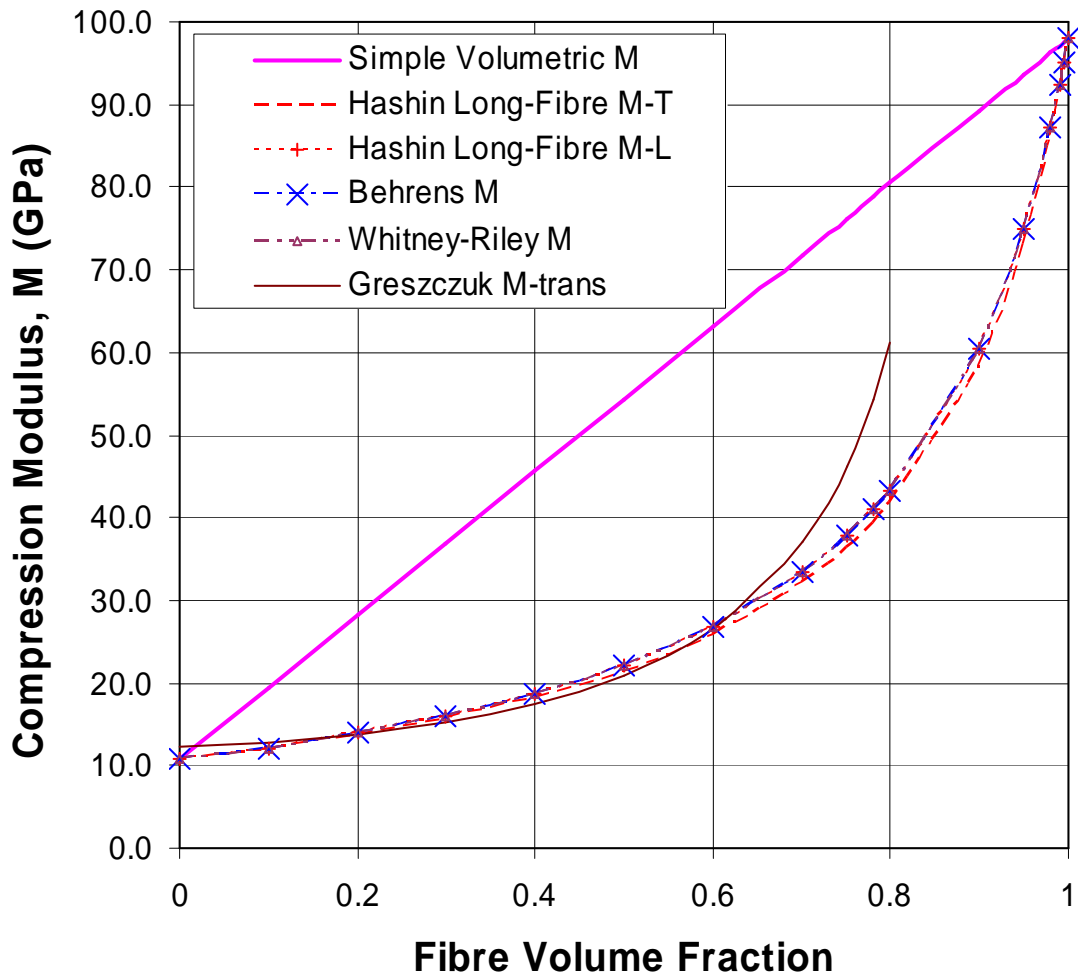


Figure 3-3. Comparison of compression modulus for S-glass fibre epoxy composite calculated using various methods from the literature. The Greszczuk modulus is actually the transverse modulus (across the fibres). The Hashin moduli have been calculated using the lower bounds for both longitudinal shear (1-2 plane) and transverse shear (2-3 plane) modulus.

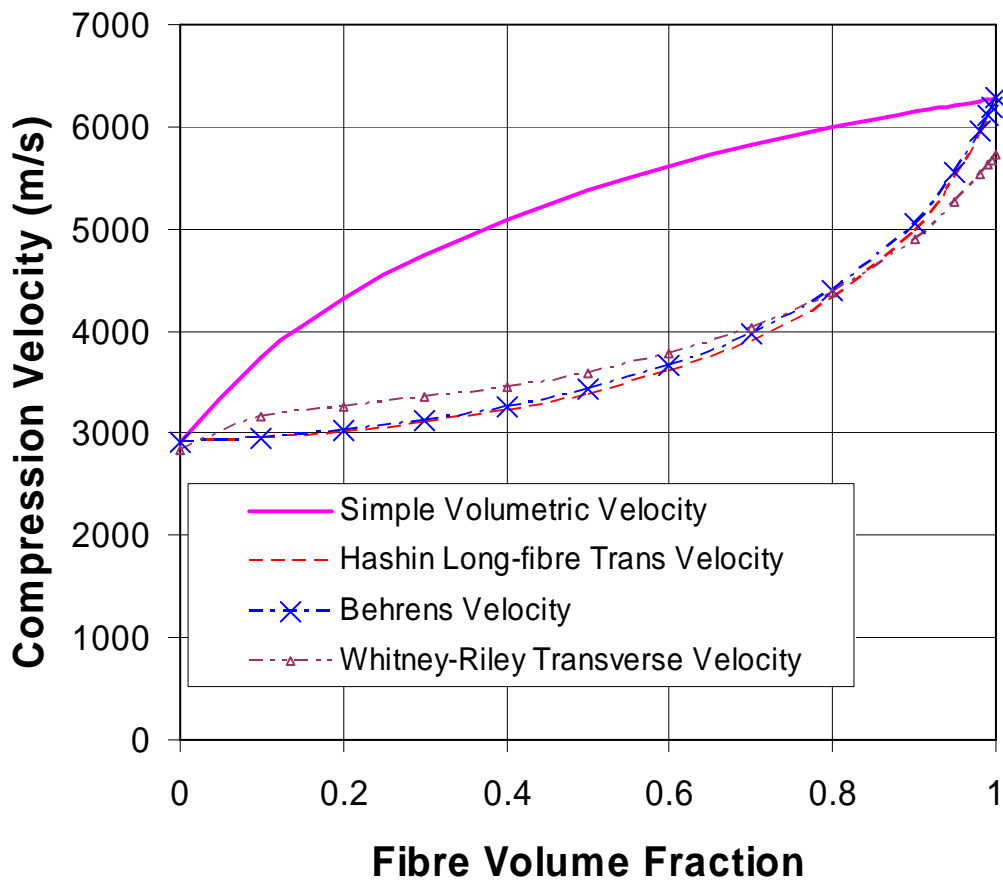


Figure 3-4. Comparison of transverse ultrasonic velocity for (isotropic) S-glass fibre composite calculated using the various models for fibre composites. Greszczuk is not included due to the difficulty of determining velocity

3.4.3.4 Validation of isotropic long-fibre models

Validation of these theoretical equivalent-medium models has been minimal. Whitney and Riley (1966) used static methods to determine tensile and shear modulus in comparison with Hashin and Rosen (1964), Tsai (1962a; 1962b), and their own model. They obtained good agreement between experimental results and their own model, and with the Hashin and Rosen upper-bound theoretical predictions for the transverse moduli, but not with Tsai's model. For Poisson's ratio the trend with fibre volume fraction was in good agreement but the absolute values measured were considerably lower than predicted. They suspected that the type of strain gauge used was reinforcing the material in the transverse direction and causing the discrepancy. For shear modulus their

comparison was with the Hashin and Rosen equation only, and agreement with just two experimental data points of their own, and one from an external source, was poor. Tsai (1964) has suggested using a 'contiguity factor' to adjust the predicted values and there is also an issue of the difference between static and dynamic stiffness. Whitney and Riley point out that neither they, Tsai nor Hashin and Rosen have considered the interaction between adjacent filaments in their model, which may be of considerable importance for composites under shear load.

Greszczuk (1966) compared transverse and longitudinal Young's Modulus, and shear modulus, with experimental data from Tsai (1964) and Schneider (1964) and claimed good correlation. However, a fairly simple assessment shows that all the methods shown in Figure 3-3, apart from the simple mixture rule, would have correlated well with this experimental data.

Zimmer and Cost (1970) used ultrasonic velocity measurement of longitudinal and shear waves in various directions through a glass-fibre composite as a method for obtaining elastic stiffness constants, and thereby testing the above three theories for elastic properties of a fibre composite. Glass fibre has a much higher stiffness than carbon fibre, giving a much bigger difference in properties between fibre and matrix, so this was a choice that gave true potential for determining the validity of the theories. Although problems of dispersion in the composite were investigated, Zimmer and Cost were able to justify neglecting them on the basis that they are not appreciably greater than the experimental error in the method. Experimental measurements of the five elastic constants were compared by Zimmer and Cost with predictions from three earlier theories (Hashin and Rosen, 1964; Whitney and Riley, 1966; Greszczuk, 1966). They reported that the Greszczuk theory was the only one to come within the measurement uncertainties in most cases and this was not unexpected because they regarded this model as the most realistic, comprising fibres in a continuous matrix rather than repeated composite elements. In addition, the Greszczuk theory predicted a C_{33} modulus (the one that is relevant to transverse ultrasonic propagation across a fibre-composite ply when the fibres are in the '1' direction) that was very close to Zimmer and Cost's experimental

value, whilst the other two theories' predictions underestimated by more than 30%. This comparison was made after Zimmer and Cost had applied a 40% mark-up in modulus of the epoxy resin matrix in the three models to allow for the difference between static and dynamic moduli of a viscoelastic material. It is unclear how justifiable such a mark-up is as it will be very dependent on the state of cure of the resin. Zimmer and Cost referred to Bodner and Lifshitz (1967) and Schultz and Tsai (1968) to justify it. However, whilst Greszczuk's method gave the best absolute values of modulus, the trend in Greszczuk's Young's Modulus with angle to the fibres does not match the experimental data as well as either the Hashin and Rosen or Whitney and Riley methods. Also, Zimmer and Cost failed to correct the mistake in Whitney and Riley (1966) for plane-strain bulk modulus, so it is unclear whether they were using the corrected equations to plot the predictions (see Appendix F).

3.4.4 Anisotropic fibre reinforcement of elastic matrix

According to R E Smith (1972), silica and glass fibres are isotropic materials but carbon or graphite fibres are only isotropic perpendicular to the fibre axis and can have a factor of 10 (carbon) to 20 (graphite) higher axial modulus than transverse modulus. Therefore it is important to consider anisotropic fibre properties when modelling carbon or graphite fibres.

Behrens (1967a; 1967b; 1969a; 1969b; 1971) considered anisotropic fibres in an anisotropic matrix and derived equations for the stiffness matrix components in terms of the Lamé parameters for the fibre and matrix. He assumed cylindrical point symmetry for the individual fibres, and thus transverse isotropy of the composite. The expressions generated by Behrens were subsequently quoted by R E Smith (1972) in a form that is more consistent with the nomenclature of Appendix F where they are presented. They were also subsequently quoted by Martin (1977) in a slightly different form.

In a PhD thesis, Silnutzer (1972) moved from what are essentially second-order bounds in the Hashin (1965) and Hill (1964) treatments to third-order bounds because they are exact up to the third order in the difference in the phase properties. The expressions derived are considerably more complex involving

evaluation of microstructural parameters which are defined as triple integrals related to probabilities of finding certain morphologies in the matrix or fibre phases respectively.

Martin (1977) clearly distinguishes between isotropic fibres and anisotropic fibres. For anisotropic fibres he quotes R E Smith (1972) and Behrens (1969a) with equations in a different form, by making some assumptions that the matrix will be isotropic. Using the assumed equivalences, the new equations can be seen to be equivalent to those of R E Smith (1972) and Behrens (1969a) – see Appendix F.

Hashin (1979) extends Hashin and Rosen (1964) and Hashin (1965) to allow for carbon and graphite fibres, which are highly anisotropic. In fact the expressions for transverse bulk modulus, transverse shear modulus and axial shear modulus are identical in form to those in Hashin (1965) except that they are more specific about which moduli in the constituent materials should be used. More detail and the new equations are provided in Appendix F.

Tsai and Hahn (1980) produced a book which reviewed the current methods for modelling composite materials but it has not been possible to trace a copy of this, just references to it by others such as Chao and Chaturvedi (1997).

Kantor and Bergman (1982) proposed a new approach to determining an 'effective stiffness matrix' for a homogeneous sample that exactly matches the boundary conditions and the volume-average properties of the inhomogeneous material in question. It then determines the eigenstates of individual fibres before going on to determine the eigenstates for the whole composite. This can then be applied to a hexagonal or square lattice of cylindrical fibres. A matrix perturbation technique is then used to allow an exact expansion of the elastic constants in terms of the fibre volume fraction. The equations for a hexagonal lattice are exact equivalents of Hashin and Rosen (1964) for bulk modulus and Hashin (1970) for shear modulus. For a square lattice the expressions are much more complicated but this is more appropriate for Boron fibres than for carbon fibre composites.

Datta et al (1984) consider random but homogeneous distributions of identical long and parallel fibres and the propagation of longitudinal and shear waves perpendicular to the fibre direction. A multiple scattering approach is used to determine a dispersion relationship in the long-wavelength limit. Fibres are considered to be anisotropic and the outcome is expressions for elastic constants over the whole range of fibre volume fractions. The expressions obtained for the longitudinal and transverse shear moduli were identical to the lower bounds of Hashin (1965) and the plane-strain bulk modulus matched Hashin (1965) exactly.

Lado and Torquato (1986) introduced microstructural parameters to the formulations of Hashin and Rosen (1964) in a similar way to Silnutzer (1972). Torquato and Lado (1992) extend the work of Lado and Torquato (1986) and of Silnutzer (1972) but only treat impenetrable cylinders, which do not include any of the anisotropic fibres being considered here. However, they did produce a simplified form of Silnutzer's expressions for effective elastic constants which otherwise only reside in a PhD thesis.

Wilczynski (1992) and later Ward and Wilczynski (1993) presented a rather lightweight simplification of the problem and declared that much of this computation for structural design purposes was being carried out using finite element analysis by this time.

Therein lies the key to why there is a sudden lack of reported work on analytical effective-medium methods – they were no longer needed for structural design purposes because finite-element analysis provided a far more versatile and application-specific method of modelling exact structures and composite materials. Indeed, Hashin, one of the main authors in this field, summarised his work in a major review (Hashin, 1983) and then diverted his attention from about 1980 to modelling damaged composites – particularly fatigue cracks in the matrix.

The most recent published work that has been found is Chao and Chaturvedi (1997), where a new unified framework is presented based on Helmholtz and Gibbs free energy functions and micromechanical models involving average

stresses and strains in the composite using the approach of Eshelby (1957). Both isotropic and anisotropic fibres are catered for. This model accounts for interaction between the fibres and matrix, and so is more advanced than many of the other methods such as Hashin and Rosen (1964) and its derivatives. A comparison of Chao and Chaturvedi methods with others is given in Appendix F. The new methods are claimed to fit experimental data well and to be more accurate for certain elastic constants, as well as being more versatile, than the earlier models. However, the fact that the Chao and Chaturvedi (1997) stress and strain models give functions of volume fraction that are even more widely spaced than the upper and lower bounds of Hashin and Rosen (1964) means that there is little benefit in escalating the complexity of the formalism this much.

3.5 Discussion

3.5.1 *Modelling porosity*

The scattering model of Adler (1986) for forward scattering from porosity in solids provides a useful analytical solution that is easily coded, and it can be combined with the Pinfield (2010) model for backscattering from a porous layer, which is a suitable configuration for layered composites. An alternative to Pinfield's model is the Hashin (1962) model for effective moduli of spherical inclusions in a solid, but this does not include the frequency dependence of backscattering, which is itself pore-size dependent. It was decided to include both of these options – Adler with either Hashin or Pinfield - in the model for this project.

3.5.2 *Modelling multi-layered structures*

The modelling requirement for this project is limited to normal-incidence ultrasound but a simple analytical model is required that has the potential for running rapid calculations as part of a model-based decomposition method. For this reason, a much reduced transfer matrix approach is suitable, catering for just normal incidence and producing analytical expressions for transmission and reflection coefficients of three-layer structures with two interfaces. By allowing the interfaces to have complex reflection and transmission coefficients, it is

possible to apply this expression multiple times to build up the response of a multi-layered structure.

3.5.3 Modelling long-fibre/resin composites

The remaining aspect is the prediction of the transverse compression velocity in long-fibre composites. The Hashin (1965) expressions for effective bulk and shear modulus (Equations F-33 and F-35) were selected to derive the compression velocity because they are in agreement with most of the other credible models that have been developed, even using different physical principles to arrive at the effective parameters. Where other models deviate from the Hashin (1965) predictions, they have subsequently failed to agree with the later models, whilst Hashin (1965) has been shown to be equivalent to these. A simple volumetric mixture rule is accurate for density.

CHAPTER 4 **MODELLING OF ULTRASOUND PROPAGATION IN LAYERED STRUCTURES**

4.1 Introduction

4.1.1 *Motivation*

In order ultimately to decompose the ultrasonic response from monolithic composite materials into components related to material properties, it is necessary to gain a deep understanding of the ultrasonic propagation through layered inhomogeneous materials. The use of a model fulfils this requirement and also enables prediction of the ultrasonic response of the material and extensive testing of various proposed decomposition methods.

For the purposes of this project the model can be restricted to normal incidence, because that is the acquisition method already in use in industry, and plane-wave propagation for simplicity. Diffraction corrections due to finite sized planar transducers or focused transducers could be added at a later date but generally only weak focusing (eg 75 mm focal length in water from a 12.5 mm diameter probe) was used in this project, where the plane-wave approximation is sufficiently valid. The normal-incidence restriction allows the transversely isotropic composite plies to be considered without concern for the direction of the anisotropy. This enables a ply to be represented by an equivalent homogeneous medium with material properties determined as some combination of properties of the constituent phases (fibre, matrix, voids, etc).

4.1.2 *Model development*

Such a model requires three main components: 1) a layer model, allowing the stacking of multiple plies of these equivalent homogeneous media and the determination of its impulse response to normal-incidence ultrasound, 2) a transducer model, or equivalent, to simulate a realistic pulse of ultrasound with which the impulse response can be convolved, and 3) an equivalent-medium

model, which determines the equivalent material properties of the specific mixture of phases in a ply.

During this project the three parts of the model were developed in the following sequence chronologically: layer model, transducer model and then equivalent-medium model. However, in order to test and validate the layer model by benchmarking against other models it was necessary to use a simple volumetric equivalent-medium mixture rule. During this period, extensive research was undertaken into other equivalent-medium models to find those most suited to use for this project and it transpired that the considerable amount of literature on the subject from 1960 to 1990 (documented in Chapter 3 and Appendix F) was in a poor state, with many errors and confusing comparisons of methods. The most suitable equivalent-medium models would be those that could run rapidly as part of an analytical multi-layer model, with the potential for use in a model-based decomposition method or an iterative inversion algorithm. The chosen equivalent-medium models were then used in the model as it progressed to include porosity and other types of defects.

4.1.3 Validation of the model

Experimental validation of all aspects of the model from scratch would be an extremely time-consuming exercise. Fortunately this was not necessary because extensive validation against experiment and other models had already been undertaken for the MLM-Propmat model when it was developed at the University of Keele (Freemantle, 1995), and the current model could be validated by comparison with MLM-Propmat. Other aspects of the model were compared with experimental results and the comparisons are documented in this chapter in the appropriate sections.

4.1.4 Organisation of the chapter

Section 4.2 is a broad treatment of the complexity of the ultrasonic response of composite materials in terms of the contributions to the frequency response from different material properties. It is not a rigorous treatment but sets the scene for the development of the model and played a crucial role in determining which assumptions and constraints would be appropriate.

Section 4.3 describes the development, testing and benchmarking of an analytical layer model comprising a single-ply between two thin resin layers, embedded in composite, using a simple volumetric mixture rule. This was used to test some theories about how the frequency dependence of the single-ply response depends on ply thickness, resin layer thickness and fibre volume fraction (FVF) – the proportion of a given volume that comprises the fibre phase of the mixture. In order to test, debug and validate it, the model was compared with the University of Nottingham's 'MLM-Propmat' model, which also used a simple volumetric mixture rule at the time and had been extensively tested against other models and experimental data (Freemantle, 1995; Mienczakowski et al, 2006).

Section 4.4 describes the extension of the analytical model to multiple plies separated by thin resin layers, where the properties (thickness, FVF, properties of phases) for each ply can be stipulated, as can the thickness and properties of the resin layers. At this stage the option for the entry and exit media to be water was included. Again the model was benchmarked against MLM-Propmat.

Section 4.5 deals with convolution of the impulse response with realistic ultrasound pulses, either generated from a transducer model, measured experimentally, or generated from a simple Gaussian frequency-response model.

In Section 4.6 porosity is added to the model by inserting a frequency-dependent attenuation due to scattering and changing to micro-mechanical mixture rules allowing the equivalent-medium model to include a spherical-particle model for porosity and a cylindrical fibre model for the long fibres.

Section 4.7 adds the ability to investigate a single thick resin layer whilst Section 4.8 looks at using the model to show how to distinguish between porosity and thick resin layers.

4.2 Frequency-dependence of ultrasonic interactions

4.2.1 Multiple Frequency Dependencies

At the start of this project it was well known that in composite materials there are many inhomogeneities that cause different frequency-dependent effects when ultrasound propagates through the material. Previous experiments have shown that the frequency range used can dictate which frequency-dependent interaction dominates the response. For example, above 10 MHz the inter-ply layer reflections become significantly larger than the visco-elastic damping effects. The following sub-sub-sections briefly introduce the interactions that are summarised in Table 4-1 and Figure 4-1. Then the resonances are treated in more detail.

Normal incidence Interaction	Backscatter	Transmission
Smooth surface	Independent of f $R \propto f^0$	Independent of f $T \propto f^0$
Porosity (size \gg wavelength) (Smith, 2005)	Independent of f $R \propto f^0$	Independent of f $T \propto f^0$
Inter-ply layer reflections	$R \propto f$	$\sqrt{1-T^2} \propto f$
Ply Resonant Frequency	$f_{res} \propto 1/\text{ply thickness}$	$f_{res} \propto 1/\text{ply thickness}$
Visco-elastic damping in resin	$-\text{Log}R \propto f$	$-\text{Log}T \propto f$
Rough Surfaces (Nagy & Rose, 1993)	$-\text{Log}R \propto f^2$	$-\text{Log}T \propto f^2$
Porosity (size \ll wavelength) (Adler et al, 1996)	$\text{Log}R \propto f^4$	$-\text{Log}T \propto f^4$

Table 4-1. Summary of frequency dependence of normal-incidence ultrasonic interactions.

4.2.1.1 Smooth surface reflection/transmission

These smooth surface reflections are independent of frequency at normal incidence. They can be measured by extrapolating spectral attenuation effects back to DC (0 Hz). At a smooth interface there should be minimal scattering and conservation of energy, which requires that the energy in the incident wave

equals the sum of the energies in the reflected and transmitted waves. See Appendix B to this thesis for a full treatment.

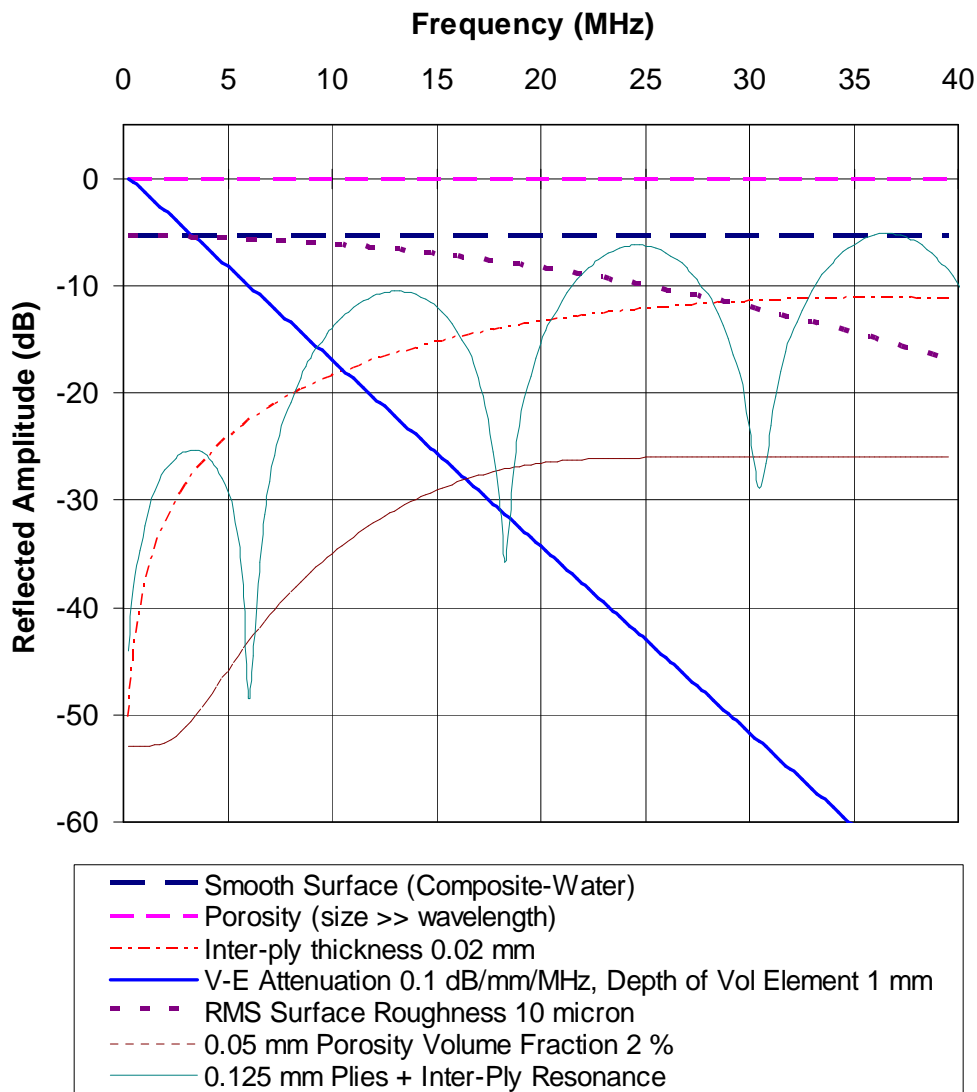


Figure 4-1. Graphical illustration of the multiple frequency-dependencies involved in understanding the interaction of ultrasound with carbon-fibre composites. This graph shows the reflected response of the structure as a function of frequency.

4.2.1.2 Rough surfaces

At a rough interface there will be energy loss due to scattering. This effect increases as the frequency increases. In Appendix B to this thesis it is shown, using a phase-screen approximation presented by Nagy and Rose (1993), that the logarithm of both the reflection and the transmission coefficients are proportional to frequency squared.

In fact, measurements of the reflection coefficient at the interface over a range of frequencies can be used to determine the rms roughness (Smith and Bruce, 2001; Birt et al, 2004), and potentially for removing the effects of roughness from other measurements. The extrapolated value for 0 Hz will also provide a method for determining the surface losses for rough surfaces.

4.2.1.3 *Visco-elastic damping in resin*

In general the logarithm of the attenuation coefficient is proportional to frequency for this type of damping. Hence, as the frequency increases, the amplitude decreases.

4.2.1.4 *Inter-ply layer reflections*

If thickness is small relative to a wavelength then the actual reflected amplitude from the layer (combined interfaces) is approximately proportional to frequency. Hence, log amplitude (eg in dB) is proportional to log frequency.

4.2.1.5 *Ply resonances*

The inter-ply reflections (above) also cause ply resonances, the frequencies of which depend on the ply thickness and the amplitude on the inter-ply resin layer thickness.

4.2.1.6 *Porosity*

In the long wavelength limit ($ka \ll 1$) the scattered power vanishes as k^4 (Adler et al, 1986). In the short-wavelength limit a large pore looks like a delamination or a smooth surface. Obviously these are over-simplifications of the real situation with porosity, but they are useful for considering how the different frequency-dependencies compete for dominance.

The graph for 2% porosity where the porosity is smaller than the wavelength ($ka \ll 1$) in Figure 4-1 uses the long-wavelength equation 4 from Adler et al, 1986, where the scattering attenuation coefficient $\alpha(k)$ is given by:

$$\alpha(k) = \frac{3\phi_v\beta(ka)^4}{4a} \quad (4-1)$$

where ϕ_v is the void volume fraction, k is the wavenumber, a is the porosity size and $\beta(\eta)$ is a function which governs the long-wavelength behaviour of the reduced cross-section and depends on η , the ratio of shear to longitudinal velocities, with the following values in Table 4-2. For the composite application a value of η of 0.5 was used.

η	β
0.3	20
0.4	7
0.5	2.5
0.6	1.7
0.7	1.1

Table 4-2. Approximate values of $\beta(\eta)$ for different values of η , the ratio of shear to longitudinal velocities. Data taken from Adler et al (1986), calculated from Ying and Truell (1956).

4.2.2 Inter-ply resin layer resonances

The interaction of ultrasound with the fibres is dominated by the reflection from the thin inter-ply resin layer that exists between plies of different fibre orientation. This layer is much thinner than a wavelength of ultrasound at the frequencies being investigated and resonance occurs at 35 MHz for a 0.02 mm resin layer, as shown in Figure 4-1 by the ‘inter-ply thickness 0.02 mm’ curve. Figure 4-2 illustrates that, in the case of thin layers, the overall reflection coefficient of the resin layer is highly dependent on the layer thickness. It is for this reason that an impression of the fibre tows both above and below the resin layer are present in C-scan images plotting the reflection amplitude from the resin layer (see Figure 4-3).

Changes in FVF may change the thickness of the resin layer but the effect of this may only be detected as a variation in reflection amplitude if the resonant frequency of the resin layer is higher than it is proposed to operate.

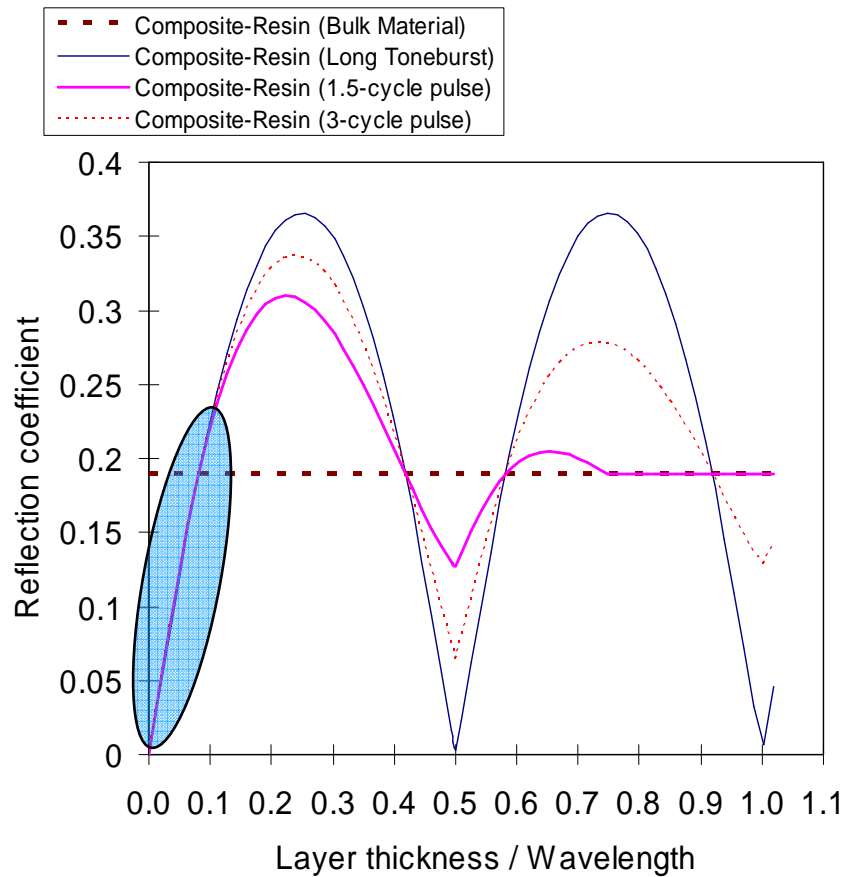


Figure 4-2. Graph of the variation in reflection coefficient of a thin resin layer between two carbon-fibre composite plies. The properties of the layers were kept constant while the resin-layer thickness was varied. Plots are for three different pulse lengths and a single interface, based on bulk material acoustic impedance. The blue shading shows the region where the thin inter-ply resin layers occur and shows how sensitive their reflection coefficient is to thickness.

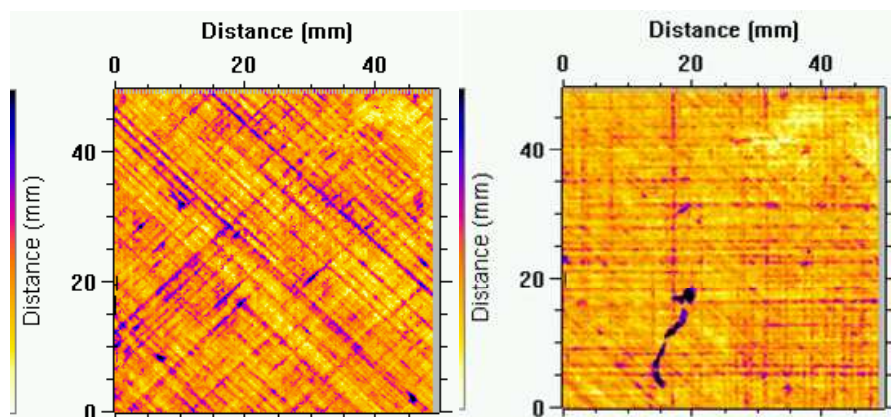


Figure 4-3. Amplitude C-scans obtained from inter-ply resin layer reflections at different depths in a 16-ply skin. Note that generally there is an impression of fibre tows in two ply orientations –one above and one below the resin layer.

4.2.3 Ply resonances

The composite plies themselves are half-wave resonant layers with a resonant frequency (the *second* resonance) at approximately 12 MHz for 0.125 mm thickness plies – see the ‘0.125 mm plies + inter-ply resonance’ curve in Figure 4-1. The *first* resonance is not a classical resonance as a half-wave resonator should have a maximum at zero frequency, but when it is multiplied by the frequency response of the thin resin layer it then has a minimum at zero frequency and a first resonance at approximately a quarter of the second resonance. This corresponds to groups of four plies vibrating together.

By tracking the ply resonances from each volume element in the structure, it should be possible to obtain a measurement of the local FVF. In order to use this it would be necessary to calibrate an ultrasonic parameter against FVF. There are two possible ultrasonic parameters: peak frequency or peak amplitude (reflection coefficient). In practice it is usually more reliable to use a frequency-based parameter because amplitude measurements are more susceptible to other variations – as in the benefits of frequency-modulated radio over amplitude-modulated radio. Such a variation that could affect a ply-resonance amplitude (reflection coefficient) parameter is a change in the inter-ply reflection coefficient due to thickness variations in the thin resin layer (see Figure 4-2).

It has been shown in Appendix C to this thesis, using a further development of the author’s simple analytical model described in Appendix A, that both the resonant frequencies and the reflection coefficients at resonance are proportional to local ply-thickness changes. If an assumption is made that fibres do not move sideways along the ply in bulk, over the width of the ultrasonic beam, then this change in ply spacing can be assumed to be inversely proportional to FVF. A full treatment and explanation is given in Appendix C where proposed equations for determining FVF have been developed. These show that, given the above assumption, a change in the resonance frequency is proportional to the *fractional* change in FVF. This allows the generation of equations that apply to any composite system provided the nominal ply thickness and nominal FVF are known. The equations developed by the author for this purpose are:

$$FVF = \alpha_n f_n t FVF_{nom} \quad (4-2)$$

$$FVF = \beta_n R_n t \quad (4-3)$$

where f_n is the resonance frequency of the n th harmonic resonance, R_n is the corresponding reflection coefficient for the n th harmonic, t is the nominal ply thickness, FVF_{nom} is the nominal FVF and α_n and β_n are the calibration coefficients. The values for α_n and β_n for the first two resonances ($n=0$ and 1) are shown in Table 4-3 (and plotted on graphs in Appendix C) and it can be seen that there is little variation in these coefficients for different nominal FVFs.

Calibration Coefficient	Nominal Fibre Volume Fraction			
	60%	70%	80%	90%
$\alpha_0 (mm^{-1} MHz^{-1})$	2.5	2.4	2.4	2.4
$\beta_0 (mm^{-1})$	120	120	120	120
$\alpha_1 (mm^{-1} MHz^{-1})$	0.62	0.61	0.61	0.61
$\beta_1 (mm^{-1})$	21	21	21	21

Table 4-3. Calibration factors (to 2 significant figures) for converting resonant frequency and reflection coefficient measurements into FVF measurements. These apply for the designated nominal FVFs. Material properties used were: fibre density 1.69 kg/dm³ and bulk modulus 16 GPa, resin density 1.27 kg/dm³ and bulk modulus 10.7 GPa.

Thus, the parameters that need to be entered in order to calibrate such a FVF meter are the nominal ply thickness and the nominal FVF. Then the measurements of peak frequency and amplitude can be converted to estimates of local FVF. This is potentially a major breakthrough and makes the 3D profiling of FVF a real possibility. However, it is likely that there will be certain cases where this method will not work – such as deep in structures with thin ply thicknesses where the low frequency required for penetration is below the lowest ply resonance frequency.

4.3 Analytical Layer Modelling

For the purposes of investigating the potential for fibre volume fraction (FVF) measurement, a simple model for predicting resonant frequencies was required. The choice of model was based on the need for a high computational speed for ultimate use in a model-based decomposition method for 3D characterisation of FVF and porosity in composites. The chosen type of model is a simplified normal-incidence version of a recursive stiffness-matrix model presented by Wang and Rokhlin (2003), as reviewed in Chapter 3.

The basic principle behind this model is that, if it is possible to describe a combination of two interfaces in terms of complex transmission and reflection coefficients, then that combination can be treated as a single interface characterised by those coefficients. The method used to calculate the complex reflection and transmission coefficients includes multiple reflections between the interfaces by employing a Geometric Progression (GP) principle, ar^n , where the sum to infinity ($n \rightarrow \infty$) is well defined, provided the multiplier, r , meets the condition: $|r| < 1$.

4.3.1 *Single-ply analytical model*

At first, this model only needed to handle 3 layers (two resin layers separated by a composite ply) embedded in a medium because the intention was to use small volume elements in the structure that only encompassed one or two plies.

If the interface pairs are symmetrical (ie they have the same medium either side of them – see Figure 4-4) then two such interface pairs can then be combined in the same way. The frequency dependence of the ultrasonic response, and hence the impulse response of the structure, will be contained in those complex reflection coefficients.

The full treatment of this single-ply model is given in Appendix A to this thesis. It is referred to in many graph legends as the ‘RAS Model’.

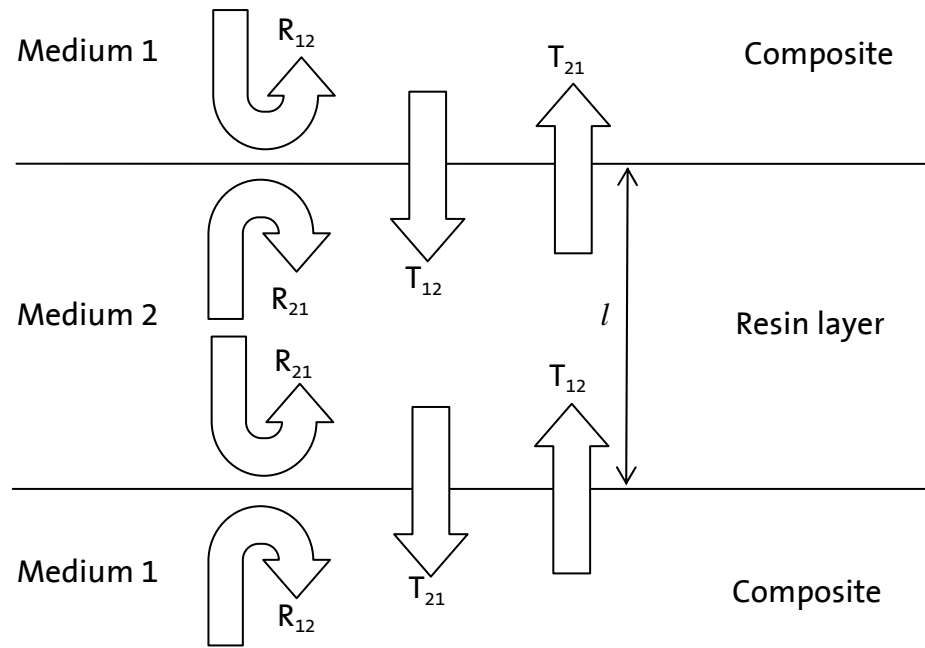


Figure 4-4. Diagram showing how an interface pair can be described by complex reflection and transmission coefficients.

4.3.2 Simple mixture rule

For each layer the model uses single values for the compression modulus, M , and density, ρ , to derive single values of phase velocity, c , and acoustic impedance, Z . This assumes that each layer is a homogeneous medium. As only normal incidence is considered, transversely isotropic layers are satisfactorily dealt with by the model. If a layer is actually inhomogeneous then it is possible to approximate its properties to an 'equivalent' homogeneous medium using a mixture rule. For the purposes of comparison with other models such as MLM-Propmat, the simplest of these mixture rules was used initially - the volumetric rule, which assumes that the proportionate contribution of each component of the mixture depends predominantly on its volume fraction in the mixture – as shown in Equations 4-4 and 4-5 for a two-component fibre-resin mixture.

$$M = \phi_f M_f + (1 - \phi_f) M_r \quad (4-4)$$

$$\rho = \phi_f \rho_f + (1 - \phi_f) \rho_r \quad (4-5)$$

where ϕ_f is the fibre volume fraction, M_f and M_r are the compression moduli in the propagation direction of the fibre and the resin respectively, and ρ_f and ρ_r are the densities of fibre and resin respectively. More comprehensive mixture rules are considered later for long-fibre composites and where porosity is added to the mixture.

4.3.3 Benchmarking the single-ply analytical model

The analytical model from Appendix A was implemented in an MS Excel spreadsheet in order to predict the frequency response of up to two resin layers separated by a composite ply. In order to test, debug and validate it, the model was compared with the University of Nottingham's MLM-Propmat model for a limited number of layers – see Figure 4-5 – and it compared favourably. Both models were using the simple volumetric mixture rule as described above.

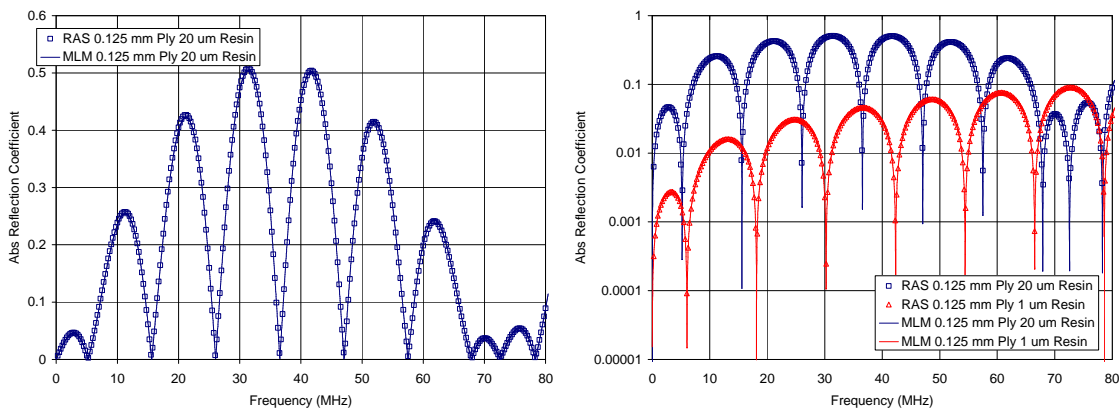


Figure 4-5. Comparison of the Excel version of the (RAS) analytical model with MLM-Propmat for a single 0.125 mm thick composite layer (80% Fibre Volume Fraction) sandwiched between two 0.020 mm (blue) and 0.001 mm (red) thick resin layers on a linear scale (left) and a logarithmic scale (right).

Then attenuation in the resin layer was added and a further comparison with MLM-Propmat – see Figure 4-6 – also showed good agreement but with a slight discrepancy in the peak reflection coefficients at the higher resonant frequencies. This discrepancy was removed later by a change in the way attenuation was applied to the resin part of the mixture in MLM-Propmat – see later comparison in Figure 4-13.

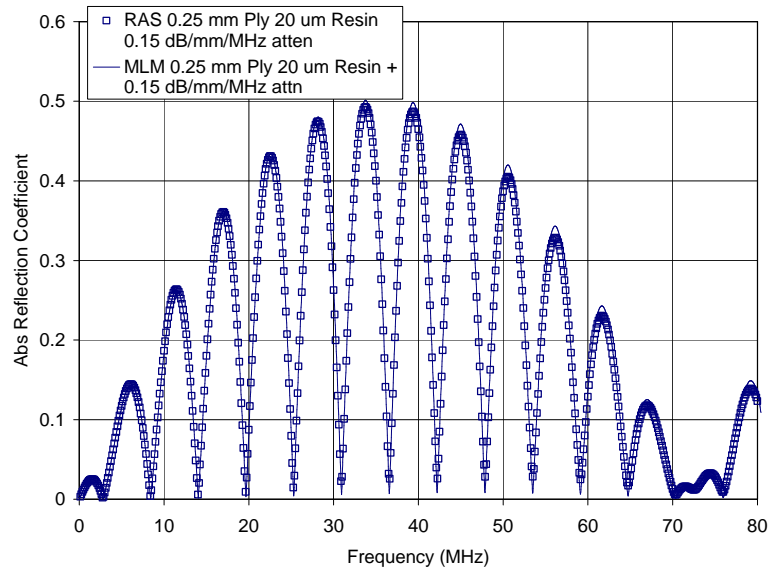


Figure 4-6. Comparison of the Excel version of the (RAS) Analytical model with MLM-Propmat for a single 0.25 mm ply sandwiched between two 0.02 mm resin layers with 0.15 dB/mm/MHz attenuation in the resin.

4.3.4 Effect of fibre volume fraction changes

The ultimate aim of the modelling exercise was to investigate the effects of changes in Fibre Volume Fraction (FVF) on the time-frequency ultrasonic response in a realistic structure containing many plies. Firstly, these FVF effects were modelled using a single ply with a constant number of fibres per unit width across the fibres – assuming that changes in FVF would be reflected in ply thickness changes. Figure 4-7 shows that a linear relationship exists between FVF and resonant frequency as described by Equation 4-2, where f_n is the n th resonant frequency, t is the nominal ply spacing, and α_n is the constant of proportionality for the n th resonance.

4.3.5 Dependence on ply thickness and ply spacing

In order to determine whether the composite ply thickness or the ply spacing (sum of the composite and resin layer thicknesses) dominated in determining the resonant frequency, the model was used to generate values of α_n for a) variable resin thickness with the same composite ply thickness, and b) variable resin thickness but a constant ply spacing (composite + resin thickness). Figure 4-8 shows evidence that it is the ply spacing that dominates in determining the resonant frequency rather than just the composite ply thickness. This result

means that the resonant frequency is a suitable metric for mapping 3D variations in FVF, but it will be relatively insensitive to resin-rich areas within a given ply spacing.

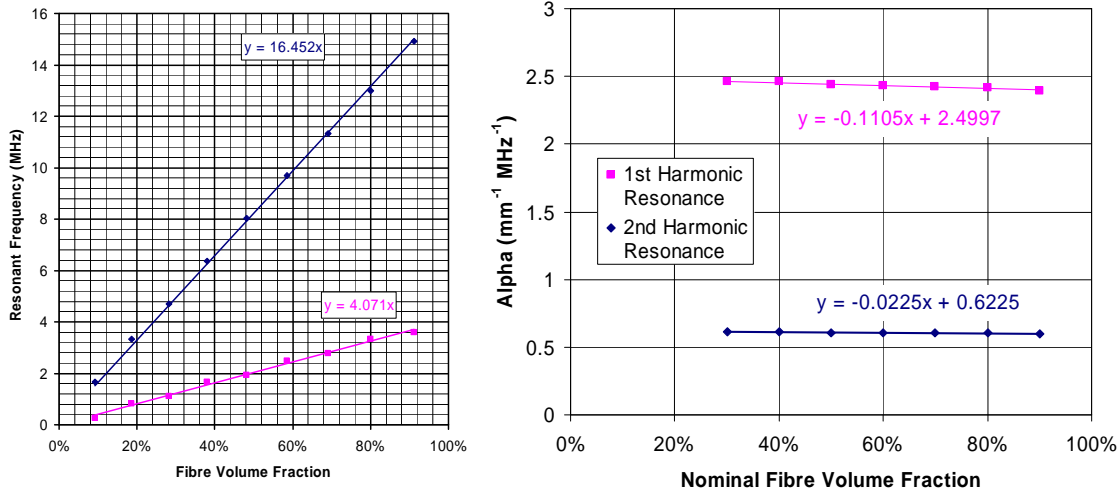


Figure 4-7. Relationship between resonant frequency and local FVF for a nominal 80% FVF 8 plies/mm composite, with a nominal 0.113 mm composite layer between two 0.012 mm thick resin layers (left) and how the slope of this dependency varies with nominal FVF (right). Only the first two resonances are shown, the first in pink and the second in blue.

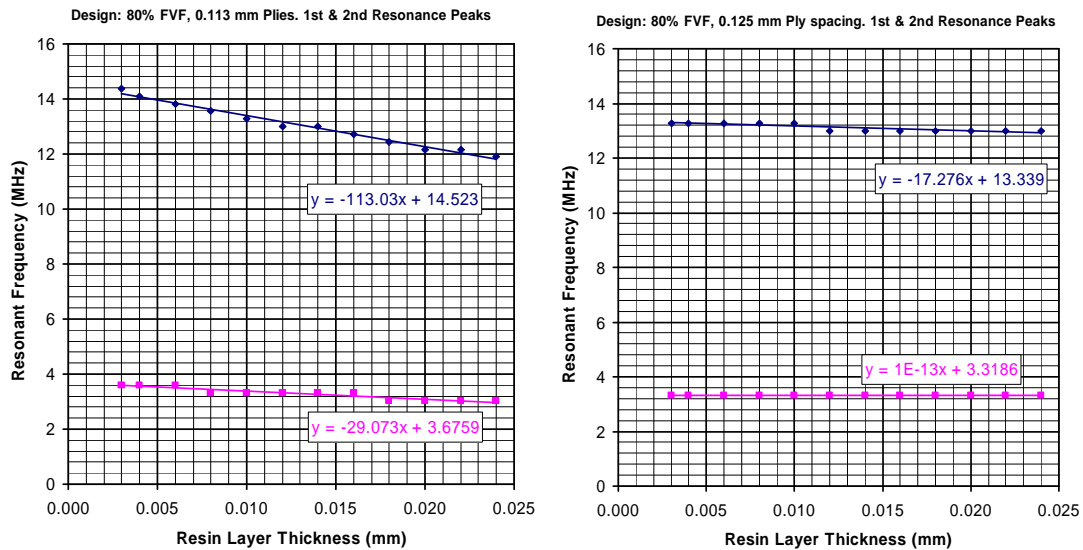


Figure 4-8. Comparison of the effect on the first two resonant frequencies of varying the resin layer thickness with (left) constant (80% FVF) composite ply layer thickness of 0.113mm, and (right) constant ply spacing of 0.125 mm. Only the first two resonances are shown, the first in pink and the second in blue.

4.4 Multi-Layer Analytical Modelling

4.4.1 ANDSCAN version

In order to extend the model to include multiple layers, and then to produce a time-domain response to a typical transducer pulse input, the model was migrated into Microsoft 'C'. It was embedded within the ANDSCAN® Waveform application in order to use all ANDSCAN's signal processing, image processing and display capabilities, and to provide direct comparisons with real data. The model produces an impulse response that can then be convolved with the front-wall echo from a real structure, which represents a typical ultrasonic pulse.

The migration into ANDSCAN was achieved by writing a *Modelling.c* module incorporating new functions for complex number arithmetic, and routines for calculating complex reflection and transmission coefficients for combinations of interfaces. A user interface was provided for input of material properties, numbers of layers and their thicknesses etc – see Figure 4-9.

The screenshot shows a 'Layer Modelling Parameter Entry' dialog box with the following fields and values:

- Inter-Ply Thickness: 0.020 mm
- Composite Thickness: 0.250 mm
- Fiber Volume Fraction: 80 %
- Time Offset: 1.000 μs
- Amplitude: 1
- Water Surround:
- % Randomness: 0 %
- Number of Plies: 1
- % Porosity: 0.0 %
- Porosity Radius: 10 μm

Material Properties:

Property	Resin Value	Fiber Value
Compression Modulus C ¹¹	10700000000 N/m ²	16000000000 N/m ²
Density	1270 kg/m ³	1690 kg/m ³
Attenuation Coefficient	0.150 dB/mm/MHz	0.000 dB/mm/MHz

Inter-Ply Layer Material: Resin, Aluminium, Titanium

Convolution To Give Time Domain Wfm In Memory 1:

- Delta-Function: Center Frequency (MHz) 10.00, Q-Factor: 0.80
- Gaussian Pulse: Water Stand-off (mm): 0.00
- UoN Pulse: Spectrum: 1
- Frozen Spectrum

Buttons: OK, Apply, Cancel

Figure 4-9. User interface for input of material properties, layers and their thicknesses, whether surrounded by water or composite, as-designed FVF etc.

The extension of the model involved using a more generalised method for determining the complex reflection and transmission coefficients for a given group of layers. The basic concept was similar to a finite-element approach where the effect of each ply (composite layer plus resin layer) is added sequentially.

Figure 4-10 illustrates the principle of adding a single ply to a stack and calculating the new values for the forward and back reflection and transmission coefficients of the new expanded system: R_{fwd} , R_{back} , T_{fwd} and T_{back} . When the next ply is added R_{fwd} becomes the new R_{12} , R_{back} becomes R_{21} , T_{fwd} becomes T_{12} and T_{back} becomes T_{21} . The new resin layer at interface 2-3 itself comprises two interfaces, each of which has real reflection and transmission coefficients that can be calculated in the usual way using the impedances of the resin and composite and then combined using the same equations given below. Because the thicknesses and FVFs of each layer may vary, the reflection and transmission coefficients R_{23} , R_{32} , T_{23} and T_{32} must be calculated from the impedances in this way for each new ply.

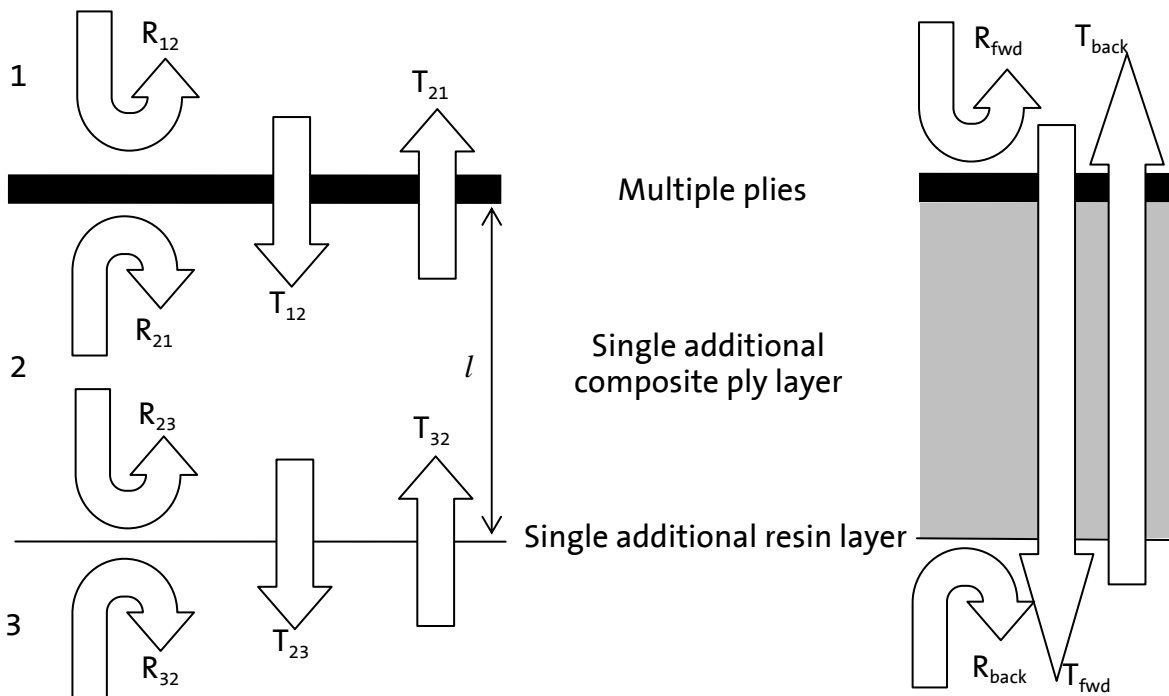


Figure 4-10. Diagram showing how an additional ply can be added to a group of plies to give new complex reflection and transmission coefficients for the now expanded system of plies.

The equations, including attenuation, for calculating the reflection and transmission coefficients for this generalised system are as follows (Equations 4-6 to 4-9), where l is the thickness of the new layer of composite. Any variation in thickness of the new resin layer will need to be incorporated in a fresh calculation of R_{23} , R_{32} , T_{23} and T_{32} for the additional resin layer.

$$R_{fwd} = R_{12} + \frac{R_{23}T_{12}T_{21}e^{-2l(\alpha+ik)}}{1 - R_{21}R_{23}e^{-2l(\alpha+ik)}} \quad (4-6)$$

$$R_{back} = R_{32} + \frac{R_{21}T_{32}T_{23}e^{-2l(\alpha+ik)}}{1 - R_{23}R_{21}e^{-2l(\alpha+ik)}} \quad (4-7)$$

$$T_{fwd} = \frac{T_{12}T_{23}e^{-l(\alpha+ik)}}{1 - R_{21}R_{23}e^{-2l(\alpha+ik)}} \quad (4-8)$$

$$T_{back} = \frac{T_{32}T_{21}e^{-l(\alpha+ik)}}{1 - R_{23}R_{21}e^{-2l(\alpha+ik)}} \quad (4-9)$$

4.4.2 Comparison for 3 layers with MLM-Propmat

For validation purposes, comparisons between MLM-Propmat and the MS Excel and ANDSCAN versions of the analytical model were performed using a simple resin-composite-resin three-layer stack surrounded with composite. Again, both methods used the simple mixture rule described above. These are documented in Figure 4-11 and Figure 4-12 for the case with no attenuation, and in Figure 4-13 for visco-elastic attenuation in the resin of 0.15 dB/mm/MHz.

Note that in in Figure 4-13 the discrepancy in peak reflection coefficient at the resonant peaks evident in Figure 4-6 has been solved through a modification in MLM-Propmat.

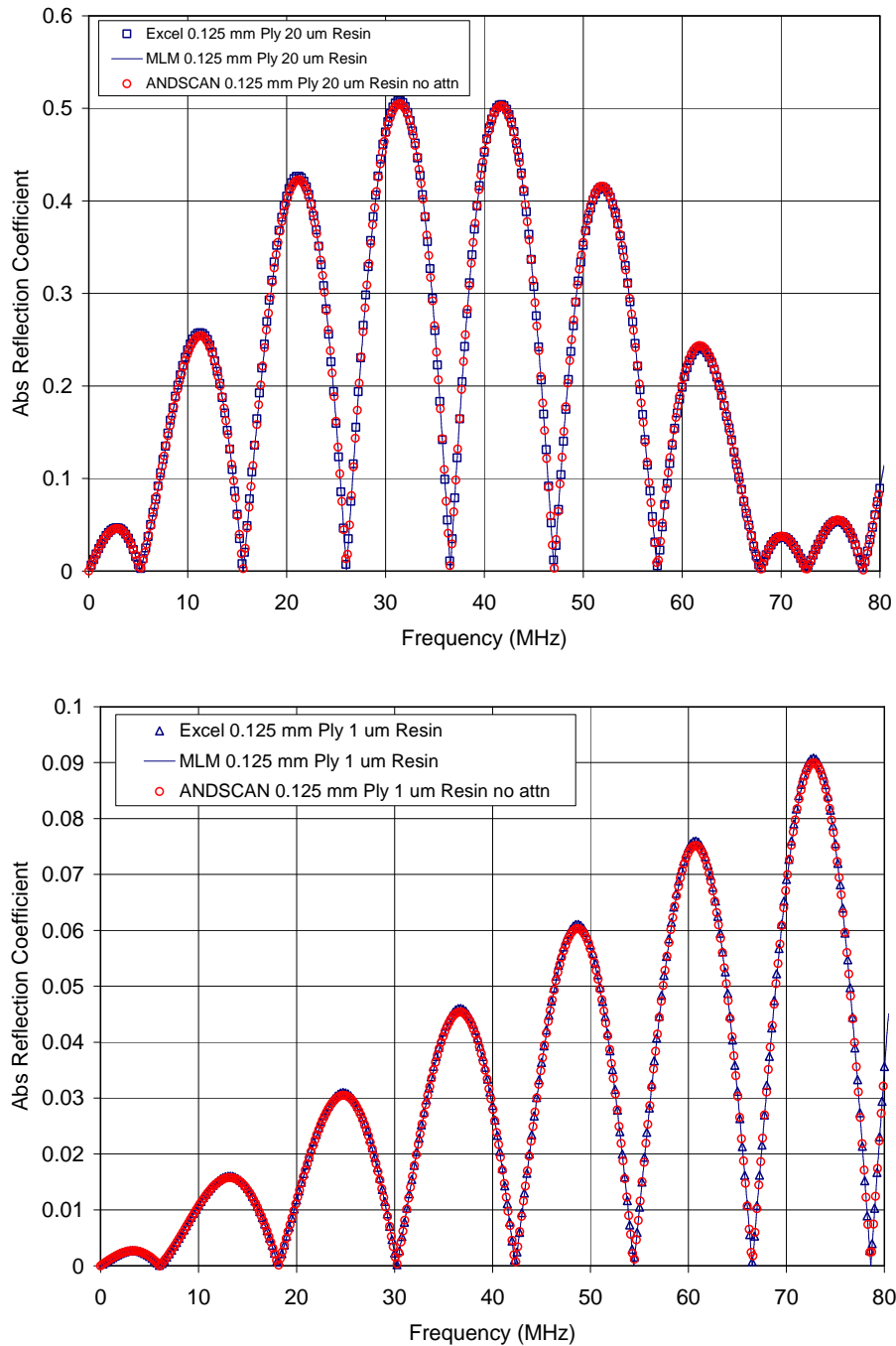


Figure 4-11. Comparison of the ANDSCAN Waveform version of the (RAS) Multi-layer Analytical Model with the original MS Excel version and with MLM-Propmat for a single 0.125 mm thick composite layer (80% Fibre Volume Fraction) sandwiched between two 0.020 mm (top) and 0.001 mm (bottom) thick resin layers.

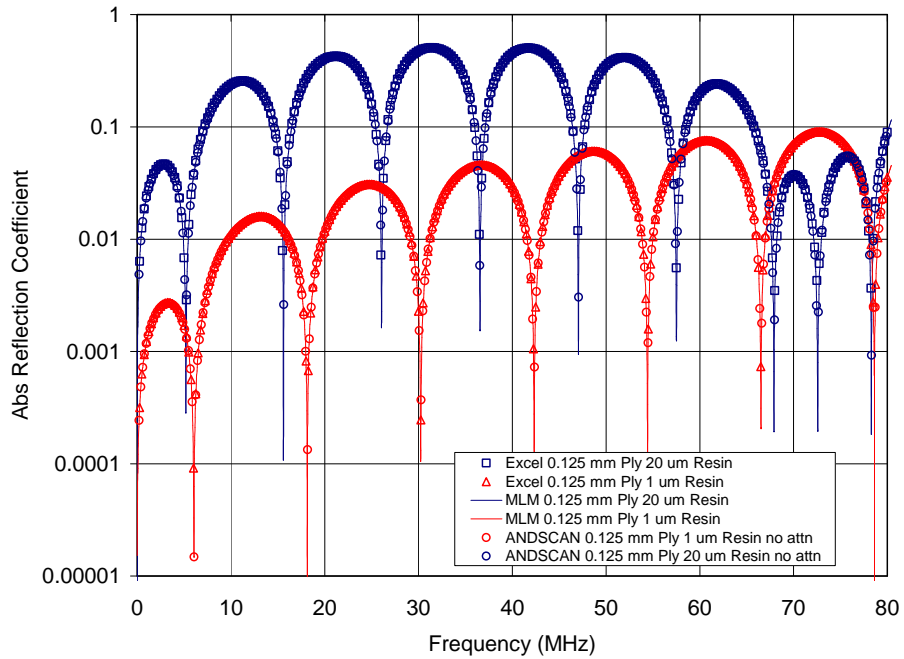


Figure 4-12. Comparison of the ANDSCAN Waveform and Excel versions of the (RAS) Multi-layer Analytical Model with MLM-Propmat for a single 0.125 mm thick composite layer (80% Fibre Volume Fraction) between two 0.020 mm (blue) and 0.001 mm (red) thick resin layers on a logarithmic scale.

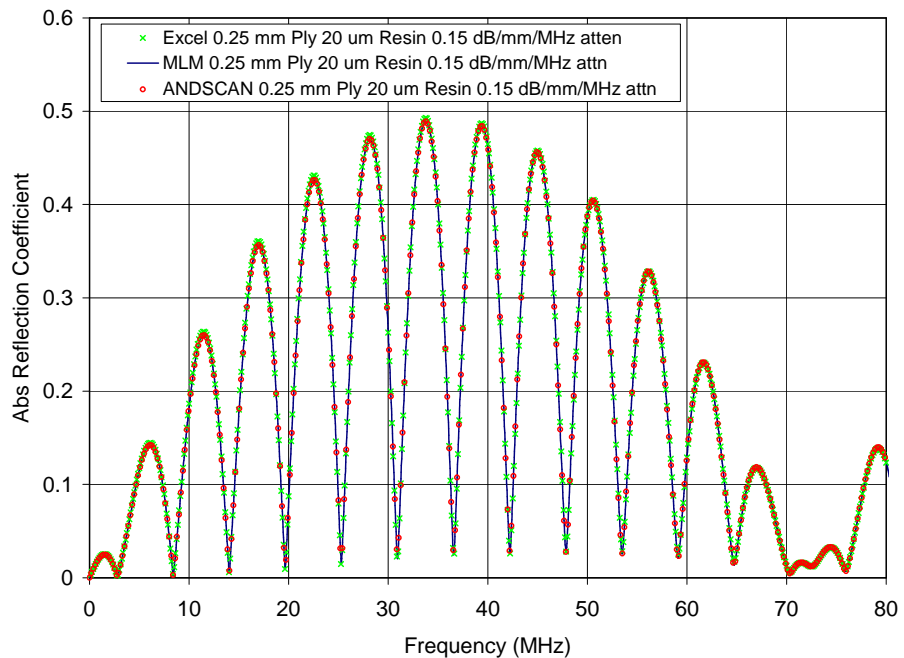


Figure 4-13. Comparison of the ANDSCAN Waveform and Excel versions of the (RAS) Multi-layer Analytical Model with MLM-Propmat for a single 0.25 mm thick composite layer (80% Fibre Volume Fraction) between two 0.020 mm thick resin layers but with 0.15 dB/mm/MHz visco-elastic attenuation in the resin.

4.4.3 Results for multiple plies

4.4.3.1 Embedded in composite

After this validation process, frequency responses and temporal impulse responses were produced for different numbers of 60% FVF plies embedded in composite, firstly assuming no attenuation (see Figure 4-14 and Figure 4-15) and then with a visco-elastic attenuation of 0.15 dB/mm/MHz (see Figure 4-16 and Figure 4-17).

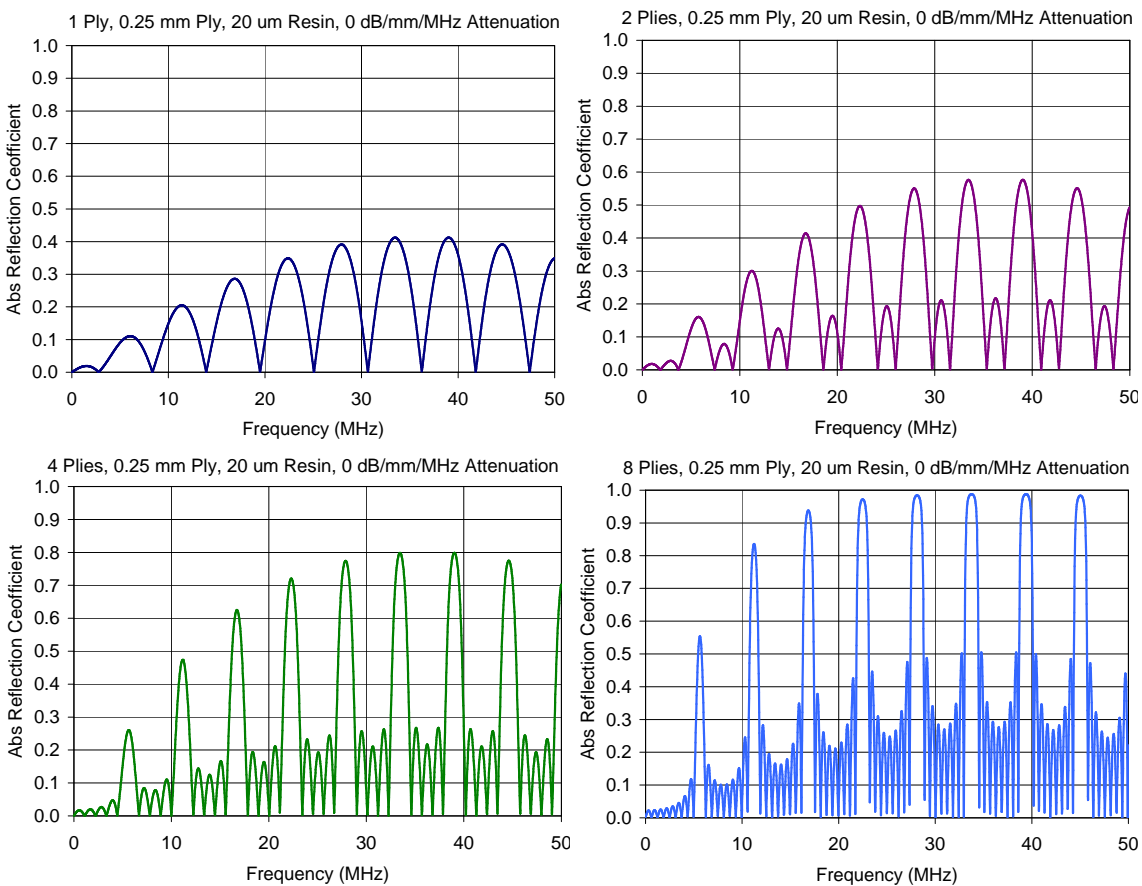


Figure 4-14. Reflection coefficient frequency responses calculated for (left to right, top then bottom) 1, 2, 4 and 8 plies of 60% FVF and thickness 0.25 mm, separated by 0.02 mm resin layers, neglecting attenuation and embedded in composite.

As the number of plies increases, the resonance peaks become much narrower. Note that when there is no attenuation included in the model, the magnitude of the total reflection coefficient can approach very close to unity at the resonant frequencies for a large number of plies.

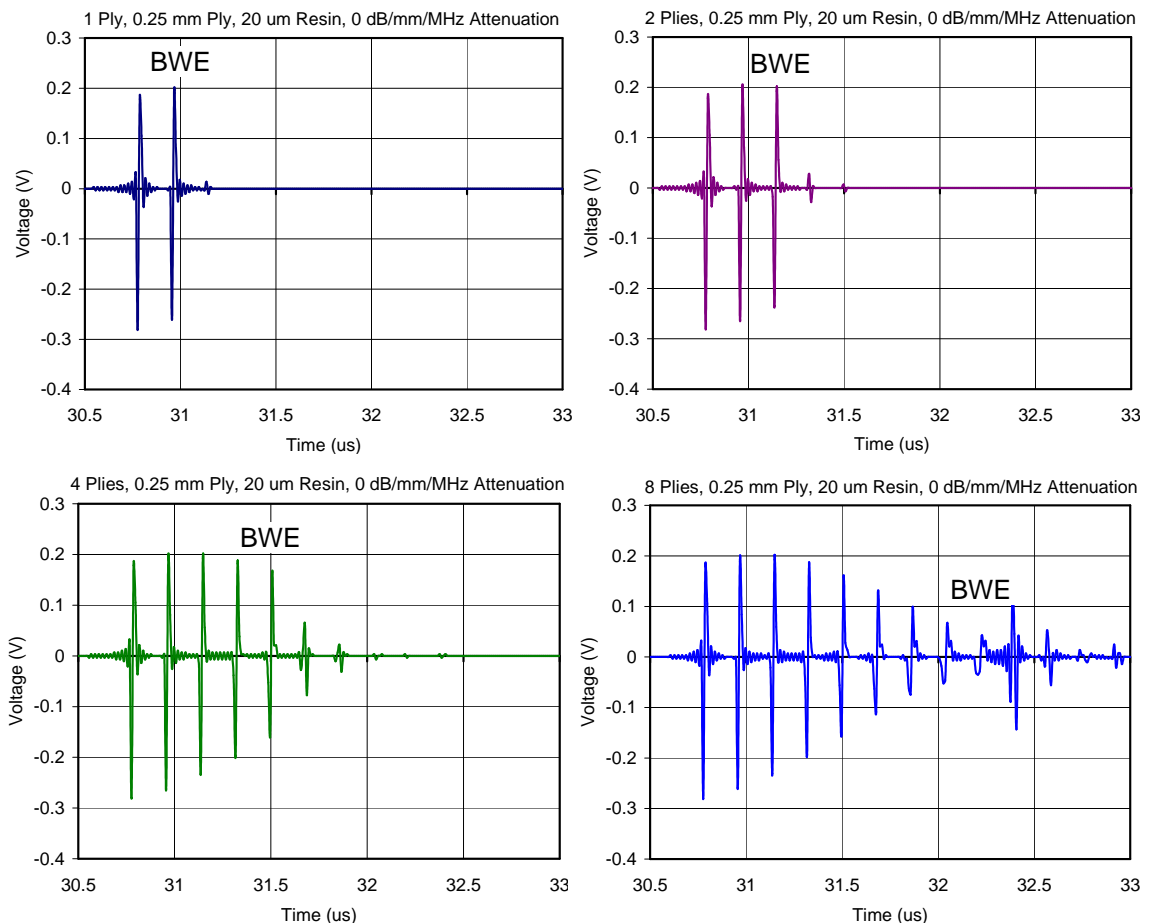


Figure 4-15. Reflection temporal impulse responses calculated for (left to right, top then bottom) 1, 2, 4 and 8 plies of 60% FVF and thickness 0.25 mm, separated by 0.02 mm resin layers, neglecting attenuation and embedded in composite. In each case, 'BWE' indicates the back-wall echo reflection.

At this stage the responses have not been convolved with a realistic waveform from a transducer so they are impulse responses. In addition, the structure is effectively embedded in composite whereas when the surrounded medium is water the front-wall and back-wall reflections will dominate the spectrum.

An interesting effect in Figure 4-17 (bottom-right) is in the waveform predicted for 8 plies where the echo from one ply *beyond* the back-wall echo is actually a higher amplitude than from the back-wall itself. The model has been checked for artefacts in the Inverse Fourier Transform (IFT) by doubling the sample rate – extending the Nyquist frequency up to 100 MHz. This still produced the same effect, which can also be seen for 5, 6 and 7 plies, suggesting it is a real response of the structure, maybe due to the lack of a real interface at this depth to cause destructive interference with the multiple reflections from earlier plies.

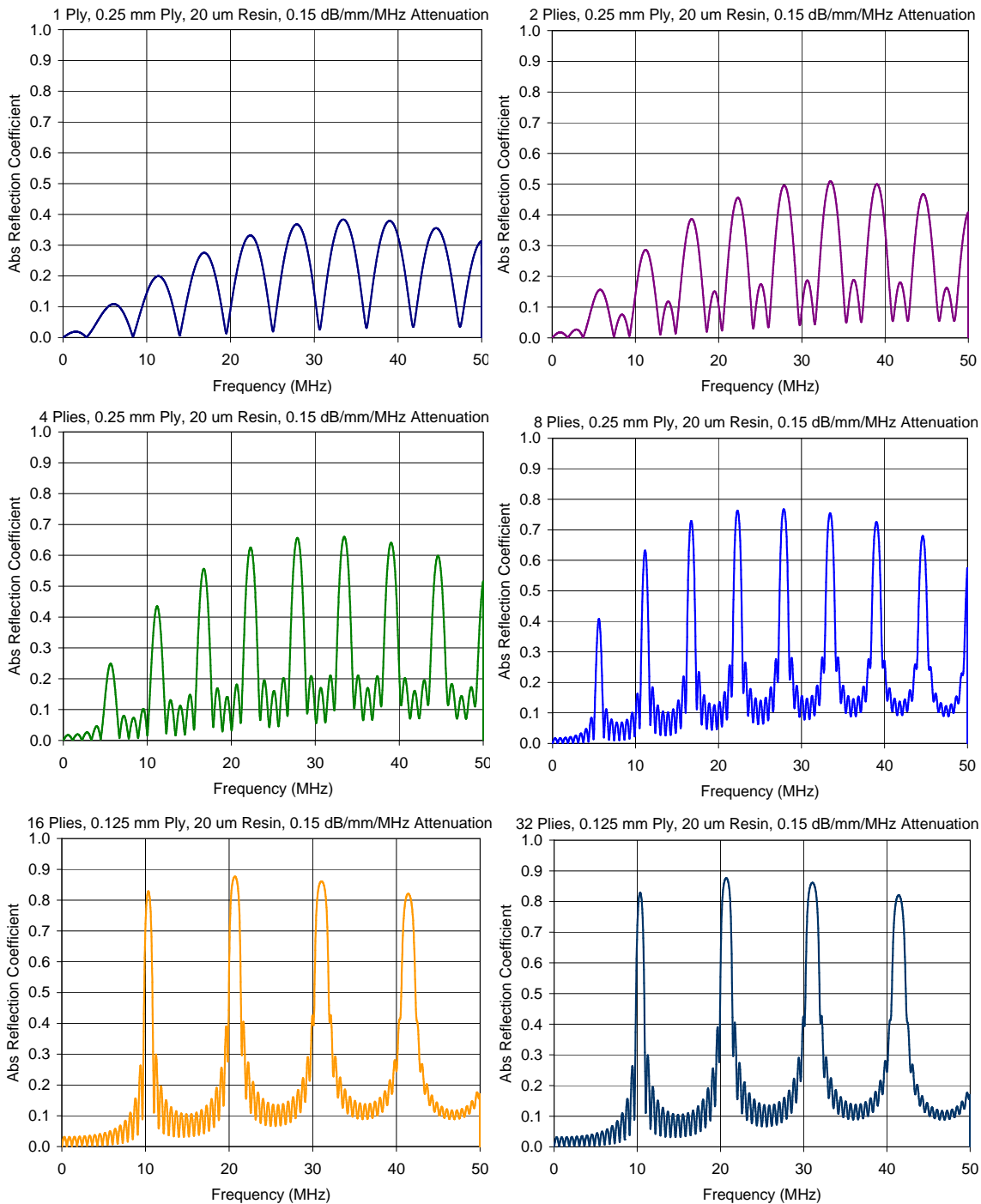


Figure 4-16. Reflection coefficient frequency responses calculated for 1 and 2 (top), 4 and 8 (middle) plies of 60% FVF and thickness 0.25 mm, each separated by 0.02 mm resin layers, using 0.15 dB/mm/MHz visco-elastic attenuation in the resin and embedded in composite. Also shown (bottom) are 16 and 32 plies of 0.125 mm thickness with the same resin thicknesses and attenuation.

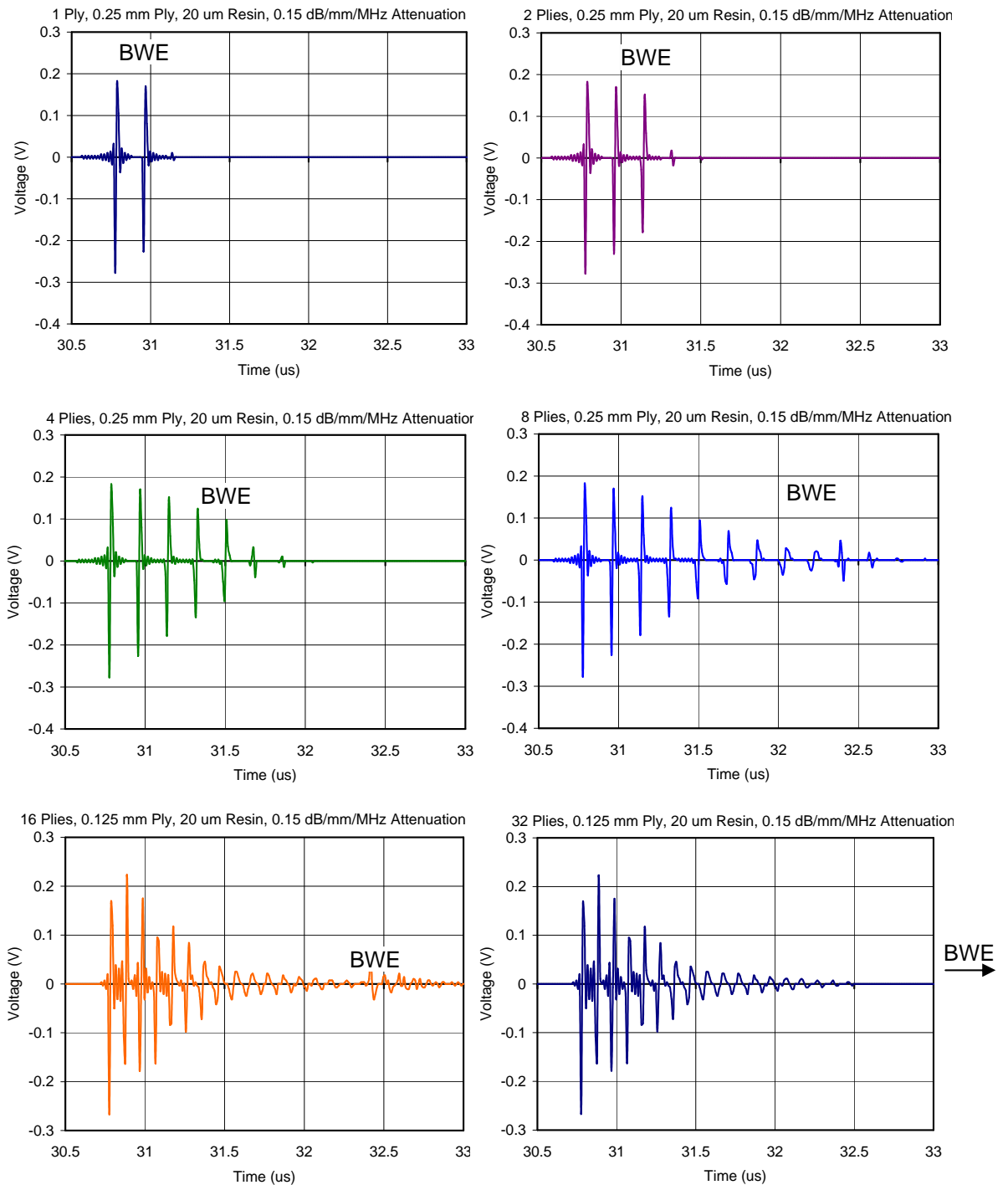


Figure 4-17. Reflection temporal impulse responses calculated for 1 and 2 (top), 4 and 8 (middle) plies of 60% FVF and thickness 0.25 mm, each separated by 0.02 mm resin layers, using 0.15 dB/mm/MHz attenuation in the resin, embedded in composite. Also shown (bottom) are 16 and 32 plies of 0.125 mm thickness. In each case, 'BWE' indicates the back-wall echo reflection.

4.4.3.2 Embedded in water

When water is used as the embedding medium the front-wall and back-wall reflections are phase-reversed and dominate the waveform. The frequency response then exhibits a quarter-wave resonance instead of a half-wave resonance, as shown in Figure 4-18 with time-domain responses in Figure 4-19.

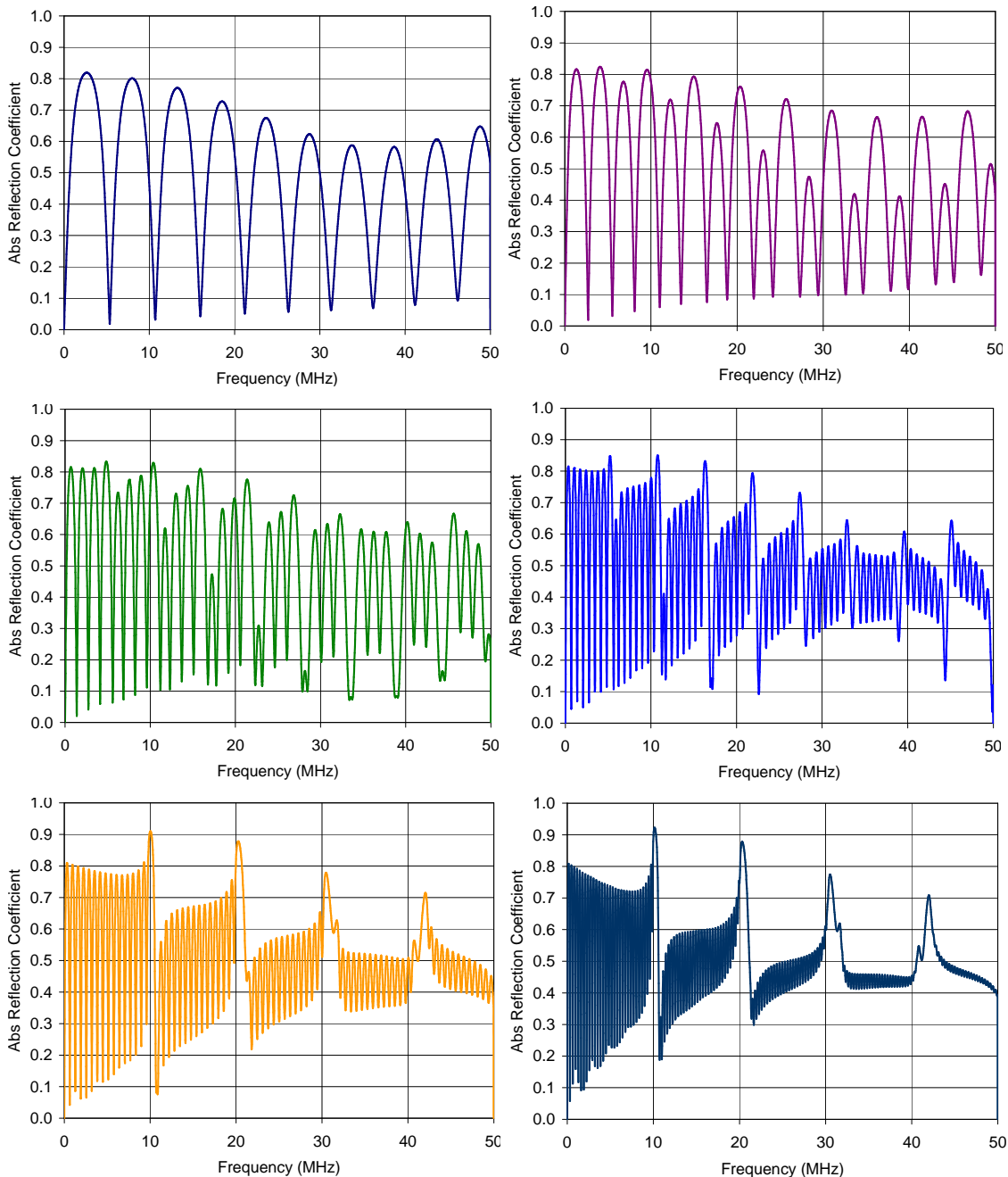


Figure 4-18. Reflection coefficient frequency responses calculated for 1 and 2 (top), 4 and 8 (middle) 0.25 mm plies of 60% FVF, each separated by 0.02 mm resin layers, using 0.15 dB/mm/MHz attenuation in the resin, and embedded in water. Also shown (bottom) are 16 and 32 plies of 0.125 mm thickness.

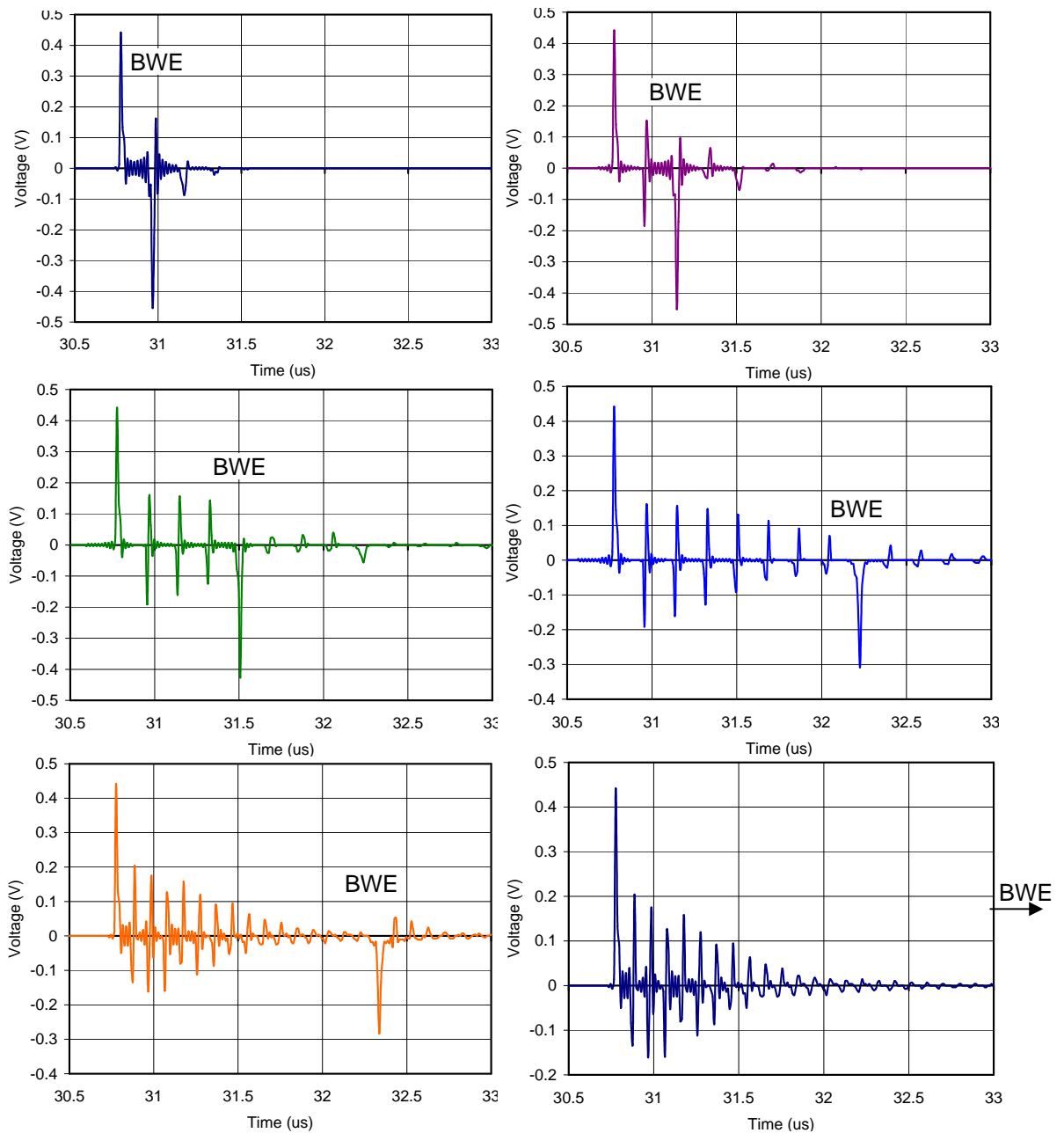


Figure 4-19. Reflection temporal impulse responses calculated for 1 and 2 (top), 4 and 8 (middle) plies of 60% FVF and thickness 0.25 mm, each separated by 0.02 mm resin layers, using 0.15 dB/mm/MHz attenuation in the resin and embedded in water. Also shown (bottom) are 16 and 32 plies of 0.125 mm thickness.

4.4.4 Comparison with MLM-Propmat for multiple plies

The comparison with MLM-Propmat was performed for a 32-ply stack of 0.125 mm thick plies separated by 2 μ m resin layers, all surrounded by water. The impulse response spectrum is shown in Figure 4-20 and Figure 4-21; both

showing good agreement. There was also good agreement with the simulated waveforms and spectra from Wang and Rokhlin (2003).

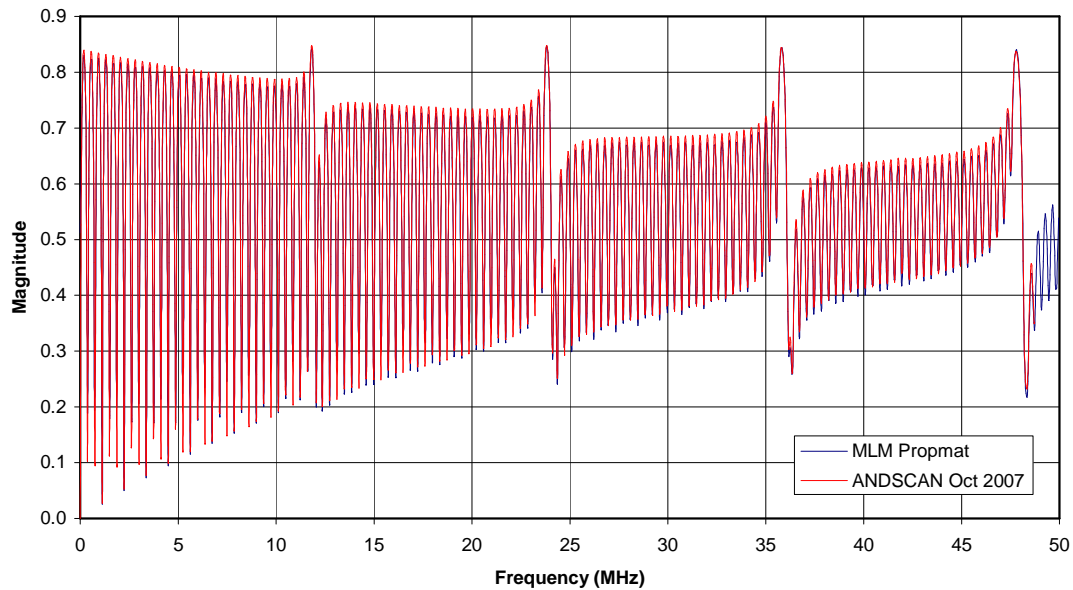


Figure 4-20. Comparison of the ANDSCAN version of the model with MLM-Propmat for a 32-ply stack of 0.125 mm-thick plies separated by 2 μm resin layers, surrounded by water, using 0.15 dB/mm/MHz attenuation in the resin.

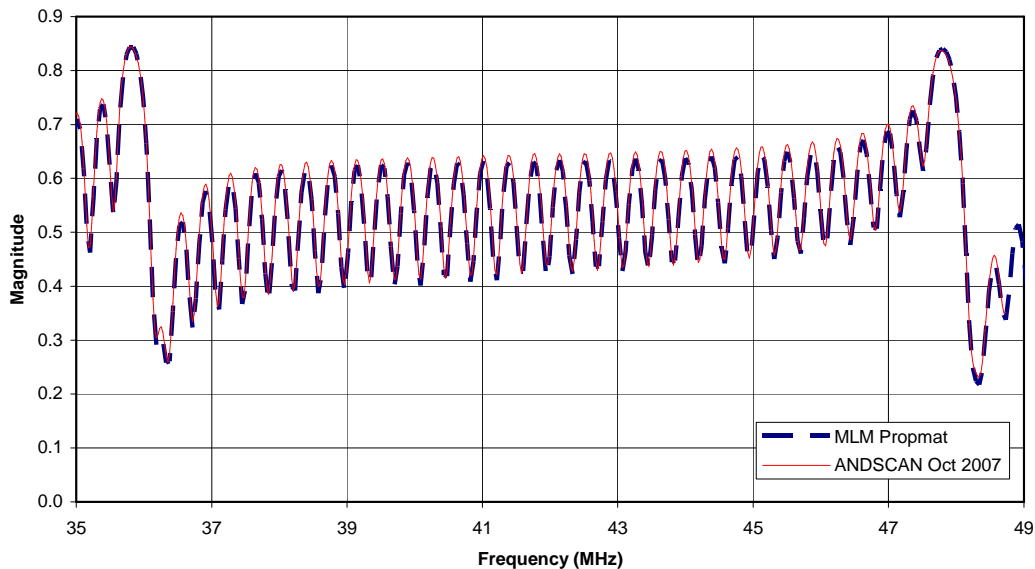


Figure 4-21. Expanded view of Figure 4-20 for better comparison.

A further comparison, but for 20 μm resin layers, surrounded by water is shown in Figure 4-22, demonstrating excellent agreement between the ANDSCAN (RAS) model and MLM-Propmat.

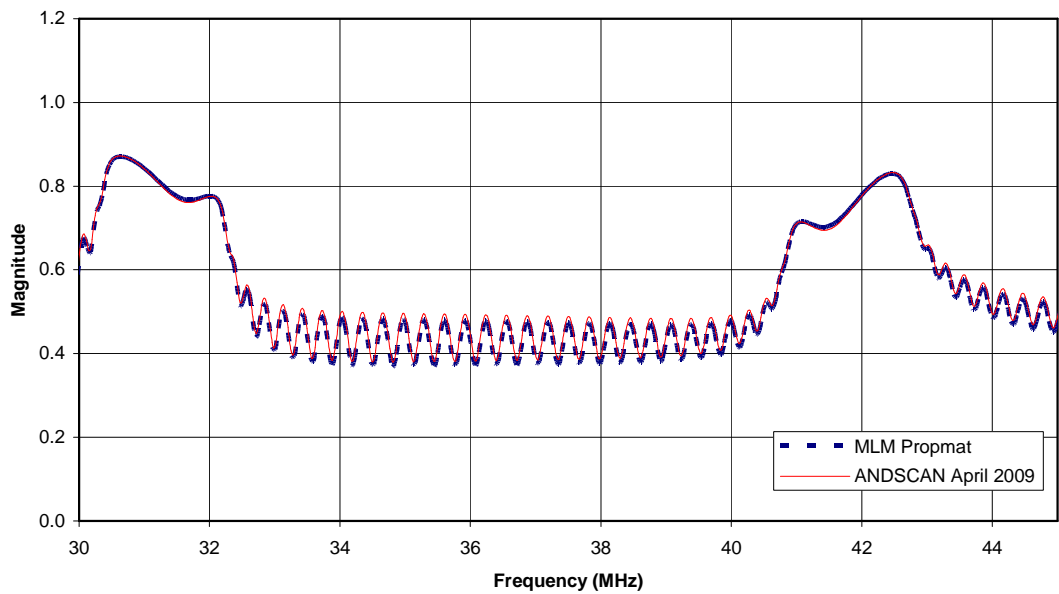
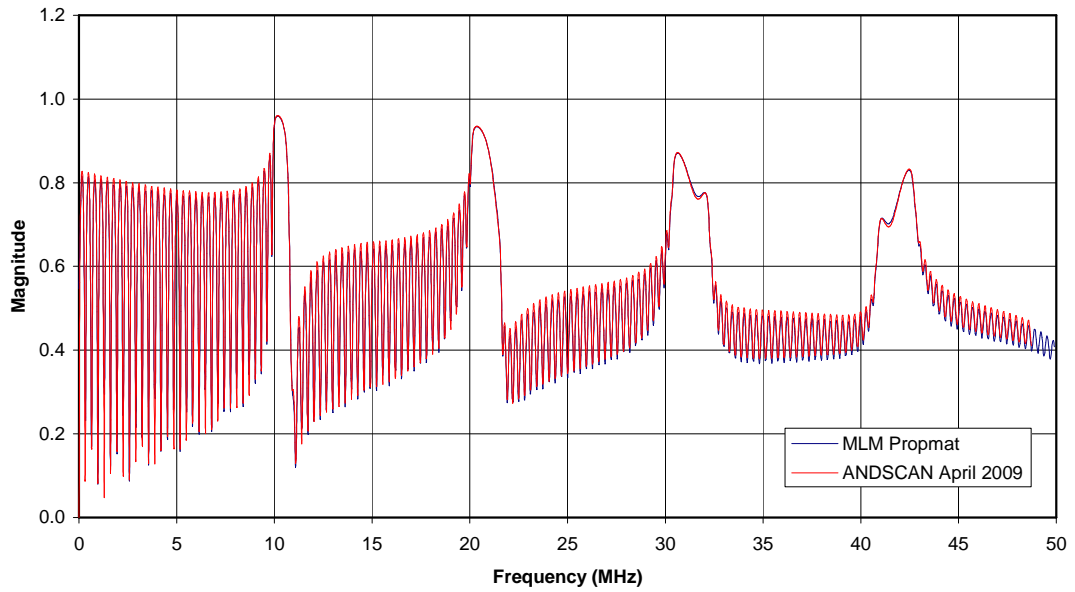


Figure 4-22. Comparison with MLM-Propmat for a 32 ply stack of 0.125 mm-thick plies, 80% FVF, separated by 20 μm resin layers, surrounded by water, using 0.15 dB/mm/MHz attenuation in the resin. The lower graph is an expanded view of the same comparison.

4.5 Convolution with Realistic Pulses

In order to simulate a real waveform and validate against experimental data, the impulse responses shown above need to be convolved with a realistic ultrasonic pulse, which can be generated in various ways. The reflected pulse from a

perfect reflector can be captured experimentally and used; the actual front-wall reflection from the specimen is generally adequate but less satisfactory. Alternatively, it can be formed from the transmit waveform (a step or short pulse) convolved twice with the impulse response of the transducer (ie transmit and receive filtering by the transducer), or the transducer itself can be modelled. All three options are considered here.

4.5.1 Use of front-wall echo

Convolution of the impulse response with a real ultrasonic pulse waveform is also possible if a front-wall echo signal is gated and then windowed using a Hanning taper before convolving with the impulse response calculated using the model. Although the front surface signal also includes interference from deeper plies, to a first approximation the water-to-composite interface will dominate this reflection. A 72-ply 18 mm-thick specimen is shown in Figure 4-23.

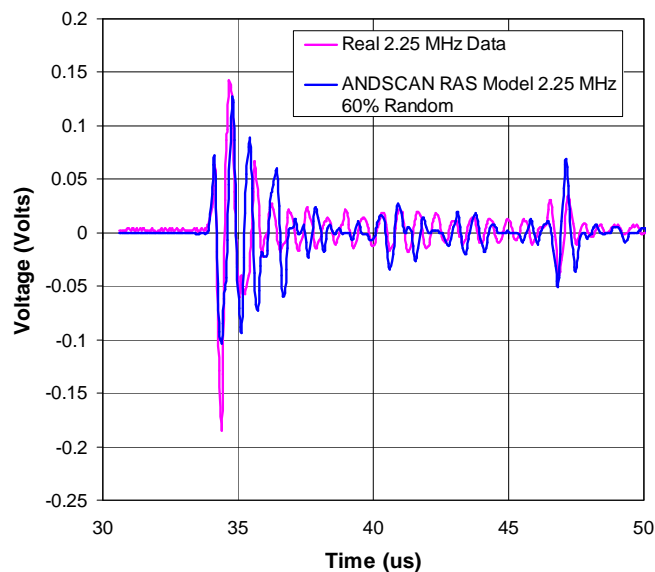


Figure 4-23. 2.25 MHz 38 mm focal-length (in water) focused-probe experimental and plane-wave modelled waveforms for a 72-ply 18 mm-thick composite specimen. The focus was at the mid-plane. The front surface signal from the experimental waveform was convolved with the impulse response from the model, having randomised the ply thickness by up to 60% of the nominal value.

Although agreement is far from exact, the actual ply spacings are unknown and cannot be modelled accurately, so randomised ply spacings, l , were used, allowing up to $q=60\%$ variation of the nominal ply spacing, l_0 .

The randomness was introduced using the following equation:

$$l = l_0[1 + 2(rand - 0.5)q] \quad (4-10)$$

where *rand* is a pseudo-random number generator embedded in Microsoft C, which generates equally distributed values (see Figure 4-24 for over 5000 samples) from 0 to 1 so that the range of thicknesses is $(1 - q)l_0$ to $(1 + q)l_0$.

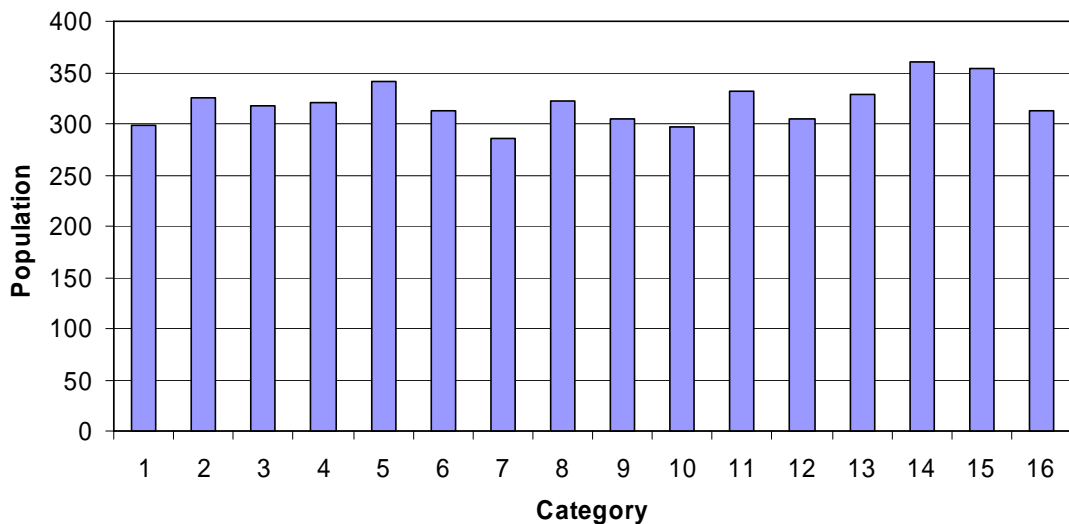


Figure 4-24. Distribution of pseudo-random numbers produced by Microsoft C *rand()* function – over 5000 samples divided into 16 equal categories in the output range.

In addition, the model automatically recalculates the fibre volume fraction to be the ratio l_0/l of the ‘designed’ fibre volume fraction. Inclusion of this randomness was necessary to obtain some similar amplitudes of ply reflections, relative to the front-wall echo, to those found experimentally in Figure 4-25.

The effect of increasing the randomness in layer thicknesses can be seen in Figure 4-26. With reference to Figure 4-25 it can be seen from the time-frequency plots that the experimental data seems to include less than 10% randomness and yet the signals from the ply resonances seem much larger than from the model, relative to the front surface signal. The 38 mm focal-length probe was focused at the mid-plane of the specimen. This could have artificially increased the mid-ply resonance amplitudes relative to the front-surface signal.

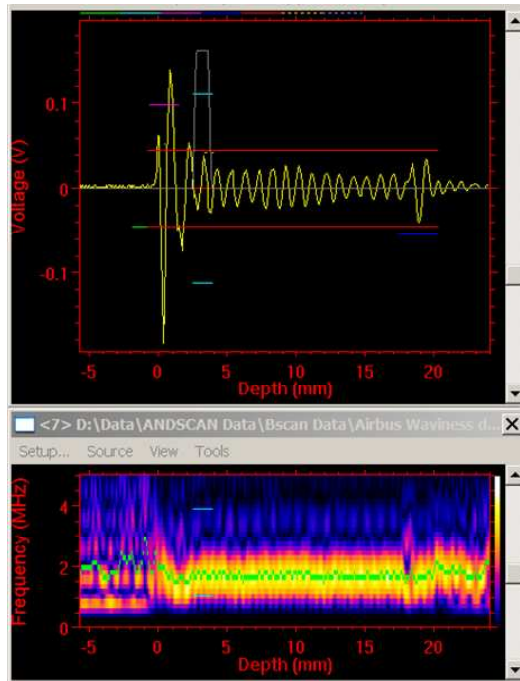


Figure 4-25. Experimental waveform (top) and corresponding band-pass filtered time-frequency plot (bottom) from a 72-ply 18 mm thick composite using a 2.25 MHz focused probe. Note that the calculated first resonance for this structure occurs at 1.7 MHz – very close to the green energy-centroid frequency line shown on the time-frequency plot.

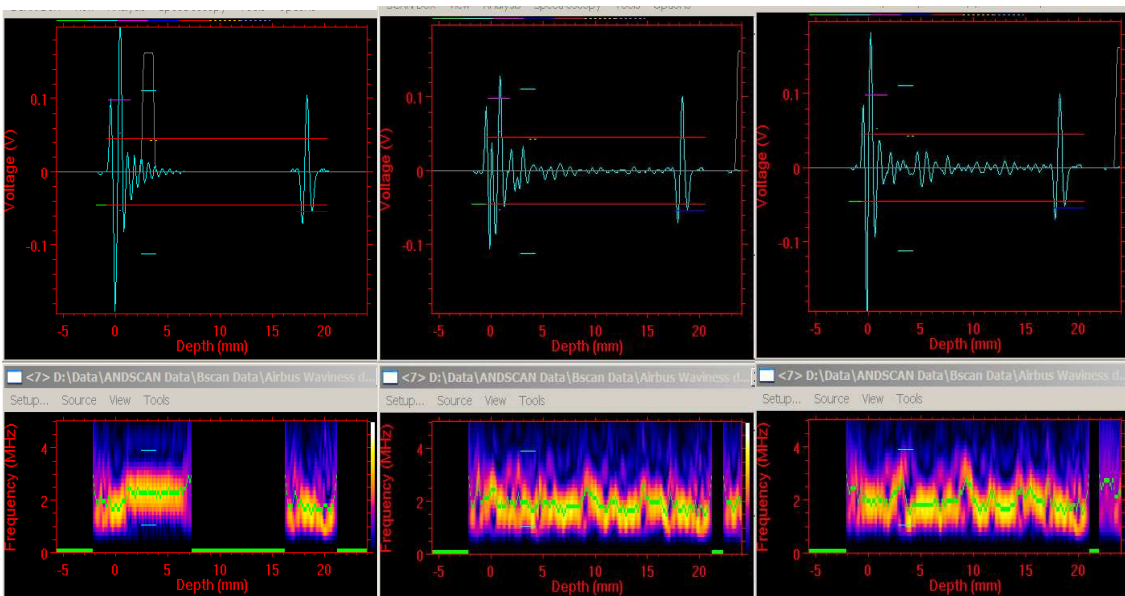


Figure 4-26. The effect of increasing randomness in the composite layer thickness in a 72-ply stack modelled using 0.25 mm plies separated by 20 μm resin layers. Amounts of randomness are (left to right) 0%, 10% and 20%.

A band-gap in transmission at the resonant frequency has caused attenuation of the resonances in the left image of Figure 4-26 to such an extent that a spectrum could not be generated from the sub-digitisation-level amplitudes of the later inter-ply reflections. It is only when there is no randomness in ply spacing that such a significant and narrow band gap is generated. This, and the effect of randomness on that transmission band-gap are discussed in Chapter 5.

However, when this specimen was examined more closely by micro-sectioning, it was found to contain stitched groups of four plies and that the stitching caused a thicker layer every four plies. This was then simulated using 18 plies of thickness 0.85 mm separated by 0.17 mm resin layers – see Figure 4-27.

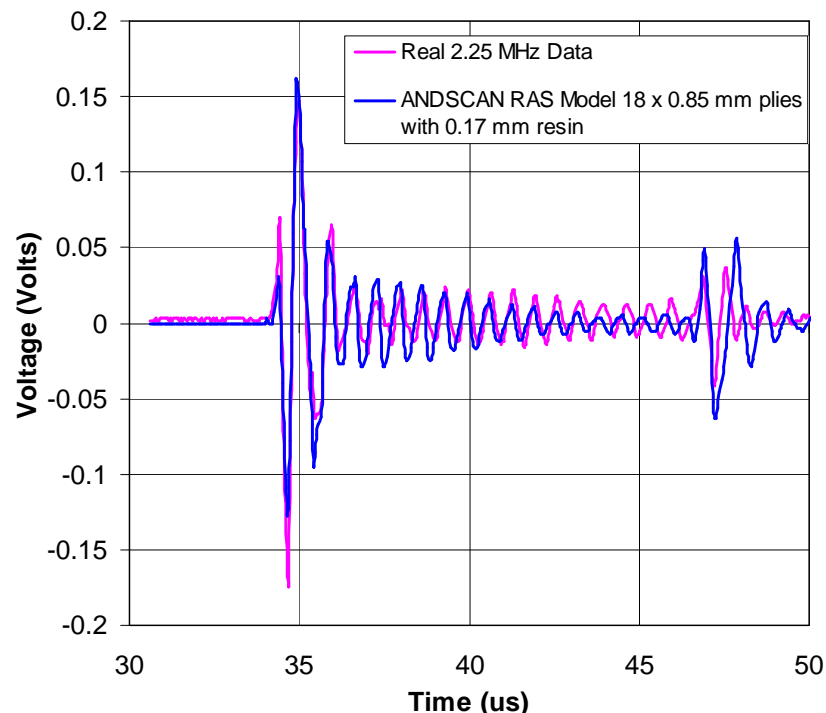


Figure 4-27. Result of convolving a 2.25 MHz front-surface reflection with the impulse response from 18 layers 0.85 mm thick with 0.17 mm resin layers for the stitching. FVF was set at 80% and resin attenuation at 0.15 dB/mm/MHz.

The specimen used for the experimental data contained regions of out-of-plane fibre waviness and two waveforms from such regions are shown in Figure 4-28. It can be seen that the time-frequency plot does seem to identify these regions with a change in the energy-centroid frequency.

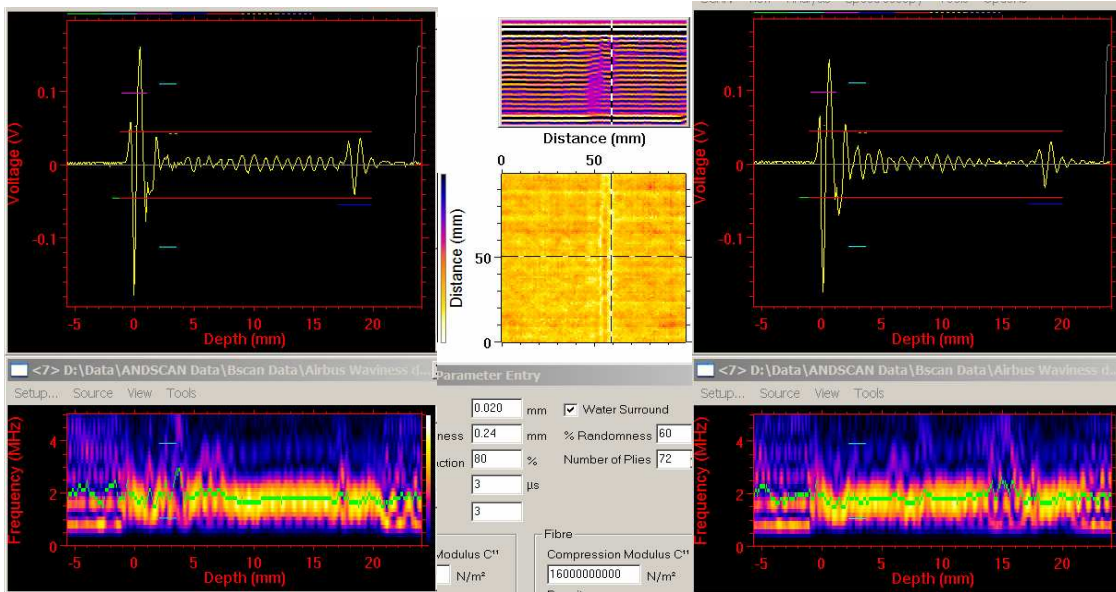


Figure 4-28. Experimental 2.25 MHz waveforms from the same specimen as Figure 4-25 but over a region with out-of-plane waviness near the front of the specimen (left image) and near the back of the specimen (right image). Note that in these regions the time-frequency plot shows a change in the energy-centroid frequency (green line).

Further comparisons of experimental and modelled waveforms - at 25 MHz for a 24-ply 3 mm thick composite - are shown in Figure 4-29 and Figure 4-30. Note that approximately 20% randomness in thickness (Figure 4-26, right) is required to give a similar time-frequency plot to the experimental data (Figure 4-28).

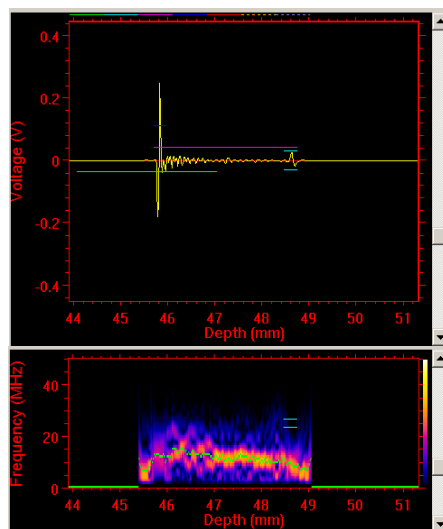


Figure 4-29. 25 MHz waveform, averaged over a small region, from a 24-ply, 3 mm thick composite.

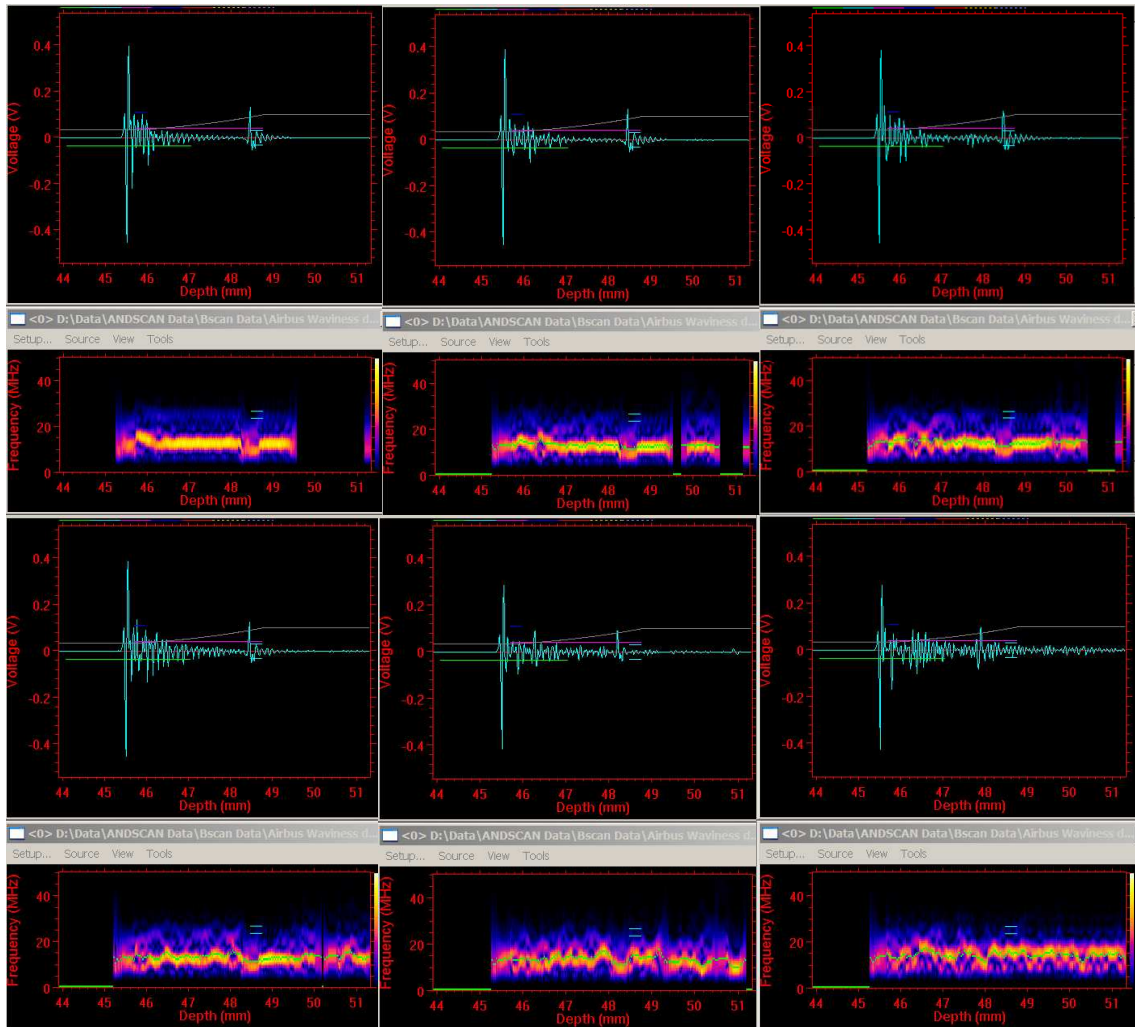


Figure 4-30. 25 MHz modelled waveforms using different amounts of randomness in the 24 composite layers: (top, left to right) 0%, 4%, 8%, (bottom, left to right) 20%, 40%, 60% of randomness in ply thickness.

4.5.2 Use of a modelled transducer response

The transducer response has been modelled previously (Phang 2006) using a convolution of the impulse response of the transducer front and back interfaces with a half-cycle of a sine wave. In the current work, this convolution is performed in the frequency domain so it is easy to apply the response twice - simulating transmit and receive responses - and then filter it using a low-pass filter to represent the attenuation of water (if water is the coupling medium). The result is a realistic pulse waveform. The Q-factor can be varied by changing the reflection coefficients of the two interfaces of the transducer – a higher reflection coefficient giving a narrower bandwidth and hence a higher Q-factor. Spectra and waveforms are shown in Figure 4-31 and Figure 4-32 respectively.

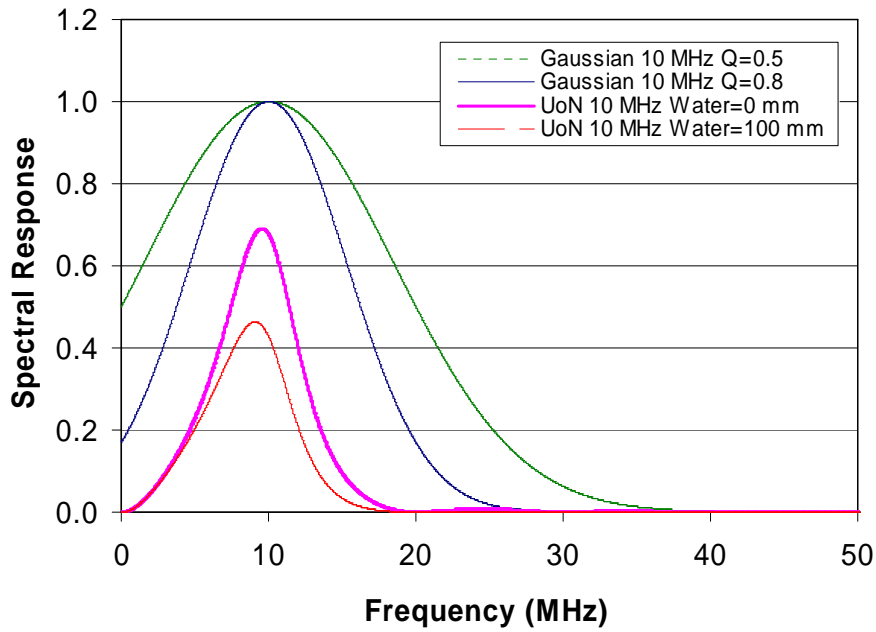


Figure 4-31 Simulated spectral responses corresponding to the pulse-echo waveform from a reflector placed at the front of the specimen.

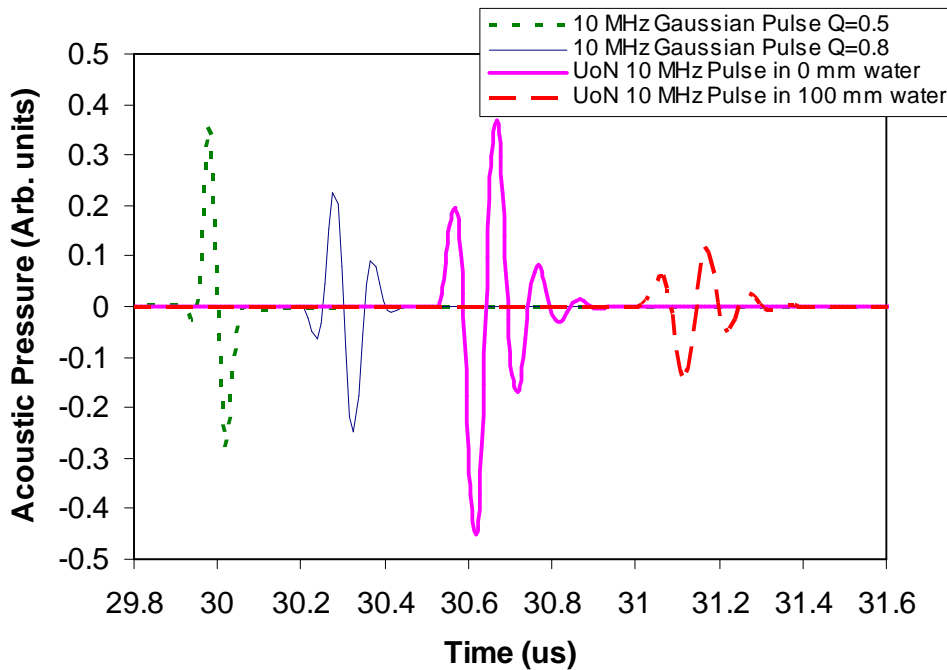


Figure 4-32 Simulated temporal responses corresponding to the pulse-echo waveform from a perfect reflector placed at the front of the specimen. Time delays have been applied to separate the pulses for ease of viewing and the first two (left-most) pulses are from the Gaussian pulse envelope method, whilst the 3rd and 4th (right-most) pulses were generated using the transducer model.

4.5.3 Use of a Gaussian pulse envelope

If the transducer is approximated as a Gaussian band-pass filter, it is possible to control the Q-factor of the pulse quite easily. The equation for the spectrum depends on the centre frequency f_0 and the half-bandwidth at half-height, w_{6dB} , which is calculated from the Q-factor, Q ($w_{6dB} = f_0/2Q$):

$$A(f) = A_0 e^{-\frac{(f-f_0)^2 \ln(2)}{w_{6dB}^2} + i\pi \sin \theta} \quad (4-11)$$

where the phase response is forced to follow a sine-wave profile varying from $-\pi$ to $+\pi$ as the resonance is transitioned, given by:

$$\theta = \frac{\pi(f - f_0)}{4w_{6dB}} \text{ but is constrained by: } \frac{\pi}{2} \geq \theta \geq -\frac{\pi}{2}$$

Spectra and waveforms are also shown in Figure 4-31 and Figure 4-32 respectively, by comparison with the modelled transducer response.

4.6 Modelling a Porous Layer

4.6.1 Porous layers in the model

The model changes the material properties of each ply based on the specified amount of porosity. The simple volumetric mixture rule described above was used initially to calculate local changes in modulus, ultrasonic velocity and density, thus giving the averaged changes in impedance across each layer as a result of porosity. However, an investigation of more comprehensive mixture rules (documented in Section 4.6.5) revealed that the simple volumetric rule is probably too simple for the inclusion of porosity into composite.

There is also enhanced attenuation due to scattering from the porosity. This can be modelled in various ways but the method of Adler et al (1986) was used for the convenience of an analytical expression.

If multiple plies containing porosity are modelled, it is possible to include an element of randomness in the void volume fraction ϕ_v in each adjacent layer. The randomness was introduced using the following equation:

$$\phi_v = \phi_0[1 + 2(rand - 0.5)q] \quad (4-12)$$

where ϕ_0 is the nominal void volume fraction and $rand$ is the above-mentioned pseudo-random number generator embedded in Microsoft C, which generates evenly distributed but random values from 0 to 1 so that the range of void volume fractions is from $(1 - q)\phi_0$ to $(1 + q)\phi_0$.

4.6.2 Enhanced attenuation due to scattering

The basis of the increased attenuation due to scattering in a porous layer for the long-wavelength limit is Equation 4-13, which is derived from Adler et al (1986) and links the frequency dependence to pore size via the reduced scattering cross-section $\Gamma(ka)$.

$$\alpha(k) = \frac{3\phi_v}{4a} \Gamma(ka) \quad (4-13)$$

where ϕ_v is the void volume fraction, k is the wavenumber and a is the porosity radius. Thus the size of the individual pores has to be specified in order to determine the frequency-dependent attenuation. At this stage, no allowance was made for the return of backscattered energy to the transducer except in the sense of changes in reflection coefficient at the composite-resin boundaries due to changes in average impedance of the composite layer due to porosity.

A transition between long-wavelength and short-wavelength expressions for $\Gamma(ka)$ is required in order to match the frequency responses given by Adler et al (1986) in Figure 4-33. For $ka < \psi$ (where $\psi = 0.7$ works well because that is the peak in the Adler curve) the long-wavelength expression is used (from Equations 3-1 and 3-2). For $ka > \psi$ the long-wavelength expression is modified to Equation 4-14 and it is mixed with the short-wavelength limit $\Gamma(\infty)$ (which still seems to depend on η) based on the ratio $(\psi/ka)^2$. The modified long-wavelength expression is:

$$\Gamma(ka) = \beta(\eta)(ka)^{4-n} \psi^n \quad (4-14)$$

where η is the ratio of shear to longitudinal velocities and n is used to adjust the rate of transition from the long- to short-wavelength expressions. The full equation for reduced scattering cross-section (Equation 4-15) best matched the graphs of scattering cross-section of Adler et al when $n = 3$, see Figure 4-33.

$$\Gamma(ka) = \left(\frac{\psi}{ka}\right)^2 \beta(\eta)(ka)^{4-n} \psi^n + \left[1 - \left(\frac{\psi}{ka}\right)^2\right] \Gamma(\infty) \quad (4-15)$$

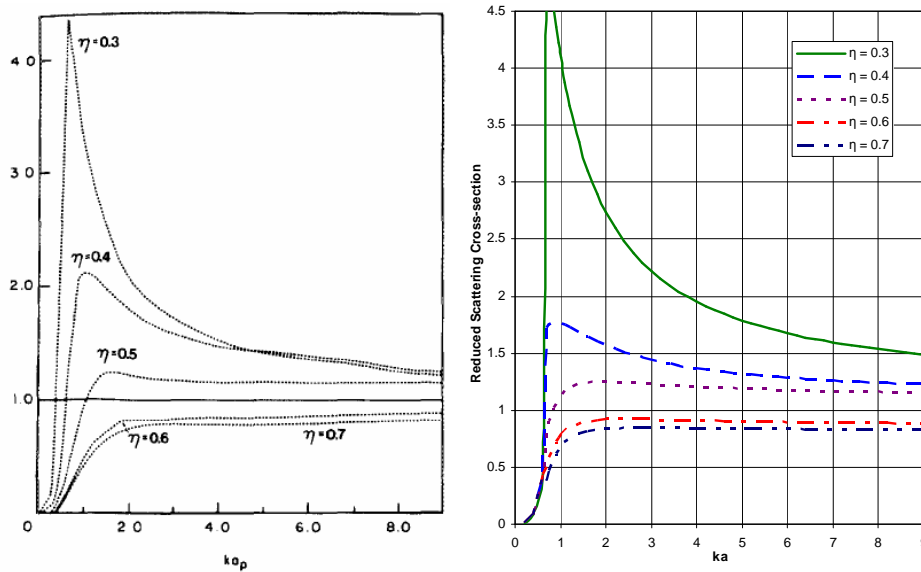


Figure 4-33. Adler et al (1986) (left) and modelled version (right) of the reduced scattering cross-section for $n=3$ and for different values of η .

The complete equation used for calculating the scattering attenuation coefficient $\alpha(k)$ is shown in Equation 4-16.

$$\alpha(k) = \frac{3\phi_v}{4a} \left\{ \left(\frac{\psi}{ka}\right)^3 \beta(\eta)(ka)^{4-n} \psi^n + \left[1 - \left(\frac{\psi}{ka}\right)^3\right] \Gamma(\infty) \right\} \quad (4-16)$$

4.6.3 Single-ply frequency response of porosity

In order to simulate the response from a small volume element in the way that the 3D porosity profiling is intended to work, a simple 3-layer system (resin-composite-resin, embedded in composite) was investigated first as this could be an ideal layer thickness for a volume element. Examples of the frequency-response variations with the inclusion of varying amounts of porosity in the

single composite layer in the middle of the volume element are given in Figure 4-34 for both 60% and 80% fibre volume fraction.

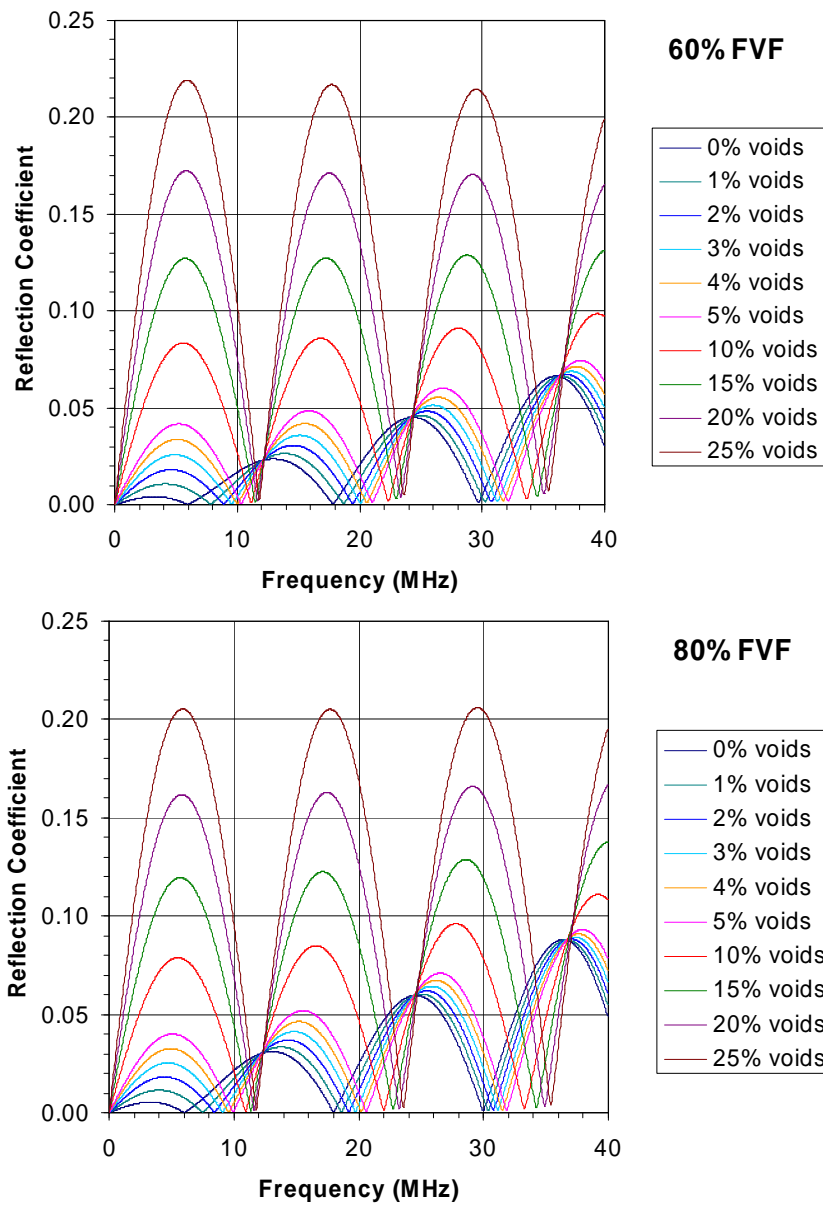


Figure 4-34. The effect of varying porosity levels in a single ply on the local resin-ply-resin frequency-dependent reflection coefficient for 60% fibre volume fraction (top) and 80% (bottom). The simple volumetric mixture rule was used.

It is very interesting that only a small amount of porosity is required to completely change the nature of the ply resonance from a $\frac{1}{2}$ -wave resonance to a $\frac{1}{4}$ -wave resonance. This is due to the resin and composite impedances being very similar, so a very small lowering of the impedance of the composite layer results in a reversal of the resin-composite reflection coefficient, thus changing

the nature of the reflection in the thin resin layer. From these modelling results it is possible to envisage the use of the amplitude response at the resonant frequency, or the resonant frequency itself, to measure porosity. Possible calibration curves are shown in Figure 4-35.

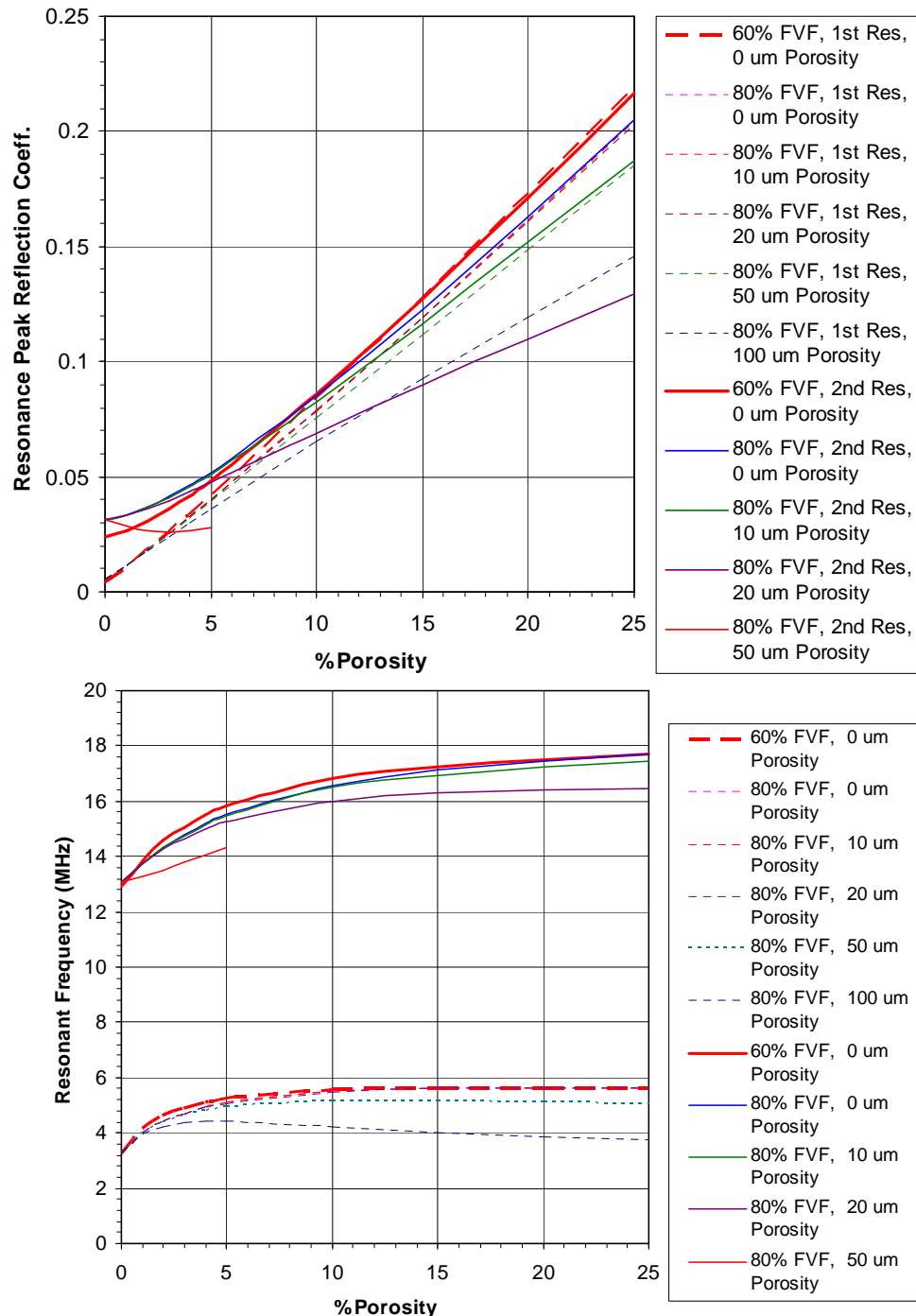


Figure 4-35. The calibration curves for single-ply porosity against resonant amplitude reflection coefficient (top) and resonant frequency (bottom). These are given for different void sizes at 80% fibre volume fraction and, at a zero size, for 60% (thick red lines) and 80% fibre volume fraction..

If the amplitude response is used, it is likely to be very susceptible to other material variations, such as thickening of resin layers, so there may be a need to use the resonant frequency shift as a classifier to determine whether porosity is present or not.

4.6.4 Micromechanical mixture rules

Various mixture rules have been proposed in the literature (see Chapter 3 and Appendix F). Several of these methods are derived from, or use the work by Hashin (1962), often providing further validation of his work against experiment. For this reason, the Hashin (1962) spherical-inclusion method was chosen to provide a comparison with the simple mixture rule for porous composite, and the Hashin (1965) method for long-fibre composites was chosen for the fibre composite. If carbon fibres are being modelled, which are anisotropic, it is important to use the transverse modulus and Poisson's ratio for ultrasonic propagation across the plies, in which case the isotropic-fibre expressions of Hashin (1965) still apply – as shown by Hashin (1979).

The modulus that is required for compression-wave propagation of ultrasound is the compression (or longitudinal) modulus, M , which can be derived from the bulk (K) and shear (G) moduli as in Equation 4-17 (App. F has a full treatment):

$$M = K + \frac{4}{3}G \quad (4-17)$$

It is also noted that the simple mixture rule (Equation 4-5) is still valid for calculating density.

4.6.5 Mixture rules for porosity in composite

In Appendix F a comparison of mixture rules from the literature is made. For spherical inclusions such as porosity, the Hashin (1962) method has been shown to be adequate (see Figure 4-36).

Three of the methods for determining the modulus of porous composite proposed in Appendix F – Hashin, Hashin-Bezier and the Pinfield et al (2010) scattering model - were all built into the model as optional mixture rules to use.

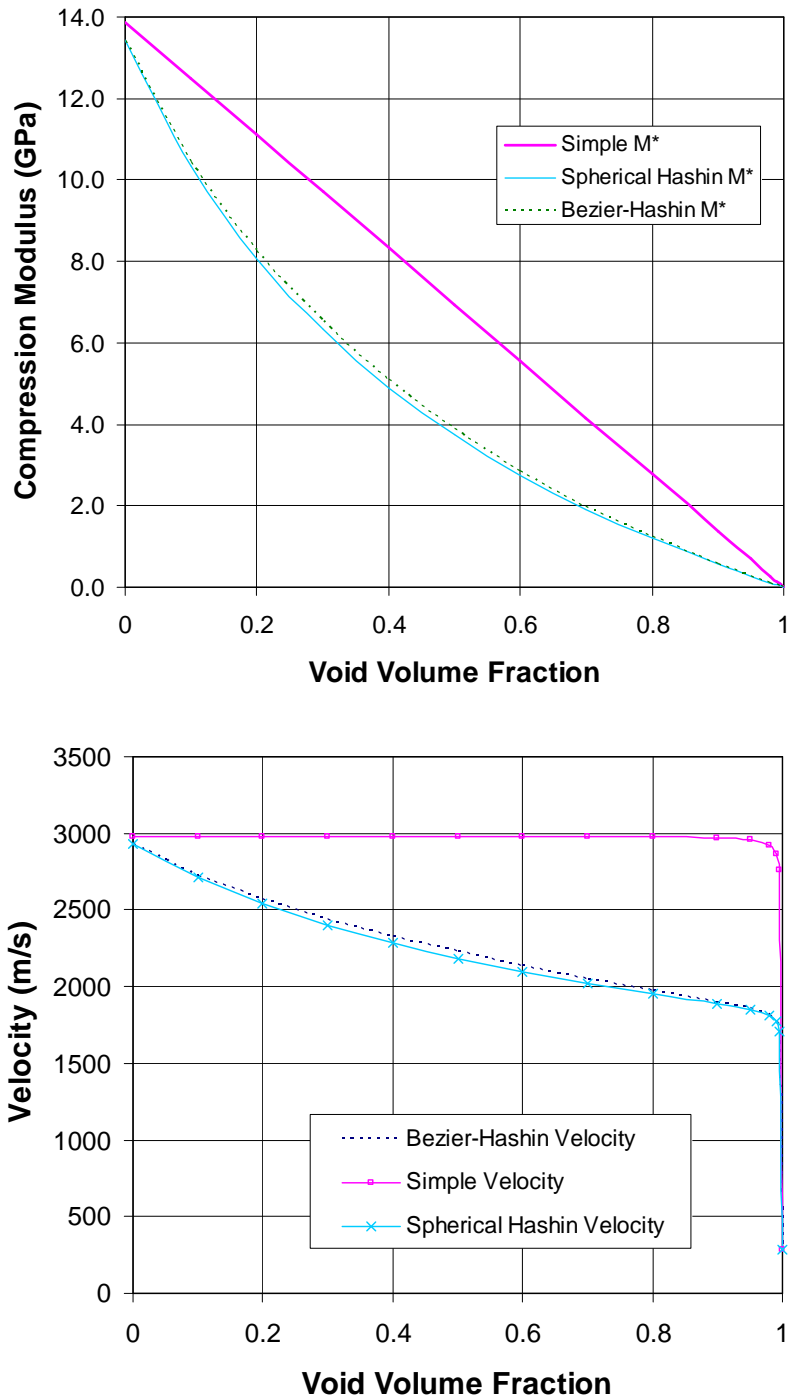


Figure 4-36. Comparison of compression modulus (top) and velocity (bottom) for porous carbon-fibre epoxy composite calculated using the methods presented in Appendix F.

The Hashin and Hashin-Bezier methods are indistinguishable, but the Pinfield scattering method affects both the frequency response and the phase of the backscattered signal and this can be seen in the normalised time-frequency analysis shown in Figure 4-37. The additional $\pi/2$ phase shift at all frequencies,

noted by Pinfield et al (2010), has the effect of changing the reflected pulses from even to odd functions (see A and B labels in Figure 4-37).

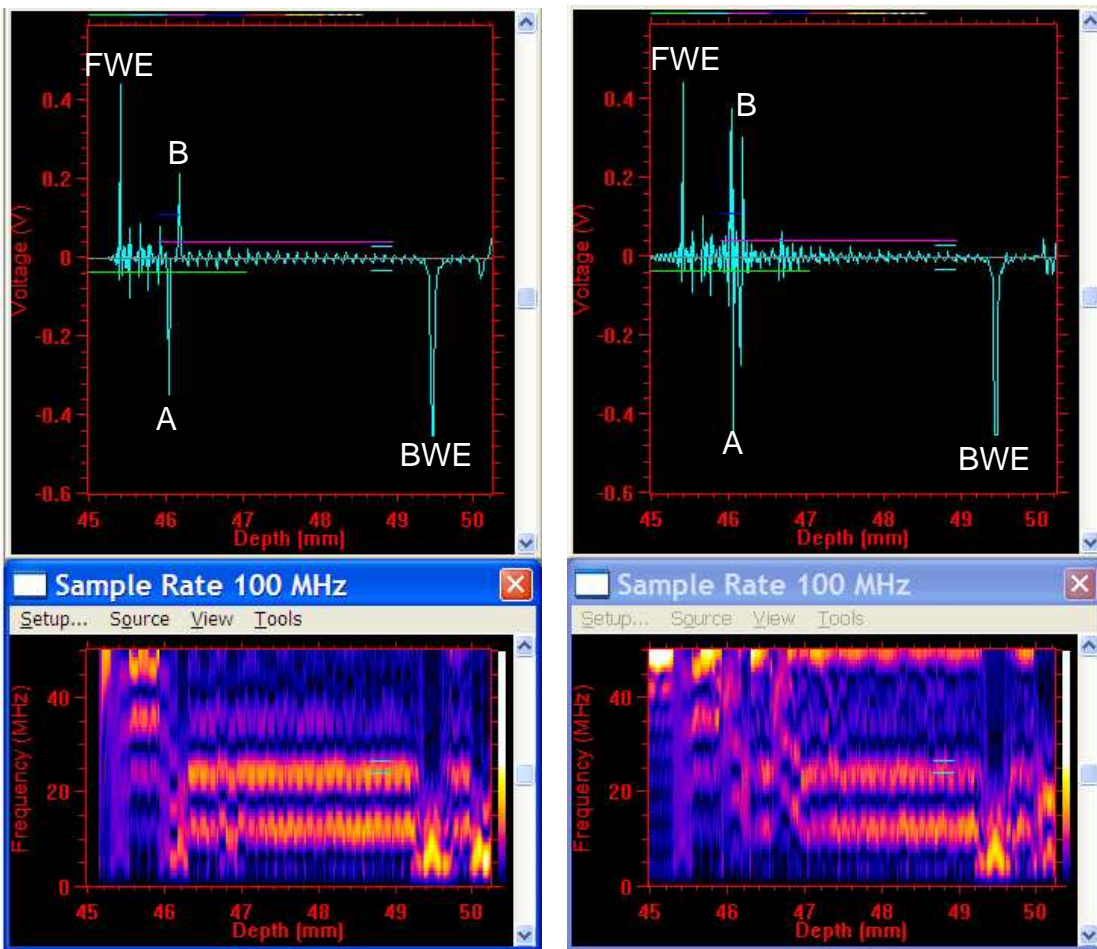


Figure 4-37. Comparison of the Hashin mixture rule (left) and the Pinfield et al (2010) scattering mixture rule (right) for the simulated impulse response of a single porous 0.125 mm ply in a 32-ply stack, where 10% porosity comprising 10 μm radius pores has been inserted at ply 6. Time-domain waveforms (top) and time-frequency analysis with a Hanning window on 20% of the gate width (bottom) are both shown. Front (FWE) and back-wall (BWE) echoes are indicated along with the front and back of the porous layer (A and B).

4.6.6 Comparison of mixture rules for fibre-resin composite

The simple volumetric mixture rule is a lot closer to the more exact Hashin (1965) analysis for carbon fibres in resin than for glass fibres or porosity in resin. This is because carbon fibre has a transverse modulus that is much nearer to that of the resin matrix – see Figure 4-38.

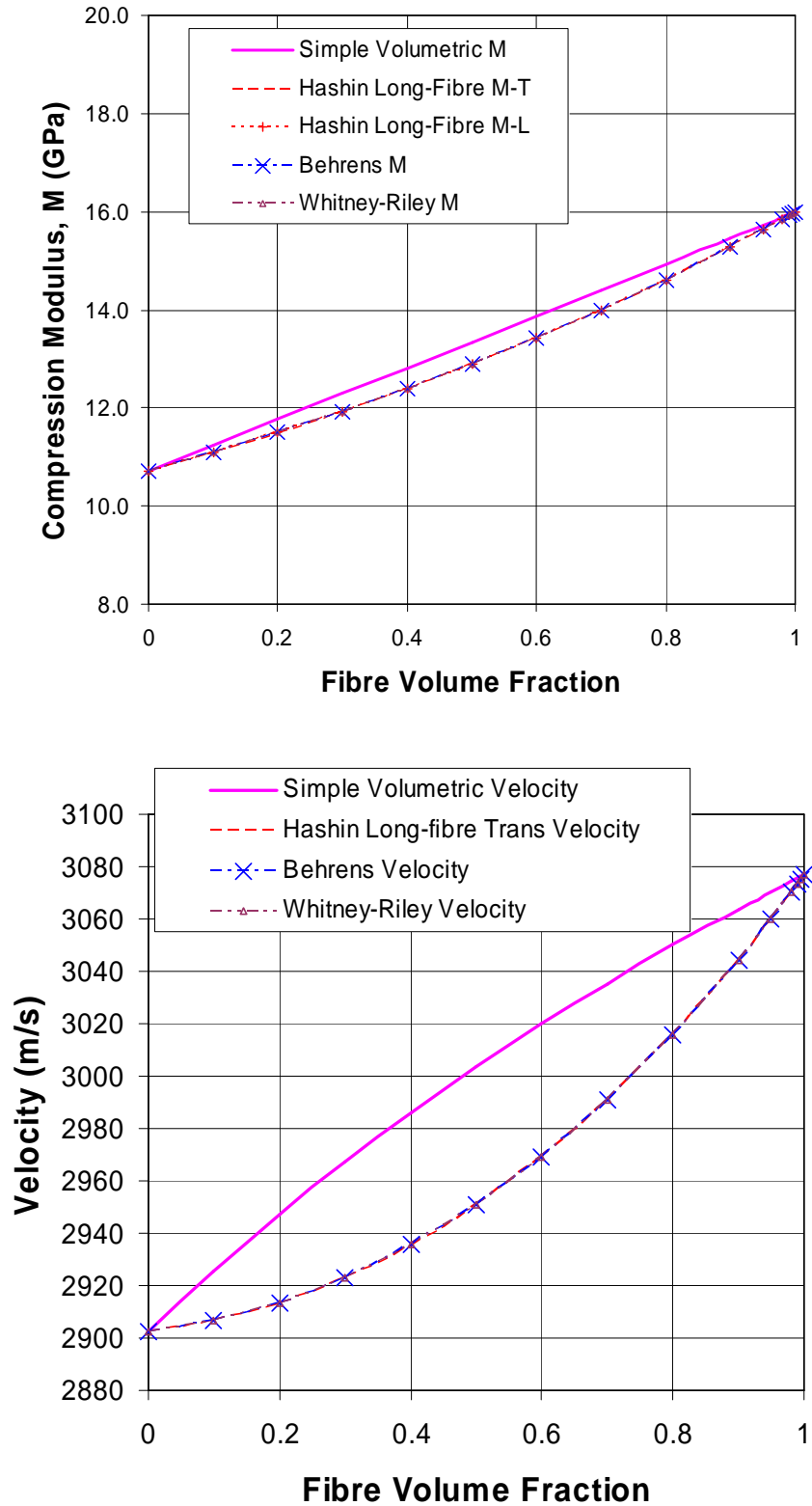


Figure 4-38. Comparison of compression modulus (top) and transverse velocity (bottom) for carbon-fibre epoxy composite calculated using various methods from the literature. The Hashin moduli have been calculated using the lower bounds for the shear moduli.

Figure 4-38 shows that there is a maximum 4% difference (at 60% FVF) in modulus and 1.7% difference (also at 60% FVF) in velocity between the simple volumetric and the more complex mixture rules for carbon-fibre composite. This is relatively trivial and suggests that the work in this project using the model with the simple volumetric mixture rule is still valid in terms of the conclusions that were drawn as a result.

4.6.7 Effect of mixture rules on porosity modelling

The modelling of porosity in composite addressed above used the simple volumetric mixture rule, before the Hashin method was programmed into the model. Figure 4-39 illustrates the difference that the velocity change modelled by Hashin (1962) has on the resonances in porous composite layers – resonant frequencies are downshifted at higher porosity levels due to a velocity overestimate by the simple volumetric rule by 20% for a 30% void volume fraction (see Figure 4-36). The reflection coefficients are up to 50% greater in magnitude using the Hashin method than the simple volumetric method.

This downshift in the first two resonant frequencies is also illustrated in Figure 4-40 (top) and is relatively independent of void size, although the amplitude at the resonance in Figure 4-40 (bottom) is dependent on void size.

For local porosity up to a volume void content of 30% there is insufficient downshift in the second resonant frequency for it to coincide with the normal ply resonance frequency – shown at 0% porosity on the graph in Figure 4-40 (top) and also in Figure 4-39.

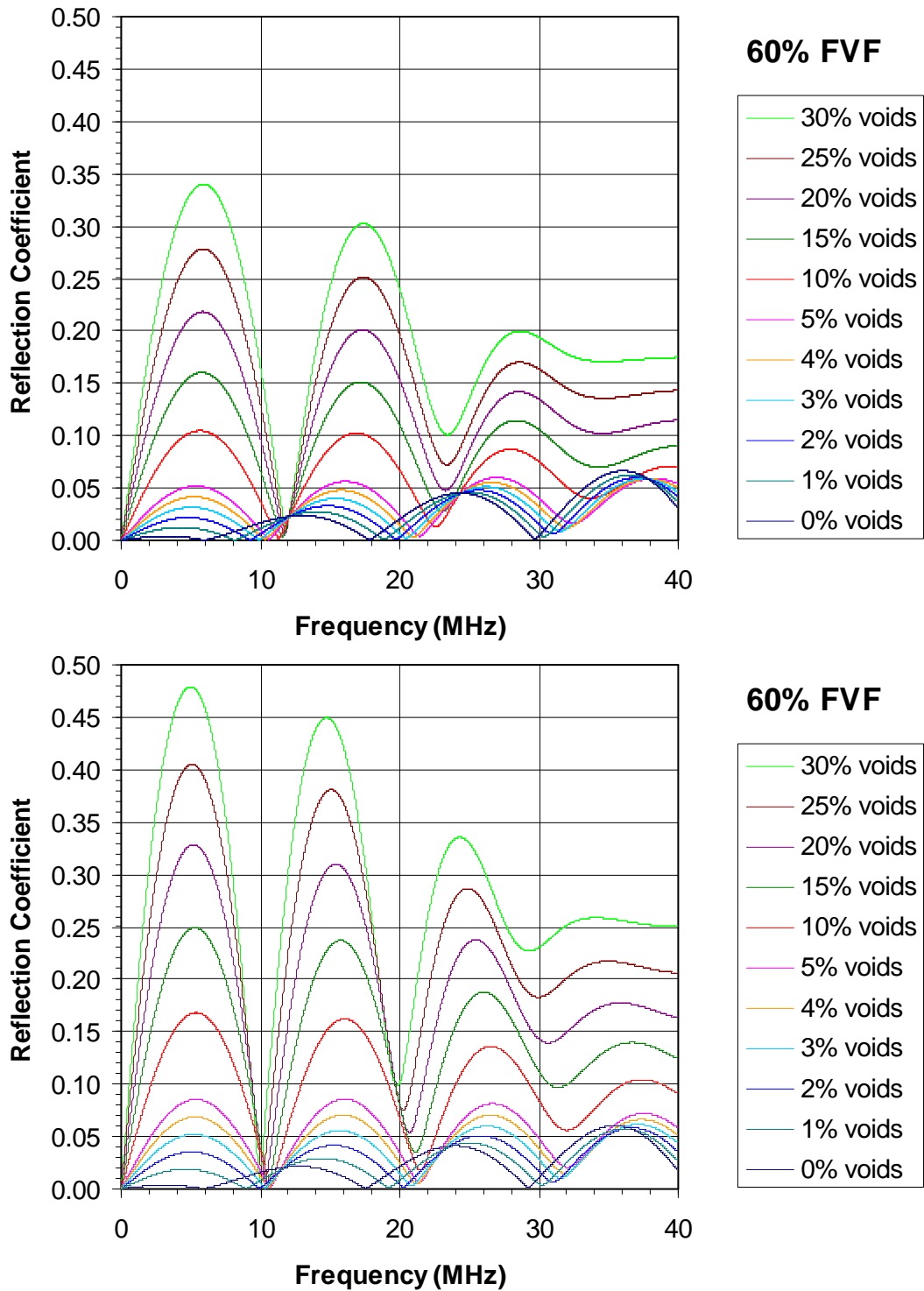


Figure 4-39. Simple volumetric (top) and Hashin-Bezier (bottom) mixture rules applied using the (RAS) analytical model to 10 μm porosity in a single 0.125 mm ply of 60% FVF composite sandwiched between two 0.002 mm resin layers. Note that the velocity change modelled in the Hashin-Bezier mixture rule (bottom) causes a downshift in resonant frequency for larger amounts of porosity.

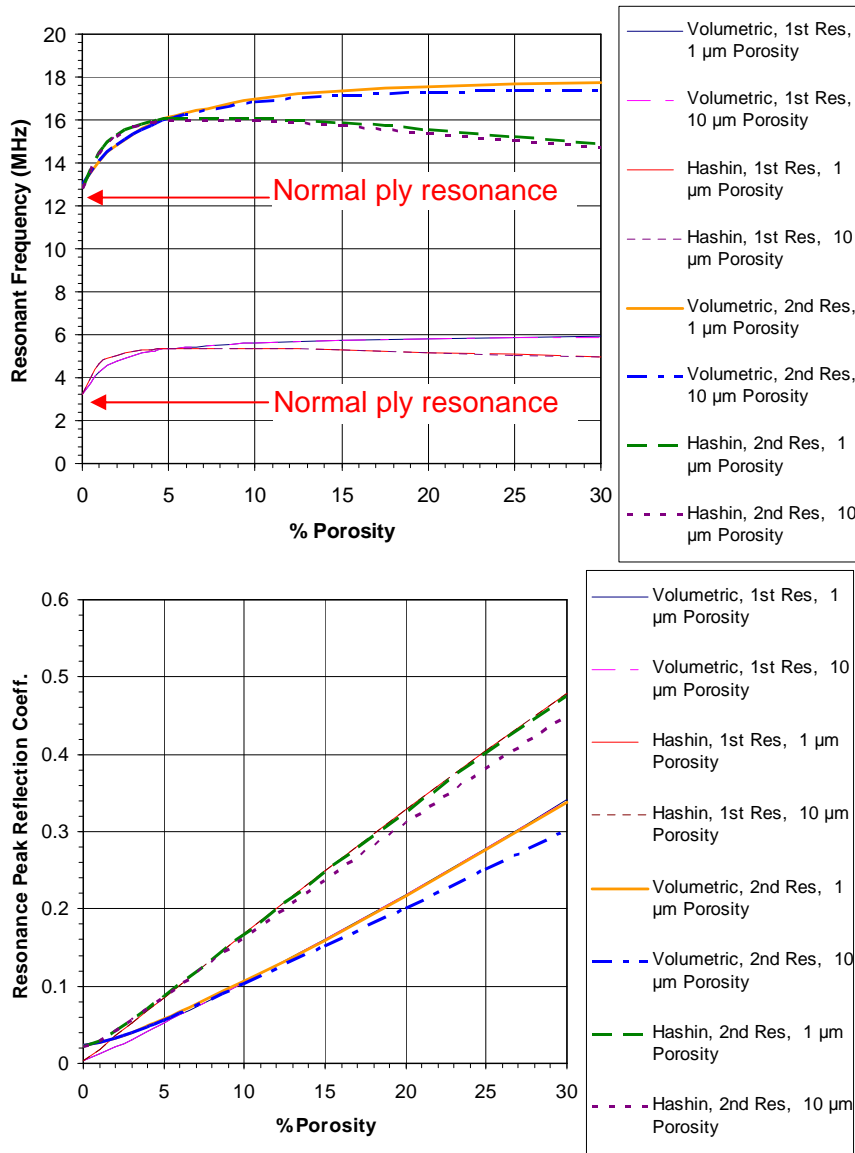


Figure 4-40. Resonant frequency and amplitude at resonance using the (RAS) analytical model for the first two resonances as a function of porosity level, for 1 μm and 10 μm radius pores in a single 0.125 mm ply of 60% FVF composite between 0.002 mm resin layers. Both simple volumetric and Hashin-Bezier mixture rules are shown. Note that pore size only affects reflection amplitude, resonant frequency being less sensitive, but downshifted at high porosity levels.

4.6.8 Time-domain response of single-ply porosity

Examples of modelled time-domain waveforms are shown in Figure 4-41 for a pulse generated from a Gaussian spectrum with a Q factor of 0.8, and a range of typical local porosity (void volume fraction) levels in ply 12 of a 32-ply stack, which may be present even when the thickness-average porosity is only 2%.

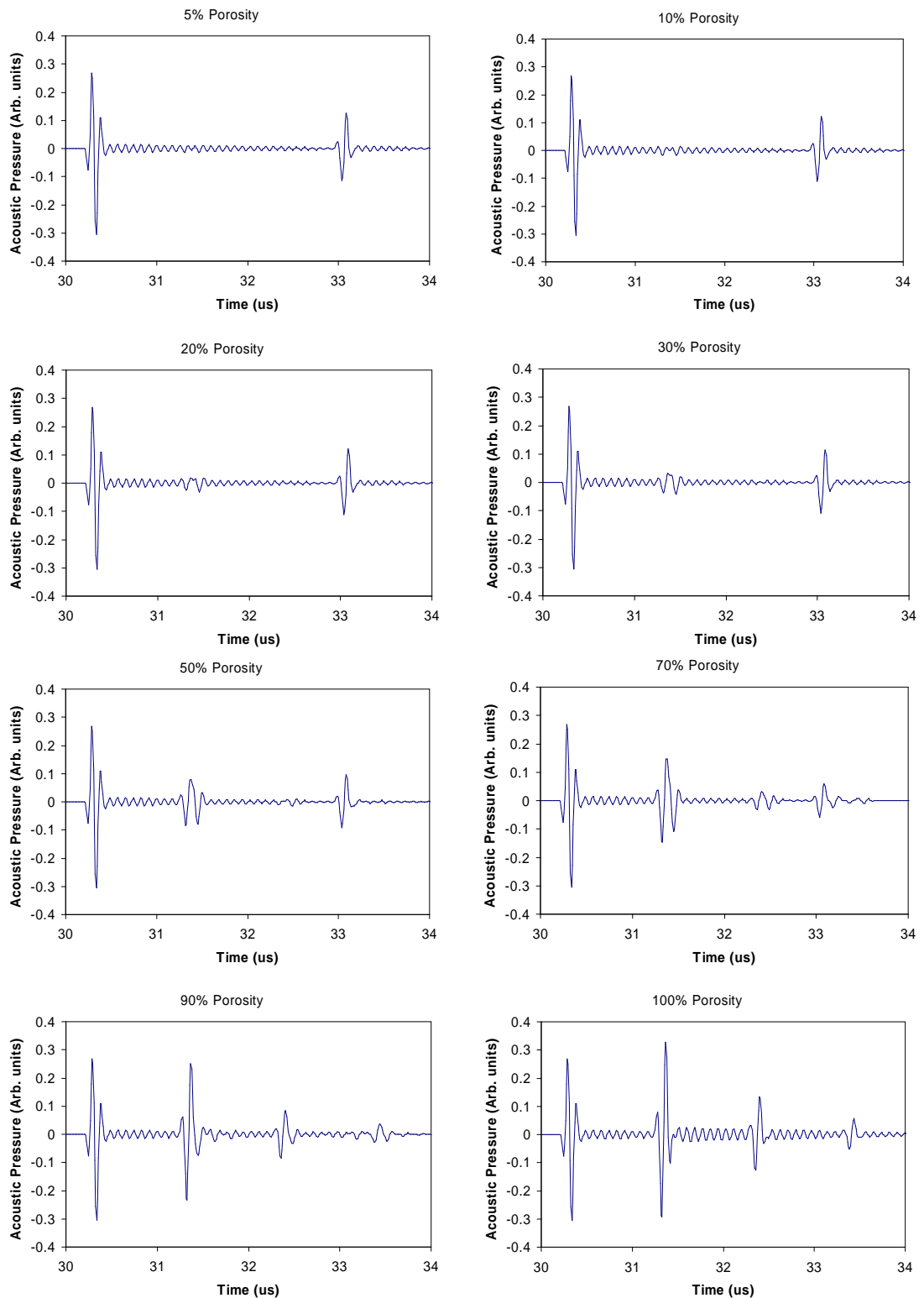


Figure 4-41. Modelled time-domain responses from a porous ply in a 32-ply stack of 0.125 mm 70% FVF plies separated by 0.005 mm resin layers. A Gaussian $Q=0.8$ pulse profile centred at 10 MHz was used. Different percentage porosities at a pore size of $10\ \mu\text{m}$ are shown.

4.6.9 Back-wall attenuation due to single-ply porosity

The traditional method of inspecting composite for porosity is to monitor the back-wall echo in comparison with a standard, and assume any additional attenuation is caused by scattering at porosity. The model can be used to determine how this back-wall echo depends on percentage porosity (void volume content) and the result is shown in Figure 4-42 for 5 and 10 MHz centre-frequency pulses and 10 μm radius pores.

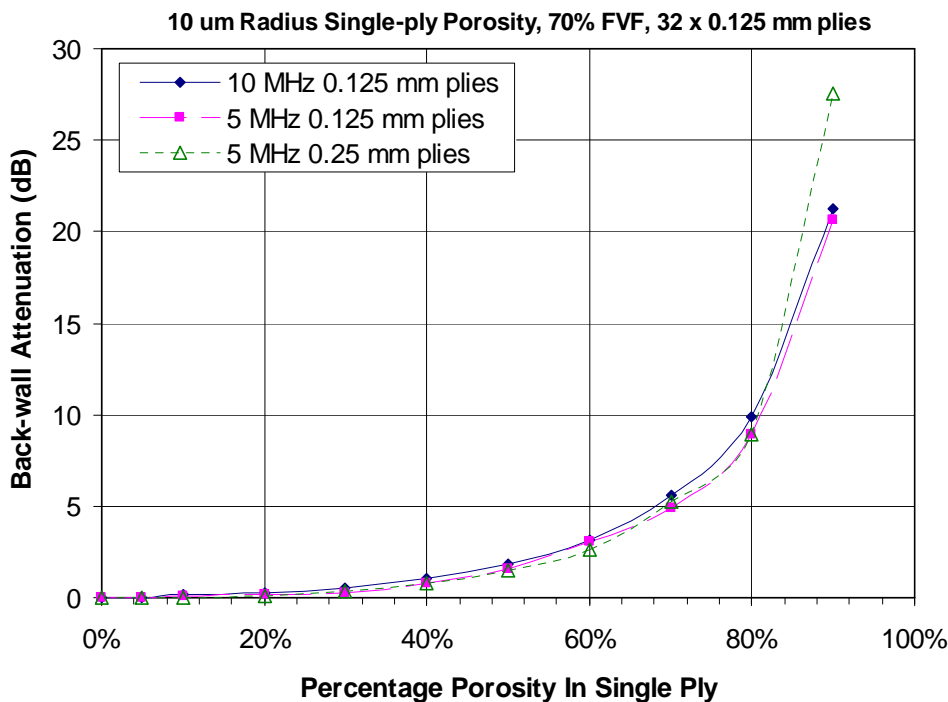


Figure 4-42. 5 and 10 MHz (UoN pulse) modelled back-wall attenuation as a function of percentage of 10 μm radius porosity ($ka = 0.21$) in the 14th ply of a 32-ply stack of 0.125 mm or 0.25 mm thick 70% FVF plies separated by 5 μm resin layers.

Figure 4-43 shows how back-wall echo attenuation is affected by pore radius for different ply spacings, l , and frequencies (and therefore wavenumbers, k).

However, it is worth determining what scaling factors apply, so Figure 4-44 is plotted against ka showing that the 5 MHz 0.25 mm plies data agrees well with the 10 MHz 0.125 mm ply data, because the response depends not just on ka but the ply-spacing-wavenumber product: kl .

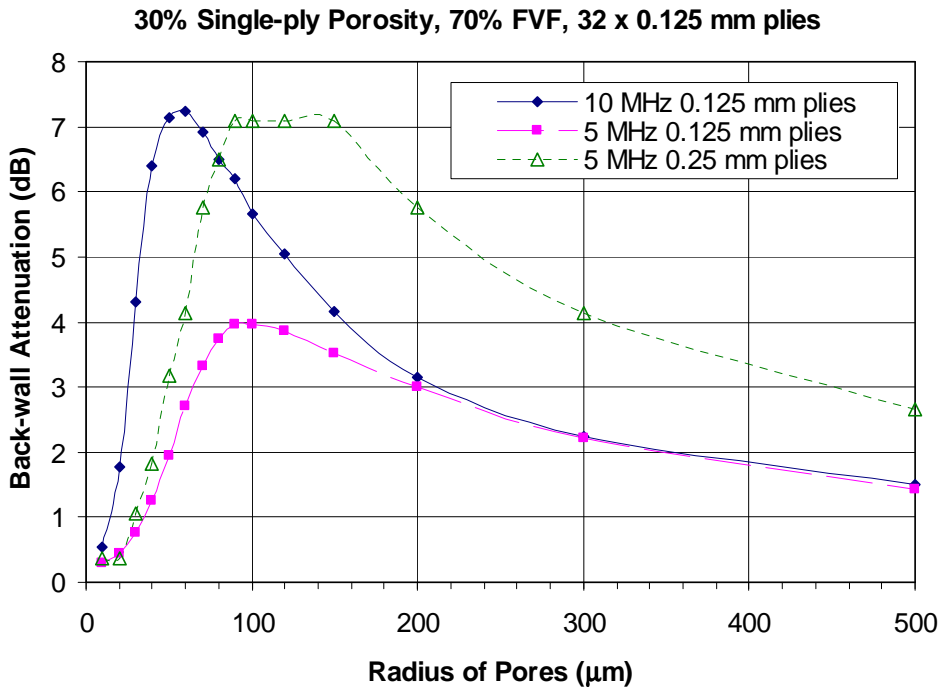


Figure 4-43. 5 and 10 MHz (UoN pulse) modelled back-wall attenuation as a function of radius of pores in the 14th ply of a 32-ply stack of 0.125 mm or 0.25 mm thick 70% FVF plies separated by 5 μm resin layers.

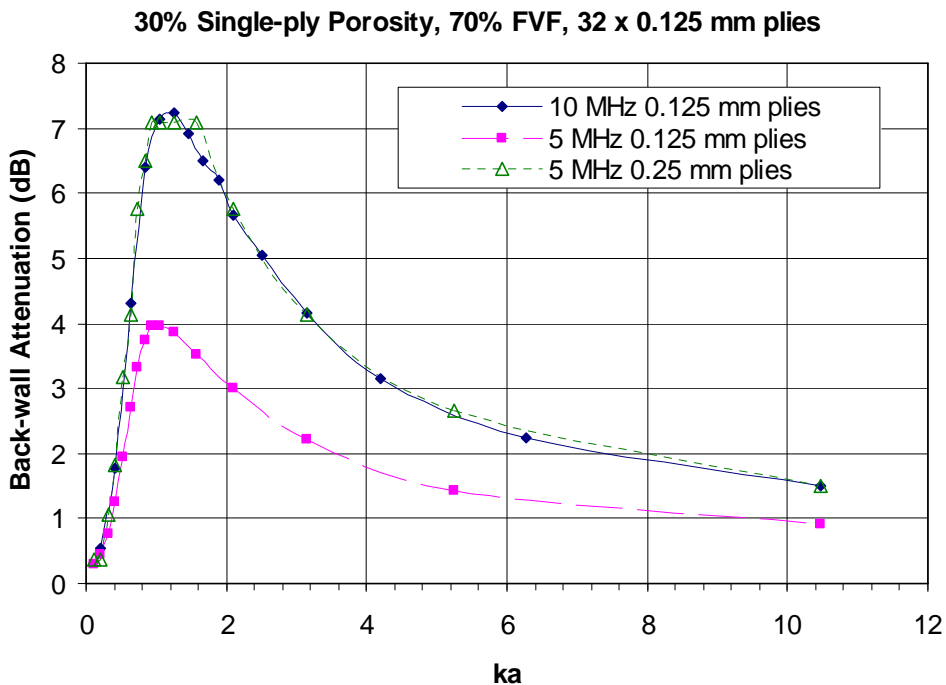


Figure 4-44. As Figure 4-43 but plotted against ka showing that the response depends on ka and the ply spacing * wavenumber product kl .

4.6.10 Time-frequency response of single-ply porosity

In order to decompose the response of a real composite into contributions from normal plies, thick plies, porosity or thick resin layers, it is necessary to understand the response to each of these individually. This can be achieved by using a time-frequency analysis of the modelled response. In the case of a single porous ply, this is shown in Figure 4-45.

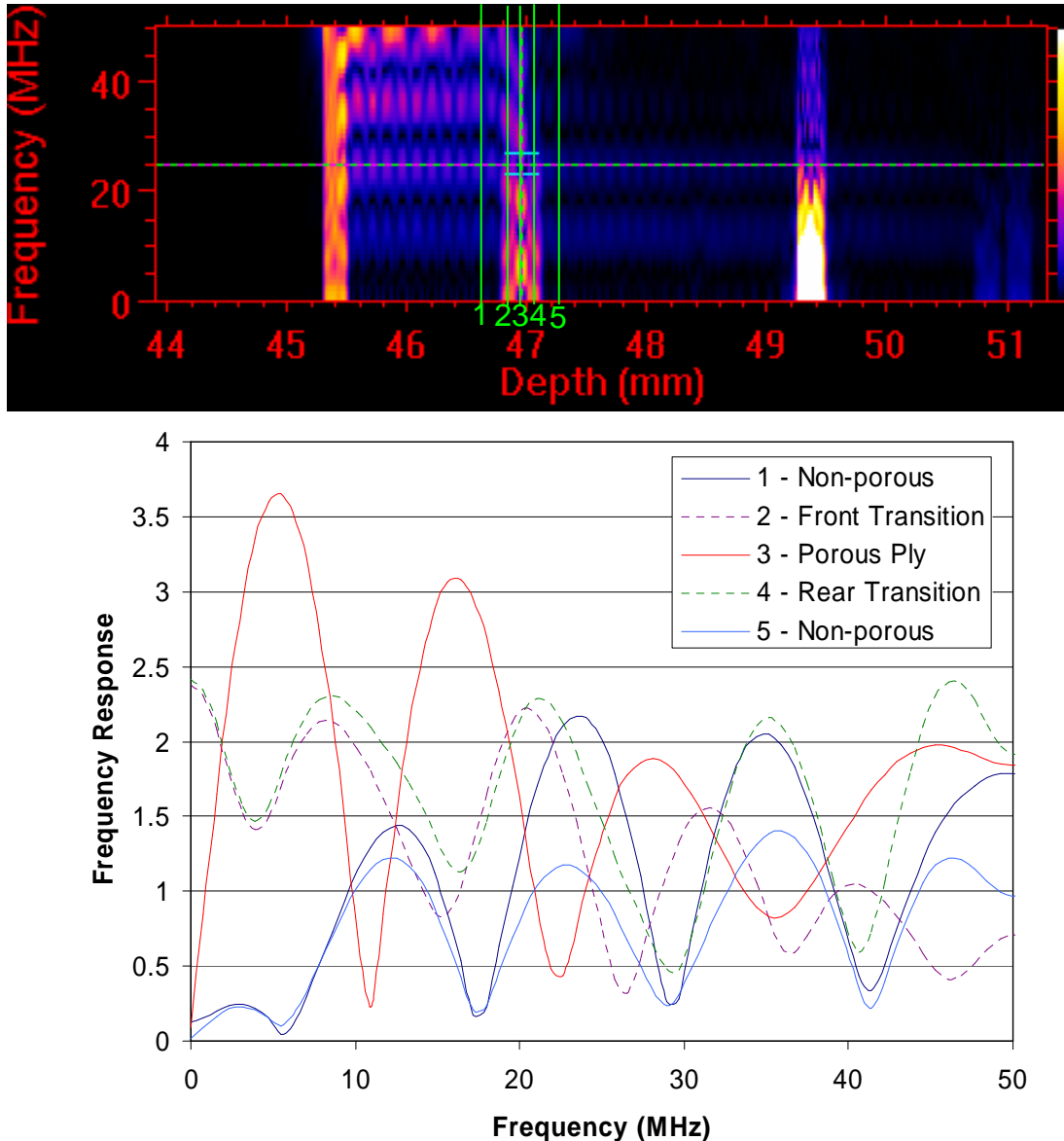


Figure 4-45. Modelled impulse-response time-frequency spectrum (top) for a 32-ply stack of 125 μm thick 80% FVF plies and 5 μm resin layers with a single ply (centred at green label '3') containing 20% porosity (10 μm radius pores), and (below) spectra taken from five different time windows in the waveform, labelled as 1 to 5 on the above time-frequency spectrum.

The response of a normal ply (region 1 in Figure 4-45) is that of a $\frac{1}{2}$ -wave resonance, whilst the response at the centre (region 3 in Figure 4-45) of the porous ply is a $\frac{1}{4}$ -wave resonance. As explained above, this is because only a very small amount of porosity is required to lower the impedance of the ply below that of the resin layers.

Interestingly, there is a difference between the spectra for transition region 2 and transition region 4 at the higher frequencies in Figure 4-45. The former retains an intermediate response between non-porous and porous plies, whilst the latter moves towards the non-porous response at higher frequencies. This may be a differentiator between increasing and decreasing porosity but it is unlikely to be of practical value because the frequencies involved are too highly attenuated.

From this analysis there appears to be potential for using the shift in type of resonance as a means of decomposing the single-ply spectral response into contributions from non-porous and porous plies. Further investigations show how the spectrum from an individual ply changes with percentage porosity in the presence of certain effects, namely:

1. 10% randomness in the ply spacing (Figure 4-46), showing that this does not completely prevent the change in resonance type being used as a differentiator, but that some form of ply-spacing assessment may be necessary;
2. different bandwidths of the incident pulse (Figure 4-47), showing that a broader bandwidth (lower Q-factor) allows better differentiation.

In Figure 4-46 it is important to note that an increase in porosity level in a ply of the nominal ply spacing results in an equal shift in all the resonant frequencies, such that the n th resonant frequency shifts from nf_1 at 0% porosity to $nf_1 + \Delta f$, where f_1 is the frequency of the second resonance at the nominal ply spacing. This shift Δf has been modelled and illustrated above, in Figure 4-40, for both the simple volumetric mixture rule (as used in Figure 4-45) and the Hashin (1965) mixture rule. In contrast, an increase in ply spacing by a factor κ , results

in a frequency scaling of the spectrum by a factor $1/\kappa$ so that the n th resonance peak is at $(nf_1 + \Delta f) / \kappa$.

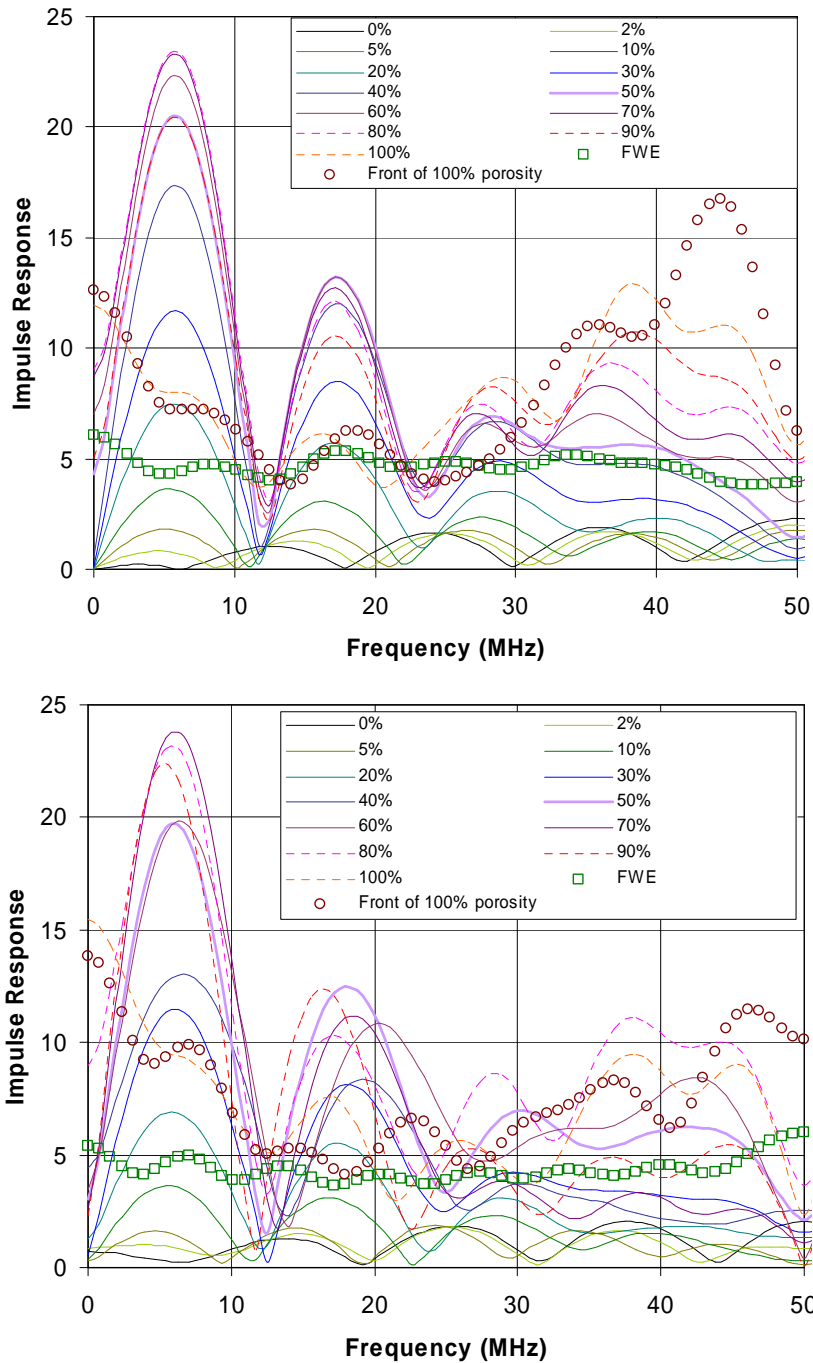


Figure 4-46. Frequency response taken from the central region (region 3 from Figure 4-45) of a region of porosity in a 32-ply stack of 125 μm thick 70% FVF plies and 5 μm resin layers with no randomness (top) and with 10% randomness (bottom) in ply thickness. Multiple curves represent different levels of porosity in the single porous ply.

Also shown on these graphs are spectra from the front-wall reflection, and from the front of a ply with 100% porosity – which is like an air-backed back-wall reflection and tends to reflect the full spectrum of the incident pulse.

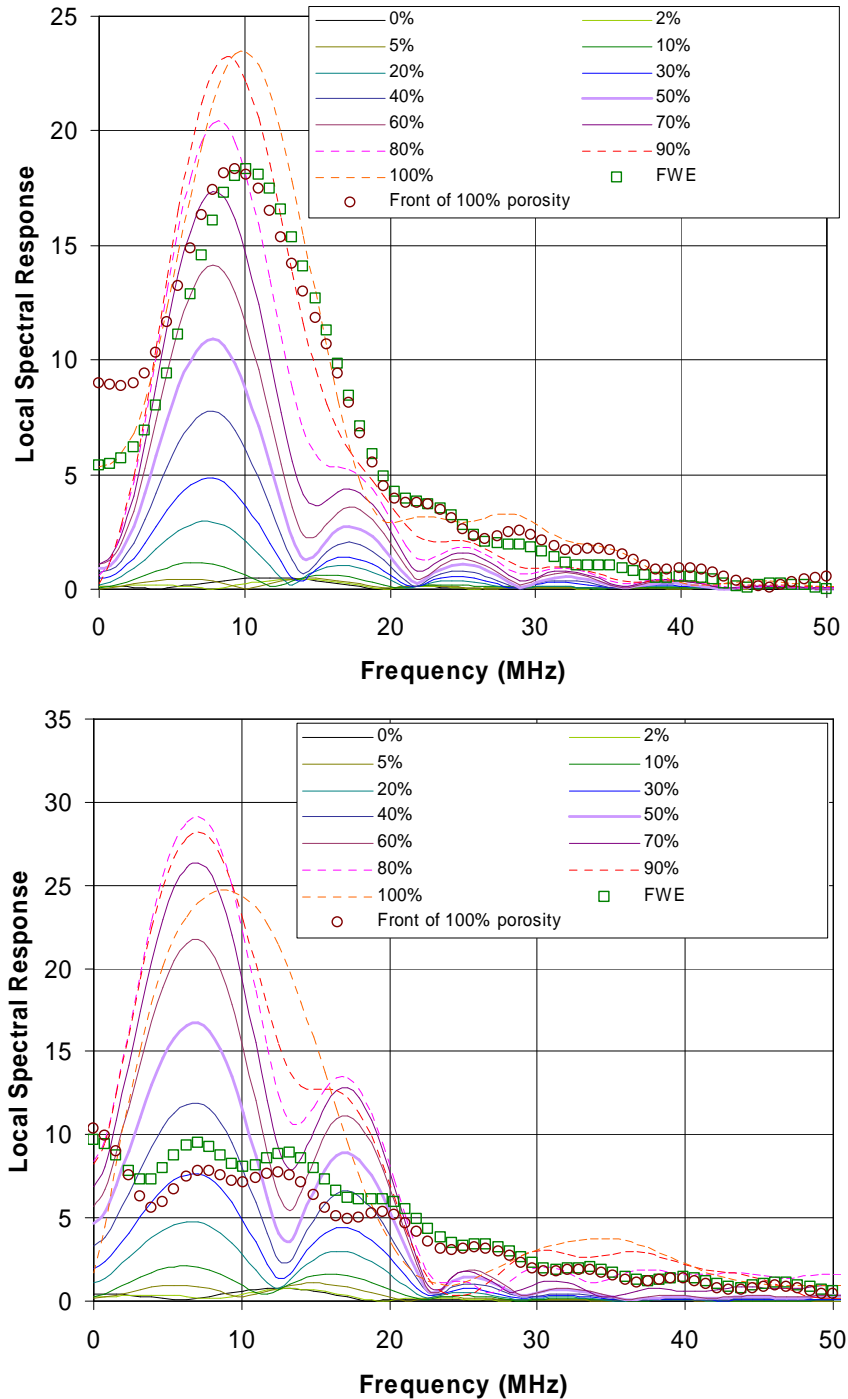


Figure 4-47. Responses to porosity for a 10 MHz Gaussian pulse with $Q=1.0$ (top) and $Q=0.5$ (bottom) from the central porous region (region 3 from Figure 4-45) of a 32-ply stack of $125\ \mu\text{m}$ thick 70% FVF plies and $5\ \mu\text{m}$ resin layer.

Finally, Figure 4-48 shows that, using a Q-factor of 0.7, there is a significant difference between non-porous and porous ply spectra, except at high levels of porosity where the ultrasound does not penetrate the porous layer enough to change the type of resonance.

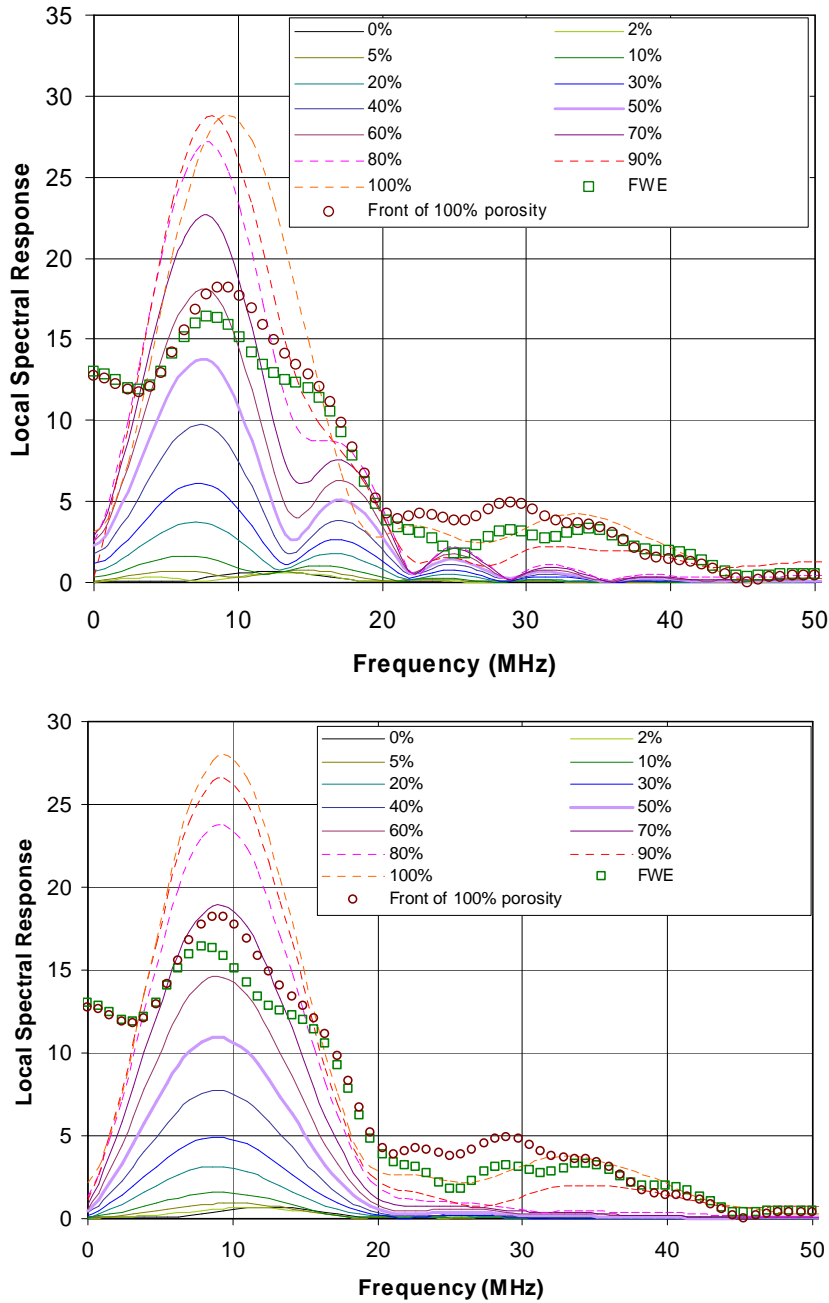


Figure 4-48. 10 MHz Gaussian $Q=0.7$ pulse responses from central porous region 3 (top) and non-porous region 1 (bottom) of Figure 4-45 in a 32-ply stack of 125 μm thick 70% FVF plies and 5 μm resin layers.

The above results suggest that this change in resonance type may be used to distinguish porous from non-porous plies, but there are several options for parameters that might quantify this. One possible parameter is the bandwidth of the resonance peak so this is plotted in Figure 4-49 to show its dependence on porosity level. Unfortunately, the variation in this parameter is not sufficient for it to be a viable contender. The modelling of thick resin layers is covered in the following section, whilst Chapter 5 deals with the search for a method to reliably decompose the single-ply spectra into contributions from normal plies, porous plies and thick resin layers.

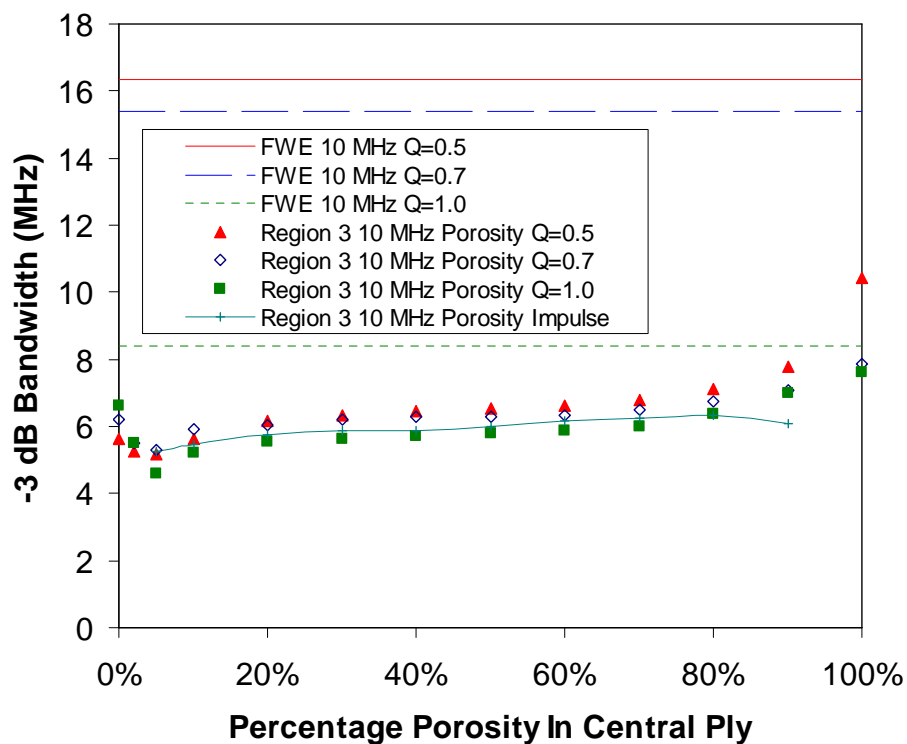


Figure 4-49. Trend in -3 dB Bandwidth as a function of porosity in the centre of a porous ply in a 32-ply stack of 125 μm thick 70% FVF plies and 5 μm resin layers.

4.7 Modelling a Thick Resin Layer

4.7.1 Thick resin layers in the model

In order to model a thick resin layer, or even an adhesive bondline between two adherends, it is necessary to allow at least one resin layer to have an

independent thickness. The model incorporates, as an input parameter, an array of thicknesses for the inter-ply (resin) layers as well as arrays for both the ply thicknesses and fibre volume fractions of the plies themselves. The default thickness for all the inter-ply layers is a single nominal value but a different thickness can be provided for one specified inter-ply layer. The model allows the option to automatically adjust the adjacent composite ply layer in thickness and fibre volume fraction to retain the same ply spacing and total volume of fibres in the local region, if required.

4.7.2 Back-wall echo response from a thick resin layer

Experimental observation of the back-wall echo C-scans of composites suggest that an ‘impression’ of fibre directions is sometimes evident. The small effect of a single thick resin layer on the back-wall echo attenuation is modelled in Figure 4-50 for a 10 MHz centre-frequency pulse. This suggests that variations of less than 1 dB are possible in a back-wall echo C-scan where the impression of fibre directions could be the result of small undulations in resin-layer thickness between the finite-width fibre tows in each ply.

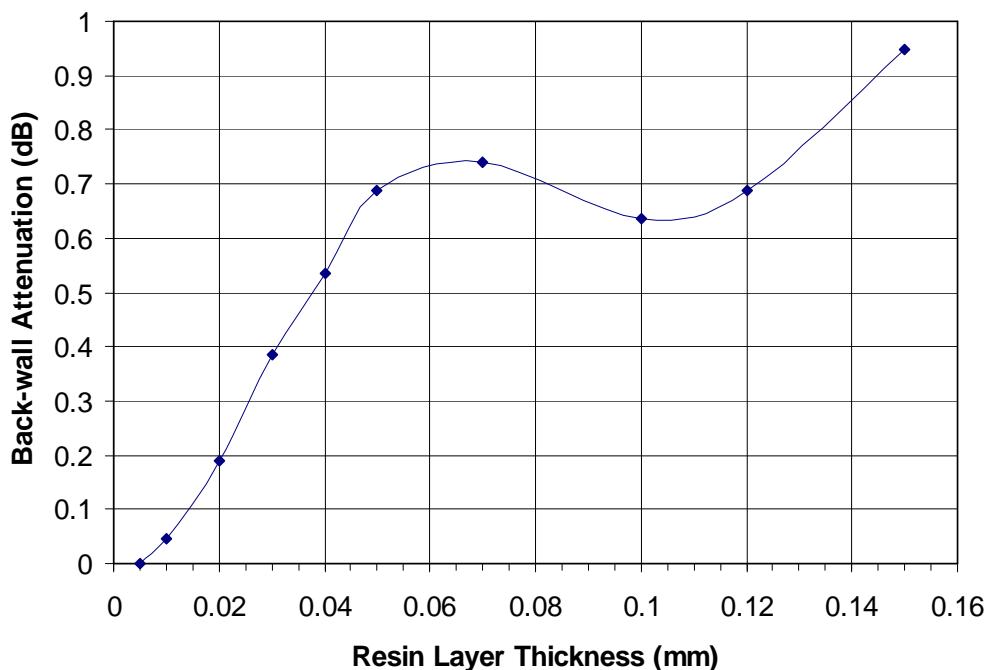


Figure 4-50. 10 MHz (UoN pulse) back-wall additional attenuation as a function of resin-layer thickness before the 18th ply in a 32-ply stack of 0.125 mm thick 70% FVF plies with 0.005 mm standard resin layer thickness.

4.7.3 Time-frequency Analysis for a thick resin layer

In order to investigate whether the spectrum from a thick resin layer can distinguish it from porosity or any other effect, a time-frequency analysis was conducted on the modelled waveform, looking at five different depths spanning the depth of the thick resin layer. The spectra are shown in Figure 4-51.

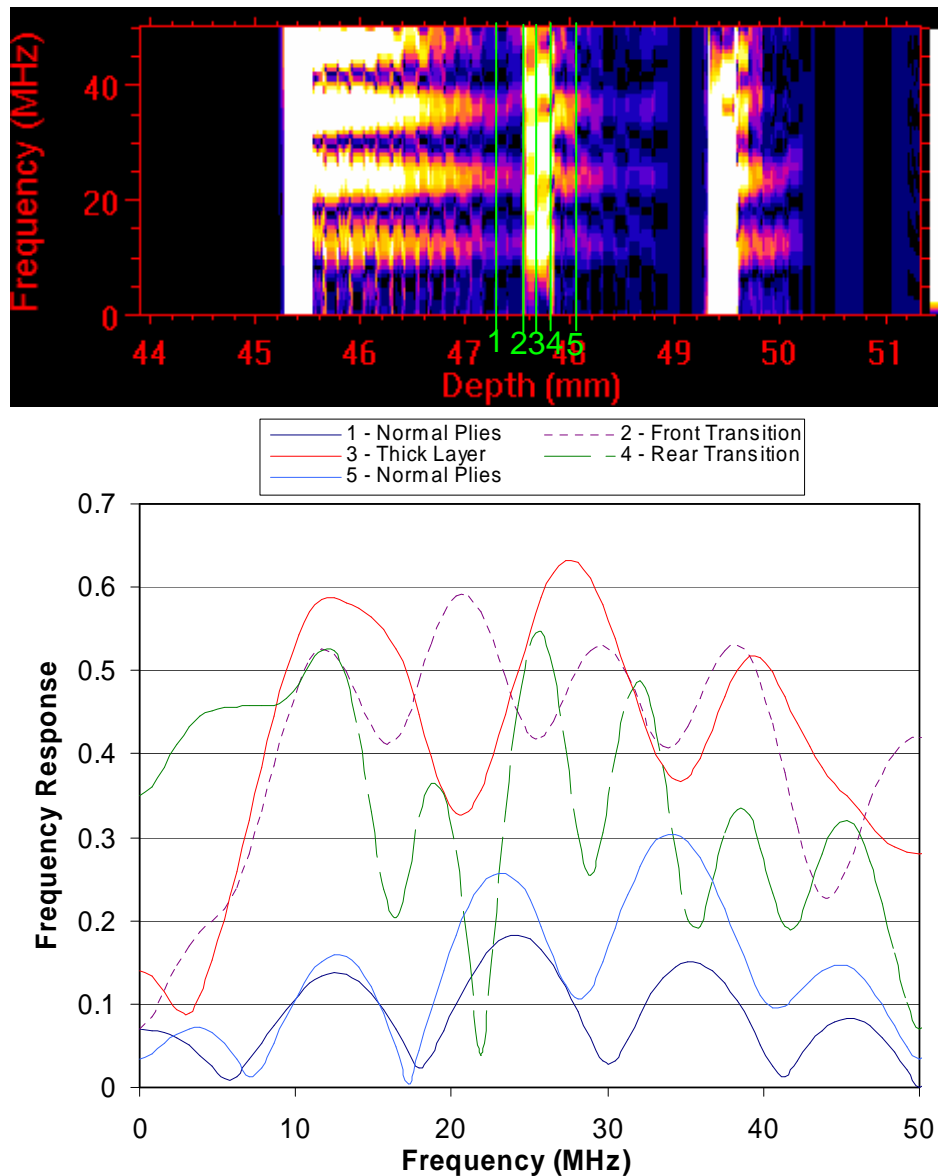


Figure 4-51. Modelled impulse-response time-frequency spectrum (top) for a 32-ply stack of 125 μm thick 80% FVF plies and 5 μm resin layers, with a single 20 μm thick resin layer, and (below) spectra taken from five different time windows in the waveform, labelled as 1 to 5 on the above time-frequency spectrum.

Although the frequency and bandwidth of the second ply resonance are affected by the resin-layer thickness when considering the impulse response, these effects are considerably reduced when a realistic pulse spectrum is used. This is shown in Figure 4-52, suggesting that neither resonant frequency nor bandwidth are suitable parameters for quantifying resin layer thickness.

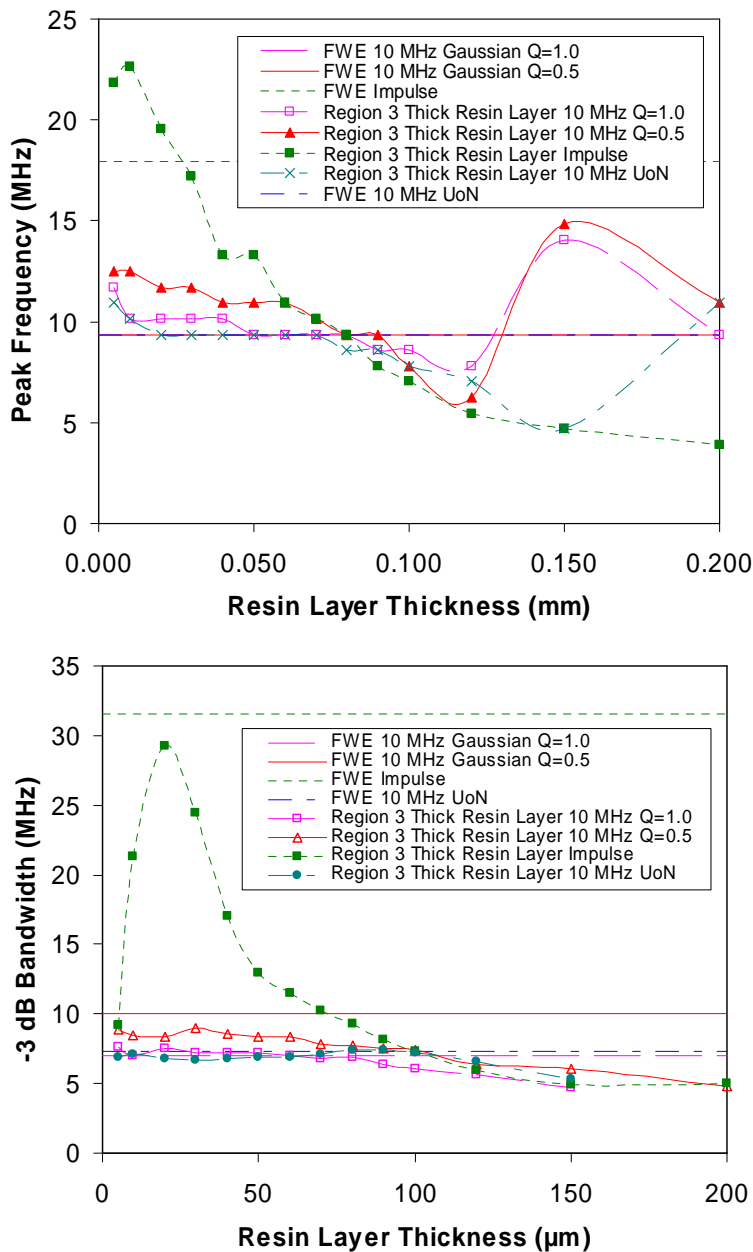


Figure 4-52. Resonant frequency (top) and bandwidth (bottom) as a function of resin-layer thickness using various incident pulses from an impulse response to a Q-factor of 1.0. Both front-wall echo and the centre of the reflected signal from the thick resin layer (Region 3 in Figure 4-51) are plotted for comparison.

The effect of a thick resin layer on the spectrum of the adjacent ply can be considered in terms of the convolution of the ply resonance with the resin-layer resonance. As the resin layer increases in thickness, its resonant frequency decreases, resulting in a significant rise in the low-frequency gradient – see Figure 4-53 – and this can be seen in the time-frequency plot in Figure 4-51.

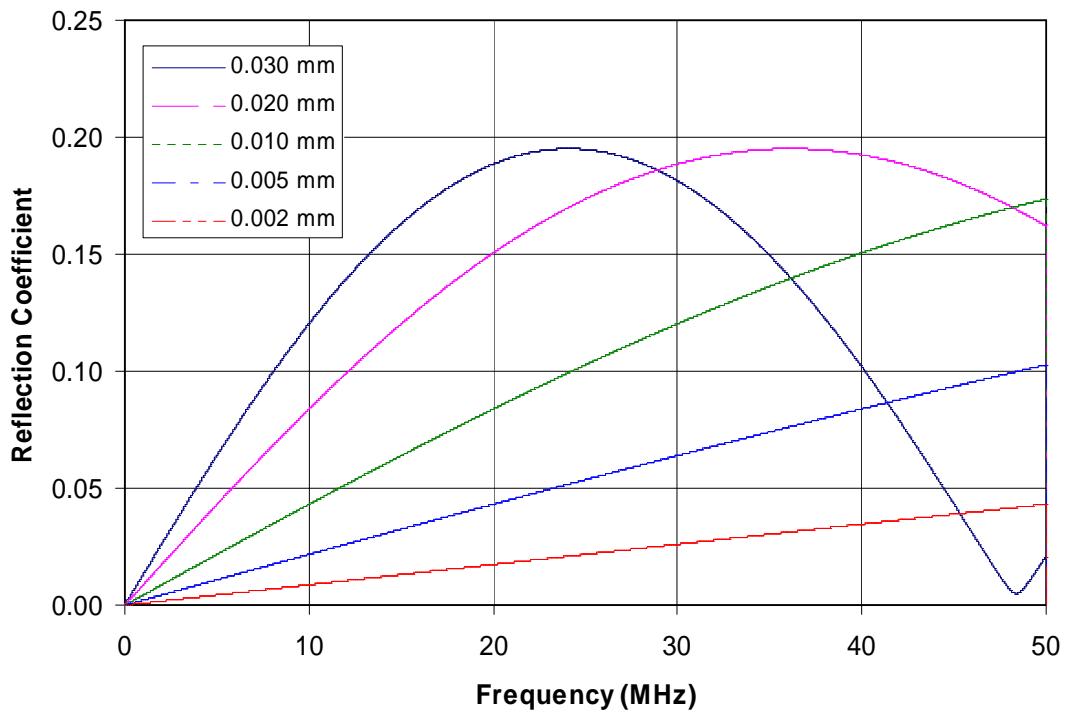


Figure 4-53. Resonance spectra for different thicknesses of thin resin layer, illustrating that at low frequencies, the main effect is the increase in gradient with increasing thickness.

4.8 Distinguishing between porosity and a thick resin layer

To the extent that both produce increased amplitude reflections, a thick resin layer can masquerade as local porosity in a ply. However, the above two sections have shown that a porous layer results in a minimum (anti-resonance) at the normal ply-resonance frequency, while the thick resin layer enhances the amplitude of the normal ply resonance but does not significantly change its frequency. These effects can be clearly seen in the time-frequency comparison in Figure 4-54 and can be used to distinguish between the two causes.

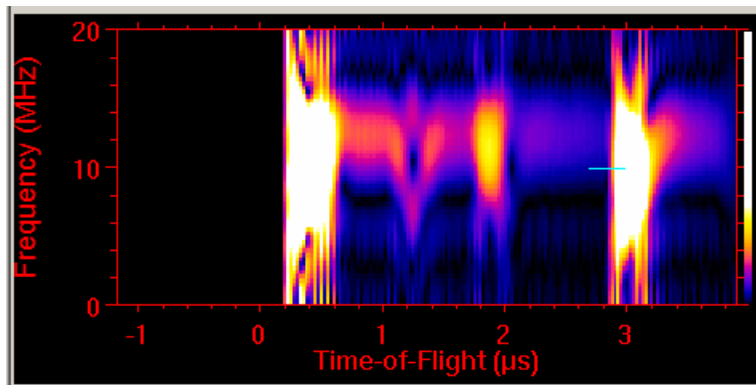
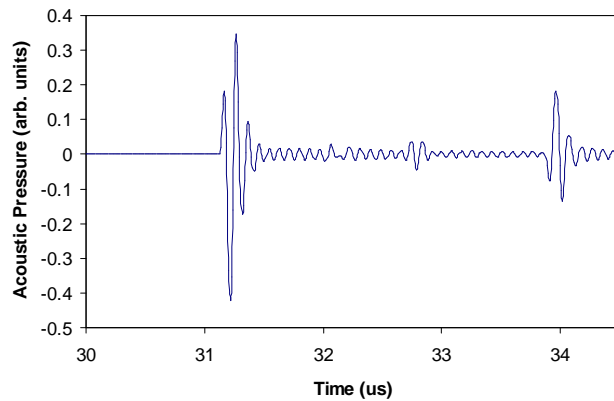


Figure 4-54. Time-frequency response using a 10 MHz UoN-simulated transducer pulse of a 32-ply stack of 120 μm 70% FVF plies and 5 μm resin layers. The 10th ply has 10% of 10 μm radius porosity and the 18th ply has a 20 μm resin layer followed by a 105 μm thick ply, with increased FVF to compensate.

This analysis provides the key to decomposing the spectral response of a ply into contributions from normal ply resonance, porosity and thick resin layers.

4.9 Benefits of the model

Throughout the development and use of the model it has gradually increased in its versatility and it has also found applications in modelling adhesive-bonded joints in metals and metal-composite hybrid laminates such as GLARE. As well as forming the basis of the model-based decomposition method (see Chapter 5) it has also been incorporated into a multi-dimensional optimisation method developed by a colleague of the author and has been successfully adapted for electromagnetic wave (microwave) propagation in multiple dielectric layers by another colleague.

CHAPTER 5 ISOLATION OF LOCALISED PROPERTIES IN LAYERED STRUCTURES

5.1 Motivation

5.1.1 *Material properties*

A fundamental part of achieving the objectives of this project is the extraction from full-waveform ultrasonic data of independent parameters that can be related to specific material properties at each location in the structure. Many composite materials comprise layers, or plies, which produce resonances, even in 'good' material without defects. These resonances are strong in composites with phases of very different stiffness, such as GFRP, and quite weak when the phases have similar stiffness, such as CFRP. In developing methods for isolation of material properties, these resonances cannot be ignored. Instead, they can be exploited and, by studying their characteristics, can actually be used to measure material properties. This chapter considers the isolation of several material properties of layered fibre-matrix composites; in particular: ply spacing, matrix inter-layer thickness, fibre volume fraction and void volume fraction (porosity). Fibre orientation and waviness, and ply wrinkling, are considered in Chapters 6 and 7.

5.1.2 *Background*

In addition to the reviews in Chapters 2 and 3 of this thesis, some previous work has been reviewed specific to the characterisation of composite materials using advanced waveform-processing methods and is summarised here.

Buoncristiani and Smith (1985) reported a method of extracting two generic frequency-dependent parameters characterising a composite material and its status, using a model of the frequency-dependent propagation in the composite. The first parameter is dependent on the dispersion and attenuation within the sample and scales with thickness. The second parameter relates to the

properties of local scattering centres within the bulk of the material. The model used accounts carefully for the steady-state acoustic flux established in the material but requires an assumption that the scattering and attenuation processes occur uniformly through the structure.

Smith and Buoncristiani (1986) extended this method by analysing a complex analytical function, formed by combining the backscattered waveform (the real part) with its Hilbert Transform (the imaginary part – see Appendix D), statistically to provide a distribution of scatterers within the material. This was an early attempt at producing a 3D distribution of material properties in a composite. They reported that the method compared well with experiment for delaminations caused by impact damage but did not test the method with porosity or investigate how it is influenced by the thickness of resin layers between plies. The problem of shadowing of deeper defects by shallower ones was identified in this work because it is a more significant problem when dealing with virtually impenetrable delaminations than with porosity.

Lorraine et al (2003) published a patent covering the decomposition of backscattered sonic waveforms from composites into a set of time-domain basis functions, each representing characteristics of material or defects. The coefficients associated with the basis functions may be non-zero when a defect is present, thus allowing rapid defect detection.

The above literature failed to address the problem of thick inter-ply resin layers masquerading as porosity and therefore did not solve the primary concern of this chapter – the isolation of the effect of each material property and defect type. In fact the work in this chapter shows that neither Smith and Buoncristiani nor Lorraine et al would have succeeded in differentiating between porosity and thick resin layers. Therefore, a new approach was required in this project to distinguish between these two material properties and quantify them.

5.1.3 3D data presentation

This chapter is primarily concerned with the generation and presentation of three-dimensional information about material properties. A crucial part of the presentation is the imaging technique employed. It needs to help the user to

assimilate the information and rapidly understand the implications of what is being presented.

Many of the applications addressed here require the same processing to be applied to each volume element within a structure. In ultrasonics this involves waveforms from one or more beams that pass through the given volume element. These beams may be combined in some way (eg averaging or array processing) to form one waveform. That waveform may then have further signal processing performed before the application of a time-gate (or window), which defines the volume element. The portion of the waveform in that time-gate may then be processed and analysed to determine scalar values for one or more material properties for that volume element.

Because of this importance of presenting data, the first section of this chapter deals with the presentation of a 3D array of scalar quantities representing the 3D-profile of a material property.

5.2 Presentation of 3D localised properties

5.2.1 3D-Profile layers

In order to accommodate 3D profiles within the ANDSCAN software, a new type of 'layered' measurement channel was introduced, which stores multiple layers of scalar data. During this project, the 3D-profile method was developed to include all measurement parameters available in ANDSCAN, plus some new ones, so that any parameter can be plotted as a 3D profile. In general the third axis (layer number) represents depth in the structure (propagation time in fact), but in some cases, such as for ultrasonic resonance analysis or low-frequency (5 kHz – 40 kHz) vibration analysis, it has been found beneficial to use frequency as the third axis and effectively visualise the spectral response of the structure.

In the normal 'C-scan' type of display, only one layer can be displayed at a time. However, there are other ways of displaying this 3D profile, which are discussed below.

5.2.2 Cross-sectional View

The cross-section windows in ANDSCAN can display slices through the 3D-profile layers.

An example of the single-layer C-scan with cross-sectional slices is shown in Figure 5-1. This was produced by allowing any measurement type in ANDSCAN that is applied within a time gate to be automatically plotted as a 3D parameter where the time gate is systematically moved deeper in the structure and a new scalar value is calculated for each successive layer.

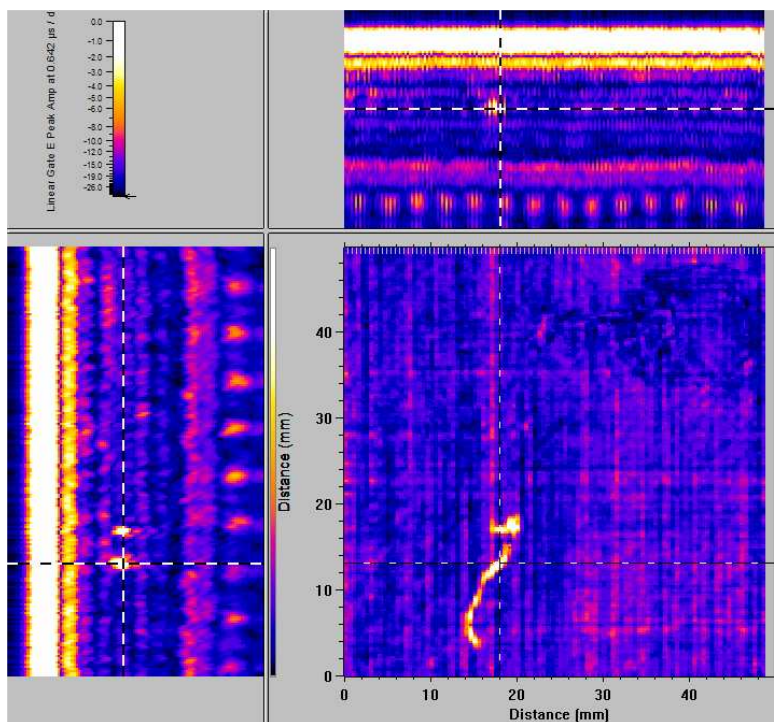


Figure 5-1. Cross-sectional view of a 3D profile of the Peak Amplitude in a short gate for each volume element in the structure of a six-ply carbon-fibre composite skin on a honeycomb core. The crosshairs illustrate the location of the cross-sectional slices in the other dimensions. Note that the worm-hole porosity can be seen in the two cross-sectional slices through the 3D profile as well as in the single layer C-scan.

The new measurement type illustrated in Figure 5-1 is: “Gate 1 Peak Amp Layers in Gate 2”, where Gate 1 is a short gate that is scanned through a longer Gate 2, and these can be selected to be any of the gates available. The amount of overlap between successive gate depths can be preset.

For this type of presentation it is important that the operator can navigate through the 3D structure and have feedback about the current position. Navigation is by moving cross-hairs using the mouse cursor on the C-scan (in-plane section) view, or by clicking on one of the vertical slice cross-sections. In addition, the mouse-wheel is used to rapidly change layers whilst over the C-scan view. Feedback of current location is achieved through the crosshairs on each cross-section as seen in Figure 5-1, as well as a read-out of layer number and (x,y,z) coordinates in the status bar in a real-space coordinate system and selectable units (mm or inches).

5.2.3 Projection View

The 'projection' or 'elevation' mode of display is based on the methods used in technical drawings where side and end elevations are provided together with a plan view. Essentially this is akin to 'projecting' the data from the object onto three perpendicular surfaces. The level of effective transparency, allowing different depths to be viewed simultaneously, should be selectable, as should the width, length, height and location of the 'projection volume' that is to be projected. This is achieved in ANDSCAN by allowing the operator to select the number of voxels (3D pixels) in a given dimension that are in the projection volume, centring it on the current cursor location, and allowing the operator to move it through the 3D structure as with the cross-sectional view.

An example of this method is given in Figure 5-2 by comparison with the cross-section method. The specimen is a tape-layup CFRP skin where a simple amplitude 3D profile easily detects the butt-joints of thick resin between adjacent tapes in each ply. It is important to check that these resin lines, which can cause effective stress concentrations, do not line up from one ply to another, causing a weakness in the structure. In the cross-sectional view the resin lines appear as single dots in the vertical slices and just one layer is shown in the C-scan slice at a time. This makes it difficult to check whether plies of the same orientation have the same location of butt-joints. By contrast, the projection (lower) view clearly shows multiple layers in the C-scan and it is clear that the butt-joints are staggered in plies of the same orientation.

Feedback to the operator of the projection volume size and location is provided by showing two sets of crosshairs in each projection, which effectively define the boundaries of the projection volume. These can be seen in Figure 5-2. Another option would be to just show the bounds of projection volume itself as a rectangle.

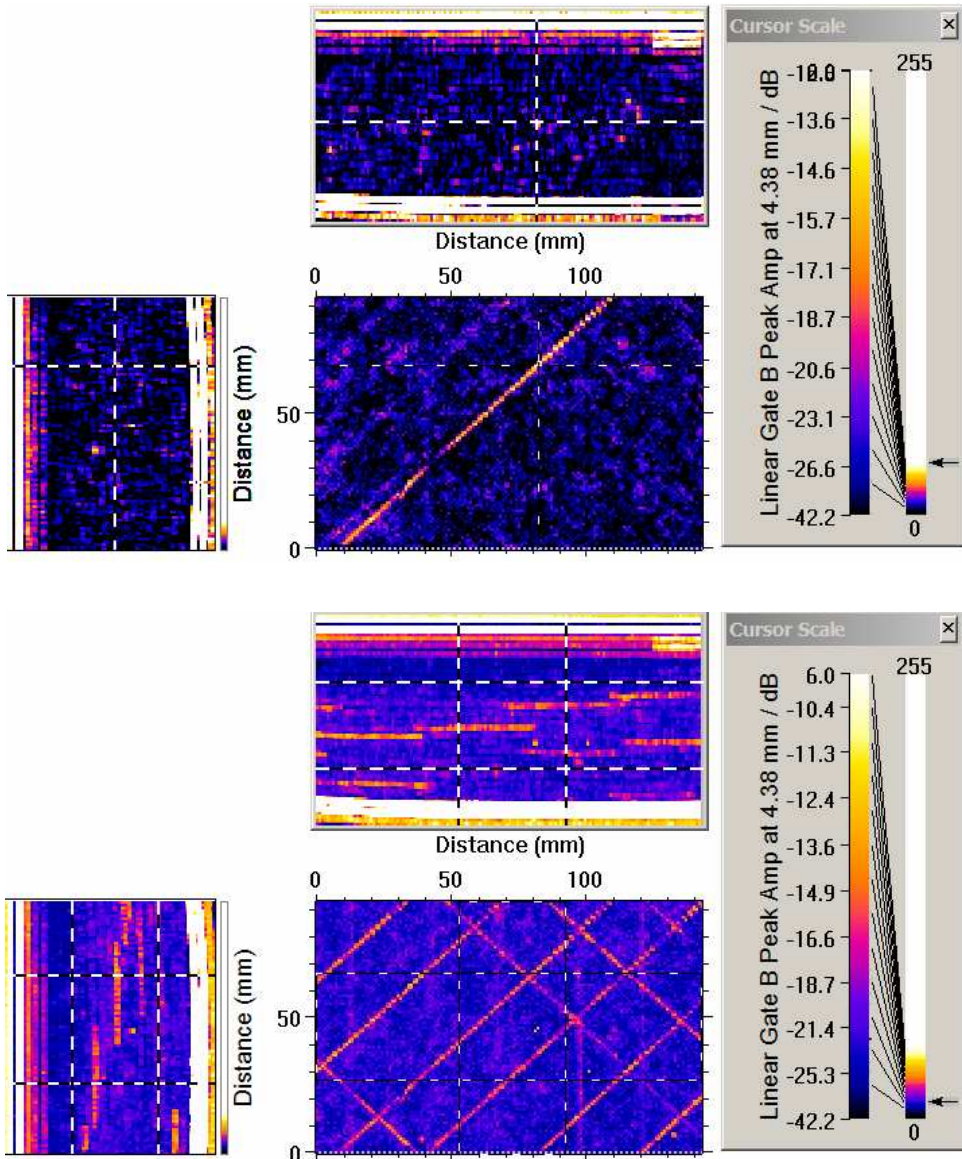


Figure 5-2. Illustration of the difference between cross-sectional view (top) and projection view (bottom) for a 3D profile of peak amplitude in a short gate. The specimen is a simple CFRP panel manufactured using tape lay-up, where the resin butt-joints between adjacent tapes can be clearly seen.

5.2.4 Rotating pseudo-3D images of layers

The pre-existing Pseudo-3D imaging software in ANDSCAN was modified on this project to allow the display of 3D-profile layered data. This extended the capability where previously only one 3D value per surface location could be plotted – creating just a surface in 3D space. Now the complete 3D profile is plotted. An example of the type of pseudo-3D image of a 3D profile of amplitude is given in Figure 5-3 for the same specimen as shown above in Figure 5-1. The worm-hole porosity and the hexagonal honeycomb cells are very clearly seen.

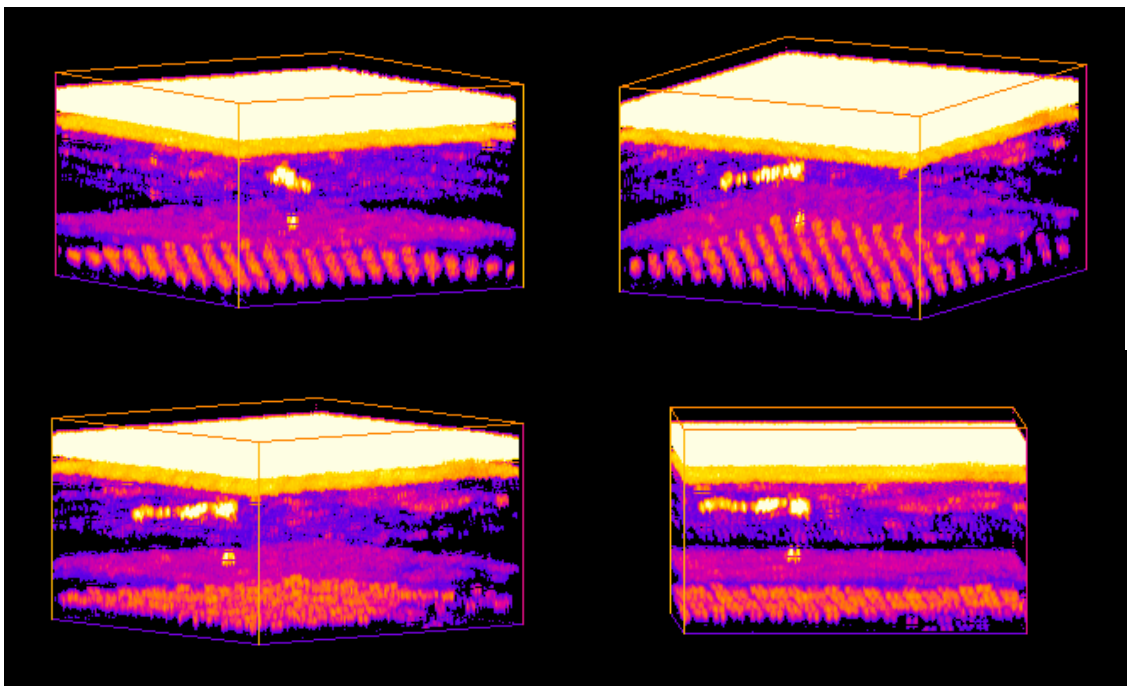


Figure 5-3. An example of a full 3D layered data set displayed as pseudo-3D images, which can be rotated and viewed from any angle. This is the same amplitude data as shown in Figure 5-1 with six composite plies above honeycomb, the hexagonal pattern of which shows up at the bottom of the images.

In order to plot all points from the 3D profile, various problems had to be solved. Firstly, if all points are plotted then the observer would only see the outside of the cuboid of data being displayed. There needs to be a process whereby the most important data takes precedence. This is achieved in two ways.

- Firstly, a Noise Reject Threshold is applied, below which 3D points are not plotted, cleaning up the presentation considerably.

- Secondly, the user can choose whether to display the ‘nearest’ or the ‘brightest’ points when they overlap. This has the effect of reducing the influence of any low-amplitude noise, as well as making bright reflectors visible through the more transparent lower-amplitude voxels.

The pre-existing method of treating each possible height in the 3D image as a single pixel in depth does not work with 3D-profile layered data because the layers can have large gaps between them and it no longer looks like a continuous 3D profile. For this reason the software was modified to fill in the gaps between layers – effectively making the layers thicker.

Processing time is much greater for the 3D profiles than for a 2D image plotted as a surface, although the expected increases in speed of computer processors should soon make up for the current delay of a second or two in recalculating the image on a relatively slow laptop computer. A dual-core processor could also be specifically instructed to dedicate one core to the 3D-to-2D coordinate calculations, leaving the other core to cope with displaying the image.

5.3 Fibre-resin effects

5.3.1 Ply spacing

It has been shown in Appendix C to this thesis that a useful relationship exists between ply resonant frequencies and ply spacing. In order to analyse this further, an analytical expression for the resonant frequencies as a function of ply spacing and other material properties was sought.

Equation 4-6 in Chapter 4 can be used to represent the frequency-dependent reflection coefficient from a single ply between two thin resin layers, each of which act as an interface with complex reflection and transmission coefficients. If the density and acoustic velocity in the plies were to remain constant when the ply thickness changes, the frequency responses for the scenarios tabulated in Table 5-1 would change as shown in Figure 5-4.

Material properties used were: fibre density 1.69 kg/dm^3 and fibre modulus 16 GPa , resin density 1.27 kg/dm^3 and resin modulus 10.7 GPa .

Total Thickness (mm)	No. of plies	Ply Thickness (mm)	Fibre Volume Fraction
1	7	0.143	80%
1	8	0.125	80%
1	9	0.111	80%

Table 5-1. Values for an available and representative specimen used for the simple analytical model from Chapter 4, the results of which are in Figure 5-4.

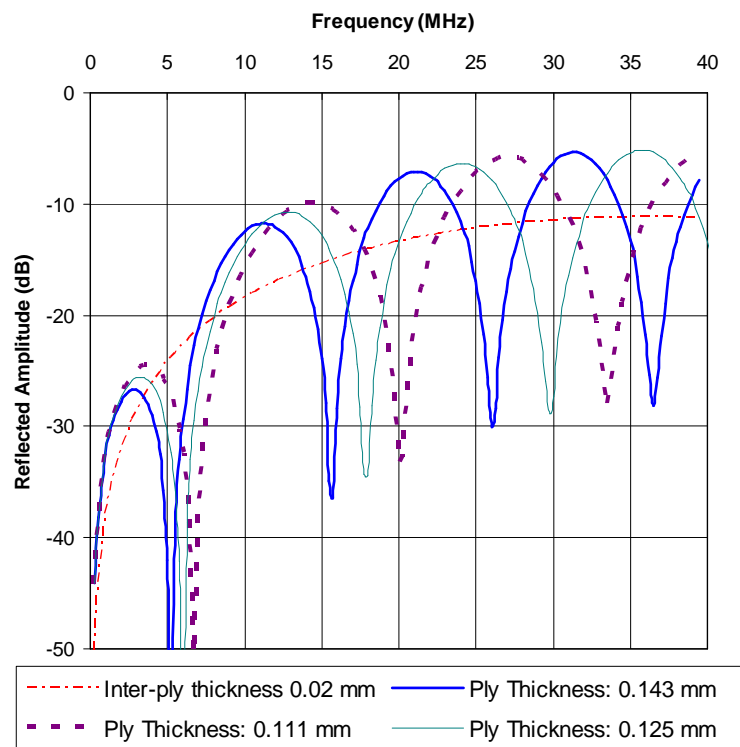


Figure 5-4.. Theoretical frequency response of the ply resonance for ply thicknesses corresponding to 7, 8 and 9 plies per mm of unidirectional pre-preg material, with the inter-ply layer reflection amplitude for a 0.02 mm layer shown too. The theoretical model was the analytical one from Chapter 4, and was set up to assume the same density and acoustic velocity for the plies regardless of ply thickness.

In order to find an analytical expression for the resonant frequencies it is necessary to differentiate the magnitude of the reflection coefficient expression of Equation 4-6 in Chapter 4 with respect to frequency, or in this case the

wavenumber k , to find the turning points. This was attempted but is very difficult because the resin-layer interface reflection and transmission coefficients are complex and dependent on its thickness. However, an easily differentiated approximation to the magnitude of the complex reflection coefficient can be made by considering the response as a convolution of the impulse response of a single resin layer of thickness d with the impulse response of two single infinitesimally thin interfaces separated by distance l (see Figure 5-5).

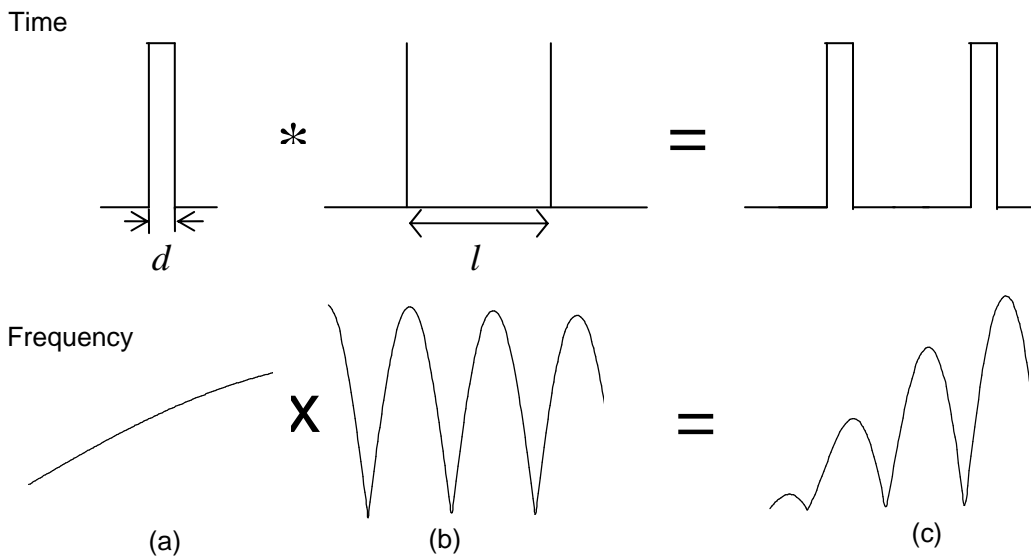


Figure 5-5. Diagram showing the principle of convolution for a time-domain propagation (top) and the equivalent frequency response (bottom) for finite-thickness two interfaces. The responses are for a) a single thickness d resin layer, b) two infinitesimal thickness interfaces at spacing l , and c) two thickness d resin layers at spacing l .

In the frequency domain this becomes a simple rectified cosine curve (dependent on the ply spacing l) modulated by a sine curve (dependent on the resin layer thickness d):

$$R \propto |\sin(2kd)\cos(kl)| \quad (5-1)$$

For typical multi-ply carbon-fibre composite with 4 or 8 plies per millimetre thickness and resin layers of $2 \mu\text{m}$ thickness, Figure 5-6 shows that there is a

close similarity between the simple expression in Equation (5-1) and the magnitude of the reflection coefficient calculated using the full model of Chapter 4 with various different visco-elastic damping coefficients for the resin. Of particular note is that the resonant frequencies are very similar for the simple equation and the full model.

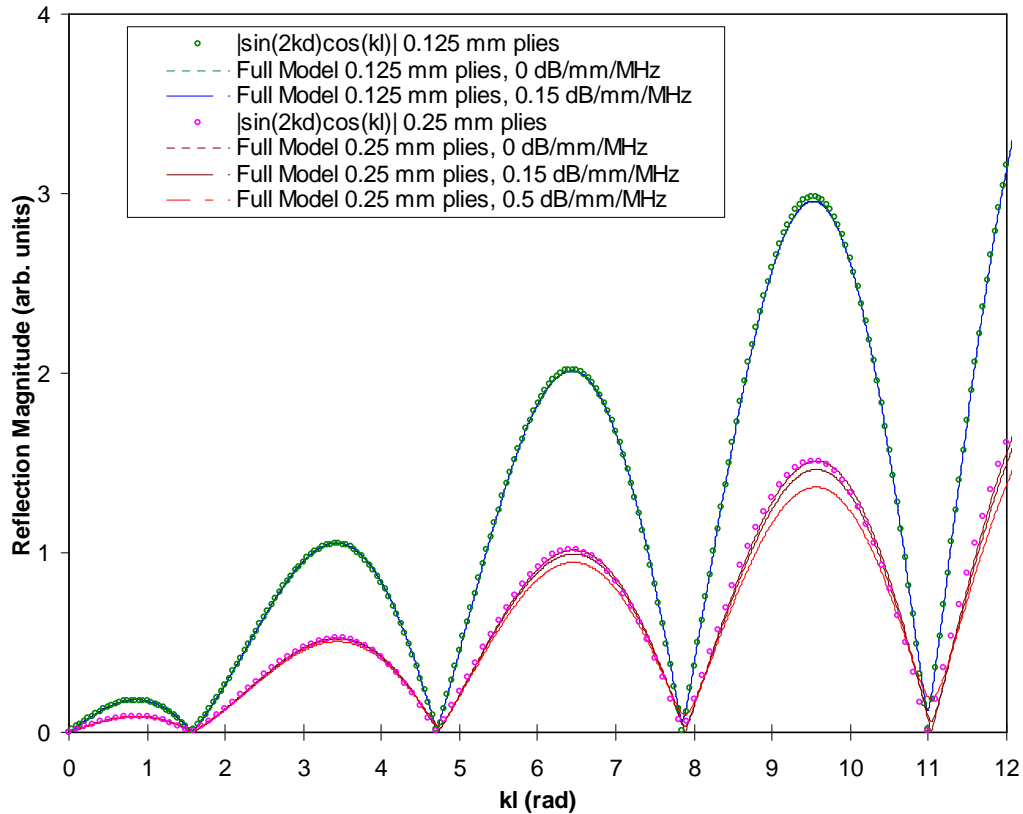


Figure 5-6. Illustration of the similarity of the full modelled response and the simplified equation $|\sin(2kd)\cos(kl)|$ for a 0.125 mm ply and a 0.25 mm ply of 60% FVF composite between two resin layers of thickness 0.002 mm. Different visco-elastic attenuations in the resin have been used in the full model and are indicated in the legend.

The derivative of this new simplified expression is required to determine the maxima and is given below:

$$\frac{d}{dk}[\sin(2kd)\cos(kl)] = 2d \cos(2kd)\cos(kl) - l \sin(2kd)\sin(kl) \quad (5-2)$$

The n th turning point occurs when the magnitude of this expression is equal to zero, which is when:

$$\tan(k_n l) = \frac{2d}{l \tan(2k_n d)} \quad (5-3)$$

When the resin layer thickness d , is small compared with the ply spacing ($d \ll l$), the resonant frequency becomes independent of the resin layer thickness:

$$\tan(k_n l) \approx \frac{1}{k_n l} \quad (5-4)$$

The n th resonant peak frequency, f_n is related to the wavenumber as follows:

$$f_n = \frac{(k_n l)c}{2\pi d} \quad (5-5)$$

where l is the ply spacing and c is the ultrasonic compression-wave velocity.

Note that what is called the 'second resonance peak' corresponds to $n=1$.

The expressions in Equation 5-3 and Equation 5-4 also cannot be solved analytically, but Figure 5-7 illustrates that the first four maxima are at the intersections of the graphs of the functions from the two sides of Equation 5-3.

For $d = 0.002$ mm, these intersections occur at $k_n l = \theta_n$ where θ_n takes the values 0.862, 3.425, 6.44 and 9.53 radians for $n = 0, 1, 2$ and 3 respectively. These resonant frequencies are higher than for an infinitesimal resin layer, where they would be at $n\pi$ radians.

For the first four solutions when $d = 0.002$ mm (circled in Figure 5-7), Equation 5-5 becomes:

$$f_n = \frac{\theta_n c}{2\pi d} \quad (5-6)$$

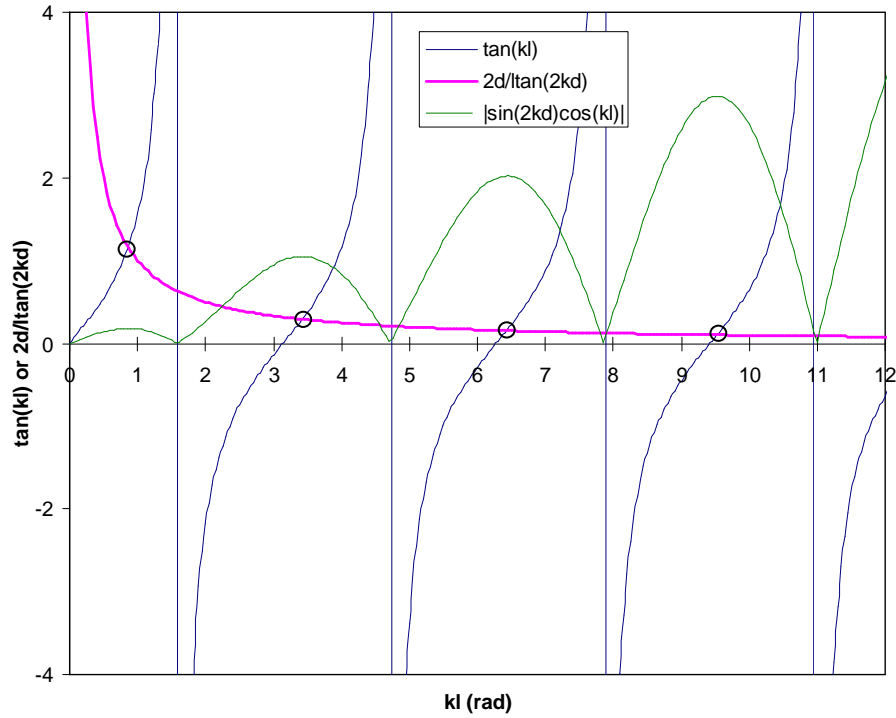


Figure 5-7. Graph of the left and right sides of Equation 5-3, illustrating peak resonant frequencies (circled intersections of the two curves) when a finite resin layer thickness $d=0.002$ mm modulates the response of the ply resonance. Also shown (dashed) is Equation (5-1) for the magnitude of the response to demonstrate that the maxima are correctly identified by the intersections of the curves.

The α_n value defined in Chapter 4 Equation (4-2) is also defined as:

$$f_n = \frac{1}{\alpha_n l} \quad (5-7)$$

so it follows that:

$$\alpha_n = \frac{2\pi}{(k_n l)c} \quad (5-8)$$

or:

$$\alpha_n = \frac{2\pi}{\theta_n c} \quad (5-9)$$

Equation (5-4) assumes that the resonant frequencies are independent of the resin layer thickness, provided it is thin relative to the wavelength. But for thicker resin layers (and Chapter 4 used 20 μ m thickness where $d \approx l/6$) the

effect is to change the resonant frequencies and hence the values of $k_n l$ (see Figure 5-8) and α_n .

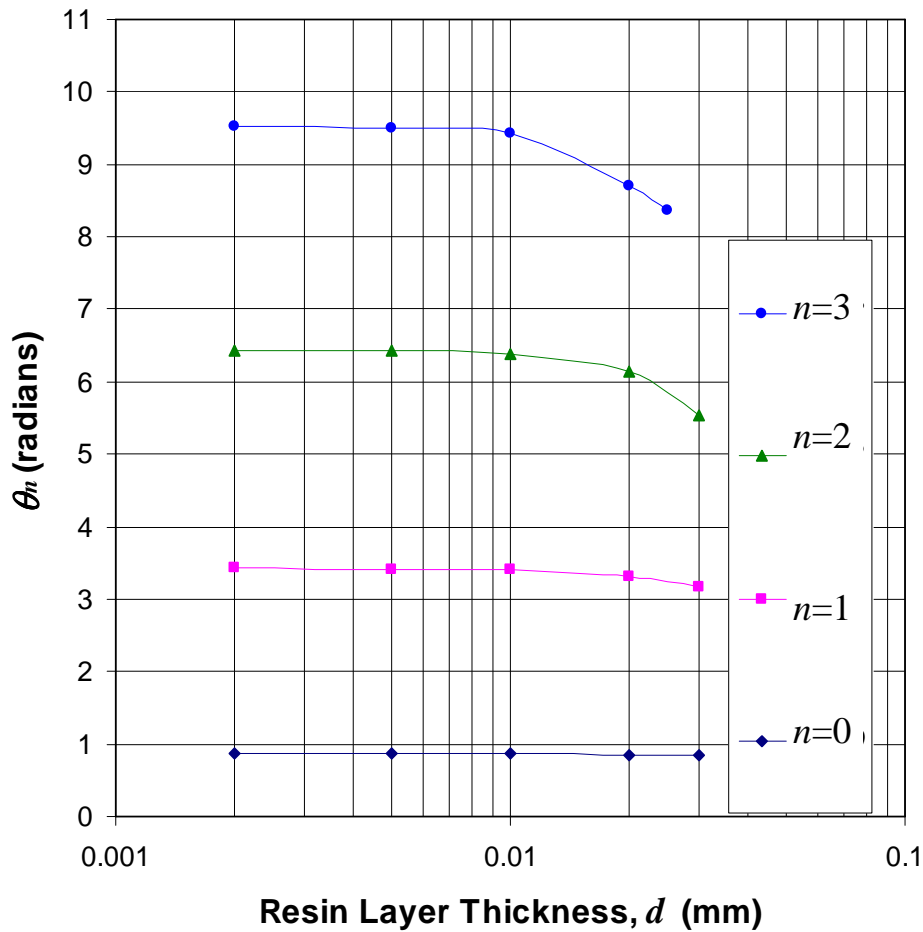


Figure 5-8. Graph showing how sensitive the θ_n value is to resin layer thickness for the first four resonances of a ply spacing $l = 0.125$ mm. Note that the $n=3$ resonance is not plotted beyond $23 \mu\text{m}$, where the resin-layer anti-resonance (minimum in the modulation function) is below the ply resonance frequency.

If a resin layer thickness d of 0.02 mm is used instead, $k_l l$ falls by 3% to 3.31 giving an α_l value of $0.622 \text{ mm}^{-1}\text{MHz}^{-1}$ using a compression velocity c of 3050 m/s. Thus, for the same material parameters as used in Appendix C, this α_l value compares well with the value of $0.629 \text{ mm}^{-1}\text{MHz}^{-1}$ determined by graph plotting from the full model in Chapter 4 Equation 4-2.

For most normal resin-layer thicknesses, up to 0.01 mm, the values of $k_n l$ can be regarded as invariant at $\theta_n = 0.862, 3.425, 6.44$ and 9.53 radians for $n = 0, 1, 2$ and 3 respectively.

In order to measure the ply spacing a resonant frequency f_n should be measured and the equation to use will be:

$$l = \frac{\theta_n c}{2\pi f_n} \quad (5-10)$$

The value for the compression velocity c will need to be calculated based on the fibre volume fraction using an appropriate mixture rule. However, for carbon-fibre composites, the FVF has little effect on the compression velocity (see Appendix F and Figure 4-38 in Chapter 4), a reduction in FVF from 60% to 40% producing a reduction in velocity of just 1%. Therefore, it is probably sufficient to use a single value for velocity in CFRP, but not in GFRP (see Figure 3-7 in Chapter 3), where the velocity can reduce by as much as 12% for this reduction in FVF due to the much higher transverse modulus of glass than carbon fibre.

5.3.2 Fibre Volume Fraction (FVF)

If assumptions are made that:

- average fibre volume per unit lateral surface area is constant, and
- fibres do not move laterally within a ply even when the ply thickness changes,

then it follows that ply thickness changes are accompanied by corresponding local FVF changes, and that measurement of local ply spacing may provide a method for measuring local FVF, ϕ_f . This has been investigated in Appendix C using the layer model and an expression derived based on a constant product $\phi_f l$, the average fibre volume per unit lateral ply area. Thus:

$$\phi_f = \phi_{f,nom} \frac{l_{nom}}{l} \quad (5-11)$$

where $\phi_{f,nom}$ and l_{nom} are the *designed* values for FVF (typically 60%) and ply spacing respectively.

Substituting Equation 5-10 into Equation 5-11 results in an expression for FVF in terms of resonant frequency...

$$\phi_f = \phi_{f,nom} l_{nom} \frac{2\pi f_n}{\theta_n c} \quad (5-12)$$

Local FVF changes modify the effective bulk modulus and density in the equivalent medium according to an appropriate mixture rule (see Chapter 4), thus causing a change in compression velocity, c and this may need to be accounted for in FVF measurement of GFRP plies, as explained above, but probably not in CFRP according to results in Appendix C.

For GFRP and CFRP respectively, the compression velocity varies with FVF (see Figure 5-9) approximately following a parabola:

$$c = \gamma_f \phi_f^2 + c_m \quad (5-13)$$

where γ_f is related to the acoustic velocity in the fibre, ϕ_f is the fibre volume fraction and c_m is the compression velocity of the matrix – 2903 m/s for the example simulated in Figure 5-9. Using the Hashin (1965) equivalent medium model to plot the equivalent-medium compression velocity, γ_f takes values 1954 m/s and 185 m/s for S-glass fibre and carbon fibre composite respectively to generate the fit illustrated in Figure 5-9 which is optimised for 50% to 70% FVF – the likely range to be found in a composite material with a designed FVF of 60%. These two values for γ_f are radically different because γ_f represents the difference between the velocity in the composite and that in the matrix only, and whilst carbon fibres have a similar velocity to resin, glass fibres are much stiffer and have a much higher velocity.

The method for calculating the value of γ_f optimised for the range of FVF (see Figure 5-9) is to find the mean value from three Hashin (1965) calculations of

compression velocity c_1 , c_2 and c_3 at $\phi_{f,1} = \phi_{f,nom} - 0.1$, $\phi_{f,2} = \phi_{f,nom}$ and $\phi_{f,3} = \phi_{f,nom} + 0.1$ as follows:

$$\gamma_f = \sum_{i=1}^N \frac{c_i - c_m}{N\phi_{f,i}^2} \quad (5-14)$$

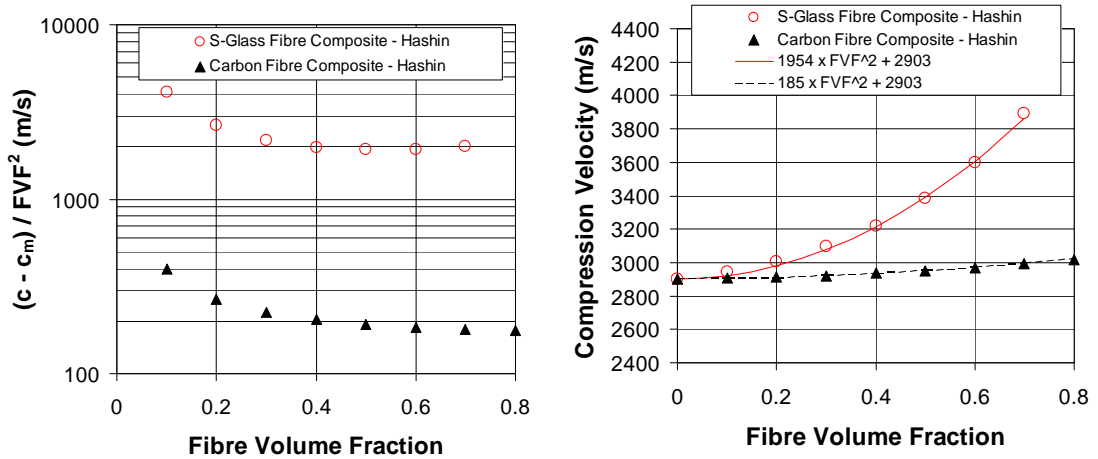


Figure 5-9. Simplified equations to fit the compression velocity of GFRP and CFRP (right), based on γ_f values calculated using Equation 5-14 with values plotted against FVF (left).

5.3.3 Combined Ply Spacing and Fibre Volume Fraction

The effect of FVF on compression velocity, discussed above, results in the need to account for this in measurements of both ply spacing and FVF. Equations 5-10 and 5-12 are probably adequately accurate for CFRP as the sound velocity is relatively independent of FVF and the velocity corresponding to the designed nominal FVF will suffice: c_{nom} giving the following:

$$l = \frac{\theta_n c_{nom}}{2\pi f_n} \quad (5-15)$$

$$\phi_f = \phi_{f,nom} l_{nom} \frac{2\pi f_1}{\theta_n c_{nom}} \quad (5-16)$$

In this case Equation 5-13 can be substituted into Equation 5-10 and then combined with Equation 5-11 to give the following cubic expressions for ply spacing, l and FVF, ϕ_f :

$$\frac{2l^3}{\theta_n} - \frac{c_m l^2}{\pi f_1} = \frac{C_f}{\pi f_1} \quad (5-17)$$

$$\theta_n \phi_f (\gamma_f \phi_f^2 + c_m) = 2\pi \phi_{f,nom} l_{nom} f_1 \quad (5-18)$$

where C_f is a combination of nominal (as designed) material properties and is defined as:

$$C_f = l_{nom}^2 \gamma_f \phi_{f,nom}^2 \quad (5-19)$$

The *real* solutions of Equations 5-17 and 5-18 (there being two other *complex* solutions) link the ply spacing, l and FVF, ϕ_f to the resonant frequency and are:

$$l = \frac{1}{6} \left(\frac{\theta_n c_m}{\pi f_1} + \frac{\theta_n^2 c_m^2}{2^{2/3} \pi^2 f_1^2 G_1^{1/3}} + (4G_1)^{1/3} \right) \quad (5-20)$$

$$\phi_f = \frac{1}{\gamma_f} \left(\frac{F_1}{18} \right)^{1/3} - c_m \left(\frac{2}{3F_1} \right)^{1/3} \quad (5-21)$$

where F_1 and G_1 are functions of the first resonant frequency f_1 and are defined as follows:

$$G_1 = \frac{\theta_n^3 c_m^3}{4\pi^3 f_1^3} + 3 \sqrt{\frac{3(\theta_n^4 c_m^3 C_f + 27\theta_n^2 \pi^2 f_1^2 C_f^2)}{2\pi^2 f_1^2}} + \frac{27\theta_n C_f}{2\pi f_1} \quad (5-22)$$

$$F_1 = \frac{18\pi f_1 l_{nom} \gamma_f^2 \phi_{f,nom}}{\theta_n} + \sqrt{3\gamma_f^3 \left(4c_m^3 + \frac{108\pi^2 f_1^2 C_f}{\theta_n^2} \right)} \quad (5-23)$$

5.3.4 Measurement of resonant frequency

Measurement of resonant frequency is not straightforward. A gate width has to be chosen for defining the portion of the waveform for spectral analysis. This

gate must include two ply interfaces in order for its spectrum to contain the ply resonances. Experience has shown that choosing a gate of approximately two ply thicknesses, combined with a 20% Hanning window (10% of the gate width at each end), ensures that there are always just two interfaces in the gate.

There are two main sources of error in measuring the resonant frequency: the influence of the incident pulse spectrum, and the algorithm for measuring a single resonance frequency. These two sources of error are interlinked because the incidence pulse will influence each measurement algorithm differently.

Examples of four algorithms are shown in Figure 5-10 and Figure 5-11.

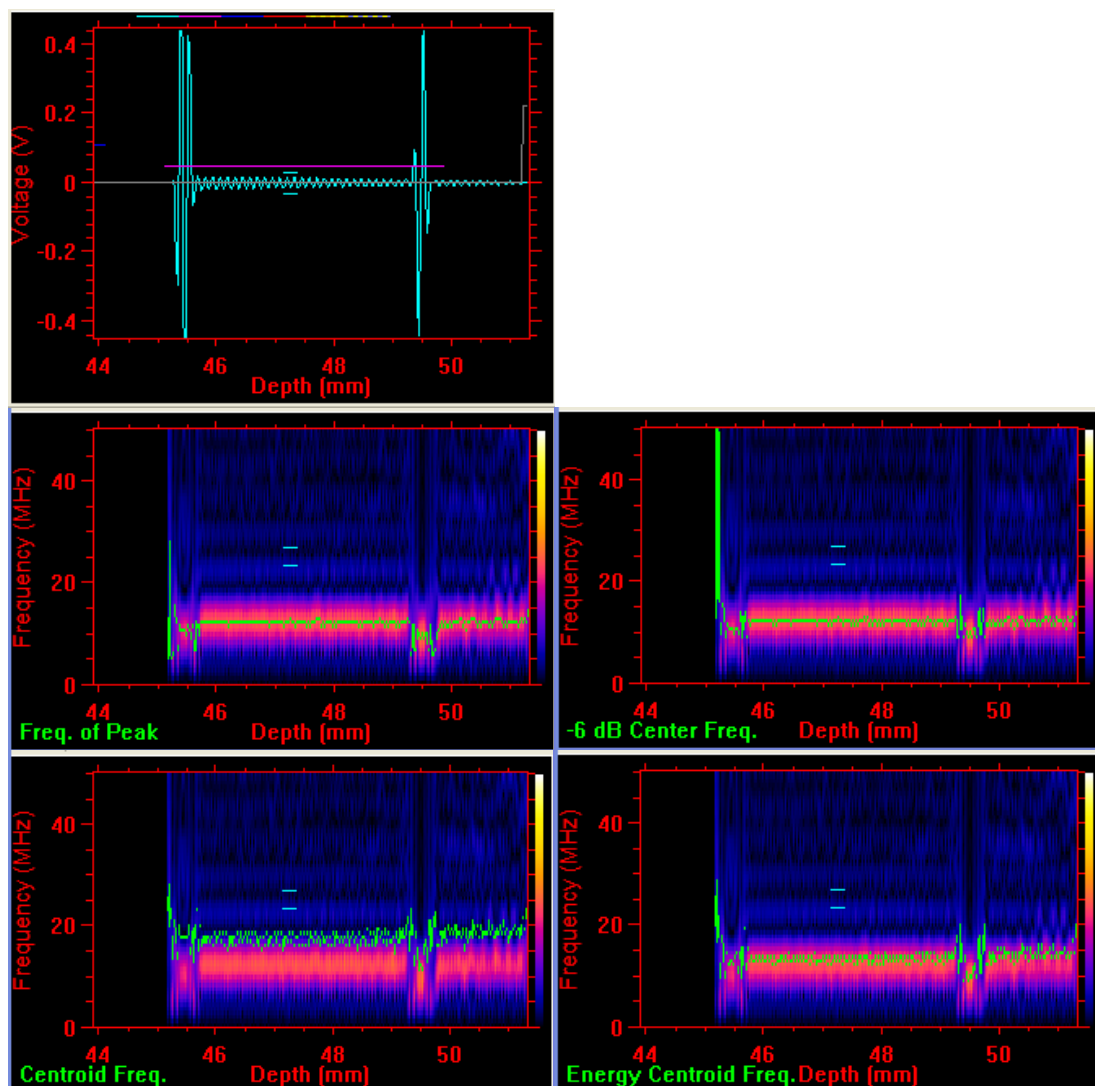


Figure 5-10. Waveform (top) and time-frequency plots for a simulated 32-ply stack of constant-thickness 0.125 mm plies, each showing a different algorithm for determining resonant frequency (labelled in green bottom-left in each plot).

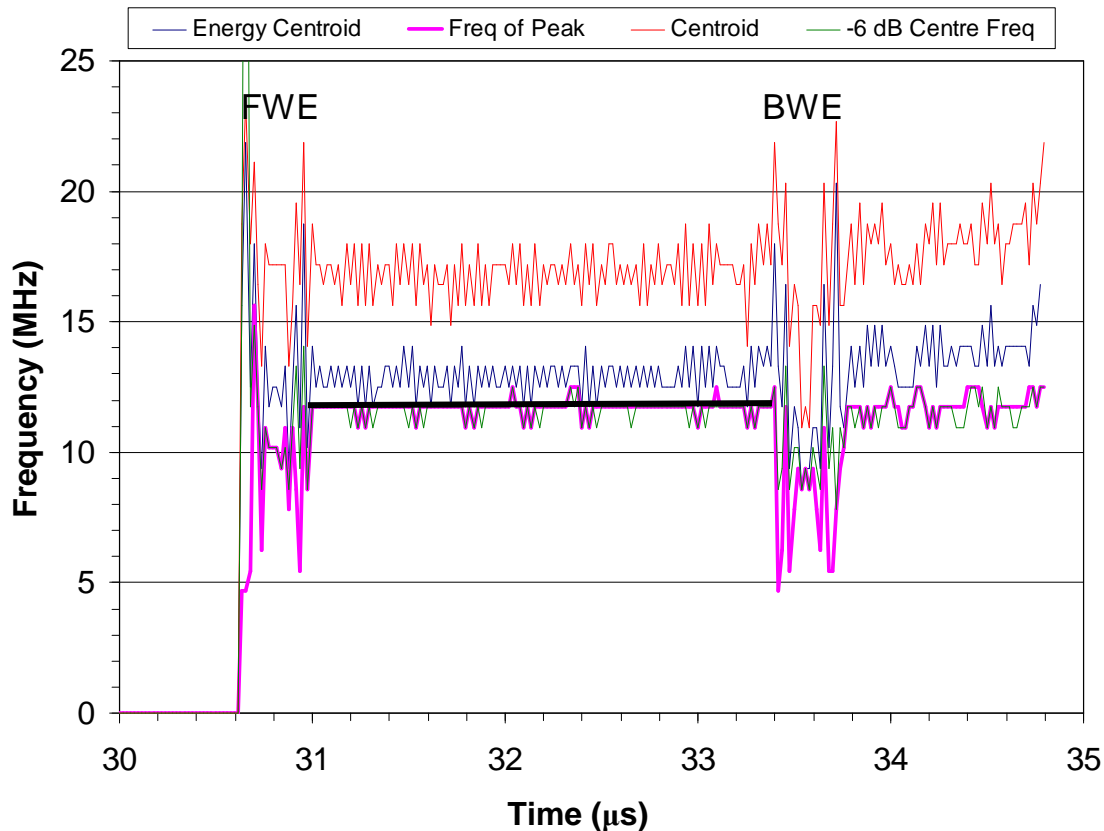


Figure 5-11. Comparison of algorithms for measuring the resonant frequency for the simulated 32-ply stack of 0.125 mm constant-thickness plies shown in Figure 5-10, with a 10 MHz Gaussian-profile simulated incident pulse shape. The thick black line indicates the modelled resonant frequency in the region between the front-wall echo (FWE) and back-wall echo (BWE) as marked.

Even with constant ply spacing in the above example, the four different algorithms measure different resonant frequencies. The Frequency of Peak algorithm fails when the peak is flat-topped or when it is split by an anti-resonance and the algorithm decides which is the correct peak to take, based on amplitude. The -6 dB Centre Frequency algorithm copes well with flat-topped peaks but can be confused by multiple peaks that do not go below -6 dB between them. The Centroid Frequency measurement is too heavily influenced by the low parts of the spectrum unless these are deliberately filtered out, but then the filter influences the value. The Energy-Centroid Frequency is less susceptible to the low amplitude parts of the spectrum because it uses the square of the amplitude, but still gives a value that is influence by the spectrum length or filter bandwidth, if one is used. Having decided that the Frequency of

Peak and -6 dB Centre Frequency are the best performing metrics, similar problems are evident for 30% randomness in ply spacing, as in Figure 5-12.

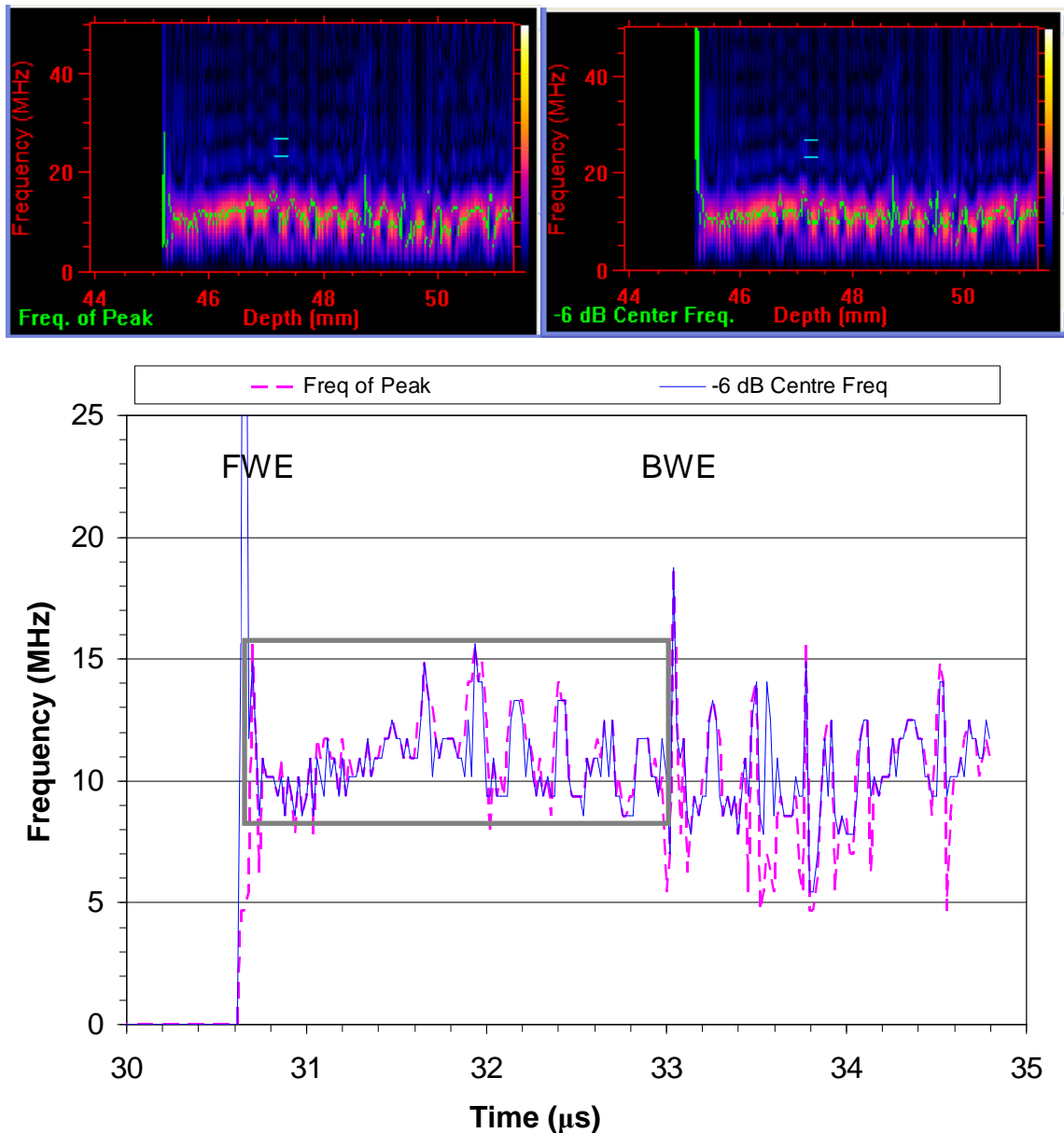


Figure 5-12. Time-frequency plots and resonant frequency calculations for 32-ply simulated material with 30% randomness in the ply spacing. The same waveform was used for each analysis. The rectangular grey box between the front-wall echo (FWE) and back-wall echo (BWE) shows the modelled resonant frequency band for 30% randomness in ply spacing.

Next, a single thick ply was simulated at ply 10 of the 32-ply stack and the resulting FVF at each ply from the model was plotted with the measured resonant frequency using the two methods in Figure 5-13.

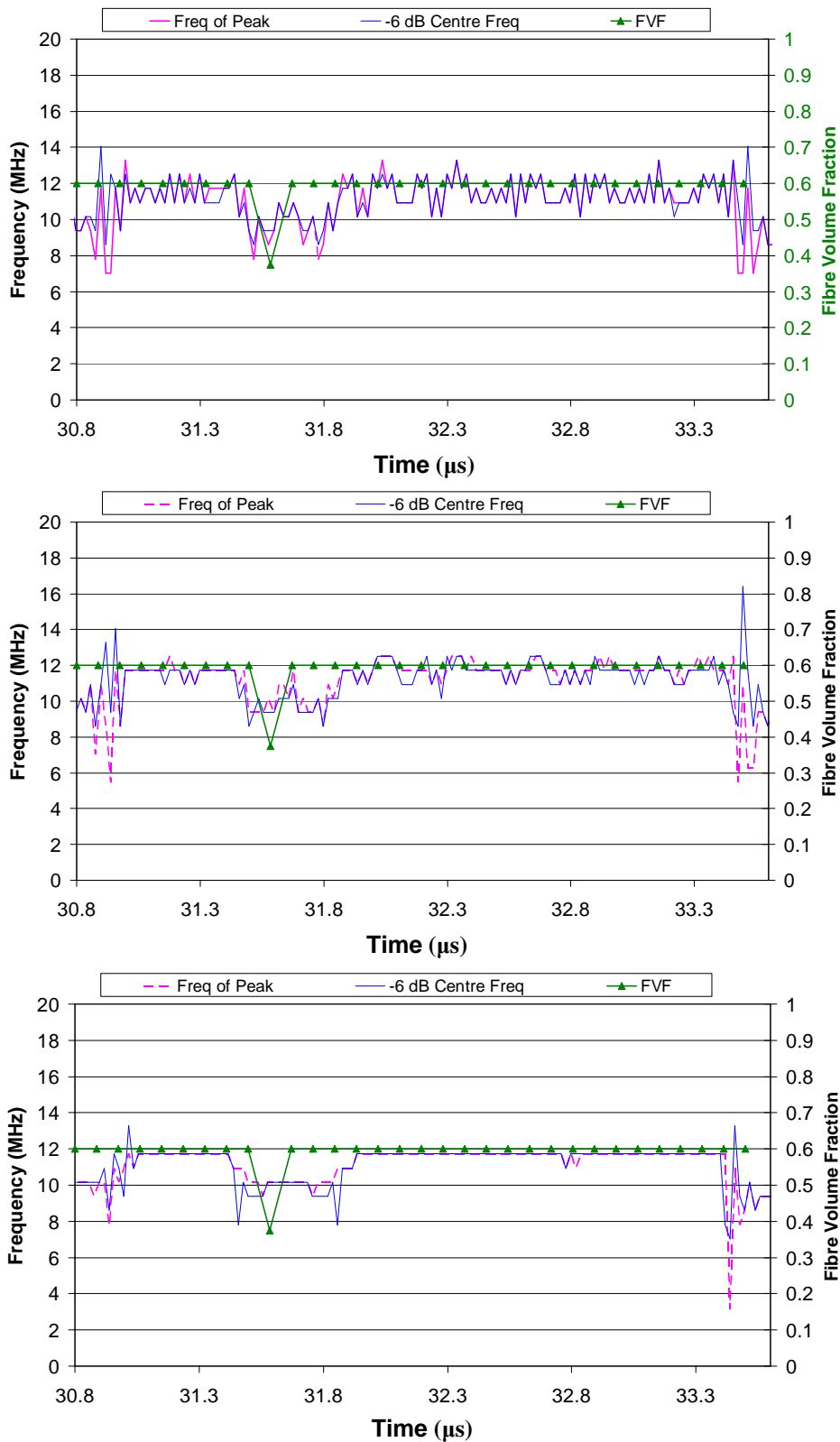


Figure 5-13. Resonant frequencies measured using gates of width 0.2 mm (top), 0.24 mm (middle) and 0.4 mm (bottom) for a thick (0.2 mm) ply at ply 10 (31.6 μs) in a 32-ply stack of 0.125 mm thick plies. The calculated FVF for each ply is also plotted (green) to show the thick ply.

This shows promise as the resonant frequency is responding to the change in ply spacing and FVF. However, when a high level of variability is introduced, it is not clear that either algorithm for resonant frequency is adequately following the FVF – see Figure 5-14.

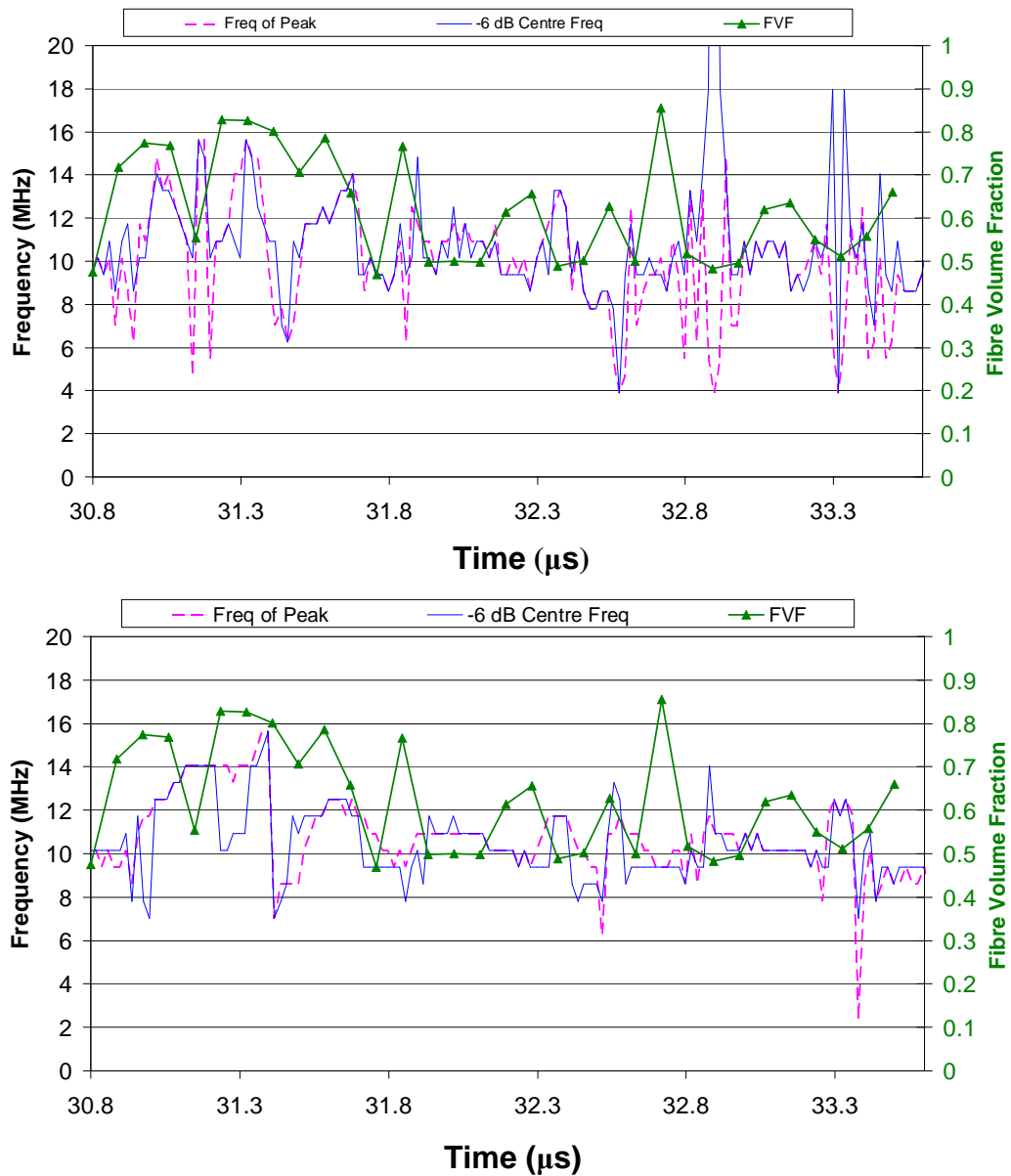


Figure 5-14. Resonant frequencies measured using gates of width 0.24 mm (top) and 0.4 mm (bottom) for 30% randomness in ply spacing in a 32-ply stack of 0.125 mm thick plies. The calculated FVF for each ply is also plotted (green) to show variation, which should be matched by the resonant-frequency measurements.

5.3.5 Cross-correlation algorithm for resonant frequency measurement

A new algorithm has been developed that uses the multi-layer model to generate a 'reference' spectral response of a single layer bounded by two resin layers and compares this with the measured spectrum at each depth. By performing a log-transform on the frequency axis of both the measured and reference spectra prior to cross-correlation, it then compares the relative scale factors for the two spectra and produces a peak at the scaling giving the best match. The result is a factor that gives the ratio of measured resonant frequency to the reference resonant frequency.

In order to improve this method it will be necessary to include the incident pulse spectrum in the calculation of the reference spectrum, or to remove it from the measured spectrum, prior to cross-correlation. The examples in Figure 5-15 to Figure 5-18 use a reference spectrum with a simulated incident pulse spectrum applied to the modelled single-ply spectrum. The cross-correlations of the log-transformed spectra are demonstrated in Figure 5-16 and Figure 5-17 for a normal-thickness (0.125 mm) simulated ply and a 0.25 mm thick simulated ply.

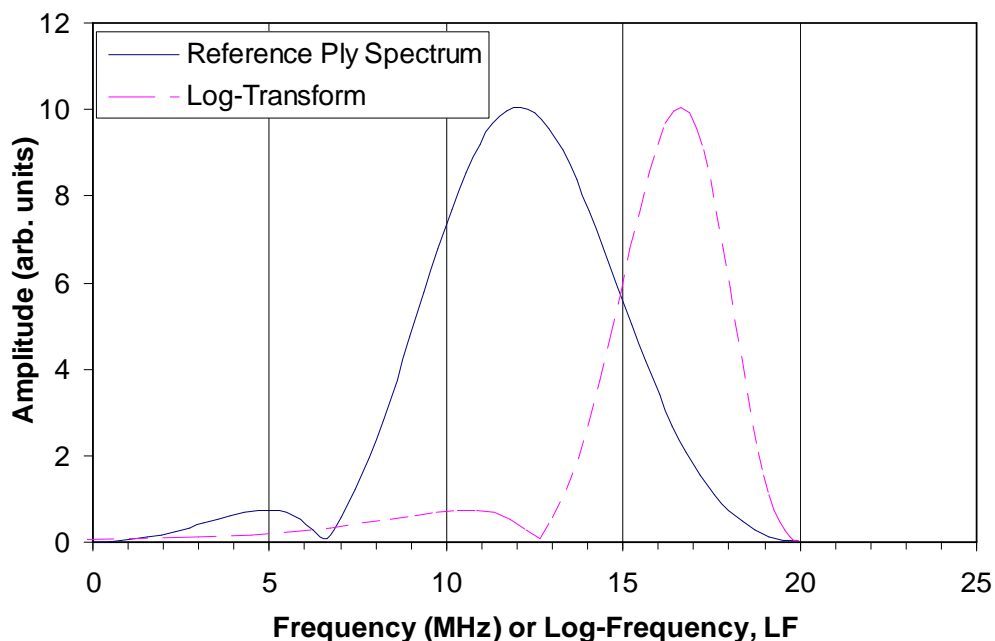


Figure 5-15. The reference spectrum (blue solid curve) generated by the analytical model, and the dimensionless log-transform LF (pink dashed curve) defined as: $LF = 20 \log_{10}(f \text{ re: } 1\text{MHz}) / \log_{10} 20$ where f is the frequency in MHz.

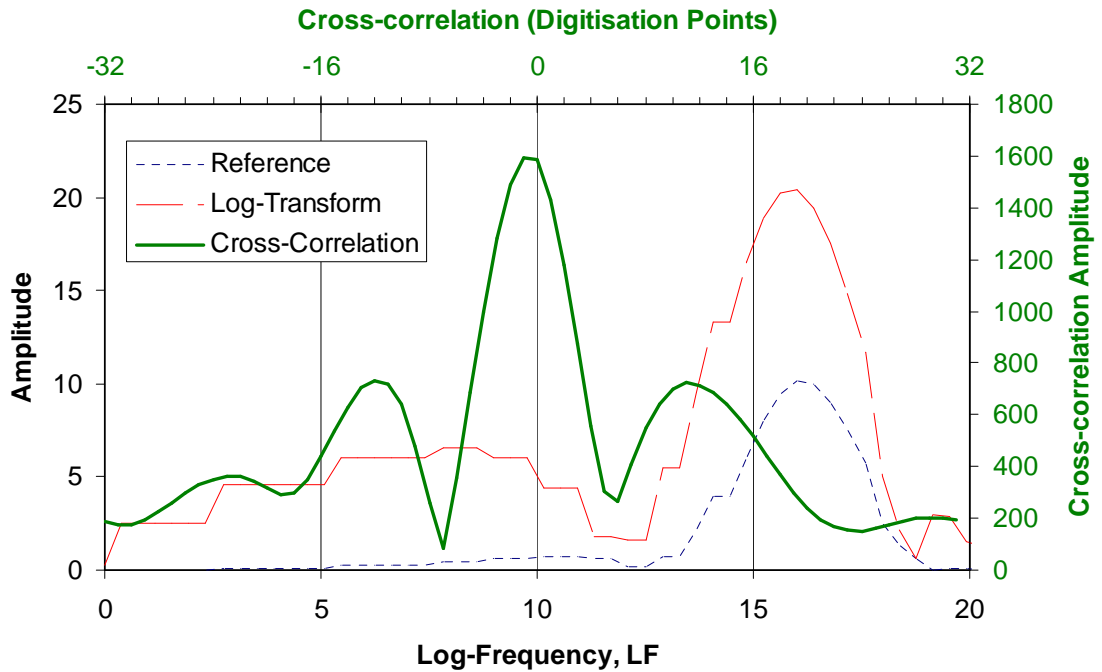


Figure 5-16. The reference (blue dotted) and locally measured (red dashed) log-transformed spectra for a 0.125 mm ply, and the output of the cross-correlation algorithm (green solid) with point 0 corresponding to scaling of unity, and the peak between points -1 and 0 shows that the spectra are scaled by $-\frac{1}{2}$ a point.

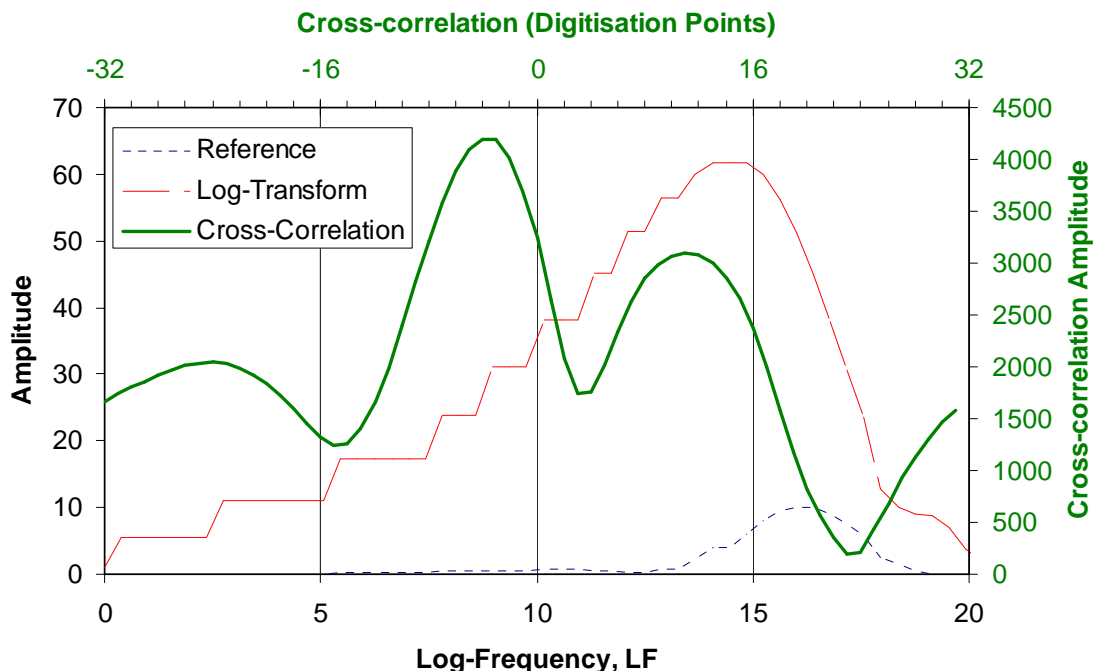


Figure 5-17. As in Figure 5-16 but for a single simulated 0.25 mm ply in a stack of 32 simulated plies of thickness 0.125 mm, showing that the cross-correlation peak is between points -4 & -3 so the two spectra are scaled by -3.5 points.

The method measures the resonant-frequency shift but gives very similar results to the Frequency of Peak method, as shown in Figure 5-18 for a modelled simulation, and takes longer to calculate. Thus it is concluded that the log-transform cross-correlation method is not worth pursuing further.

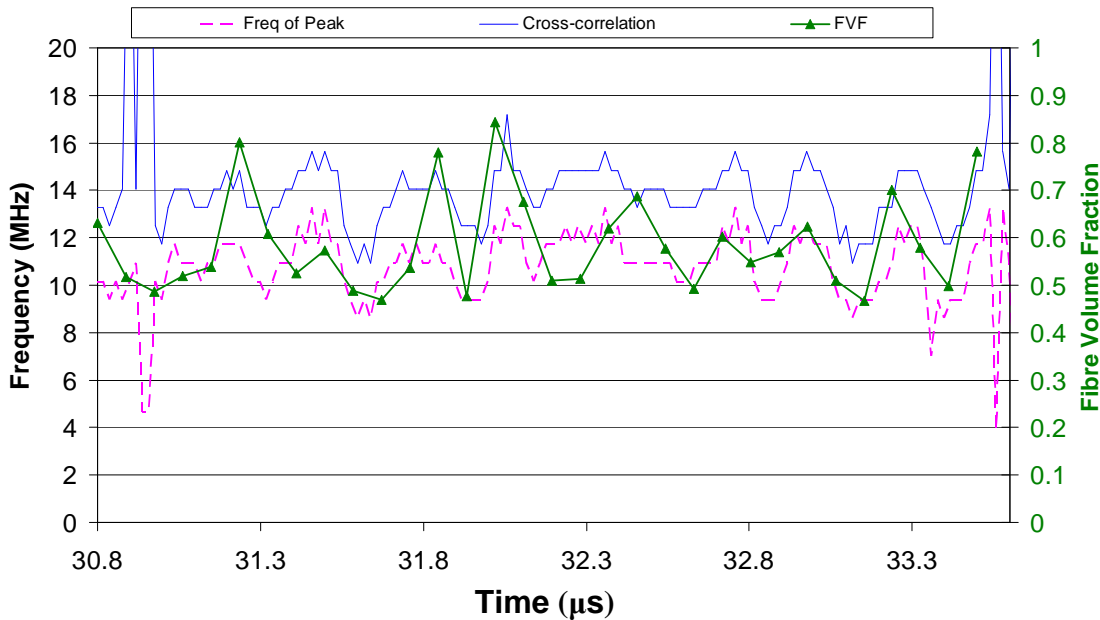


Figure 5-18. Resonant frequencies measured using gate of width 0.28 mm for 30% randomness in ply spacing in a 32-ply simulated stack of 0.125 mm thick plies. The calculated FVF for each ply is also plotted (green) to show variation, which should be matched by the resonant-frequency measurements.

5.3.6 Summary of 3D characterisation of fibre-resin effects

Algorithms have been developed for relating both ply spacing and FVF to local resonant frequency. The five methods that have so far been tested for measuring local resonant frequency have had some success with single thick plies in a stack of otherwise uniform plies. However, they all deteriorated as the ply spacing became more random. This suggests that if significant randomness exists, the local ultrasonic resonance is affected by adjacent ply spacings as well as the ply spacing on which it is centred. Some promising initial work has been done on the use of multi-dimensional optimisation methods to determine the thicknesses of multiple adjacent plies with the analytical model as part of the feedback loop. This may point the way ahead for ply spacing measurements in highly random laminates but is beyond the scope of this project.

5.4 Porosity – Amplitude method

5.4.1 Rationale

A possible metric for porosity could be amplitude-based rather than frequency-based but it would be susceptible to numerous other influences on amplitude that could masquerade as porosity or affect its measurement. For example:

- The response from a particular depth will be modified by what happens to the ultrasound in the shallower layers through which it passes. This includes any visco-elastic damping, reflections at interfaces, and scattering from voids or inclusions. In particular the amplitude of the response will be affected, so a correction must be applied before any calibration can occur.
- Other changes in the material, such as a variation in thickness of a resin layer between plies, can increase the amplitude of a reflection from a particular layer, thus masquerading as porosity. This material variation may also be significant, but it needs to be distinguishable from porosity itself.

In this section, a method is proposed for deriving a parameter that is sensitive to porosity and can be corrected for depth in the structure, calibrated, and supplemented by a method for distinguishing porosity from other sources of increased amplitude.

5.4.2 Basis of an amplitude method

It is possible that porosity can be measured by measuring the local reflection coefficient in each volume element. If this is the case then it is necessary to correct the amplitude response for depth in the structure and calibrate the relationship in order to determine porosity distribution. A possible scenario for using this method is shown schematically in Figure 5-19.

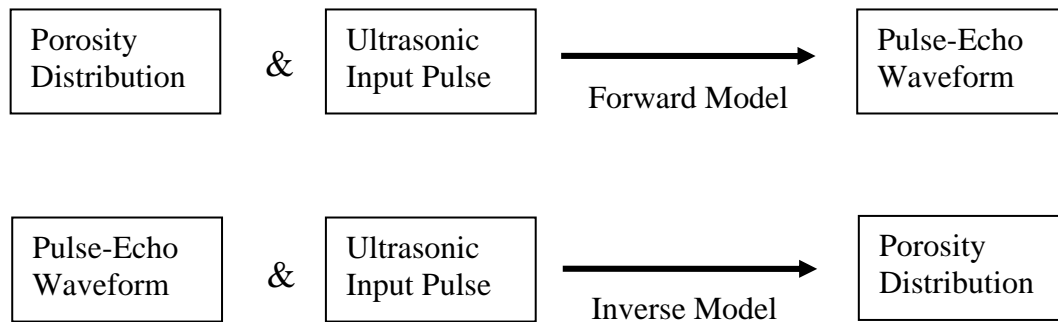


Figure 5-19. Schematic illustrating how a calibrated inverse model could be used to determine the porosity distribution based on the ultrasonic waveform.

5.4.3 Assumptions

The following assumptions are required in order to pursue an amplitude method for porosity measurement and develop it using the model from Chapter 4:

- That actual backscattered energy from porosity can be modelled sufficiently accurately by varying the bulk material properties that affect the acoustic impedance of a layer, thus ignoring the frequency dependence and the angular dependence of the response.
- That the response at a particular time in the waveform is dominated by the product of the reflection coefficient and incident energy at the corresponding depth. For this to apply, multiple reflections will probably need to be 10 dB to 20 dB lower in amplitude than the primary reflection from that depth, which is realistic for CFRP, but GFRP may violate this condition because the inter-ply reflections are stronger.
- That beam profile variations with distance have negligible effect.
- That the instantaneous acoustic intensity is proportional to the instantaneous acoustic pressure-squared. This is usually only the case when the pressure and particle velocity are in quadrature phase – ie in a plane or spherical wave. However, combining the original signal (the real component) with its Hilbert Transform (the imaginary component – see Appendix D) to form the complex analytic signal, and taking the modulus of the result gives the envelope representing the instantaneous amplitude, removing the effect of phase, and so should solve this problem.

- That the front-surface reflection is captured, unsaturated, as part of the waveform, and is unaffected by surface roughness causing a change in the reflection coefficient and the introduction of a frequency dependence, and hence can be used to help determine the incident energy.

5.4.4 Proposed amplitude method

It is proposed that a modified waveform could be produced that is the per-point quotient of a 'reflection amplitude' waveform and a derived 'incident amplitude' waveform, thus correcting for shadowing of nearer-surface porosity or other material variations, and determining the actual reflection coefficient from each depth. The reflection amplitude waveform can be generated by first combining the received signal (the real component) with its Hilbert Transform (the imaginary component – see Appendix D) and taking the modulus of the result, giving the envelope representing the instantaneous amplitude of the response reaching the transducer from each depth. It is then low-pass filtered and high-pass filtered to remove any residual effects of normal ply resonances superimposed on it.

In order to correct for the gradually changing amplitude of the pulse incident at each depth, an 'incident amplitude' curve is required. For each volume element at time t , the pressure-squared (equivalent to the transducer voltage squared) is integrated in the waveform up to the time of interest to determine the reflected energy from all material shallower than the volume element.

Through conservation of energy, assuming only forward or backward scattering and neglecting scattering in other directions and visco-elastic (or internal friction) thermal losses:

$$\textit{Incident energy} = \textit{reflected energy to time } t + \textit{transmitted energy beyond } t$$

The integrated reflected energy profile is thus used to determine the energy transmitted to each volume element and its use is similar to that of an energy DAC curve. By square-rooting this incident energy curve, an 'incident amplitude' curve is obtained, and dividing the reflection curve by it results in a plot of the reflection coefficient at each volume element – the maximum value being unity.

The initial energy incident on the whole structure is not known directly but it can be derived from the front-surface signal and the front-surface amplitude reflection coefficient, R_I . R_I can be calculated using simple effective impedances derived from mixture rules and the modulus and density of fibre and resin:

$$R_I = 0.535 \text{ for } 80\% \text{ FVF}$$

$$R_I = 0.524 \text{ for } 70\% \text{ FVF}$$

If the signal is not saturated, the front-wall amplitude-squared over the pulse can be integrated and divided by the intensity (or energy) reflection coefficient (R_I^2) to give an approximate initial incident energy.

The time of the end of the front-surface reflected pulse, t_I needs to be determined for each waveform so that the front-surface reflected pulse can be integrated. It could be the time at which the FWE envelope falls below some percentage of its peak height, but a consistent method must be developed as this will be fundamental to the calibration.

The reflected energy density (energy per unit area across the beam), E_r prior to each time τ is given by:

$$E_r(\tau) = \frac{1}{\rho c} \int_0^{\tau} p^2 dt \quad 5-24$$

For the front surface reflection, the reflected energy density, E_{rI} is calculated:

$$E_{rI} = \frac{1}{\rho c} \int_0^{t_I} p^2 dt \quad 5-25$$

where p is the instantaneous acoustic pressure amplitude in the beam, ρ is the density, c is the sound speed, and t_I is the time of the end of the front-surface reflection. Hence the incident energy density, E_i is:

$$E_i = \frac{E_{rI}}{R_I^2} = \frac{1}{\rho c R_I^2} \int_0^{t_I} p^2 dt \quad 5-26$$

Then the transmitted energy density at each time τ , $E_t(\tau)$ is given by:

$$E_t(\tau) = E_i - E_r(\tau) = E_i - \frac{1}{\rho c} \int_0^{\tau} p^2 dt \quad 5-27$$

Instantaneous reflection coefficients (from each volume element) are required, because this is what the model uses to determine calibration curves, and they need to be calculated from instantaneous intensity, I , where:

$$I = \frac{p^2}{\rho c} \quad 5-28$$

In order to convert the energy density in the incident pulse into an instantaneous intensity, an assumption can be made that the maximum instantaneous intensity in a pulse is what contributes to the ‘reflected amplitude’ waveform (ie. the filtered modulus of the complex analytic waveform – the real original waveform combined with its imaginary Hilbert Transform – see Appendix D). In this case, an effective pulse length T_{eff} can be defined, which converts the integrated energy density in the pulse into a maximum instantaneous intensity. For the front-wall incident pulse this can be calculated as follows:

$$T_{eff} = \frac{E_{r_i}}{I_{max}} \quad 5-29$$

where I_{max} is the maximum instantaneous intensity in the incident pulse. The instantaneous reflection coefficient at each time τ , $R(\tau)$ is given by:

$$R(\tau) = p(\tau) \sqrt{\frac{T_{eff}}{\rho c E_t(\tau)}} \quad 5-30$$

Substituting for $\rho c E_t(\tau)$ in Equation 5-30 from Equations 5-26 and 5-27,

$$R(\tau) = p(\tau) \sqrt{\frac{T_{eff}}{\frac{1}{R_1^2} \int_0^{t_1} p^2 dt - \int_0^{\tau} p^2 dt}} \quad 5-31$$

Assuming that the instantaneous voltage amplitude V from the non-filtered modulus of the combined transducer output (real part) and its Hilbert Transform (imaginary part – see Appendix D) is proportional to acoustic pressure amplitude p then it is possible to re-write the above Equation 5-31 as:

$$R(\tau) = V_1(\tau) \sqrt{\frac{T_{eff}}{\frac{1}{R_1^2} \int_0^{t_1} V^2 dt - \int_0^{\tau} V^2 dt}} \quad 5-32$$

where V_1 is the *filtered* modulus of the complex analytic signal (the combined original waveform and its Hilbert Transform – see Appendix D).

If the incident energy density D_i is to be calculated globally, prior to the analysis of each waveform, the parameter that needs to be calculated is:

$$D_i = \frac{1}{R_1^2} \int_0^{t_1} V^2 dt \quad 5-33$$

and the equation to which it applies is then:

$$R(\tau) = V_1(\tau) \sqrt{\frac{T_{eff}}{D_i - \int_0^{\tau} V^2 dt}} \quad 5-34$$

5.4.5 Evaluation of the amplitude method

An example of this analysis is shown in Figure 5-20 for simulated porosity and a thick resin layer. The biggest potential problem with this amplitude method is the potential for thick resin inter-ply layers to masquerade as porous plies because they give an increased amplitude response that is potentially indistinguishable from that of porosity when just using the modulus of the complex analytic waveform generated from a Hilbert Transform (see Appendix D), as shown in Figure 5-21 (top).

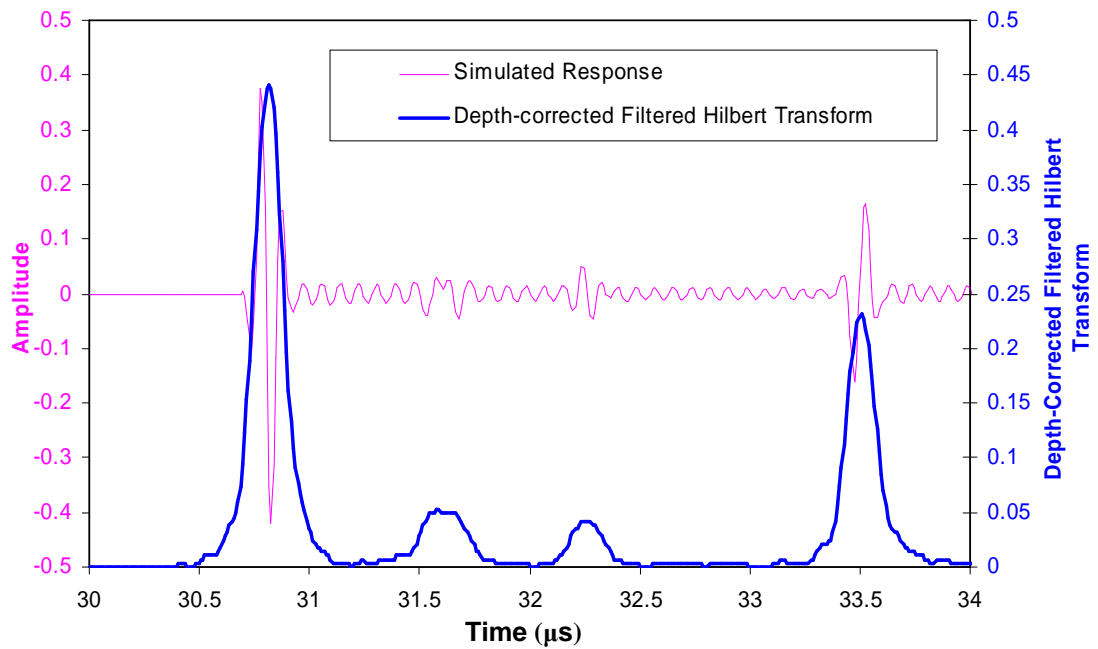


Figure 5-20. Simulated temporal response (magenta), and instantaneous reflection coefficient $R(\tau)$ calculated by correcting the filtered Hilbert-transformed waveform for transmitted energy at each depth. The simulation used a 10 MHz $Q=0.8$ Gaussian pulse with a 32-ply stack of 120 μm 70% FVF plies and 5 μm resin layers. The 10th ply (at 31.6 μs) has 10% of 10 μm radius porosity and the 18th ply (at 32.2 μs) has a 20 μm resin layer followed by a 105 μm thick ply, with increased FVF to compensate.

However, it is possible to use the phase of the complex analytic waveform, formed by combining with the Hilbert Transform (see Appendix D). This is effectively the instantaneous phase of the response - and shows different characteristics for porosity and thick resin layers. The phase is plotted in Figure 5-21 (bottom) after subtracting the instantaneous phase of the centre frequency of the resonance in the structure. For porosity, the phase increases rapidly on entering the first porous ply, increases further during the thickness of the porous ply, and also on exiting the porous ply, ending at a different phase to the entry phase. For a thick resin layer, there is only one increase in phase, *followed by dropping back to the original phase again*. The latter effect is important as the porosity response does not do this and it offers potential for use as a differentiator between porosity and thick resin layers but the work required to

understand these phase responses was beyond the scope and time available for the current project.

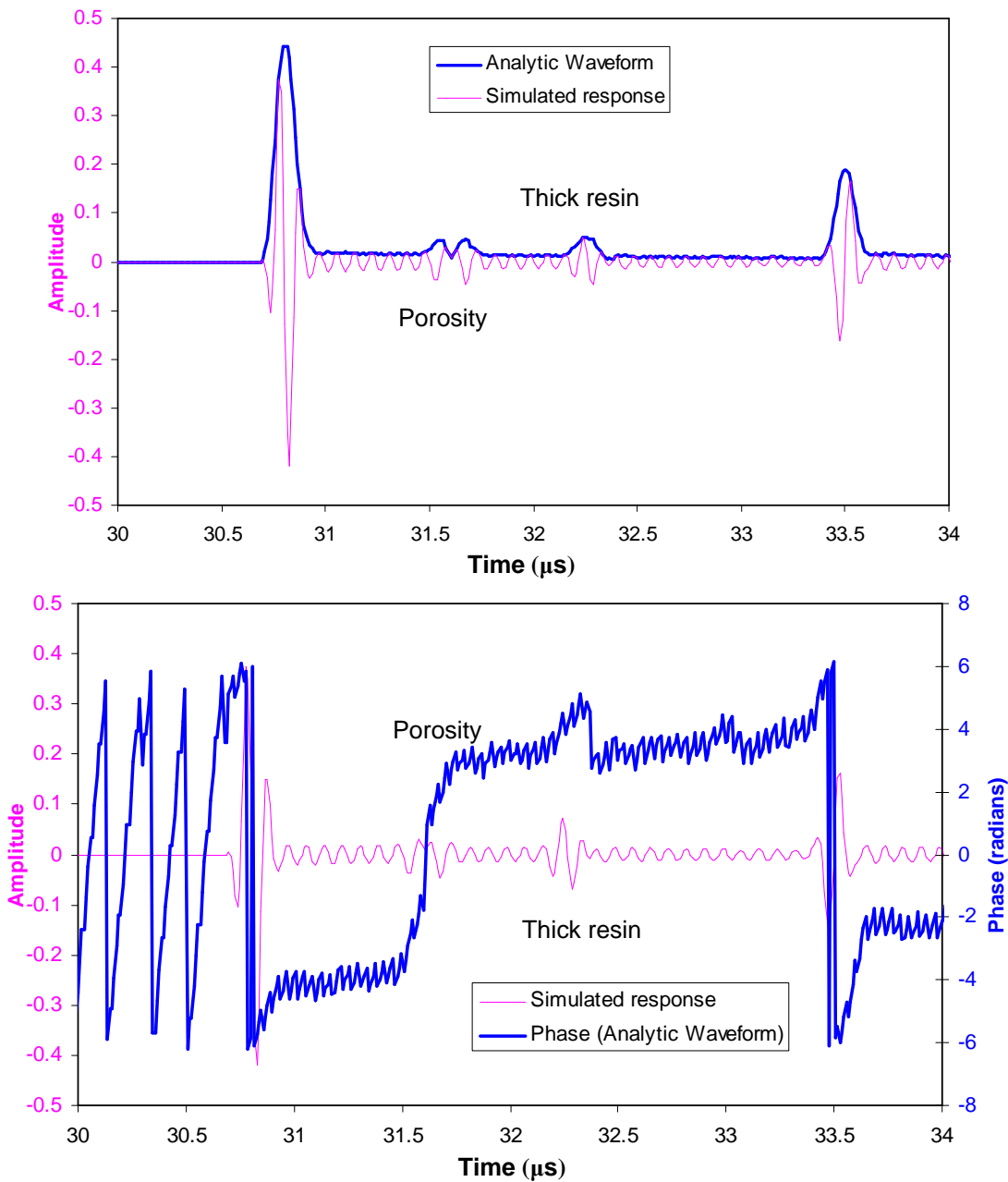


Figure 5-21. Simulated temporal response (magenta) with the magnitude (top, blue) and phase (bottom, blue) of the complex analytic waveform after combination with its Hilbert Transform (see Appendix D). A 10 MHz $Q=0.8$ Gaussian pulse was simulated propagating into a 32-ply laminate of $120 \mu\text{m}$ 70% FVF plies and $5 \mu\text{m}$ resin layers. The 10th ply (at $31.6 \mu\text{s}$) contains 10% of $10 \mu\text{m}$ radius porosity and the 18th ply (at $32.2 \mu\text{s}$) has a $20 \mu\text{m}$ resin layer followed by a $105 \mu\text{m}$ thick ply, with increased FVF to compensate.

5.5 Porosity – Model-based decomposition method

5.5.1 Rationale

The main aim of this chapter of the project is to develop quantitative 3D methods that differentiate between local porosity and fibre-resin effects such as ply spacing, resin layer thickness and fibre volume fraction. In order to achieve this, the ultrasonic response from the complex composite materials needs to be decomposed into components from each of the important material properties and defect types.

The above amplitude method exhibits cross-talk between the various defect types such as porosity and thick resin layers. This is fundamentally caused by the fact that the links between the ultrasonic parameters and the material properties have not been independent. A method is required that decomposes the ultrasonic response from each volume element into substantially independent (orthogonal) components, each of which is the result of a different material property. For this reason an actual *decomposition* method was investigated and is reported here

5.5.2 Frequency-domain decomposition

The work that has been reported above on modelling and studying composite structures has resulted in a good understanding of the underlying physics of the interaction between ultrasound and composite materials. This understanding has led to a realisation that it is the *frequency spectrum* of the response from each volume element that contains the differentiating information and therefore may be decomposed into a linear combination of *basis* functions that are linked to material properties. By definition, basis functions are substantially independent and can be combined linearly. Equation 5-35 shows how the modelling has indicated this could work to decompose $F(\omega)$, the signal response from a single-ply volume element, where ω is the angular frequency.

$$F(\omega) = a_0 N + A_0 T^2(\omega) D(\omega, d) [a_1 S(\omega) R(\omega, t_{norm}) + a_2 C(\omega, t_{thick}) + a_3 P(\omega)] \quad (5-35)$$

where: t_{norm} is the thickness of a ‘thick resin layer’,

t_{thick} is the thickness of a normal-thickness resin layer

A_0 is the incident signal amplitude,

T is the transducer response,

D is a correction for the incident spectrum at each depth d ,

$a_0 - a_3$ are the coefficients of the basis functions in the linear combination.

and the following four basis functions have been identified:

1. SR is the normal ply resonance, S , multiplied by the normal resin layer resonance, R
2. C is a thick resin layer,
3. P is the single porous layer response, and
4. N is white noise.

The aim of the work reported in this section is to establish whether such basis functions can be identified, develop a decomposition method and then evaluate how independent the basis functions are for the purposes required, using modelled waveforms. Finally, the decomposition method was tested on real data and these results are shown in subsequent sections.

5.5.3 Evaluation of decomposition methods

There are various decomposition methods available but Singular Value Decomposition (SVD) (Press et al, 2002) was chosen as a) the most suitable method in this application because of the ease of using weightings, and b) because it had already been included in the ANDSCAN toolset for other purposes (transient eddy currents). Similar results were obtained with another decomposition method (least squares decomposition) but the SVD method seemed more tolerant of basis-function amplitude levels.

In order to test the SVD implementation for the specific type of basis functions required, test spectra were artificially generated by adding together basis functions with different coefficients and then using SVD to recalculate those coefficients using the test spectrum and the basis functions. For this purpose, simplified basis functions were used (see Figure 5-22) as follows:

1. A half-wave resonance amplitude modulated by a linear slope with frequency, to represent a normal ply resonance: $S(\omega)R(\omega, t_{norm})$ where:

$$S(\omega) = |\cos(\omega/\omega_0)|$$

$$R(\omega, t_{norm}) = (\omega/2\pi).10^{-6}$$

and ω_0 is the resonant angular frequency.

2. A simple linear slope with frequency to represent the low-frequency part of a thick resin layer response: $C(\omega, t_{thick}) = (\omega/2\pi).10^{-6}$
3. A quarter-wave resonance to represent layer porosity:
 $P(\omega) = |\sin(\omega/\omega_0)|$ where ω_0 is the resonant angular frequency.
4. A constant, representing white noise : $N = 1$.

The trials showed that SVD is very accurate, in the absence of noise, at determining the various coefficients of these basis functions – see Table 5-2.

A more realistic test of the SVD method would be when there are spectral effects that do not readily fall into one of the categories represented by the basis functions. Normal ‘white’ noise is represented by the fourth basis function, so it was decided to add ‘random spectral fluctuations’ of different amplitudes to the simulated spectra before running the SVD algorithm.

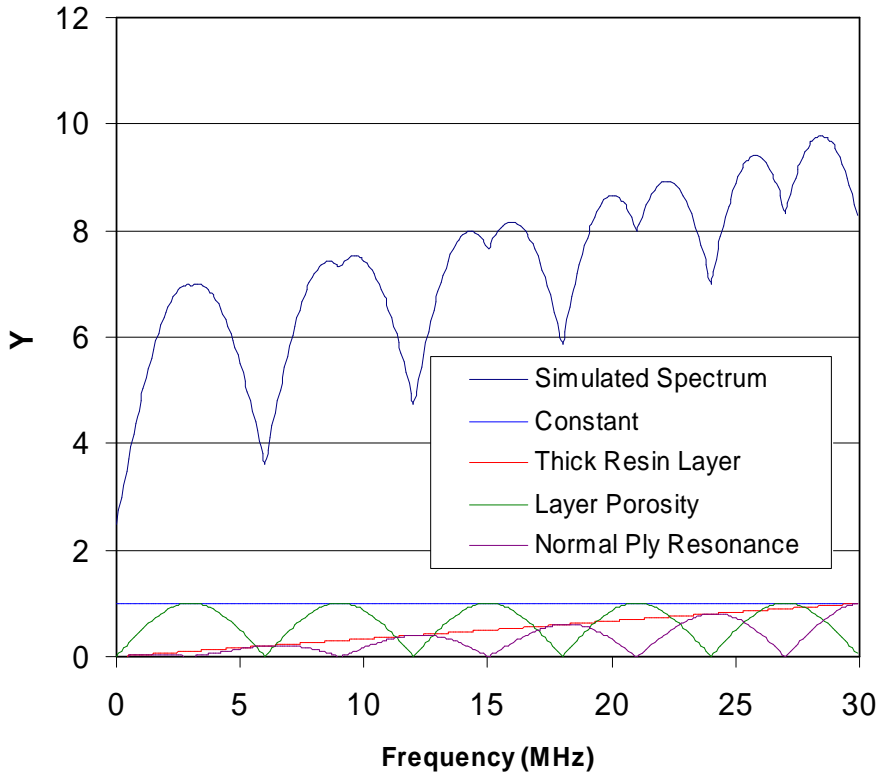


Figure 5-22. Figure showing the four simple basis functions and the simulated spectrum that was then decomposed into the four basis functions.

Basis functions:	N	$C(\omega, t_{\text{thick}})$	$P(\omega)$	$S(\omega)R(\omega, t_{\text{norm}})$
Input coefficients:	2.50	1.70	4.30	3.90
SVD output coefficients:	2.50	1.70	4.30	3.90

Table 5-2. Comparison of input coefficients (bold) used to create the simulated spectrum, and the output coefficients determined by SVD.

With increasing amplitude of random spectral fluctuations (Figure 5-23) the SVD method becomes less accurate, as shown in Table 5-3, where the spectral fluctuations are in the same arbitrary units as all the other coefficients of basis functions. The single-attempt data is shown as a function of peak-to-peak random spectral fluctuation level in Figure 5-24, together with the standard deviations as error bars.

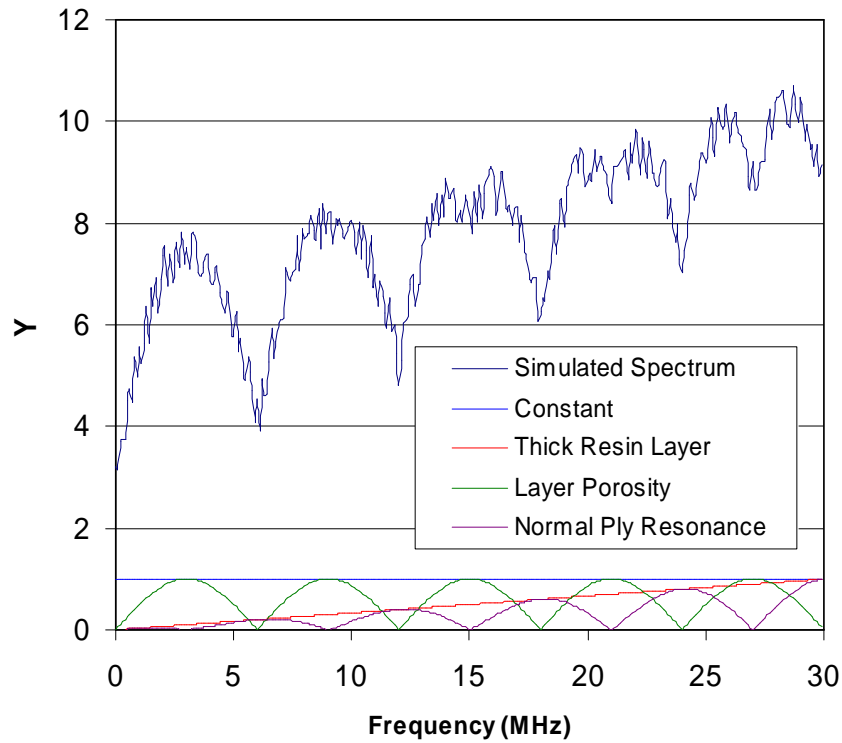


Figure 5-23. Figure showing the same decomposition as Figure 5-22 but for a random spectral random fluctuation level with a peak-to-peak amplitude of 1.0.

Basis functions:	p-p Random Spectral Fluctuations	N	$C(\omega, t_{\text{thick}})$	$P(\omega)$	$S(\omega)R(\omega, t_{\text{norm}})$
Input coefficients:		2.50	1.70	4.30	3.90
SVD output coefficients:	0	2.5	1.7	4.3	3.9
	0.5	2.83	1.71	4.20	3.81
	1	2.98	1.8	4.29	3.84
	1.5	3.24	1.72	4.26	4.02
	2	3.45	1.87	4.35	3.75
	2.5	4	1.37	4.22	3.91
	3	4.32	2	3.8	3.41
	3.5	3.94	1.53	4.54	4.25

Table 5-3. Comparison of input coefficients (bold) used to create the simulated spectrum, and the output coefficients for each basis function determined by a single attempt at SVD, as a function of the level of random spectral fluctuations.

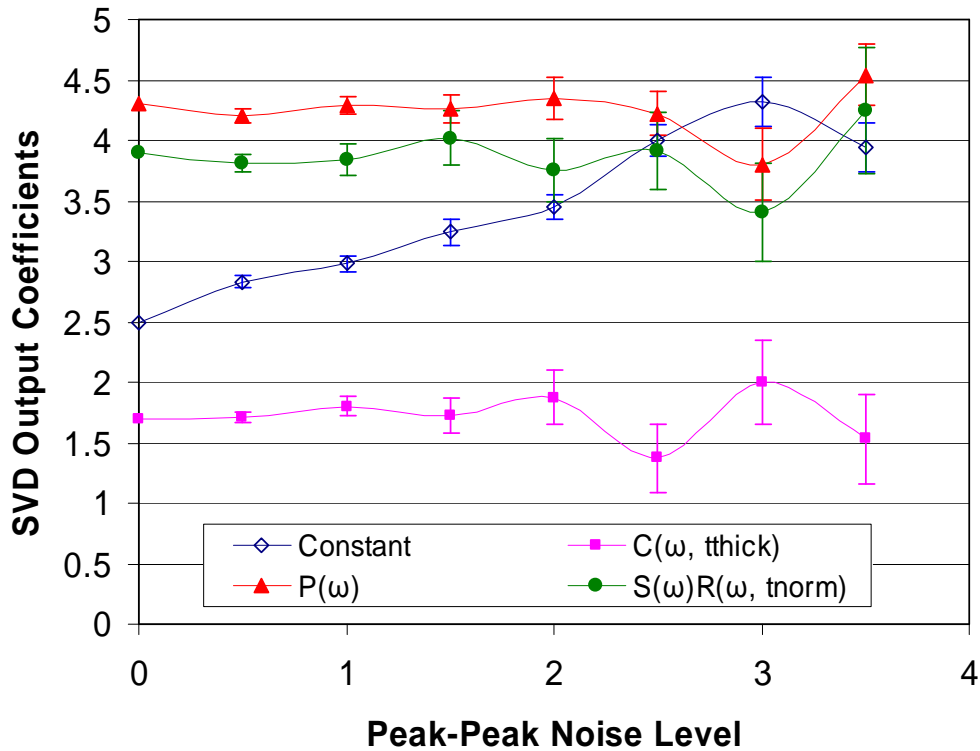


Figure 5-24. Single SVD attempts with different random spectral fluctuation levels, showing Standard Deviation error bars that increase with random fluctuation level, as expected. The curve labelled 'Constant' is the white noise basis function coefficient N .

In order to determine whether the trend with random spectral fluctuation level is systematic, SVD was repeated 18 times for each different level of random spectral fluctuations, using different input spectra, and the mean and 'standard error on the mean' (SEOM) values are plotted in Figure 5-25.

Figure 5-25 shows that there is no increase in systematic errors (accuracy) as the random spectral fluctuation level increases, purely an increase in random errors (precision), for all basis functions except the 'white noise' basis function, N . The coefficient for the latter basis function understandably increases with increasing peak-to-peak random spectral fluctuation as it has a positive mean level and has been added to the spectrum. These results were very encouraging and were followed by a more rigorous evaluation of the model-based decomposition approach.

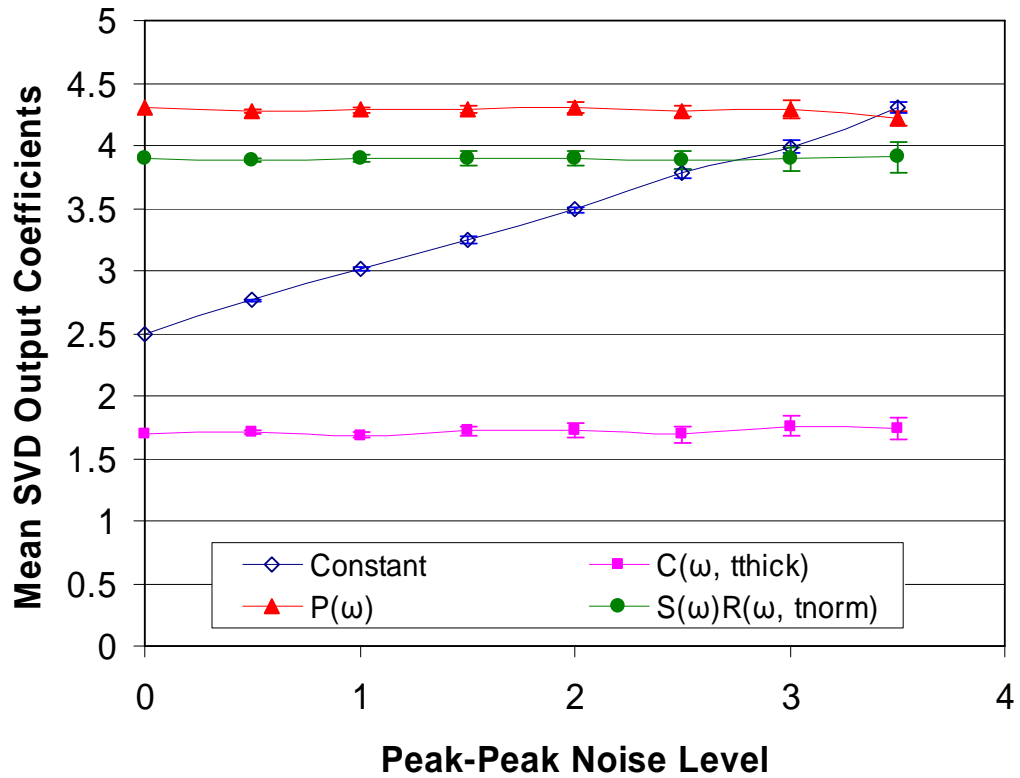


Figure 5-25. Mean of 18 SVD attempts, with Standard Error on the Mean error bars. The curve labelled 'Constant' is the white-noise coefficient N .

5.5.4 ANDSCAN Implementation of SVD working on modelled spectra

The SVD method was then coded into the ANDSCAN software and evaluated using four basis functions, broadly matching the ones used above. An adaptation was implemented whereby if the porosity coefficient is negative, the porosity basis function is removed and the SVD is repeated with just three basis functions. Then, if the thick resin layer coefficient is negative, SVD is repeated with just two basis functions (white noise and ply resonance).

The ply resonance and porosity basis functions needed to use the ply spacing and the composite velocity to determine the resonant frequency, and the full implementation uses the ANDSCAN version of the analytical model to generate the basis functions (see Chapter 4).

Initially, no transducer response, T , was applied to either the modelled spectra or the basis functions so effectively the impulse and frequency responses were

being considered. Figure 5-26 to Figure 5-28 show that the fit is good and this was confirmed by the ANDSCAN display of the coefficients where porosity gave a positive coefficient for porosity that seemed approximately linear with percentage porosity, and the thick resin layer coefficient was zero for a porous region (Table 5-4). Similarly the thick resin layer coefficient seemed approximately linear with resin layer thickness and the porosity coefficient was zero for a thick resin layer. This is exactly the desired response.

	N	$C(\omega, t_{\text{thick}})$	$P(\omega)$	$S(\omega)R(\omega, t_{\text{norm}})$
Good material	7.44	0	0	4.27
20 μm Resin Layer – ply 4	68.95	5.7	0	6.82
10% (1 μm) porosity – ply 8	12.22	-4.41	228.26	3.69

Table 5-4. Initial coefficient values from simulated good structure, a thick resin layer, and a porous ply.

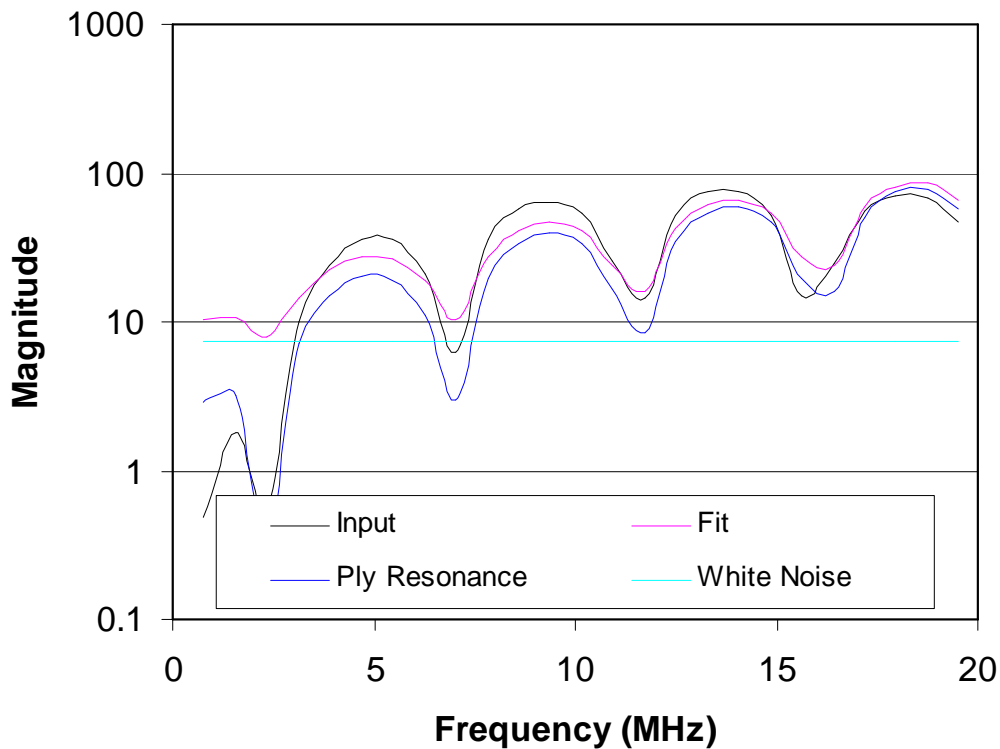


Figure 5-26. [Impulse] frequency response modelled spectra (Input – black) and the fitted spectra (Fit – pink) for good 0.33 μm ply structure using a 2.2-ply gate width.

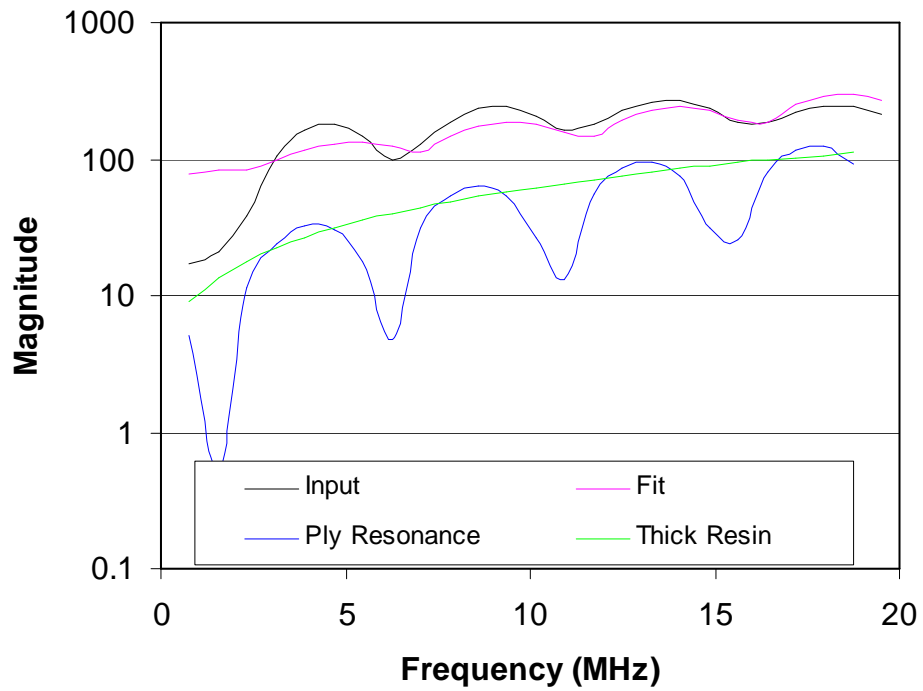


Figure 5-27. Impulse-response modelled spectra (Input – black) and the fitted spectra (Fit – pink) for a $0.33\ \mu\text{m}$ ply structure with a $20\ \mu\text{m}$ thick resin layer using a 2.2-ply gate width. Note that the vertical scale is logarithmic so the thick resin layer basis function (Gradient – green) is curved.

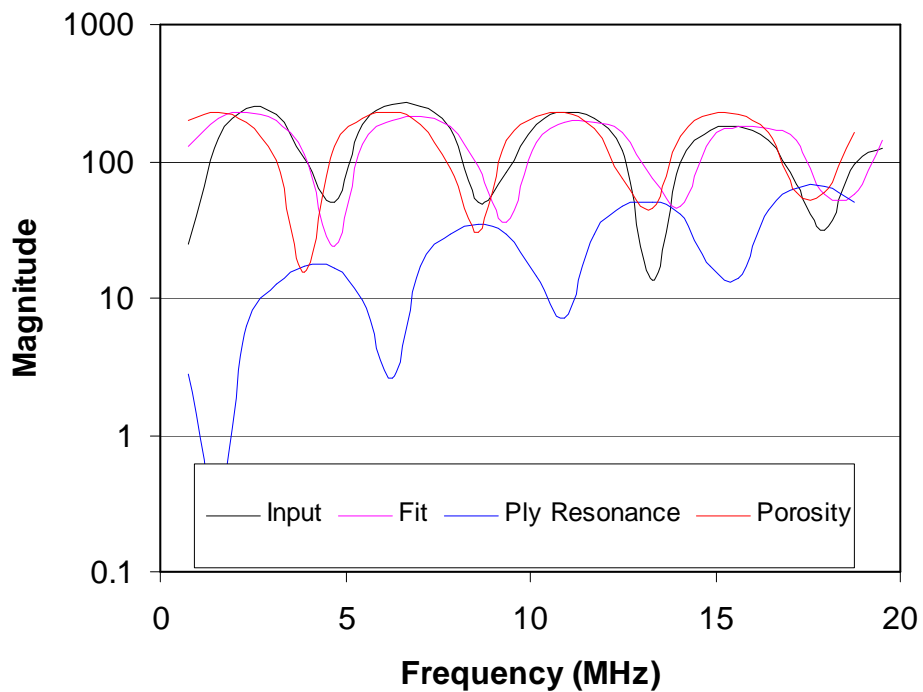


Figure 5-28. Impulse-response modelled spectra (Input – black) and the fitted spectra (Fit – pink) for a $0.33\ \mu\text{m}$ single-ply structure with 10% of $1\ \mu\text{m}$ porosity using a 2.2-ply gate width.

5.5.5 Inclusion of the transducer response

Initially, a test was made to see if it is necessary to use the transducer response in the decomposition at all. The test used the simulated impulse response from a thick resin layer, multiplied by the transducer response of a 10 MHz transducer with a Q-factor of 0.8. The transducer response was deliberately not applied to the basis functions. The result is shown in Figure 5-29 where the fit is very poor.

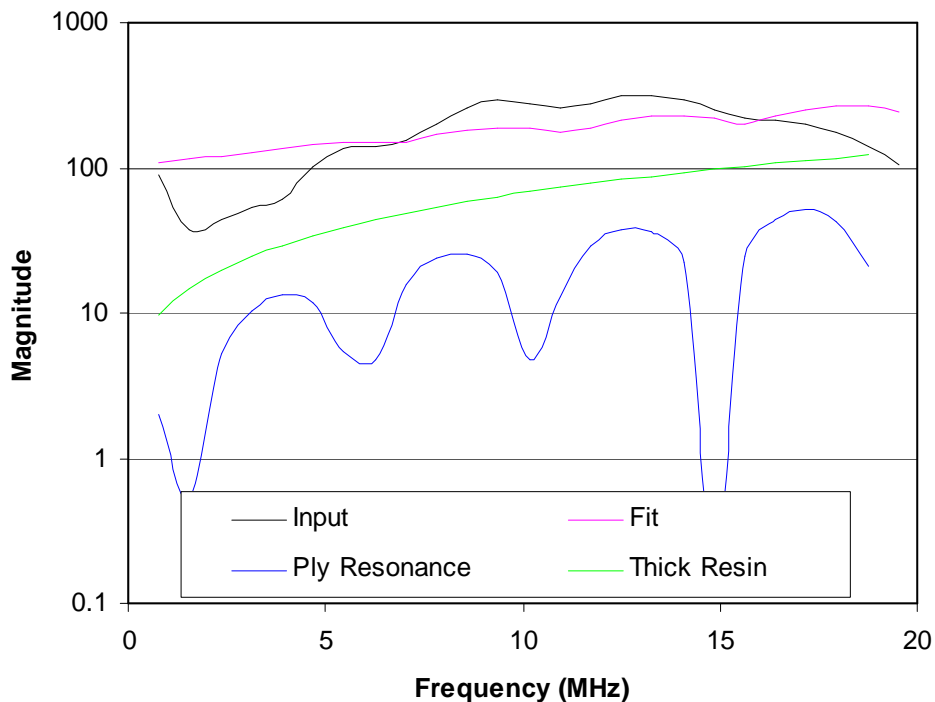


Figure 5-29. Transducer response applied to modelled impulse response spectrum of 20 μm thick resin layer but not to the basis functions.

The next stage was to decide whether to apply the transducer response to the basis functions or to divide the ultrasonic spectrum by it. The latter is a deconvolution and is notoriously problematic, especially in cases like this where the low-level noise at both high and low frequencies would be artificially emphasised. An initial check that this is the case was sufficient confirmation and it was decided to multiply each basis function by the transducer response squared (to allow for both transmit and receive responses in pulse-echo mode). After further consideration and some experimentation, it was decided not to apply the transducer response to the white noise basis function, N .

Examples of the resultant fits obtained for thick resin layers and porosity are shown in Figure 5-30 and Figure 5-31 respectively and are highly satisfactory.

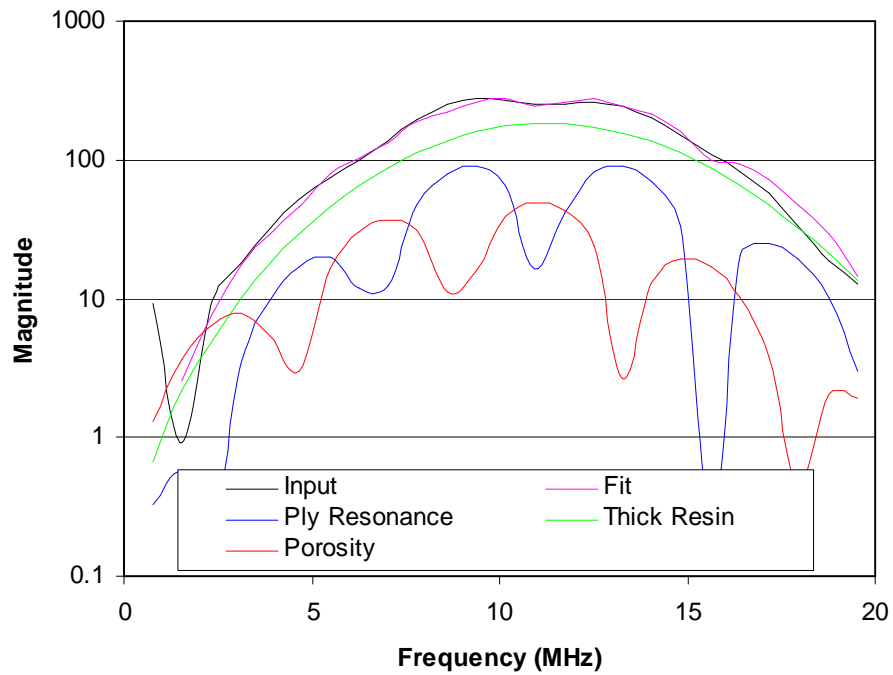


Figure 5-30. Transducer response convolved with modelled impulse response data of 20 μm thick resin layer and with three basis functions (all except the constant).

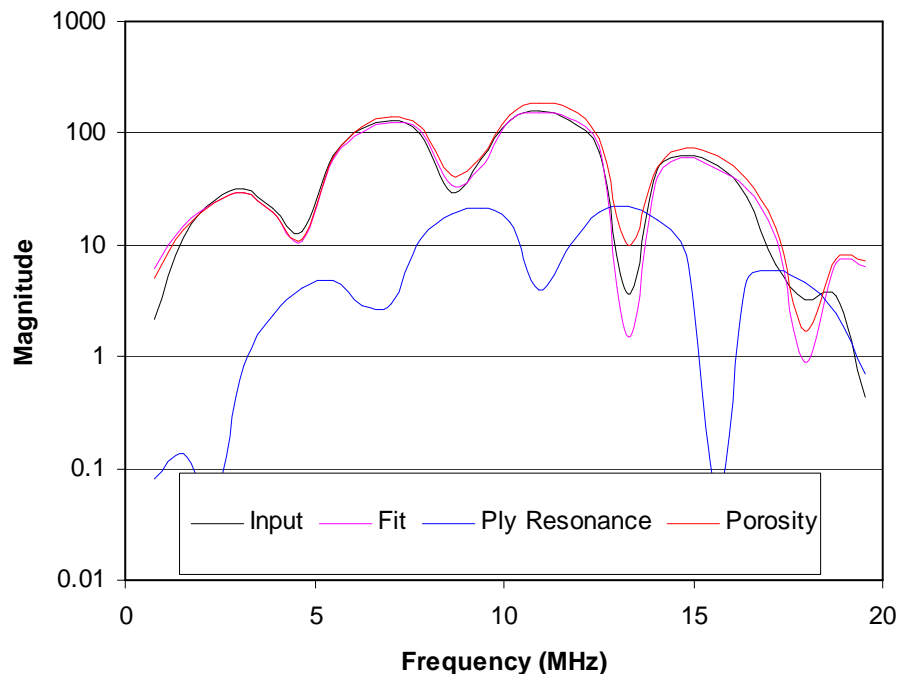


Figure 5-31. Transducer response convolved with modelled impulse response data of 10% (1 μm) porosity in ply 8 and with three basis functions (all except the constant).

A standard evaluation of the performance and cross-talk of the decomposition method was carried out using simulated, modelled waveforms (see Chapter 4) of a 32-ply stack of 0.125 mm plies, a 10 MHz, Q=0.8 transducer and a 2.2-ply gate width. The simple volumetric mixture rule was being used in the model at this time. The values of the porosity and thick-resin layer coefficients were plotted when centred on the depth of the defect and then various amounts of either porosity or thick resin layer were simulated, with results in Figure 5-32. At this stage the porosity and thick resin layer coefficients appeared to respond quite linearly, and with little cross-talk, but further work was required, and is reported in subsequent sections, to understand why the porosity coefficient was multiple-valued above 70% porosity and zero below 10% porosity in a ply.

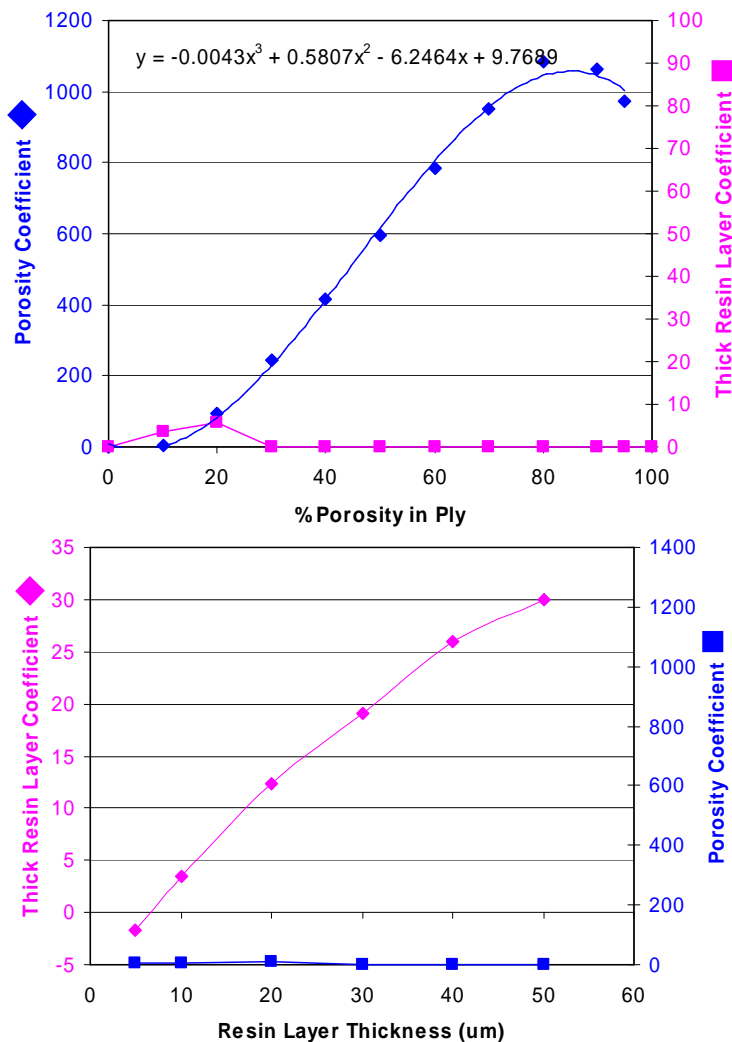


Figure 5-32. Evaluation of the decomposition method using modelled responses of structure with a single porous ply (top) or a single thick resin layer (bottom). The equation is a cubic polynomial fit to the porosity coefficient.

5.5.6 Effect of shadowing by nearer-surface flaws

Then the thick resin layer was moved to the 13th ply in a 15-ply stack, with a 10% porosity layer at ply 8. At this depth, the visco-elastic attenuation of the resin, reflections at ply interfaces, and any scattering from porosity at ply 8 will have effectively applied a frequency-dependent filter, which is likely to decrease the thick resin layer coefficient. This was tested at 10 MHz by changing the size of the pores in the simulation of the 10% porosity layer at ply 8, above a thick resin layer at the 13th ply, with results shown in Table 5-5, and at 5 MHz with results in Table 5-6:

Pore radius	N	$C(\omega, t_{\text{thick}})$	$P(\omega)$	$S(\omega)R(\omega, t_{\text{norm}})$
1 μm pores	-2.49	6.67	86.3	10.9
10 μm pores	-4.17	3.85	104.61	12.47
20 μm pores	-7.91	-6.27	168.18	16.74

Table 5-5. 10 MHz transducer results for a 20 μm thick resin layer at ply 13 beyond a 10% porosity layer at ply 8 which attenuates the signal with frequency-dependent attenuation.

Pore radius	N	$C(\omega, t_{\text{thick}})$	$P(\omega)$	$S(\omega)R(\omega, t_{\text{norm}})$
1 μm pores	2.97	5.7	52.2	16.11
10 μm pores	2.97	5.7	52.2	16.11
20 μm pores	1.85	4.53	56.85	16.9

Table 5-6. 5 MHz transducer results for a 20 μm thick resin layer at ply 13 beyond a 10% porosity layer at ply 8 which attenuates the signal with frequency-dependent attenuation.

The conclusion from these results is that frequency-dependent effects occurring above a defect can influence the measurement of that defect and they may need to be corrected for. At 5 MHz, the scattering of the longer wavelength from the porosity is much less significant and so the additional frequency-dependent attenuation is reduced compared with that at 10 MHz.

5.5.7 Modification to include a new 'delamination' basis function

It became evident that a further basis function, R_0 , may be required – the response of a single interface with a frequency-independent reflection coefficient, such as the BWE, FWE, a delamination, or high-percentage layer porosity. This would modify Equation 5-35 to give the following equation:

$$F(\omega) = a_0N + A_0T^2(\omega)D(\omega, d)[a_1S(\omega)R(\omega, t_{norm}) + a_2C(\omega, t_{thick}) + a_3P(\omega) + a_4R_0] \quad (5-36)$$

It can be seen from Figure 5-33 that including this delamination basis function has the desired effect of picking out high levels of porosity as delaminations rather than porosity, but there is undesirable interaction with the thick resin layer basis function, which is quite similar to the delamination basis function.

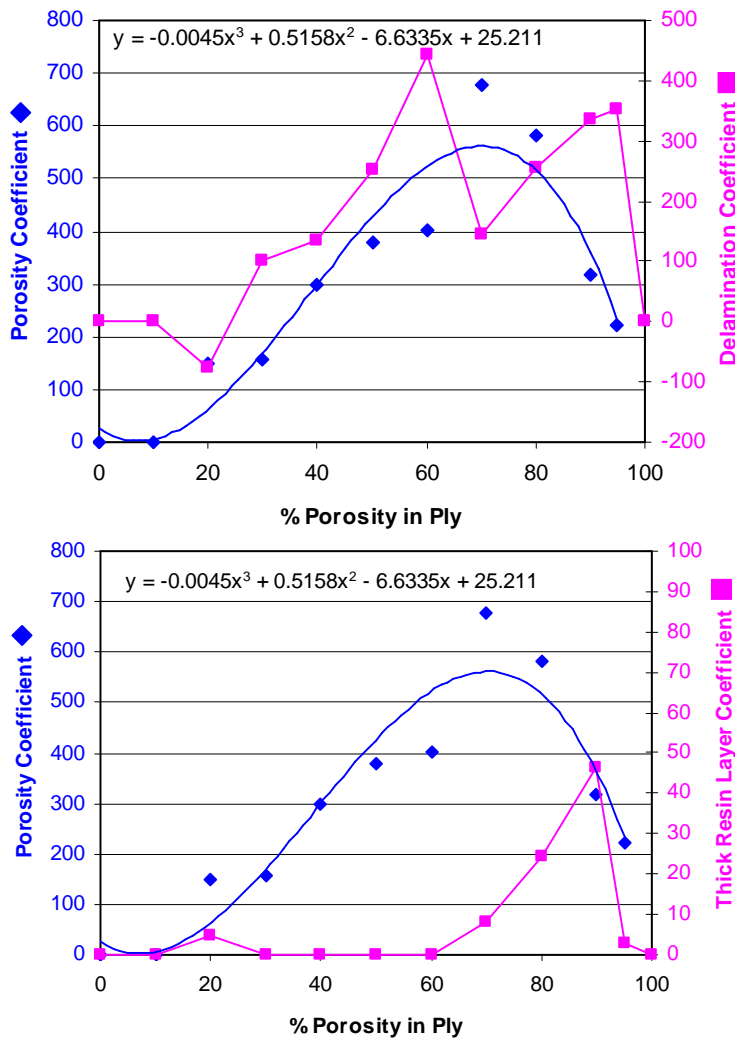


Figure 5-33. The effect of including a new basis function to represent a delamination, or FWE or BWE reflections. The equations are cubic polynomial fits to the porosity coefficient.

It was concluded that the decomposition had been more successful *without* the delamination basis function so it was removed from the processing.

5.5.8 Removal of ply resonance basis function if negative

Up to this stage the ply resonance basis function had been allowed to have a negative coefficient - often the case for a porous layer. However, this does not have a physical basis, so it was decided to limit it to being positive by removing the basis function if the coefficient goes negative, and reprocessing. The software was then modified accordingly and results are shown in Figure 5-34.

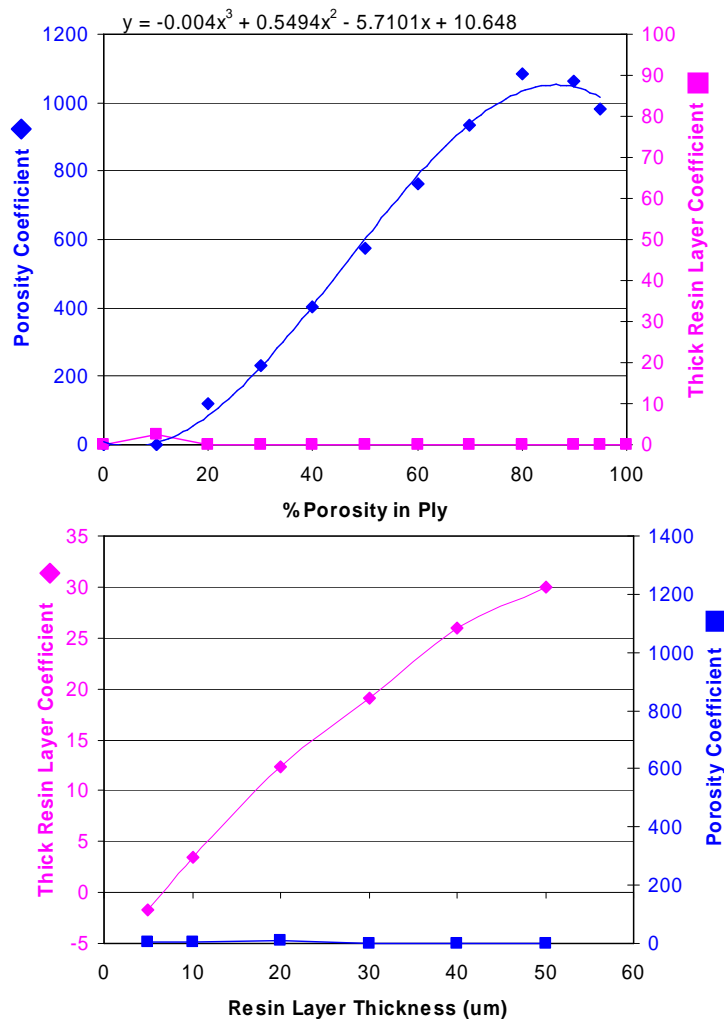


Figure 5-34. Removal of ply resonance basis function if the coefficient is negative. The equation is a cubic polynomial fit to the porosity coefficient.

It can be seen that the level of cross-talk is very low and the response of each coefficient is relatively linear. However, the minimum detectable level of porosity is still 10%. Given that current allowable through-thickness average porosity

levels are around 2%, the minimum measurable porosity level in a given ply should be less than 2% in case all plies contain 2% porosity. Thus the 10% threshold is higher than desired. The reason is that the resonant frequency of the layer does not increase to that of the porosity basis function until this porosity level is reached (see Chapter 4, Figure 4-39 and Figure 4-40). Chapter 4 suggests that the choice of mixture rule also affects the calculated resonant frequency. The next stage was to adapt the porosity basis function to optimise the fit from the decomposition and then to test it with different mixture rules.

5.5.9 Adaptive modification of porosity basis function

Adaptively modifying the porosity basis function and optimising the fit from the SVD improves the sensitivity to low levels of porosity - see Figure 5-35.

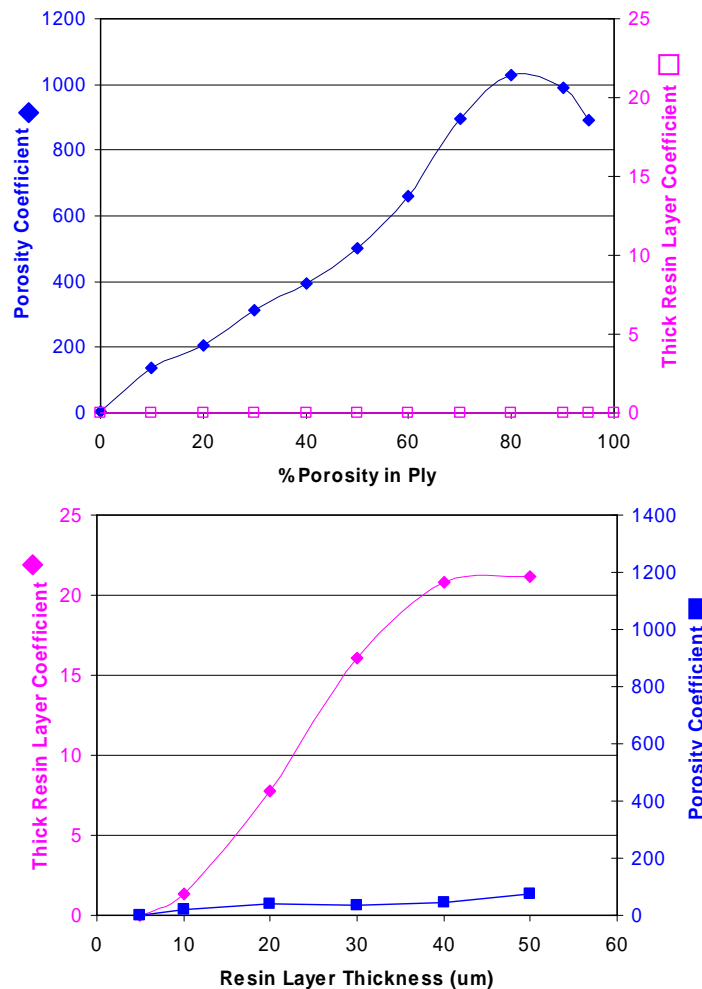


Figure 5-35. The result of using an adaptive resonant frequency shift for the porosity basis function - improved measurement of low values of porosity simulated using the simple volumetric mixture rule.

The adaptive method involves reducing the resonant frequency in the porosity basis function if the porosity coefficient is low, then re-processing the SVD to see if the porosity coefficient increases. If it does, a further reduction in the resonant frequency is applied until the SVD porosity coefficient is maximised.

5.5.10 Effect of single versus multiple porous plies

At this initial stage the method was assessed in terms of how it responds to single or multiple porous plies. Examples of the two coefficients (porosity and thick-resin layer) superimposed on a time-frequency image of simulated single-ply porosity and a single thick resin layer are shown in Figure 5-36.

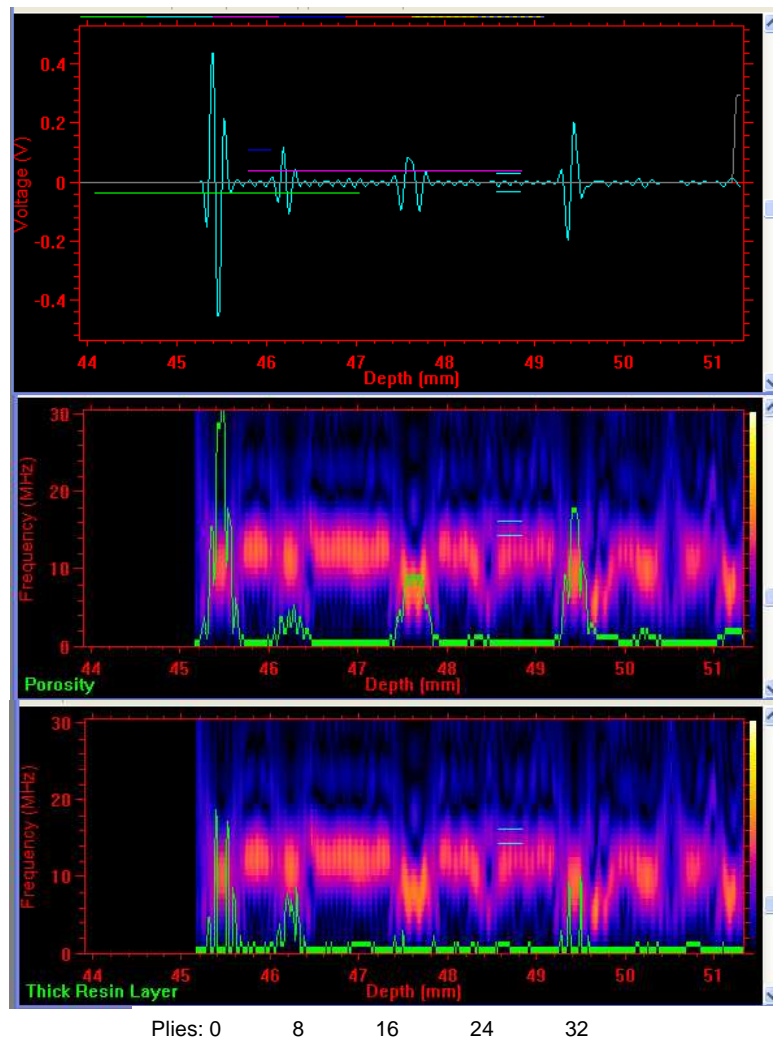


Figure 5-36. Example of the response of the porosity coefficient (green in middle image) and thick-resin layer coefficient (green in bottom image) to a simulated 32-ply stack of 0.125 mm plies with 30 μm thick resin layer at ply 7 (45.2 mm) and 30% porous layer at ply 18 (47.6 mm). Porosity was simulated using the Hashin mixture rules.

However, it was found that intermediate layers in a multi-layer stack of porosity give no response in the porosity coefficient. This is shown for 5 plies of 30% porosity in Figure 5-37 and is thought to be because the basis function has been generated to apply to a single porous ply surrounded by non-porous plies.

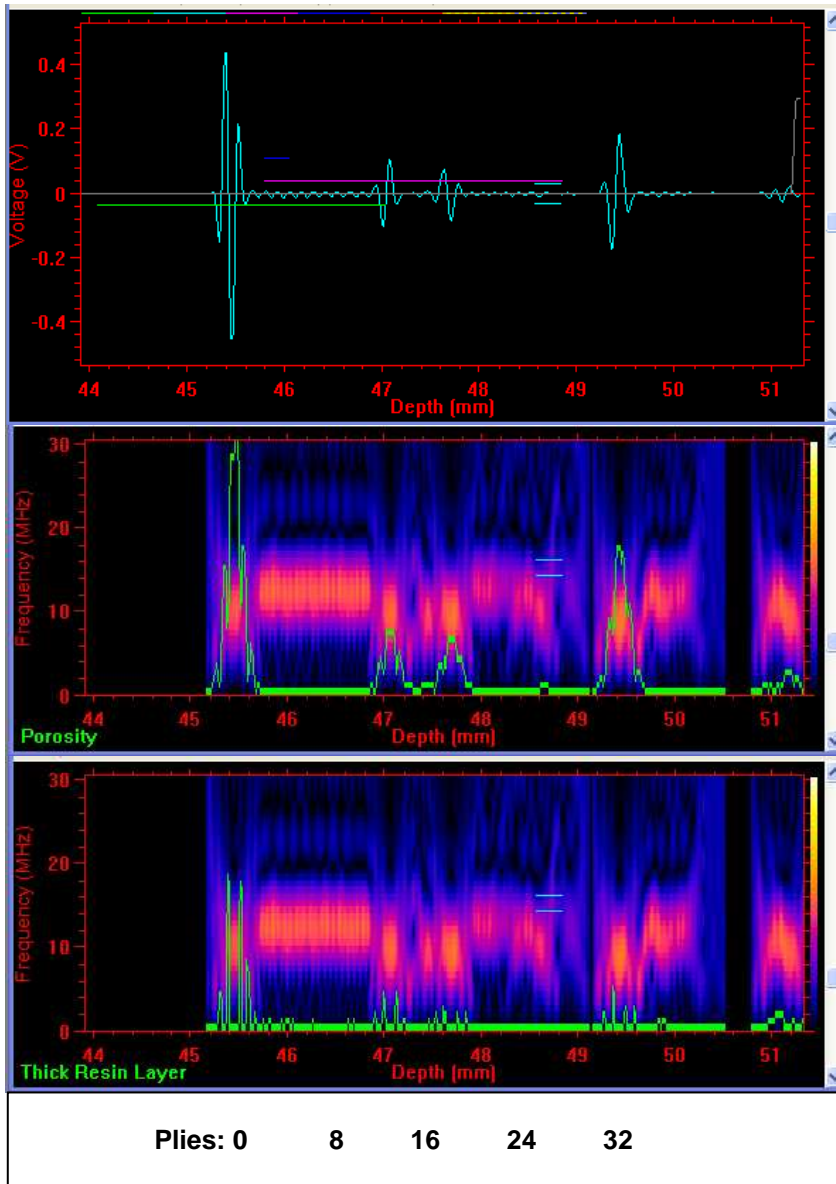


Figure 5-37. Example of the response of the porosity coefficient (green in middle image) and thick-resin layer coefficient (green in bottom image) to a simulated 32-ply stack of 0.125 mm plies with 30% porous plies from ply 14 (47.1 mm depth) to ply 18 (47.6 mm depth) inclusive. Porosity was simulated using the Hashin mixture rules.

5.5.11 Effect of ply spacing

Another problem was shown when variations in ply spacing are induced in the porous ply or the ply next to the thick resin layer. A thick ply can potentially move resonances into the location of peaks expected for porosity. This was investigated and the results are shown in Figure 5-38.

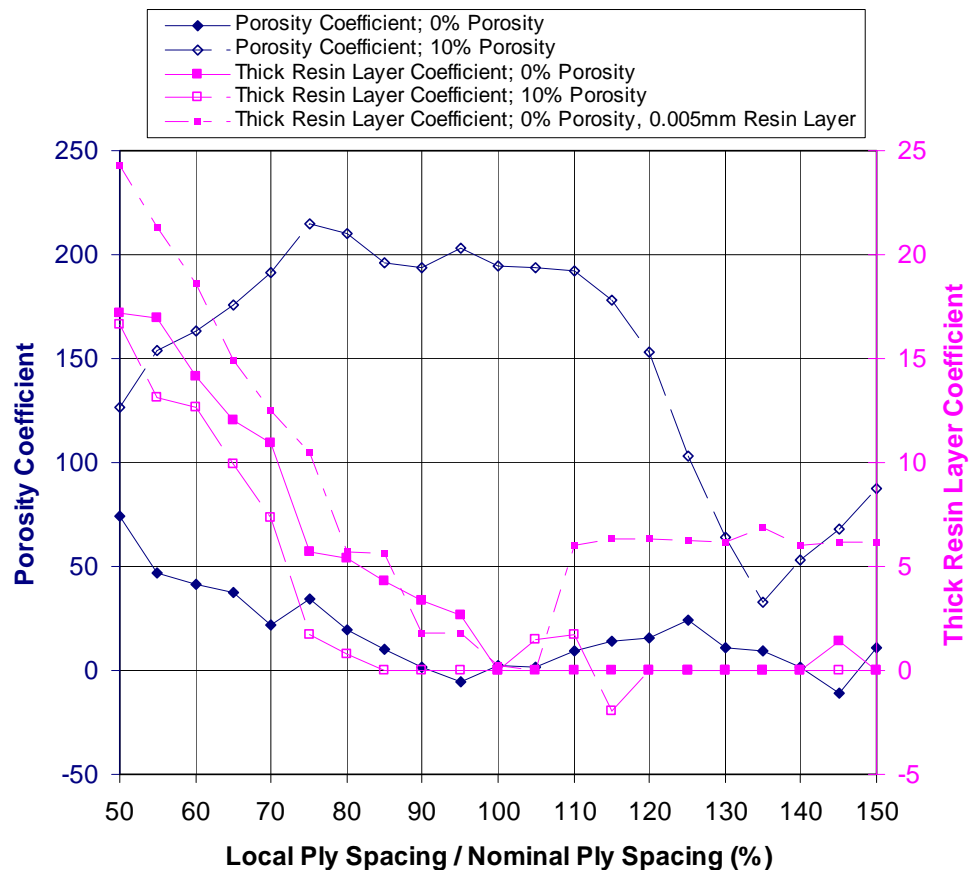


Figure 5-38. The response of the decomposition method porosity and thick resin layer coefficients to changes in local ply spacing, for both 0% and 10% porosity, and for a thick (5 μm) resin layer. The defects were put at the 20th ply in a 32-ply stack of 125 μm plies, with a 10 MHz transducer function and Q-factor of 1.0.

The conclusion of this investigation was that an increase in ply spacing above about 10% can cause an underestimate in porosity coefficient, and a reduction in ply spacing can cause an overestimate in thick resin layer coefficient. Future work will investigate whether it would be preferable to determine the ply spacing before computing the basis functions to be used in the decomposition.

5.5.12 Calibration of the decomposition method

In order to calibrate the decomposition method's coefficients it is first necessary to determine which factors will influence the calibration of coefficients a_2 (porosity) and a_3 (thick resin layer) from Equation 5-35. Assuming that these two coefficients are actually linear functions of the material property on which they have been modelled, as demonstrated by the above modelling, then:

$$a_2 = f_2(t_{thick}) \quad \text{which approximates to:} \quad a_2 = b_2 t_{thick} + const$$

$$a_3 = f_3(V_v) \quad \text{which approximates to:} \quad a_3 = b_3 V_v \text{ for } V_v < 0.8$$

and:

$$F(\omega) = a_0 N + A_0 T^2(\omega) D(\omega, d) [a_1 S(\omega) R(\omega, t_{norm}) + f_2(t_{thick}) C(\omega, t_{thick}) + f_3(V_v) P(\omega)] \quad (5-37)$$

Inversion of the above gives:

$$t_{thick} = g_2(a_2) \quad \text{where } g_2(a_2) = a_2 / b_2 + c_2 t_{nom} \quad [c_2 \text{ may equal unity}]$$

$$V_v = g_3(a_3) \quad \text{where } g_3(a_3) = a_3 / b_3$$

The significance of these functions is that calibration coefficients b_2 , b_3 and c_2 are sufficient to calibrate the porosity and resin layer thickness decomposition coefficients.

5.5.12.1 Correction for depth

The incident spectrum at each depth will change as the ultrasound propagates deeper in the structure. In order to correct for this the incident spectrum can be corrected using the model to determine the double-pass transmission frequency response of the structure above the depth of interest. This will be a frequency-dependent and depth-dependent correction $D(\omega, d)$ from Equation 5-35 where d is the depth in the structure, or the number of plies passed. $D(\omega, d)$ will need to be calculated for each depth or ply, and $A_0 T^2(\omega) D(\omega, d)$ is the incident spectrum at each depth or ply d . If the analytical model is used to generate $D(\omega, d)$, Figure 5-39 and Figure 5-40 show this function (effectively the transmission coefficient) for 0% to 30% randomness in ply separation. The

trend is an increased attenuation of higher frequencies with a particularly high loss at the resonant frequency of the plies, which forms a narrow band-gap in the transmission spectrum. However, as the randomness of ply spacings increases the band gap becomes broader and less distinct, as expected.

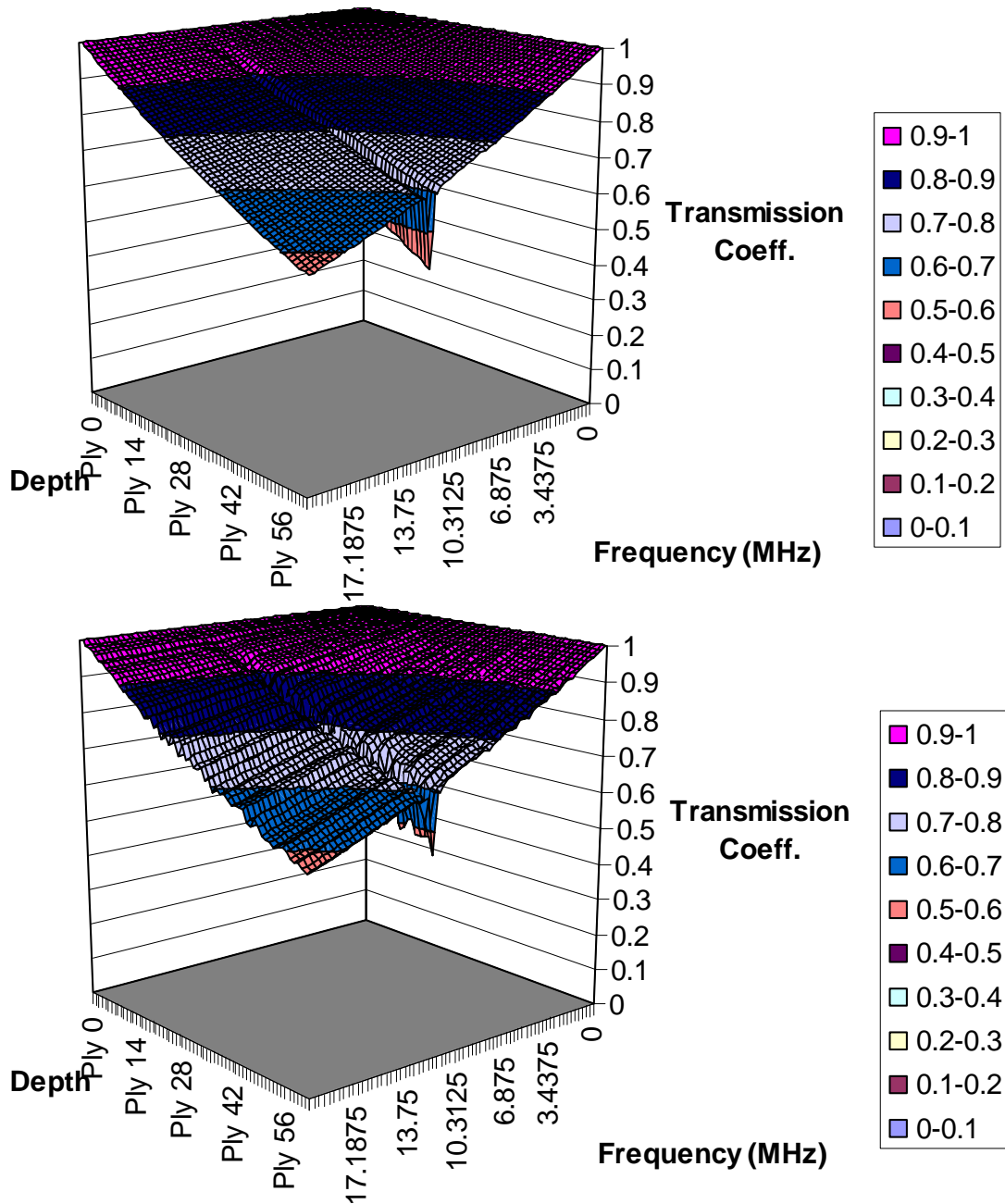


Figure 5-39. Depth-dependent incident spectrum for 0% (top) and 10% (bottom) randomness.

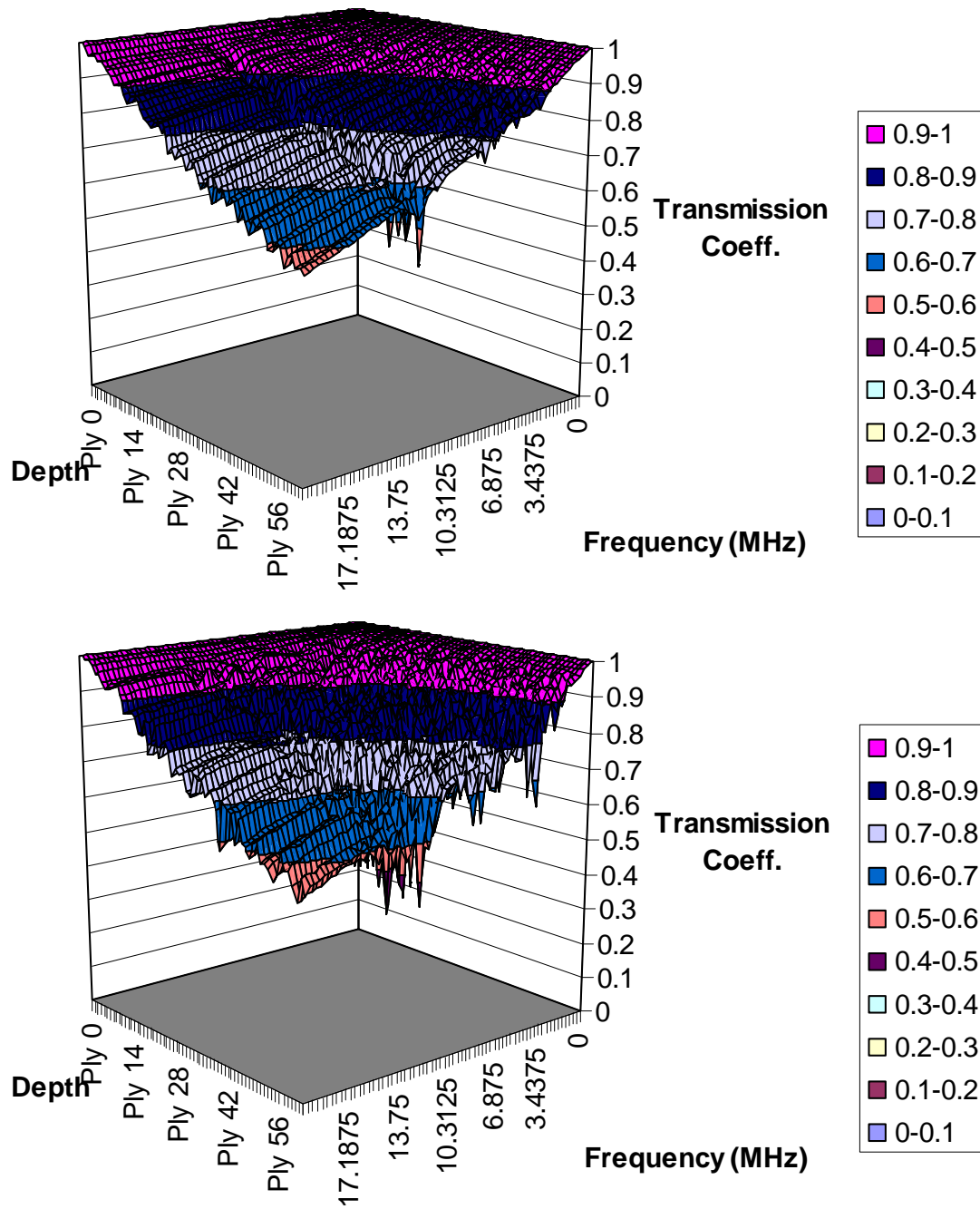


Figure 5-40. Depth-dependent incident spectrum for 20% (top) and 30% (bottom) randomness.

Then, using simulated waveforms from a layer of 30% porosity in ply 29 of a 32 ply stack, the results in Figure 5-41 were obtained, showing that the fit improves if the depth is corrected for.

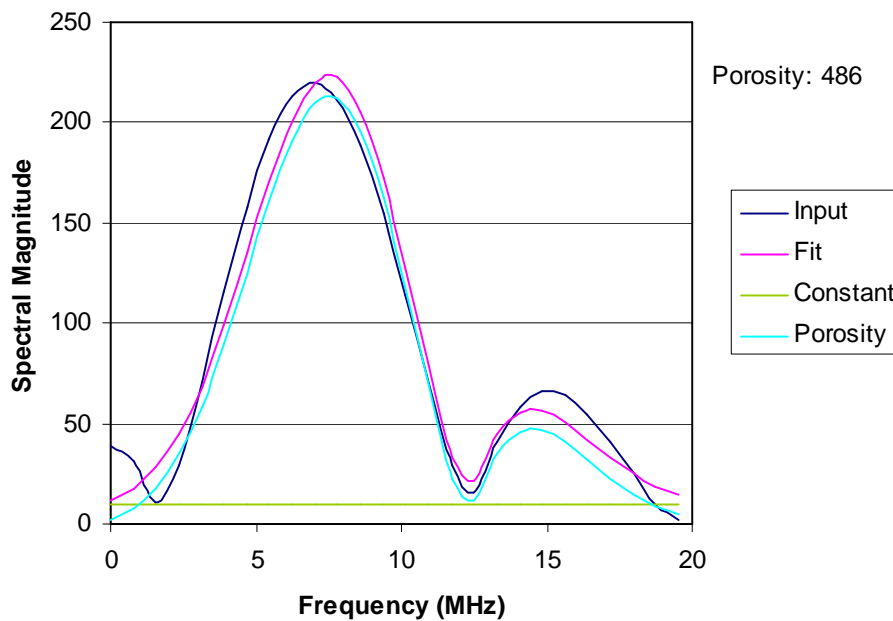
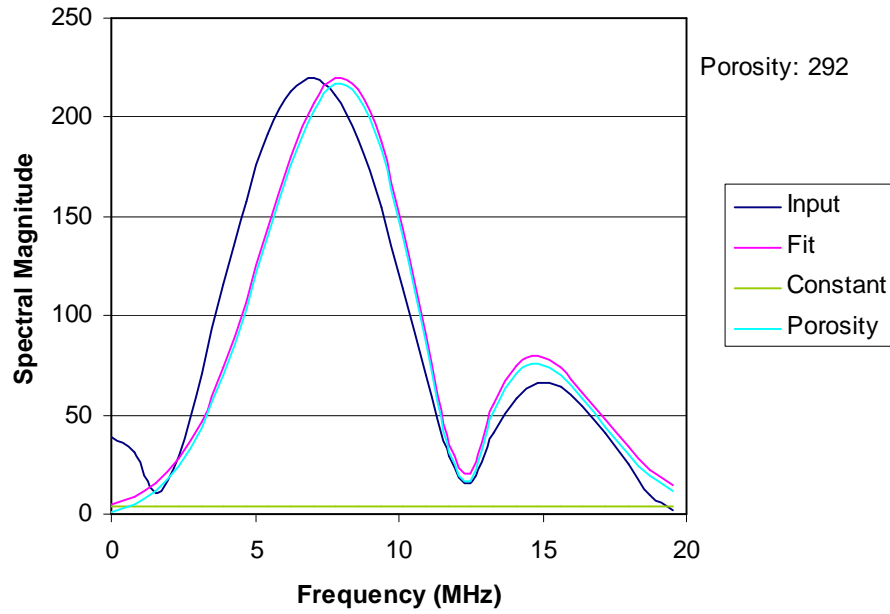


Figure 5-41. 30% porosity ($10\ \mu\text{m}$ radius pores) in ply 29 of a 32 ply 0.125 mm ply spacing stack. Standard basis functions (top) and corrected by $D(\omega, d)$ (bottom) using 10% randomness in the preceding 28 plies. The porosity value quoted is the value of the porosity coefficient determined by decomposition.

Using modelled waveforms, several depths were then tested for both 10% porosity and 30% porosity with the depth correction implemented, and also for 30% porosity with no depth correction. The results, shown in Figure 5-42,

illustrate that the depth dependence of the porosity coefficient has been very effectively removed using this model-based correction of the basis functions.

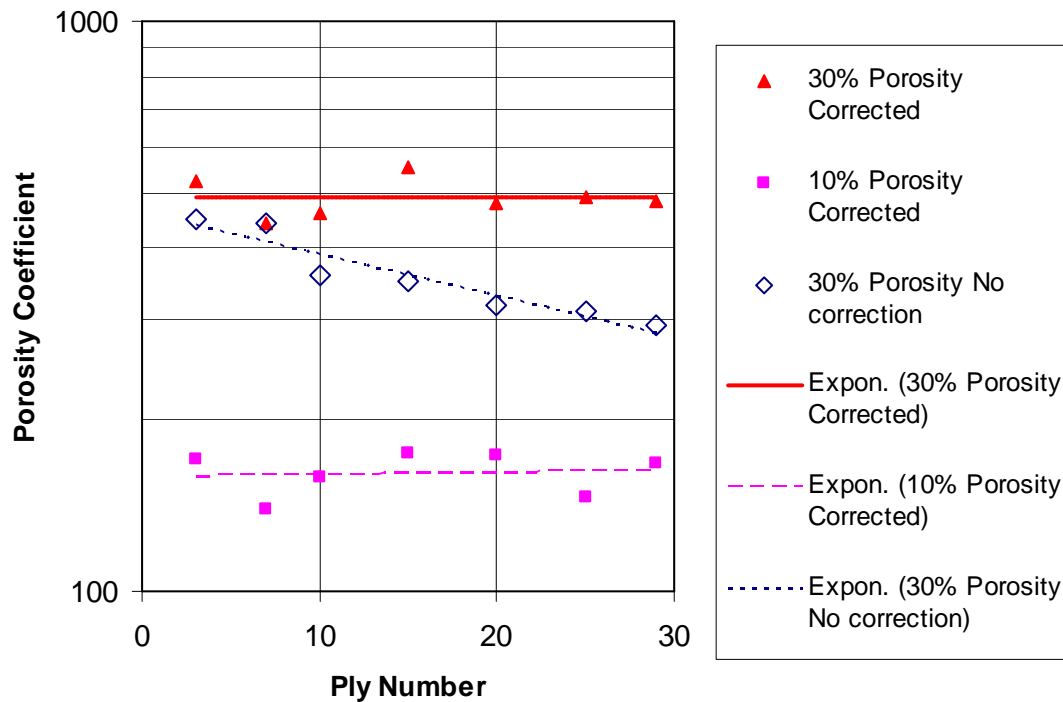


Figure 5-42. Graph showing how the depth correction (with 10% randomness in ply spacing to generate the correction factors) removes the depth dependence of the porosity coefficient.

Finally, the linearity and cross-talk were investigated for the new depth-corrected method as before, using simulated waveforms for porosity and thick resin layers at ply 29 in a 32-ply stack. Graphs of the relationships between the coefficients and their associated material properties are shown in Figure 5-43 for ply 29. These graphs show an improvement in both cross-talk and linearity for both coefficients.

5.5.12.2 Use of Front-Wall Echo

$A_0 T^2(\omega)$ must be determined in some way in order to calibrate the coefficients.

An option is that both A_0 and $T^2(\omega)$ may be obtained from the front-wall echo, thus saving the need to use a modelled spectrum for $T(\omega)$. This removes dependence on the system setup, transducer response and gain of the pulser-

receiver, digitiser etc, as well as determining a value for A_0 . However, obtaining a good front-wall echo signal is not necessarily straightforward, especially if it has saturated the acquisition system in order to obtain good signal strength from internal reflectors and scatterers.

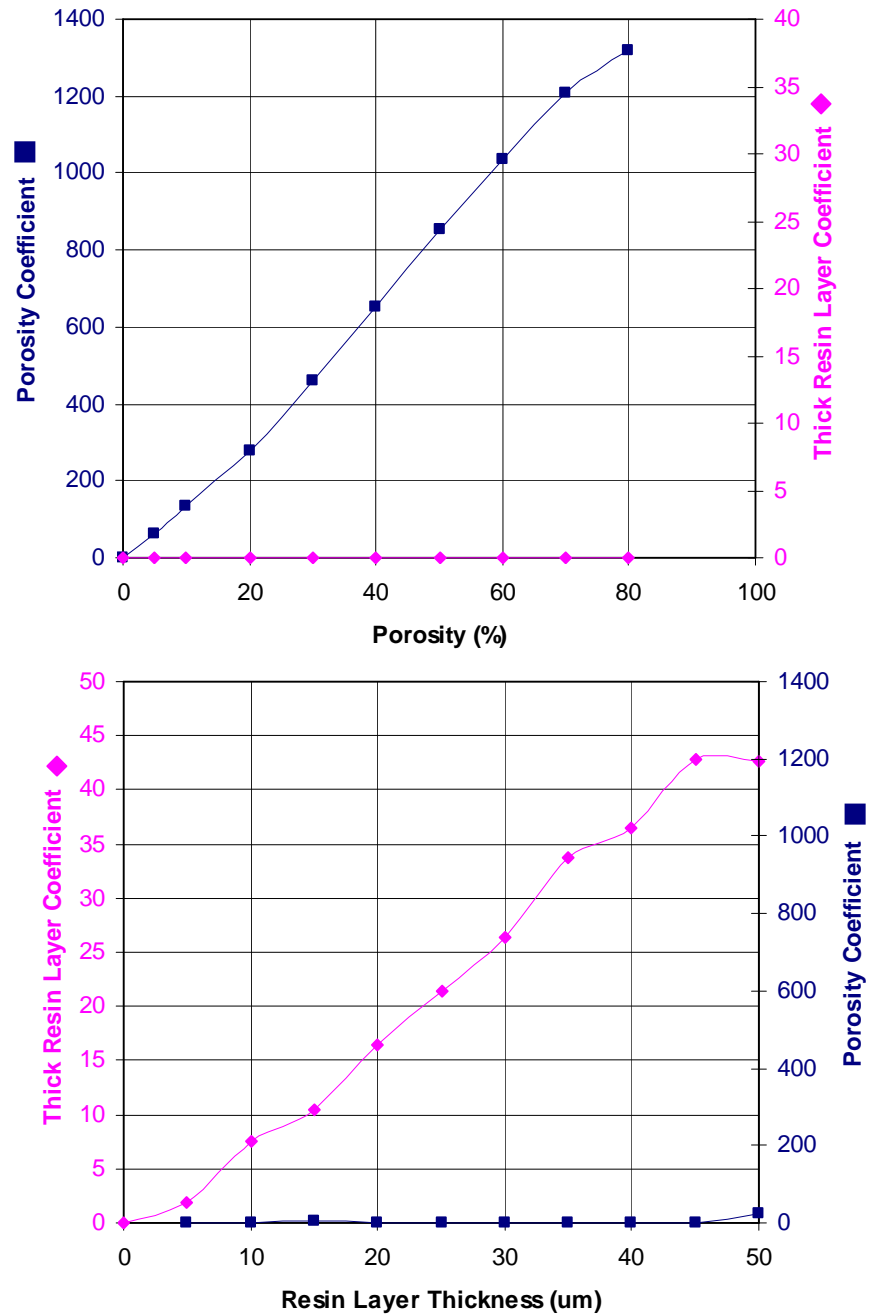


Figure 5-43. Ply 29 porosity (top) and thick resin layer (bottom) using 10% randomness to generate the depth dependent incident spectrum correction $D(\omega, d)$. The simple volumetric mixture rule was used.

5.5.12.3 *Other dependencies of calibration coefficients*

It was found that the porosity calibration, which is dependent on the absolute amplitude in the spectrum, varies with both:

- the number of points in the gate
- the type and extent of the taper windowing used

but not with:

- the number of zero padding points

Two corrections were made to allow for this.

- the time-domain values were divided by approximately the amount that the window had reduced them:

$$\frac{1}{b-a+1} \int_a^b W(\omega) d\omega$$

where W is the windowing function and the gated region is from points a to b inclusive. This affects only the absolute values obtained in the subsequent spectral analysis, not the shape of the spectrum itself.

- the porosity coefficient and thick resin layer coefficient were both divided by the number of points in the gate.

5.5.12.4 *Calibration of basis-function coefficients*

This leaves the need to calibrate the coefficients to extract actual % porosity and resin-layer thickness. One option is to determine the calibration coefficients b_2 , b_3 and c_2 for the above inversion equations, based on the graphs from simulated waveforms from the model.

However, using the model to determine amplitude-based coefficients relies on the mixture rule being accurate and the pore size and attenuation and backscattering being allowed for correctly. Hence any calibration using the model would itself have to be calibrated against known reference specimens.

A preferred option is to use real data from real structures, but then the problem is the accurate measurement of porosity in the small 3D volumes that have been scanned and evaluated ultrasonically. Various methods of doing this are being investigated including micro-CT X-ray and X-ray diffraction methods, as well as micro-sectioning.

5.5.13 *The problem of multiple porous plies*

The above decomposition method has been evaluated primarily with simulated waveforms of single porous plies in stacks of multiple non-porous plies. In this situation it has been shown to deliver a coefficient that is linearly related to the porosity levels in the single ply of interest. However, the investigation of multiple porous plies demonstrated that the coefficient did not respond except for the first and last porous ply. This suggests that it is sensitive only to changes in porosity levels. An investigation ensued into the possibility of using the decomposition method to find a basis function that is a differential measure of porosity, giving a different value for increasing and decreasing levels of porosity.

The investigation followed from the recently developed Pinfield (2010) model of porosity as a random array of scatterers (see Chapter 4) where the combined response can be calculated by integrating the response over all the scatterers. This showed that there is a $\pi/2$ difference in phase, at all frequencies, between the reflection at an increase in porosity compared with that at a decrease in porosity. It follows that there should be a method of distinguishing between increasing and decreasing porosity levels, then tracking and integrating the change in porosity to calculate the porosity profile through the depth.

Section 4.6.10 in Chapter 4 showed that the time-frequency plot for a waveform of a single porous ply exhibits transition regions with resonances at frequencies that do not correspond to resonances of single plies, whether porous or not. It is intended to develop basis functions for these transition regions and use them with the SVD decomposition method to see if it is possible to track changes in porosity levels and calculate porosity profiles.

5.5.14 Summary of 3D porosity measurement

The objective of measuring 3D quantitative profiles of porosity was ambitious at the outset. Considerable progress has been made in isolating the effects of porosity from other effects that masquerade as porosity. By using the local spectral response of a volume element it has been possible to distinguish porosity from thick resin layers, which have a similar time-domain amplitude response. This method has been embodied in a SVD decomposition approach for which a patent has been applied.

The method has been successful on simulated porosity in single plies, but porosity does not appear like this in real composites. The amounts of porosity vary within plies and there can be multiple plies with porosity, but each with different amounts. It is intended in the future to extend the decomposition method to track increases and decreases in porosity levels, and thereby determine, through integrating the depth profile of the coefficient with respect to depth, a profile of porosity levels through the depth of the material.

5.6 Summary of property isolation in layered structures

Considerable progress has been reported in this chapter in isolating the many interfering influences on ultrasonic pulse-echo responses of composite structures. Methods have been developed to produce separate 3D profiles of ply spacing, fibre volume fraction, porosity and thick resin layers. However, the quantitative measurement of each of these material properties in three dimensions is still some way off. Chapter 7 reports on some attempts to apply these methods qualitatively to both simulated and real composite structures and begins to look at validation methods that can be applied in the future.

CHAPTER 6 FIBRE ORIENTATION MEASUREMENT AND MAPPING

6.1 Introduction

6.1.1 Motivation

As civil airframes contain more composite components, including primary structures such as wings and fuselage, there are growing concerns about quality assurance in terms of ply stacking sequence and straightness of fibres in CFCs, and about fibre spacing in titanium metal-matrix composites (TiMMCs). Current methods for assurance of these parameters are purely optical and can only be applied at the surfaces and edges of components. This does not provide for checking stacking sequence over thinner central regions of components, nor for detecting wrinkling in the middle of a component at a radius – a location where it is most likely to occur. If an ultrasonic method can be developed to automatically measure 3D fibre orientation (including ply inclination) across the whole component then this could be used as a detection and auditing tool.

6.1.2 Background

The original work on fibre orientation by the author, in 1994, was to determine ply stacking sequence non-destructively for CFC/honeycomb sandwich structure and was reported in an external paper (Smith & Clarke 1994). Subsequent work by Prof David Hsu at Iowa State University, published in 2002 (Hsu *et al* 2002), reproduced this original DRA work and then went on to use 2D Fourier Transforms accurately to determine ply orientation for carbon-fibre composites (CFCs). At the start of the current work reported here, the author implemented Hsu's 2D Fourier Transform method in QinetiQ's ANDSCAN analysis software and began applying it to TiMMC, as well as to CFC. Since then the technique has been improved and adapted to provide accurate ply stacking sequences, ply fingerprinting for woven fabrics and full 3D profiles of in-plane waviness and out-plane ply wrinkling.

6.1.3 Description of method

Ultrasound is reflected by acoustic-impedance mismatches at boundaries. The fibre-to-resin boundaries in carbon-fibre composite therefore reflect ultrasound. Also, if each inhomogeneous fibre-resin composite layer can be regarded on a macro scale as a mixture with a single *effective* stiffness and density, then each change in fibre volume fraction will be an acoustic-impedance change and will result in a reflection (see Chapters 3 and 4). Between plies there are two such boundaries, either side of a pure resin layer. This resin layer is of variable thickness, but it is always thin relative to the ply thickness. The reflection coefficient of the resin layer is directly related to its thickness according to the graph in Figure 6-1, derived from a full treatment of this thin-layer reflection, which can be found in Chapter 4 and Appendix A. In carbon-fibre composites this resin layer is much thinner (around 2 μm for 7 μm diameter fibres) than one-tenth of a wavelength at normal inspection frequencies (less than 20 MHz) and therefore the reflection coefficient will be approximately linearly proportional to the thickness of the resin-rich layer.

It is fortunate in CFRP and GFRP that the fibres are generally inserted into a ply in bunches, known as 'tows'. This creates a natural undulation in the resin layer thickness such that lines of slightly thicker resin occur between the tows. As mentioned above, the reflection coefficient from a thicker resin layer is greater and this causes the lines to show up on a C-scan of amplitude from a time gate at the depth of the resin layer.

The reflections from the resin layers can also be tracked - in B-scan cross-sections where they follow the profile of any ply wrinkles.

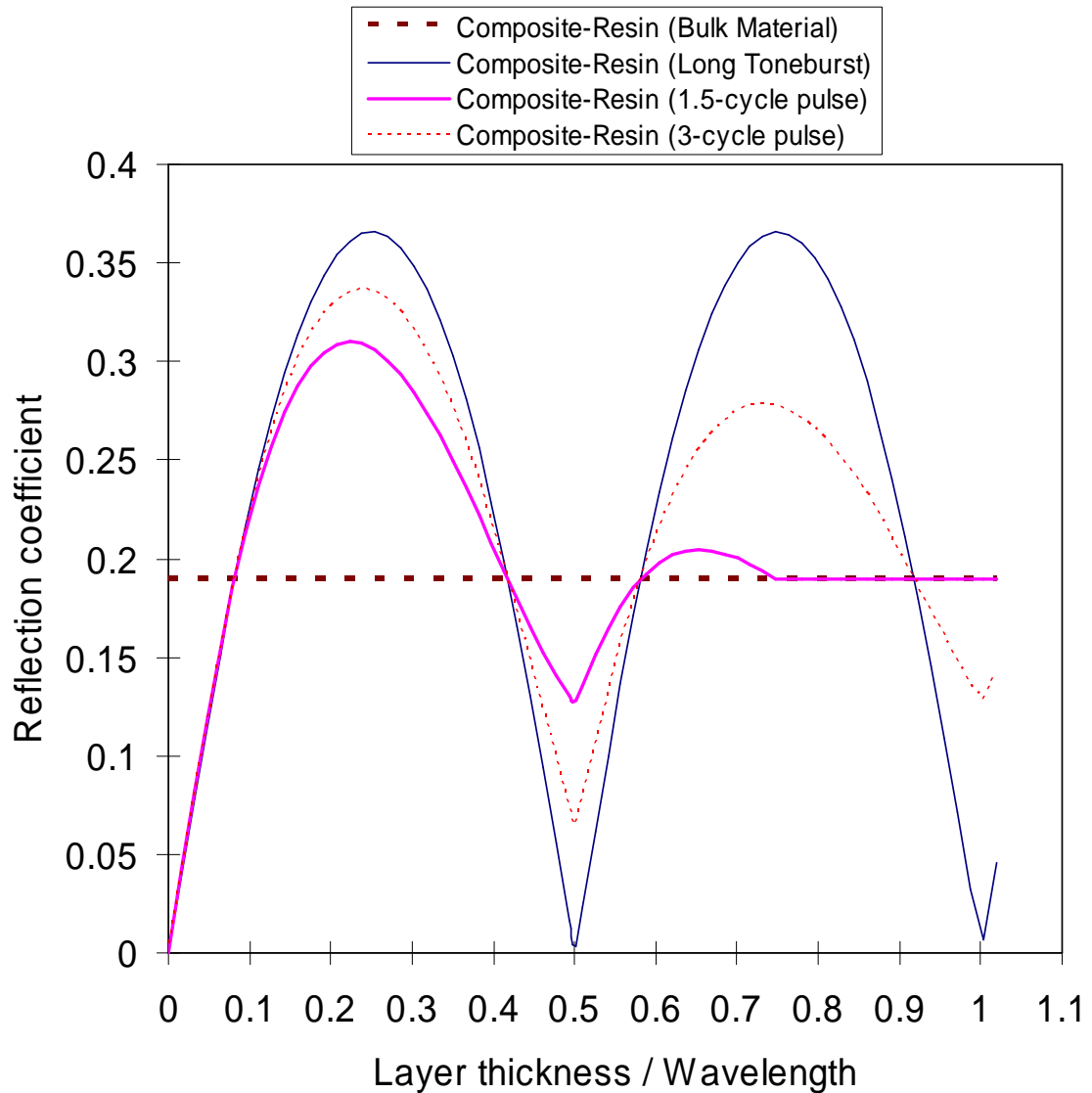


Figure 6-1. Calculated reflection coefficient for a thin layer of resin within a CFC material for a long tone-burst (thin line). The dashed brown straight line shows the reflection coefficient level for a single interface of composite to resin. The thick pink line is the result of a simulation of a short, 1.5-cycle pulse where the resonance effect decreases as the thickness increases because interference between the incident and reflected pulses decreases. When the specimen is thinner than half the pulse duration then the reflection coefficient will depend on the exact thickness-to-wavelength ratio. As the specimen becomes thicker than half the pulse length in the material then the thickness-mode resonance disappears and the single-interface reflection coefficient (dashed straight line) dominates.

6.1.4 The method applied to Ply Stacking Sequence

The ply stacking sequence method can be applied to C-scans of each ply interface reflection to determine the sequence of dominant fibre orientations. The C-scan generally shows lines in two directions - those of the fibre tows in the plies above and below the interface (because both contribute superimposed ripples on the resin layer thickness). A two-dimensional Fast Fourier Transform (2D FFT) is applied to the C-scan and the relative power at each angle is calculated. Peaks in this angular power distribution indicate the dominant ply orientations. A resolution of less than one degree appears to be achievable.

Examples of this method applied to the first four ply orientations in the same specimen used for the earlier work (Smith & Clarke 1994) are shown in Figure 6-2 to Figure 6-5.

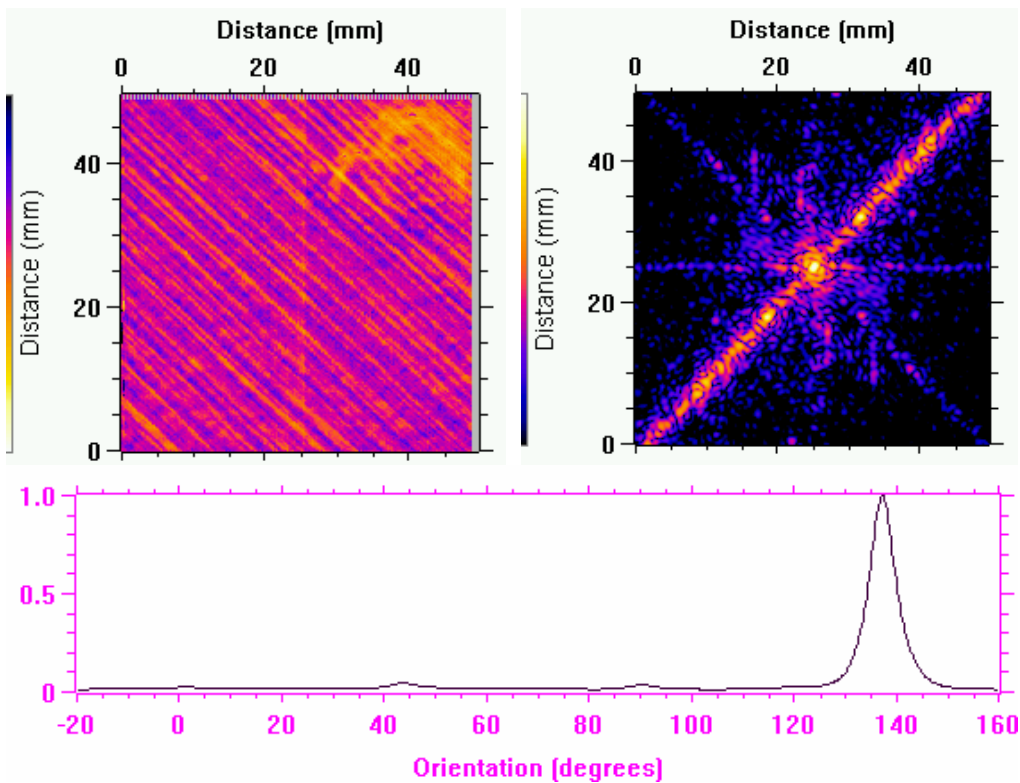


Figure 6-2. First ply interface showing C-scan (top-left), 2D FFT from the whole scan (top-right) and resultant logarithmic plot of angular analysis of ply orientation (bottom) with a peak at approximately 137° (-43°).

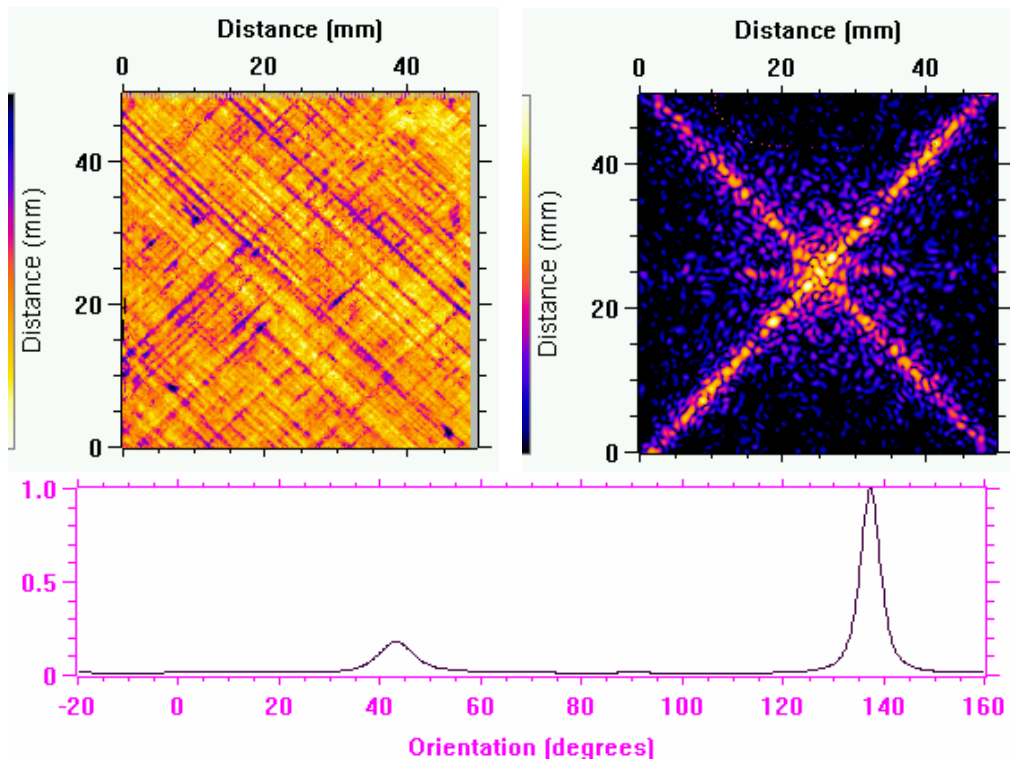


Figure 6-3. Second ply interface showing C-scan (top-left), 2D FFT from the whole scan (top-right) and resultant logarithmic plot of angular analysis of ply orientation (bottom) with a peaks at approximately 137° (-43°) and 43° .

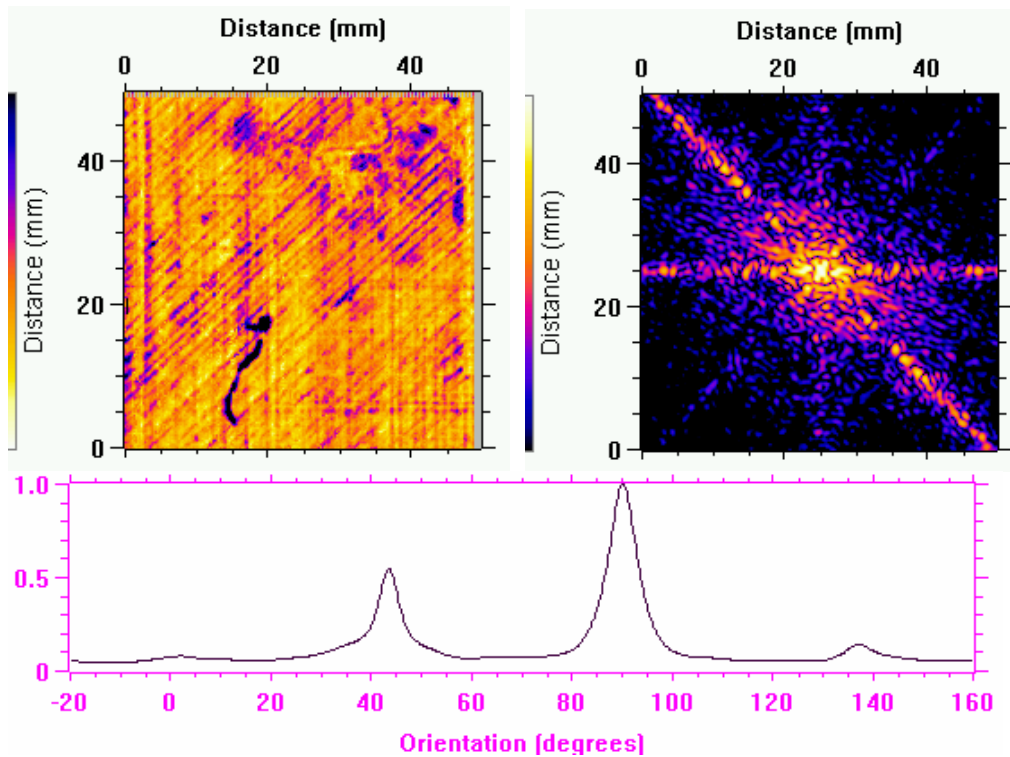


Figure 6-4. Third ply interface showing C-scan (top-left), 2D FFT from the whole scan (top-right) and resultant logarithmic plot of angular analysis of ply orientation (bottom) with a peaks at approximately 43° and 90° .

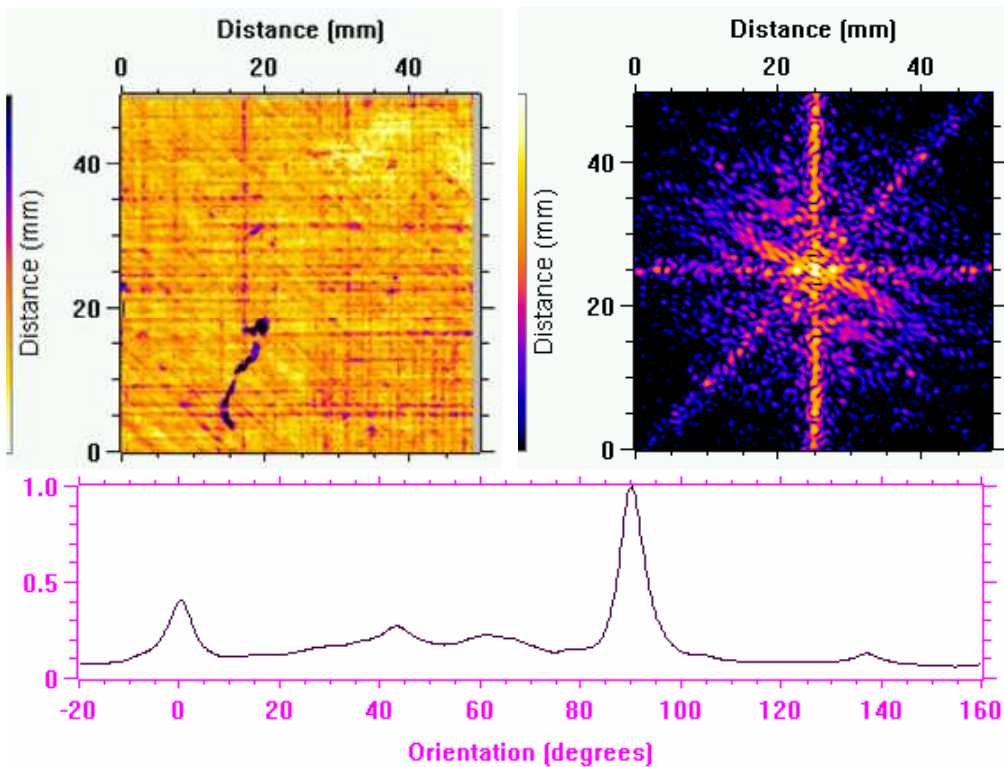


Figure 6-5. Fourth ply interface showing C-scan (top-left), 2D FFT from the whole scan (top-right) and resultant logarithmic plot of angular analysis of ply orientation (bottom) with a peaks at approximately 0° and 90° .

6.1.5 Use of 3D profile layers

Both the ply stacking sequence and the in-plane waviness applications require C-scans to be produced from the amplitude in a gate moved down through the structure. 3D-Profile layered channels were developed in this project (see Chapter 5) specifically for this type of application so that the same processing can be repeated for each layer in a structure. Depth-angle distribution images of ply stacking sequence have been shown by Hsu *et al* (2002) and the use of 3D profile layers means that they can now be produced by ANDSCAN using a range of different processing methods, depending on the application.

6.2 2D FFT method

This is a conventional 2D FFT with pre-specified windowing and 'mean-value-padding' (as the mean value is not zero) allowing improved spatial-frequency resolution if required. The magnitude alone of the 2D FFT is analysed to obtain the angular power distribution and plotted as a graph— see Figure 6-6.

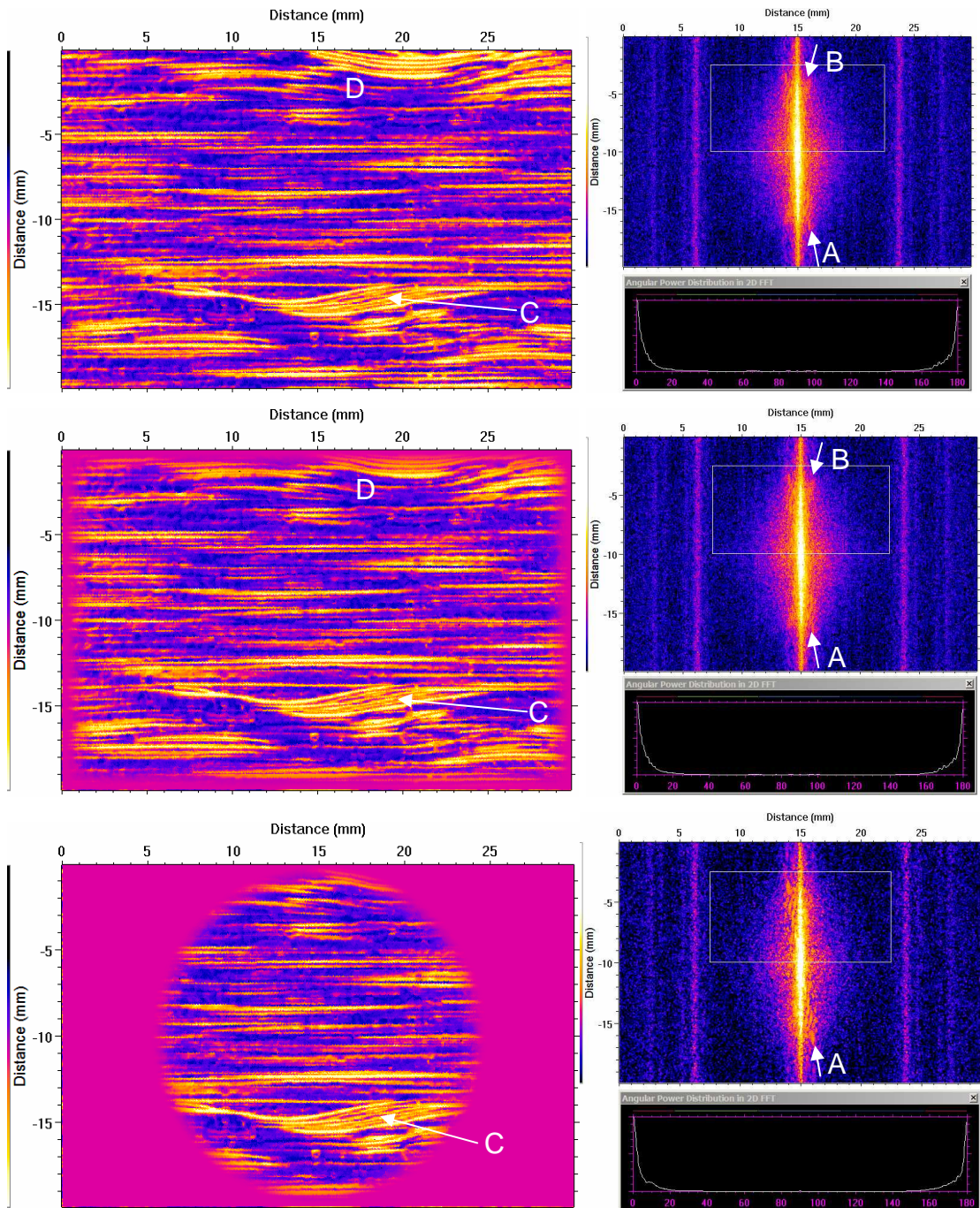


Figure 6-6. Example of the effect of a Hanning window applied to just 20% of the image width or height - 10% each side. The left-hand images are the windowed C-scan data from a single ply of TiMMC, and the right-hand images are the corresponding 2D FFTs and computed angular distribution: without windowing (top), rectangular mode (middle) and circular mode (bottom). The thin line in the FFTs marked 'A' corresponds to the wrinkle marked 'C' in the original C-scans, whilst the line marked 'B' is caused primarily by the wrinkle at the top of the scan marked 'D'

6.2.1 Windowing

A 'windowing' function can be applied to avoid *spectral leakage*. Spectral leakage is caused by the truncation of the image at its edges, which effectively convolves the actual (non-truncated) image of the structure with a rectangular 2D step function (Challis & Kitney 1991, Oppenheim & Schaffer 1975). A choice of window types was added into the software:

- Bartlett
- Parzen
- Hanning
- Hamming
- Blackman
- Welch
- Finite Gaussian
- Infinite Gaussian

The choice of rectangular or circular application of the windowing function was investigated in an attempt to avoid any bias in the angular distribution calculation. Figure 6-6 compares these two window application methods for a 2D FFT of a whole scan. It appears that the main difference is to do with what angles are present in the portion of the image that is excluded by the window. For example, the circular-windowed FFT in Figure 6-6(bottom) has one, rather indistinct, diagonal line (marked 'A') at approximately 5 degrees anticlockwise to the vertical, whereas the other FFTs also have a mirror-image line (marked 'B'). This is caused by the waviness at the top of the image (marked 'D'), which has been excluded by the circular window.

With a Hanning window applied within this software a study of the difference in angular distributions for rectangular versus circular windowing was performed. This showed negligible difference between the two types of windowing in terms of an expected bias towards 0° and 90° for the rectangular window (Figure 6-7).

Hence, the circular windowing has the disadvantage of reducing the amount of useful data used for the FFT, especially if the area selected has an aspect ratio that deviates significantly from unity – see Figure 6-8 and the resulting angular power distributions in Figure 6-9.

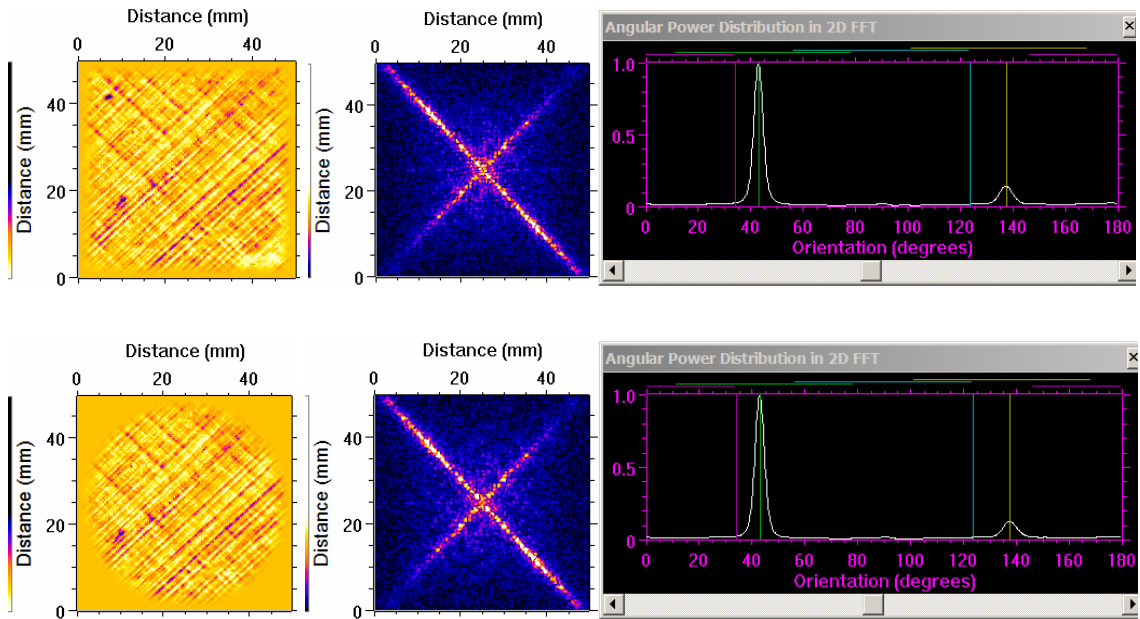


Figure 6-7. Difference between rectangular (top) 20% windowing and circular (bottom) 20% windowing on a scan with a unity aspect ratio. The central image shows the 2D FFT resulting from the left hand image. Apart from a slightly clearer low-frequency 90° line on the 2D FFT from the rectangular window, there is negligible difference that would actually affect the angular distribution.

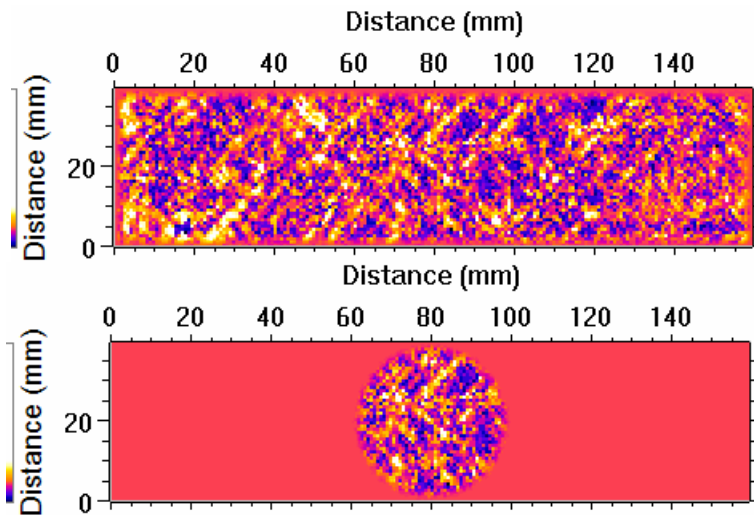


Figure 6-8. Comparison of rectangular (top) and circular (bottom) windowing on a high aspect-ratio image. Circular windowing removes most of the useful data.

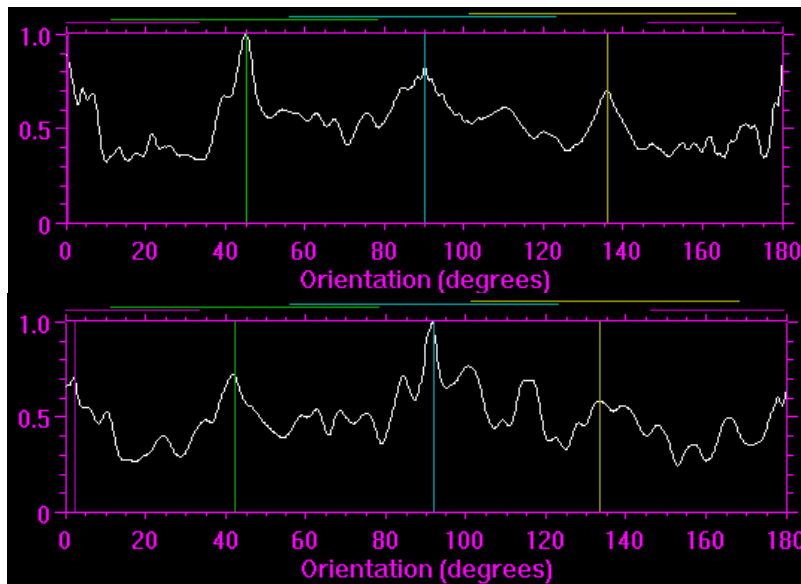


Figure 6-9. Resulting angular power distributions from rectangular (top) and circular (bottom) windowing on the high aspect ratio image from Figure 6-8, where circular windowing removes most of the useful fibre orientation data.

A similar analysis of the effect of varying the percentage of the image used for windowing showed that there is no noticeable benefit, in terms of faithful angular distribution, from extending the window over more than 20% of the image. However, there is a detrimental effect; a window spread over a greater percentage area reduces the amount of usable data. This analysis shows that the optimum windowing is a rectangular 20% Hanning window.

6.3 Angular power distribution

6.3.1 2D FFT of C-scan images with unity aspect ratios.

6.3.1.1 The Polar Transformation Algorithm

A polar transformation is performed on the 2D FFT data to determine the angular power distribution, but it is not straightforward for various reasons. Firstly, the central region of the 2D FFT contains a largely angle-independent distribution, which just raises the background level for the angular power distribution. Secondly, the 2D FFT image is pixelated and some directions, such as 0°, 90°, 45° and 135°, are better populated with pixels than others (see

Figure 6-10). And thirdly, there is an angle-dependent variation in amplitude, which has to be corrected to prevent bias in the measured angle

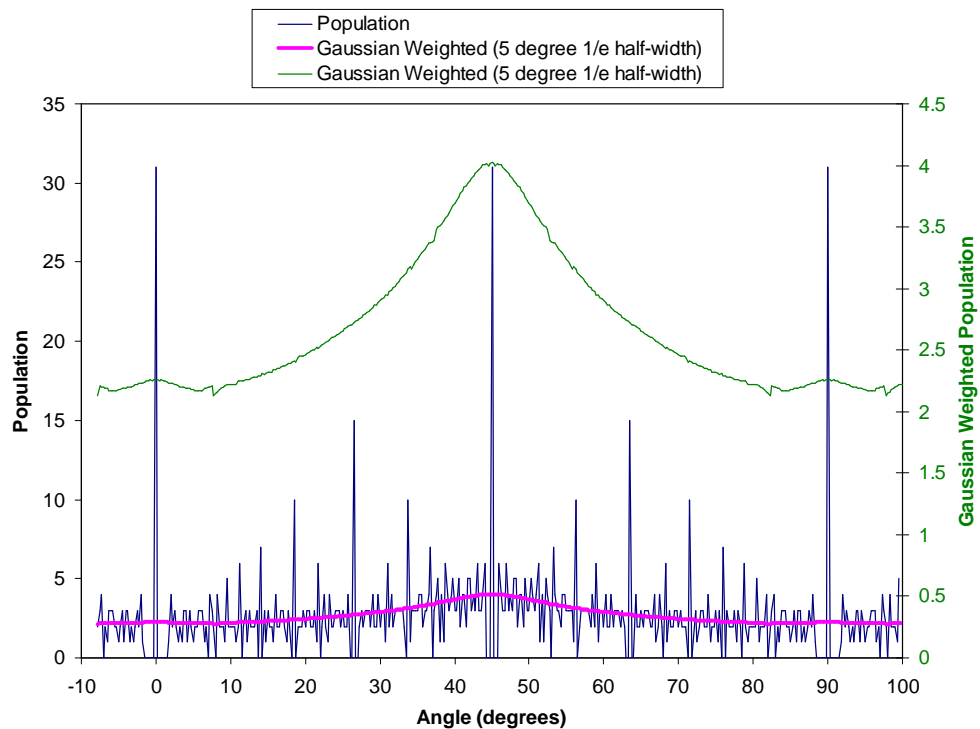


Figure 6-10. Population of angles (blue thin line) for 16 x 16 pixels of a 2D FFT of an image with an aspect ratio of 1:1. 720 angle bins of width 0.25° were used. The pink thick line (left axis) and green thin line (right axis) is the result of applying the Gaussian shading function with a 1/e half-width, φ , of 5 degrees.

The first two effects can be seen in Figure 6-4 particularly, where the 90° peak is extremely narrow due to the large number of pixels in this direction, and there is always a small peak at 0° and 90°, even when no plies at these angles can be seen.

A solution was found by applying a weighting function (in angle) to the contribution from each pixel, effectively ‘blurring’ it in the angular direction (ie convolving with the weighting function) so each pixel contributes to the integral at more than one angle. In the first instance, linear (triangular) and Gaussian weighting functions were tested and the Gaussian function was chosen because it more consistently removed the 0° and 90° spikes in the angular

distribution. Equation 6-1 shows how the angular distribution $F(\theta)$ is calculated with Gaussian weighting:

$$F(\theta) = \frac{\sum_x \sum_y [a(x, y)]^2 e^{-[\arctan(y/x) - \theta]^2 / \varphi^2}}{\sum_x \sum_y e^{-[\arctan(y/x) - \theta]^2 / \varphi^2}} \quad (6-1)$$

where x , y and a are the coordinates and value of each point in the 2D FFT, and φ is the 1/e point on the Gaussian shading function. Note that the amplitudes are squared so it is really an angular power distribution. This is in order to enhance the peaks in the distribution. Finally, the function is normalised to the sum of the weighting at each angle to allow for the fact that angles have differing numbers of contributors. An example is shown in Figure 6-10 of the effect of using a Gaussian shading function with $\varphi=5^\circ$.

It was found that no detrimental effect was observed by truncating the summation when the Gaussian weighting function became smaller than $1/e^2$ and, by calculating this in advance, a considerable computation-speed advantage could be achieved.

The value of φ , the 1/e point on the Gaussian shading function, was found to be important. Too large a value caused too much smoothing and loss of angular resolution in the angular power distribution. Too small a value failed to adequately remove the effects of pixelation, giving preference to 0° , 45° , 90° and 135° . The optimum value was shown to depend a) on the number of points in the 2D FFT because the angular spacing between angles with contributing pixels becomes greater as the number of points decreases (compare Figure 6-11 with Figure 6-10) and b) on the aspect ratio of pixel spacing (see next subsection).

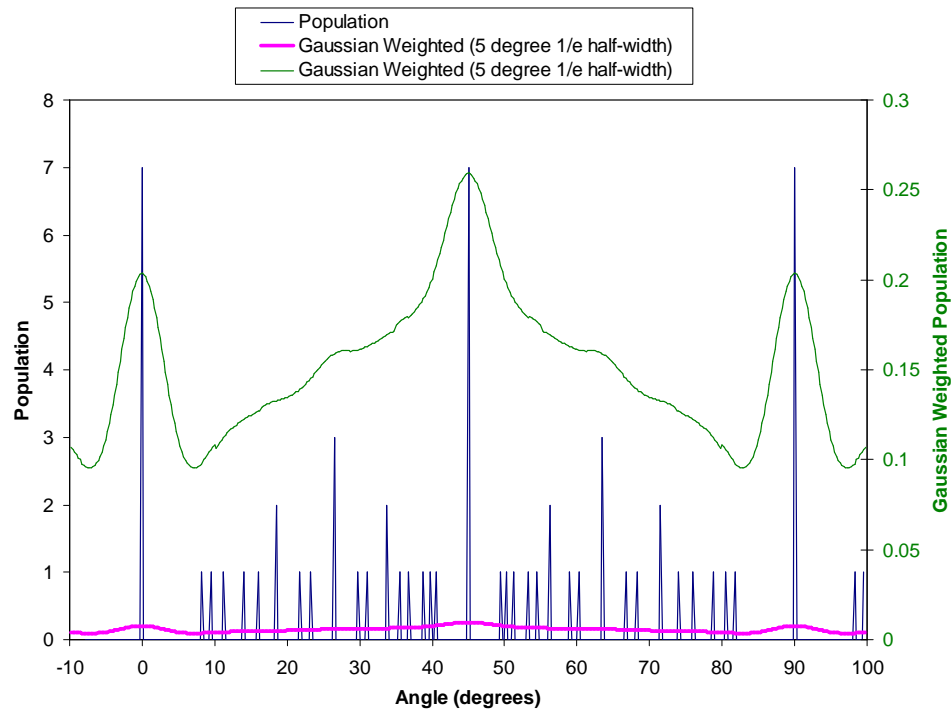


Figure 6-11. Population of angles (blue thin line) for 8 x 8 pixels of a 2D FFT of an image with an aspect ratio of 1:1. 720 angle bins of width 0.25° were used. The pink thick line (left axis) and green thin line (right axis) is the result of applying the Gaussian shading function with a 1/e half-width, φ , of 5 degrees.

A method was implemented that uses a larger value of φ (ie a wider angular width to the weighting function) as the number of contributing points in the 2D FFT decreases:

$$\varphi \propto \frac{1}{n.m} \quad (6-2)$$

where n and m are the number of points in the two directions of the rectangular portion of the image used for the 2D FFT. An example of the improvement is shown in Figure 6-12. This was implemented as a spatial-frequency-dependent Gaussian half-width that decreases with increasing spatial frequency, with a high-pass filter that limits the influence of the low spatial-frequencies.

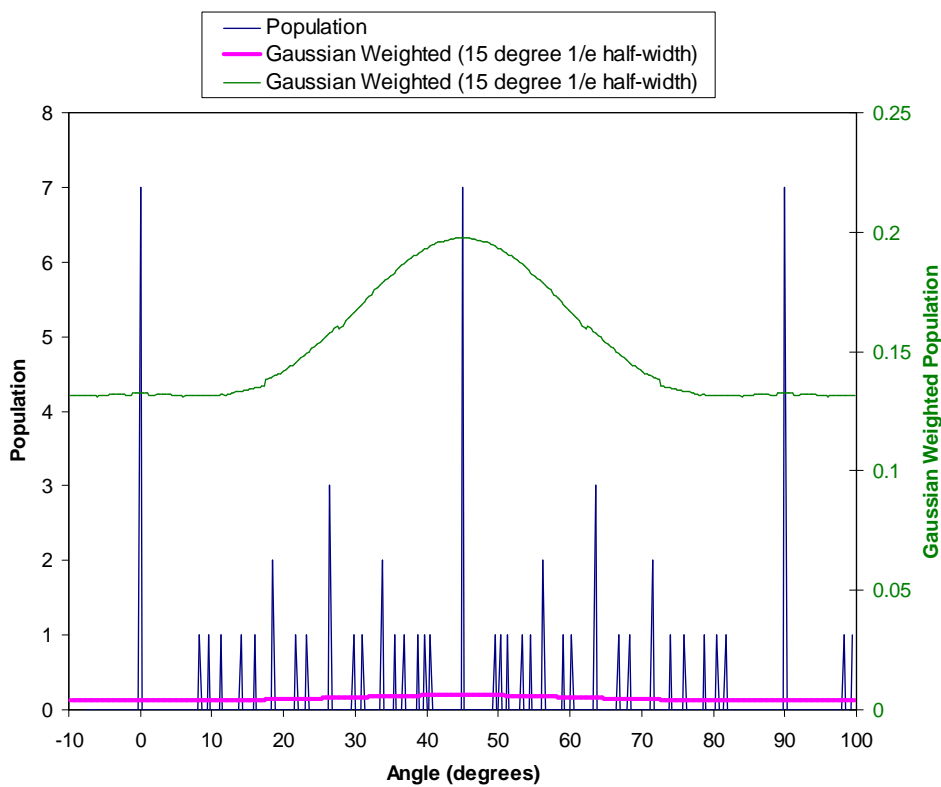
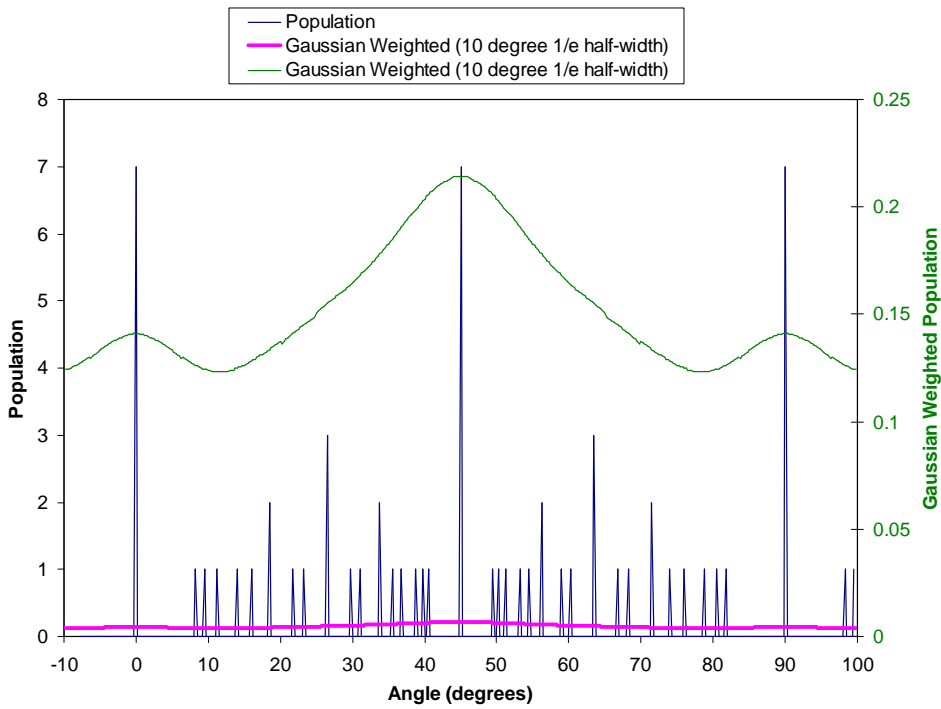


Figure 6-12. As for Figure 6-11, the pink thick lines (left axis) and green thin lines (right axes) are the result of applying the Gaussian shading function with a $1/e$ half-width, φ , of 10 degrees (top) and 15 degrees (bottom)

6.3.1.2 Angle-dependent Correction – Square Images

Finally, an angle-dependent correction is required for the angular power distribution because the peak amplitude from a given angle of fibres decreases from 0 or 90 degrees towards 45 or 135 degrees. This is illustrated in Figure 6-13 for a square region extracted from simulated fibre-tow C-scan images with different fibre orientations (see Appendix G on simulation of fibre tows).

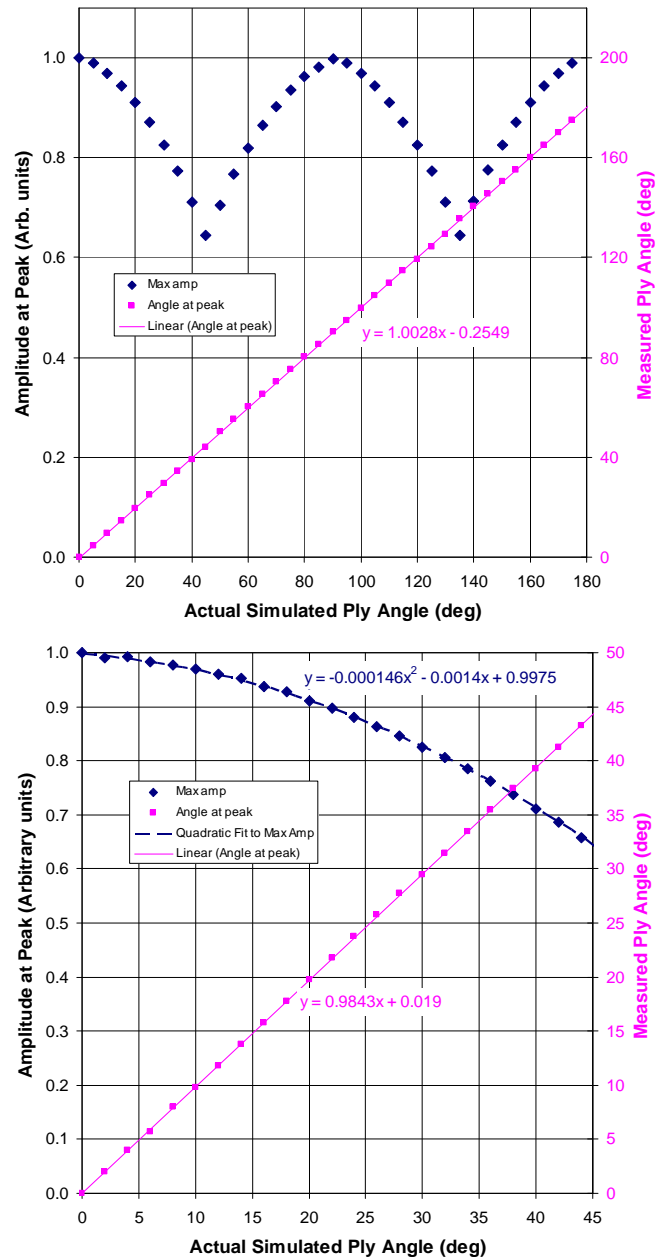


Figure 6-13. The measured ply angle and peak amplitude in a square region 20x20 mm for fibre tows simulated at 2 mm spacing and at angles ranging from 0° to 180° in 5° steps (top) and 0° to 45° in 2° steps (bottom).

It is possible that a correction is justified based on the varying spatial-frequency area of each 0.25° segment of the square 2D FFT. The variation in spatial-frequency area A , is given by:

$$A = \frac{\Delta\phi}{2 \cos^2 \phi} \frac{w_{FFT}}{2} \quad (6-3)$$

where w_{FFT} is the width of the 2D FFT. A possible correction factor is the normalised variation with angle, given by $1/\cos^2 \phi$. Such a correction factor, applied to the analysis of the 16x16 population of pixels used above, is illustrated in Figure 6-14.

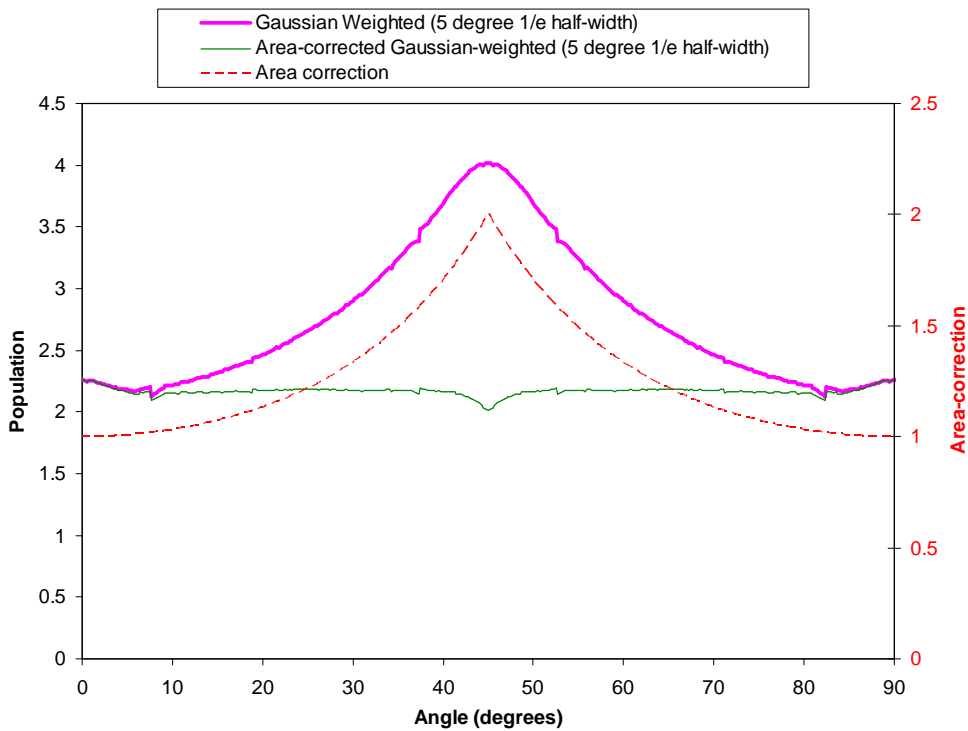


Figure 6-14. 5° 1/e half-width Gaussian weighting and $1/\cos^2 \phi$ area correction applied to a 16x16 pixel region as shown in Figure 6-10.

The correction clearly appears to produce a flatter amplitude response as a function of angle. However, when applied to the amplitudes obtained from the actual simulated fibre tows used for Figure 6-13, it is obvious (in Figure 6-15) that the $1/\cos^2 \phi$ correction is not appropriate and that the varying area is not the cause.

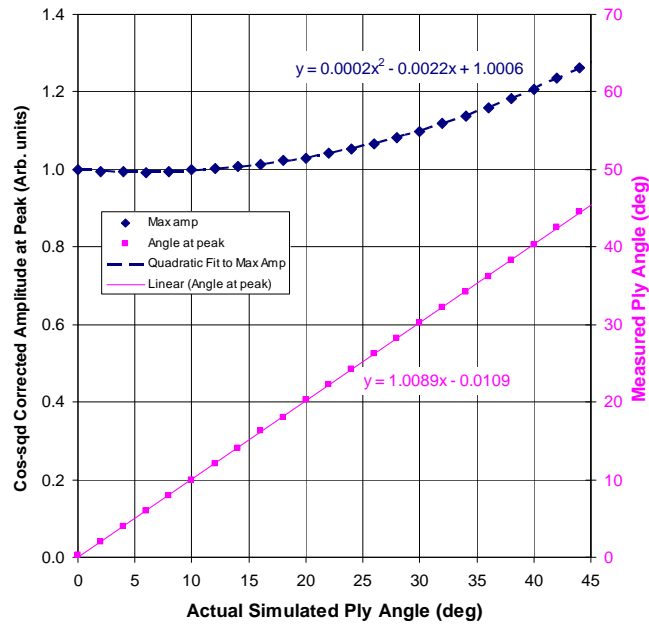


Figure 6-15. Data from Figure 6-13 corrected using the proposed $1/\cos^2 \phi$ segment-area correction, showing that this does not solve the problem.

An alternative cause of this correction requirement is the finite ‘aperture’ or region of image chosen, which is effectively multiplied by the image of fibre-tows. In the spatial-frequency domain this becomes a convolution of the FFT of the aperture with the FFT of the fibre tows (two dots either side of the zero-frequency centre point) – see examples in Figure 6-16. It can be understood why this introduces a rotational symmetry of order 4 for square regions.

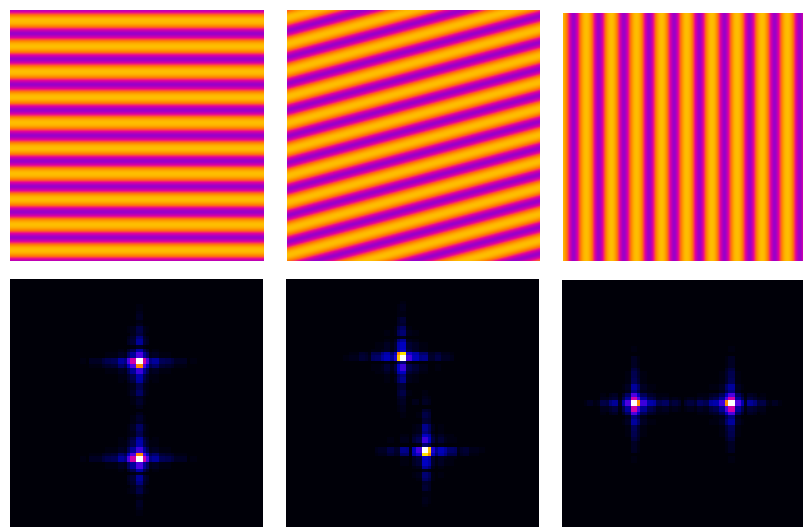


Figure 6-16. Square regions of fibre-tow images (top) and their corresponding 2D FFTs (bottom) for fibre orientations (left to right) 0° , 8° and 90° .

A quadratic fit to the data in Figure 6-13 provides a quadratic correction, κ for a square image region, for ϕ in degrees, in Equation 6-4, giving a relatively flat amplitude response with angle, as shown in Figure 6-17

$$\kappa = \frac{1}{1 - 0.014\phi - 0.000146\phi^2} \quad (6-4)$$

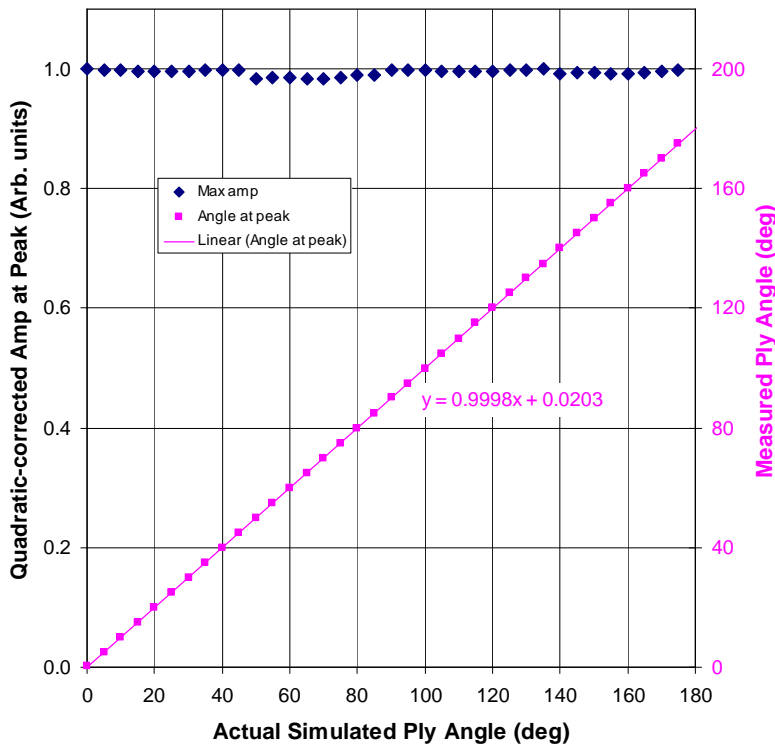


Figure 6-17. Data from Figure 6-13 corrected using the quadratic correction factor κ , showing a considerable improvement in peak amplitude uniformity and accuracy of orientation measurement.

Note that the measurement of ply angle is also more accurate when the correction has been applied, as shown in Figure 6-17.

An example of the analysis of a simulated stack of plies in 5-degree steps is shown in Figure 6-18 and this non-normalised data illustrates that the quadratic correction produces uniform, angle-independent amplitudes.

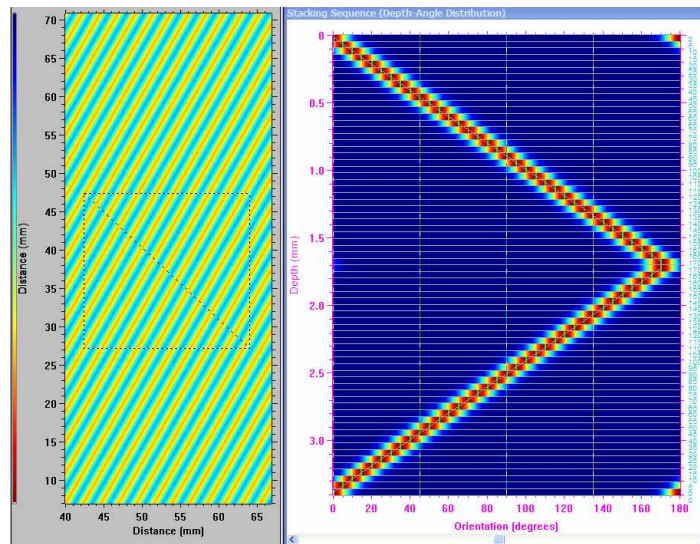


Figure 6-18. Simulated ply angles in 5 degree increments measured accurately with the quadratic correction factor. This data is not normalised in each layer so it would demonstrate any changes in amplitude if the correction had failed..

6.3.1.3 Angle-dependent Correction – Rectangular Images

The above quadratic correction is only applicable to *square* analysis regions. For *rectangular* analysis regions (see Figure 6-19) the effect is more complicated because the FFT for each of the two points is stretched in one direction and now has rotational symmetry of order two.

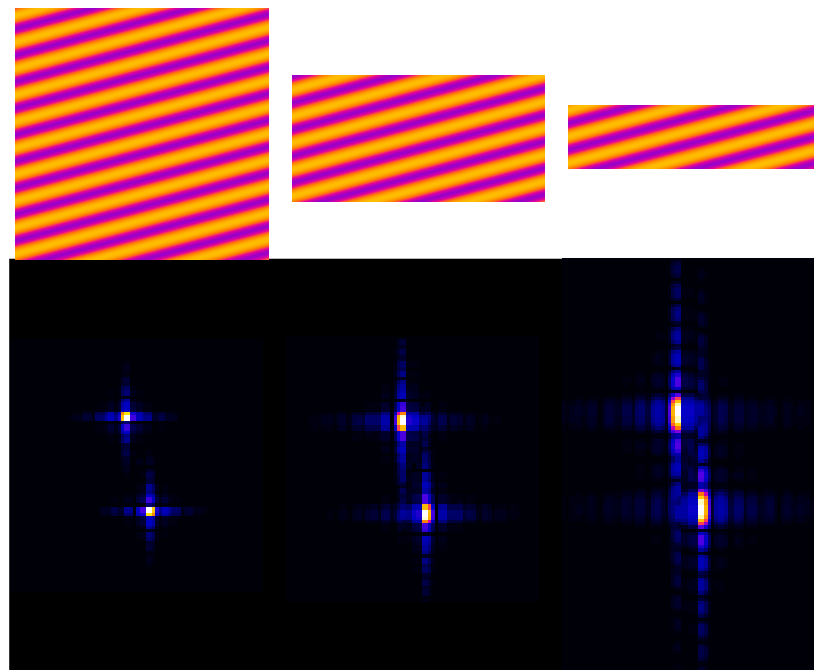


Figure 6-19. Rectangular regions of fibre-tow images (top) and corresponding 2D FFTs (bottom) for aspect ratios (left to right) 1, 2 and 4.

The effect of this on the angle-dependent peak amplitude in the 2D- FFT is shown in Figure 6-20 where the rotational symmetry of order two is clearly superimposed on the rotational symmetry of order four.

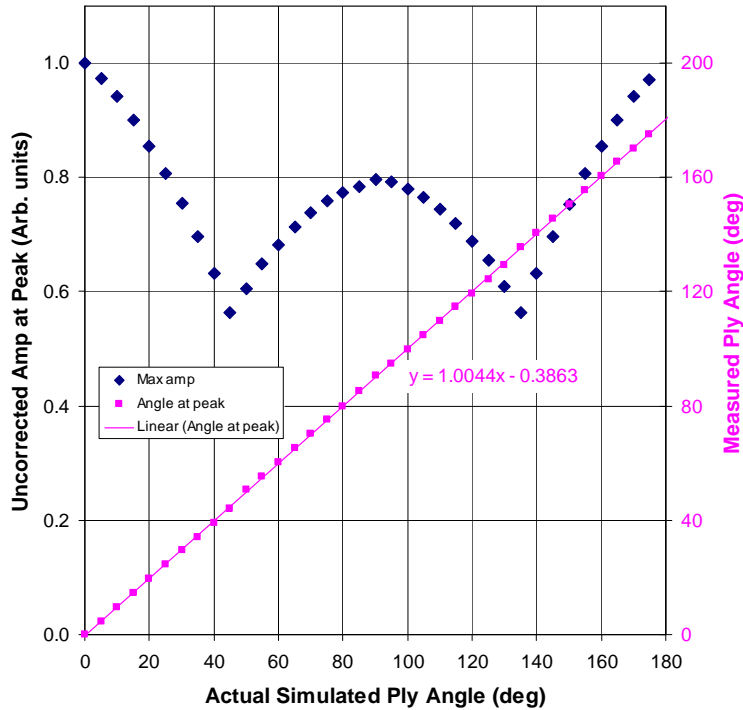


Figure 6-20. Uncorrected response from a 20 mm wide, 10 mm tall rectangular region from the C-scan image.

If these two effects are superimposed, it may be possible to correct for them separately. If the quadratic correction is applied first to correct for rotational symmetries of order 4 (see Figure 6-21), the remaining angle-dependent variation may be due purely to effects with rotational symmetry of order 2.

Based on this method, corrections were derived that fitted the remaining symmetry order 2 effects. For aspect ratios where the width is greater than the height, the correction is given by:

$$1 - \alpha \sin \phi \tag{6-5}$$

and for aspect ratios where the width is less than the height:

$$1 + \beta(1 - \cos \phi) \tag{6-6}$$

where α and β depend on the aspect ratio (width / height) of the analysis region.

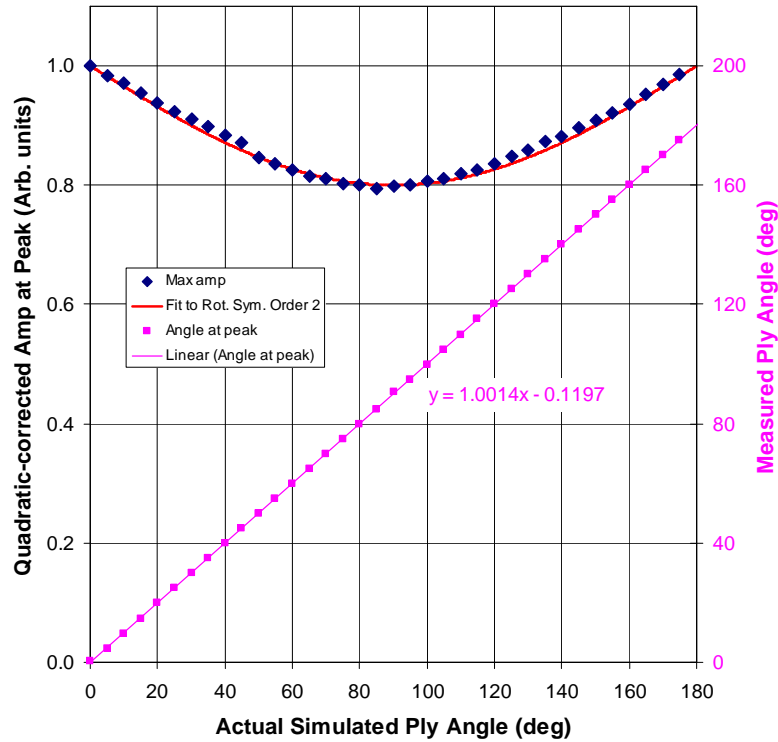


Figure 6-21. Response from Figure 6-20 but corrected using the quadratic correction described above for square regions. The red line is the proposed correction for the effects with rotational symmetry of order 2.

Using the simulated fibre-tow images, it was possible to determine empirically the apparent optimum values of α and β as a function of aspect ratio in Figure 6-22. From curves of best fit through these values, the following equations for α and β as a function of aspect ratio (of width w to height h) can be derived:

$$\alpha = -0.0178(w/h)^2 + 0.2545(w/h) - 0.2337 \quad (6-7)$$

and for aspect ratios where the width is less than the height:

$$\beta = 4.044e^{-5.5118w/h} \quad (6-8)$$

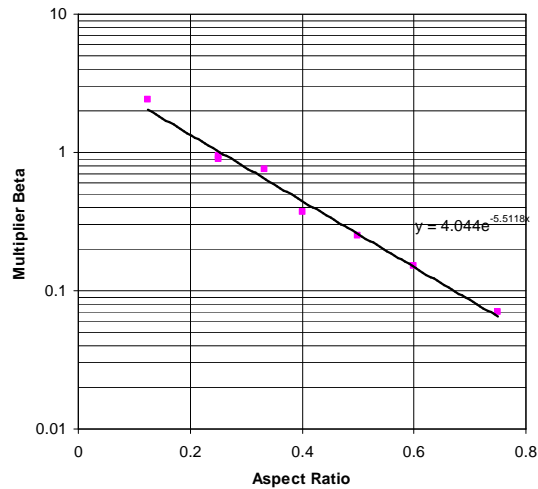
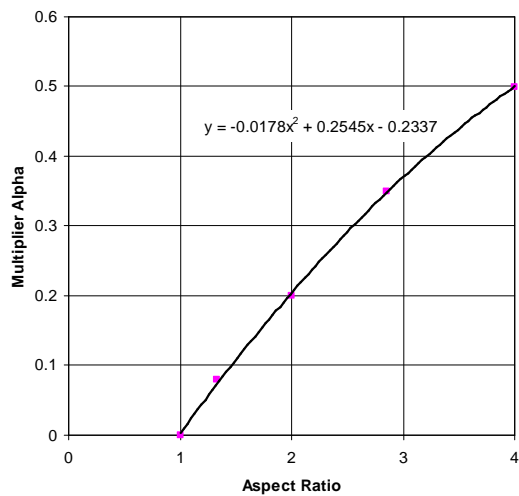
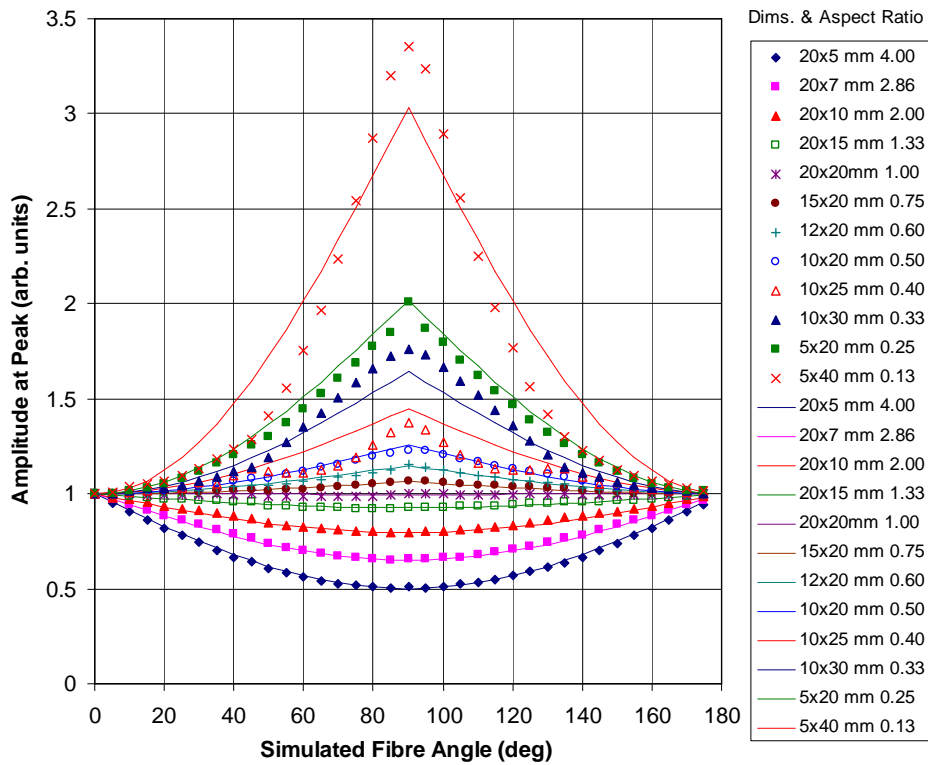


Figure 6-22. Corrections for rotational symmetry of order 2 are shown (curved lines) in the top graph and are compared with the measured peak amplitudes (symbols) from various aspect ratios of regions on simulated fibre-tow images. Also shown (bottom) are values for the multipliers α (left) and β (right) as a function of aspect ratio, based on the best fit to the data in the top graph.

In order to test this two-stage correction methodology, five regions with different aspect ratios were tested - see Figure 6-23. Whilst the correction is not perfect, the variation in amplitude with angle has been reduced to less than 6%.

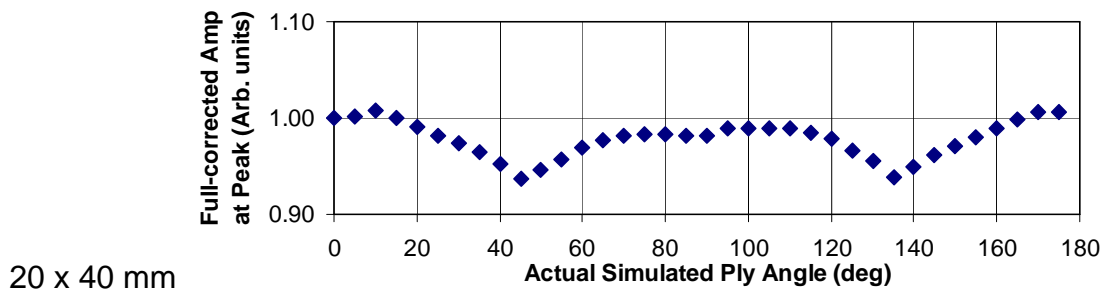
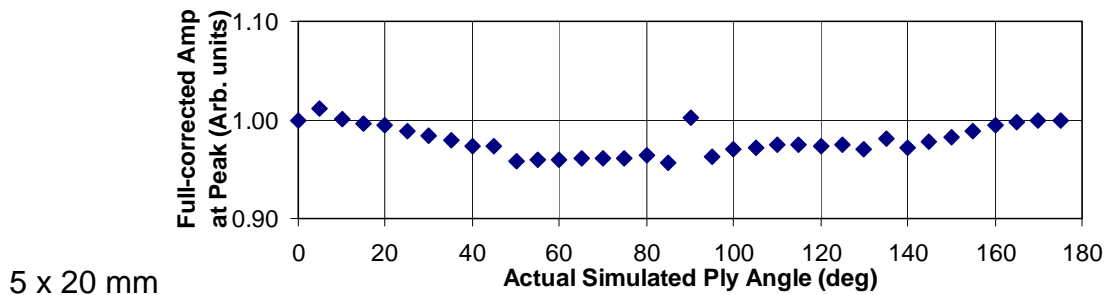
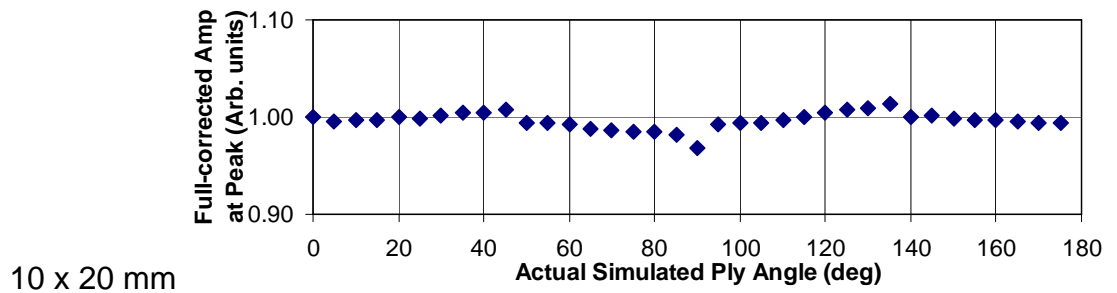
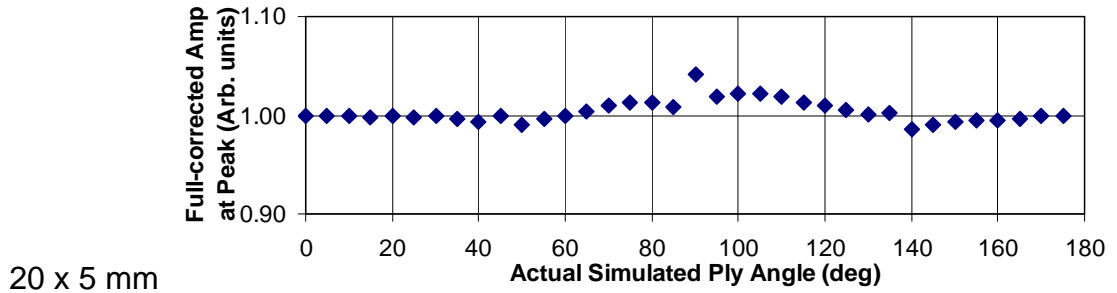
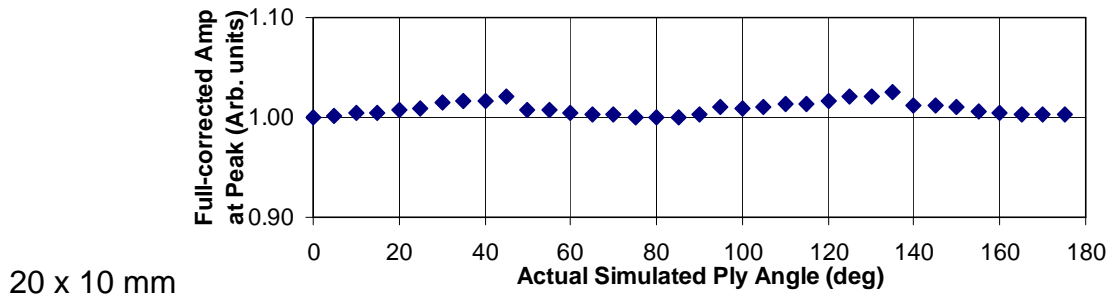


Figure 6-23. Implementation of the two-stage correction for angular dependence of amplitude for rectangular regions of dimensions (width x height): Top to bottom: 20 x 10 mm, 20 x 5 mm, 10 x 20 mm, 5 x 20 mm and 20 x 40 mm.

6.3.2 2D FFT of B-scans (images with non-unity aspect ratios).

In order to use the angular distribution method for measurements of out-of-plane ply wrinkling it is necessary to analyse out-of-plane B-scan slices, which are very different to the in-plane C-scan slices used so far. B-scans are cross-sectional slices built up from multiple waveforms spaced at a given scan step size. The pixel separation in the time domain, corresponding to the depth axis in the structure is usually much smaller than the pixel separation along the surface of the structure between waveforms. This leads to a non-unity aspect ratio which changes the symmetry in the 2D FFT and needs addressing in order to produce an unbiased angular power distribution. In the example shown in Figure 6-24 the aspect ratio (width:depth) is 13.6:1 and this translates into an aspect ratio in the spatial frequency (2D FFT) domain of 1:13.6 as illustrated. Consequently, the distribution of pixels contributing to angles in the angular power distribution is skewed considerably (Figure 6-25). Although there are many contributors at 0°, there are none for a wide range of adjacent angles.

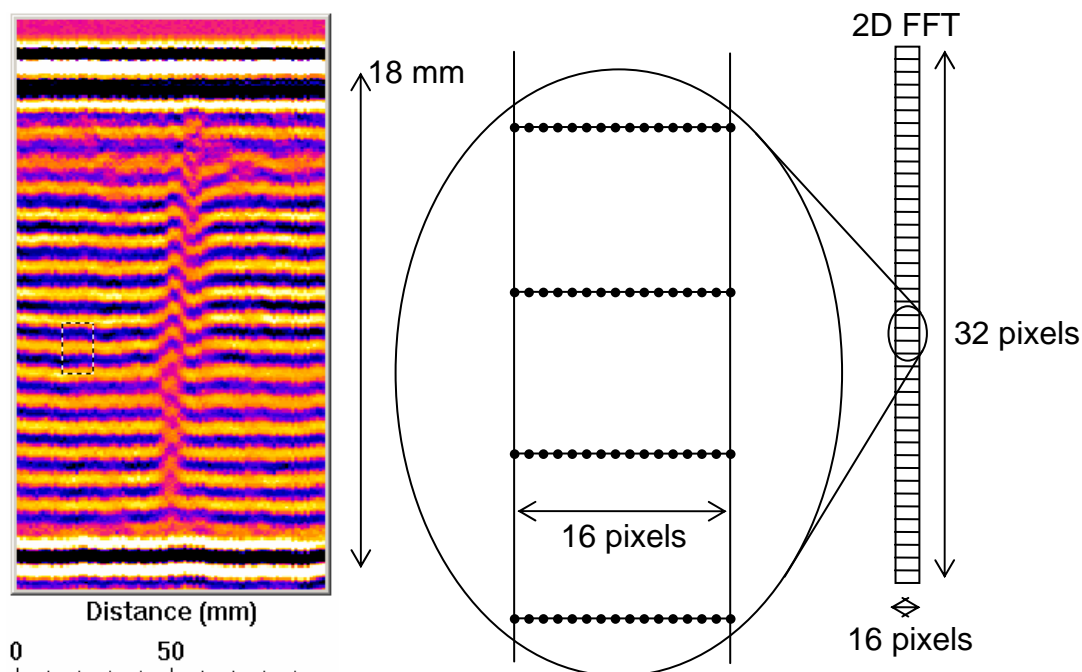


Figure 6-24. Typical B-scan of out-of-plane fibre waviness in an 18 mm thick 72-ply carbon-fibre composite skin (left). The pixels in the actual B-scan are 1 mm wide and only 74 μm tall. The box illustrated on the B-scan is actually 10 mm (10 pixels) wide and 2 mm (27 pixels) tall. A 2D FFT of this box is shown diagrammatically (right) and will typically be tall and thin.

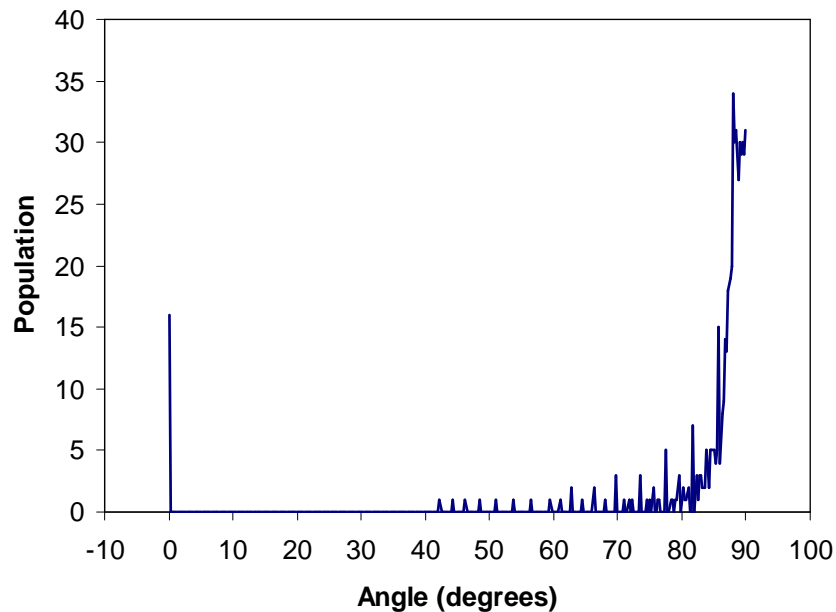


Figure 6-25. Population of angles in the 2D FFT for a 16 x 32 pixel 2D FFT of a B-scan with an aspect ratio of 13.6:1. 720 angle bins of width 0.25° were used. Note that 90° in the FFT corresponds to 0° lines in the B-scan.

One solution was to use a much larger value of φ (the 1/e point on the above-mentioned Gaussian shading function) for the 0° pixels and the adjacent angles, whilst reverting to a smaller value of φ when the population is non-zero. This was a relatively time-consuming algorithm, especially considering that most of the time was spent applying a wide shading function to the 0° 2D-FFT angles, whilst the plies in the B-scan are orientated close to 0°, corresponding to 90° in the 2D FFT, where the angles are well populated.

A second, more efficient solution was found: as only one orientation angle exists in the B-scan – the ply angle of inclination – it is possible to just calculate the ‘power centroid’ for the raw angular power distribution, with no shading function applied at all. This works mainly because that one ply angle is at 90° in the 2D FFT – a well-populated region.

6.4 2D map of orientation

In order to detect local variations in orientation of fibres or fibre tows in composites, it was decided that a local assessment of orientation was required. This could be achieved by applying the 2D FFT and angular distribution

analysis to a small region at a time and then raster-scanning that region over the image. When developing this method, it became obvious that the 2D spacing of orientation information would be equal to the increment with which the box is moved, so a smaller increment (larger overlap) is advantageous when raster-scanning the box across the image. Initially the processing was very time-consuming and so the increment chosen was half the size of the box in each direction. Later, the algorithm for B-scan (out-of-plane) analysis was speeded up using the power-centroid' method and the increment was reduced to a quarter of the box size. In order to fill in the gaps between the sparsely-distributed values of orientation (at the centre of each box location), a linear interpolation method was initially used (see Figure 6-26).

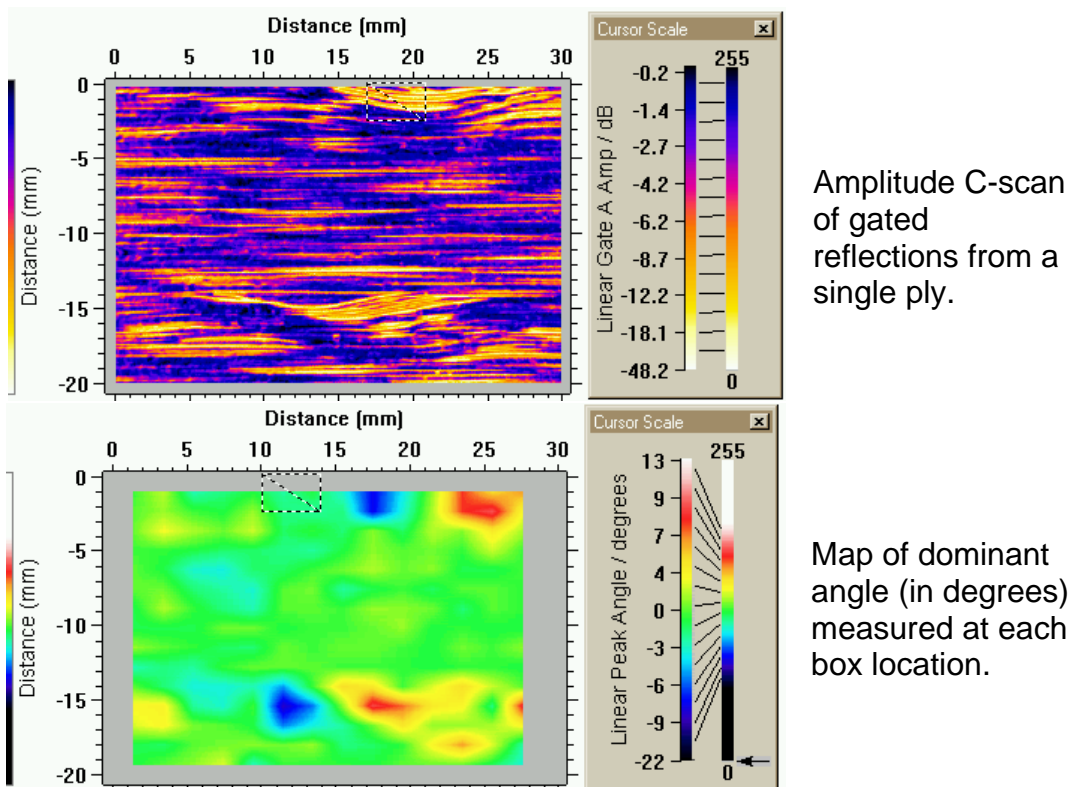


Figure 6-26. An example of 2D mapping of fibre orientation for the scan of wavy SiC fibres in a Ti matrix (top). The lower image plots as a colour the dominant angle at each location of the analysis box (shown dashed in both images), which is then raster-scanned over the whole image using a 50% overlap of adjacent box positions and linear interpretation between adjacent box centres.

However, this did not perform well in all situations such as on B-scans with high aspect ratios so a different method using weighted averaging was introduced.

After experimenting with different weightings, an elliptical Gaussian weighting function, with the ellipse matched to the aspect ratio of the image, was found to produce the best results. The size of the Gaussian weighting function (ie its spatial influence) was linked to the increment of the box (the % overlap) rather than the box size. An example of this method of interpolation is shown in Figure 6-27 for wavy fibres in a single ply of carbon-fibre composite. It is also possible to superimpose the original image on the orientation map.

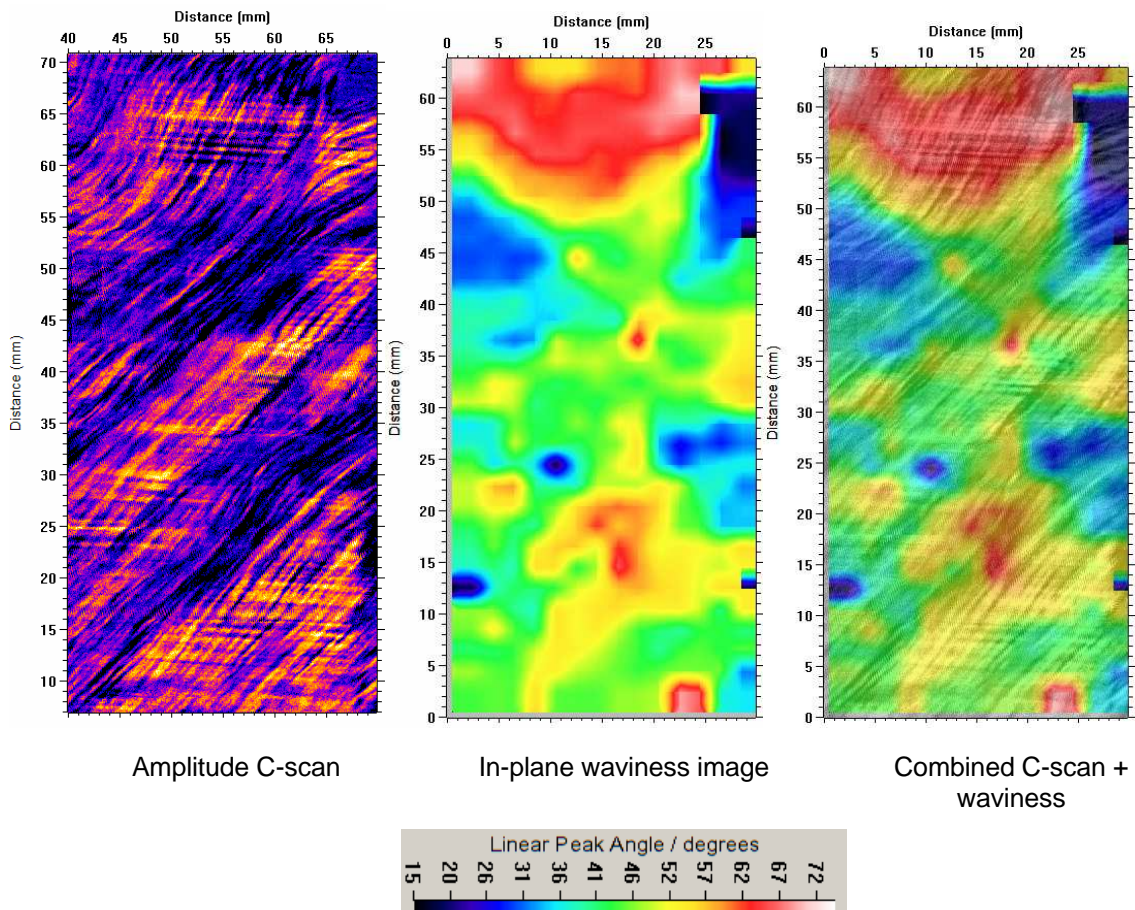


Figure 6-27. Optimised in-plane waviness image (middle) with the C-scan from which it was generated (left) and a combination of the two images (right). A 5 x 5 mm box size was used with 60% overlap and 40% rectangular Hanning windowing and an elliptical Gaussian weighted average.

Figure 6-28 shows an example of a B-scan (left) and the ply-angle cross-section result (right) of applying the 2D FFT with 50% overlap of box locations and elliptical Gaussian-weighted averaging. Whilst the wrinkle can be visualised in the B-scan, it can be completely quantified in the ply-angle cross-section

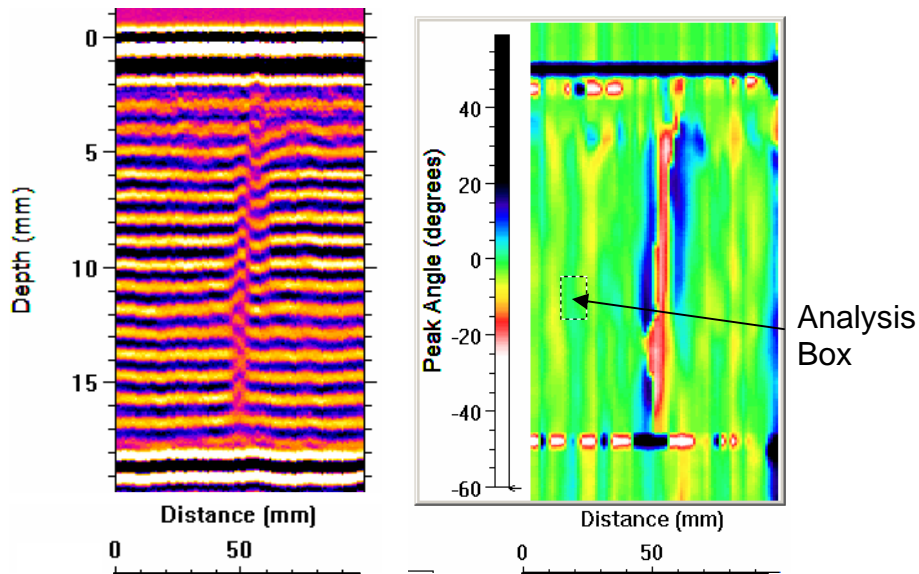


Figure 6-28. 2D mapping of out-of-plane ply wrinkling in an 18 mm thick CFC specimen. The B-scan cross-section (left) has been analysed using a 2D FFT in an analysis box as marked, scanned with a 50% overlap and elliptical Gaussian weighted average. The output shows cross-sections of ply inclination (right).

Bands of high-angle measurements at the top and bottom surfaces of the specimen are evident in Figure 6-28. This was solved by moving to the power-centroid method of determining the dominant ply angle of inclination. It is therefore thought that this was an aberration caused by the original method of Gaussian shading to determine the angular power distributions. An example of the cleaner output from the power-centroid method is shown in Figure 6-29.

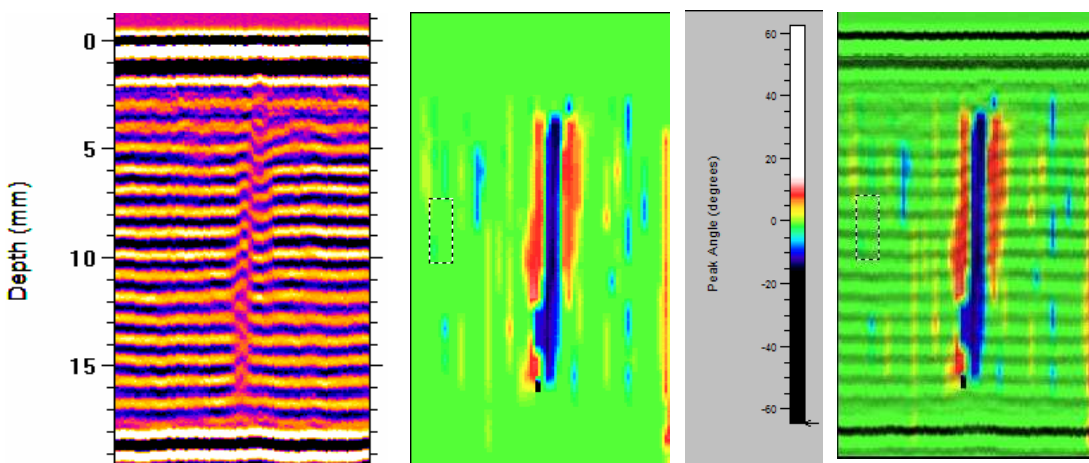


Figure 6-29. B-scan (left) and corresponding power-centroid method ply-inclination analysis (centre), with the two superimposed (right).

6.5 1D profile of stacking sequence

By taking the Angular Power Distribution for each layer in a 3D Profile and plotting it as a grey-scale image, it is possible to visualise the ply stacking sequence in the structure. Figure 6-30 shows such an image in the six-ply carbon-fibre composite skin, adhesively-bonded to honeycomb, that was used for Figure 6-2 to Figure 6-5. The skin has the following ply lay-up: 135°, 45°, 90°, 0°, 135°, 45°. In fact, the design was for a ‘balanced’ structure with 135° plies on the outside on both sides, furthest from the centreline, so this skin had been incorrectly manufactured.

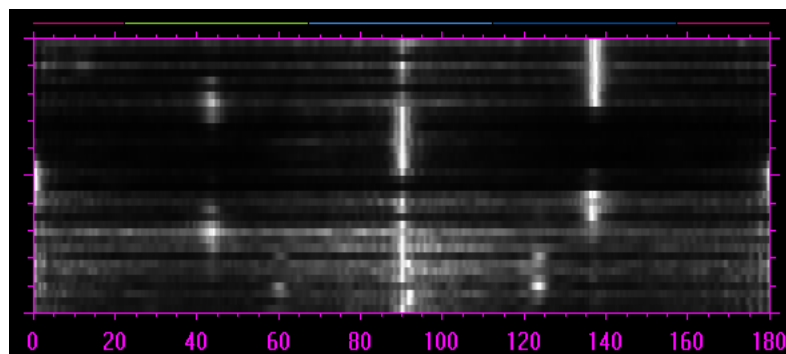


Figure 6-30. Ply stacking sequence shown as a greyscale image highlighting the dominant orientation as a function of depth in the structure, culminating in the hexagonal lattice of the honeycomb bond-line.

6.5.1 Visualisation

Ideally the output from this ply stacking sequence analysis would be a definitive list of the ply orientations in depth order. Whilst the automation of such a process is the ultimate aim, there will always be a need for a method of visualisation so that the operator can check the automated analysis. The grey-scale image method has already been introduced in Figure 6-30, and in the following section there is a discussion of the issues of normalisation in order to assist the operator to distinguish the dominant orientation. In addition, horizontal lines can be added to the image to delineate where the plies occur and vertical lines to show where the expected orientations of 0°, 45°, 90° and 135° (pseudo-isotropic carbon-fibre composite lay-up) occur.

Additional features have been added to the ANDSCAN software to allow improved operator verification. For example, when the operator clicks the

mouse on a layer of interest on the image, the C-scan layer shown in ANDSCAN automatically changes to the layer clicked on, allowing immediate confirmation of the ply orientation at that depth.

6.5.2 Normalisation

A rigorous study of the application of this stacking sequence method was applied to a range of specimens. The aim was to determine the optimum acquisition settings: scan step size, probe frequency and bandwidth, and optimum analysis parameter settings for the variables that had been written into the software by the author: gate width, gate overlap, window size, type and extent of windowing for the FFT, etc. The peak amplitude in the angular distribution varies considerably as the C-scan layer descends down through the stack, due to attenuation. The initial normalisation method to overcome this – normalising to the peak in each layer - was found to be inadequate because it could give poor contrast-to-noise for low amplitude reflections. Various other methods of normalisation were attempted and are compared in Figure 6-31.

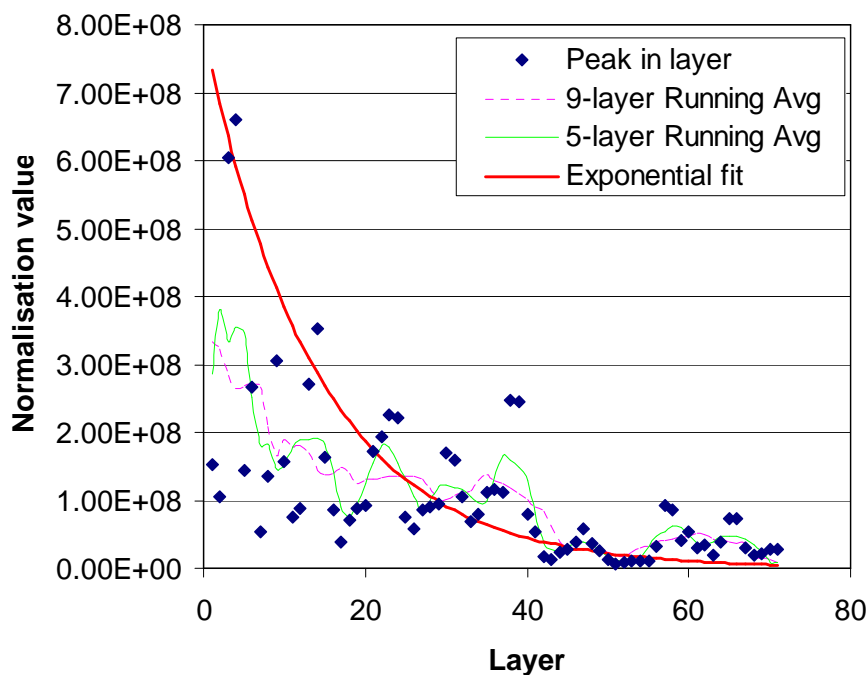


Figure 6-31. Three methods for normalising the stacking sequence image. Each layer is normalised to: the peak in that layer; the average of a specified number of layers above/below (5 and 9 shown); an exponential fit to the layers from 25% to 75% of the range of layers.

Whilst the exponential fit produces potentially the most realistic curve shape, matching attenuation in the structure, it has proven to be the most difficult to adapt to different scans and different structures. This is because, if the front or back surface reflections are included in the data that is fitted, a completely unrepresentative exponential curve can result. The exponential fit shown in Figure 6-31 was produced using the central 50% of the range of layers in an attempt to avoid the front and rear surface effects. However, then the exponential normalisation can be erroneous near the front and rear surfaces.

Using a running average across a range of layers proved to be more consistent in implementation although this method is sensitive to the number of layers used for the average. If the range of layers averaged is less than a single composite ply, the desired result is not achieved, because contrast between plies can be lost in the normalisation process. This can be seen in Figure 6-32 where the different normalisation methods shown in Figure 6-31 are demonstrated on the 6-ply honeycomb structure.

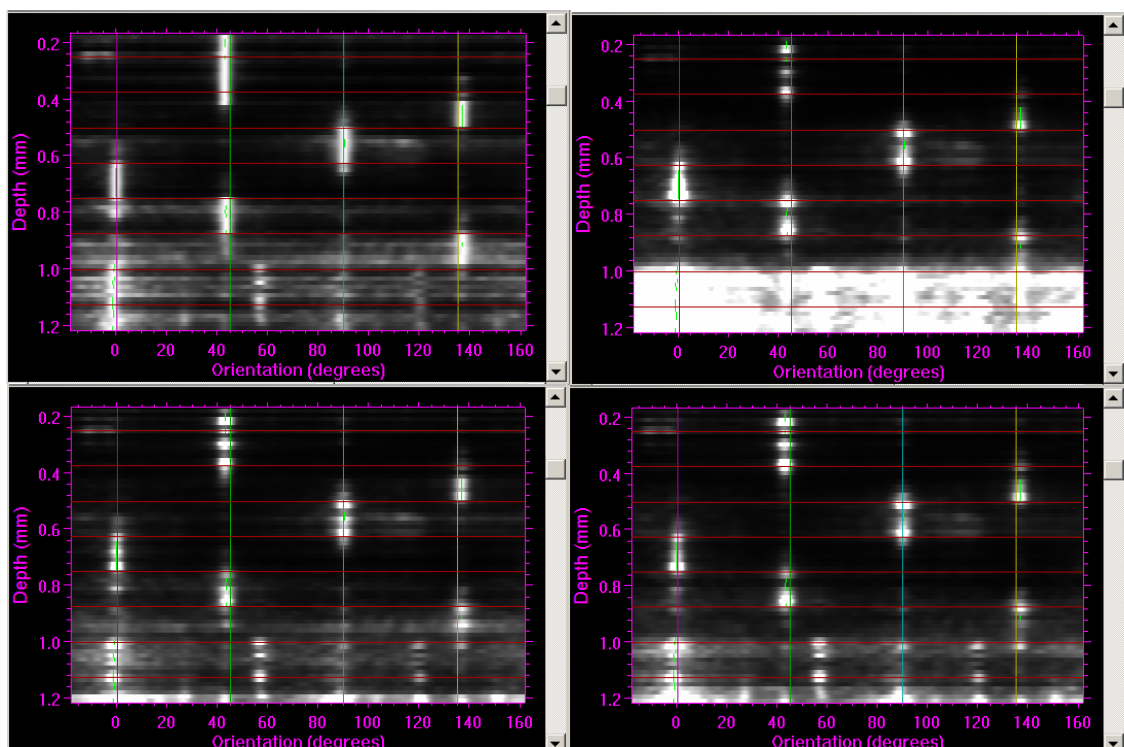


Figure 6-32. Examples of different normalisation methods: peak in layer (top-left), exponential fit (top-right), 5-layer running average (bottom-left), 9-layer running average (bottom-right).

6.5.3 Max-Min normalisation.

The biggest problem with the above normalisation methods is that the noise level in the angular distribution is also affected. Noise manifests itself mainly as an angle-independent elevation in amplitude in the angular distribution.

Therefore, a method of spreading the colour or greyscale levels over just the range from the maximum to the minimum angular amplitude, results in setting all the background levels to black and providing a uniform background against which the peaks can be more easily observed. Max-min normalisation has become the standard for ply stacking sequence visualisation and analysis.

6.5.4 Resolution requirements

It is known from the modelling work discussed in this thesis that the source of reflections within the composite is the inter-ply resin layer, the thickness of which dictates the amplitude of the reflection. However, the dominant resonances in the response are at frequencies governed by the ply spacing and the variations in resin layer thickness just modify the amplitude of the resonant response. It is also known that the main cause of variations in the inter-ply resin layer thickness is the presence of fibre tows, or bunches of fibres within each ply. It is these variations that are imaged and used to determine fibre orientation.

For adequate stacking sequence determination, the basic requirement is to resolve the in-plane variations in local reflection amplitude due to the fibre tows in each ply in the stack. These fibre tows have a width from 1 mm to 5 mm, depending on the method of manufacture of the composite material. Thus it is necessary to ensure that the ultrasonic pulse-echo beamwidth is less than the fibre-tow width over the whole depth of the structure being inspected.

For an acquisition system with a fixed focal length (ie without phased-array dynamic focusing or full-matrix capture and array processing) it is therefore necessary to choose a focused transducer to achieve this requirement, and focus it at the mid-depth in the structure.

The two focusing requirements are:

1. -6 dB pulse-echo focal beamwidth < fibre tow width
2. -6 dB pulse-echo range of focus > thickness of the structure

Initially dealing with these requirements separately, the focal beamwidth is defined as follows (see Appendix E on focused fields):

$$w_f = 1.032\lambda_w F_w \quad (6-9)$$

where w_f is the -6 dB pulse-echo focal beamwidth, λ_w is the wavelength in water and F_w is the F-number in water, defined as in optics, as:

$$F_w = \frac{z_f}{D} \quad (6-10)$$

where z_f is the focal length and D is the aperture (transducer) diameter.

The resonant frequency required for stacking sequence imaging is the half-wave resonance where the wavelength in the composite λ_c is twice the ply spacing, z_{ps} . The resonant wavelength in water λ_w can then be determined:

$$\lambda_w = 2z_{ps} \frac{c_w}{c_c} \quad (6-11)$$

where c_w is the speed of sound in water and c_c is the speed of sound in composite. As the speed in water is approximately half that in composite, the following approximation can be made without undue effect on the conclusions of this treatment of resolution.

$$\lambda_w \approx z_{ps} \quad (6-12)$$

Substituting into Equation 6-9, a similar approximation can be made, to determine the focal beamwidth:

$$w_f \approx z_{ps} F_w \quad (6-13)$$

If the requirement is that the focal beamwidth w_f should be less than the fibre-tow width w_t then the following requirement defines the upper limit on F-number, based on the ratio of fibre tow width and ply spacing:

$$F_w < \frac{w_t}{z_{ps}} \quad (6-14)$$

Secondly, the requirement for the range of focus to be greater than the material thickness d provides a lower limit on F-number. An equation for the -6 dB pulse-echo range of focus in water z_r is derived in Appendix E and is equivalent to:

$$z_r = F_w (5.44\lambda_w F_w + 0.072D) \quad (6-15)$$

Appendix E also shows that this can be approximated to the following for focal gains in the range that we are expecting to use: 0.2 to 0.7.

$$z_r \approx 6\lambda_w F_w^2 \quad (6-16)$$

As the requirement is for z_r to be greater than the material thickness d in composite, or approximately $2d$ in water, and Equation 6-12 links the wavelength to the ply spacing, the following approximation to the requirement for minimum F-number can be made:

$$F_w > \sqrt{\frac{d}{3z_{ps}}} \quad (6-17)$$

Combining these two requirements gives the following limits on F-number:

$$\sqrt{\frac{n}{3}} < F_w < \frac{w_t}{z_{ps}} \quad (6-18)$$

where n is the number of plies in the specimen and is equal to d/z_{ps} .

Practical examples are shown in Table 6-1 with the limiting cases shown in bold. These limiting cases show the maximum number of plies in the stacking sequence for a given ply spacing and fibre-tow width.

Ply Spacing (mm)	Number of plies	Fibre-Tow Width (mm)	Material Thickness (mm)	Minimum F-number	Maximum F-number
0.125	64	1	8	4.6	8
0.125	192	1	24	8	8
0.25	64	1.5	16	4.6	6
0.25	108	1.5	16	6	6
0.25	64	2	16	4.6	8
0.25	192	2	48	8	8
0.25	256	3	64	9	12
0.25	432	3	108	12	12

Table 6-1. Examples of minimum and maximum F-number for various carbon-fibre composite material specifications. Limiting cases are shown **bold**.

It can be seen that the limiting number of plies n_{max} is given by the following equation and is shown graphically in Figure 6-33:

$$n_{max} = 3 \left(\frac{w_t}{z_{ps}} \right)^2 \quad (6-19)$$

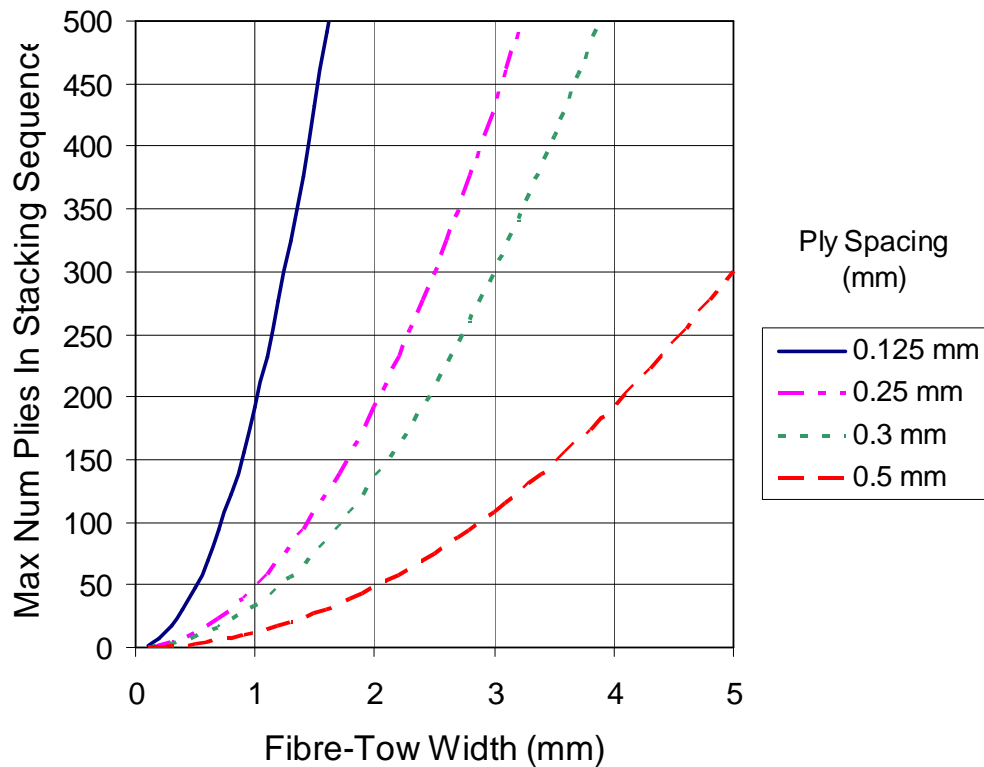


Figure 6-33. Maximum number of plies that can be resolved in the ply stacking sequence if the optimum transducer F-number is selected.

6.6 Spatial-frequency energy distribution and spatial filtering

The spatial-frequency energy distribution is a profile of the all-angle sum of the amplitude-squared at each spatial frequency from the 2D-FFT output. This can be useful for determining fibre-tow widths.

Spatial filtering has various uses within fibre orientation analysis, but primarily the benefits are: a) to speed up the processing by reducing the number of points in the 2D-FFT that need to be analysed, b) to remove the low spatial frequencies where the angles are sparsely populated, or c) to preferentially remove certain frequencies that are adversely influencing the assessment of fibre orientation. High-pass filtering is useful for ply stacking sequence and in-plane orientation or waviness analysis, while low-pass filtering is useful for out-of-plane wrinkling analysis. A notch filter is useful for removing the effects of regularly-spaced stitching in a non-crimp fabric (NCF).

6.6.1 Spatial-frequency distribution

The spatial frequency distribution is calculated from the 2D FFT and suffers similar problems of sparse populations, particularly at low spatial frequencies (Figure 6-34).

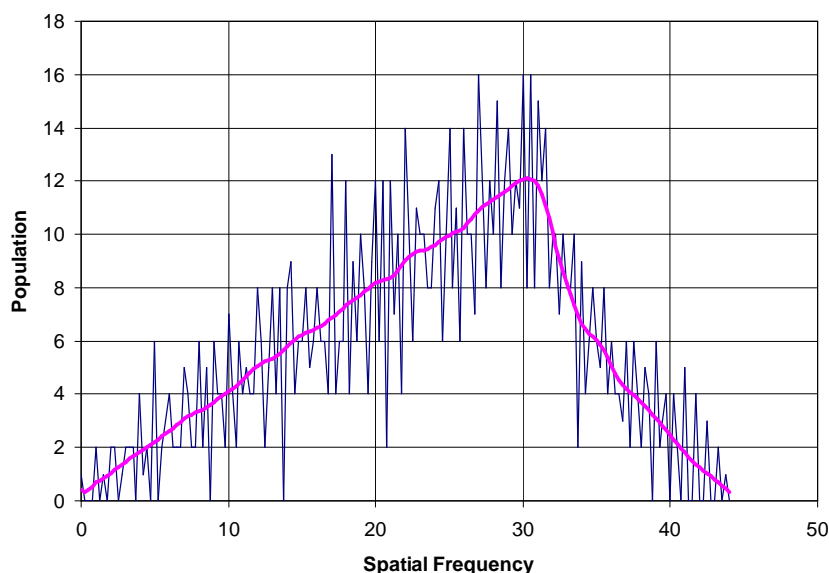


Figure 6-34. Population of spatial frequencies in the FFT (blue) from a 16x16 pixel region and the result of using the Gaussian weighting function (pink) with a $1/e$ half-width of 1 pixel in spatial frequency.

This is overcome by populating spatial-frequency ‘bins’ using a weighting based on a Gaussian function. The $1/e$ half-width of the Gaussian is one spatial-frequency spacing and this is applied out to three half-widths (where the weighting has fallen to $1/e^3$) – see Figure 6-34.

6.6.2 High-pass spatial filtering

A half-Gaussian-shaped edge is used for the cut-off of a high-pass filter in cases where it is known that most of the information is at the high-frequency end of the spectrum. This is the case when the lines in the image are caused by fibre tows and the resolution of the scan has been chosen to be approximately half or a quarter of the fibre-tow spacing. Both the ply stacking sequence and the in-plane waviness imaging methods use the fibre tows as the source of the lines in the image so the operator is asked to specify the maximum fibre tow width and the software uses this to calculate the minimum spatial frequency required, thus defining the high-pass filter cut-off spatial frequency. This is shown for a 10 mm maximum fibre tow spacing in Figure 6-35.

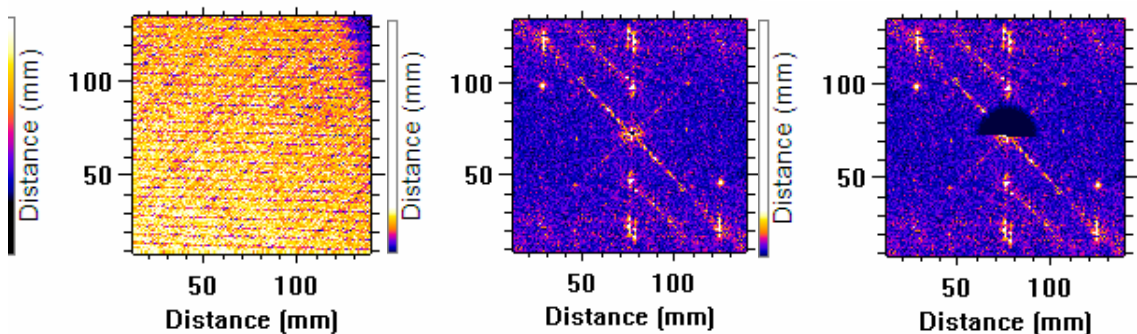


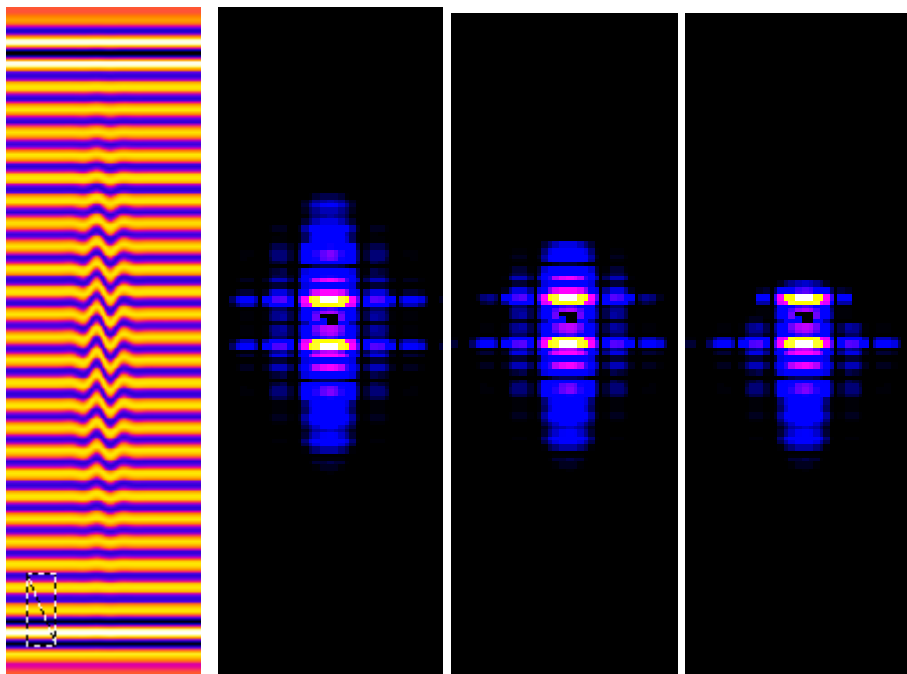
Figure 6-35. C-scan of $+45^\circ/-45^\circ$ plies with 5 mm stitching aligned to the 0° direction (left), the corresponding 2D-FFT (centre) and an example of applying a 10 mm high-pass filter to the top half of the 2D-FFT and the right half of the central (zero frequency) row are used for angular analysis.

6.6.3 Low-pass spatial filtering

A half-Gaussian-shaped low-pass filter cut-off is used in cases where the line spacing is a large proportion of the width or height of the image, which is the case for out-of-plane wrinkling imaging, where just two or three plies are

included in the boxed image. In this case the high spatial frequencies can be ignored and the algorithm runs faster if there are fewer frequencies to process.

It was found that, for out-of-plane wrinkling, the $1/e$ cut-off frequency can be reduced to a fraction $4/n$ of the Nyquist frequency where n is the number of pixels between adjacent lines in the image. Reducing the cut-off frequency further resulted in corruption of the angular information because the main spatial frequency of the plies was being affected – as can be seen in Figure 6-36 where the filter for 16 pixel spacing is beginning to influence the main peak in the 2D-FFT from a 14-pixel line-spacing image..



Filter cut-off for line-spacing: 1 pixel 8 pixels 16 pixels

Figure 6-36. Examples of low-pass spatial filtering applied to the top half of 2D-FFTs from the box (20 x 42 pixels) in the B-scan on the left, where the line spacing is approximately 14 pixels. The cut-off frequencies shown in the 2D-FFT images correspond to line spacings, n , of (left to right) 1, 8 and 16 pixels. Only the top half of the 2D-FFT is used for angular analysis.

6.6.4 Notch Filtering

A notch filter is useful for removing the effects of regularly-spaced stitching in a non-crimp fabric (NCF). In this case a band-gap notch has to be introduced not

only for the fundamental spatial frequency of the stitches, but also for its harmonics. The filter has to go to zero for a region of frequencies either side of the harmonic in order to remove the stitching effects. Thus the function chosen to define this notch filter is...

$$\frac{1 + \sin \chi}{2} \quad (6-20)$$

where χ is limited to a maximum value of $+\pi/2$ and a minimum value of $-\pi/2$ and is defined as follows:

$$\chi = \frac{\pi}{2} + \pi\psi \left(1 - \left| 1 - \frac{2\eta}{f_s} \text{MOD} \left(\frac{f}{f_s} \right) \right| \right) \quad (6-21)$$

where f is the spatial frequency, f_s is the stitching spatial frequency, $\text{MOD}(x/y)$ is a function that takes the remainder of a division of x by y , ψ is the sharpness of the filter and η adjusts the width over which the filter has zero value. Figure 6-37 shows the filter when $\psi = 2$ and $\eta = 1.05$ and Figure 6-38 shows the 2D-FFT with the filter applied, excluding the notch at zero frequency.

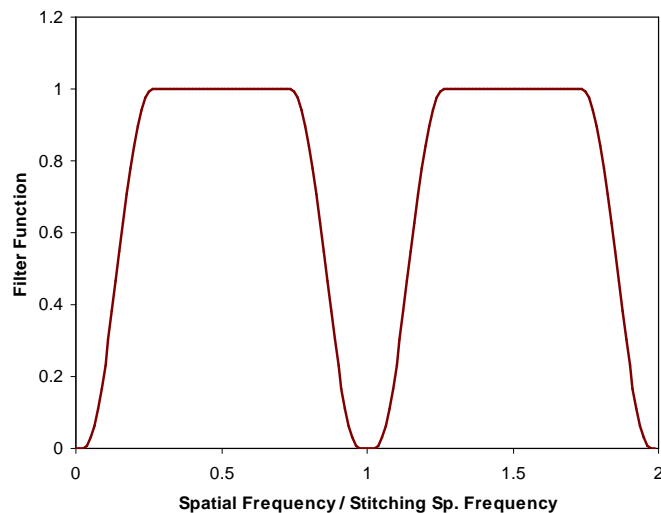


Figure 6-37. Graph showing the first two cycles of the notch filter function when $\psi = 2$ (sharpness of the filter cut-off) and $\eta = 1.05$ (width of the zero region).

Figure 6-39 illustrates the benefit of using this filter for the $+45^\circ / -45^\circ$ panel from Figure 6-35 with $0^\circ/90^\circ$ stitching.

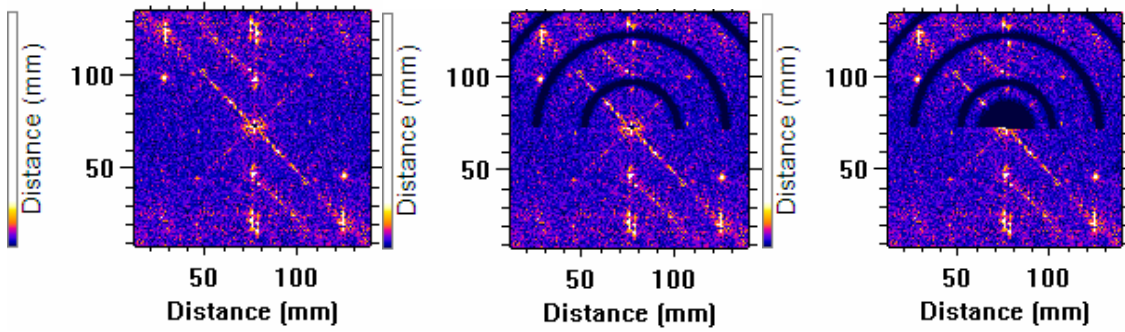


Figure 6-38. The result of applying the notch filter (centre) to the 2D-FFT from Figure 6-35 (left). The notch centred at zero frequency has not been applied, but the high-pass filter can be superimposed (right).

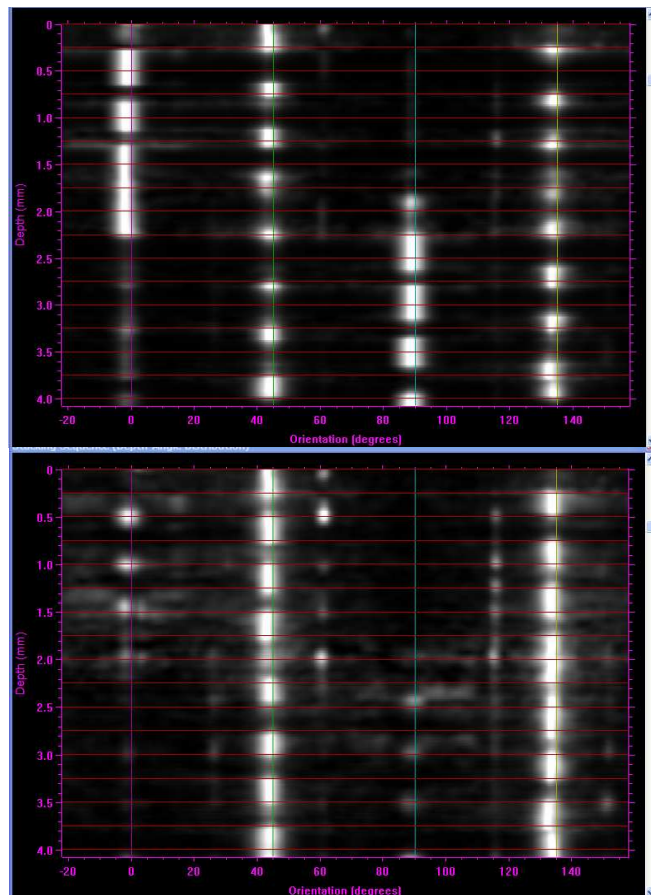


Figure 6-39. Comparison of the ply stacking sequence without (top) and with (bottom) a stitching notch filter for a panel comprising alternating $+45^\circ$ / -45° plies with stitching spaced at 5 mm in the 0° and 2.6 mm in the 90° direction.

It can be seen that the majority of the $0^\circ/90^\circ$ indications have been filtered out. However, there are now some weak $0^\circ/60^\circ/120^\circ$ indications, which appear to come from the points in the 2D-FFT (see Figure 6-38) that have been missed by

the omni-directional notch spatial-filter. This result suggests that it may be necessary to calculate different spatial filters in different directions by requesting the operator to input multiple stitching directions and spacings.

This was investigated next, for the same panel where, in the top half of the panel, the stitching is at 5 mm spacing in the 0° direction but at 2.6 mm spacing in the 90° direction. Figure 6-40 shows the filters being applied separately and illustrates that all the stitching responses (dots in the 2D-FFT) have been effectively removed. The result is shown in Figure 6-41 (top) where the mainly 0° stitching has been removed.

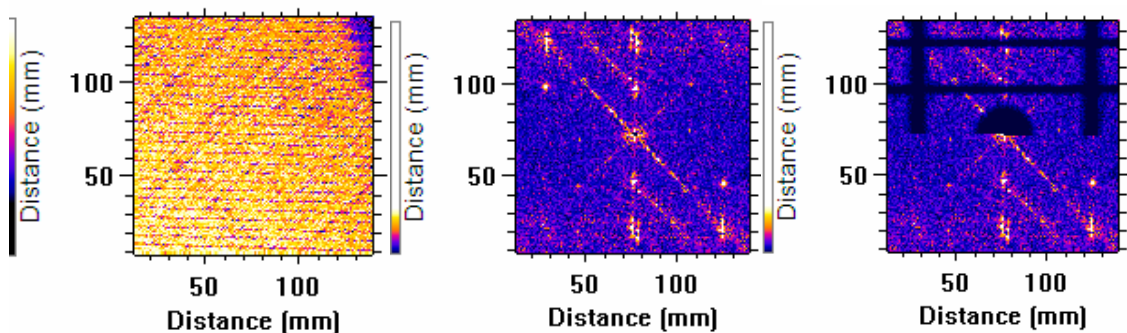


Figure 6-40. Separate $0^\circ/5\text{mm}$ and $90^\circ/2.6\text{mm}$ notch filters applied (right) to the same 2D-FFT (centre).

However, in the lower half of the panel the plies are turned over and round by 90° , giving 90° stitching at 5 mm spacing. The stitching has not been removed in the lower half of the panel because, whilst 2.6 mm is close to a harmonic of 5 mm, the reverse is not true, so the best option is to filter out 5 mm stitching at both 0° and 90° - see Figure 6-41 (bottom).

In the case of the panel illustrated, the separate stitching filters are very successful, but there are instances where this is not the case, such as when both fibre directions and stitching directions coincide.

6.7 Discussion

In this chapter a complete basis for ultrasonic fibre orientation measurement has been outlined, including refinements for improved processing and visualisation of the results and avoidance of aberrations.

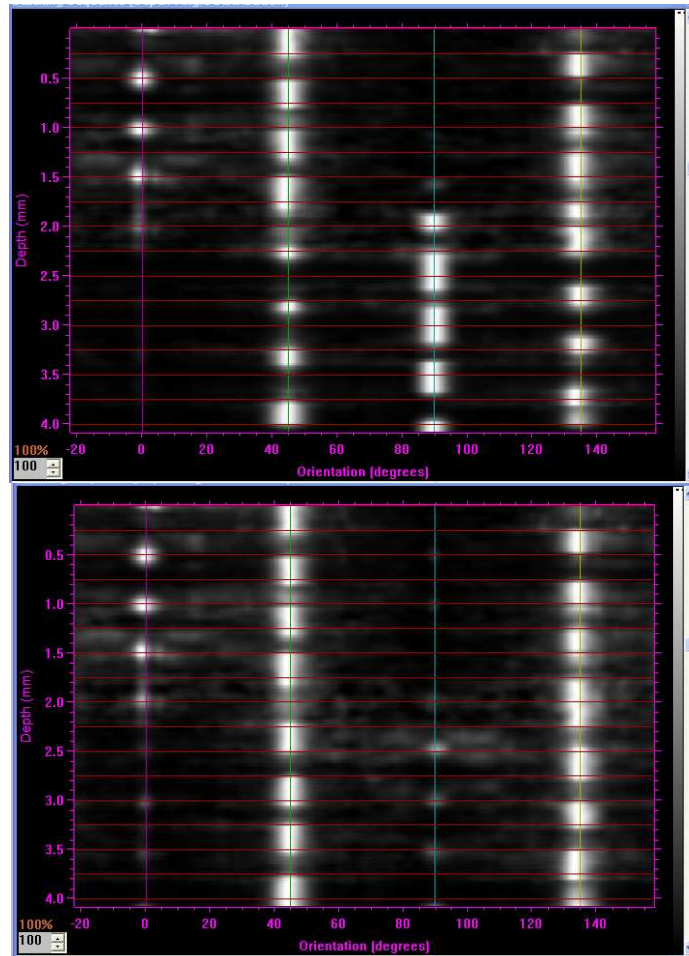


Figure 6-41. Comparison of the ply stacking sequence with (top) separate $0^\circ/5\text{mm}$ and $90^\circ/2.6\text{mm}$ notch spatial filtering and with (bottom) separate $0^\circ/5\text{mm}$ and $90^\circ/5\text{mm}$ notch filters for a panel comprising alternating $+45^\circ / -45^\circ$ plies with stitching spaced at 5 mm in the 0° and 2.6 mm in the 90° direction.

Various corrections have been identified, calculated, and applied to the data in order to provide unbiased measurements of fibre orientation and further validation of these will be discussed in Chapter 7. An important factor is that the data should be of adequate quality and a recommended specification for the focal characteristics of the transducer have been provided to ensure good resolution of fibre tows for in-plane orientation.

The application of the method to ply stacking-sequence determination, in-plane waviness and out-of-plane wrinkling has also been described, paving the way for a complete 3D characterisation of the 3D fibre orientation, which will also be described in Chapter 7 on *Validation and Application*.

CHAPTER 7 VALIDATION AND APPLICATION

7.1 Ply spacing and fibre volume fraction mapping

7.1.1 *Rationale*

The research work reported in Chapter 5 went a long way towards solving the problems associated with 3D mapping of ply spacing and fibre volume fraction (FVF) in composites. There are remaining issues to do with the measurement of local resonant frequency, from which the ply spacing measurement is derived. These have been taken as far as possible within the current project and will be revisited in the near future. In this chapter it is important to address the validation and application of the methods to real composite structures. In addition, certain assumptions were made in Chapter 5, which need to be considered in this chapter in terms of their validity and practicality.

The equations derived in Chapter 5, Section 5.3.3 for combined ply spacing and FVF assessment have been put into a function: *CalculatePlySpacingAndFVF()* within the ANDSCAN software package in order to allow comparison in this chapter with data from simulated and real specimens.

7.1.2 *Validation of assumptions*

During the derivation of the equations, the Hashin (1965) equivalent-medium mixture rule was used as it has been shown to be valid for long carbon fibres in resin. This assumes even distribution of fibres in the resin and such an assumption needs ultimately to be tested against real components using micro-sectioning, but over the size of volume element dictated by the ultrasound beam – about 2.5 mm for a typical focused probe, and around one ply in depth – the average distribution should be fairly even.

The other assumption that was made when deriving these equations was that fibres do not move laterally within a ply when the ply gets thicker or thinner. This assumption needs to be valid over the size of the ultrasound beam – about 2.5 mm for a typical focused probe – meaning that the average number of fibres in a 2.5 mm width of a ply should remain approximately constant. At this stage it

is not known if this assumption is valid, but a programme of work is commencing at QinetiQ to determine this using analysis of micro-sections.

The method for ply-spacing and FVF determination assumes that the operator inputs 'as designed' nominal values for both parameters. However, knowledge of these parameters may not be well established, so the method is really designed just to measure 3D variations in the two parameters. For this reason the software was designed to output %-change in ply spacing or FVF. Even then, the UoN/QQ model is required to calculate the 'as designed' nominal resonant frequency, making assumptions about modulus and density for both fibre and resin. Any inaccuracies in the nominal values for ply spacing, FVF, modulus or density would merely result in an overall offset in ply spacing and FVF across the whole panel.

7.1.3 Measurement of Resonant Frequency

Work reported in Section 5.3.4 on the measurement of local resonant frequency as a way of determining ply spacing and FVF has shown that this is not straightforward. Five different methods have been tested and three of them (Frequency of Peak, -6 dB Centre Frequency, and Cross-Correlated Resonant Frequency) work well on single simulated thick plies embedded in a stack of equally-spaced plies. However, as the randomness in ply spacing increased, the tracking of the ply spacings became gradually less accurate, suggesting a need to further develop the method in the future for more variable ply spacings.

In Figure 7-1 and Figure 7-2 an additional dependence of resonant-frequency measurement on the incident pulse spectrum is illustrated. When the centre frequency of the incident waveform is *not* exactly at the resonant frequency of the plies, both the centre frequency and the pulse-echo bandwidth influence the measured peak frequency. For this reason an inverse filter has been developed to correct for the incident pulse spectrum before measurement of resonant frequency. However, it has been difficult to keep this stable because an inverse filter of this kind tends to amplify the high and low frequencies.

The quantitative 3D profile method for ply spacing and FVF would therefore benefit from further work on resonant frequency measurement.

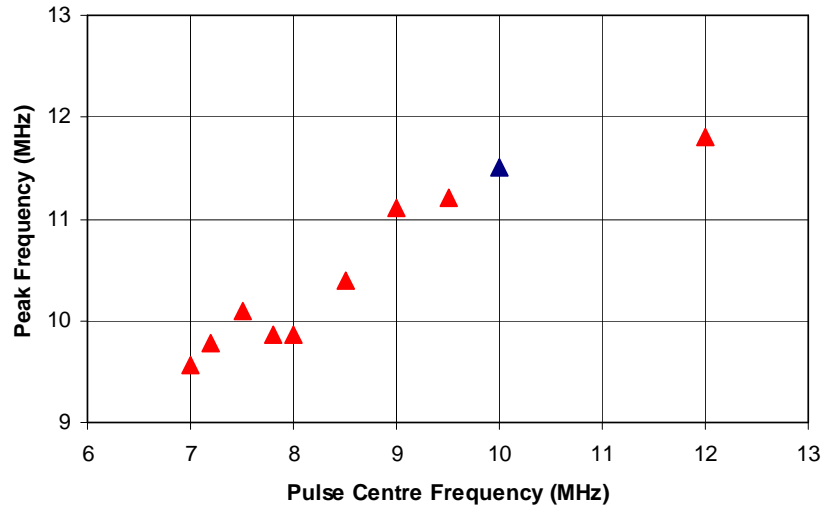


Figure 7-1. Dependence of measured resonant frequency of 0.125 mm plies on the incident pulse frequency for a simulated incident pulse with Q factor 0.8. The blue triangle is the 10 MHz, Q=0.8 point at which this graph crosses the one in Figure 7-2.

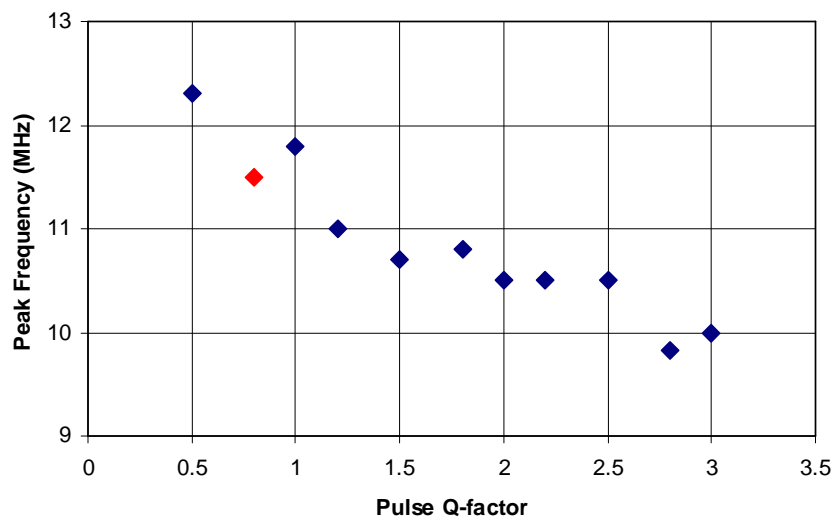


Figure 7-2. Dependence of measured resonant frequency of 0.125 mm plies on the incident pulse bandwidth (Q-factor) for a simulated incident pulse with centre frequency of 10 MHz. The red diamond symbol is the 10 MHz, Q=0.8 point at which this graph crosses the one in Figure 7-1.

7.1.4 Simulated changes in ply spacing and FVF

A simulated wrinkle is a good example of changes in ply spacing and simulated wrinkles were produced using the Gaussian-weighted sine-wave method from Appendix G to test the ply spacing and FVF analysis – see Figure 7-3.

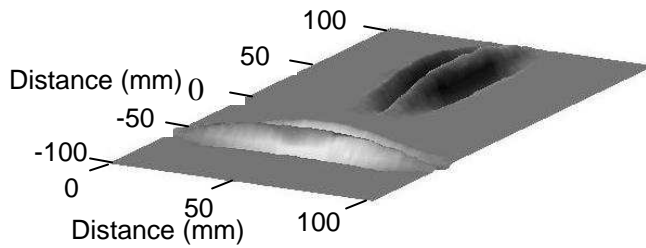


Figure 7-3. Picture of two simulated 0.5 mm amplitude wrinkles used for testing.

For FVF determination (Figure 7-4), the Frequency Of Peak method (Section 5.3.4) was used to determine resonant frequency, with a quadratic fit to the top five points of the resonance peak to measure its frequency more accurately.

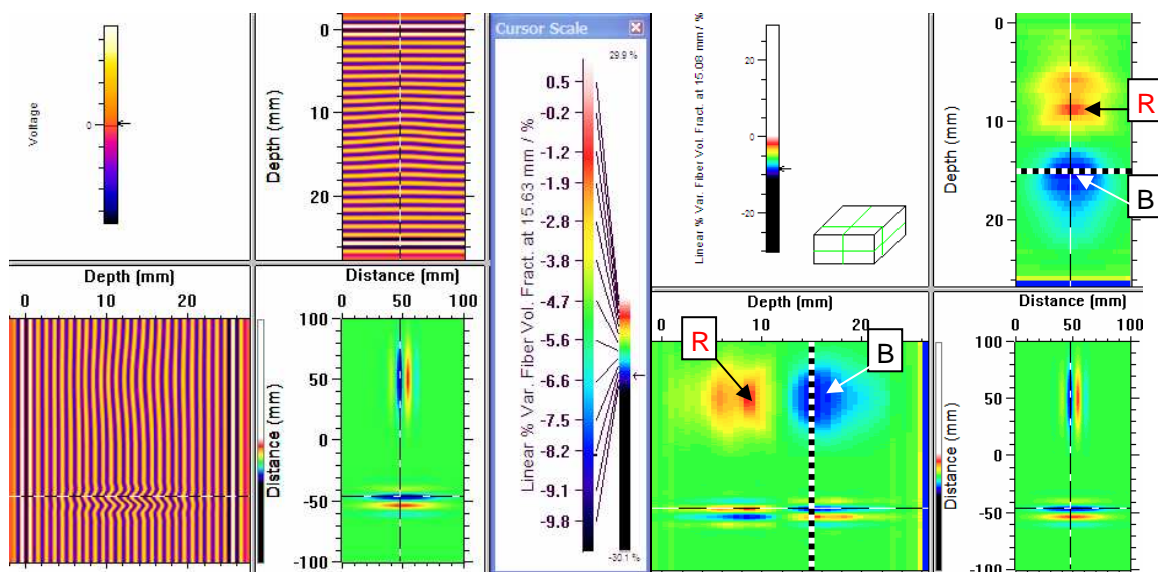


Figure 7-4. B-scan cross-sections (left) and cross-sections through a 3D profile (see Section 5.2.2) of percentage variation in FVF (right). Red (R) represents a 5% increase in FVF where plies have been squashed together. Blue (B) is a 5% reduction where plies have been separated. 50% Hanning windowing was used.

In the lower part of the simulated specimen in Figure 7-4, a gradual increase in ply spacing (reduction in FVF) has resulted in a blue roughly-spherical volume in the FVF 3D-profile – shown as blue circular area ‘B’ in the cross-sections. A gradual decrease in ply spacing results in an orange-red ‘R’ spherical volume.

It was found that the gate width used to create the spectrum at each depth is quite critical. A gate of just over two cycles of the normal resonant frequency is recommended, with a 50% Hanning window applied. Reducing the windowing to 20% of the gate results in banding through the depth, as shown in Figure 7-5.

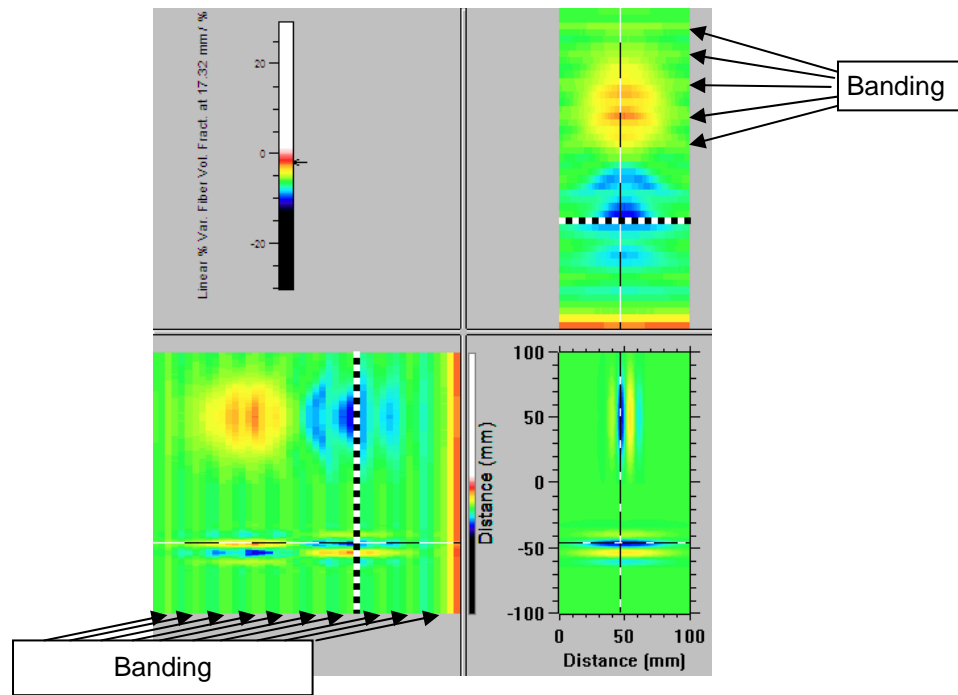


Figure 7-5. Image of the 3D profile of FVF showing that with just 20% Hanning windowing there is ‘banding’ through the depth as marked.

7.1.5 FVF and ply spacing changes in a real specimen

A similar FVF analysis (50% Hanning window on a gate just wider than two cycles of the resonant frequency) was performed on experimental data from the *real* wrinkle shown pictorially in Figure 7-6, and the results are in Figure 7-7.

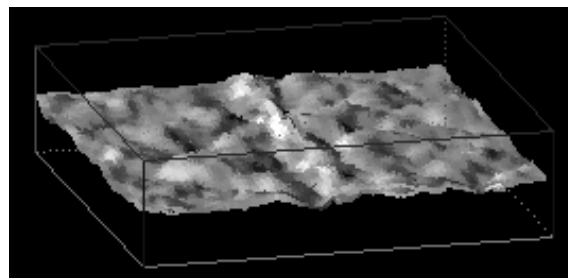


Figure 7-6. A rendered Pseudo-3D image of the surface heights of a ply 2/3 of the way through a real specimen, produced using the method from Chapter 6.

Considering the poor agreement of this FVF method with simulated 30%-random ply spacings in Section 5.3.4, the FVF profile in Figure 7-7 seems remarkably plausible. This is because ply-spacing variations in a wrinkle are *not* random and the ultrasound resonant frequency can respond gradually through the thickness, as for the well-behaved simulated wrinkle in Figure 7-4.

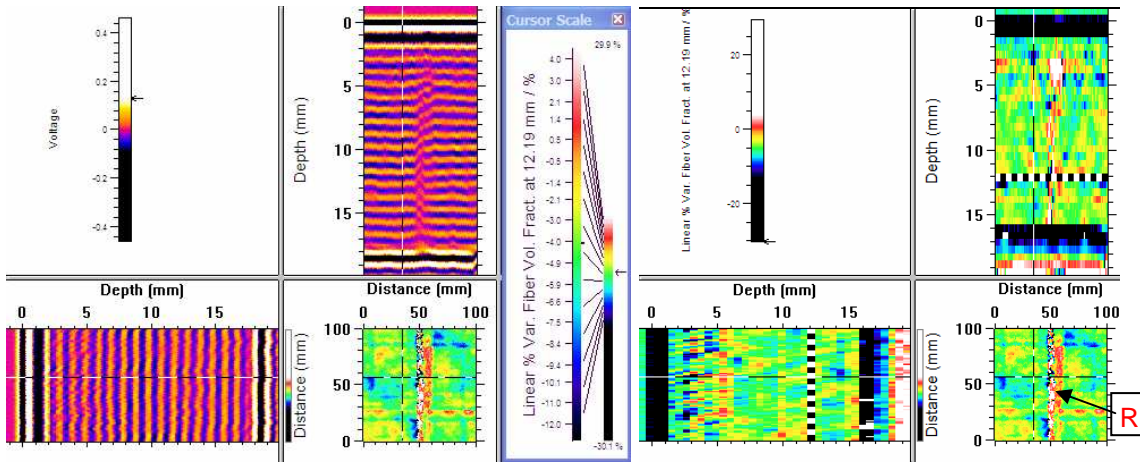


Figure 7-7. Experimental data from a real wrinkle in the 18 mm thick composite panel shown in Figure 7-6. B-scans (left) and 3D profile of FVF (right). As above, red (R) is a 5% increase in FVF and blue a 5% decrease.

The final example for FVF profiling is the 32-ply pre-preg panel with removed and added triangular ply cut-outs, shown diagrammatically in Figure 7-8.

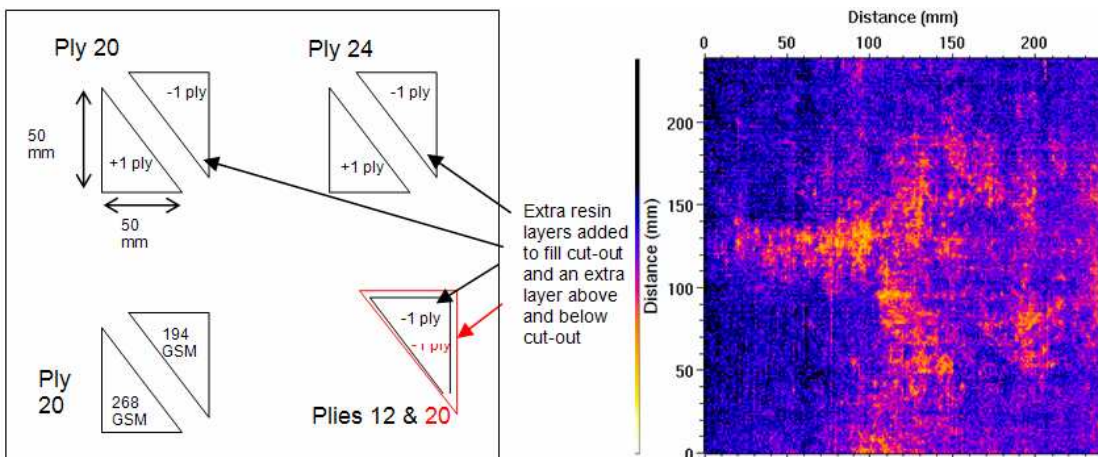


Figure 7-8. Diagram (left) and experimental data from a back-wall echo C-scan (right) for the 32-ply panel with triangular ply cut-outs at the pre-cure lay-up.

This is an extreme case of FVF variation. However, as a measure of ply spacing variation, it is a useful example. Where there is a ply cut-out there is generally a localised region of twice the ply spacing but with one ply's worth of fibres, giving a halving of FVF (60% down to 30%). This is seen in the FVF 3D-profile (see Section 5.2.2) in Figure 7-9 where blue-black regions quantify a 20-30% reduction in FVF. But when a ply has been added, the ply spacings even out through the thickness giving just a 1/32 increase in FVF (60% to 62%).

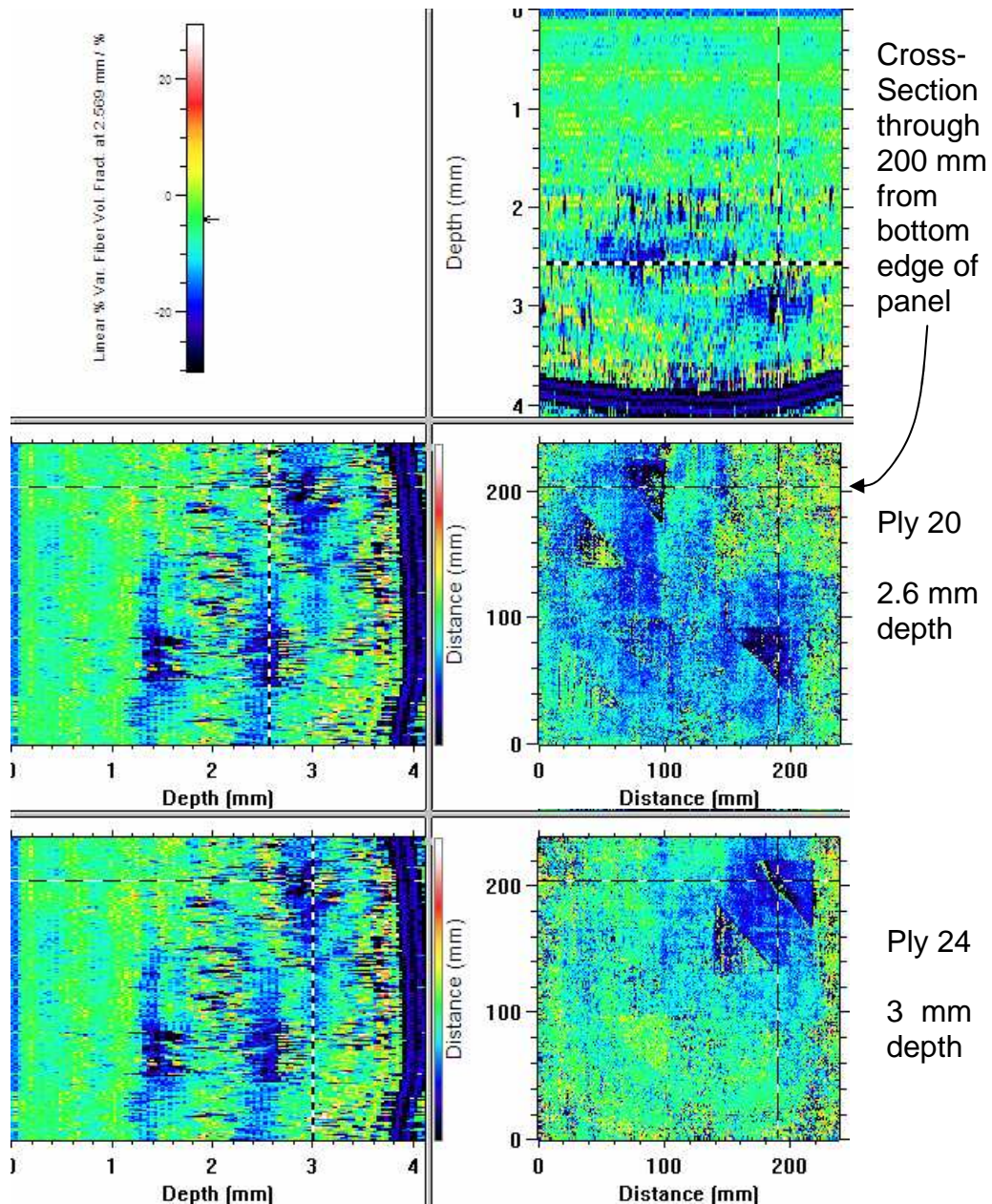


Figure 7-9. Cross-sections through a 3D FVF profile (see Section 5.2.2) created for the 32-ply stack of 0.125 mm plies – see Figure 7-8 - where triangular cut-outs have been removed at ply 20 (middle row, 2.57 mm depth) and ply 24 (bottom row, 3.01 mm depth) and extra triangular-shaped plies have been inserted. Note that the removed plies result in a reduction from 60% to 30% FVF and the added plies result in an increase from 60% to 62% (discussed in the main text).

In all these examples on real structures, the Frequency of Peak method used to calculate resonant frequency has been successful in generating plausible 3D profiles of FVF, suggesting that ply-spacing randomness is not a major problem.

7.2 Porosity and thick resin layer mapping – The Porosity Meter

The Decomposition Method (Section 5.5) was clearly the most promising method developed so far, with potential for becoming a 3D *porosity meter*. Initially the decomposition method was tested using the model to simulate waveforms from a 32-ply stack of 0.125 mm plies. Section 5.5 included quantitative studies of this work but the current section is looking at the implementation in ANDSCAN and is leading to use of the method on data from real structures.

7.2.1 Performance of the Decomposition Method

The first assessment was made qualitatively to assess cross-talk between the porosity and thick-resin-layer coefficients (Section 5.5.12). It is important that the coefficients correctly distinguish between the two defect types. The method of determining cross-talk is by measuring both coefficients in the presence of just one of the defect types. This is illustrated on time-frequency plots from ANDSCAN in Figure 7-10 to Figure7-12. The analytical model was used to simulate waveforms from a 32-ply stack of 125 μm thick plies separated by 2 μm resin layers with a thick resin layer before ply 7 and a layer of porosity at layer 18. The gate width was the equivalent of 2.2 plies (280 μm) and a Hanning taper window was used over 50% of the gate (25% at each end).

These images seem to show more cross-talk between the two coefficients – porosity and thick resin layers – than the quantitative assessment in Section 5.5.12 (Figure 5-43) would suggest. However, in Section 5.5.12, no windowing was used on the gated waveform segment before transforming it to the frequency domain. When the windowing was turned off, the analysis of the same simulation from Figure7-12 was improved to give a much lower cross-talk (see Figure7-13). This suggests that windowing can cause cross-talk between the two coefficients, which may be explained as follows. The thick-resin-layer basis function is a constant slope in the frequency domain (for frequencies well below the resonance of the resin layer), whilst the porosity basis function is a series of quarter-wave resonances and anti-resonances. The cross-talk shown

in Figure7-12 suggests that windowing causes a response from simulated porosity in the thick-resin-layer basis function due to the presence of energy at the expected anti-resonances, flattening the spectrum.

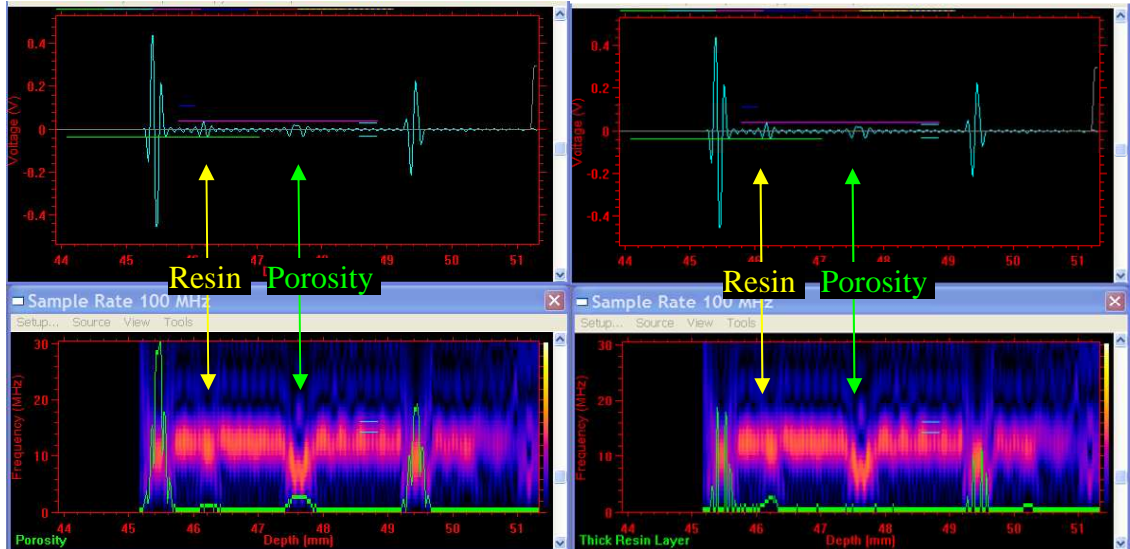


Figure 7-10. Simulated waveforms (top) and time-frequency plots (bottom) for 10 μm thick resin layer at ply 7, 10% porosity (10 μm radius) at ply 18 in a 32-ply stack, showing the porosity coefficient (left) and the thick resin layer coefficient (right) in green overlaid on the time-frequency plot.

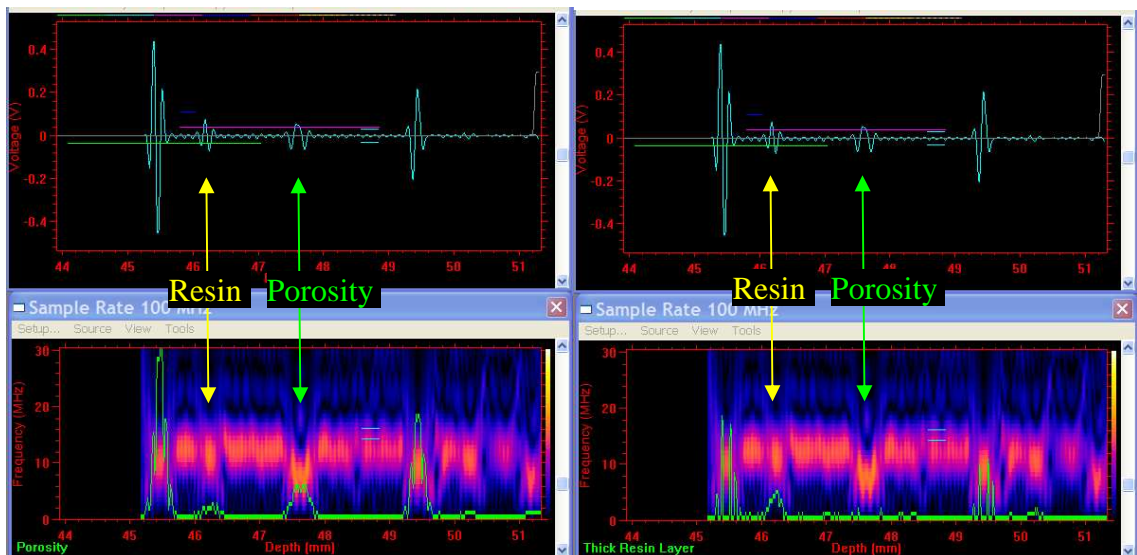


Figure7-11. Simulated waveforms (top) and time-frequency plots (bottom) for 20 μm thick resin layer at ply 7, 20% porosity (10 μm radius) at ply 18 in a 32-ply stack, showing the porosity coefficient (left) and the thick resin layer coefficient (right) in green overlaid on the time-frequency plot.

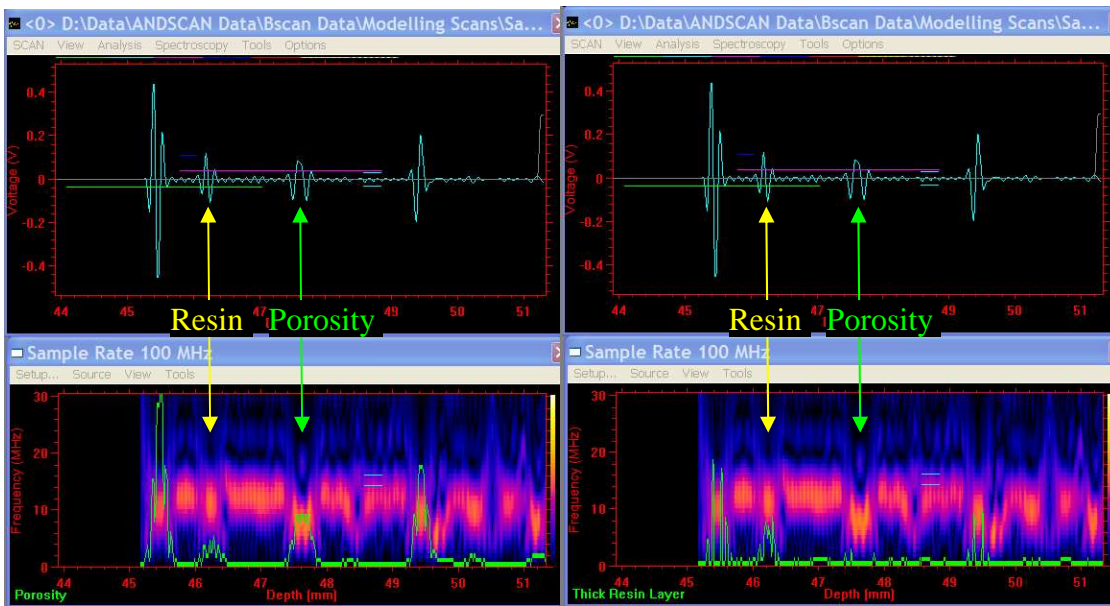


Figure 7-12. Simulated waveforms (top) and time-frequency plots (bottom) for 30 μm thick resin layer at ply 7, 30% porosity (10 μm radius) at ply 18 in a 32-ply stack, showing the porosity coefficient (left) and the thick resin layer coefficient (right) in green overlaid on the time-frequency plot.

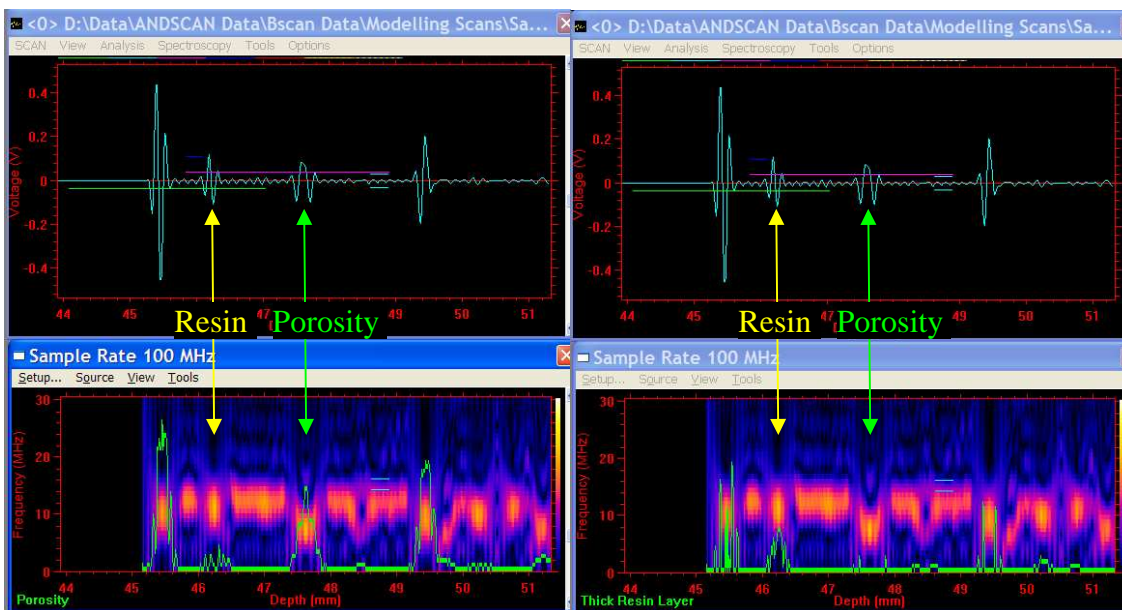


Figure 7-13. The same simulation as in Figure 7-12 but without windowing the gated waveform before transforming to the frequency domain, resulting in reduced cross-talk between the two effects – porosity and thick resin layers.

Further work is required to investigate and understand this effect and then determine how to minimise its effect. Additional trials will determine whether windowing is required and, if so, what kind of windowing is optimum.

7.2.2 Multiple layers of similar porosity levels

It was found that, due to the way the porosity basis function works, it is not sensitive to porosity in layers that are between other layers with the same amount of porosity (see Figure 7-14). At present it is not clear how detrimental this will be for the 3D porosity meter, because it is thought unlikely that identical amounts of porosity will exist in adjacent volume elements. An initial test using simulated waveforms with random amounts of porosity (Figure 7-14) suggested that, even with 20% variation in porosity, this still does not increase the sensitivity to intermediate plies significantly.

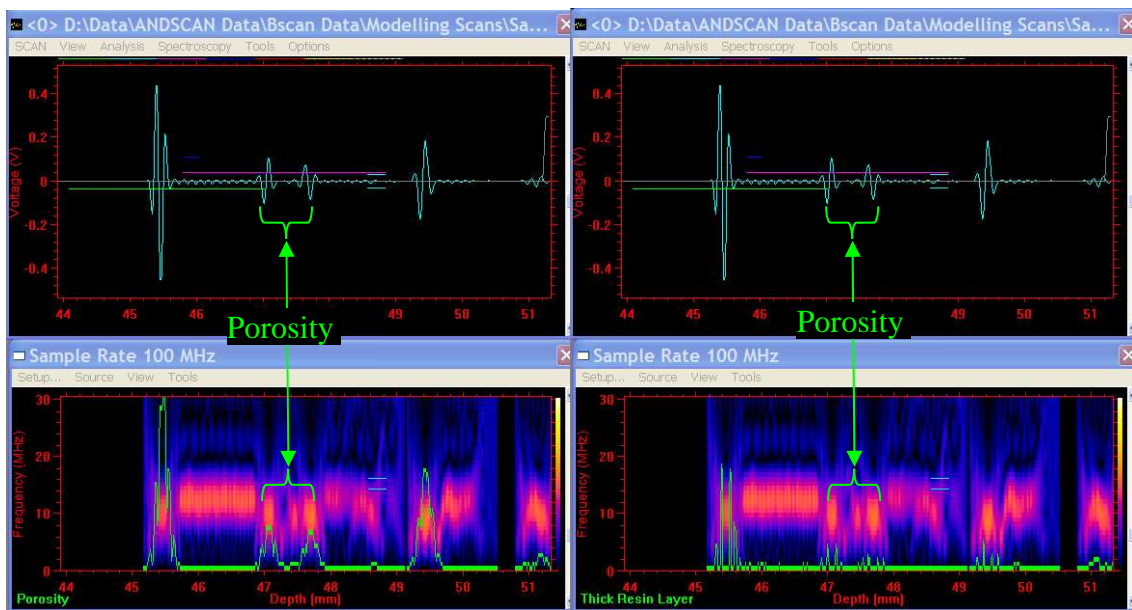


Figure 7-14. 30% \pm 6% porosity in plies 14 to 18 (ie with 20% randomness in the amount of porosity in adjacent plies), showing the porosity coefficient (left) and the thick resin layer coefficient (right) in green overlaid on the time-frequency plot. Note that only the first and last plies really register with the porosity coefficient.

7.2.3 Performance on real components

Figure 7-15 shows 3D profiles of porosity and thick resin layers generated using the Model-based Decomposition Method for the 32-ply panel shown in Figure 7-8. At present too little is known about the actual 3D distribution of porosity and thick resin layers to use this as any sort of validation. However, micro-sections suggest there is porosity in regions with high porosity coefficients in this image.

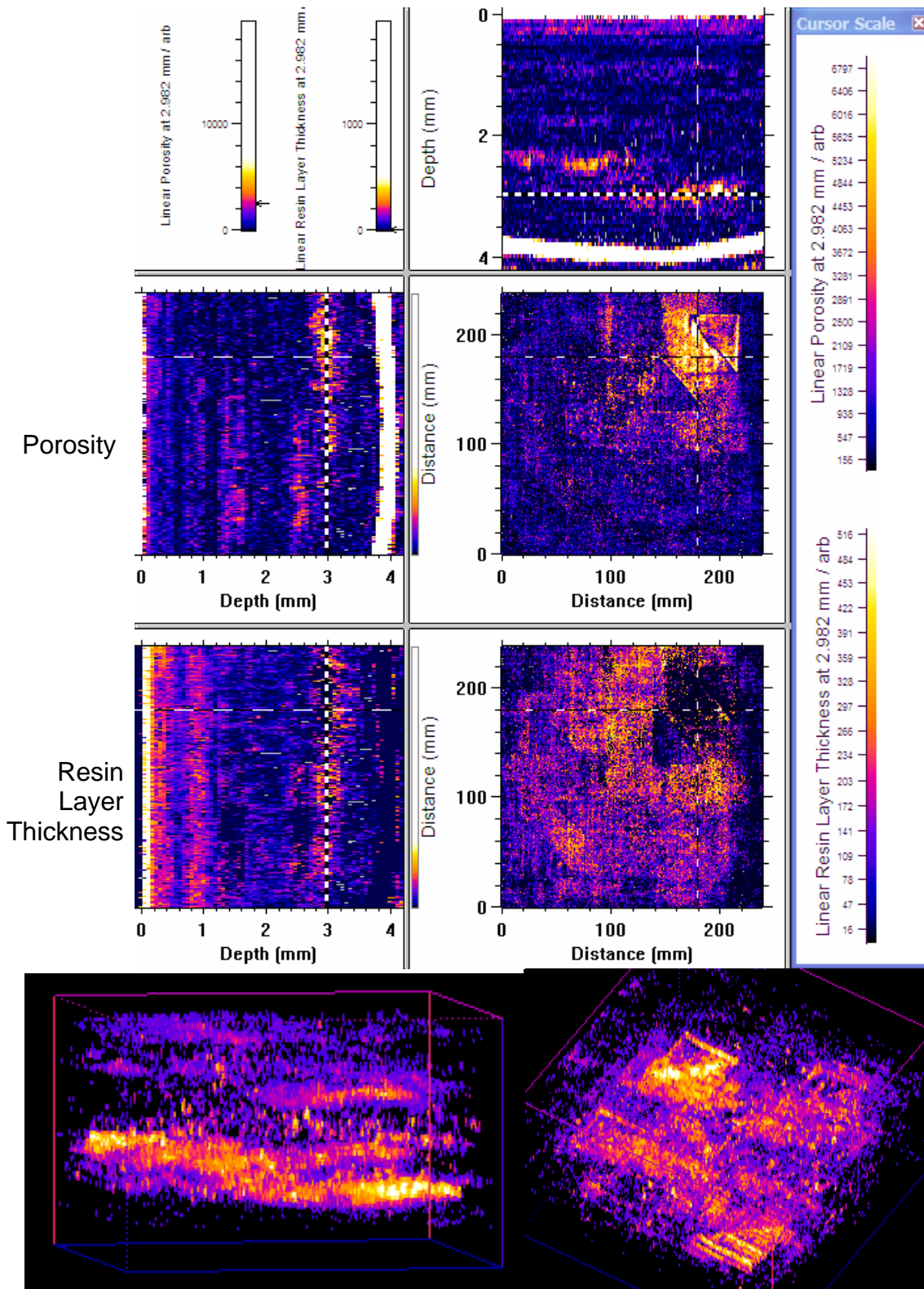


Figure 7-15. 3D profiles (see Section 5.2.2) of the porosity (top images and scale) and thick-resin-layer (middle images, bottom colour scale) coefficients. Pseudo-3D profiles of the porosity coefficient (bottom). Experimental data from the 32-ply panel in Figure 7-8 containing triangular ply cut-outs from which porosity has formed. Coefficients are uncalibrated and are in arbitrary units.

Micro-CT X-Ray provides a possible method for qualifying ultrasonic 3D porosity-characterisation methods. Recent Micro-CT images of some parts of this panel show significant amounts of porosity, mainly long tubular voids following the fibre orientations. Figure 7-16 has less than 1% average porosity.

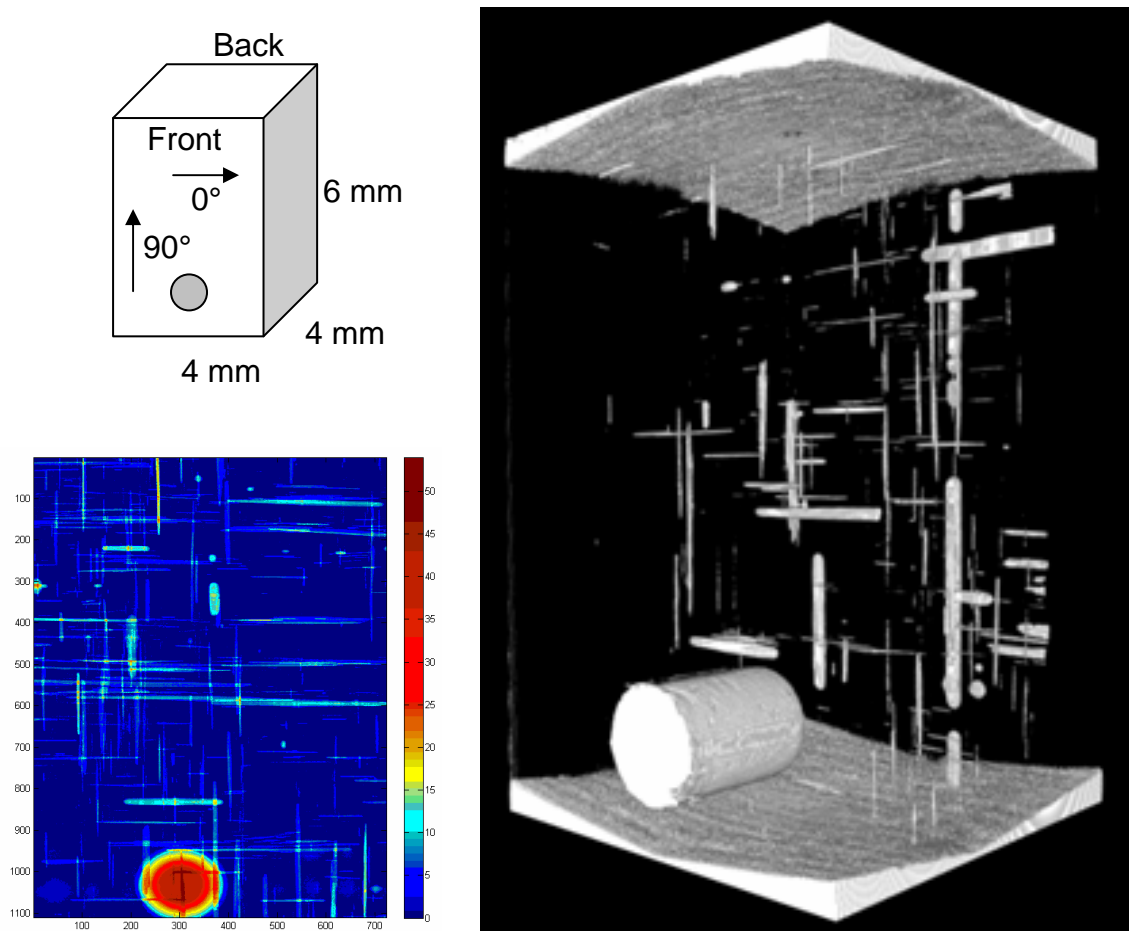


Figure 7-16. Micro-CT X-ray data of porosity in a 4 mm x 4 mm x 6 mm section of the same 0/90° specimen. The voxel size is approximately 5 μ m in width, length and height. The large cylindrical feature at the bottom is a hole drilled to provide accurate registration of the ultrasonic data with the Micro-CT data. The colour map is the through-thickness average porosity from the Micro-CT data.

In order to ensure that the porosity seen in Figure 7-16 is all that there is, and that there is no cloud of small voids, through-thickness summation of pixels below a threshold was performed for a range of thresholds. The results, plotted in Figure 7-17, and the 3D images at each threshold (eg Figure 7-18) showed that only porosity existed below a threshold of 60 [8-bit levels], but that the fibres themselves started contributing at thresholds above 60.

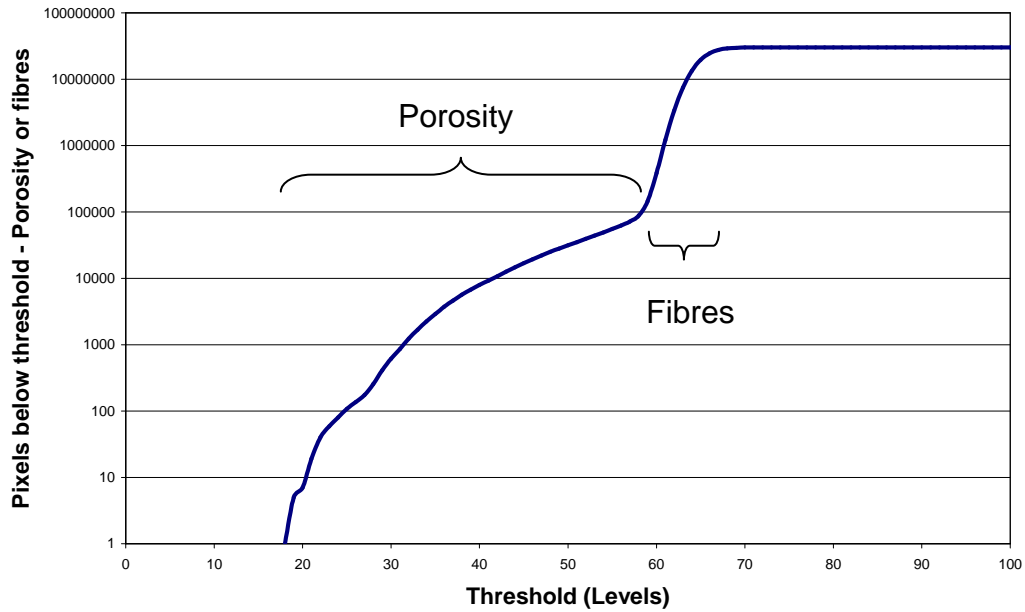


Figure 7-17. The number of pixels below the threshold as a function of threshold level. The sudden sharp rise beyond a threshold of 60 (8-bit) levels is where the fibres start to be counted. Below 60, just the porosity is counted.

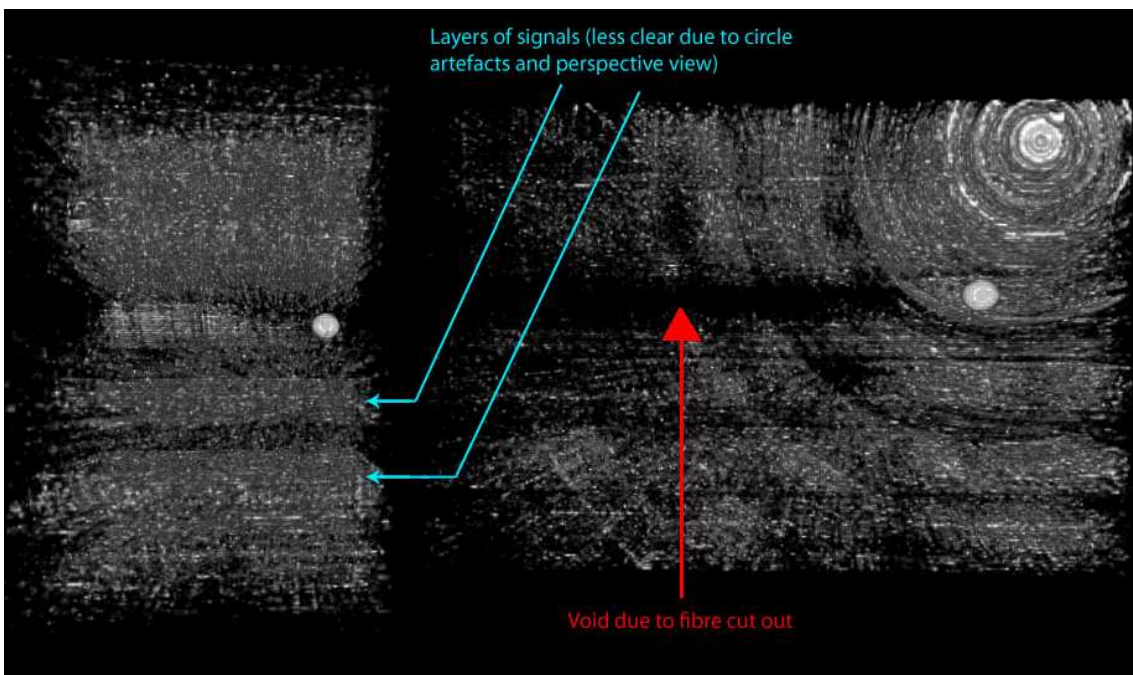


Figure 7-18. Two Micro-CT images of the same specimen with a threshold above 60 levels, showing that fibres are contributing a significant amount, except in the ply cut-out region where only resin exists. Both images show a vertical stack of plies in perspective view but from different viewing angles.

In addition, the back-wall echo attenuation from the ultrasonic data was compared with the through-thickness average porosity from the Micro-Ct data in order to check that the expected trend would be observed. All current porosity inspections are based on this trend and a correlation coefficient (R) of 0.925 is observed from the analysis in Figure 7-19.

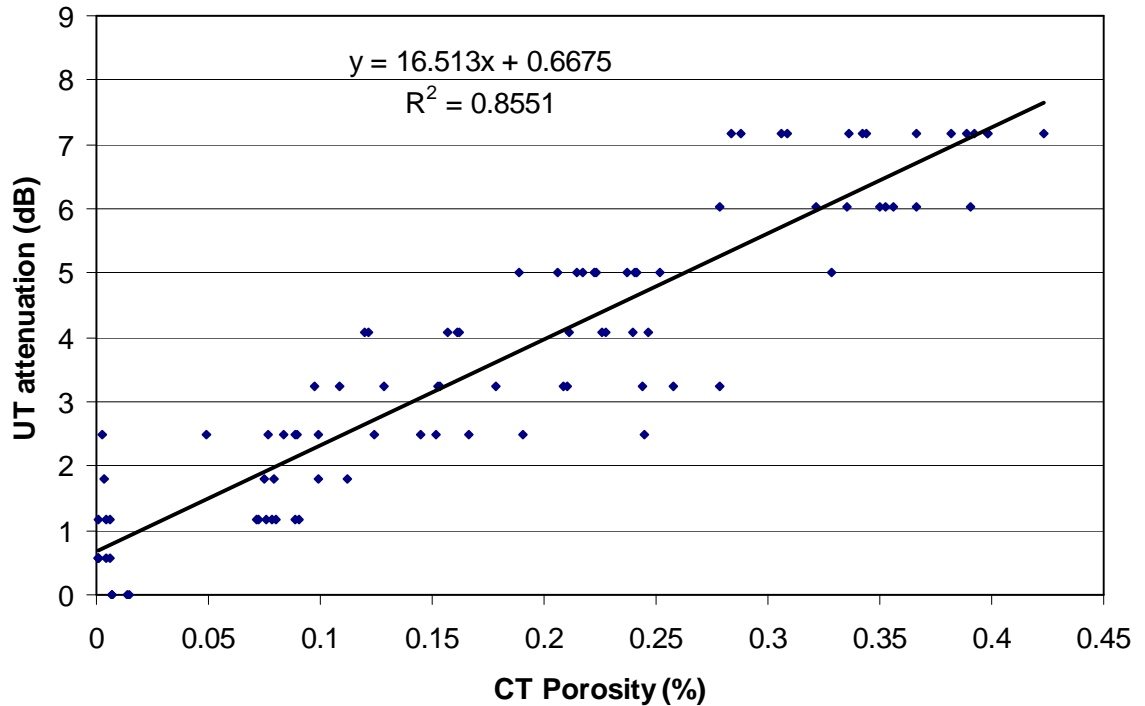


Figure 7-19. Back-wall echo ultrasonic attenuation compared with through-thickness average porosity from the Micro-CT data. The correlation coefficient R is 0.925.

Comparison of a 3D analysis of the porosity in the Micro-CT data with the 3D profile of the decomposition porosity coefficient gave very poor correlations of less than 0.1. When looking at just individual plies, some of the plies gave correlation coefficients as high as 0.5. Initial observations suggest that, in most cases, the decomposition porosity coefficient is acting as a differential parameter – responding to an increase or decrease in porosity rather than an absolute porosity level. This is confirmed by the work of Pinfield et al (2010). The ongoing analysis work will concentrate on using decomposition to determine the rate of increase or decrease in local porosity levels. Using an integration algorithm, it may then prove possible to reconstruct the actual porosity levels at each depth.

7.3 Fibre Orientation Mapping

7.3.1 Background

Chapter 1 contained the background information on the requirement for fibre orientation mapping in polymer matrix composites, Chapter 3 reviewed previous work and Chapter 6 contained the current methodology for fibre-orientation mapping. This chapter describes how it has been applied to carbon fibre composites to solve three different quantitative inspection requirements:

- Ply stacking sequence
- In-plane waviness
- Out-of-plane wrinkling

Most of the work on optimising the parameters for data acquisition for in-plane fibre orientation was carried out by using the ply stacking-sequence analysis method as it is very sensitive to changes in parameters.

7.3.2 Accuracy of in-plane fibre orientation measurement.

Appendix H contains an accuracy assessment for in-plane fibre orientation. The results of this analysis are incorporated in the following recommendations for optimised parameters. In summary, a region of size at least 100 x 100 pixels is required, containing at least 20 fibre tows, to obtain an accuracy of better than $\pm 0.25^\circ$. This is generally achievable for ply stacking-sequence measurements, but not for in-plane waviness where a size of just a few fibre tow widths is the maximum in order to avoid flattening the peak in the angular deviation. In simulations of waviness with a wavelength of 10 to 20 fibre tows, use of a square region 5 fibre-tows wide resulted in flattening of the 45° peak deviation equivalent to a 4% underestimate, with a $\pm 2^\circ$ uncertainty.

7.3.3 Accuracy of out-of-plane wrinkling measurement.

Appendix H contains an initial accuracy assessment for out-of-plane wrinkling but ongoing work beyond this project will be required to complete it. The angular accuracy depends on the wrinkle wavelength, the box size used to define the analysis regions and the number of pixels in that box. As with in-plane waviness, the box needs to be narrow relative to a wrinkle wavelength in order

not to spatially-average the peak angle, but it needs to be as many pixels wide as possible to improve the accuracy of the measurement of angle. Thus a small incremental step size in the original scan is beneficial as this maximises the number of pixels per wrinkle wavelength.

The number of plies included in the box height is also important. A good compromise includes 4 plies in the box height and 50 pixels in the box width, provided this is less than a quarter of a wrinkle wavelength. Then the accuracy of the ply angle should be within $\pm 1^\circ$.

7.4 Ply Stacking Sequence

7.4.1 Acquisition and analysis parameters and procedure

Because of the ability of ply stacking-sequence analysis to rapidly demonstrate improvements in the output of the process, a major part of the investigations has been focused on this method. Some of the evaluation was performed by a third party under the supervision of the author. Aspects requiring investigation were divided into three key areas, as follows:

- 1) Probe frequency
- 2) Ultrasonic acquisition parameters
- 3) Analysis parameters

7.4.1.1 Probe frequency: improving stacking sequence resolution at depth

As expected, use of a lower-frequency ply resonance increases the depth to which adequate stacking-sequence information can be generated. The first resonance is not available for stacking sequences because this does not show all the ply reflections and averages the effects of four plies. Thus the lowest available resonant frequency is the second resonance, which is at approximately 6 MHz for a panel with 0.25 mm ply spacing (4 plies/mm), and approximately 12 MHz for 0.125 mm spacing (8 plies/mm).

It has been confirmed, using piezo-composite focused probes centred at various frequencies, that using the second resonance frequency produces an

optimum compromise between high-resolution stacking-sequence images from higher frequencies and better depth penetration from lower frequencies.

7.4.1.2 Acquisition parameters

As a result of the above accuracy analysis and probe frequency trials, the recommended acquisition parameters are:

- a scan pitch of between a half and a fifth of the width of the fibre tows, ie between 0.4 mm and 1.0 mm for fibre tows 2.0 mm wide.
- at least 100 x 100 waveforms acquired in the scan area, containing between 20 and 50 fibre-tow widths in each direction.
- a probe frequency close to the second ply resonance frequency: 6 MHz for 0.25 mm ply spacing (4 plies per mm) or 12 MHz for 0.125 mm ply spacing (8 plies per mm).
- a DAC (depth-amplitude correction) applied at acquisition, prior to digitisation, to compensate for attenuation, allows better penetration (see Section 7.4.2 below).

The limit on probe frequency means that stacking sequence and waviness measurements can only be achieved down to approximately 9 mm in 0.125 mm ply (8 plies per mm) material, 18 mm in 0.25 mm ply (4 plies per mm) material, or 13 mm in 0.070" (0.175 mm) ply material. However, if 0.5 mm plies are used for material thicker than 18 mm then it would be possible to image ply orientation down to 36 mm in this material.

7.4.1.3 Analysis procedure

The following analysis procedure was found to give the best resolution stacking-sequence images and in-plane waviness C-scans, and was programmed in to ANDSCAN as an automated procedure:

- Use the modulus of the waveform combined with its Hilbert Transform (see Appendix D) before processing the C-scans, removing phase effects.
- Set a gate width equal to one sample point in the waveform, with a 0% overlap so each sample point produces one layer in the 3D profile.

- Use a 100% scan magnification - anything higher wastes analysis time.
- A reasonable compromise in accuracy and analysis time is achieved using a 120 x 120 pixel area for analysis. This achieves $\pm 0.25^\circ$ accuracy.
- Only zero pad to the next power of two larger than the sample size (ie 128 x 128 for the recommended sample size).
- Use a Hanning taper over 20% of the scan, as a rectangular window.
- Use Max-Min normalisation for displaying angular power distribution.
- Use a colour scale to dramatically improve stacking-sequence imaging
- Use a logarithmic distribution of colours and variable dynamic range.

The benefit of these optimum settings can be seen in the example in Figure 7-20 for a 25 MHz focused probe scan of a 16-ply stack of $[(45^\circ/135^\circ/90^\circ/0^\circ)_2]_8$ lay-up with a ply spacing of 0.125 mm (8 plies/mm), over a honeycomb core.

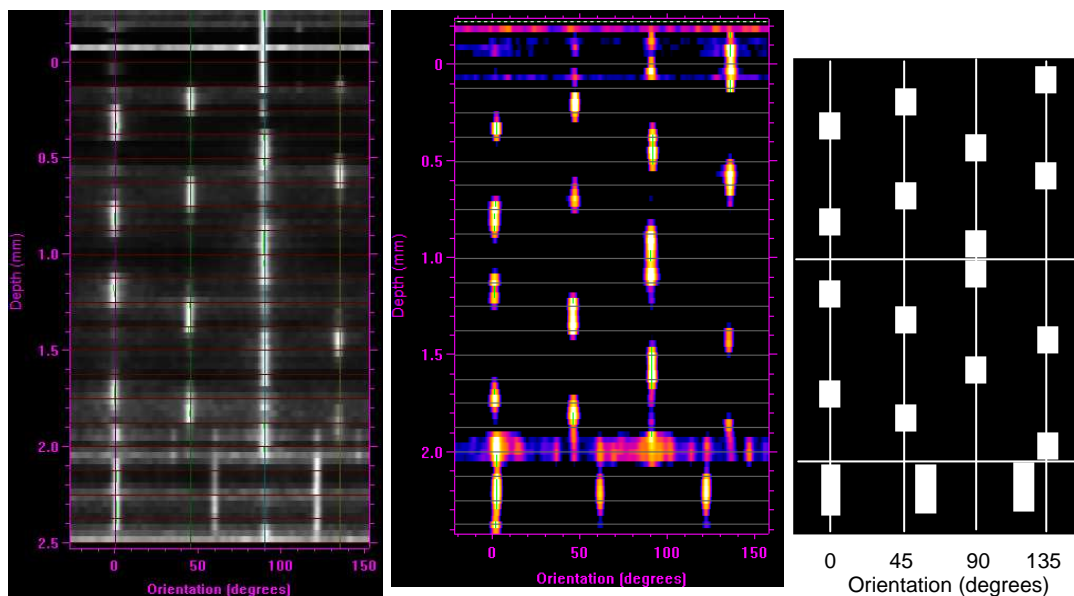


Figure 7-20. Ply stacking sequence for a 16-ply laminate (note back-wall at 2.0 mm depth) over honeycomb (note $0^\circ/60^\circ/120^\circ$ angles). A 25 MHz focused probe was used. Comparison of images prior to optimisation (left), with the benefits of the optimisation and software refinements (middle), and the correct lay-up shown diagrammatically (right).

The optimisation improvements have made it possible to determine stacking sequence to a much greater depth, and even in the most difficult ply lay-ups.

7.4.2 Ply Stacking Sequence Depth Penetration

Depth of penetration is dependent on the frequency, because visco-elastic attenuation in the resin is frequency-dependent, as is scattering from the fibres and any porosity. However, the optimum frequency for determining ply stacking sequences is the second resonance (see above) which is approximately 6 MHz for ply spacings of 0.25 mm and 12 MHz for ply spacings of 0.125 mm. Thus it will be possible to penetrate deeper in the thicker ply materials, which is advantageous as the thicker plies are generally used for thicker structures.

In order to counter some of the attenuation effects a DAC (depth-amplitude correction) can be applied, which is a time-dependent gain. If this can be done at acquisition time, prior to digitisation, then it does not get applied to digitisation 'noise' and hence improves the signal-to-noise ratio at depth if digitisation is the most significant noise source. An example of the ability of the technique to determine errors in stacking sequence to 15 mm depth is shown in Figure 7-21.

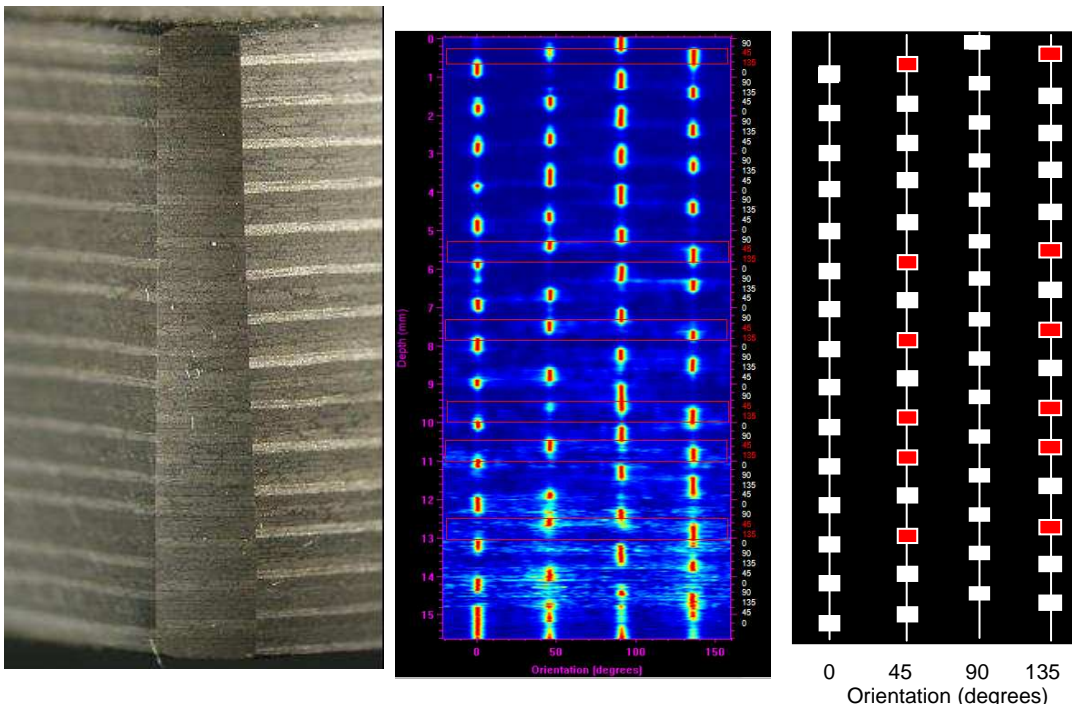


Figure 7-21. Stacking sequence in a 15 mm thick laminate with 0.25 mm plies, shown photographically (left) and as an ultrasonic ply stacking sequence (middle) with stacking sequence listed on the right - incorrect lay-ups indicated in red. The 'as designed' stacking sequence is shown diagrammatically (right). The probe centre frequency was 5 MHz. A DAC was applied at acquisition.

7.4.3 Automated calculation of ply stacking sequence

The key to automated determination of the fibre angle in a particular ply is first to determine the depths of the ply centres. This has been achieved by detecting the depth of the hand-over of the peak amplitude from one angle to the next. These hand-over depths are not necessarily the ply interface depths due to varying reflected amplitudes from each interface. However, the centres of the plies can be assumed to be located close to the mid-depths between these hand-over depths. At the ply centre the peak angle can then be determined and this reliably identifies and measures the fibre angle provided the data has been acquired and analysed using the above optimum parameters. An example of this automated analysis is shown in Figure 7-22, where the hand-over depths are shown as horizontal lines and the selected ply angles are joined by a zig-zag line. The measured ply angles are shown as a column of numbers colour-coded based on the four expected orientations.

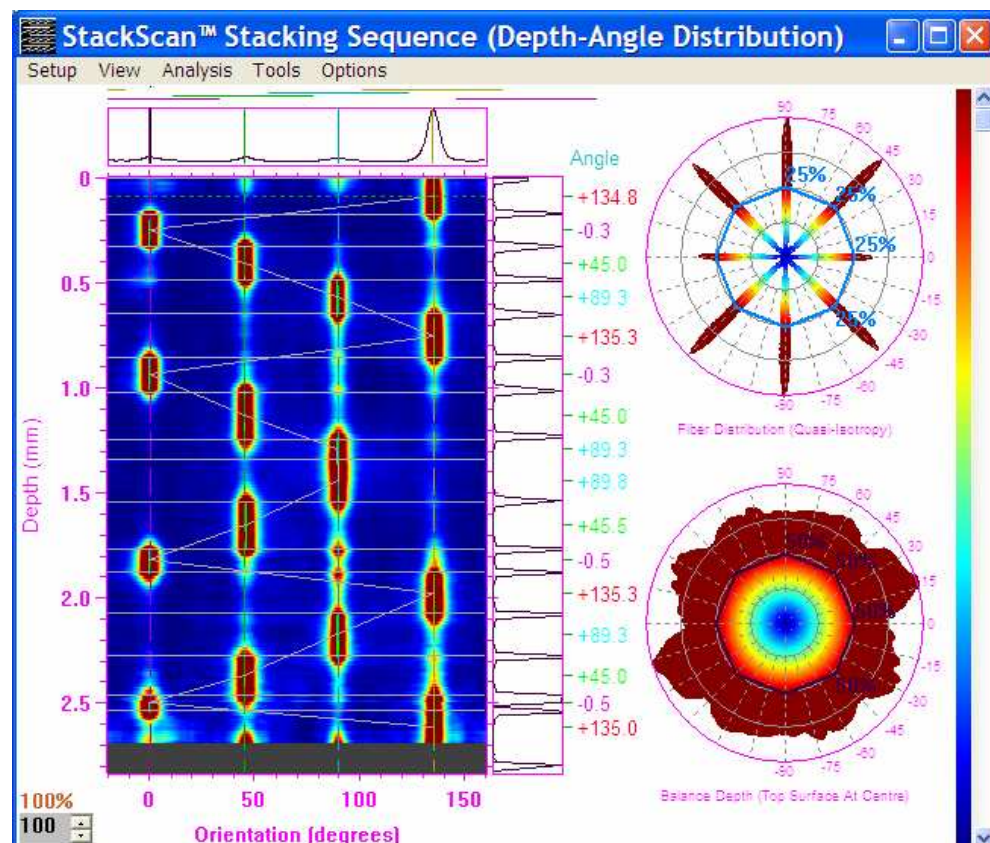


Figure 7-22. An example of ply stacking-sequence determination, where the ply interfaces have been detected automatically and the Quasi-isotropy and balance depth are plotted on the right (see later discussion).

7.4.4 Polar displays summarising ply stacking sequence.

Also illustrated in Figure 7-22 is a method for summarising the results of the ply stacking-sequence analysis in terms that would be understood by materials scientists and composite stress engineers. The two most important design criteria for the lay-up of a monolithic composite panel are the number of plies at each angle, and the order in which they are positioned in the sequence.

The number of plies at a given angle will determine the stiffness and strength in that direction. Often a panel will be designed to have quasi-isotropic properties by putting equal numbers of plies at each of the four angles. The top-right polar plot in Figure 7-22 displays the extent of quasi-isotropy of the measured stacking sequence by plotting a light-blue line joining points defined by the fibre angle and the proportion of plies at that angle. This quasi-isotropic stacking sequence (all four angles represented in equal numbers) should have all points on the mid-radius circle marked as $\frac{1}{4}$ of plies on the diagram in Figure 7-23 (left).

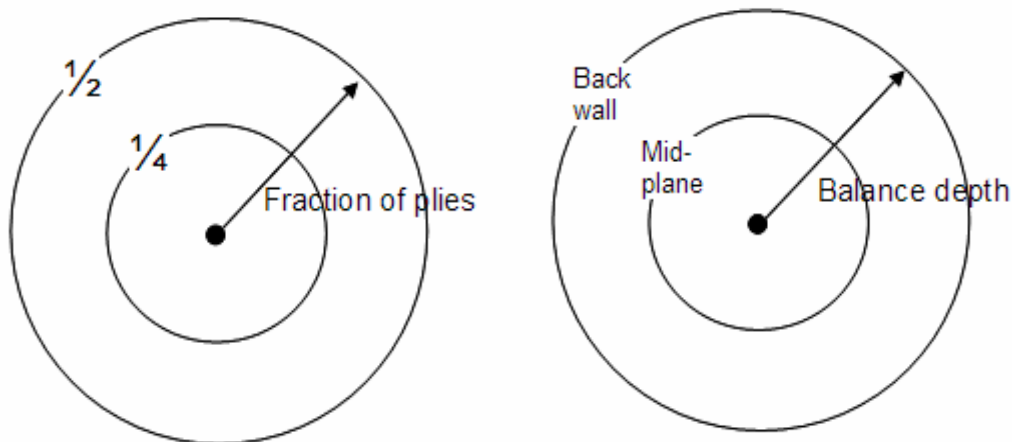


Figure 7-23. Diagram explaining the polar plots used to assess the extent of quasi-isotropy (left) and the balance depth (right).

The order of plies in the stacking sequence is critical and it is usually desirable to have a *balanced* stacking sequence – where the mid-plane of the laminate is a plane of symmetry and all ply angles are repeated in the opposite half of the panel depth, at the same distance from the mid-ply. A method of displaying the extent to which the panel is balanced (see bottom-right in Figure 7-22) is shown diagrammatically on the right of Figure 7-23. The mean (or ‘balance’) depth of

plies at a given angle is plotted as the radius on a polar diagram where the mid-radius is mid plane, the centre is the front surface of the panel, and the outer circumference is the back of the panel. Hence a balanced stacking sequence would have all points on the mid-plane circle at mid-radius, as illustrated in Figure 7-24 using some real data.

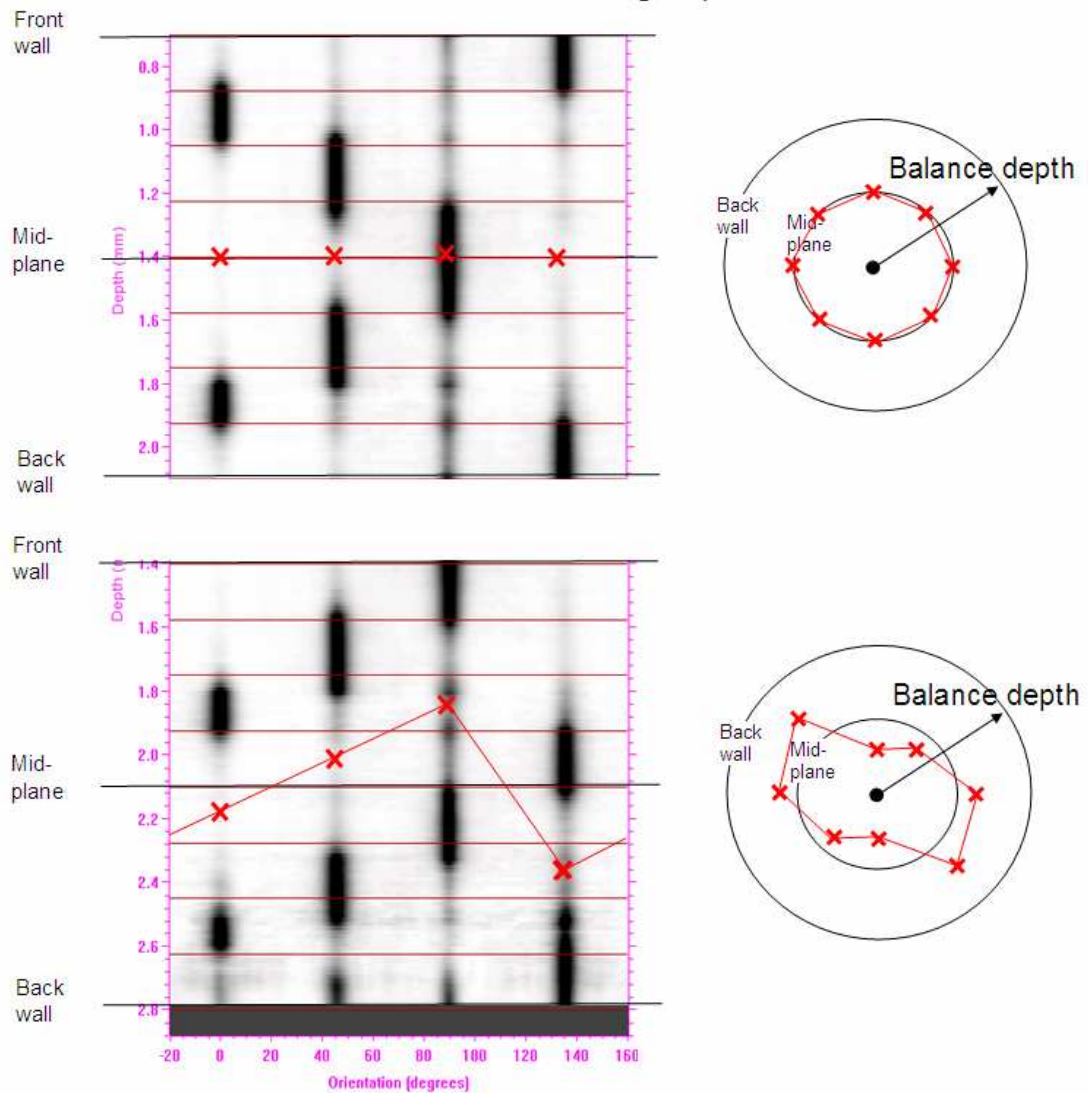


Figure 7-24. Balance-depth polar plots (right) for a balanced (top-left) stacking sequence and an unbalanced (bottom-left) stacking sequence. The mean depth (or ‘balance depth’) for each angle is shown as a cross on the diagrams.

Finally, in Figure 7-22, the actual mean ultrasonic amplitude at each angle is plotted as the radius of a background colour map in the quasi-isotropy plot (top-right) and the weighted-mean (or centroid) depth of the ultrasonic amplitudes as

the radius at each angle on the balance-depth plot (bottom-right). The latter display needs some refinement because the low signal-to-noise angles (between the four main ply orientations) are currently included and tend to dominate the display. It may be necessary to use colour, where the brightness increases or the colour changes with amplitude at the angle, as in Figure 7-25.

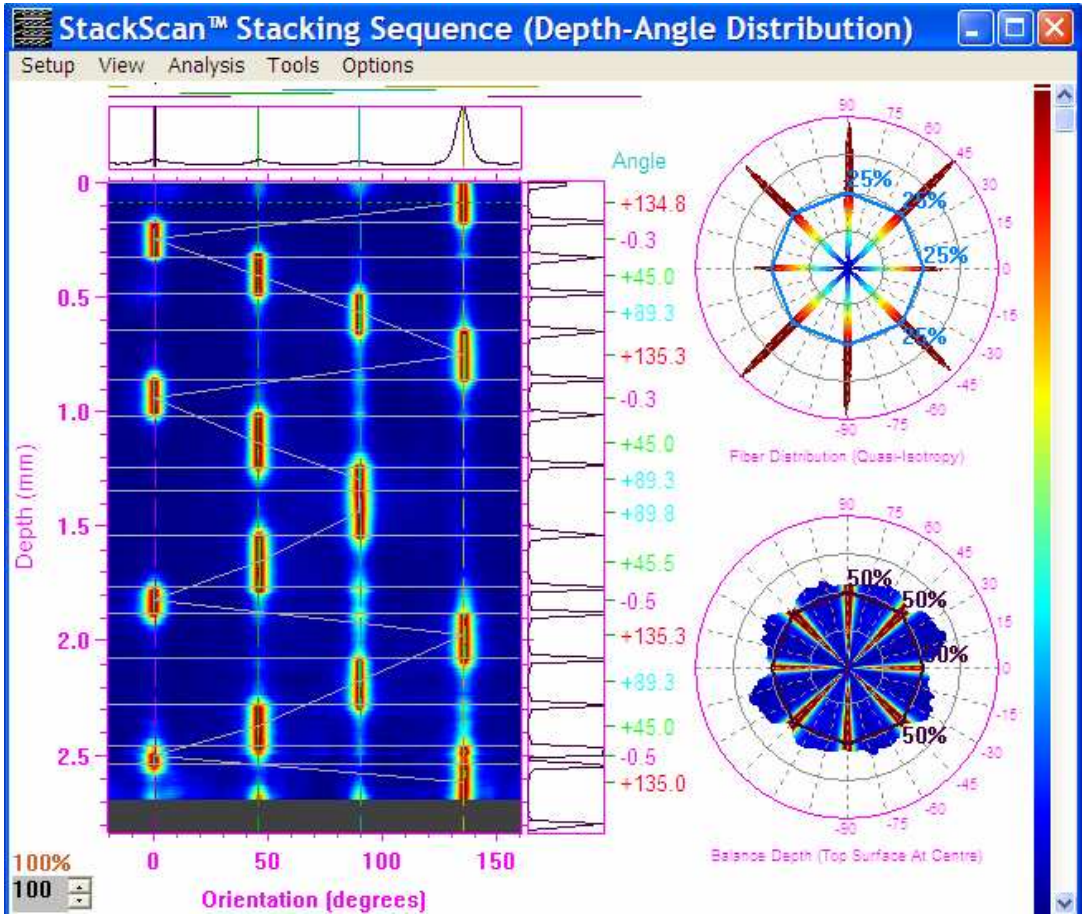


Figure 7-25. Same data as for Figure 7-24 but with modified balance-depth polar plot (bottom-right) using colour to show which ply angles are present.

7.5 In-plane Waviness

7.5.1 In-plane waviness evaluation

Acquisition parameters and generation of a 3D-profile layered image from the data is covered under the stacking-sequence work in Section 7.4. Conversion of a C-scan into a waviness map is required to quantify the effects observed by eye in the C-scan. To do this, a box is passed over the scan with some overlapping, and the angular distribution is assessed at each box location as

described in Section 6.2. For in-plane waviness, pixels in the C-scan usually have an aspect ratio of unity so this is not as significant an issue as for out-of-plane waviness.

Appendix H covers the effect of the box size on the accuracy of the fibre orientation measurements. For the only specimen with in-plane waviness available for this project (Figure 6-27), the best parameters were determined experimentally to be: a 5 x 5 mm box with 60% overlap and a rectangular Hanning window over 40% of the scan.

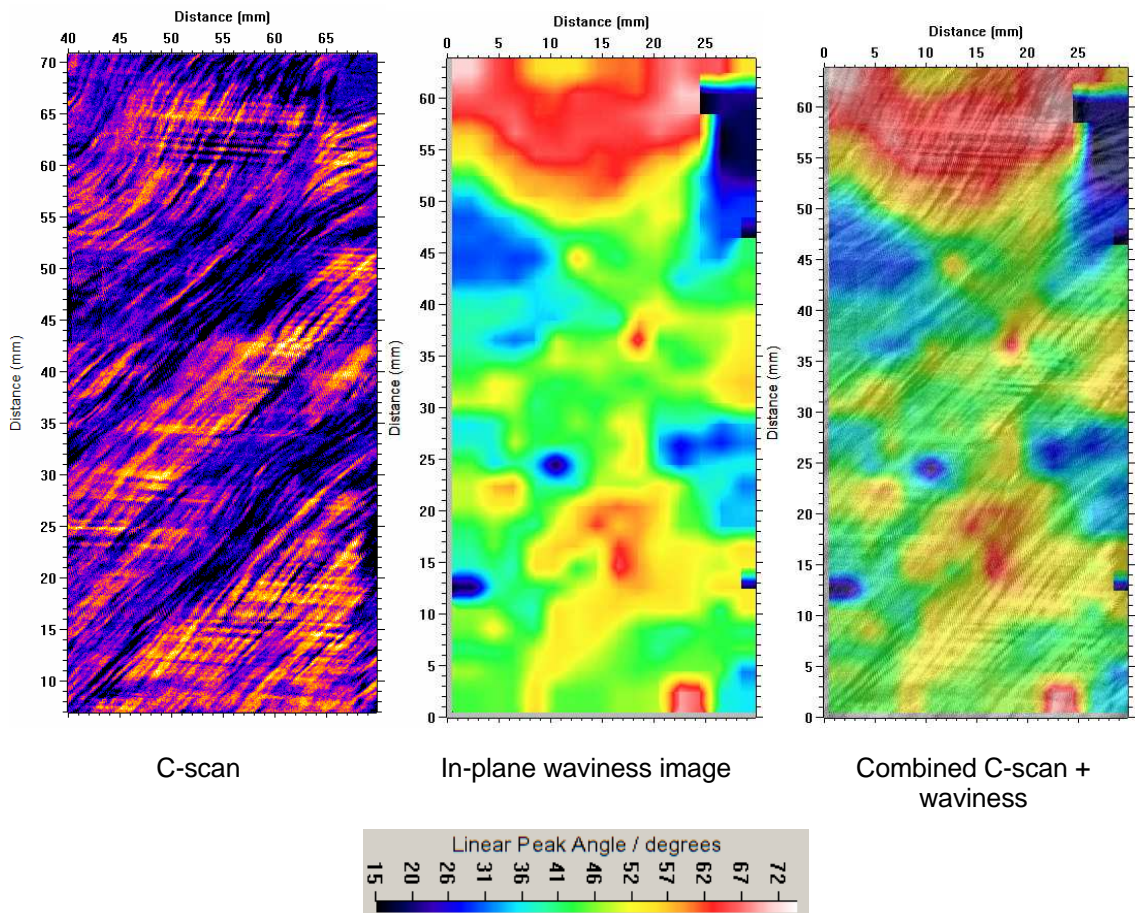


Figure 7-26. In-plane waviness image (middle) with the C-scan from which it was generated (left) and a combination of the two images (right). A 5 x 5 mm box size was used with 60% overlap and 40% rectangular Hanning windowing.

At this stage, the selection of analysis parameters can be guided by the accuracy work in Appendix H, but it is an ongoing exercise to optimise these parameters for a range of fibre-tow widths and fibre wavelengths.

7.5.2 In-plane waviness visualisation

The combined orientation (colour) and C-scan (greyscale) image shown in Figure 6-27 is a very convincing and useful method of presentation. The colour scale still gives quantitative orientation information, whilst the greyscale gives qualitative confirmation that the processing is correct to give that orientation information.

This method of combining quantitative colour and qualitative greyscale images was then implemented in the ANDSCAN software via 24-bit RGB colour bitmaps where previously only 8-bit Palette bitmaps were available – see Figure 7-27. Both scales can be modified independently in terms of brightness (offset) and contrast (gain) in order to produce the desired result, and quantitative information can be gained from the colour scale as the cursor is moved over any location, or by analysis of the scan.

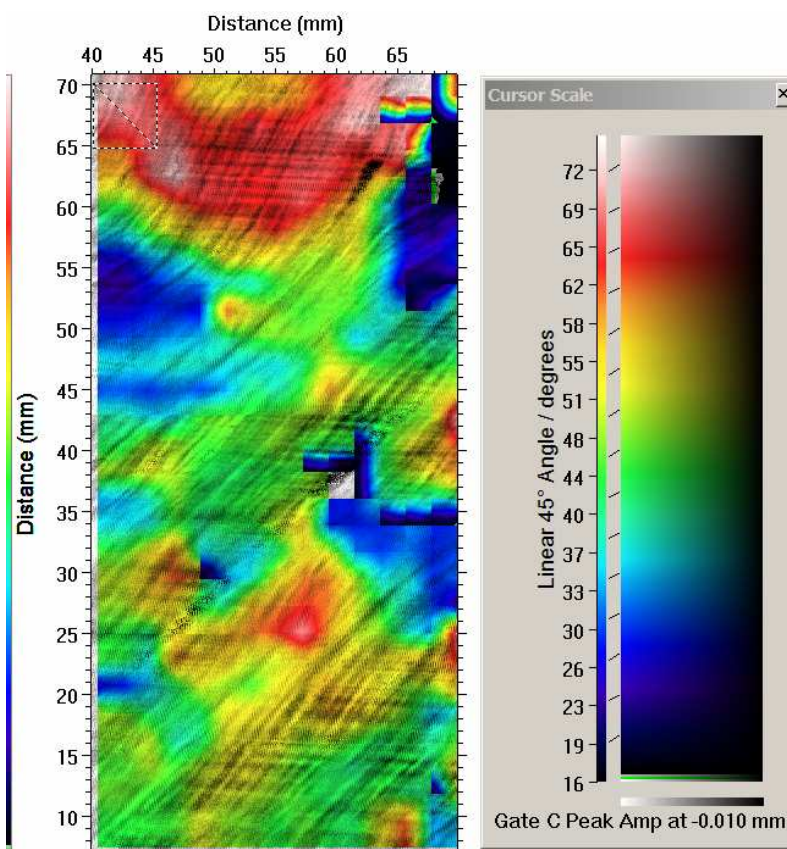


Figure 7-27. Example of the ANDSCAN implementation of the combined quantitative colour and qualitative greyscale images. The scales can be adjusted by dragging either end of either scale in the window on the right.

7.5.3 Application to 3D in-plane waviness

By performing this analysis for every layer in a 3D profile of amplitude response from a laminate, the 3D in-plane waviness can be visualised. This is shown in Figure 7-28 for a nominally ‘good’ 16-ply quasi-isotropic composite laminate – the same one used for Figure 7-25.

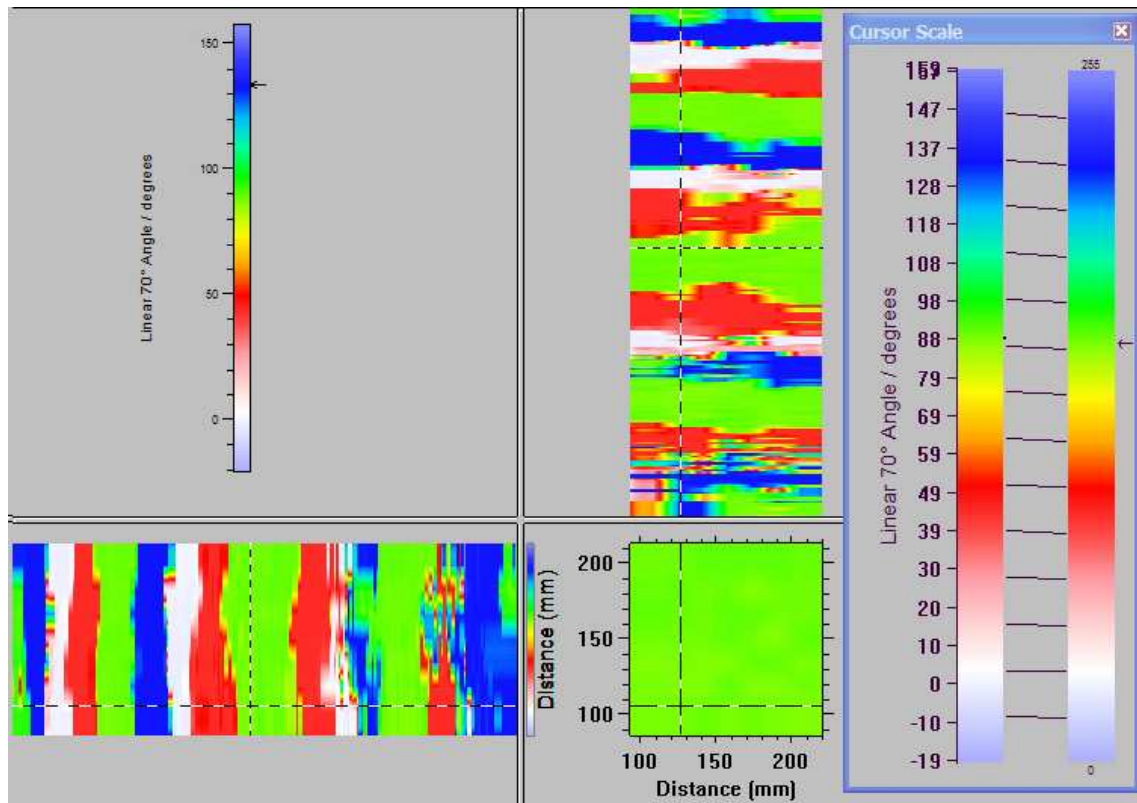


Figure 7-28. An example of a 3D in-plane waviness profile for a composite with no simulated waviness, showing the different ply angles in the cross-sections (top and left).

Experience with other in-plane waviness samples suggests that they often also contain out-of-plane wrinkling, resulting in cross-talk between plies – plies of a different angle encroaching on the layer being imaged. The future 3D method will need to use out-of-plane wrinkling information (see next section) to pre-determine the depth of each ply and track the plies through the structure to produce in-plane C-scans of each ply on which in-plane waviness can be determined.

7.6 Out-of-plane Wrinkling

7.6.1 Out-of-plane ply-wrinkling visualisation

Figure 7-29 shows an example of a B-scan with the ply inclination analysis (Section 6.2) applied in ANDSCAN. As with in-plane waviness, it is advantageous to present an image of combined quantitative colour orientation overlaid with qualitative greyscale image of the wavy plies (Figure 7-29(d)). This has also been implemented in ANDSCAN, this time in the cross-section windows, as 24-bit RGB bitmaps, again with both colour and greyscale scales (Figure 7-29(c)) adjustable.

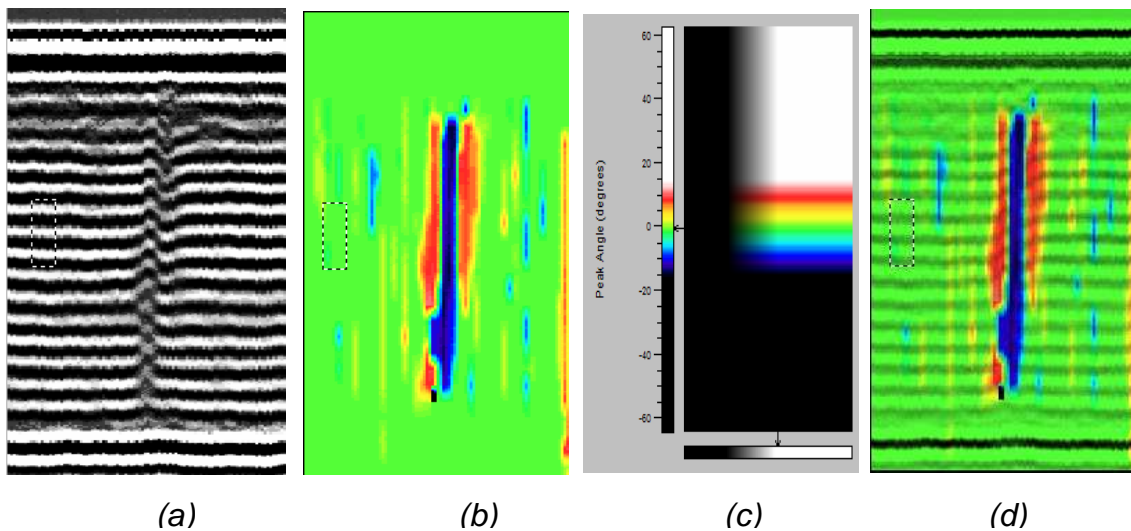


Figure 7-29. Example of the ANDSCAN implementation of qualitative greyscale for B-scan (a) combined with a quantitative colour ply orientation (b) image of out-of-plane waviness. The combined image (d) uses the colour and greyscale scales shown in (c) and is still quantitative in terms of ply angle.

7.6.2 3D Mapping of Ply Wrinkling

7.6.2.1 Horizontal and Vertical Ply Angles

The above analysis of horizontal and vertical B-scans produces values for the horizontal and vertical ply angles, α and β respectively as shown in Figure 7-30. These values are sufficient to fully describe the local inclination of a flat plane and they can be calculated at every 3D location in the structure,

populating two 3D arrays, one for α and one for β . These are stored in two channels in ANDSCAN.

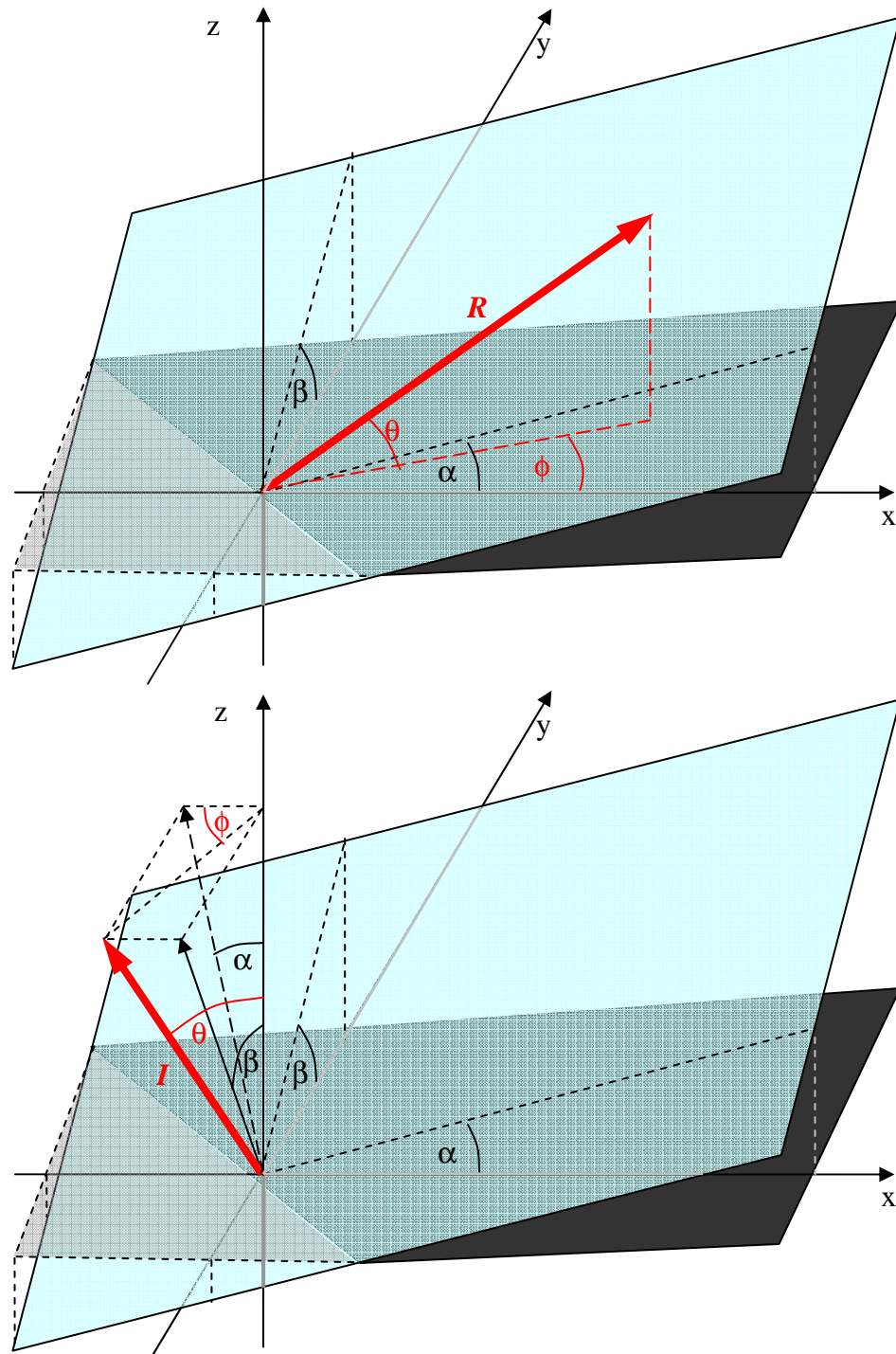


Figure 7-30. Diagram showing the calculation of horizontal (α) and vertical (β) ply angles, and then peak ply angle θ and azimuthal direction ϕ .

3D data is easier to visualise in videos and animations than in a paper report, but, for two simulated wrinkles, the horizontal and vertical angles are shown in Figure 7-31 as cross-sectional slices through the 3D data.

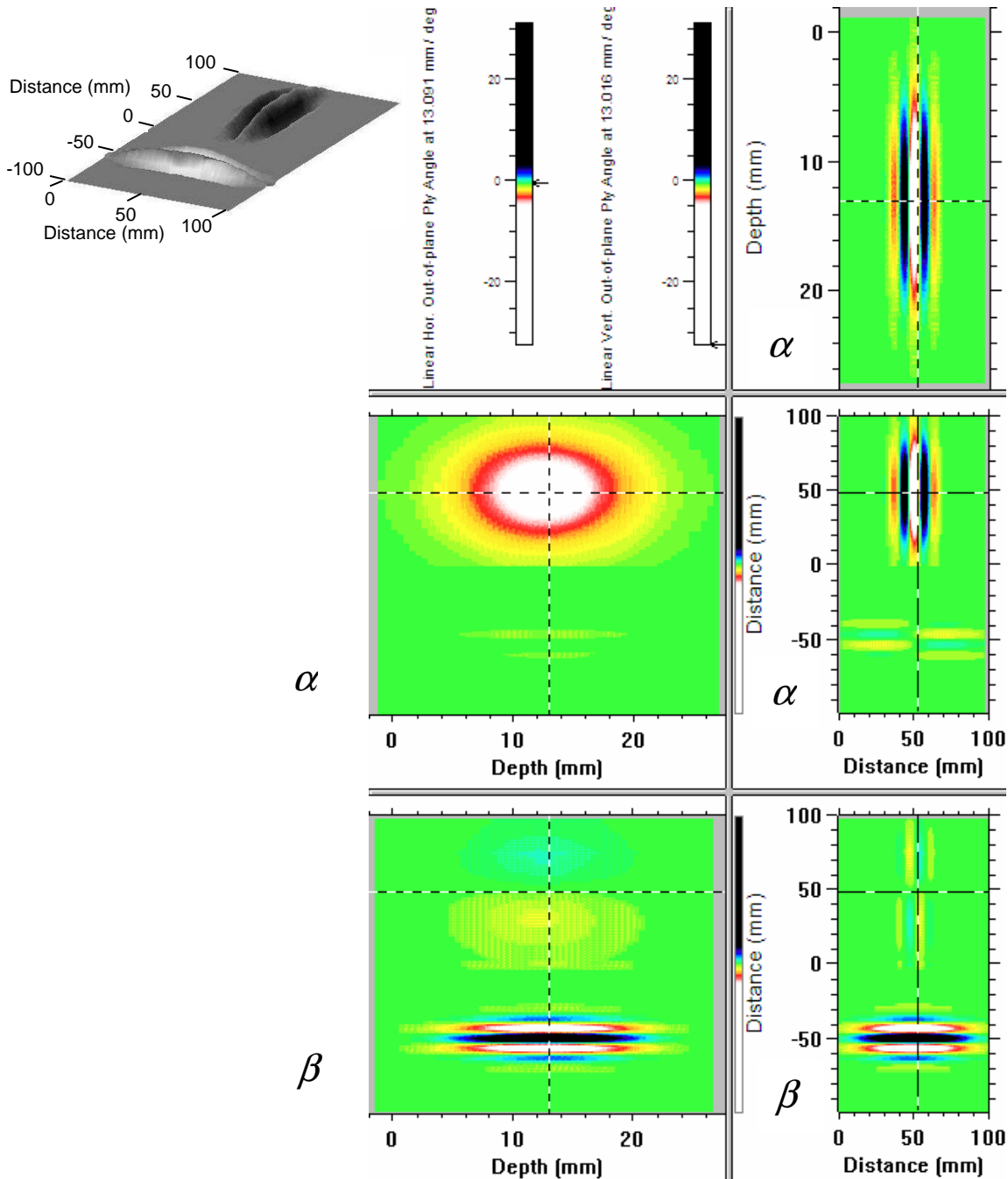


Figure 7-31. Cross-sections through horizontal α (top and middle) and vertical β (bottom) ply angles as 3D data sets for two simulated wrinkles. The top cross-section is along a horizontal line and the left cross-sections are along a vertical line. Also shown (top left) is a pseudo-3D image of the simulated wrinkles showing their orientation.

7.6.2.2 Measurement of Ply Wrinkles

Although two 3D profiles of α and β are not necessarily the generic parameters required for quantification of wrinkles in any direction, they are sufficient to generate whatever other parameters are required. It is possible to measure the wrinkle severity (peak angle), wavelength and volume for wrinkles lying in the vertical or horizontal directions of the scan, as shown in Figure 7-32.

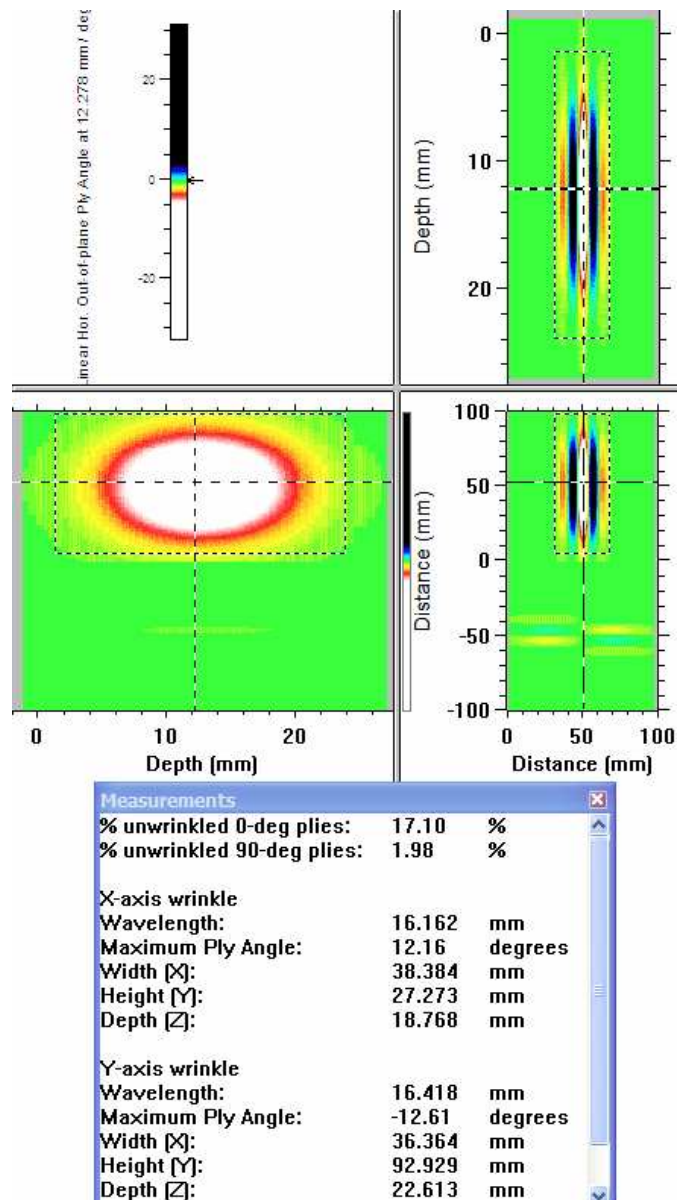


Figure 7-32. An example of quantification of the horizontal and vertical wrinkles in the simulated data using the α and β parameter 3D profiles. The extent of the wrinkled volume is represented by a cuboid, marked visually on each of the cross-sections as a box. Measurements appear in the window at the bottom.

What follows is the conversion of these two 3D profiles of α and β into other profiles that more closely match the required metrics for ply wrinkles.

7.6.2.3 Peak Ply Angle and Direction

In order to transform the two 3D orthogonal ply-angle data sets (α and β) into two 3D data sets giving the local peak angle of inclination of the plane θ , and its azimuthal direction ϕ (see Figure 7-30), it is necessary to transform the data as follows.

If $\mathbf{I} = (x, y, z)$ is the unit vector perpendicular to the inclined plane of the ply at the origin (see Figure 7-30), then:

$$\begin{aligned}x^2 + y^2 + z^2 &= 1 \\ \tan \alpha &= x / z \\ \tan \beta &= y / z \\ \tan \phi &= y / x \\ \cos \theta &= z\end{aligned}\tag{7-1}$$

and from these equations, the following expressions can be derived:

$$\begin{aligned}\tan \phi &= \tan \beta / \tan \alpha \\ \tan^2 \theta &= \tan^2 \alpha + \tan^2 \beta\end{aligned}\tag{7-2}$$

The angle θ is always positive (see the analysis of simulated wrinkles in *Figure 7-33* top and middle) and is the angle of inclination of the ply at each 3D location. In fact, the major benefit of the transformation into these θ and ϕ parameters is that the peak ply angle of inclination, regardless of direction, can more easily be determined by finding the peak of the 3D profile of θ . This means that wrinkles that do not align with the x or y axes can now be accurately measured as well. An outcome of this transformation is that the azimuthal angle ϕ undergoes 180° inversions as the wrinkle is traversed from positive to negative slopes. This effect can be easily seen in *Figure 7-33* (bottom).

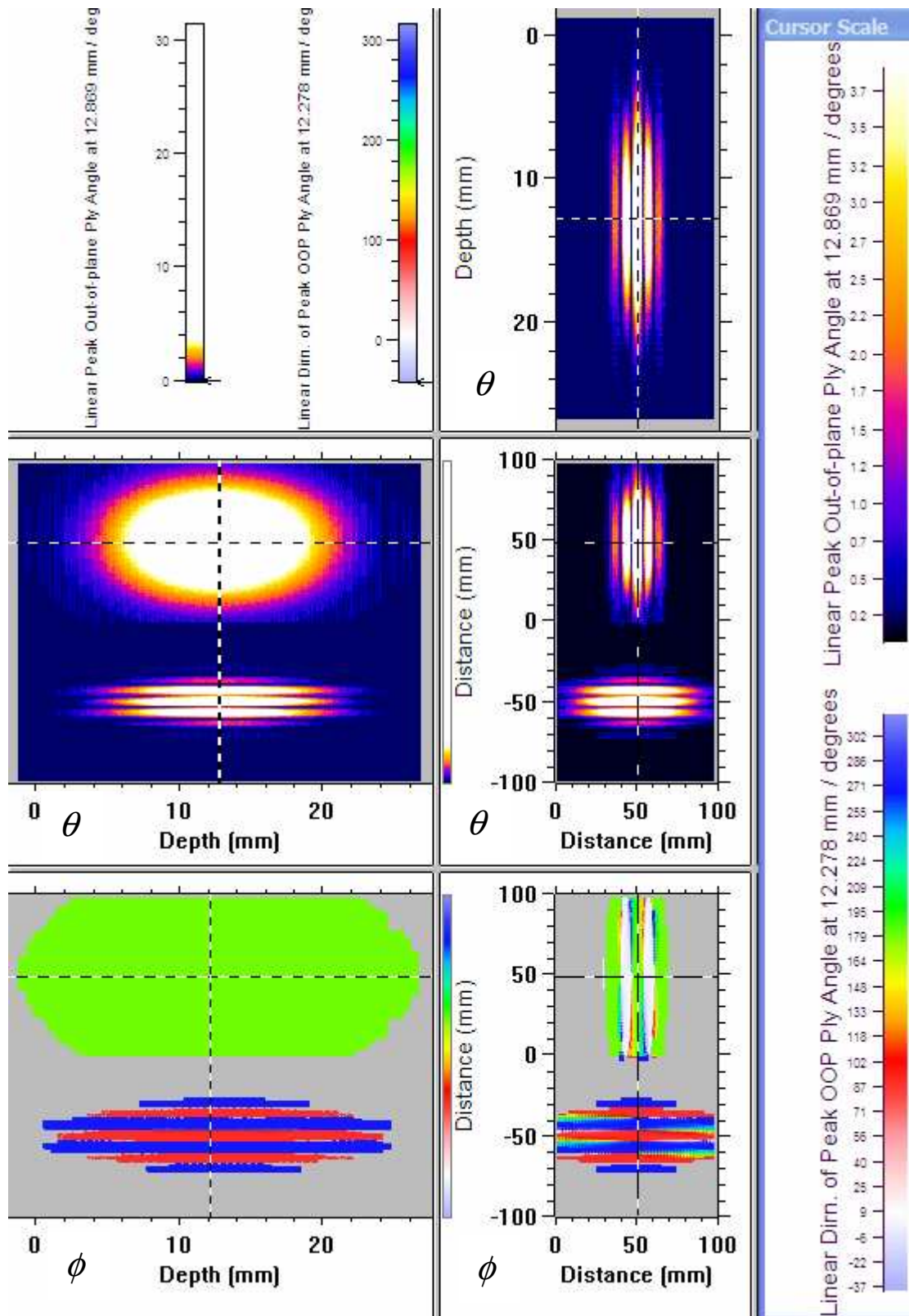


Figure 7-33. Angle of inclination θ (top and middle profile, and left-hand colour scale), and azimuthal angle ϕ (bottom profile and right-hand colour scale) for the two simulated wrinkles.

7.6.2.4 Calculation of ply surface depth.

Although the actual deviation of the ply depth is unlikely to be a parameter that is required quantitatively, it is extremely useful for visualisation of wrinkles (see Figure 7-34). Such visualisation is important for describing the wrinkles to composites structural experts who have the job of deciding on concessions.

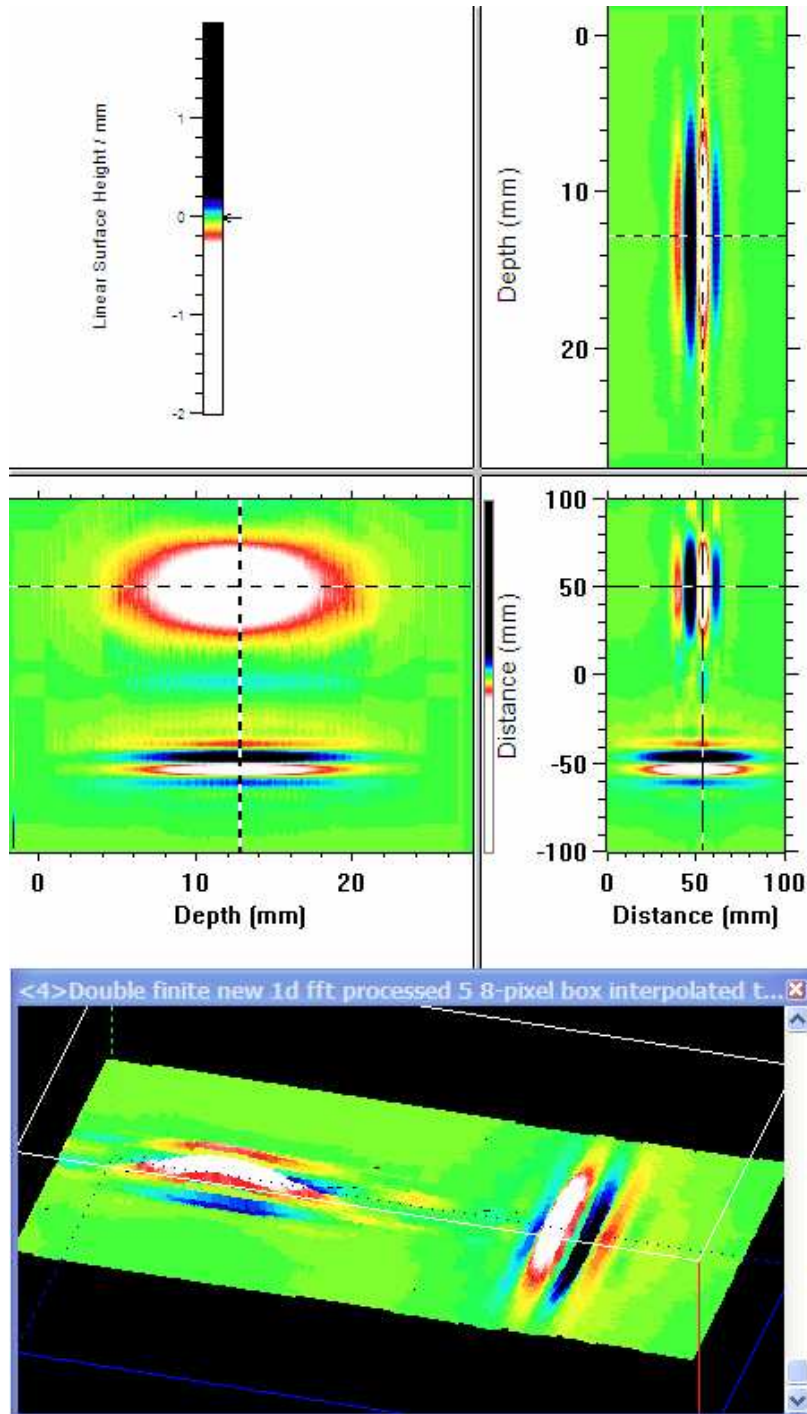


Figure 7-34. Surface height 3D profile showing deviation of the ply depth.

The surface depth profile is calculated from the horizontal and vertical angles α and β by first converting angle to gradient for an in-plane slice of each 3D profile and then integrating them both before combining the two results. The integration is undertaken in the frequency domain in order to use the angular information from the whole in-plane slice. The result is a process that is robust and copes well with missing data from angles of inclination that are too steep to measure. Other integration methods that worked from point to point proved unreliable because multiple small rounding or digitisation errors rapidly build up into ramps and large deviations in surface height.

7.6.3 *Illumination of rendered surfaces.*

Two methods for illuminating a rendered surface have been tested. The first determines a scalar quantity representing brightness by taking the dot product of I with an 'illumination' unit vector L , where -1 is black and +1 is white. An alternative method uses an 'embossed' kernel-processing method to determine local slope in a particular direction. The latter method (Figure 7-35 and Figure 7-36) is much faster but does not allow different vertical angles for the illumination direction.

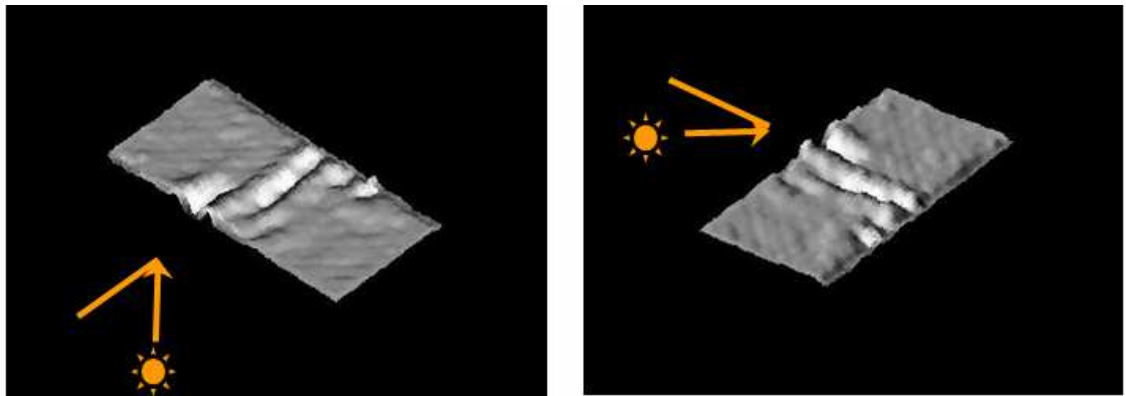


Figure 7-35. Two different rendered image views of a ply wrinkle in a real component showing the 45° illumination direction.

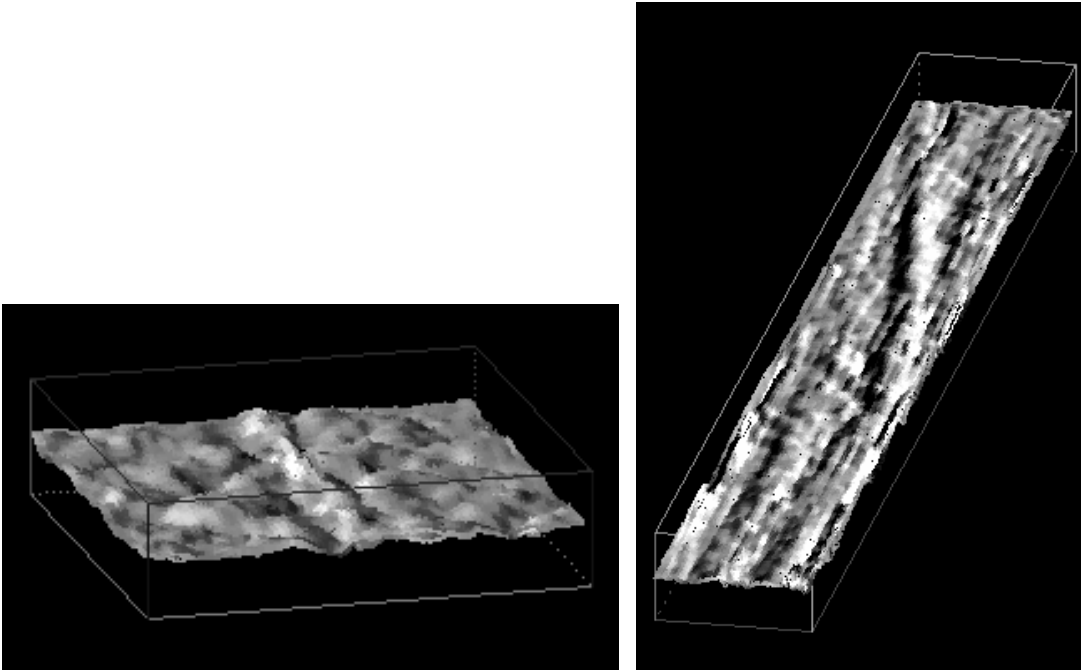


Figure 7-36. Two examples of ply surface height 3D rendered images with illumination.

7.7 Applications summary

Examples have been given of the 3D characterisation toolset developed in this project applied to both simulated and real composites. Further work is still required on the validation of 3D porosity, ply spacing and fibre volume fraction mapping. The fibre orientation mapping methods (ply stacking sequence, in-plane waviness, and out-of-plane wrinkling) have been validated using simulations and now need extensive validation against real components that will need to be sectioned in order to determine what really exists in them.

During the course of this project there has been interaction with manufacturers of composite aerospace components and there is considerable interest at present in the unique capability for ply-wrinkling characterisation in order to ensure complex components have no internal wrinkling. The uniqueness and impact of this work is evidenced by the winning of several related contracts by the author's employer, QinetiQ, including a key one in the USA where the invitation to tender was very widely circulated.

CHAPTER 8 DISCUSSION AND CONCLUSIONS

8.1 Initial position and motivation

At the start of this project, in 2005, most inspection of composite materials at manufacture and in service was already being performed using ultrasound because of its ideal properties. In particular, wavelengths for ultrasound in the low-Megahertz frequency range are of the order of a composite ply thickness. Also, achievable beamwidths of a few millimetres provide adequate detection and sizing of the kind of defects found at manufacture and in service.

Despite considerable research effort during the period from the early 1970s to 2005, it was apparent that the real benefits of ultrasound inspection had still not been fully exploited for composites. For example, most inspection was performed using analysis of either A-scan waveforms, or two-dimensional in-plane C-scan maps. These C-scans generally provided a through-thickness average parameter representing the attenuation (or insertion loss) for the whole specimen. A variant of the C-scan, the Depth-scan (or D-scan) did plot the depth of a signal, and Pseudo-3D images of the same data were developed in the 1990s, but depth-dependent information was rare and full B-scan cross-sections were rarely used.

The main reason for this predominance of through-thickness average information was the complexity of the response of the laminated structure to ultrasound. Attempts to understand this response and generate parameters that accurately reflected structural variations in the laminate had merely shown how difficult the problem was.

Another impasse in the development of composite inspection methods was the inability to provide measurements of actual material properties and thereby remove the need for expert NDT interpretation of results. This has been a constant source of frustration for manufacturers of composite materials who have repeatedly requested advanced automated analysis methods, which can output quantitative plots of real material properties, requiring no interpretation.

During the 1990s the author and other research teams, had begun to explore the response of composite plies and resin inter-ply layers to ultrasound. In parallel, the Applied Ultrasonics Laboratory at the University of Nottingham had been developing an understanding of the scattering of ultrasound from small particulate inclusions in liquids and solids, and of the propagation of ultrasound in multi-layered adhesively-bonded structures. The current project was thus established as a synergistic collaboration aimed at extending the inspection of composites to include three-dimensional quantitative characterisation of the laminate itself and any deviations from the designed structure in terms of porosity, ply spacing, fibre-volume fraction, ply stacking sequence, in-plane fibre waviness and out-of-plane ply wrinkling.

This project has been necessarily broad in terms of the range of material properties considered but just one model, one signal-processing method and one image-processing scheme sufficed for all of these.

8.2 Approach

Early in this project it was realised that a multi-layer inhomogeneous-medium normal-incidence ultrasonic propagation model would be required in order to understand the interaction of ultrasound with composite laminates. This model would also prove extremely useful for testing various approaches and the validity of relationships between potential ultrasonic parameters and material properties. If possible, a fast analytical model was required so that it could be built into the code for calculating material properties if necessary. This has transpired to be an essential requirement for decomposing the complex response into various contributory material characteristics.

At this stage the research branched into two approaches, one using spectral analysis of small 3D voxels to determine ply spacing, fibre-volume fraction and void-volume fraction (porosity), and the other using 2D Fourier analysis of cross-sectional images to determine local fibre-tow and ply angles. The above-mentioned model proved beneficial for understanding both approaches, but additional simulation methods were required for validation of the fibre-waviness and ply-wrinkling methods.

Validation of the methods has relied heavily on simulation, mainly because of the difficulty of obtaining actual 3D information about real laminates. Only towards the end of the project was Micro-CT X-ray imaging beginning to provide some real validation information for porosity measurement, and photo micro-graphic sectioning for fibre volume fraction and ply wrinkling. Several validation programmes are now commencing with composites manufacturers and end users now that interest in the 3D characterisation methods has been aroused.

8.3 The wave propagation model

A multi-layer wave propagation model was required from the start of this project to understand the complex response of composite laminates to ultrasound propagation, but how comprehensive would that model need to be?

Even before the project started it was clear that only normal-incidence ultrasound inspection would be acceptable for manufacturers of composites because there is only time in the production cycle for one inspection of the structure. Whilst full-waveform data had rarely been captured up to this time, the ramp-up to Boeing 787 manufacture – the first wide-body civil aircraft made largely from composites – saw full-waveform data being captured as standard. Previous work by the author had suggested that the thickness of the thin resin layer between composite plies was very important in governing the local reflection coefficients.

These factors bounded the model requirements and resulted in the need for a normal-incidence propagation model that could cope with multiple layers comprising fibre-resin mixtures alternating with thin resin layers. It was considered adequate to model each composite ply as an effective homogeneous medium with properties calculated using one of the mixture rules developed for modelling material properties in the 1960s-1970s. The use of normal-incidence ultrasound and the transversely-isotropic (see Appendix F) nature of each ply greatly simplified the model.

The importance of the thin resin layer between plies led to a decision to build a simple implementation of the well-established transfer-matrix approach around

the *composite-resin-composite* three-layer interface. The thickness of the resin layer and any visco-elastic attenuation were included by making the reflection and transmission coefficients of the three-layer interface complex. Thus the basic building block was an interface element with complex normal-incidence frequency-dependent reflection and transmission coefficients calculated for both propagation directions. Any number of plies could then be modelled by adding additional elements and the properties of each ply could be varied using the mixture rules to pre-calculate the effective moduli and density. A study of the literature on mixture rules for composites resulted in the adoption of two options for fibre-resin mixture rules. The first option was a simple volumetric rule whilst the second used Hashin (1965) for anisotropic fibres in resin.

The model was initially built and tested in MS Excel in order to understand the importance of various parameters on its performance. Then the model was easily ported into MS Visual C as a dynamic-link library, which was callable from ANDSCAN or from MATLAB for testing purposes.

This basic model sufficed for understanding the effects of ply thickness, resin-layer thickness and fibre volume fraction, but then it was necessary to include the effects of porosity. Initially porosity was incorporated as a simple volumetric mixture rule and an additional frequency-dependent attenuation in the propagation using an adaptation of the Adler et al (1986) formulation for forward scattering. Then the Hashin (1962) mixture rule for spherical inclusions in a solid was incorporated and finally the Pinfield et al (2010) model was added, which condenses the integrated backscattering from randomly distributed pores into a complex frequency-dependent effective impedance for a porous layer.

Throughout the development and use of the model it has gradually increased in its versatility and it has also found applications in modelling adhesive-bonded joints in metals and metal-composite hybrid laminates such as GLARE. As well as forming the basis of the model-based decomposition method (see below) it has also been incorporated into a multi-dimensional optimisation method developed by a colleague of the author. In addition, the concept of the three-layer interface building-block was successfully adapted for electromagnetic wave (microwave) propagation in multiple dielectric layers by another colleague.

8.4 3D characterisation of composites

8.4.1 *Isolation of responses*

It was quickly realised that the key to the localised 3D response of a composite to ultrasound lay in the frequency response. It is only in the spectra that the variations in response due to changes in layer thicknesses, fibre volume fraction and porosity can be observed.

The multi-layer composite laminate behaves towards ultrasound propagation as multiple resonators in series. For carbon-fibre composite the reflection coefficients are small because the transverse acoustic impedance of a carbon fibre is similar to the resin matrix. This means that multiple reflections are very much second- or higher-order effects, which do not result in much cross-talk between plies in the structure. However, glass fibres have a much higher stiffness than resin, resulting in much higher reflection coefficients, more cross-talk between plies, and smaller overall transmission through the structure. This latter effect is well-known in the NDT community but is commonly (and erroneously) thought to be the result of higher intrinsic absorption in glass-fibres, rather than stronger internal reflections.

Decomposing the ultrasonic response of the structure falls conveniently into two stages. Firstly, a porosity assessment can be applied because this is most likely to cause a structurally significant defect. Only if the porosity is less than the minimum reportable threshold is it important to move on to assess ply spacing or fibre volume fraction. Often it is the case that any zone in a structure is only susceptible to either porosity *or* ply spacing / fibre volume fraction, but rarely both. Having said this, it transpired during the project that the porosity assessment requires a knowledge of the local ply spacing and fibre volume fraction, so it may be that all parameters will need to be determined at every 3D voxel.

8.4.2 *Ply spacing and fibre volume fraction*

Ply spacing can be determined from a measurement of local resonant frequency, but if accompanied by a fibre volume fraction change, the resultant

variation in velocity will also contribute to the modification of the resonant frequency. In order to extract both ply spacing and fibre volume fraction from a single measurement of resonant frequency it is therefore necessary to make an assumption that links these two material properties. The chosen assumption was based on experience with viewing optical micrographs. It is that fibres rarely move laterally in a laminate enough to change the total number of fibres in the width of an ultrasound beam, even a focused beam. There may be a need to provide a correction for this assumption in radius regions for example. Using this assumption, which is in the process of being validated by quantitative assessment of many micrographs, it has been possible to derive analytical expressions for percentage variations in both ply spacing and fibre volume fraction in terms of resonant frequency changes. The propagation model has proved invaluable in this task, both for validation purposes and also as part of the algorithm to determine the baseline 'as designed' resonant frequencies.

Initial validation trials suggest that the algorithm works well for either single-ply changes or gradual variations in the structure, such as from ply wrinkling, but totally random fluctuations in ply spacing are more difficult to track. This limitation is thought to be due to the cross-talk between plies – effectively the overlap of ring-down resonances in adjacent plies. A programme is just starting using multi-dimensional optimisation methods combined with the propagation model to better track random fluctuations in ply spacing.

8.4.3 Porosity and thick resin layers

Two methods were tested for quantifying local 3D porosity. The first is based on measuring the backscattered energy from the voids and assumes a monotonic relationship between the backscattered energy and the void volume fraction. According to the literature, combination of the received signal with its Hilbert Transform to form a complex analytic signal, and then using the modulus of this signal, should result in a good measure of backscattered energy. This method was implemented but unfortunately there were two problems: 1) other sources of backscattered energy such as normal ply interfaces or enhanced reflections from thick resin layers, and 2) the interference effect between multiple

scatterers (Pinfield et al, 2010) resulting in a reduction in backscattered energy from multiple porous plies (thick porous layers).

The second method was aimed primarily at differentiating between porosity and thick resin layers, both of which give a strong amplitude response but differ in the frequency domain. Thickening of a single resin layer merely increases the amplitude of the reflection at that interface so the spectral response does not change shape or phase, just amplitude. In contrast, a small amount of porosity in a carbon-fibre ply is sufficient to lower the effective acoustic impedance below that of resin, changing the sign of the reflection coefficients and converting a half-wave resonance into a quarter-wave resonance for the porous ply. Thus, all the single-ply resonant frequencies increase as the porosity level increases, until they reach the frequencies of the previous minima (anti-resonances) for 5% porosity or more. The assumption in this analysis is that porosity is confined to a single ply and is homogeneously, but randomly distributed in that ply.

In order to decompose the single-ply frequency response at each volume element into contributions from 1) a normal ply, 2) a thick resin layer, 3) porosity and 4) noise, four basis-function spectra are generated using the model and singular value decomposition (SVD) is used to determine the coefficients of each basis function contributing to the measured response. This frequency-domain decomposition method was refined by testing using model-simulated waveforms with different kinds of defects. It is necessary to apply the incident spectrum to each basis function and adaptively modify the porosity basis function in order to accurately measure porosities of less than 10%. Depth dependence can be corrected for by using a different incident spectrum for each depth, calculated using the model in transmission-coefficient mode. Using simulated waveforms the decomposition method was shown to exhibit minimal cross-talk between the porosity and thick-resin coefficients, successfully differentiating between the two defect types and quantifying them up to 80% porosity or 50 μm resin layers.

During further testing it was found that if the porosity basis function is created using the model for a single porous ply between adjacent non-porous plies, then

it becomes insensitive to multiple porous plies, only detecting the first and last porous ply. This was confirmed using Micro-CT X-ray analysis of a real porosity specimen. Such a basis function results in a differential porosity coefficient, which is only sensitive to increases or decreases in porosity. The next and ongoing stage of this research is to generate a basis function that can differentiate between increases and decreases in porosity levels. Such a coefficient could be plotted as a function of depth in the structure and integrated to determine absolute local porosity levels.

Calibration of the output coefficients from the decomposition will be required before the method can be implemented and the first stage of this will be an assessment of what material and inspection parameters the calibration is dependent on. This work has been started and is ongoing.

8.5 3D fibre orientation in composites

8.5.1 Ply stacking sequence

At the start of this project the author had previously established that ply stacking sequence can be determined by producing amplitude C-scans at each depth in the structure (for each time in the waveform) and imaging the variations due to fibre tows (bundles of fibres as laid down in the ply). The actual mechanism for seeing these fibre tows in C-scans is that the primary reflector – the resin inter-ply layer – varies in reflection coefficient as a function of resin-layer thickness, which in turn varies following an undulating pattern dictated by the original fibre tows in the ply. It is thought that the undulations from both interfaces adjacent to a ply constructively interfere, giving a strong impression in the C-scan from the fibre-tow direction of that ply.

This original ply stacking-sequence method (Smith and Clarke, 1994) was enhanced during the current project using the 2D-FFT method of Hsu et al (2002). Following numerous improvements, an automated method has been developed for determining the ply stacking sequence from a full-waveform scan and presenting this in a form that is understood by structures and design engineers, without the need for NDT interpretation. The technique has been

shown to work down to at least 15 mm depth when plies are 0.25 mm in thickness, and deeper for thicker plies. An accuracy assessment has shown that $\pm 0.25^\circ$ accuracy is possible provided at least 100 x 100 pixels are present in each C-scan and this contains at least 20 fibre tows.

Despite some of the principles behind this tool being in the public domain, no actual implementation of a ply stacking-sequence tool is known to the author.

8.5.2 *In-plane waviness*

An extension to the above stacking sequence method involves using a smaller sample region on each C-scan, determining the dominant fibre direction and plotting its measured value as a function of location of the sample region in the C-scan. The output is a 3D profile of in-plane fibre angle, which is sensitive to, and can map, in-plane fibre waviness.

An accuracy assessment has shown that the smaller sample region results in a reduced angular accuracy compared with the ply stacking-sequence method. The region cannot be increased in size beyond a quarter of a wavelength of the waviness without causing an unacceptable underestimate in angular deviation. However, the accuracy can be recovered if a finer-pitch scan is performed in the wavy-fibre region. Ongoing work is investigating whether improved accuracy can be achieved through better signal processing or image processing alone.

Another issue with 3D in-plane waviness mapping is that any out-of-plane wrinkling or variation in ply thickness can cause bleed-through to a particular depth from adjacent plies, resulting in a confusing map of fibre angles at that depth. Future work will include pre-processing the data for out-of-plane wrinkling to determine the surface profile of each ply and then tracking the ply through the structure to generate an in-plane C-scan of a single ply without any bleed-through from adjacent plies.

8.5.3 *Out-of-plane wrinkling*

Finally, the same processing for local orientation can be applied to B-scan cross-sections in order to determine ply angles and map out-of-plane wrinkling. This is a more complicated analysis because the pixels no longer have a unity

aspect ratio. Again the accuracy suffers if the box width has a reduced number of pixels but this can be partially recovered with a finer-pitch original scan.

The initial output of this method is two 3D profiles of ply angle in two perpendicular orientations – sufficient information from which most other parameters can be calculated. Further processing can determine the maximum ply inclination at each 3D location and from this data a quantitative evaluation and comparison with acceptance criteria can be made.

The last processing stage is a 2D integration of each in-plane slice through the ply-angle data, generating the surface profile of each ply in the laminate. This is useful for visualisation of any wrinkles and presentation to structural and design engineers who need to decide whether the wrinkle can be allowed to remain in the structure or needs to be repaired.

The ability to pull out of the ultrasonic data the actual profile of a wrinkled ply at any depth has been acknowledged as a significant and unique advance in the NDT of composites. As a result, the author's employer has been included in numerous programmes to pursue the quality control of ply wrinkling, allowing the potential removal of weight from structures where thicknesses have been increased to mitigate risk due to the an inability to quantify ply wrinkling.

8.6 Benefits

3D characterisation of the inner quality of composite laminates offers considerable benefits to the aerospace industry as it moves towards high volume production of wide-body civil aircraft from composite materials. This benefit is partly medium-term in quality control and better-informed disposition of manufacturing defects. But the main benefit will be in the long-term, once the new ability to determine 3D distributions of porosity and other defects is realised by composites designers and 3D acceptance criteria can be built into their designs. This then offers the potential for weight reductions, opening up the design space and allowing a full realisation of the potential of composite structures.

New European targets for CO₂ emissions from aircraft require a reduction of 50% by 2020, equating to a 50% reduction in fuel usage. This will primarily be achieved through structural weight savings, although aerodynamics and engine efficiency will also play a part. It is hard to see how these savings in weight will be possible without a step change in the design philosophy and 3D acceptance criteria for composites is just such a step change. At present the structural models used in the design process are not able to deal with 3D acceptance criteria, and the mechanical test programmes have not been carried out, but in the long term there is a great opportunity offered by 3D characterisation of composites.

8.7 Recommendations for future work

In each of the tools developed for this project there is a future work plan, either for validation or for further development followed by validation. For fibre-resin effects the ply spacing measurement needs to be extended to use multi-dimensional optimisation. The frequency-domain decomposition method needs a modified porosity basis function that can respond differently to the increase or decrease in porosity level.

The three tools for fibre orientation measurement (ply stacking sequence, in-plane waviness and out-of-plane wrinkling) have been combined into an application called StackScan™, which is based on the ANDSCAN® libraries developed in this project. Various composite manufacturers and end-users of composites are starting programmes to evaluate StackScan on real components on the production line or in-service for repairs. The future route for these three tools includes: more versatile automation of ply stacking sequence generation, improvement in the angular accuracy of waviness and wrinkling measurements, and the pre-processing of C-scans for in-plane waviness using the ply-wrinkling information.

Various other techniques such as the polar-backscattering technique of Blodgett et al (1986) and Yuhas et al (1986) deserve revisiting using full matrix capture with arrays.

8.8 Final Conclusions

An ultrasonic three-dimensional characterisation toolset has been developed for determining the inner quality of composite laminates, incorporating six output parameters that have never been assessed quantitatively in this way before. These six parameters are actual material properties, not NDT parameters, and can be understood without the need of NDT interpretation. They are: ply spacing, fibre volume fraction, porosity, ply stacking sequence, in-plane fibre waviness and out-of-plane ply wrinkling. To a large extent the generation of these parameters has been automated and validation has commenced with simulated data. Quantitative comparisons with acceptance criteria can be performed using these output parameters, and visualisation methods have been developed to help explain the results to structures or design engineers. However, further refinement is still required, particularly for the 3D porosity parameter, where a new basis function for the decomposition must be developed as well as a calibration strategy.

By the end of this project in 2009 there had been no other reported work in the literature attempting to compete with the approaches described herein to achieve the same objectives. This does not rule out other undisclosed work, but the two patent applications made by QinetiQ in October 2008 have not so far resulted in the discovery of competing work, or prompted a challenge to the originality of this work.

REFERENCES

- Achenbach & Hermann, 1968 J D Achenbach and G Hermann, "Dispersion of free harmonic waves in fiber-reinforced composites," *AIAA Journal*, Vol 6, No 10, pp 1832-1836, 1968.
- Adams & Cawley 1988 R D Adams and P Cawley, "A review of defect types and non-destructive testing techniques for composites and bonded joints," *NDT International*, Vol 21, pp 208-222, 1988.
- Adler et al 1986 L Adler, J H Rose and C Mobley, "Ultrasonic method to determine gas porosity in aluminum alloy castings. Theory and experiment." *J. Applied Phys.*, Vol 59, pp 336-347, 1986.
- Aduda & Rawlings 1990 Aduda and R D Rawlings, *Proc. VII CIMTEC*, Montecatini, Italy, Elsevier, 1990.
- Allegra & Hawley 1972 J R Allegra and S A Hawley, "Attenuation of sound in suspensions and emulsions: theory and experiments." *J. Acoust. Soc. Am.*, Vol 51, pp 1545-1564, 1972.
- Allen et al 1986 A J Allen, C F Coleman, and F A Smith, "A feasibility study on the non-destructive determination of the moisture content of aerospace fibre-resin composites from positron annihilation lifetime measurements", *Harwell Lab. Report No. AERE G 3837*, March 1986.
- Anderson & deLacy 1972 R T Anderson and T J deLacy, "Nondestructive testing of advanced composites." *Met. Prog.*, Vol 102, pp 88-92, 1972.

- Ashton et al 1969 J E Ashton, J C Halpin and P H Petit, *Primer on Composite Materials: Analysis*, Technomic, Stamford, Conn., Chapter 5, p 77, 1969.
- ASM Handbook ASM Handbook, Vol 17 "Non-destructive Inspection and Quality Control", Ultrasonic Inspection Chapter, pp 231-277.
- Attenborough & Walker 1972 K Attenborough and L A Walker, *J. Acoust. Soc. Am.*, Vol 51, p 192, 1972.
- Azzi & Tsai 1965a V D Azzi and S W Tsai, "Elastic moduli of laminated anisotropic composites – Experimental programme," *Exp. Mechanics*, Vol 5, No. 6, pp 177-185, 1965.
- Azzi & Tsai 1965b V D Azzi and S W Tsai, "Anisotropic strength of composites," *Experimental Mechanics*, Vol 5, No 9, pp 283-288, 1965.
- Bach et al 2002 M Bach, L-K Shark, B J Matuszewski, S P Platt, and J P Smith, "Inspection of carbon fibre composite aircraft components using acoustographic system," *Proc NDT2002, Annual Conf of the British Institute of NDT*, Southport, pp 113-118, September 2002.
- Bacon 1982 D R Bacon, "Characteristics of a PVDF membrane hydrophone for use in the range 1-100 MHz," *IEEE Transactions on Sonics and Ultrasonics*, Vol SU-29, No 1, pp 18-25, 1982.
- Bar-Cohen & Crane 1982 Y Bar-Cohen and R L Crane, "Acoustic-back-scattering Imaging of sub-critical flaws in composites", *Mat. Eval.*, Vol 40, pp 970-975, 1982.

- Bartels et al 1998 R H Bartels; J C Beatty and B A Barsky, "Bézier Curves." Ch. 10 in *An Introduction to Splines for Use in Computer Graphics and Geometric Modelling*. San Francisco, CA: Morgan Kaufmann, pp 211-245, 1998
- Bartle 1983 P M Bartle, "Acoustic pulsing - A condition monitoring technique developed at the Welding Institute," *The Welding Institute Research Report No. 227/1983*, December 1983.
- Behrens 1967a E Behrens, "Elastic constants of filamentary composites with rectangular symmetry," *J. Acoust. Soc. Am.*, Vol 42, pp 367-377, 1967.
- Behrens 1967b E Behrens, "Sound propagation in lamellar composite materials and averaged elastic constants," *J. Acoust. Soc. Am.*, Vol 42, pp 378-383, 1967.
- Behrens 1969a E Behrens, "Elastic constants of composite materials," *J. Acoust. Soc. Am.*, Vol 45, pp 102-108, 1969.
- Behrens 1969b E Behrens, "Elastic constants of filamentary composites with hexagonal symmetry," *J. Acoust. Soc. Am.*, Vol. 45, pp.1567-1570, 1969.
- Behrens 1971 E Behrens, "Elastic constants of fiber-reinforced composites with transversely isotropic constituents," *ASME J. Appl. Mech.*, Vol. 38, pp. 1062-1065, 1971.
- Berens 2001 A P Berens, "What Metric Should be Used to Measure Intrinsic Capability? Is it only Probability of Detection and False Call Probability, or is it Theoretical?" *Mat. Eval.*, Vol 59, pp 42-48, 2001.

- Beltzer & Brauner 1984 A I Beltzer and N Brauner, "Waves of an arbitrary frequency in random fibrous composites," *J. Acoust. Soc. Am.*, Vol 76, No 3, pp. 962-963, 1984.
- Bergquist 1978 B D Bergquist, "An electronic speckle pattern interferometer for the examination of surface areas of up to 1.0m diameter," *University of Loughborough - Final Report of MOD contract A93b/197*, April 1978.
- Birt 1998 E A Birt, "Damage detection in carbon-fibre composite using ultrasonic Lamb waves," *Insight - The Journal of The British Institute of NDT*, Vol 40, No 5, pp 335-339, May 1998.
- Birt & Smith 2004 E A Birt and R A Smith, "A review of NDE methods for porosity measurement in fibre-reinforced polymer composites," *Insight - The Journal of The British Institute of NDT*, Vol 46, No 11, pp 681-686, 2004.
- Birt et al, 2004 E A Birt, R A Smith, C B Scruby and L D Jones, "Improved Ultrasonic Spectroscopy Procedure for Roughness Measurement of Hidden Corroded Surfaces". *Insight – J. British Institute of NDT*, Vol 46, No 3, pp 151-156, March 2004.
- Bishop & McLaughlin 1979 S M Bishop, and K S McLaughlin, "Thickness effects and fracture mechanisms in notched carbon-fibre composites," *RAE Technical Report No. TR 79051*, November 1979.
- Blodgett et al 1986 E D Blodgett, L J Thomas III and J G Miller, "Effects of porosity on polar backscatter from fibre reinforced composites," *Rev. Prog. in QNDE*, Ed. D O Thompson & D E Chimenti, Vol 5B, pp 1267-1274, 1986.

- Bodner and Lifshitz 1967 S R Bodner and J M Lifshitz, "Experimental Investigations on the Dynamic Strength of Composites," *Proc. Intern. Conf. Mech. Composite Materials*, 1967.
- Bond-Thorley et al 2000 A Bond-Thorley, H Wang, and J S Sandhu, "Application of acoustography for the ultrasonic NDE of aerospace composites," *NDE of Aging materials and Composites IV*, Editors: G Y Baaklini, C A Lebowitz, E S Boltz, *Proc. SPIE*, Vol. 3993, Paper 3993-06, 2000.
- Brant 1984 C P Brant, "Development of ultrasonic spectroscopy for the characterisation of carbon fibre composites," *British Aerospace Technical Report*, Nov. 1984.
- Briggs et al 1993 G A D Briggs, C W Lawrence, and C B Scruby, "Acoustic microscopy of ceramic-fibre composites," *J Microscopy* Vol 169, pp 139-153, 1993.
- Broughton & Sims 1996a W R Broughton, and G D Sims, "Review of Procedures for Ultrasonic C-Scan Inspection of Polymer Matrix Composites - Part 1: Industrial Practices and Requirements," *NPL Report CMMT(C)5*, 1996.
- Broughton & Sims 1996b W R Broughton, and G D Sims, "Review of Procedures for Ultrasonic C-Scan Inspection of Polymer Matrix Composites - Part 2: Operational Procedures," *NPL Report CMMT(C)6*, 1996.
- Broughton et al 1998 W R Broughton et al "Overview of DTI-funded programme on 'Standardised procedures for ultrasonic inspection of polymer matrix composites,'" *Insight - Journal of the British Institute of NDT*, Vol 40, No 1, pp 8-11 & 27, 1998.

- Broughton et al 1999 W R Broughton, M J Lodeiro, G D Sims, B Zeqiri, M Hodnett, R A Smith and L D Jones, "Standardised procedures for ultrasonic inspection of polymer matrix composites," *Proc 12th International Conference on Composite Materials (ICCM-12)*, Paris. Paper 1030, April 1999.
- BSI 1999a "Ultrasonic C-scan inspection of composite structures. Part 1. Operational Procedures," *Draft Standard, BSI Reference: 99/701577*, 1999.
- BSI 1999b "Ultrasonic C-scan inspection of composite structures. Part 2. Transducer calibration procedure," *Draft Standard, BSI Reference: 99/701578*, 1999.
- BSI 1999c "Ultrasonic C-scan inspection of composite structures. Part 3. Preparation of reference defects and reference panels," *Draft Standard, BSI Reference: 99/701579*, 1999.
- Buoncristiani & Smith 1985 Buoncristiani, A M and Smith, B T, "Backscatter of acoustic signals from inhomogeneities in composites," *Proc. 1985 Ultrasonics Symposium*, pp. 1068-1071, 1985.
- Burchett 1972 O J Burchett, "Analysis techniques for the inspection of structures by holographic interferometry." *Materials Evaluation*, Vol 30, pp 25-30, 1972.
- Buttle & Scruby 1988 D J Buttle, and C B Scruby, "Acoustic Characterisation of an aluminium silicon carbide metal matrix composite", *Harwell Laboratory Report No. AERE R 13273*, October 1988.

- Buttle & Scruby 1989 D J Buttle, and C B Scruby, "Acoustic Emission Source Location in Fibre Reinforced Plastic Composites," *J. Ac. Emission*, Vol 7, p 211, 1989.
- Castaings & Hosten 1993 M Castaings and B Hosten, "Transmission coefficient of multilayered absorbing anisotropic media. A solution to the numerical limitations of the Thomson-Haskell method. Application to composite materials." *Proc. Ultrasonics International 93*, 1993.
- Castaings & Hosten 1994 M Castaings and B Hosten, "Delta operator technique to improve the Thomson-Haskell method stability for propagation in multilayered anisotropic absorbing plates." *J. Acoust. Soc. Am.*, April 1994.
- Cawley 1985 P Cawley, "The operation of impedance instruments based on the impedance method," *J. Composite Structures*, Vol 3, pp 215-228, 1985.
- Cawley 1987 P Cawley, "The Sensitivity of the Mechanical Impedance Method of Non-Destructive Testing," *NDT International*, Vol 20, pp 209-215, 1987.
- Cawley 1989 P Cawley, "The Sensitivity of an NDT Instrument Based on the Membrane Resonance Method," *NDT International*, Vol 22, pp 209-216, 1989.
- Cawley 1990 P Cawley, "The detection of delaminations using flexural waves," *NDT International*, Vol 23, pp 207-213, 1990.
- Cawley 1994 P Cawley, "The rapid nondestructive inspection of large composite structures," *Composites*, Vol 25, pp 351-357, 1994.

- Cawley & Adams 1988 P Cawley and R D Adams, "The Mechanics of the Coin-Tap Method of Non-Destructive Testing," *J. Sound and Vibration*, Vol 122, pp 299-316, 1988.
- Cawley & Adams 1989 P Cawley and R D Adams, "The Sensitivity of the Coin-Tap Method of Non-Destructive Testing," *Materials Evaluation*, Vol 47, pp 558-563, 1989.
- Cawley et al 1985 P Cawley, A M Woolfrey and R D Adams, "Natural frequency measurements for production quality control of fibre composites," *Composites*, Vol 16, pp 23-27, 1985.
- Challis & Kitney 1991 R E Challis and R I Kitney, "Biomedical signal processing (in four parts). Part 2. The frequency transforms and their inter-relationships," *Medical and Biological Engineering and Computing*, Vol 29, pp 1-17, Jan 1991.
- Challis et al 1998a R E Challis, J S Tebbutt and A K Holmes, "Equivalence between three scattering formulations for ultrasonic wave propagation in particulate mixtures." *J Phys D: Appl. Phys.*, Vol 31, pp 3481-3497, 1998.
- Challis et al 1998b R E Challis, A K Holmes, J S Tebbutt and R P Cocker, "Scattering of ultrasonic compression waves by particulate fillers in a cured epoxy continuum." *J. Acoust. Soc. Am.*, Vol 103, pp. 1413-1420, 1998.
- Chen et al 2001 A S Chen, D P Almond, and B Harris, "Measurement Acoustography as a means of monitoring damage in composites during fatigue loading," *Science and Technology*, Vol. 12, 2001, pp. 151-156.

- Chao & Chaturvedi 1997 C-P Chao and S K Chaturvedi, "A thermo-micromechanical theory for effective elastic constants of composite materials," *J. Reinforced Plastics and Composites*, Vol. 16, pp. 392-413, 1997.
- Chubb & Abbiss 1973 T W Chubb and J B Abbiss, "Particle size measurement by in-line holography," *RAE Technical Report No. TR 72229*, March 1973.
- Compton 1971 R Compton, "An inspection system for the non-destructive testing of composites." *Composites*, Vol 2, pp 152-153, 1971.
- Connolly 1992 M P Connolly, "The measurement of porosity in composite materials using infrared thermography," *J of Reinforced Plastics and Composites*, 11, pp. 1367-1375, December 1992.
- Connor 1988 P J Connor, "The feasibility of detecting impact damage in carbon-fibre laminates using EMAT's", *TI Research Report No. SLS42B/396 - K2855/CLS*, February 1988.
- Connor 2005 A J Connor, "Automated Analysis and Sentencing of Large Area Ultrasonic Data – Final Report," *QinetiQ Technical Report No. QINETIQ/FST/STT/CR050363/1.0*, February 2005.
- Datta et al 1984 S K Datta, H.M. Ledbetter and R.D. Kritz, "Calculated elastic constants of composites containing anisotropic fibres," *Int. J. Solids & Structures*, Vol 20, pp 429-438, 1984.
- Davis 1979 M C Davis, *J. Acoust. Soc. Am.*, Vol 65, p 387, 1979.

- Degrieck et al 2003 J Degrieck, N F Declercq and O Leroy, "Ultrasonic polar scans as a possible means of non-destructive testing and characterisation of composite plates," *INSIGHT*, Vol 45, pp 196-201, March 2003.
- deLacy 1982 T J deLacy, "Nondestructive testing to study stress-relaxation in advanced composites for telecommunications satellites." *SAMPE Journal*, Vol 18, pp 8-15, 1982.
- Deng et al 2002 W Deng, B J Matuszewski, L-K Shark, J P Smith, A Ciliberto, and G Cavaccini, "CAD based simulation and visualisation for non-destructive testing," *Proc NDT2002, Annual Conf of the British Institute of NDT*, Southport, September 2002, pp. 119-124.
- Dingwall 1973 P F Dingwall, "Transducers for the detection of stress wave emission," *RAE Technical Memo Structures 829*, February 1973.
- Dingwall & Mead 1974 P F Dingwall, and D M Mead, "The testing of carbon fibre reinforced plastic missile fins using acoustic emission," *RAE Tech. Memo: Structures 845*, June 1974.
- Dominguez & Mascarot 2006 N Dominguez and B Mascarot, "Ultrasonic non-destructive inspection of localised porosity in composite materials," *Proc. European Conf. on NDT – ECNDT-2006*, Berlin, Paper Tu.2.1.4, Oct 2006.
- Dreumel & Speijer 1983 W H M van Dreumel and J L Speijer, "Polar-scan, A non-destructive test method for the inspection of layer orientation and stacking order in advanced fiber composites," *Materials Evaluation*, Vol 41, pp 1060-1062, 1983.

- Dunkin 1965 J W Dunkin, "Computation of modal solutions in layered elastic media at high frequencies." *Bull. Seism. Soc. Am.*, Vol 55, pp 335-358, 1965.
- Epstein 1941 P S Epstein, in *Contributions to Applied Mechanics, Theodore Von Karman Anniversary Volume* (California Inst of Technology, Pasadena), pp 162-168, 1941.
- Epstein & Carhart 1953 P S Epstein and R R Carhart, "The absorption of sound in suspensions and emulsions. I. Water fog in air." *J. Acoust. Soc. Am.*, Vol 25, pp 553-65, 1953.
- Eshelby 1957 J D Eshelby, "The xetermination of the elastic field of an ellipsoidal inclusion and related problems," *Proc. Roy. Soc., Series A*, Vol 241, pp 376-396, 1957.
- Ewins & Ham 1973 P D Ewins and A C Ham, "The nature of compressive failure in unidirectional carbon fibre reinforced plastics," *RAE Technical Report No. TR 73057*, August 1973.
- Faran 1951 J J Faran, "Sound scattering by solid cylinders and spheres," *J. Acoust. Soc. Am.*, Vol 23, pp 405-418, 1951.
- Flax & Dragonette 1978 L Flax and L R Dragonette, "Theory of elastic resonance excitation by sound scattering," *J. Acoust. Soc. Am.*, Vol 63, No 3, pp 723-731, 1978.
- Freemantle 1995 R J Freemantle, "Ultrasonic compression wave evaluation of adhered metal sheets and thin sheet materials," *PhD Thesis*, Ultrasonics and Digital Signal Processing Laboratory, Dept of Physics, Keele University, 1995.

- Frisch & Simha 1956 H I Frisch and R Simha, "The viscosity of colloidal suspensions and macro-molecular solutions," Chapter 14 in *Rheology*, Ed. F.R. Eirich, Vol. 1, Academic Press, New York, 1956.
- Gabor 1946 D Gabor, "Theory of Communication." *J. Inst Electrical Engrs.* Vol 93, pp 429–457, 1946.
- Gammell 1981 P M Gammell, "Improved ultrasonic detection using the analytic signal magnitude" *Ultrasonics*, Vol 19 (2), pp 73-76, 1981.
- Garrett 1983 R A Garrett, AGARD-CP-355, "Effects of defects on aircraft composite structures," pp 19-1 - 19-34, 1983.
- Gassert 1983 H-J Gassert, "New System-185 B-scanner for resin bonded carbon fibre composite testing," *Sonarnews*, No 3, p 3, March 1983.
- Gaunaurd & Überall 1983 G C Gaunaurd and H Überall, "Resonance effects and the ultrasonic effective properties of particulate composites," *J. Acoust. Soc. Am.*, Vol 74 No 1, pp 305-313, 1983.
- Gray et al 1995 S Gray, S Ganchev, N Qaddoumi, G Beauregard, D Radford and R Zoughi, " Porosity level estimation in polymer composites using microwaves," *Materials Evaluation*, Vol 53, No 3, pp 404-408, 1995.
- Green 1974 G A Green, "An acoustic emission transducer having a selectable resonant frequency," *AML Memorandum ME 156/74*, August 1974.
- Green et al 2004 G A Green, P Campbell and R Zoughi, "An investigation into the potential of microwave NDE for maritime applications," *16th World Conference on NDT – WCNDT 2004*, Montreal, Canada, 2004.

- Green & Lane 1978 G A Green and G Lane, "Acoustic emission attenuation and velocity measurements on the surface of a Hercules wing section," *Admiralty Marine Technology Establishment Technical Memo No. AMTE(M) TM 78110*, June 1978.
- Green et al 1979 G A Green, M Phillips and J Taylor, "An automated system for the capture and analysis of acoustic emission events," *Admiralty Marine Technology Est. Tech. Memo No. AMTE(M) TM 79112*, Oct. 1979.
- Greszczuk, 1966 L B Greszczuk, "Theoretical and experimental studies on properties and behaviour of filamentary composites," Douglas paper 3550, Feb 1966, Santa Monica, Calif. Also: *Proc. 21st Annual Conf. Society of the Plastics Industry, Chicago, Illinois, 1966*.
- Greszczuk 1971 L B Greszczuk, "Interfiber Stresses in Filimentary Composites", *J. AIAA*. Vol 9. pp 1274-1284, 1971.
- Grolemund & Tsai 1998 D Grolemund and C S Tsai, "Statistical moments of backscattered ultrasound in porous fibre reinforced composites," *IEEE Trans on Ultrasonics, ferroelectrics and frequency control*, Vol 45, No 2, pp 295-304, 1998.
- Gubernatis & Domany 1984 J E Gubernatis and E Domany, in *Review of Progress in Quantitative NDE – July 1983*, Vol 2A, p 833, and *Wave Motion*, Vol 6, p 579, 1984.
- Guo & Cawley 1993 N Guo and P Cawley, "The interaction of Lamb waves with delaminations in composite laminates," *J. Acoust. Soc. Am.*, Vol 94, pp 2240-2246, 1993.

- Guo & Cawley 1994a N Guo and P Cawley, "Lamb wave reflection for the quick NDE of large composite laminates," *Materials Evaluation*, Vol 52, pp 404-411, 1994.
- Guo & Cawley 1994b N Guo and P Cawley, "The non-destructive assessment of porosity in composite repairs," *Composites*, Vol. 25, pp 842-850, 1994.
- Habeger 1982 C C Habeger, "The attenuation of ultrasound in dilute polymeric fiber suspensions," *J. Acoust. Soc. Am.*, Vol 72, No 3, pp 870-878, 1982.
- Hagemaiier et al 1970 D J Hagemaiier, H J McFaul and J T Parks, "Non-destructive testing techniques for fiberglass, graphite fiber and boron fiber composite aircraft structures." *Materials Evaluation*, Vol 28, pp 194-204, 1970.
- Hagemaiier & Fassbender 1979 D J Hagemaiier and R H Fassbender, "Nondestructive testing of advanced composites," *Materials Evaluation*, June 1979, pp. 43-49.
- Hale & Ashton 1988 J M Hale and J N Ashton, "Ultrasonic attenuation in voided fibre-reinforced plastics," *NDT International*, Vol 21, pp 321-326, 1988.
- Hall 1985 R F C Hall, "Investigation into the attenuation and velocity of acoustic emissions in carbon fibre composite aircraft structures," *British Aerospace PLC Report No. Bae-KGT-R-Gen-01349*, Sept. 1985.
- Halpin 1992 J C Halpin, *Primer on composite materials analysis - Second edition, Revised*, Technomic Publ. Co. Inc., Lancaster, Penn., USA, ISBN 0-87762-754-1, Chapter 6, pp 153-191, 1992.

- Hashin 1958 Z Hashin, "The moduli of an elastic solid containing spherical particles of another elastic material," *Proc. IUTAM Symposium on non-homogeneity in elasticity and plasticity*, Warsaw, Poland, No 17, 1958, Pergamon Press, New York, pp 463-478, 1959.
- Hashin 1962 Z Hashin, "The elastic moduli of heterogeneous materials," *J. Appl. Mech.*, Vol 29, pp 143-150, 1962.
- Hashin 1964 Z Hashin, "Theory of mechanical behavior of heterogeneous media," *Appl. Mech. Rev.*, Jan 1964.
- Hashin 1965 Z Hashin, "On elastic behaviour of fiber reinforced materials of arbitrary transverse phase geometry," *J. Mech. Phys. Solids*, Vol 13, pp 119-134, 1965.
- Hashin 1970 Z Hashin, "Theory of fiber reinforced materials," NASA Langley Res. Center, Hampton, Virginia, 1970
- Hashin 1979 Z Hashin, "Analysis of properties of fiber composites with anisotropic constituents," *J. Appl. Mech.*, Vol 46, pp 546–550, 1979.
- Hashin 1983 Z Hashin, "Analysis of composite materials – A survey," *J. Appl. Mech.*, Vol 50, pp 481-505, 1983.
- Hashin & Rosen 1964 Z Hashin and B W Rosen, "The elastic moduli of fiber reinforced materials," *J Appl. Mech.*, Vol 31, Ser. E, pp 223-232, 1964.
- Haskell 1953 N A Haskell, "Dispersion of surface waves on multilayered media." *Bull. Seism. Soc. Am.*, Vol 43, pp 17-34, 1953.
- Heyser 1971 R C Heyser, "Determination of Loudspeaker Signal Arrival Times: Part III." *J. Audio Eng. Soc.*, Vol 19, pp 902–905, 1971.

- Hill 1964a R Hill, "Theory of mechanical properties of fibre-strengthened materials: I. Elastic behaviour," *J. Mech. Phys. Solids*, Vol 12, pp 199-212, 1964.
- Hill 1964b R Hill, "Theory of mechanical properties of fibre-strengthened materials: II. Inelastic behaviour," *J. Mech. Phys. Solids*, Vol 12, pp 213-218, 1964.
- Hill 1965a R Hill, "Theory of mechanical properties of fibre-strengthened materials: III. Self-consistent model," *J. Mech. Phys. Solids*, Vol 13, pp 189-198, 1965.
- Hill 1965b R Hill, "A self-consistent mechanics of composite materials," *J. Mech. Phys. Solids*, Vol 13, pp 213-222, 1965.
- Hobbs et al 1991 C P Hobbs, D Kenway-Jackson and J M Milne, "Quantitative measurement of thermal parameters over large areas using pulse video thermography," *Proc SPIE*, Vol 1467, Thermosense XIII, pp 264-277, 1991.
- Hobbs & Temple 1993 C P Hobbs and A Temple, "The inspection of aerospace structures using transient thermography", *Brit J NDT*, Vol 35, 1993, pp 183-189.
- Hobbs et al 1994 C P Hobbs, D Kenway-Jackson and M D Judd, "The application of transient thermography for the nondestructive testing and evaluation of aerospace materials," *Proc Int Symp Advanced Materials for Lightweight Structures '94*, Noordwijk, Netherlands, ESA WPP-070, 1994, pp 645-653.

- Hosten & Castaings 1993 B Hosten and M Castaings, "Transfer matrix of multilayered absorbing and anisotropic media. Measurements and simulations of ultrasonic wave propagation through composite materials." *J. Acoust. Soc. Am.*, Vol 94, pp 1488-1495, 1993.
- Hsu et al 2002 D Hsu, D Fei and Z Liu, "Ultrasonically mapping the ply layup of composite laminates," *Materials Evaluation*, Vol 60, No 9, pp 1099-1106, 2002.
- Hsu & Nair 1987 D K Hsu and S M Nair, "Evaluation of porosity in graphite epoxy composite by frequency dependence of ultrasonic attenuation," *Review of Progress in QNDE*, Edited by D O Thompson and D E Chimenti, Vol 6B, pp 1185-1193, 1987.
- Jemison et al 1988 S M Jemison, E A Culpan and J Taylor, "Preliminary investigation into the use of acoustic emission techniques on three-point bend tests on aluminium metal matrix composites," *Admiralty Research Establishment Engineering Note No. ARE DN (UMM) 88401*, March 1988.
- Jemison & Culpan 1989 S M Jemison, and E A Culpan, "Evaluation of brazed aluminium metal matrix composite samples using X-ray and ultrasonic techniques," *Admiralty Research Establishment ARA DN (UMM) 89401*, March 1989.
- Jemison et al 1993 S M Jemison, G A Green and E A Culpan, "Investigation of non destructive evaluation techniques for aluminium metal matrix composite materials," *Defence Research Agency Technical Memorandum No. DRA TM (AWMC) 93424*, September 1993.

- Jeong & Hsu 1995 H Jeong and D K Hsu, "Experimental analysis of porosity-induced ultrasonic attenuation and velocity change in carbon composites," *Ultrasonics*, Vol 33, No 3, pp 195-203, 1995.
- Jones 1998 R M Jones, *Mechanics of composite materials*, Routledge ISBN: 156032712X, 1998.
- Jones & Stone 1976 B R Jones and D E W Stone, "Towards an ultrasonic attenuation technique to measure void content in carbon-fibre composites," *Non-destructive Testing*, pp 71-79, April 1976.
- Jones et al 1998 L D Jones, D A Bruce, and R A Smith, "Ultrasonic inspection of next-generation carbon-fibre composite materials," *Proceedings of NDT '98, The British Institute of NDT*, pp 50-53, 1998.
- Judd & Wright 1978 N C W Judd and W W Wright, "Voids and their effects on the mechanical properties of composites – an appraisal," *SAMPE Journal*, pp 10-14, Jan. 1978.
- Kantor & Bergman 1982 Y Kantor and D J Bergman, "Elastostatic resonances - a new approach to the calculation of the effective elastic constants of composites," *J. Mech. Phys. Solids*, Vol 30, pp 355-376, 1982.
- Kite et al 2008 A H Kite, D K Hsu and D J Barnard, "Determination of porosity content in composites by micrograph image processing," *Review of Progress in Quantitative Nondestructive Evaluation – July 2007*, Vol 27, pp 942-949. 2008.

- Knollman et al 1978 G C Knollman, D Carver and J J Hartog, "Acoustic imaging of composites - the ultrasonic test that requires no interpretation." *Materials Evaluation*, Vol 36, pp 41-47, 1978.
- Knopoff, 1964 Knopoff L, "A matrix method for elastic wave problems," *J. Bull. Seism. Soc. Am.*, Vol 54, pp 431-438, 1964.
- Kollgaard et al 2008 J R Kollgaard, C A Decker, T L Aljundi, D K Hsu and D Barnard. "Approaches to porosity assessment in composites", *Review of Progress in Quantitative Nondestructive Evaluation – July 2007*, Vol 27, pp 934-941, 2008.
- Krautkramer & Krautkramer 1969 J Krautkramer and H Krautkramer, *Ultrasonic Testing of Materials*, Springer-Verlag, 1969.
- Lado and Torquato 1986 F Lado and S Torquato, "Effective properties of two-phase disordered composite Media. I. Simplification of bounds on the conductivity and bulk modulus of dispersions of impenetrable spheres," *Phys. Rev. B*, Vol 33, pp 3370-3378, 1986.
- Lamb 1945 H. Lamb, *Hydrodynamics* (Dover, New York), 6th Edn., 1945.
- Lane 1988 G J Lane, "Eddy current non destructive examination of metal matrix composite sample discs, plate and torpedo nose cone," *Admiralty Research Establishment Engineering Note No. ARE DN (UMM) 88402*, June 1988.

- Lawrence et al 1993a C W Lawrence, G A D Briggs and C B Scruby, "Acoustic microscopy of ceramic-fibre composites: I Glass matrix composites," *J. Mats. Sci.*, Vol 28, pp 3635-3644, 1993.
- Lawrence et al 1993b C W Lawrence, G A D Briggs and C B Scruby, "Acoustic microscopy of ceramic-fibre composites: II Glass-ceramic matrix composites," *J. Mats. Sci.*, Vol 28, 1993, pp 3645-3652.
- Lawrence et al 1993c C W Lawrence, G A D Briggs and C B Scruby, "Acoustic microscopy of ceramic-fibre composites: III Metal matrix composites," *J. Mats. Sci.*, Vol 28, pp 3653-3660, 1993.
- Lines 1998 D I A Lines, "Rapid inspection using integrated ultrasonic arrays," *INSIGHT – J. British Inst. NDT*, Vol 40, No 8, pp 573-577, 1998.
- Lines et al 1999 D I A Lines, K R Dickson, G Filippi and T Moir, "A real-time image acquisition and processing system for ultrasonic arrays in NDT," *Proceedings of NDT'99, The British Institute of NDT* (ISBN 0 903132 27 3), pp 11-17, 1999.
- Lines et al 2003 D I A Lines, R A Smith, D Edgar, J M Bending and L D Jones, "Rapid, low-cost, full-waveform mapping and analysis using ultrasonic phased arrays," *Proceedings of NDT2003, 42nd Annual Conference of the British Institute of NDT*, 2003.
- Lloyd & Wright 1986 P A Lloyd and M A Wright, "An introduction investigation into the performance of an Ultrasonic Imaging System," *RAE Technical Report No. TR 86063*, October 1986.

- Lloyd 1989 P A Lloyd, "Ultrasonic system for imaging delaminations in composite materials," *Ultrasonics*, Vol 27, January 1989.
- Lorraine et al, 2003 P W Lorraine, M Dubois, R J Filkins and B Venchiarutti, "System and method for detecting defects in a manufactured object," Patent Publicn. No. WO 03/067245 A1, 2003.
- Lowe 1995 M J S Lowe, "Matrix techniques for modelling ultrasonic waves in multilayered media." *IEEE Trans. Ultrasonics, Ferroelectrics and Frequency Control*, Vol UFFC-42, No 4, pp 525-542, July 1995.
- Maigret & Jube 1971 J P Maigret and G Jube, "Advanced NDT methods for filament wound pressure vessels and composites in general." *Proc. Materials '71, SAMPE, 16th Nat. Symp. and Exhib.*, pp 123-137, 1971.
- Marchant 1974 M J N Marchant, "Holographic interferometry of CFRP honeycomb panels," *RAE Technical Report No. TR 73192*, March 1974.
- Marchant 1978 M J N Marchant, "Holographic interferometry of CFRP wing tips," *RAE Technical Report No. TR 78105*, August 1978.
- Marchant & Snell 1981 M J Marchant and M B Snell, "Determination of the flexural stiffness of thin plates from small deflection measurements using optical holography. Part 1," *RAE Technical Report No. TR 81083*, July 1981.
- Markham 1969 M F Markham, *Proc. Ultrasonics for Industry 1969*, p1, Iliffe Science and Technology Pub. Ltd, 1969.

- Martin 1976 B G Martin, "Ultrasonic attenuation due to voids in fibre-reinforced plastics," *NDT International*, Vol 9, pp 242-246, 1976.
- Martin 1977 B G Martin, "Ultrasonic wave propagation in fibre-reinforced solids containing voids," *J. Appl. Phys.*, Vol 48, pp 3368-3373, 1977.
- Matuszewski et al 2000 B J Matuszewski, J P Smith, L-K Shark and M R Varley, "Automatic mosaicing with error equalisation of non-destructive testing images for aerospace industry inspection," *Proc 15th World Conference on Non-Destructive Testing*, Rome, Italy, October 2000.
- Matuszewski et al 2001 B J Matuszewski, J P Smith, L-K Shark and M R Varley, "Sparse image mosaic construction for radiographic inspection of large structures," *Proc NDT2001, Annual Conf of the British Institute of NDT*, Coventry, pp 221-226, September 2001.
- Matuszewski et al 2002 B J Matuszewski, L-K Shark, A Ciliberto and G Cavaccini, "Large size image mosaic construction for ultrasonic inspection of primary aircraft structures," *Proc NDT2002, Annual Conf of the British Institute of NDT*, Southport, pp 99-104, September 2002.
- Mienczakowski et al 2008 M J Mienczakowski, A K Holmes and R E Challis, "Modelling of ultrasonic wave propagation in composite airframe components." *Review of Progress in QNDE., AIP Conf. Proc.*, Vol 975, pp 995-1001, 2008.
- Milne & Reynolds 1985 J M Milne and W M Reynolds, "Applications of thermal pulses and infrared thermal imagers for observing sub-surface structures in metals and composites," *Proc SPIE*, Vol 590, pp 293-297, 1985.

- Morse 1948 P M Morse "Vibration and Sound" McGraw-Hill Book Company, New York, 2nd Edition, 1948.
- Mummery et al 1991 P A Mummery, B Derby, D J Buttle and C B Scruby, "Micromechanisms of fracture in particle-reinforced metal matrix composites: acoustic emission and modulus rejection." *Proc Euromat 91*, Cambridge, UK, July 1991.
- Mummery et al 1993 P A Mummery, B Derby and C B Scruby, "Acoustic emission from particulate metal matrix composites," *Acta Metal & Mater*, Vol 41, pp 1431-1445, 1993.
- Nagy & Rose 1993 P B Nagy and J H Rose, "Surface Roughness and the ultrasonic detection of subsurface scatterers." *J Appl Physics*, Vol 72, No 2, pp 566-580, 1993.
- Nayfeh & Chimenti 1991 A H Nayfeh and D E Chimenti, "Elastic wave propagation in fluid-loaded multiaxial anisotropic media." *J. Acoust. Soc. Am.*, Vol 89, pp 542-549, 1991.
- Nelson et al 2006 L J Nelson, R P Dalton, E A Birt, L D Jones and R A Smith, "A new low-frequency vibration technique for blind-side inspections," *Insight - J. British Institute of NDT*, Vol 48, No 3, pp 149-154, 2006.
- Nevadunsky et al (1975) J J Nevadunsky, J J Lucas and M J Salkind, "Early fatigue damage detection in composites." *J. Composite Materials*, Vol 9, pp 394-408, 1975.
- Nurse 2000 A D Nurse, J M Huntley, J N Petzing, D C Panni, P.J. Sherratt and J R Tyrer, "Developments in inverse analysis for in-situ flaw detection in composite material structures," *Proc 13th European Conf on Fracture (ECF13), Fracture Mechanics: Applications and Challenges*, San Sebastian, Spain, Sept. 2000.

- O'Donnell et al 1978 M O'Donnell, E T Jaynes and J G Miller, "General relationships between ultrasonic attenuation and dispersion," *J Acoust. Soc. Am.*, Vol 63, pp. 1935-1937, 1978.
- O'Neil 1949 H T O'Neil, "Theory of focusing radiators." *J. Acoust. Soc. Am.*, Vol 21, pp 516-526, 1949.
- Oppenheim & Schafer 1975 Oppenheim, A V and Schafer, R W, "Digital Signal Processing," Prentice Hall, New Jersey, 1975.
- Owston 1976 Owston, C N, "Eddy-current methods for the examination of carbon fibre reinforced epoxy resins," *Materials Evaluation*, Vol 34, pp 237-250, 1976.
- Panametrics 1993 "Ultrasonic Transducers for non-destructive testing", Panametrics, 1993, or "Ultrasonic Transducers Technical Notes", Olympus NDT, 2006.
- Percival & Birt 1997 W J Percival and E A Birt, "A study of Lamb wave propagation in carbon-fibre composites," *Insight - Journal of the British Institute of NDT*, Vol 39, pp 728-735, 1997.
- Petzing et al 2002 J N Petzing, W S Wan Abdullah and J R Tyrer, "Investigating Error Sources in Shearography and their Influence on Non-Destructive Testing," *Proc. BSSM International Conference on Advances in Experimental Mechanics, Stratford-upon-Avon, UK*, ISBN 0-94825605-2, pp 45-48, 2002.
- Phang 2006 A P Y Phang, "An integrated ultrasonic correlation spectrometer." PhD thesis, School of Electrical and Electronic Eng., University of Nottingham, UK, 2006.

- Pialucha 1992 T P Pialucha, "The reflection coefficient from interface layers in NDT of adhesive joints." PhD Thesis, Mech. Eng. Dept., Imp. Coll., London, 1992.
- Pinfield et al 2010 V Pinfield, R E Challis, A Holmes, R A Smith and M.J. Mienczakowski, "Reflected and backscattered signal from a porous layer in solid matrix," submitted to *J Acoust Soc Am.*, 2010.
- Powell 1988 S E A Powell, "Report on the development of the EMI CT5005 X-ray body scanner for WHL use," *Westland Helicopters Ltd Report No. LR 88062*, Feb. 1988.
- Prakash & Owston 1976 R Prakash and C N Owston, "Eddy-current method for the determination of lay-up order in cross-plyed CFRP laminates," *Composites*, Vol 7, No 2, 88-92, April 1976.
- Prakash & Owston 1977 R Prakash, and C N Owston, "Ultrasonic determination of lay-up order in cross-plyed CFRP," *Composites*, Vol 8, 100-102, 1977.
- Press et al, 2002 Press, W H, Teukolsky, S A, Vetterling, W T, and Flannery, B P, "Numerical Recipes in C++. The art of scientific computing." Cambridge Univ. Press, 2002.
- Quek & Almond 2005 S Quek and D P Almond, "Defect detection capability of pulsed transient thermography," *Insight – J. British Institute of NDT*, Vol 47, pp 212-215, 2005.
- Rayleigh 1896 J W Strutt (Baron Rayleigh), "The Theory of Sound" McMillan, London, 1896 ; reprinted by Dover Publications, New York, 1945.
- Reiner 1958 M Reiner, "Rheology," in *Encyclopedia of Physics*, Ed. S. Flugge, Vol 6, "Elasticity and Plasticity," Springer Verlag, Berlin, Germany, pp 522-534, 1958.

- Reynolds 1974 W N Reynolds, "Ultrasonic and dynamical testing of resins and composites." *Proc. Carbon Fibres – 2nd Intl. Conf.*, 1974.
- Reynolds 1985 W N Reynolds, "Quality control of composite materials by thermography," *Metals and Materials*, Vol 1, No 2, pp 100-102, February 1985.
- Reynolds & Wilkinson 1978 W N Reynolds and S J Wilkinson, "The analysis of fibre-reinforced porous composite materials by the measurement of ultrasonic wave velocities," *Ultrasonics*, Vol 16, pp 159-163, 1978.
- Richardson et al 2000 M O Richardson, Z Y Zhang and J R Tyrer, "Evaluation of Progressive Damage Development under Flexural Loading of Pultruded GRP Composites using Electronic Speckle Pattern Interferometry (ESPI)," *ECCM 9 - European Conference on Composite Materials, ECCM*, Brighton, pp 48-58, June 2000.
- Rokhlin & Wang 2002a S I Rokhlin and L Wang, "Stable recursive algorithm for elastic wave propagation in layered anisotropic media:Stiffness matrix method." *J. Acoust. Soc. Am.*, Vol. 112, pp 822-834, 2002.
- Rokhlin & Wang 2002b S I Rokhlin and L Wang, "Ultrasonic waves in layered anisotropic media: characterization of multidirectional composites." *Int. J. Solids. & Structures*, Vol. 39, pp. 5529-5545, 2002.
- Rose et al 1973 J L Rose, J M Carson and D J Liedel, "Ultrasonic procedures for inspecting composite tubes." *ASTM Special Technical Pub. 521*, pp 311-325, 1973.

- Sanders 1973 M C Sanders, "Detection of sub-surface faults in CFRP panels using holographic interferometry," *Internal RAE Memo*, August 1973.
- Schneider 1964 M H Schneider, "Experimental determination of the elastic constants for fibreglass laminates," Douglas Aircraft Company Inc., (Internal Technical memorandum), 1964.
- Schultz and Tsai 1968 A B Schultz and S W Tsai, "Dynamic moduli and damping ratios in fiber-reinforced composites," *J. Composite Materials*, Vol. 2, p. 368, 1968.
- Sewell 1910 C T J Sewell, *Phil Trans Soc* (London), Vol A210, p 239, 1910.
- Shark et al 2001 L-K Shark, B J Matuszewski, J P Smith and M R Varley, "Automatic feature-based fusion of ultrasonic, radiographic and shearographic images for aerospace non-destructive testing," *Insight - Journal of the British Institute of NDT*, Vol 43, No 9, pp 607-615, 2001.
- Shaw & Fenwick 2003 Shaw, B. and Fenwick, A.J. "Scattering from anisotropic structures - selection of materials" QinetiQ Working Paper: QinetiQ/FST/WP023330, Nov 2003.
- Sheldon 1978 W H Sheldon, "Comparative evaluation of potential NDE techniques for inspection of advanced composite structures." *Materials Evaluation*, Vol 36, pp 41-46, 1978.
- Skelton & James 1992 E A Skelton and J H James, "Acoustics of anisotropic planar layered media." *J. Sound & Vib.*, Vol 152, pp 157-174, 1992.

- B T Smith 1990 B T Smith, "Ultrasonic characterisation of porosity in composites," *Review of Prog. in Quantitative Non-destructive Evaluation*, Vol 9, pp 1535-1540, 1990.
- B T Smith & Buoncristiani 1986 B T Smith and A M Buoncristiani, "Digital signal processing methods for ultrasonic backscattered waves in composite materials," *Proc. 1986 Ultrasonics Symposium*, pp 1041-1046, 1986.
- B T Smith et al 1986 B T Smith, J S Heyman, J G Moore, S J Cucura and S M Freeman, *Review of Prog. in Quantitative Non-destructive Evaluation*, Vol 6B, pp 1239-1244, 1986.
- Smith 1994 R A Smith, "Ultrasonic defect sizing in carbon-fibre composites - an initial study," *Insight - Journal of the British Institute of NDT*, Vol 36, pp 595-605, 1994.
- Smith 1995a R A Smith "Evaluation and accuracy assessment of ANDSCAN - a non-destructive portable scanner, Part 1. ANDSCAN hardware and software," *Insight – J. British Inst. of NDT*, Vol 37, pp 284-289, 1995.
- Smith 1995b R A Smith, "Evaluation and accuracy assessment of ANDSCAN - a non-destructive portable scanner, Part 2. NDT applications and specialised features; accuracy and repeatability," *Insight – J. British Inst. of NDT*, Vol 37, No 5, pp 352-357, 1995
- Smith 1996 R A Smith, "Full ultrasonic waveform capture for in-service inspection using ANDSCAN," *DRA Tech. Report DRA/SMC/TR962009*, DRA Farnborough, UK, 1996.

- Smith 2004 R A Smith, "Advanced Ultrasound Waveform Analysis Package For Manufacturing And In-Service Use", *Proc. World Conf on NDT*, Montreal, August 2004, Paper WP46.
- Smith, 2005 R A Smith, "Composite Material Properties for measurement and Mapping – LOCOCAM 3.2/1", *QinetiQ Customer Report No. QinetiQ/D&TS/Air/CR0510692/1.1*, December 2005.
- Smith, 2006 R A Smith, "Initial Strategy for isolation of CFRP parameters – LOCOCAM 3.2/2a&3a", *QinetiQ Customer Report No. QINETIQ/D&TS/AIR/CR0510289*, February 2006.
- Smith & Bruce, 2001 R A Smith and D A Bruce, "Pulsed ultrasonic spectroscopy for roughness measurement of hidden corroded surfaces." *Insight - The Journal of The British Institute of NDT*, Vol 43, pp 168-172, 2001.
- Smith & Clarke 1994 R A Smith and B Clarke, "Ultrasonic C-scan determination of ply stacking sequence in carbon-fibre composites," *Insight - Journal of the British Institute of NDT*, Vol. 36, No. 10, pp. 741-747, 1994.
- Smith & Jones 1992 R A Smith and L D Jones, "The development and evaluation of ANDSCAN - a non-destructive portable scanner", *Defence Research Agency Technical Report No. TR 92070*, December 1992.
- Smith & Willsher 1998 R A Smith and S J Willsher, "Multi-element ultrasonic transducers for rapid lap-joint inspection," *Proc. NDT '98, British Inst. of NDT*, pp 87-90, 1998.

- Smith & Hugo 2001 R A Smith and G R Hugo, "Transient eddy current NDE for ageing aircraft - capabilities and limitations." *INSIGHT – J. Brit. Inst. NDT*, Vol 43, pp 14-25, 2001.
- Smith et al 1997 R A Smith, A B Marriott and L D Jones, "Delamination sizing in fibre-reinforced plastics using pulse-echo amplitude," *Insight - Journal of the British Institute of NDT*, Vol 39, No 5, pp 330-336, 1997.
- Smith et al 1998a R A Smith, L D Jones, B Zeqiri and M Hodnett, "Ultrasonic C-scan standardisation for fibre-reinforced polymer composites - minimising the uncertainties in attenuation measurements," *Insight – J. British Institute of NDT*, Vol 40, pp 34-43, 1998.
- Smith et al 1998b R A Smith, B Zeqiri, L D Jones and M Hodnett, "Nonlinear propagation in water and its effect on ultrasonic C-scanning," *Insight - Journal of the British Institute of NDT*, Vol 40, No 1, pp 12-19, 1998.
- Smith et al 1998c R A Smith, L D Jones, S J Willsher and A B Marriott, "Diffraction and shadowing errors in -6 dB defect sizing of delaminations in composites," *Insight – J. British Inst. NDT*, Vol 40, pp 44-49, 1998.
- Smith et al 1998d R A Smith, D A Bruce, L D Jones, A B Marriott, L P Scudder and S J Willsher, "Ultrasonic C-scan standardization for polymer-matrix composites - Acoustic considerations," *Review of Progress in Quantitative Non-destructive Evaluation*, Ed. D O Thompson & D E Chimenti, Plenum Press, New York, Vol. 17B, pp. 2037-2044, 1998.

- Smith et al 1999a R A Smith, S J Willsher and J M Bending, "Linear array systems for aerospace NDT," *Proc. 9th Int. Symp. on the Nondestructive Characterisation of Materials*, Sydney, pp. 502-509, June 1999.
- Smith et al 1999b R A Smith, L D Jones, B Zeqiri and M Hodnett, "Nonlinear propagation in water and its effect on NDT," *Proc. 9th International Symposium on the Nondestructive Characterisation of Materials*, Sydney, pp. 522-527, June 1999.
- Smith et al 2003a R A Smith, J M Bending, L D Jones, T R C Jarman and D I A Lines, 'Rapid Ultrasonic Inspection of Ageing Aircraft', *INSIGHT – J British Inst NDT*, Vol 45, pp 174-177, 2003.
- Smith et al 2006 R A Smith, I Pettigrew and K J Kirk, "High Frequency Ultrasonic NDE of Titanium Metal Matrix Composites," *Review of Prog. in Quantitative Non-destructive Evaluation*, Vol 25, pp 1035-1042, 2006.
- R E Smith 1972 R E Smith, "Ultrasonic elastic constants of carbon fibres and their composites." *J. Appl. Phys.*, Vol 43, No 6, pp 2555-2561, 1972.
- Snell 1979 M B Snell, "Initial buckling performance of some CFRP structures and the validity of classical plate theory predictions," *RAE Technical Report No. TR 79128*, October 1979.
- Spencer 2001 F W Spencer, "Estimating Probability of Detection Curves from Regression Data." *Materials Evaluation*, Vol 59, pp 866-870, 2001.

- Stone 1974 D E W Stone, "Some problems in the non-destructive testing of carbon-fibre-reinforced plastics." *Proc. Carbon Fibres – 2nd Intl. Conf.*, 1974.
- Stone & Clarke 1974 D E W Stone and B Clarke, "Non-destructive determination of the void content in carbon fibre reinforced plastics by measurement of ultrasonic attenuation," *RAE Technical Report No. TR 74162*, December 1974.
- Stone & Clarke 1975 D E W Stone and B Clarke, "Ultrasonic attenuation as a measure of void content in carbon-fibre reinforced plastics," *Non-Destructive Testing*, June 1975, pp 137-145.
- Sturgeon 1978 J B sturgeon, "Fatigue mechanisms, characterisation of defects and their detection in reinforced plastics materials." *British J. NDT*, Vol 20, pp 303-310, 1978.
- Summerscales 1990b J Summerscales (editor), "Non-destructive testing of fibre-reinforced plastics composites. Volume 2." Elsevier Applied Science, Barking, Essex, Chapter 6, pp 316-325, 1990.
- Thacker 1984 R I Thacker, "Defects, damage and repairs to carbon fibre composites - final NDT progress report - phase 1," *British Aerospace Report No. MDR 0707*, 1984.
- Thomson 1950 W T Thomson, "Transmission of elastic waves through a stratified solid medium." *J. Appl. Phys.*, Vol 21, pp 89-93, 1950.
- Thompson 1950 W T Thompson, "Transmission of elastic waves through a stratified solid medium," *J. App. Phys.*, Vol 21, pp 89-93, 1950.

- Thompson & Rawlings 1991 I Thompson and R D Rawlings, "Monitoring thermal shock of alumina and zirconia-toughened alumina by acoustic techniques," *J. Mat. Sci.*, Vol 26, 1991, pp 4534-4540.
- Tsai 1962a S W Tsai, "A variational formulation of two-dimensional heterogeneous media," Aeronutronic Publication U-1698, 1962.
- Tsai 1962b S W Tsai, "Composite stiffness of fiber-reinforced media," Aeronutronic Publication U-1699, 1962.
- Tsai 1964 S W Tsai, "Structural behavior of composite materials," NASA Report CR-71, 1964.
- Tsai and Hahn 1980 S W Tsai and H T Hahn, "Introduction to composite material," Technomic Publishing Co. Inc., Lancaster PA, USA, 1980.
- Uhl et al 1988 K M Uhl, B Lucht, H Jeong and D K Hsu, "Mechanical strength degradation of graphite fibre reinforced thermoset composites due to porosity," Review of Prog. in QNDE, Edited by D O Thompson and D E Chimenti, Vol 7B, pp 1075-1082, 1988.
- UKAEA 1983 "Transient thermography using pulsed radiant energy source provides nondestructive testing technique for detecting internal defects in a body," UKAEA, *European Patent No 0-089-760-A*, Nov 1983.
- Urlick 1953 R J Urlick, *J. Acoust. Soc. Am.*, Vol 20, p 553, 1953.
- Wadsworth et al 1972 N J Wadsworth, B F Billing and M J N Marchant, "The measurement of local in-plane surface displacements using a Moire technique," *RAE Technical Report No. TR 72046*, April 1972.

- Wang & Rokhlin 2001 L Wang and S I Rokhlin, "Stable reformulation of transfer matrix method for wave propagation in layered anisotropic media." *Ultrasonics*, Vol 39, pp 413-421, 2001.
- Wang and Rokhlin, 2003 L Wang and S I Rokhlin, "Ultrasonic wave interaction with multidirectional composites: Modelling and experiment," *J. Acoust. Soc. Am.*, Vol 114, No 5, pp 2582-2595, 2003.
- Whitney and Riley, 1966 J M Whitney and M B Riley, "Elastic properties of fiber-reinforced composite materials," *AIAA Journal*, Vol 4, No 9, pp 1537-1542, 1966.
- Wilczynski & Klasztorny 2000 A P Wilczynski and M Klasztorny, "Determination of complex compliances of fibrous polymeric composites." *Journal of Composite Materials*, Vol 34, No 1, pp 2-26, 2000.
- Williams et al 1975 J H Williams, H Nayeb-Hashemi and S S Lee, "Ultrasonic attenuation and velocity in AS/3501-6 graphite fibre composite," *J of NDE*, Vol 1, No 2, pp 137-148, 1980.
- Willsher & Smith 1998a S J Willsher and R A Smith, "Rapid large-area composite scanning using ultrasonic arrays," *Proc. NDT '98, British Inst. of NDT*, pp 46-49, 1998.
- Willsher & Smith 1998b S J Willsher and R A Smith, "Multi-element ultrasonic scanning of in-service airframes," *Insight - Journal of the British Inst. of NDT*, Vol 40, pp 154-159, 1998.

- Worsdell 1982 A W Worsdell, "An investigation into the non-destructive testing of composite components by laser holographic interferometry," *Research & Technology Note No. 82043, Westland Helicopters Ltd, Yeovil, UK, October 1982.*
- Wright 1973 M P Wright, "In situ non-destructive testing of aircraft structures by holographic interferometry," *RAE Technical Report No. TR 72218, February 1973.*
- Ying & Truell 1956 C F Ying and R Truell, "Scattering of a plane longitudinal wave by a spherical obstacle in an isotropically elastic solid." *J Applied Phys, Vol 27, pp 1086-1097, 1956.*
- Yuhas et al 1986 D E Yuhas, C L Vorres and R Roberts, "Variation in ultrasonic backscatter attributed to porosity," *Review of Progress in QNDE, Edited by D O Thompson and D E Chimenti, Vol 5B, pp 1275-1284, 1986.*
- Zeqiri et al 1998 B Zeqiri, M Hodnett, R A Smith and L P Scudder, "An assessment of pulse-echo and hydrophone methods for characterising ultrasonic NDT transducers," *Insight - Journal of the British Institute of NDT, Vol 40, No 1, pp 20-27, 1998.*
- Zhang et al 1997a Z Y Zhang, M O Richardson and J R Tyrer, "Non-destructive Evaluation of Cracks in Pultruded GRP Composites by ESPI in Conjunction of Thermal Excitation," *Macro Group UK Spring Meeting, Leeds, pp 35-42, April 1997.*

- Zhang et al 1997b Z Y Zhang, M O Richardson and J R Tyrer, "Application of Phase Stepping ESPI to Non-destructive Testing of GRP Composite Materials," *International Conference of NDT in Civil Engineering*, Liverpool, pp 12-24, April 1997.
- Zhang et al 1997c Z Y Zhang, M O Richardson, M Wisheart, J R Tyrer, and J N Petzing, "Non-destructive testing of GRP composite materials containing impact damage by ESPI," *Proc. Inst. of Materials, CF715, 5th Int. Conf. on Automated Composites (ICAC '97)*, Glasgow, pp 395-405, 4th September 1997.
- Zimmer and Cost, 1970 J E Zimmer and J R Cost, "Determination of the elastic constants of a unidirectional fiber composite using ultrasonic velocity measurements," *J. Acoust. Soc. Am.*, Vol 47, No 3, pp 795-803, 1970.